



Efwita Astria, SPd MSi

Encapsulation of Carbohydrate-based Molecules in Metal-Azolate Frameworks

DOCTORAL THESIS

to achieve the university degree of
Doktorin der Naturwissenschaften

submitted to

Graz University of Technology

Supervisor

Univ.-Prof. Dott. mag. Dr., Paolo Falcaro
Institute of Physical and Theoretical Chemistry
Faculty of Technical Chemistry, Chemical and Process Engineering and Biotechnology

Graz, December 2020

AFFIDAVIT

I declare that I have authored this thesis independently, that I have not used other than the declared sources/resources, and that I have explicitly indicated all material which has been quoted either literally or by content from the sources used. The text document uploaded to TUGRAZonline is identical to the present doctoral thesis.

Date, Signature

Acknowledgments

I would like to thank the following people, without whom I would not have been able to complete this research, and without whom I would not have made it through my PhD degree.

First, I would like to express my sincere gratitude to my advisor Prof. Paolo Falcaro for his continuous support during my PhD, for his guidance, motivation, important discussion, immense knowledge and moral support. Importantly, I thank Prof. Paolo for the great opportunities he gave me to work in a nice working environment. I could not have imagined having a better advisor and mentor for my PhD research.

My sincere gratitude also goes to the great colleagues in our group: Raffaele Ricco, Francesco Carraro, Mercedes Linares, Lea Brandner, Peter Wied, Marcello Solomon, Tomas Kamencek, Samir El Hankari, Michael Hafner, Alice Zanini, and Carlos Carbonell, for fruitful discussion, for the help with the experiments, for their insightful comments, encouragements, and great working environment. I would like to offer my special thanks to Miriam Velasquez for the co-supervision and support that she provided me during my PhD.

Furthermore, I sincerely thank all the collaborators: Prof. Christian J. Doonan, Prof. Heinz Amenitsch, Weibin Liang, and everyone who was involved with my research regarding carbohydrate-based MOF biocomposites. I wholeheartedly thank Prof. Jeremiah J Gassensmith for accepting to take part in the panel of experts assessing my thesis. I am deeply grateful to Mag. Christina Düss for her assistance and supports regarding my scholarship program. I thank Hilde Freißmuth, Marion Hofmeister, Christian Holly, Philipp Frühwirt, and Max Schmallegger, for their help with experiments, lab equipment, organizational questions, computer issues, and administration information.

Finally, my biggest thanks to my family and friends for all the support you have shown me through this time, the culmination of three years of distance learning. I especially thank my mama and papa, Widya, Iqbal, Nia, Tika, Okta, Dini, and Rheza for supporting me spiritually throughout my PhD and my life in general.

Abstract

Recently, Metal-Organic Frameworks (MOFs) have been integrated with biomacromolecules to construct MOF-based biocomposites with functional properties. MOF matrices provide thermal and chemical protection to the biomacromolecules located within the MOF shell upon exposure to harsh conditions. Furthermore, the porous materials allow for the on-demand release of the cargo. Metal azolate frameworks (MAFs) are a subclass of MOFs comprised of metal ions interconnected by azolate ligands. With respect to biomedicine, MAFs have been investigated as carriers for several active pharmaceutical ingredients (APIs) ranging from small drugs to larger biomolecules. By using MAF-based composites as drug delivery systems (DDS) it is possible to improve the pharmacokinetics and bioavailability of the APIs. Recently, it has been demonstrated that some MAF-based biocomposites can be readily synthesized under aqueous conditions. This facile synthetic process, termed *biomimetic mineralization*, is a self-assembly process that yields the spontaneous encapsulation of negatively charged biomacromolecules. Among the negatively charged biotherapeutics, Glycosaminoglycans (GAGs) are an important class of drugs that typically require parenteral administration. This type of administration requires careful dose monitoring, as an excess of the drug could lead to bleeding complications due to the anticoagulant properties of some GAGs. These facts make desirable the development of novel platforms that enable customized drug release properties in accordance with the requirements of the disease to be treated. This doctoral thesis focused on the encapsulation of carbohydrate-based biomolecules into MAFs. In the first part of the present work, we studied the integration of different types of carbohydrates (e.g. CM-dextran and DEAE-dextran) within $\text{Zn}(\text{mIM})_2$ shells. This study highlights the role of the electrostatic interactions between the carbohydrate (CH) and Zn^{2+} cations for the successful encapsulation of the target molecule. In the second part of this project, we explored the encapsulation of GAGs, which are high molecular weight CHs. To this aim, we studied the encapsulation of heparin (HP), hyaluronic acid (HA), chondroitin sulfate (CS), dermatan sulfate (DS), HepSYL, and GM-1111 within three different MAFs (ZIF-8, ZIF-90, and MAF-7). The different properties in terms of crystallinity, particle size, and spatial localization of the biomolecules within the biocomposites lead to the difference in release kinetics and biopreservation properties. Motivated by the fact that the formation of different crystalline phases can be tuned by varying the concentration of MOFs precursors (Zn^{2+} , HmIM), in the third part of this work, we studied two different phase diagrams for the encapsulation of bovine serum albumin (BSA) in $\text{Zn}(\text{mIM})_2$. The resultant MOF biocomposites exhibit a wide variety of phases including the novel ZIF- CO_3 -1 (aka ZIF-C). The diverse phases showed significant differences in the encapsulation efficiency and release kinetics of encapsulated proteins.

Kurzfassung

Kürzlich wurden metallorganische Gerüste (Metal-Organic Frameworks, MOFs) mit Biomakromolekülen kombiniert, um MOF-basierte Biokomposite mit funktionellen Eigenschaften herzustellen. MOF-Matrizen bieten den in der MOF-Hülle befindlichen Biomakromolekülen thermischen und chemischen Schutz, wenn sie extremen Bedingungen ausgesetzt werden. Darüber hinaus ermöglichen die porösen Materialien die Freisetzung der Biomakromoleküle auf Abfrage. Metallazolatgerüste (MAFs) sind eine Unterklasse von MOFs, die aus Metallionen bestehen, die durch Azolatliganden miteinander verbunden sind. Im Hinblick auf die Biomedizin wurden MAFs als Träger für verschiedene pharmazeutische Wirkstoffe (APIs) untersucht, die von kleinen Arzneimitteln bis zu größeren Biomolekülen reichen. Durch die Verwendung MAF-basierter Komposite als Arzneimittelabgabesysteme (DDS) ist es möglich, die Pharmakokinetik und Bioverfügbarkeit der Wirkstoffe zu verbessern. Kürzlich wurde gezeigt, dass einige MAF-basierte Biokomposite unter wässrigen Bedingungen leicht synthetisiert werden können. Dieser einfache Syntheseprozess, der als *biomimetische Mineralisierung* bezeichnet wird, ist ein Selbstorganisationsprozess, der die spontane Einkapselung negativ geladener Biomakromoleküle ermöglicht. Unter den negativ geladenen Biotherapeutika sind Glykosaminoglykane (GAGs) eine wichtige Klasse von Arzneimitteln, die typischerweise eine parenterale Verabreichung erfordern. Diese Art der Verabreichung erfordert eine sorgfältige Dosisüberwachung, da ein Überschuss des Wirkstoffs aufgrund der gerinnungshemmenden Eigenschaften einiger GAGs zu Blutungskomplikationen führen kann. Dies macht die Entwicklung neuer Plattformen wünschenswert, die maßgeschneiderte Wirkstofffreisetzungseigenschaften gemäß den Anforderungen der zu behandelnden Krankheit ermöglichen. Diese Doktorarbeit befasste sich mit der Einkapselung von Biomolekülen auf Kohlenhydratbasis in MAFs. Im ersten Teil der vorliegenden Arbeit untersuchten wir die Integration verschiedener Arten von Kohlenhydraten (z.B. CM-Dextran und DEAE-Dextran) in $\text{Zn}(\text{mIM})_2$ -Schalen. Diese Studie hebt die Rolle der elektrostatischen Wechselwirkungen zwischen dem Kohlenhydrat (KH) und den Zn^{2+} -Kationen für die erfolgreiche Einkapselung des Zielmoleküls hervor. Im zweiten Teil dieses Projekts untersuchten wir die Einkapselung von GAGs, KH mit hohem Molekulargewicht. Zu diesem Zweck untersuchten wir die Einkapselung von Heparin (HP), Hyaluronsäure (HA), Chondroitinsulfat (CS), Dermatansulfat (DS), HepSYL und GM-1111 in drei verschiedenen MAFs (ZIF-8, ZIF-90 und MAF-7). Die unterschiedlichen Eigenschaften hinsichtlich Kristallinität, Partikelgröße und räumlicher Lokalisierung der Biomoleküle innerhalb der Biokomposite führen zu unterschiedlichen Freisetzungskinetiken und Biokonservierungseigenschaften. Motiviert durch die Tatsache, dass die Bildung

verschiedener kristalliner Phasen durch Variation der Konzentration von MOF-Vorstufen (Zn^{2+} , HmIM) eingestellt werden kann, untersuchten wir im dritten Teil dieser Arbeit zwei verschiedene Phasendiagramme für die Einkapselung von Rinderserumalbumin (BSA) in $\text{Zn}(\text{mIM})_2$. Die resultierenden MOF-Biokomposite wiesen eine Vielzahl von Phasen auf, einschließlich des neuen ZIF- CO_3 -1 (auch bekannt als ZIF-C). Die verschiedenen Phasen zeigten signifikante Unterschiede in der Einkapselungseffizienz und Freisetzungskinetik eingekapselter Proteine.

Abbreviation List

API, Active pharmaceutical Ingredient; ATP, Adenosine triphosphate; ATR, attenuated total reflectance; BSA, Bovine Serum Albumin; CAT, catalase; CH, Carbohydrate; CS, Chondroitin Sulfate; CM-dextran, Carboxymethyl-dextran; Cyt c, cytochrome C; CpG ODNs, cytosine-phosphate-guanine oligodeoxynucleotides; DDS, Drug delivery system; DCC, N,N'-dicyclohexylcarbodiimide; DEAE-dextran Diethylaminoethyl-dextran; DS, Dermatan sulfate; *dia*, diamondoid; EDC, 1-ethyl-3-(3-dimethylaminopropyl) carbodiimidehydrochloride; EDTA, ethylenediaminetetraacetic acid; FTIR, Fourier-transform Infrared spectroscopy; GAG, Glycosaminoglycan; GOx, glucose oxidase; HA, Hyaluronic acid; HP, Heparin; HmIM, 2-methyl-imidazole; HRP, horseradish peroxidase; HAS, human serum albumin, IR, Infrared: In, Insulin; *kat*, katesenite; LD50, median lethal dose; MOF, Metal-Organic Framework; NHS, N-hydroxysuccinimide OVA, Ovalbumin; PVP, Polyvinylpyrrolidone; PXRD, Powder X-ray diffraction; PG, proteoglycan; ROS, reactive oxygen species; SEM, Scanning Electron Microscopy; *sod*, sodalite; UV-vis, Ultraviolet-visible spectroscopy; WAXS, Wide-angle X-ray scattering; small-angle X-ray scattering (SAXS); ZIF, Zeolitic Imidazolate Framework; 2MtIMDC, 2-methyl-1H-imidazole-4,5-dicarboxylic acid.

Table of Contents

1. Introduction	1
1.1 Synthesis of MOF-based biocomposites	4
1.1.1 Biomacromolecule-on-MOF biocomposites	4
1.1.2 biomacromolecule@MOF composites	6
1.2 Main properties of MOF-based biocomposites	11
1.2.1 Biocompatibility of MOF-based biocomposites	11
1.2.2 Particle size of MOF-based biocomposites	12
1.2.3 Protection properties of MOF-based biocomposites	14
1.2.4 Release properties of MOF-based biocomposites	16
1.3 The application of MOFs as drug delivery systems	17
1.3.1 The application of MOFs as the carriers for Carbohydrate-based drugs	17
1.3.2 The application of MOFs as the carriers for Protein-based drugs	19
1.4 Methodology	21
1.4.1 Fourier-transform infrared spectroscopy (FTIR)	21
1.4.2 Powder X-ray diffraction (PXRD)	22
1.4.3 Scanning Electron Microscopy (SEM)	24
1.4.4 Ultraviolet-visible Spectroscopy (UV-vis)	24
2. Publications	27
2.1 Carbohydrates@MOFs	27
2.2 Modulation of metal-azolate frameworks for the tunable release of encapsulated glycosaminoglycans	101
2.3 Phase dependent encapsulation and release profile of ZIF-based biocomposites	143
2.4 Towards applications of bioentities@MOFs in biomedicine	179
3. Conclusion and Outlook	225
4. References	227
5. Appendix	234
5.1 List of Scientific Publications	234
5.2 List of Presentations at Scientific Conferences	235
5.3 Fundings and Awards	235

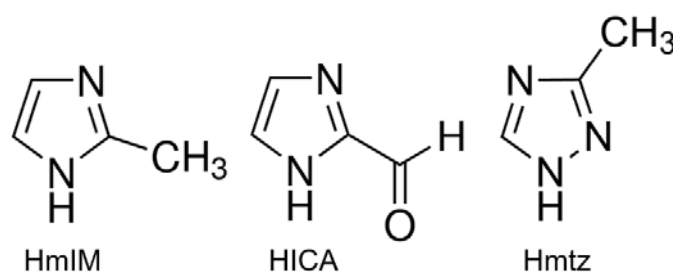
1. Introduction

Metal-Organic Frameworks (MOFs) are a class of porous crystalline materials constructed through the self-assembly of inorganic nodes (metal ions or clusters) interconnected by multitopic organic linkers.^[1,2] This bottom-up synthetic approach allows for tuning the properties of MOFs, including pore and particle size, surface area, and chemical functionality, by the judicious selection of the MOF molecular building blocks.^[2] These properties provide opportunities for different applications such as gas storage, catalysis, chemical sensing, and separation.^[3] More recently, progress has been made in the application of MOFs in different areas of biotechnology and biomedicine.^[4,5] This includes biosensing,^[6–8] biocatalysis,^[9] biospecimen preservation,^[10–13] and drug delivery.^[4,14] For the latter, MOFs that exhibit high surface area and large pore volume are particularly attractive as they can be loaded with a wide variety of APIs for their application as drug delivery systems (DDS).^[4] Pioneering studies by the Falcaro group and other groups have demonstrated that the use of MOFs can be further extended for the encapsulation of biomacromolecules including proteins,^[10,15,16] nucleic acids,^[17,18] viruses,^[12,13,19,20] and cells^[21,22] to synthesize MOF-based biocomposites.^[23–25] Moreover, the encapsulated species can be easily recovered via the MOF degradation by applying external stimuli, such as pH changes or by exposure to chelating species. The easy degradation of the MOF shells is particularly attractive for the design of stimuli-responsive drug delivery systems (DDS).^[26–28] Moreover, it has been shown that the integration of active pharmaceutical ingredients (APIs) within MOF materials allows overcoming some of the most common issues associated with the administration of free drugs.^[4] These include rapid biodegradation, systemic side effects, low specificity, poor solubility, and the inability of some biotherapeutics to cross cell membranes.^[4,29] Moreover, the integration of proteinaceous biotherapeutics into MOF matrices enhances their stability when subjected to hostile environments (e.g. temperature) during transport, handling, and storage that can compromise their potency.^[30]

Progress has been made for the integration of a wide variety of APIs, nevertheless, a reliable protocol for the encapsulation of high-molecular-weight and low-molecular-weight carbohydrates into MOFs was missing. Carbohydrates (CHs) are one of the four major classes of biomacromolecules together with proteins, lipids, and nucleic acids.^[31] Carbohydrates play a key role in different biological functions including cellular and intracellular interaction, bacterial adhesive, signalling molecules, and cell surface receptors.^[32] Hitherto, carbohydrate-based therapeutics have gained considerable attention for the treatment of cancer, diabetes, AIDS, influenza, rheumatoid arthritis, and bacterial infections.^[33–35] The successful integration

of carbohydrates into MOFs to yield carbohydrate@MOF composites could pave the way for the extended use of carbohydrate based-molecules in biotechnology and biomedicine.

Metal azolate frameworks (MAFs) are a subclass of MOFs that are promising for crystal engineering and material science because azolate ligands have strong and directional coordination ability in bridging metal ions.^[36,37] MAFs are constructed from azolate ligands which are the five-membered aromatic nitrogen heterocycles with two or more nitrogen atoms that can be deprotonated to form azolates anion such as imidazolate (im^-), 1,2,3-triazolate (vtz^-), 1,2,4-triazolate (tz^-), tetrazolate (ttz^-), and pyrazolate (pz^-).^[36,37] Basically, azoles have coordination behaviours because of the Sp^2 N donors. An azolium/azole/azolate ring comprising more N atoms has higher acidity or lower basicity since the N atom has an electron-withdrawing effect.^[36] For example, compared to pyridine, imidazole has higher acidity (easier to deprotonate); this can be ascribed to the higher electron density generated from six electrons which are delocalized on five atoms in imidazole. Conversely, tetrazole has an acidity like carboxylic acid, whereas other azoles are usually very weak acids. The basicity is the direct measurement of binding capability towards a proton and can be used to assess the bonding strength with transition metal ions, due to the relatively covalent coordination bonds in nature between a soft Lewis acid and base.^[36] MAFs have high thermal and chemical stability because deprotonation enables all N atoms to coordinate with the metal ions and enhances these donor's basicity.^[36,37]



Scheme 1. The selected example of azoles used in this research.

Zeolitic imidazolate frameworks (ZIFs) are one of the most important subclasses of porous MAFs with three-dimensional networks comprised of tetrahedral metal centers interconnected most typically with imidazolate ligands.^[38] In general, the topology of ZIFs is analogue to zeolites, and display permanent porosities and high thermal and chemical stability, which make them promising materials for several applications including gas separation and storage, catalysis, sensing, and drug delivery.^[38–40]

In terms of DDS, ZIFs have gained considerable attention as carriers for several drugs due to: a) ZIFs can be readily synthesized under mild conditions (aqueous media and room temperature)^[36,41]; b) ZIFs are stimuli-responsive MOFs: they can be easily degraded upon

applying external stimuli such as acidic pHs or chelating agents^[10,28,40] c) ZIFs have low cytotoxicity which is very important for the drug delivery system.^[4,42–44] One of the most widely used ZIFs is ZIF-8 (aka MAF-4) which is built from Zn²⁺ cations and 2-methylimidazole linkers (HmIM), see **Scheme 1**.^[36,45] ZIF-8 has been widely explored for encapsulation of biomolecules such as proteins, nucleic acids, viruses, and cells.^[10,15,17,19] ZIF-8, ZIF-90, and MAF-7 are isoreticular MAFs. All of them are Zn-based ZIFs with sodalite topology, however, they have different chemical properties.^[46–48] ZIF-8, ZIF-90, and MAF-7 crystallize in the same cubic crystal system in the noncentrosymmetric space group I-43m.^[48–50] ZIF-90 is constructed from Zn²⁺ and 2-imidazole carboxaldehyde (HICA) and MAF-7 is comprised of Zn²⁺ and 3-methyl-1,2,4- triazole (Hmtz), see **Scheme 1**.^[46,47,50] ZIF-90 and MAF-7 are more hydrophilic compared with ZIF-8.^[46,47] ZIF-90 has hydrophilic properties due to the aldehyde group, while MAF-7 presence uncoordinated triazolite N atoms on its pore surface.^[47,51]

This doctoral thesis describes the generalities of different protocols for the preparation MOF biocomposites, including (i) surface immobilization (adsorption and grafting), and (ii) encapsulation (infiltration and one-pot encapsulation). The one-pot encapsulation of carbohydrate- and protein-based biotherapeutics will be disclosed in detail. This includes the synthetic parameters that influence the mechanism of formation and the resultant properties of MOF-based biocomposites. Then, the salient properties of such biocomposites for biomedical applications (e.g. biocompatibility, particle size, protection, and drug release) will be examined.

1.1 Synthesis of MOF-based biocomposites

MOF-based biocomposites have been evolved towards several applications such as drug delivery, biosensing, biospecimen preservation, and cell and virus manipulation.^[23–25] Depending on the MOF biocomposite configuration, these materials can be classified into two main categories such as biomacromolecule-on-MOF and biomacromolecule@MOF^[24] (**Figure 1**). These systems are described in the following sections.

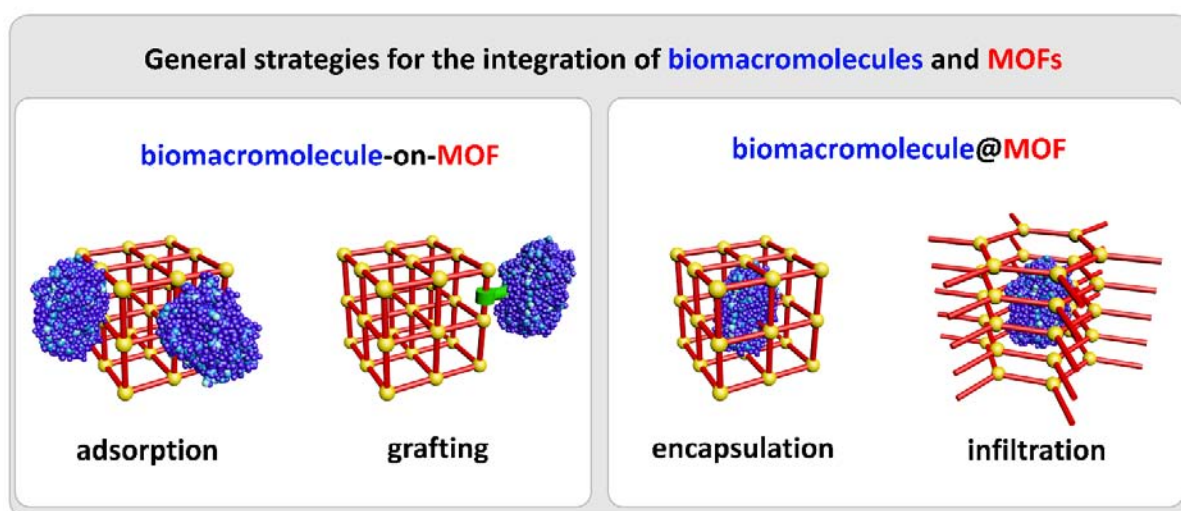


Figure 1. Schematic overview of the strategies for the preparation of MOF-based biocomposites.^[24]

1.1.1 Biomacromolecule-on-MOF biocomposites

Biomacromolecule-on-MOFs are composites in which the biomacromolecules are located on the surface of the MOF material. There are two general strategies to obtain biomacromolecule-on-MOF composites: a) adsorption and b) grafting. These two approaches are fully dependent on the immobilization strategies of biomacromolecules, but independent of the material porosity.^[23,24]

Adsorption is the process whereby the biomacromolecules are attached to the surface of the MOF particles via noncovalent interactions such as hydrophilic/hydrophobic interactions, hydrogen bonds, and electrostatic attractions.^[23,24] Experimentally, biomacromolecules are adsorbed on preformed MOF particles. Hydrophilic and hydrophobic interaction can assist the adsorption of biomacromolecules on MOFs. Particularly, it has been shown that proteins exhibit a high affinity for hydrophobic surfaces.^[52] However, strong interactions between the protein and the MOF surface can alter the structural conformation of the proteinaceous material.^[53] For instance, it has been demonstrated that catalase (CAT) adsorbed onto the surface of different MOFs exhibit different enzymatic activity for the dismutation of hydrogen

peroxide into water and oxygen depending on the hydro-philicity/phobicity of the MOF surface.^[54] The enzymatic activity was mainly retained when CAT was absorbed on hydrophilic zeolitic imidazolate frameworks (ZIFs), such as MAF-7, (obtained from Zn^{2+} and 3-methyl-1,2,4-triazolate), and ZIF-90 (obtained from Zn^{2+} and 2-imidazolecarboxaldehyde). Whereas the enzymatic activity of CAT on hydrophobic ZIF-8 (obtained from Zn^{2+} and 2-methyl-imidazole) was inhibited.^[54] Electrostatic interaction can also promote the adsorption of biomacromolecules. For example, MOFs with positively charged metal clusters can interact with negatively charged proteins.^[23] Furthermore, hydrogen-bonding interactions between functional groups from MOF ligands such as free carboxylic, amino, or imidazole with biomacromolecules can be used to favour the adsorption of biomacromolecules on MOF surfaces.^[23]

A distinct immobilization method for the preparation of biomacromolecule-on-MOF is grafting. This process involves the formation of covalent bonds between specific functional groups in the outer surface of the MOF and the target biomacromolecule.^[23–25] For example, the coupling reaction between 1-ethyl-3-(3-dimethylaminopropyl) carbodiimide hydrochloride/N-hydroxysuccinimide (EDC/NHS) or N,N'-dicyclohexylcarbodiimide (DCC) with the carboxylic or amino pendant groups in MOFs.^[55] This grafting approach has been employed for the immobilization of proteins,^[56] cells,^[57] nucleic acid,^[56] and carbohydrates on MOFs.^[58,59]

The main advantages of grafting and adsorption methods are: 1) a large number of MOFs with diverse and tunable surface chemistry are available;^[23,24,60] 2) several protocols available for adsorption and grafting strategies are accessible;^[24,55,60] 3) the post-synthetic modification is a straightforward method to integrate different functional groups on the MOF surface;^[23,24,60] 4) the bioconjugation of biomacromolecules onto the MOF surface can be conducted in biocompatible environments (aqueous or buffer solutions).^[24,61] To date, grafting and adsorption methods have been used to synthesize biocomposites for different applications including biosensing,^[62] biocatalysts,^[63–65] and the preparation of DDS.^[24,66,67] For MOF-based DDS, it has been reported that these methods could improve relevant properties of the drug carrier such as biocompatibility, colloidal stability, cellular uptake, and blood circulation time.^[67–70]

1.1.2 biomacromolecule@MOF composites

Biomacromolecule@MOFs are composites in which the biomacromolecule is incorporated within a MOF shell.^[24] Biomacromolecules@MOFs can be prepared following two approaches: 1) infiltration or 2) *one-pot* encapsulation.^[23,24]

1.1.2.1 Infiltration method

The infiltration method is performed by adding the biomacromolecule to preformed MOF crystals. The integration of biomacromolecules within the pore network of the material occurs via diffusion.^[23,24] The insertion of biomacromolecules into the MOF pores depends on 1) the equilibrium of the adsorption-desorption process, which is affected by electrostatic and hydrophobic/hydrophilic interaction between biomacromolecules and the MOF pore surface, and the particles size; 2) the pore size of the guest material with respect to the size of biomacromolecules.^[23,24] In fact, the latter represents the main limitation of this approach, as the integration of biomacromolecules requires a network with a pore window suitable for high molecular weight molecules.^[23,24] Accordingly, for the infiltration of macromolecules, it is required the use of mesoporous MOFs, which limits the number of possible MOF candidates.^[23,24] For instance, it has been demonstrated that the *Aspergillus saitoi* (2.85 nm) can be infiltrated into the mesoporous cavity of MIL-101-(Al)-NH₂ (up to 3.6 nm).^[71] Other potential limitations of the infiltration method are related to the non-covalent interactions involved in this process: this weak interaction allows for biomacromolecule leaching during recycling and washing protocols.^[24]

1.1.2.2 *One-pot* encapsulation method

The *one-pot* encapsulation method involves the self-assembly of MOF in presence of biomacromolecules (**Figure 2**). The main advantage of this approach is that the encapsulation of biomacromolecules is not limited by the pore size of MOF, as the porous material will form around the biomacromolecule. This method has been successfully employed to encapsulate large biomacromolecules such as proteins,^[10,15,16] nucleic acids,^[17,18] viruses,^[12,13,19] cells,^[21,22,72] and more recently carbohydrates.^[73,74] Depending on the systems, the presence of additives can play a major role.^[15,16] Since the encapsulation method should be able to preserve the structure and function of biomacromolecules, it is very important to conduct the synthesis in biocompatible conditions.^[24]

The formation of ZIF-8 around biomacromolecules was reported for the first time by using polyvinylpyrrolidone (PVP) as an additive; this synthetic approach was termed the *coprecipitation method*.^[15] (**Figure 2**). PVP functioned as a co-precipitating agent since it has a strong affinity with proteins^[75], and it assists the dispersion and stabilization of proteins in

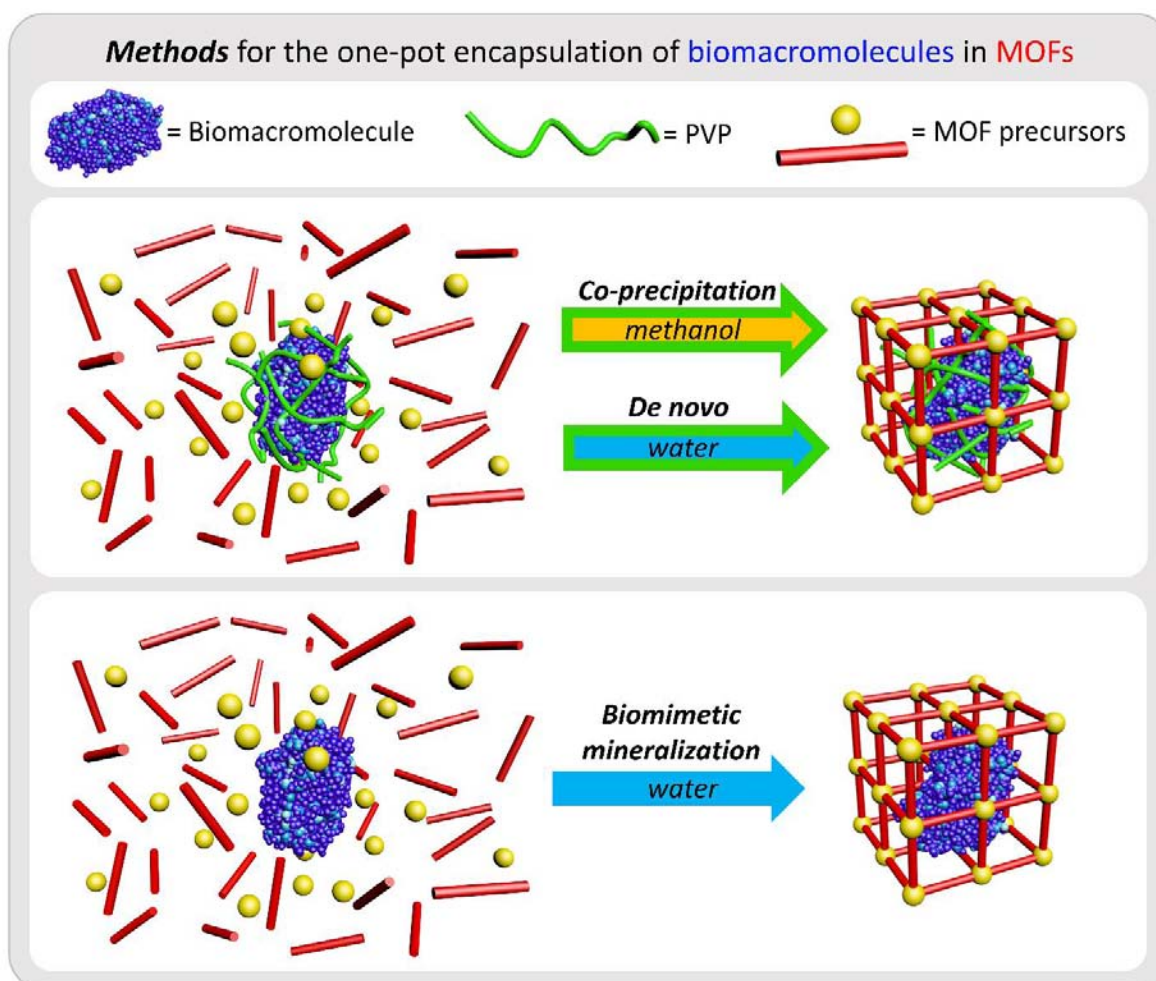


Figure 2. Schematic representation of the one-pot encapsulation strategies for the integration of biomacromolecules within MOFs.^[24]

methanol. Moreover, PVP can act as a crystallization facilitator by attracting and coordinating metal cations^[76,77], which increases the local concentration of metal cations around the protein leading to the formation of ZIF-8 around the target biomacromolecule. For instance, Ge et.al. demonstrated the successful one-pot encapsulation of cytochrome C (Cyt c) within ZIF-8 by using a PVP as the co-precipitating agent.^[15] The solution comprised of Cyt c and PVP was mixed with the precursors of ZIF-8 in methanol, which resulted in the rapid formation of the corresponding MOF biocomposite. The authors demonstrated that the enzymatic activity of encapsulated Cyt c was 10-fold higher than for the free enzyme when tested for detection of organic peroxides in solution. This method was further extended for the synthesis of other protein@MOF systems such as horseradish peroxide (HRP@MOF), and lipase (lipase@MOF). The investigation of the biopreservation properties of the resultant biocomposites revealed that the MOF shell could preserve the encapsulated proteins after being incubated in methanol.^[15] Enhanced biocompatibility was obtained by replacing alcohol

with water. This new protocol, based on PVP as a co-precipitating agent, was named as *de novo* approach.^[16]

More recently, Falcaro and co-workers demonstrated that the MOF formation can be induced by negatively-charged biomacromolecules under aqueous conditions without the addition of additives.^[10,23] (**Figure 2**) In this approach, termed *biomimetic mineralization* process, the biomacromolecules act as seeds that triggered the spontaneous formation of MOFs around biomacromolecules.^[10,54,78,79] For example, several proteins and enzymes (e.g. BSA, ovalbumin (OVA), human serum albumin (HSA), insulin, lipase, horseradish peroxidase (HRP)) trigger the formation of ZIF-8 biocomposites.^[10] The mechanism involved in the spontaneous formation of MOFs is similar to the natural biomineralization process used by several biological organisms, where biological specimens induce the heterogeneous nucleation of minerals.^[10]

Experimentally, the preparation of biomacromolecule@MOFs following the *biomimetic mineralization* approach is performed by adding the solution of biomacromolecule to the ligand solution and then mixed with the aqueous solution of metal cation.^[10,24] (**Figure 3**) To ensure the success of this process, it is required to compare the particle growth kinetics between the water-based precursor MOF with and without biomacromolecules. The biomimetic mineralization is ascertained by the rapid formation of particles in the presence of biomacromolecules.^[10,24]

Several considerations can be made when referring to the preparation of biomacromolecule@MOF biocomposites via encapsulation methods. MOF biocomposites prepared by encapsulation methods could afford high-level protection toward hostile environments (e.g. temperature, proteolytic agents, and organic solvents) compared to surface immobilization methods.^[24] For example, MOFs can protect the encapsulated enzymes and antibodies from proteolytic agents because the porous framework acts as a molecular sieve.^[54,80] MOF biocomposites prepared by encapsulation methods have improved recyclability relative to the one prepared with the surface immobilization methods.^[60] Indeed, in contrast to the adsorption method, the one-pot encapsulation method could retain the encapsulated biomacromolecules without significant leaching after repeating washing.^[16,54] Compared to the infiltration method, the one-pot encapsulation method does not require the design of MOF pores larger than the hosted biomacromolecules since MOFs are self-assembled around bioentities.^[10] In fact, the one-pot approach can be used for the encapsulation of more complex and large bioentities such as viruses and cells.^[12,13,19–22]

In general, the syntheses of MOFs can be performed under solvothermal conditions with the support of high temperature, extreme pH values, and organic solvents. Thus, the

encapsulation of biomolecules requires the selection of those MOFs that can be prepared under mild reaction conditions; this condition was found crucial for the integrity of the original biological function of the target biomacromolecule.^[10] Among the MOFs that fulfil this requirement, metal azolate frameworks (MAFs) are ideal candidates as they can be easily prepared in aqueous media and at room temperature.^[24] Another alternative involves the use of mechanochemical synthesis which could be utilized as a solvent-free method to prepare selected MOF biocomposites.^[81] In particular, the direct encapsulation of lyophilised enzymes (e.g. catalase, β -glucosidase, and invertase) in ZIF-8, UiO-66-NH₂, and Zn-MOF-74 were successfully obtained using ball milling.^[81]

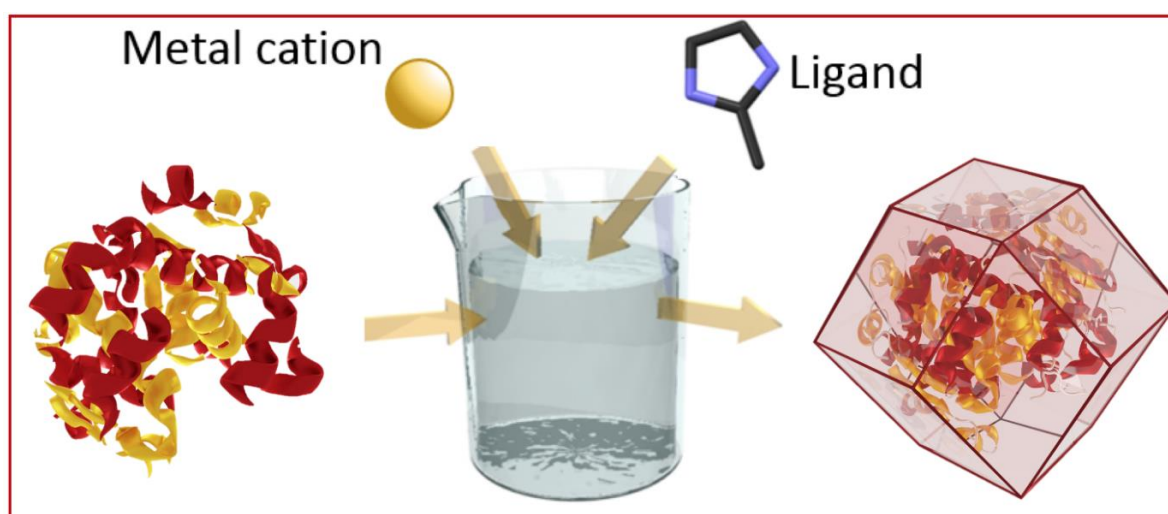


Figure 3. Schematic overview for the preparation of biomacromolecule@MOF biocomposites by the *biomimetic mineralization* method.^[25]

1.1.2.3 The Influence of synthetic parameters on mechanism formation and properties of biomacromolecules@MOFs

The encapsulation process of biomacromolecules within a MOF shell is influenced by different parameters such as co-precipitation agents and the chemical and structural features of the MAF used.^[24] It has been demonstrated that the kinetics of the biomimetic mineralization process is protein dependant,^[82] as it is influenced by the surface charges of the target biomacromolecule. In fact, subtle changes on the surface chemistry of proteins could trigger or inhibit the biomimetic mineralization process.^[19,25,73,82–84] Experimental and computational studies demonstrated that negatively-charged proteins (isoelectric point < 7) could promote the biomimetic mineralization process when using ZIF-8 precursors to induce the formation of a MAF shell.^[73,82] This observation can be extended to other negatively-charged biomacromolecules, such as polysaccharides. For instance, in carboxymethyl dextran (CM-dextran) the carboxylate moieties (COO⁻) enhance the concentration of Zn²⁺ cations around

the biomacromolecules, seeding the formation of ZIF-8 around CM-dextran following a heterogeneous crystallization process. Conversely, positively charged dextran (diethylaminoethyl dextran) depletes the Zn^{2+} ions concentration near the biomacromolecules, inhibiting the encapsulation process.^[73] A similar response to the surface charge of the MOF precursors was found to be valid for different MOFs (ZIF-90 and MAF-7) and other clinical carbohydrate-based therapeutics.^[74]

As mentioned, another parameter that has an impact on the encapsulation process is the presence of co-precipitating agents. Co-precipitating agents are additives that can assist the synthesis of biomacromolecules@MOFs when added to the solution of biocomposites precursors. For instance, bases including NaOH and NH_4OH can be used as co-precipitation agents for the synthesis of MOFs in water, as they induce ligand deprotonation accelerating the MOF self-assembly process.^[54,85]

Although the formation of MOF does not rely on the biomacromolecules size, the dimension of biomacromolecules and their assemblies could influence the spatial localization of biomacromolecules within MOF particles.^[24] For example, when analysing the MOF biocomposite, individual biomacromolecules (e.g. carbohydrates, proteins and nucleic acids) were found to be localized in different pockets in the MOF matrix.^[10,15,86] However, for bigger bioentities such as cells and viruses, the growth of a polycrystalline MOF around the specimen generates a core-shell-like configuration.^[12,13,19,20,22,87]

The properties of the biocomposites depend on the specific crystalline phase of the MOF biocomposite: distinct porosity, biopreservation capabilities, and release kinetics were observed.^[24] It has been reported that different crystalline phases such as sodalite (*sod*), diamondoid (*dia*), katsenite (*kat*), ZIF-L, ZIF-C (ZIF- CO_3 -1), and unidentified topology (U12, and U13), as well as amorphous ZIF, can be obtained by changing the concentrations of the MOF precursors.^[88–91] Each of these different phases leads to different functional properties. For example, glucose oxidase (GOx) encapsulated in amorphous ZIF has 20 times higher catalytic activity than GOx encapsulated in *sod* topology.^[90]

1.2 Main properties of MOF-based biocomposites

Several important properties should be considered for the application of MOF-based biocomposites in the field of biomedicine: biocompatibility, biopreservation capabilities, particle size, release profile, and biodegradation are salient aspects.

1.2.1 Biocompatibility of MOF-based biocomposites

The increasing interest in MOF biocomposites as DDS engenders the consideration for the biocompatibility of MOF components.^[4] Indeed, the drug delivery mechanism typically involves the degradation of the MOF carrier: the release of the therapeutic can occur simultaneously to the release of the MOF building blocks (e.g. organic ligand and the metal node). Therefore, a judicious selection of the metal nodes with a low median lethal dose (LD50) might mitigate the immune responses of the body when exposed to MOF-based drug carriers. The LD50 parameter is commonly used to compare the toxicity of different substances, and it is defined as the amount of substance that causes the death of 50% of the tested population within a selected time.^[42] Based on this parameter the preferable metal cations for the construction of MOFs are Mg^{2+} ($\text{LD50 MgSO}_4 = 5000$) > Ca^{2+} ($\text{LD50 CaCl}_2 = 1940$) > Fe^{2+} ($\text{LD50 FeCl}_2 = 984$) > Fe^{3+} ($\text{LD50 FeCl}_3 = 450$) > Zn^{2+} ($\text{LD50 Zn(OAc)}_2 = 100\text{--}600$).^[4,43] Another attractive alternative to reduce the cytotoxicity of the MOF matrix is the use of endogenous biomolecules (amino acids, peptides, proteins, nucleobases, carbohydrates, porphyrins) or exogenous bioactive ingredients (e.g. nicotinic acid, curcumin, olsalazine and some dicarboxylic acids, including fumaric acid) as organic linkers. The choice of endogenous molecules and/or bioactive molecules (cation, organic ligand, or both) is considered an effective strategy for the synthesis of biocompatible MOFs (aka bioMOFs, **Figure 4**).^[43]

In the case of ZIF-8, *in vitro* studies performed on six different cell lines demonstrated that concentrations above $30 \mu\text{g mL}^{-1}$ have significant cytotoxicity towards kidney, breast, skin, blood, bones, and connective tissue.^[44] This cytotoxicity is mainly caused by the release of Zn^{2+} in the cell media upon the degradation of the MOF shell. Thus, the $30 \mu\text{g mL}^{-1}$ threshold concentration of ZIF-8 has to be considered when using this MOF matrix as DDS.^[44] However, this amount was sufficient to deliver a therapeutic dose of insulin. It should be noticed that although *in vitro* studies provide valuable information about some cytotoxicity aspects such as cell viability, *in vivo* studies are still crucial. Indeed *in vivo* studies are needed to examine the toxicity or side effects of the MOF carriers and their related building blocks, since they could interfere with several metabolic pathways in living organisms (e.g. accumulation in organs, permanence in the circulatory system, alteration of the immune response, etc).^[92]

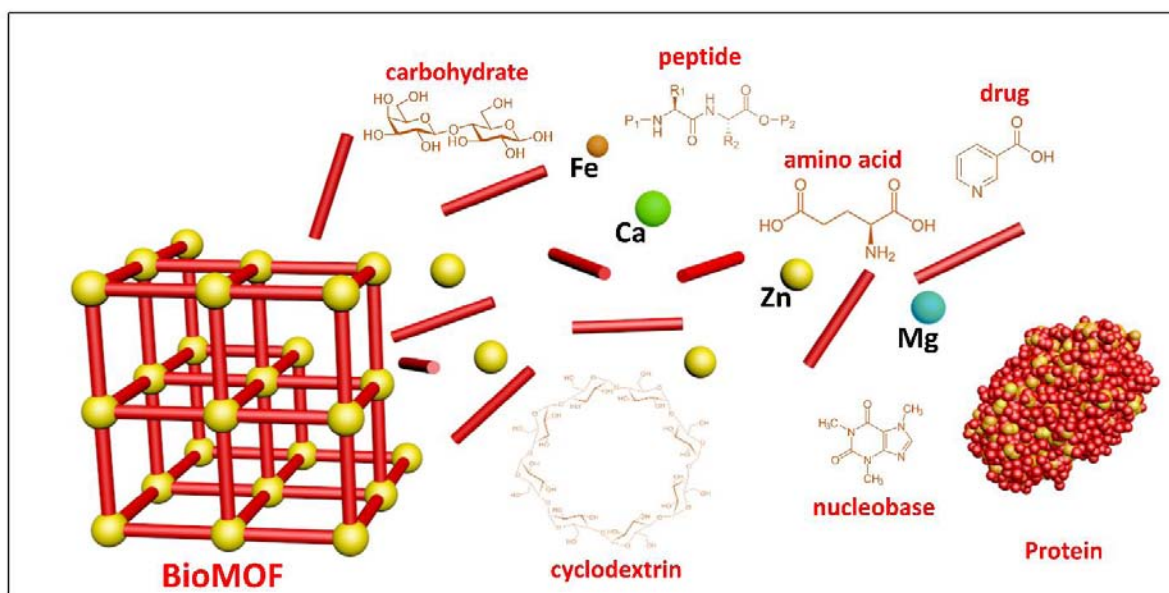


Figure 4. Natural occurring building blocks typically used for the synthesis of BioMOFs. These include endogenous/exogenous organic linkers and biocompatible cations.^[24]

1.2.2 Particle size of MOF-based biocomposites

The particle size and shape of biocomposites play a key role in their applications as DDS, since such features determine biodistribution, blood circulation time, compatibility, and cellular internalization to name the most salient aspects.^[93,94] For instance, different mechanisms in cellular internalization processes including phagocytosis, macropinocytosis, caveolar-mediated endocytosis, or clathrin-mediated are influenced by the particle size.^[95,96] Furthermore, the particle size determines the efficiency of a tumor-targeted drug delivery system. In this regard, different studies have demonstrated that larger nanoparticles (~100 nm) present higher retention in tumor tissue than smaller nanoparticles (~20 nm), even though small nanoparticles have better penetration capability compared to higher nanoparticles.^[94,97,98] Nevertheless, particles < 5 nm are rapidly removed from the circulation through extravasation or renal clearance, and particles in the 10 nm - 15 μ m range could be trapped by mechanical filtration in the spleen and then the reticuloendothelial system (RES) would remove the nanoparticles from the circulation.^[93] Additionally, mechanical filtration in the capillaries would remove the larger particles (~15 μ m) from circulation.^[93] Particles in the size range of 50–300 nm can be used for the parenteral administration route.^[4,99,100] However, some studies report that nanoparticles with a size smaller than 150 nm can leave the circulation through openings of the endothelial barrier.^[101,102] Accordingly, MOF nanoparticles from tens to hundreds of nanometers are ideal carriers for intravenous or subcutaneous administration of biotherapeutics and imaging agents.^[29,92,103] The use of MOF nanoparticles as imaging agents represent one of the most attractive applications of MOFs in theranostic,

which is defined as the combination of therapeutic and diagnostic.^[104] However, it should be noted that small nanoparticles are not suitable for all administration routes. For instance, for the transdermal administration route particles within the range of 300 nm to 1.5 μm are preferable, since nanoparticles smaller than 10 nm are unlikely to penetrate human skin through the *stratum corneum* and tend to accumulate in the hair follicle openings.^[105] On the other hand, it has been reported that biodegradable microparticles in the size range of 0.3 to 2 μm are suitable for vaccine delivery.^[101,106,107] In general, additional advantages of large particle size systems include slower degradation in buffer media and lower aggregation.^[26,91,108,109] The schematic of the different size-dependent processes and administration routes which is relevant for consideration of the particle size in DDS applications are demonstrated in **Figure 5**.

Other important aspects that should be considered for the design of DDS are particle's shape and density since such features substantially impact the biodistribution and mechanism of internalization, as well as retention and circulation time.^[93,94,101] For instance, low-density clusters with inter-particle voids can be prepared by controlling the aggregation of nanoparticles. This method can be used to modify the density of the carriers and permit higher retention in tumor tissues and deeper penetration in the case of administration to the lungs.^[94,101]

Various approaches have been used to modify the MOF particle size. For instance, the particle size of the pure MOFs could be easily tuned by adjusting the synthetic conditions this includes temperature, pH, type and amount of solvents, and reagents concentrations^[26,110] or by the introduction of additives (e.g. surfactant and coordination modulator).^[4,92,111,112] These methods are suitable to modulate the particle size of MOF-based biocomposites obtained either by the infiltration method or by the surface functionalization approach. Nevertheless, for the preparation of biomacromolecules@MOF via one-pot encapsulation, the control over particle size is more challenging, since the synthetic parameters that can be tuned are restricted by the mild conditions required to avoid the denaturation of the target biomacromolecule.^[24,25]

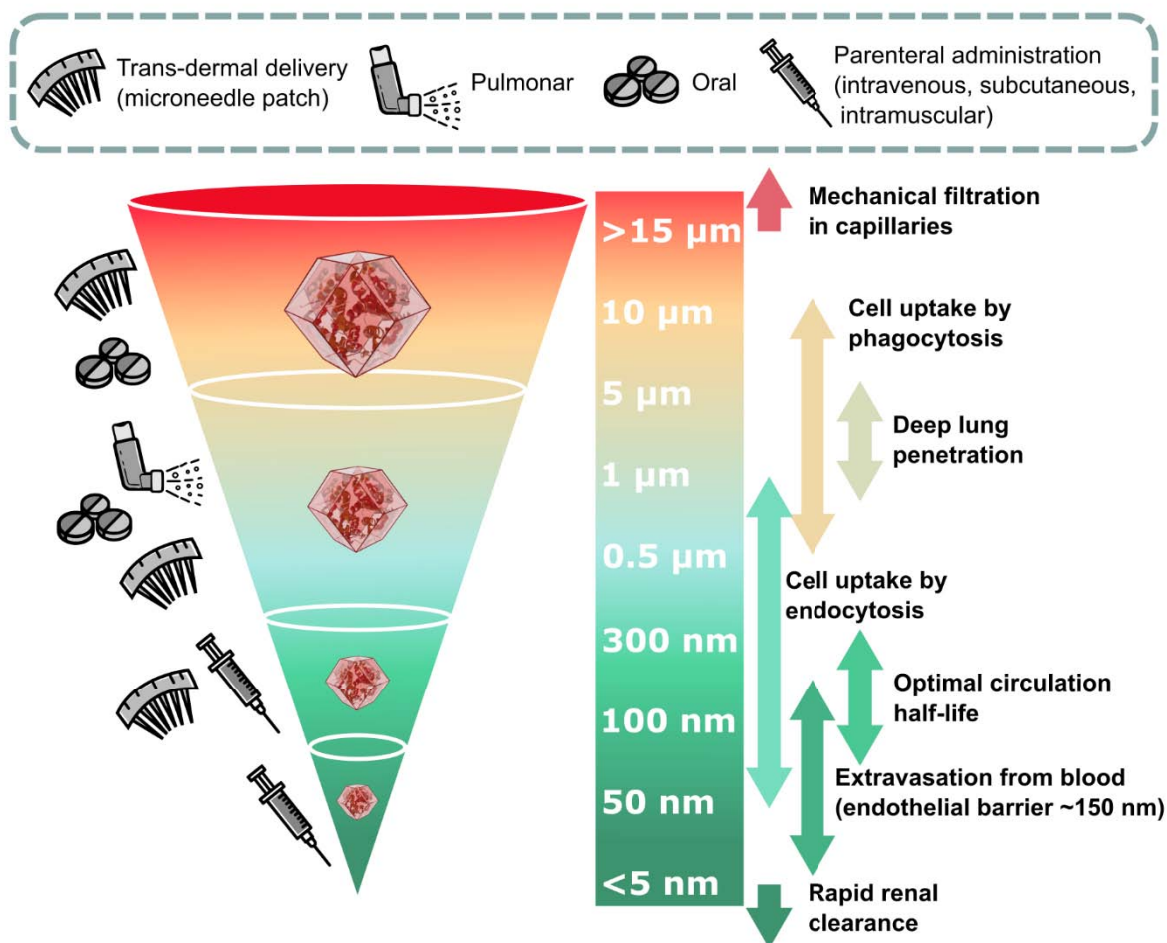


Figure 5. Consideration on the particle size and requirements for each administration route for the design of DDS.^[25]

Consequently, the research in this area is still in its infancy. Pioneering work by Carraro et al. demonstrates that the continuous flow synthesis could be employed to control the particle size of MOF biocomposites via one-pot encapsulation.^[113] This flow setup could produce BSA@ZIF-8 biocomposites in the size range of 40-100 nm.^[113] However, this setup employs ethanol as a quenching agent, which might not be fully compatible with a number of biotherapeutics. Therefore, it is still necessary for further research to investigate biocompatible synthetic conditions that allow for a tunable control of the particle size of biomacromolecules@MOF composites.^[25]

1.2.3 Protection properties of MOF-based biocomposites

An important challenge that must be addressed when using biomacromolecules or complex bioentities (cells and virus) in biomedical and biotechnological applications is the preservation of the biomolecules during storage, transport, and handling.^[20,114] By nature, biomolecules are typically unstable when removed from their natural environment and tend to degrade.

Generally, severe conditions such as increased temperature, non-native pH, or non-aqueous media can change the conformational arrangement of biomacromolecules, thereby leading to a loss of natural functions of active biomacromolecules.^[24,25] For instance, protein-based therapeutics are commonly kept at temperatures in the range of 2–8 °C since they tend to lose their natural activity when exposed to conditions outside this temperature window.^[30,115] Similarly, vaccine and virus-based therapeutics need constant refrigeration to maintain their effectivity.^[30] Whereas the bioactivity of the cells might be altered by the presence of cytotoxic compounds or after exposure to natural radiation.^[116]

Various strategies have been implemented to increase the stability and protection of proteins, viruses, and cells.^[24] An emerging protocol is the encapsulation of proteins within MOFs, as it has been shown that the integration of enzymes within MOF shells enhances the stability of the biomolecules against harsh conditions including high temperatures, organic solvents, mechanical stress, and the presence of proteolytic/chaotropic agents.^[23,24] Furthermore, MOF shells could be employed as protective synthetic coatings for virus-based therapies, and vaccines which usually need constant refrigeration (i.e. cold chain) to preserve the bioactivity towards denaturing conditions.^[12,13,20] MOFs could be interesting candidates due to the precisely tuned of their structures, chemical properties, pore size, and shape.^[117] Moreover, some MOFs (especially MAFs) can be prepared in aqueous conditions and the encapsulated biomolecules can be easily recovered upon applying external stimuli.^[28]

The biopreservation capabilities of ZIF-8-based biocomposites obtained *via* the *biomimetic mineralization* approach was reported by Falcaro and co-workers.^[10] In this work, the authors encapsulate horseradish peroxidase (HRP) enzyme within ZIF-8 to afford the corresponding HRP@ZIF-8 biocomposites. The enzymatic activities of the free HRP and HRP@ZIF-8 were investigated by exposing them to a proteolytic agent (trypsin). The HRP@ZIF-8 maintained 88% of its catalytic activity for the conversion of pyrogallol to purpurogallin, in contrast free HRP presented just 20% of its initial catalytic activity. The protective capability of ZIF-8 was compared with other porous protecting materials such as SiO₂ and CaCO₃. The catalytic activity of free HRP, HRP@ZIF-8, HRP@CaCO₃, and HRP@SiO₂ was investigated upon exposure to boiling solvents (water and DMF). After exposure to boiling water for 1 hour, HRP@ZIF-8 retained 88% and of its initial activity, whilst HRP@CaCO₃ and HRP@SiO₂ only showed 39% and 65% of the activity, respectively. Furthermore, after exposure to boiling DMF for 1 hour, HRP@ZIF-8 exhibits 90% of its catalytic activity, whilst HRP@CaCO₃ and HRP@SiO₂ showed 32% and 22% of substrate conversion, respectively. The superior protective capabilities of ZIF-8 compared to SiO₂ and CaCO₃ can be directly related to the tight encapsulation of the enzyme within the MOF matrix. Indeed, small-angle X-ray scattering

(SAXS) analysis data revealed that the pocket size in HRP@ZIF-8 was around 10-30% larger than the size of the radius gyration of the encapsulated biomacromolecules. [10]

1.2.4 Release properties of MOF-based biocomposites

When considering the carrier for therapeutics delivery, the release kinetics is one of the most important properties. The release profile is usually depicted by a plot showing the percentage of the drug released from the carrier as a function of time.^[118] The release kinetics play an important role in the efficacy of the administration method and the therapeutic effect of the drugs.^[119] A fast release is preferable for the treatment of infection-related disease,^[120] and wound treatment.^[121] In contrast, a slow-release is preferable for the extended-release of drugs when frequent administration is required and discomfort in the patient is observed.^[122,123] For example, protein-based treatments including insulin, growth hormones, or oxytocin typically need frequent administration via parenteral route generating pain and discomfort to the patient, thus a prolonged-release treatment is preferred.^[123,124]

The release profile of the drugs from nanoparticles is typically influenced by the nature of the delivery system.^[125] In most cases, the release profile of the drug can be observed by the undesirable initial rapid drug release “burst effect” followed by the slower sustained release.^[125,126] In the terms of MOF biocomposites as DDS, reducing the burst effect and providing a sustained release could be achieved by adjusting the structure of the MOFs (e.g. different topologies),^[14] composition of the MOFs (e.g. different ligands and cations) ^[14] and the localization of the drug within the carrier (e.g. different drugs immobilization methods).^[126]

Recently, the research in DDS has been progressed from regular drug delivery methods to active-targeting and stimuli-responsive carriers that can provide controllable release, localization, and dosage of drugs.^[127] It has been reported that the controlled release of biomacromolecules from MOF can be triggered by endogenous stimuli (e.g. pH, redox, and adenosine triphosphate (ATP)) and exogenous stimuli (e.g. temperature, magnetic pressure ions, and light).^[28] For instance, ZIF-8 is widely investigated as the pH-responsive MOF due to its acid sensitivity.^[10,28] Additionally, ZIF-8 can also be degraded by using a chelating agent (i.e. ethylenediaminetetraacetic acid, EDTA). Alternatively, a buffer solution such as phosphate buffer, which closely imitates the physiological conditions in terms of pH, osmolarity, and ion concentration, degrades ZIF-8 due to the presence of coordinating anions.^[26,128]

1.3 The application of MOFs as drug delivery systems

The application of MOFs as DDS has evolved since the first proof-of-principle studies and the wide variety of therapeutics and MOFs have been investigated.^[5,129] Various applications of MOFs as carriers for biomacromolecule-based therapeutics have also been reported.^[24,25] In this section, significant examples related to carbohydrates (1.3.1) and proteins (1.3.2) will be illustrated.

1.3.1 The application of MOFs as the carriers for Carbohydrate-based drugs

Carbohydrates are biomolecules constructed from carbon, hydrogen, and oxygen which play a key role in many biological functions including cellular and intracellular interactions in the form of cell surface receptors, signalling molecules, and bacterial adhesives. These carbohydrate functions underpin their potential as therapeutics and as diagnostic agents.^[32] Recently, carbohydrate-based therapeutics are clinically used for several treatments including cancer, AIDS, influenza, diabetes, rheumatoid arthritis, and bacterial infections.^[33–35] The most commercially exploited carbohydrates in biomedicine are glycosaminoglycans (GAGs).^[130] GAGs are unbranched high molecular weight polysaccharides comprised of repeating disaccharides building blocks of uronic acid (can be either β -D-glucuronic acid (GlcA) or its C5 epimerized version, α -L-iduronic acid (IdoA) and hexamine units (can be either glucose (Glc)-based (α -D- or β -D-glucosamine, GlcN) or galactose (Gal)-based, as N-acetyl- β -D-galactosamine (GalNAc)).^[130,131] GAGs are often attached to their native protein core to form proteoglycans (PGs).^[130,132] Typically, these biomacromolecules are negatively charged under physiological conditions due to the occurrence of sulfate and/or carboxylate moieties.^[131] HP, HA, DS, and CS, are the most common GAGs.^[130,131] GAGs can act as anti-inflammatories, anticoagulants, and wound healing agents. Furthermore, GAGs can be applied as therapeutics for treatments of diabetes, osteoarthritis, viral and bacterial infections.^[130–132] GAGs also can be used for vaccines, protein, and antibody modifications.^[133] ^[133] More recently, GAGs have been employed to design anti-cancer drugs due to the important functions of proteoglycans in metastasis and tumor progression.^[130,131,134]

The main challenge for using GAGs for biomedical applications lies in their low bioavailability and poor stability.^[132] For example, HP which is the most commonly employed anticoagulant tends to experience pharmacokinetic issues including fast serum clearance and poor bioavailability.^[132,135,136] Moreover, hyaluronic acid, which is used for wound healing treatments, presents low mechanical strength and is unstable in the presence of hyaluronidase enzyme and reactive oxygen species (ROS).^[137,138] To circumvent these limitations, researchers have tried various methods such as adding excipients, salts, or encapsulating the drugs in a suitable drug carrier.^[132] Regarding the administration of the therapeutics, the

efficacy of the drugs would be improved by encapsulating the drugs in the carrier that provides the protection and the tunable release profile.^[139] MOFs can be considered as promising carriers for GAGs-based therapeutics, since MOFs have been reported as suitable carriers for other polysaccharides.^[4,14,29] Furthermore, the encapsulation of carbohydrate-based drugs in MOFs could increase the bioavailability and pharmacokinetic properties of carbohydrates based therapeutics.^[74,140,141]

Several methods have been reported to integrate carbohydrates with MOFs carriers including surface immobilization (adsorption and grafting) and *one-pot* embedding strategies.^[74,140,141] For instance, MIL-101(Fe) was employed for the preparation of HP-on-MIL-101(Fe).^[141] The synthesis of HP-on-MIL-101(Fe) was carried out via the adsorption method by adding MIL-101(Fe) into HP solution. The adsorption of HP happened as a result of a partial loss of the organic linker from MIL-101(Fe) followed by heparin sulfate group chelation on iron at the defect sites in MIL-101(Fe). MIL-101(Fe) has been reported to have high adsorption capacity and prevent the leakage of heparin. Furthermore, HP-on-MIL-101(Fe) also has good biocompatibility with cytotoxicity up to 40 mM towards mammalian cells. HP-on-MIL-101(Fe) perform as HP carriers for prolonged anticoagulant activity (18% of HP was released after 12 hours).^[141]

Another example of surface immobilization for the integration of carbohydrates in MOFs is the grafting method. For example, carboxylated ZIF (FZIF), comprised of zinc ions and 2-methyl-1H-imidazole-4,5-dicarboxylic acid (2MtIMDC), was incorporated with hyaluronic acid.^[140] The hyaluronic acid was grafted to the carboxylic group in FZIF by using EDC/NHS method. The HA-on-FZIF biocomposite film has shown high mechanical strength due to the hydrogen bond between HA and FZIF-8. Moreover, good antibacterial properties, enhanced fibroblast migration, and proliferation were demonstrated when testing HA-on-FZIF biocomposite in biological systems.^[140]

The one-pot encapsulation method was employed to encapsulate carbohydrates within Zn(mIM)₂ MOFs by using the *biomimetic mineralization* approach.^[73] To prepare such CH@MOFs, the solution of carbohydrate was mixed with HmIM solution followed by the addition of zinc acetate solution. Several carbohydrates were investigated (e.g. D-glucose, D-galactose, D-mannose D-xylose, D-glucitol, meglumine, methyl-β-D-glucopyranoside, N-acetyl-D-glucosamine, D-glucosamine, sucrose, maltodextrin, D-gluconic acid-δ-lactone, dextran, diethylaminoethyl dextran (DEAE-dextran), carboxymethyl dextran (CM-dextran), and cellulose). However, only carbohydrate with negative charges (i.e. CM-dextran) was successfully integrated within the Zn(mIM)₂ to yield CH@MOF biocomposites. In particular, CM-dextran, which is a polyanionic polymer constructed from a dextran backbone with

carboxymethyl substituents, affords the formation of a CM-dextran@ZIF-8 composite with high encapsulation efficiency (100%). Furthermore, by varying the concentration of a chelating agent (i.e. EDTA), we were able to tune the release kinetic of the model drug (FITC-CM-dextran). Thus, by using 10, 20, and 40 mM EDTA, it required 40, 30, and 16 minutes to release 100% of the model drug from ZIF-8, respectively.^[73]

This study was further extended towards the encapsulation of GAGs based therapeutics, including HP, HA, CS and DS.^[74] Additionally, two preclinical drugs GM-1111 (an anti-inflammatory drug) and HepSyl (anti-carcinogenic agents) were also encapsulated within three different metal azolate frameworks, ZIF-8, ZIF-90 and MAF-7. The GAG@ZIF biocomposites exhibit different structural features including diverse crystalline phases (e.g. *sod*, *dia*, or amorphous), and various particle sizes (50 nm–7 µm). These structural differences influence the performance of GAG@ZIFs as drug delivery systems, including their corresponding encapsulation efficiency and release kinetic. The former varied from 50–100%, whereas the latter varied from 20 min to 2.5 hours, depending on the MOF matrix selected. Additionally, the study of the anticoagulant activity of HP@ZIFs demonstrated that the HP released from ZIFs maintains 95–98% of the original antithrombic activity. Furthermore, the exposure of HP@ZIFs to heparinase I (heparin lyase enzyme) revealed that the biopreservation of HP varies with the ZIF matrix used. For instance, HP release from HP@ZIF-8, after being exposed to heparinase I for 1 hour at 30 °C, retains 67% of its anticoagulant activity. Whereas HP released from HP@ZIF-90 and HP@MAF-7 presents 84% and 99% of anticoagulant activity, respectively.^[74]

1.3.2 The application of MOFs as the carriers for Protein-based drugs

Proteins are biomacromolecules comprised of one or more long chains of amino acids and significantly contribute to many cellular functions including immune response, gene regulation, and signalling. Protein deficiency or protein dysfunction may cause various health problems such as Alzheimer, Parkinson, and diabetes mellitus.^[142,143] The treatment for protein disorder may include the administration of protein-based therapeutics. For instance, insulin can be used as an effective treatment for diabetes mellitus type I and II.^[122]

Protein-based drugs have high specificity, high potency, and low toxicity compared to small drugs.^[144,145] However, the use of protein-based drugs is still limited due to the easy denaturation of proteins when exposed to temperatures outside their temperature window (2–8 °C) and mechanical stress.^[144,145] Besides, when protein-based drugs are administered to biological systems, their efficacy might be reduced due to the rapid renal clearance, fast degradation by proteolytic agents, or difficulties in crossing cell membranes.^[122,146]

Integration of proteins within MOF carriers could be a promising approach to improve the stability and intracellular delivery of protein-based therapeutics.^[10,15,23] For example, Qu et.al. showed that ZIF-8 represents a suitable nanocarrier for ovalbumin administration (OVA, a protein antigen that can induce humoral and cellular immune responses).^[147] OVA@ZIF-8 was synthesized by encapsulating OVA within ZIF-8 using the *de novo* approach. Furthermore, OVA@ZIF-8 was functionalized by adsorption of an immune adjuvant, cytosine-phosphate-guanine oligodeoxynucleotides (CpG ODNs), to create CpG-on-OVA@ZIF-8. This configuration allows for the co-delivery of the antigen and the adjuvant within the target cell. The acidic environment of lyso/endosomes induces the cytosolic release of OVA from CpG-on-OVA@ZIF-8 in the cell. The authors claim that the encapsulation of OVA within ZIF-8 improved the *in vivo* protection of the antigen against blood proteases, whereas the co-delivery of the adjuvant allows for the activation of the systemic immune system.^[147]

Another example of proteins encapsulated within MOFs was provided by Willner and co-workers.^[148] The authors developed a ZIF-8-based glucose-responsive carrier for the controlled release of insulin. Glucose responsive properties were achieved by co-encapsulated insulin and glucose oxidase (GOx) within ZIF-8, to yield In&GOx@ZIF-8 biocomposite. In presence of glucose, GOx catalyses the oxidation of glucose to yield gluconic acid and H₂O₂. This catalytic reaction produces an acidified microenvironment, that triggers the degradation of ZIF-8 shell, and by consequence the release of insulin. In this stimuli-responsive system, the accumulation of the cytotoxic by-product H₂O₂ could inhibit the enzymatic activities of GOx. Therefore, catalase (CAT) was co-encapsulated within ZIF-8 to decompose the H₂O₂ into H₂ and O₂. The authors demonstrated that the enzymatic cascade GOx/CAT could be activated or inhibited by varying the concentration of glucose, which could be useful for the on-demand control release of insulin.^[148]

1.4 Methodology

In this doctoral thesis, several experimental characterization techniques have been employed to investigate different aspects related to the encapsulation of biomacromolecules within MOFs. The main characterization techniques employed are Fourier-transform infrared spectroscopy (FTIR), Powder X-ray diffraction (PXRD), Scanning Electron Microscopy (SEM), and Ultraviolet-visible Spectroscopy (UV-vis). In the following section, an overview of each characterization technique is outlined.

1.4.1 Fourier-transform infrared spectroscopy (FTIR)

Infrared (IR) spectroscopy is an analytic technique typically used for the study of chemical functionality of the basic building blocks that constitute complex materials including polymers, biomolecules, composites, cells, among others.^[149] When IR radiation is transmitted through a sample, a specific frequency of the radiation can be absorbed by the sample while photons with other energies can pass through (transmitted).^[149,150] The absorption of infrared radiation induces direct transitions between vibrational energy levels of IR active molecules.^[150–152] The vibrational transitions that are active in IR are those that induce a change in the electric dipole moment of the molecule. Following an explanation based on the harmonic approximation, the selection rule is the following:

$$\Delta v = \pm 1$$

Where the transition $\Delta v = +1$ corresponds to absorption the $\Delta v = -1$ corresponds to emission. It should be noticed that at high frequencies the molecular motions become anharmonic and the energy levels between one transition and the other become closer which permits transitions above the fundamental frequency, which are referred as overtones. The number of vibrational modes for a non-linear molecule with N atoms is $3N-6$. Whereas for linear molecules the number of vibrational modes is $3N-5$.^[153]

The IR spectrum is typically recorded within the range of $4000-400\text{ cm}^{-1}$. The region of the spectrum between $4000-1400\text{ cm}^{-1}$ is where most of the functional groups show discrete absorption bands. Whereas the region between $1400-600\text{ cm}^{-1}$ is called the fingerprint region because is characteristic for the compound as a whole.^[153,154]

In this work, an attenuated total reflectance (ATR) accessory unit was used with Fourier transform infrared (FTIR) spectrometers. ATR accessory operates by measuring the changes occurring in an internally reflected IR radiation when the radiation meets the samples. When IR radiation is directed into the optically dense and high refractive index ATR crystal (such as diamond, zinc selenide, and germanium) at a certain angle, it will produce multiple internal

reflections and evanescent waves that extend beyond the surface of the crystal.^[149] The sample will be placed where the evanescent waves will be generated. The sample will absorb the characteristic energies in the regions of the IR spectrum and consequently, the evanescent wave will be attenuated for some frequencies. The attenuated beam will return to the crystal, and after multiple interactions with the sample, the beam will be directed to the detector. The attenuated IR beam will be recorded as an interferogram signal and used to create an IR spectrum.^[149]

In this research, FTIR was used to characterize the presence of the functional groups in MOF biocomposites. FTIR measurements can be used to ascertain the presence of biomacromolecules in MAF biocomposites. For instance, the characteristic band for carbohydrate-based molecules (CM-dextran, HP, HA, DS, CS) was observed around 1620-1608 cm^{-1} (COO^- stretching vibration).^[73,74] Furthermore, the characteristic modes of BSA were found around 1700-1610 cm^{-1} (Amide I) and 1595-1480 cm^{-1} (Amide II).^[10] Additionally, FTIR provides information related to the interaction of organic ligand and the metal ion in MAFs. The typical Zn-N stretching mode was observed at 421 cm^{-1} .^[155] In this work, FTIR spectra were characterized on Bruker ALPHA spectrometer using the attenuated total reflectance (ATR) attachment with a diamond window in the range of $\tilde{\nu}$ 4000 – 400 cm^{-1} . The samples were prepared by placing the bulk sample on the surface of the diamond crystal. The data were collected with an average of 128 scans at 2 cm^{-1} resolutions. OPUS software was used for the measurement, processing, and evaluation of the FTIR spectra.

1.4.2 Powder X-ray diffraction (PXRD)

PXRD is a rapid and non-destructive analytical technique that is mainly used for the examination of structural arrangement in crystalline substances.^{[156][157]} In general, PXRD provides important information including phase identification, crystallinity, lattice parameters, and unit cells.^[153,156] X-rays are generated in a cathode tube by heating a filament to produce electrons which are accelerated towards a target material by applying a potential difference. The accelerated electrons collide with electrons from the inner shell of the target material leading to the ejections of those inner shell electrons. Then an outer shell electron occupies this low energy level emitting X-ray radiation. The latter passes through a monochromator and collimator and then redirected to the sample. Then monochromatic-like X-rays are diffracted by the samples and create convergent radiation at the receiving slit before entering the detector.^[157]

X-ray diffraction is based on interferences. When the sample with different and spatially ordered electronic densities is exposed to X-rays, constructive and destructive interference

could occur. Constructive interference occurs when two waves with the same wavelength and moving in the same direction are in phase. Meanwhile, destructive interference occurs when the waves are out of phase. The interaction between the sample and Incident X-ray radiation generates constructive interference (also called a diffracted ray) when it satisfies Bragg's law.^[153,156]

$$n\lambda = 2d \sin \theta$$

Where θ is the angle of X-ray incident, λ is the radiation wavelength, n is an integer, and d is the space between the atomic planes.^[153] Bragg's law can be achieved by calculating the path differences between the two beams. Bragg's law explains the required conditions to occur the diffraction.^[157] The path-length difference relies on the incident angle (θ) and the spacing between the parallel crystal plane (d). The path-length should equal to one or multiple X-ray wavelengths ($n\lambda$), to keep the waves in phase.^[157]

In this work, PXRD was employed to characterize the crystalline phase of MOF biocomposites and related control (pure MOFs, metal and ligand precursors). The diffraction data of the samples on these works were characterized on a Rigaku SmartLab powder diffractometer resourced with D/teX Ultra 250 detectors equipped with Cu K α radiation ($\lambda = 1.5406 \text{ \AA}$) with the scan speed 3° min^{-1} and the step 0.01° . For the PXRD measurement, the samples were deposited on the surface of a silicon wafer, and the silicon wafer was located on the sample holder of the PXRD analyser.

Wide-angle X-ray scattering (WAXS) is the type of X-ray diffraction that is commonly employed to characterize the crystalline structure of inorganic and organic polymeric membranes.^[158,159] WAXS has a diffraction angle of $2\theta > 5^\circ$ and it usually deals with long-range periodicity in all three dimensions with a d-spacing range from a fraction of 1 \AA to 10 \AA .^[158,159] The WAXS analysis of the MOF-based biocomposites in the synchrotron beamline was particularly useful because it allows us to analyse a large number of samples with the limited amount of solid synthesized and in a faster way, which is typically a restriction for the analysis in commercial X-ray equipment. For example, in a single-phase diagram experiment, more than 100 samples were characterized. WAXS patterns of the samples were measured using the Austrian SAXS beamline at the ELETTRA synchrotron (Trieste – Italy). The operation took place at a photon energy of 8 keV with Detector: Pilatus3 100K, Dectris Ltd., Baden, Switzerland. For WAXS measurement, the sample was set in plate holes and then covered with a Kapton tape. Kapton tape was used as the background by measuring an empty plate holes cover with Kapton tape. All experiments were carried out at room temperature.

1.4.3 Scanning Electron Microscopy (SEM)

The scanning electron microscope (SEM) is a versatile technique that can be used to examine and analyse the morphology and chemical composition of the materials.^[160] SEM generates the images by scanning the sample with an electron beam. The sample is scanned simultaneously in a raster-like pattern.^[161,162] There are two main processes that occur when accelerated electrons penetrate the solid sample: 1) elastic scattering and 2) inelastic scattering. Elastic scattering occurs when the incident electron is deflected by the specimen atomic nucleus or by outer shell electrons of similar energy.^[160] In elastic scattering, the electron loses negligible energy. Backscattered electrons are primary electrons that are reflected out from the solid by scattering through an angle higher than 90 degrees as the result of elastic scattering. Backscattered electrons occur from the interaction between electrons and atomic nuclei. Backscattered electrons have high energy kinetic that allows them to leave the sample, then be re-directed almost parallel to the electron beam and collected by a detector. Backscattered electrons are useful for the investigation of multiphase samples as it is possible to qualitative map the chemical compositions of the samples.^[161] Inelastic scattering results from various interactions between incident electrons and atoms of the sample. In inelastic scattering, the electron loses energy through interaction with the sample. The secondary electrons are the result of inelastic collisions of primary electrons with the sample. Secondary electrons have lower energy than backscattered electrons.^[161,162] Secondary electrons signal can provide information about the morphology and topology of the samples. ^[161]

In this work the SEM was employed to assess the crystal size and the morphology of the pure MOFs and their corresponding biomacromolecule@MOF biocomposites. In addition, SEM was used to investigate the morphology of the different phases of biomacromolecules@MOFs including *sod*, *dia*, ZIF-C, U13, and amorphous particles. The sample was prepared by drop-casting the colloidal solution on the surface of silicon wafers (Si (100)). Once the powder was dried, the sample was and sputter-coated with gold. SEM images of the samples were collected by Philips XL30 FEG SEM. SEM micrographs and EDX spectra were measured using Tescan VEGA 3 SEM with tungsten source filament working at 20 kV.

1.4.4 Ultraviolet-visible Spectroscopy (UV-vis)

Ultraviolet-visible spectroscopy is an analytical technique in which the ultraviolet and visible regions of electromagnetic radiation are used for measuring the absorption of samples.^[163,164] UV-vis can be used for providing the data on the identification of compounds with chromophores, impurities, functional groups, compounds conjugation, qualitative and quantitative analysis.^[156]

A UV-vis spectrometer is equipped with two light sources, a deuterium lamp for the UV region and a tungsten-halogen lamp for the visible region.^[165] The light is dispersed by a prism into separate wavelengths.^[163,165] UV-vis instruments commonly record a spectrum in the 190 to 900 nm range.^[165] The data are plotted as absorbed radiations (in absorbance (A) or molar absorptivity (ϵ)) versus the energy of the incident beam.^[163] the Lambert-Beer law is used to correlate the absorption with the concentration of the chromophore.^[165]

$$A = \log \frac{I_0}{I} = \epsilon cl$$

In this equation, A is the absorbance, I_0 is the intensity of incident light, I is the intensity of transmitted light through the sample solution, ϵ is molar absorptivity coefficient, c is the concentration and l is the optical path length of the samples. According to Lambert-Beer law, the absorbance is proportional to the concentration of the absorbing species. This law is valid for monochromatic radiation and it applies mostly to dilute solutions with concentrations ≤ 0.01 M.^[166]

The absorption of electromagnetic radiations in the UV-vis range quantify the energy that is needed for electronic transitions from a ground state to an excited electronic state.^[163] In this range of frequencies, the absorption of radiation in molecules is restricted to certain functional groups (chromophores) and originated by both electrons used in chemical bonds and lone pair electrons. Electronic transitions that are possible involves electrons in n , σ , and π orbitals. Transitions from these orbitals to anti-bonding orbitals such as π - π^* , n - π^* , σ - σ^* , and n - σ^* can be observed. However, transitions of π - π^* and n - π^* are mostly responsible for the UV-vis bands in the 200 - 700 nm region.^[166]

In the carbohydrates@MOFs study, UV-vis was employed for kinetic assessment of particle formation of MOF. The study compared the formation of MOF with several dextrans with the control (BSA@MOF). The particle formation was examined with a UV-vis plate reader (FLUOstar OTPIMA, BMG LABTECH). The absorbance was measured at 595 nm for 30 min at 37°C, without shaking. UV-vis was also used for the determination of encapsulation efficiency of FITC-CM dextran@MOFs. By following the FITC at 490 nm, the supernatant of the sample can be measure by UV-Vis. Furthermore, UV-Vis was employed for the release test of FITC-CM dextran@MOFs. In the BSA phase diagram study, UV-Vis was employed for the assessment of the encapsulation efficiency and release test of BSA@MOFs. In this case, the Bradford assay^[167,168] was used for the determination of BSA in the solution. The colour change of Bradford assay from brown to blue was measured by UV-Vis at 595 nm. In the study of encapsulation of carbohydrate-based drug in MOF, UV-Vis was used for the determination of encapsulation efficiency, release test and biopreservation and anticoagulant study. For

encapsulation efficiency and release test, the carbazole assay^[169,170] was used and the absorbance was collected at 520 nm. Furthermore, biopreservation and anticoagulant activity of HP were determined by using anti IIa assay and the absorbance was recorded at 386 nm.

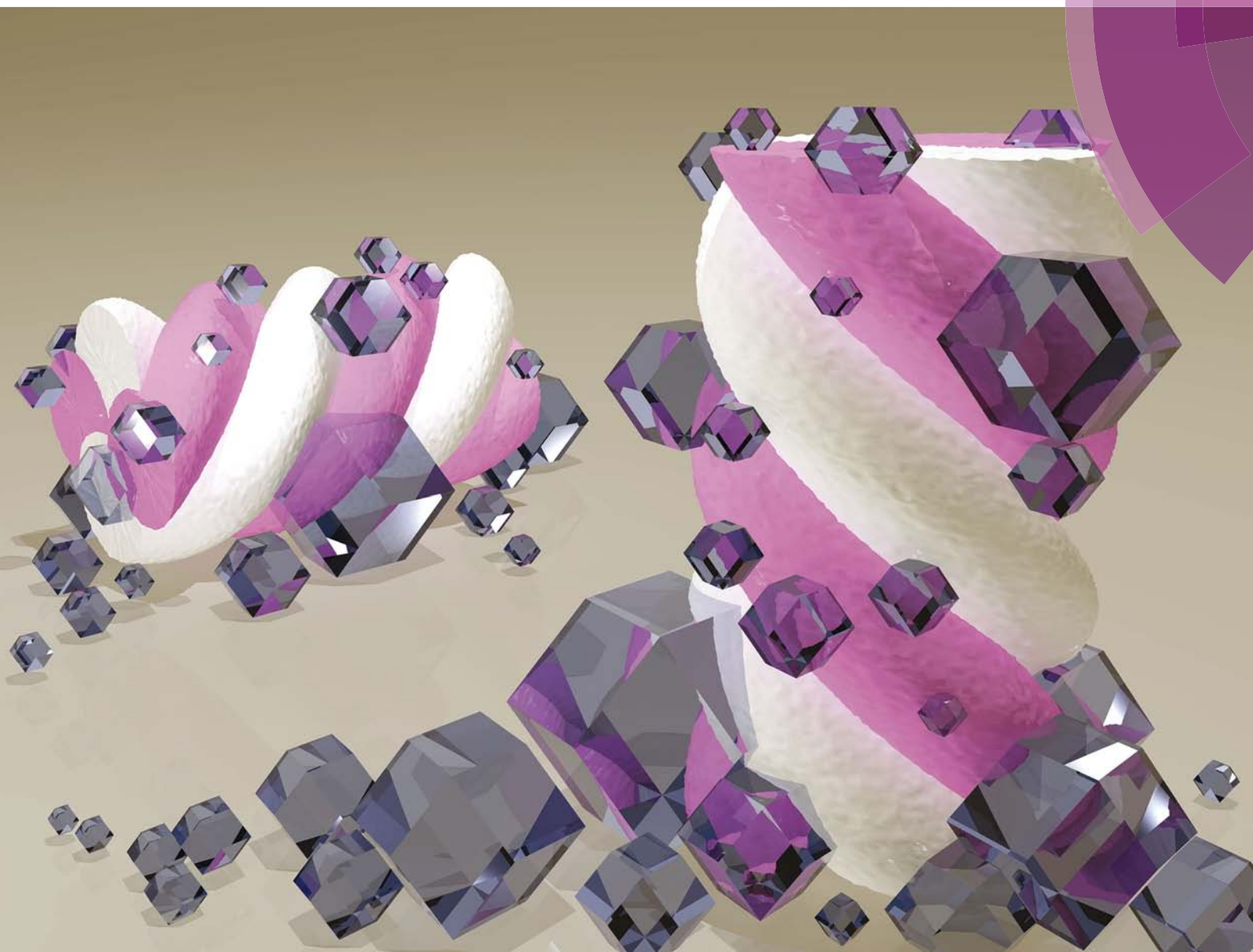
2. Publications

2.1 Carbohydrates@MOFs

In the publication entitled “Carbohydrates@MOFs”, ZIF-8 was tested for encapsulation of different carbohydrates. It is important to mention that a reliable preparation protocol for the synthesis of carbohydrate@MOF biocomposites was missing. The successful preparation of carbohydrate@MOFs and the understanding of the proper conditions for such biocomposites could pave the way for the application of carbohydrate@MOF systems in biotechnology and medicine. In this work, we examined the parameters that influence the formation of carbohydrate@MOF biocomposites. In particular, we focused on the key role of the chemical functionalization of the target CH, such as carboxylation, for the rapid self-assembly of zeolitic imidazolate framework 8 (ZIF-8). Furthermore, we determined the encapsulation efficiency and measured the release of the carbohydrate under controlled conditions. Our findings demonstrated that CH@MOF can be prepared with ZIF-8 as the matrix. Related polymorphs were formed by changing the synthetic protocol. This study paves the way for the on-demand delivery of carbohydrate-based therapeutics using ZIF-based carriers.

Materials Horizons

rsc.li/materials-horizons



ISSN 2051-6347



ROYAL SOCIETY
OF CHEMISTRY

Celebrating
IYPT 2019

COMMUNICATION

Christian J. Doonan, Paolo Falcaro *et al.*
Carbohydrates@MOFs



Carbohydrates@MOFs†

Cite this: *Mater. Horiz.*, 2019, 6, 969Received 16th December 2018,
Accepted 20th February 2019

DOI: 10.1039/c8mh01611a

rsc.li/materials-horizons

MOFs have demonstrated outstanding properties for the protection and controlled release of different bio-entities, from proteins to living cells. Carbohydrates, as pure molecules or as a component of proteins and cells, perform essential biological functions. Thus, an understanding of the role of carbohydrates in the formation of MOF-based bio-composites will facilitate their application to biotechnology and medicine. Here, we investigate the role of carbohydrate molecular weight and chemical functionalization in the formation of carbohydrate@MOF composites. We find that chemical functionalization, such as carboxylation, that leads to an enhancement of metal cation concentration at the surface of the molecule triggers the rapid self-assembly of the MOF material, zeolitic-imidazolate framework 8 (ZIF-8). Furthermore, we determine the encapsulation efficiency and measure the release properties of the carbohydrate under controlled conditions. Our findings show that MOFs can be used to prepare a new class of biocomposites for the delivery of carbohydrate-based therapeutics.

Conceptual insights

Carbohydrate-based therapeutics are relevant drugs for the treatment of cancer, diabetes, viral and bacterial infections. Therefore the efficient encapsulation and controlled release of carbohydrates has great potential in biomedicine. Here, we present a successful strategy to trigger the spontaneous crystallization of metal-organic frameworks (MOFs) on carbohydrates. The encapsulation of carbohydrates within ZIF-8 and polymorphs (zinc-imidazolate-based MOFs) can be obtained in water. The identification of conditions suitable for the successful preparation of the composite were experimentally and computationally identified. By controlling the chemical functionalization of the carbohydrate, the formation of bio-composites can be obtained in seconds. A 100% encapsulation efficiency was obtained. The controlled release of carbohydrates from the MOF biocomposite was demonstrated. This proof-of-concept study shows that a new generation of MOF biocomposites can be exploited for biomedical applications.

Introduction

Metal-organic frameworks (MOFs) are a class of crystalline porous materials that typically possess high accessible surface areas and narrow pore size distributions. In addition, the chemical functionality, on their surface or within their pores, can be precisely tuned.¹ These unique properties have led to the exploration of MOFs for application in areas such as catalysis, gas storage, separation, microelectronics, and energy production.^{2–4} In recent years, MOFs have been integrated with metallic, ceramic, and biological moieties to form novel composite materials.^{5–8} In the area of MOF bio-composites, it has been shown that MOFs can be used as carriers for therapeutics ranging from small drugs^{9,10} to large biomacromolecules.^{11,12} In the latter case, ZIF-8 has been widely investigated.^{7,8} ZIF-8, and related polymorphs,¹¹ can rapidly form in the presence of different biomacromolecules.⁷ The synthesis can be performed by adding the ZIF-8 building blocks, 2-methylimidazole (2mIM) and Zn²⁺, to proteins in the presence of a co-precipitating agent (*e.g.* polyvinyl pyrrolidone) to assist the protein encapsulation (*a.k.a.* the *de novo* approach).^{13,14} Alternatively, MOF formation can be triggered exclusively by

^a Institute of Physical and Theoretical Chemistry, Graz University of Technology, 8010 Graz, Austria. E-mail: paolo.falcaro@tugraz.at

^b Laboratory for Characterisation and Processing of Polymer, Faculty of Mechanical Engineering, University of Maribor, SI-2000, Maribor, Slovenia

^c Department of Chemistry, The University of Adelaide, 5005 Adelaide, South Australia, Australia. E-mail: christian.doonan@adelaide.edu.au

^d Institute of Inorganic Chemistry, Graz University of Technology, 8010 Graz, Austria

^e Australian Centre for Blood Diseases, Monash University, Melbourne, Australia

^f Graz Centre for Electron Microscopy (ZFE), 8010 Graz, Austria

^g Institute of Organic Chemistry, Graz University of Technology, 8010 Graz, Austria

† Electronic supplementary information (ESI) available: Additional figures, movies and experimental details. Substrates used and their formulas, schematic overviews of the performed syntheses and workups, time-dependent MOF-formation experiments induced by different carbohydrates and concentrations, yield calculations, SEM image of ZIF-8 on glass and paper, FTIR spectra of the starting materials and the obtained products, schematic of the ion-permeable spherical model, kinetics studies, UV-Vis analyses, photographs of solutions using different polysaccharides, and video showing the successful biomimetic mineralisation of CM-dextran. See DOI: 10.1039/c8mh01611a

‡ These authors contributed equally.



pure biomacromolecules.¹⁶ This method, termed biomimetic mineralisation, has been successfully employed to encapsulate proteins, DNA, enzymes, and antibodies and to coat viruses and cells with MOFs.^{7,8,15–17} In these biocomposites the ZIF-8 shell was shown to protect biomacromolecules from environments that typically lead to their degradation, to act as a gate for molecular transport, and to release the encapsulated biomolecules under controlled conditions.^{18,19} While progress has been made toward understanding the biomimetic mineralisation process for certain biomacromolecules (*e.g.* proteins), for others, *e.g.* carbohydrates (CHs), reliable preparation protocols are not yet available (*vide infra*). Nevertheless, carbohydrate-based molecules such as polysaccharides play crucial metabolic, structural, physical, and functional roles in biological systems.²⁰ The number of different biologically relevant polysaccharides (also called glycans) that an organism produces (the glycome) is estimated to be 10 to 10⁴ times larger than the corresponding number of proteins (the proteome).²¹ Because of the incremental understanding of the biological role of glycans, their importance in medicine is progressively increasing and carbohydrate-based therapies have received considerable attention in recent years.^{21–23} Pure glycans can be delivered as effective therapeutics; for example dextrin-2-sulphate was found to reduce replication of HIV-1 in patients with AIDS and to induce a gradual regression of Kaposi's sarcoma lesions.²⁴ The fusion of glycans with other biomacromolecules (glycosylation) can substantially modify the structure and function of proteins and lipids influencing intermolecular and intramolecular interactions; for instance, the type of glycan present on IgG1 antibodies contributes to determining their function, *e.g.* pro-inflammatory or anti-inflammatory properties.²⁵ Glycans can be artificially attached to proteins (glycoengineering)²⁶ to improve their robustness; the effectiveness of this method is evidenced by the commercially available glycosylated proteins.²⁷ Glycans are also active key players at the interface of viral capsids²⁸ and cell membranes as CHs regulate adaptation, differentiation, adhesion and signaling.^{22,29,30}

Motivated by our interest in the exploitation of MOFs for biotechnological applications and the widespread use of CHs in biology,^{7,8} we investigated the biomimetic mineralisation of ZIF-8 by CHs. A detailed understanding of how ZIF-8 encapsulates mono- and poly-saccharides will expand the use of MOFs in biotechnology and biomedicine.

A preliminary study that describes the facile encapsulation of polysaccharides by ZIF-8 has been recently reported.³¹ In this work, the synthesis was performed by adding polysaccharides (*e.g.* dextran, molecular weight not disclosed) to a solution of 2mIM; this solution mixture was then combined with a zinc acetate solution. We have been unable to reproduce these results in our laboratory, even after varying the reported protocol (*e.g.* order of reagents, temperature, and concentration).³¹ Thus, we considered the preparation of carbohydrates@MOF composites an open scientific challenge and carried out a systematic study to test CHs for the preparation of bio-MOF composites. In this present study, we investigated the role of mono-, di-, oligo-, and poly-saccharides as potential biomimetic mineralisation agents for the formation of CHs@ZIF-8.

Here, we show that the encapsulation of CHs within ZIF-8 and its structural polymorphs is not general. Indeed, the majority of the CHs do not lead to the formation of MOF biocomposites. More importantly, computational and experimental data show that the chemical functionality of polysaccharides is critical to the reproducible preparation of CHs@ZIF-8. Furthermore, to highlight the potential application of biomimetic mineralisation to the release of polysaccharide-based therapeutics, we used unlabelled and fluorescein isothiocyanate-labelled carboxyl-functionalized polysaccharides to study the encapsulation and release of CHs from ZIF-8 composites. In summary, we have determined a general method for preparing CHs@ZIF-8 biocomposites, which is an important first step towards exploring these materials for the release of polysaccharide-based therapeutics and for the controlled growth of MOF shells around moieties of biological interest, such as glycosylated proteins, viruses, and cells.

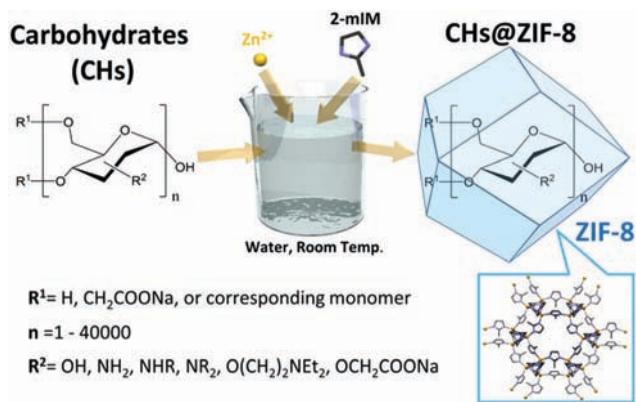
Results and discussions

Biomimetic mineralisation is a term that describes the triggered formation of MOF particles or films by single biomacromolecules or more complex biological entities (*e.g.* a virus or cell).⁷ In general, to ascertain whether the biomimetic mineralisation process takes place, it is necessary to compare the particle growth kinetics of water-based MOF precursor solutions with and without the presence of the biomacromolecules. Biomimetic mineralisation is confirmed when a difference in the formation time for MOF particles is observed in the presence of the biomacromolecules (*e.g.* faster production rate or larger amount of particles). Typically, biomimetic mineralisation leads to the formation of a MOF coating around the biomacromolecules that engenders MOF-based bio-composites that possess novel properties.⁷ We started our investigation into the preparation of CHs@ZIF-8 composites by testing a variety of basic CH units (*i.e.* monosaccharides) as potential biomimetic mineralisation agents (Scheme 1), including neutral reducing monosaccharides such as D-glucose (1), D-mannose (2), D-galactose (3), D-xylose (4); a non reducing sugar such as methyl-β-D-glucopyranoside (5) (Table S1, ESI[†]); reduced sugars such as D-glucitol (6) and meglumine (7); and monosaccharides bearing a nitrogen such as N-acetyl-D-glucosamine (8) and D-glucosamine (9).

Then, we tested water soluble oligosaccharides such as sucrose (10), a typical disaccharide, D-gluconic acid-δ-lactone (11), the oxidized form of glucose, and maltodextrin (approximately 20 α-1,4-D-glucose units). Finally, we studied structural analogues of the probed carbohydrates such as ethylene glycol (12) and N-methyl-aminoethanol (13).

Initially, we followed the literature synthesis procedure that reported the successful encapsulation of carbohydrates into ZIF-8 and structural polymorphs. The specific CH was added to an aqueous solution of 2-methylimidazole (2mIM, 160 mM) then zinc acetate (40 mM in water) was added at ambient temperature to the CH/2mIM solution (Fig. S1, ESI[†]). To ascertain the role of CHs in ZIF-8 formation, we employed varying quantities of sugars and, as an initial test, visually evaluated the opacity of





Scheme 1 Use of carbohydrates (CHs) with 2-methylimidazole (2mIM) and $\text{Zn}(\text{OAc})_2$ to trigger the biomimetic mineralisation and the subsequent formation of carbohydrates encapsulated in ZIF-8 (CHs@ZIF-8).

the solution (Table S2 and Fig. S2, ESI[†]). For the majority of the sugars used, the purported biomimetic mineralisation effects were negligible (Fig. S3–S15, ESI[†]). Only the amino functionalized monosaccharides such as meglumine, and its analogous *N*-methyl-aminoethanol (*i.e.* 7 and 13), showed a consistent increase in turbidity with respect to the control solution (Fig. 1a).

To ascertain the formation of meglumine@ZIF-8 we fixed the concentration of the ZIF-8 precursors while increasing the concentration of the monosaccharide from 0.005 to 0.5 M. The MOF particles prepared in the presence of meglumine were collected by centrifugation, washed with water and ethanol, then dried at ambient pressure and temperature. The powder samples were investigated by X-ray diffraction (XRD) and FTIR. From the XRD analysis a diamondoid topology, **dia**, was observed for a meglumine concentration below 0.05 M; increasing the concentration of meglumine to 0.125 M or above resulted in ZIF-8 of sodalite topology, **sod**. This result suggests that the framework topology depends on the concentration of

meglumine used during the synthesis (Fig. 1a(I)). After washing with water and ethanol, we performed FTIR experiments on samples prepared with different amounts of meglumine (Fig. 1a(II)). Close inspection of the data revealed vibrational bands typical of $\text{Zn}(\text{2mIM})_2$ networks: 3120 and 2926 cm^{-1} (C–H stretching of the methyl imidazole),³² 1420 cm^{-1} (ring stretching of methyl imidazole),³² 900 – 1350 (in plane bending of imidazole ring),^{33,34} 600 – 800 cm^{-1} (out of plane bending of imidazole ring), 421 cm^{-1} (Zn–N stretching).³³ However, we could not detect any infrared absorption band related to meglumine. Thus, despite our observation that the monosaccharide was acting as an initiator for MOF formation, the final crystalline material was found to be a single phase of Zn-imidazolate framework of **dia** or **sod** topology (Fig. 1b). It is worth highlighting that our SAXS investigation of the formation of ZIF-8 with a 0.5 M meglumine concentration did not reveal the presence of a crystalline material; however, a pattern consistent with **sod** was found after washing with ethanol. We monitored the transformation between the amorphous phase into **sod** (Fig. 1c). Despite the origin of the phase transformation remaining unclear, the importance of the washing procedure is demonstrated. For this reason, in this manuscript, the washing procedure used for the different sets of samples is specified.

The XRD and FTIR data lead us to conclude that meglumine, and the analogous *N*-methyl-aminoethanol, triggers the formation of MOF due to the presence of basic amino groups. Indeed, the addition of a base (*e.g.* triethanol amine) to MOF precursor solutions is an established method for the deprotonation of ligands and rapid crystallization of MOFs.^{35,36} Controlling the local formation of base with light (*i.e.* photobase generator), MOF growth was enabled in specific locations;³⁷ this demonstrates that different kinetics of the MOF formation are induced by an exogenous base. To prove this hypothesis, we measured the pH of the precursor solution of the MOF in the presence of an increasing amount of meglumine. We ascertained that

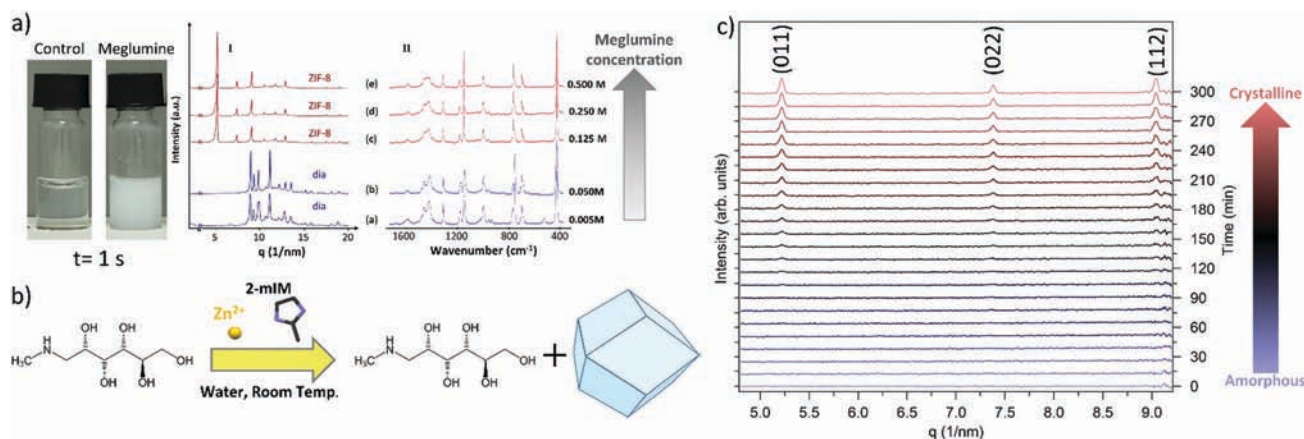


Fig. 1 (a) Photograph of a control sample (2mIM, $\text{Zn}(\text{OAc})_2$, and water) and the same solution in the presence of meglumine, diffraction patterns, and infrared spectra of the $\text{Zn}(\text{2mIM})_2$ produced using different concentrations of meglumine. A topology dependence on the amount of this monosaccharide was observed. (b) Schematic that illustrates meglumine as a crystallization agent. (c) SAXS kinetics that shows the phase transition from amorphous $\text{Zn}(\text{2mIM})_2$ to sodalite triggered by the presence of ethanol. The formation of sodalite was detected by the presence of the three peaks related to the (011), (022), and (112) reflections. The (011) reflection was observed after 120 min from the injection of ethanol in the water suspension of amorphous $\text{Zn}(\text{2mIM})_2$ particles.



the pH of the solution was in the 12–14 range (Table S3, ESI†), thus confirming the basicity of meglumine. Under specific conditions, other monosaccharides (e.g. D-glucose, methyl- α -D-glucopyranoside, D-glucitol, D-gluconic acid δ -lactone, D-glucosamine hydrochloride, N-acetyl-D-glucosamine, and D-xylose) appeared (visual inspection) to promote biomimetic mineralisation; we believe that they influence the ligand deprotonation (see details in Table S3, ESI†). To understand the effect that the preparation methods have, we studied different mixing procedures and reaction temperatures for methyl- α -D-glucopyranoside (5), glucitol (6), and meglumine (7) (Fig. S16–S18, ESI†). While meglumine induced a cloudy solution, inducing solution turbidity with the other CHs required elevated reaction temperature and/or sonication. More importantly, for the entire set of small CHs tested, FTIR analysis carried out on the solid powders after washing (H₂O and EtOH) did not provide any evidence for the encapsulation of CHs within zinc-imidazolate-based MOFs (Fig. S19–S22, ESI†).

Given these data we turned our attention to the role of the CH molecular weight in the formation of CHs@MOFs. We selected a series of dextrans of different molecular weights (*i.e.* 6, 40, and 70 kDa) as potential biomimetic mineralisation agents. Close visual inspection of these reactions gave no indication of rapid MOF formation (Table S4, ESI†). To assess these reactions more quantitatively, we performed a kinetic assessment of particle formation for 40 and 70 kDa dextran using UV-Vis spectroscopy. The solution transmittance was probed with an incident wavelength of 595 nm (Fig. S23, ESI†). No change in transmittance was observed over a time period of 30 min for either dextran. Furthermore, the change in transmittance of the negative control solution (*i.e.* a solution without the biomacromolecules) did not differ significantly from the ones containing the dextran molecules. As a positive control, bovine serum albumin (BSA) was used as the biomacromolecule; in this case, a decrease in the transmitted radiation was measured due to the formation of BSA@MOF particles. Combined, these experiments provide evidence that dextrans, regardless of molecular weight, do not induce the rapid formation of MOF-based biocomposites. To assess if the molecular structure of the polymer could play a role in the formation of a composite, we tested maltodextrin and dextran (Fig. S24, ESI†). Again, no evidence of biomimetic mineralisation was detected. Finally, we investigated solid-state CHs (cellulose) to ascertain if the surface could trigger the formation of ZIF-8. As a control, we used a glass slide. From our SEM images and FTIR investigations at 30 s and 30 min, both substrates were ineffective for inducing the growth of ZIF-8 or its polymorphs; however, within 24 hours some particles can be observed on both glass and cellulose (Fig. S25–S32, ESI†). Despite the different compositions tested and synthetic conditions used, we could not reproduce the result previously reported by Liang *et al.*³¹ Thus, we considered that the challenge of preparing CH@MOFs using a general procedure was unresolved.

Recently, we explored the role of protein surface charge on the biomimetic mineralization of ZIF-8.³⁸ By modifying the protein surface charge *via* succinylation or amination, we

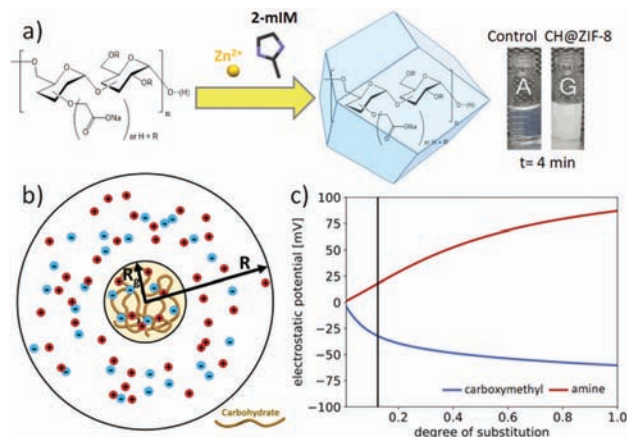


Fig. 2 (a) Schematic of the biomimetic mineralisation of CM-dextran@Zn(2mIM)₂ according to the infrared investigation; photograph of a control sample (2mIM, Zn(OAc)₂ and water) and the same solution in presence of CM-dextran. (b) Schematic of the ion-permeable sphere model of a carbohydrate molecule of radius R_0 used to calculate the electrostatic potential and ion concentrations near the molecule ($R \gg R_0$ is the radius where the potential is assumed to approach zero). (c) Calculated electrostatic potential at the center of the carbohydrate versus degree of carboxymethyl or amino functionalization.

demonstrated that it is possible to trigger or prevent the biomimetic mineralization on several enzymes.³⁸ Inspired by this work, we were motivated to establish whether the chemical functionalization of CHs could produce biomimetic mineralization agents for the preparation of CHs@ZIF-8. Thus, we used commercially available amino- and carboxylate-functionalized dextrans with similar molecular weight (10 kDa and 10–20 kDa, respectively). A 1 : 4 metal-to-ligand ratio was set for consistency with prior experiments. While the amino-functionalized CH did not show evidence of biomimetic mineralisation, the solution containing the dextran with COO[−] functionality (CM-dextran) showed a rapid transition from transparent to opalescent (Fig. 2a and Fig. S33 and related video ESI†). To study the influence of the CM-dextran on the pH, the concentration of the CH was varied in the 0–1.44 mg mL^{−1} range (Fig. S34, ESI†). In presence of the ligand, a *ca.* 3% maximum variation was measured, thus the role of the pH in the formation of the MOF was considered to be negligible.

The powder from the vial was collected *via* centrifugation and washed with water and ethanol (details in ESI†). The dried, powder was then analyzed by FTIR spectroscopy. Characteristic modes of carboxymethyl dextran (CM-dextran) were observed at approximately 1608 cm^{−1} that can be attributed to the COO[−] stretching vibration of CM-dextran,^{38,39} and at 2850–3600 cm^{−1} stretching vibrations of the OH group were observed⁴⁰ (a more comprehensive interpretation of the FTIR spectra is available in Fig. S35 ESI†). This data supports the formation of a MOF biocomposite based on CM-dextran and Zn(2mIM)₂.

To understand the impact of functional group substitution on the likelihood of dextran carbohydrates to seed ZIF-8 formation, we modelled the electrostatic potential and ion concentrations near charged dextrans as a function of their degree of substitution (DS) and the type of chain functionality.



Since most of the pervaded volume occupied by a dextran molecule is expected to be accessible to the ions in solution, we modelled the effect of adding positive charges (for amine functionalization, AM) or negative charges (for carboxymethyl functionalization, CM) to a neutral dextran backbone by calculating the electrostatic potential and electrolyte concentration surrounding an ion-permeable sphere (Fig. 2b) using the Poisson–Boltzmann (PB) equation (details in Fig. S36–S38, ESI†).⁴¹ Fig. 2c shows the electrostatic potential and zinc ion concentration enhancement at the center of the ion-permeable sphere calculated as a function of DS. In this plot, the AM functionalization depletes zinc ions near dextran, while the CM functionalization enhances the Zn^{2+} concentration in and around the biomacromolecule. In particular, at the approximate DS value of the CM-dextran, the zinc ion enhancement is around 10, which was found to lead to ZIF-8 formation around various proteins.⁴² Thus both the computational modelling and experimental results confirm the relevance of CH charge on the biomimetic mineralisation of $Zn(2mIM)_2$ MOFs. As an additional support to the role of the functionalization, COO^- functional groups were used to facilitate the formation of ZIF-8 on polymers and graphene.^{43,44}

Having identified a CH that can be used as a reliable biomimetic mineralisation agent, we turned our attention to understanding the effect of varying the $Zn^{2+}:2mIM$ ratio.

Indeed, in a previous study,¹¹ we noted that the choice of $Zn^{2+}:2mIM$ ratio affords the encapsulation of BSA within networks of different topologies, including amorphous, **sod-**, **dia-** $Zn(2mIM)_2$ and unknown phases (U12, U13, and U14).¹¹ Furthermore, it was experimentally demonstrated that the final topology of the composite can depend on the specific type of biomacromolecule used.¹¹ For the study of this CH@ZIF-8, we prepared solutions using 1:2.52 (A), 1:3.47 (B), 1:4 (C), 1:6 (D), 1:8 (E), and 1:16 (F) $Zn^{2+}:2mIM$ ratios using a fixed concentration of CM-dextran (0.36 mg mL^{-1}). After a reaction time of 24 h, the samples were investigated by XRD (Fig. 3a).

For the sample with the lowest $Zn^{2+}:2mIM$ ratio, the powdery material was found to be a mixture of phases dominated by U12¹¹ and sodalite. The biomineralised powders with 1:3.47 and 1:4 ratios were predominantly sodalite topology. A further increase of the ligand concentration (1:6) produced a pure diamond network that turned into pure sodalite for the highest ratio (1:16). The SEM images in Fig. 3b show that globular particles of *ca.* 8 μm with rough surfaces were obtained for the lowest metal/ligand ratio (1:2.52). Clusters of smaller particles were observed for 1:3.47 and 1:4 ratios (*ca.* 25 and 20 nm, respectively, Fig. S40–S41, ESI†). For the 1:6 ratio a lamellar morphology typically associated with **dia-** $Zn(2mIM)_2$ was observed, with a broad size distribution between 1 and 5 μm . This morphology was partially maintained for the 1:8 ratio,

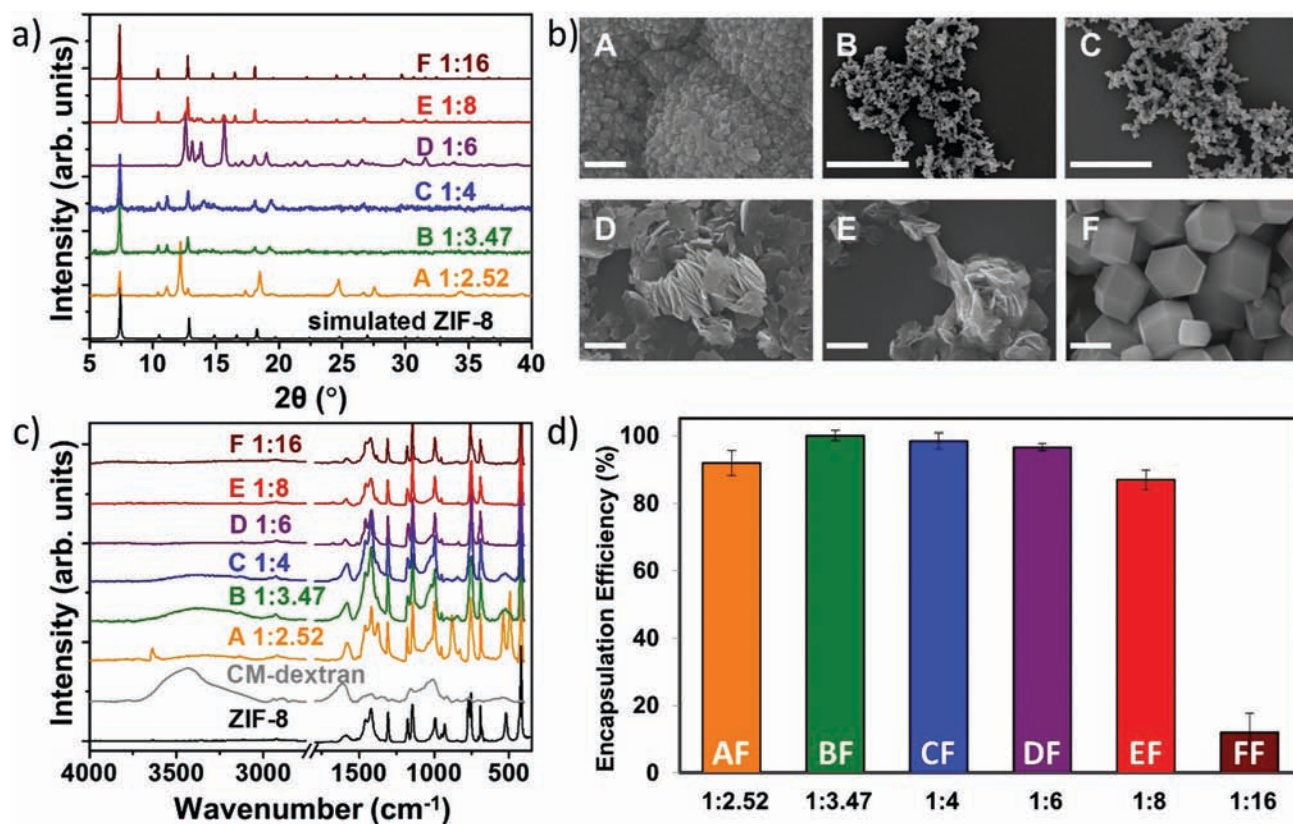


Fig. 3 (a) XRD, (b) SEM, and (c) FTIR of the CM-dextran@ZIF-8 biocomposites obtained with different metal-to-ligand ratios (A = 1:2.52, B = 1:3.47, C = 1:4, D = 1:6, E = 1:8, F = 1:16). SEM scale bar = 2 μm . (d) Encapsulation efficiency of the six systems using FITC-CM-dextran with different metal-to-ligand molar ratios (values are averages of 3 tests). The related powder X-ray diffraction plots can be found in Fig. S39, ESI†



while for 1:16 typical rhombic dodecahedron particles of *ca.* 2.5 μm were noted.

After washing the powders with water and ethanol (procedure optimized for the removal of the CM-dextran adsorbed on the surface of ZIF-8 crystals, S42, ESI[†]), samples were investigated using FTIR spectroscopy (Fig. 3c). The vibrational mode at 421 cm^{-1} , found in all samples, is assigned to the Zn–N stretching mode and thus confirms the networks are composed of 2mIM connected *via* Zn nodes.³³ Additionally, both the COO^- mode at 1608 cm^{-1} and the large OH band in the region 3600–2850 cm^{-1} indicate that CM-dextran is encapsulated. Based on the intensity of the modes engendered by CH, the amount of encapsulated CH was found to depend on the metal-to-ligand ratio. For example, a higher loading of CM-dextran was measured in the sample prepared using $\text{Zn}^{2+}:\text{2mIM} = 1:3.47$. In general, drug loading, also called encapsulation efficiency (EE), is an important parameter in drug delivery as it pertains to the amount of therapeutic within the carrier.⁸ As CH-based therapeutics can be expensive and difficult to prepare,^{45,46} we decided to run a quantitative assessment using a commercially fluorescein isothiocyanate-tagged CM-dextran, here named FITC-CM-dextran. Indeed, the use of FITC allows to use a UV-Vis spectrometer to study the release of the carbohydrate from the composite. The synthesis of the FITC-CM-dextran@ZIF-8 biocomposites was undertaken using all the previously tested $\text{Zn}^{2+}:\text{2mIM}$ ratios: 1:2.52, 1:3.47, 1:4, 1:6, 1:8, and 1:16 (here named samples AF, BF, CF, DF, EF, and FF, respectively). Then, we analysed the reaction supernatant using UV-Vis spectroscopy to quantitatively measure encapsulation efficiency (EE = 100%) at 1:3.47 (Fig. 3d). A progressive decrease in the encapsulated amount of FITC-CM-dextran with increasing concentration of 2mIM was measured. We believe that the progressive decrease in the encapsulation efficiency could be attributed to a competition between heterogeneous (biomolecule-mediated growth) and homogenous nucleation (facilitated by an increased metal-to-ligand ratio); however, further studies are needed to validate this hypothesis.

Based on parameters including a high EE and low amounts of 2mIM, we decided that the best procedure to synthesize CM-dextran@ZIF-8 (sod), was to employ $\text{Zn}^{2+}:\text{2mIM} = 1:3.47$. Using this ratio of MOF precursors we further optimized the reaction conditions by varying the CH concentration. Thus we prepared new samples named B1, B2, B3, and B4 with 0.18, 0.36, 0.72, and 1.44 mg mL^{-1} of CM-dextran solutions, respectively. Photos were taken during the reaction to record visual evidence of biomimetic mineralisation. Simultaneously, a control sample (C, Fig. 4a), with $\text{Zn}^{2+}:\text{2mIM} = 1:3.47$ prepared using the same conditions, excluding CH, was monitored to evaluate the biomimetic mineralisation effect induced by the different concentrations of CM-dextran. Fig. 4a shows photos taken after a reaction time of 2 seconds; all sample solutions (B1, B2, B3, and B4) rapidly turned opalescent confirming that the biomimetic mineralisation occurs.

Increasing the concentration of CM-dextran exceeding 3.24 mg mL^{-1} did not lead to appreciable biomimetic mineralisation; we hypothesize that this could be due to the excess of

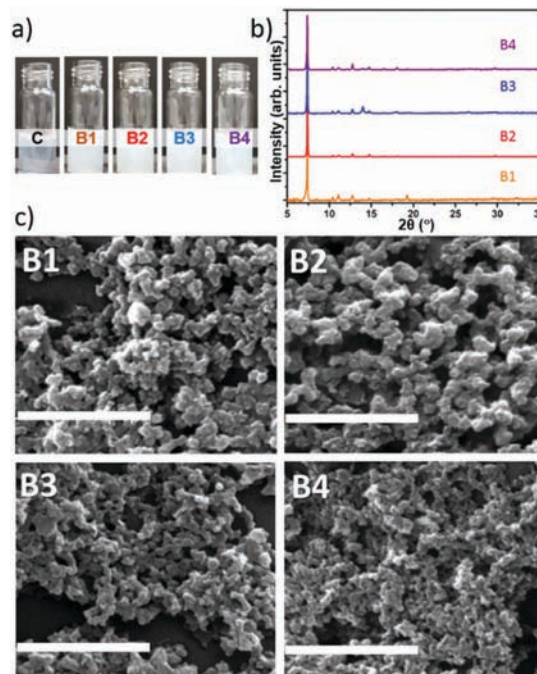


Fig. 4 (a) Photos of samples with metal/ligand ratio 1:3.47 and sugar concentrations of B1 = 0.18, B2 = 0.36, B3 = 0.72, and B4 = 1.44 mg mL^{-1} against control C without sugar. (b) Powder XRD of the same system. (c) SEM of samples B1, B2, B3, and B4 (scale bar: 1 μm).

COO^- removing Zn^{2+} cations from the MOF crystallization process.⁴⁷ After 24 h, the powders were centrifuged from each of the solutions and washed. We noted that different amounts of solid material were produced for each of the conditions (Table S5, ESI[†]). After washing, the powders were studied by FTIR (spectra reported in Fig. S43 ESI[†]). For all samples, vibrational modes attributed to the CH (*e.g.* OH band in the 3650–2850 cm^{-1}) and $\text{Zn}(\text{2mIM})_2$ (*e.g.* Zn–N stretching mode at 421 cm^{-1}) were observed. This indicates that CM-dextran gave rise to CM-dextran@ZIF-8 biocomposites for each of the concentrations. To ascertain the crystallinity of the solid material, XRD analysis was conducted on samples before and after ethanol washing. For the entire set of samples (B1–4) washed only with water, sodalite was the dominant phase obtained (Fig. 4b). This demonstrates the high selectivity of this recipe for the preparation of CM-dextran@ZIF-8.

SEM images revealed the presence of particles with average particles size below 200 nm (Fig. 4c). Although we could not find specific information on the influence the size of ZIF-8 for *in vivo* drug delivery, for other particles, this size has been identified as a critical value; indeed, nanocarriers larger than 200 nm have been shown to accumulate in the liver and spleen.⁴⁸

To study the EE as a function of the CH concentration, FITC-CM-dextran was used as a biomimetic mineralisation agent for the preparation of a set of biocomposites equivalent to the previously prepared set B. The samples prepared with FITC-CM-dextran were named set BF (*i.e.* BF1, BF2, BF3, BF4). The powders were investigated *via* SEM; surprisingly larger particles were formed (Fig. S44, ESI[†]). The confocal microscope (CLSM)



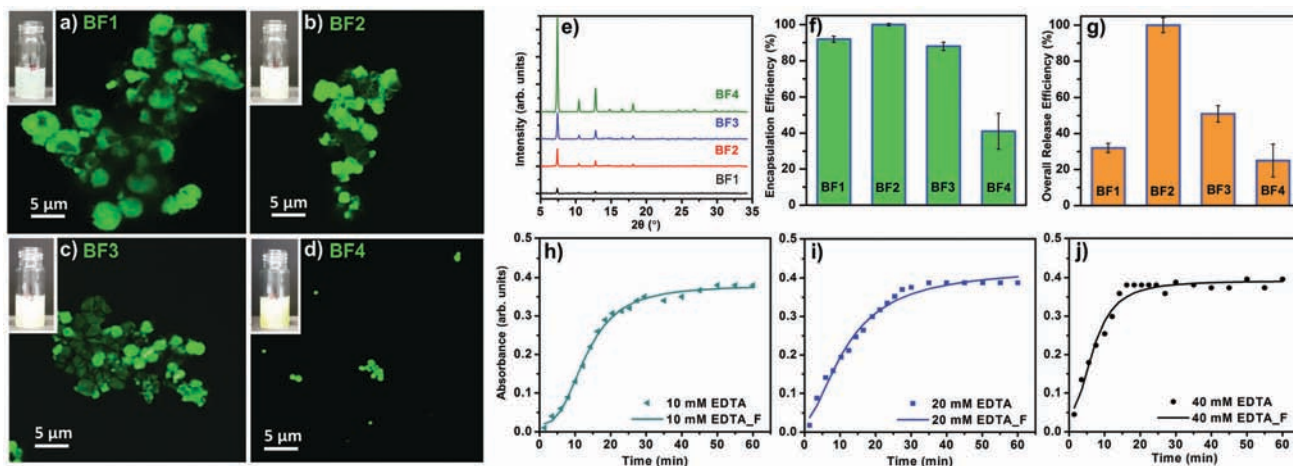


Fig. 5 (a–d) Confocal microscopy images of sample B obtained using metal-to-ligand ratio 1 : 3.47 and FITC-CM-dextran at various concentrations (BF1 = 0.18, BF2 = 0.36, BF3 = 0.72, BF4 = 1.44 mg mL⁻¹). (e) Powder XRD of the same system. (f) Encapsulation efficiency for each system (values are averages of 3 tests). (g) Overall release of the FITC-CM-dextran with respect to the original concentration used for the biomimetic mineralisation (values are averages of 3 tests). (h–j) Different release profiles on the sample BF2 using 10, 20, and 40 mM of EDTA.

confirms the different particle size (Fig. 5a–d); this variation from CM-dextran was attributed to the chemical modification of the polysaccharide.

The homogenous luminescence across the particles confirm the even distribution of the FITC-CM-dextran within the ZIF-8 particles. A PXRD analysis confirms the dominant *sod* topology for all the BF samples (Fig. 5e).

Considering the relevance of the EE in the delivery of biotherapeutics,⁴⁹ we determined the amount of FITC-CM-dextran encapsulated in ZIF-8. The assessment was performed using UV-Vis and the Lambert–Beer law with an experimental calibration of different concentrations of FITC-CM-dextran (see ESI†). As shown in Fig. 5f, the measured EE was influenced by the concentrations of the FITC-CM-dextran used as the biomimetic mineralisation agent. Intermediate concentrations of FITC-CM-dextran lead to higher EE: *ca.* 100% of the FITC-CM-dextran was encapsulated in case of BF2. For the lowest and the higher concentrations of biomacromolecules, the EE dropped to *ca.* 40% (sample BF4). We then turned our efforts to CH release. Due to the density of COO⁻ in the CH and the affinity for Zn²⁺ cations, we decided to investigate the amount of model drug available as a therapeutic that could be re-dissolved into its original molecular form. The dissolution process was performed leaving the biocomposites in presence of EDTA for 1 h (ESI†) at room temperature. In all cases, after etching the particles, a visual inspection revealed transparent solutions without a detectable amount of precipitate. Using UV-Vis, we calculated the percentage of FITC-CM-dextran from the correspondent CH@ZIF-8 (Fig. 5g). Again, BF2 showed the best performance as 100% of the loaded CH was available in solution after the release. For all the other samples, a percentage of the FITC-CM-dextran ranging from 25 to 51% was not available as a molecule in solution because of the combined losses during the encapsulation and release processes. We hypothesize that, during the dissolution of CH@ZIF-8, because of the strong affinity of carboxy-methyl functional groups with cations,⁵⁰ FITC-CM-dextran could coordinate Zn²⁺ to form

insoluble products. Because of the ideal release performance of BF2, this sample was tested to investigate the controlled release profiles, which is another important property for drug release systems.⁵¹ We used 3 different concentrations of EDTA (*i.e.* 10, 20 and 40 mM), and measured the release profile.

In Fig. 5h–j, the experimental data were fitted with a logistic fitting function that can be used in systems in which the dissolution of the carrier is involved.⁵² In particular, this model is appropriate for ZIF-8 as it is used for hydrophobic carriers.^{53–55} For the 10 mM EDTA solution, roughly 15 min were required to release 50% of the model drug; the remaining *ca.* 50% was released within 40 min. Using the 20 mM EDTA solution, in 10 min *ca.* 50% of the FITC-CM-dextran was released, while *ca.* 100% release was measured in 30 min. A further increase of the EDTA concentration (40 mM) afforded the release of 50% of the model CH in *ca.* 7 min; in 16 min a *ca.* 100% was released. These values prove that the release profile depends on the EDTA concentration, thus we demonstrated that a controlled release of CH encapsulated into ZIF-8 is possible. To ascertain the release properties using a different medium, a 100 mM sodium citrate solution (pH = 6) was tested and the release of FITC-CM-dextran from the MOF biocomposite was successfully measured (S45, ESI†).

In conclusion, we have shown that a large number of CHs do not work as biomimetic mineralisation agents. However, CHs decorated with COO⁻ functional groups can be employed reproducibly for the encapsulation of carbohydrates in MOFs (CH@MOFs). From our simulations this is can be attributed to a coulombic attraction between the functional groups and Zn²⁺ cations. By assessing synthesis conditions using different Zn²⁺:2mIM ratios and concentrations of carboxymethyl-dextran (CM-dextran) as the biomimetic mineralisation agent, we optimized a system that can form CH@ZIF-8 directly in water. We used a fluorescein isothiocyanate (FITC) tagged CM-dextran (FITC-CM-dextran) and determined conditions for the 100% encapsulation and 100% release of the model carbohydrate therapeutic.



Lastly, by varying the amount of EDTA, different release profiles were measured, showing a direct dependence between the concentration of the chelating agent and the release rate. As CHs play a number of relevant biological roles, we believe that this discovery will pave the way for the preparation of a new class of MOF-biocomposites for the delivery of carbohydrate-based biotherapeutics and for the choice of the specific CHs involved in glyco-engineering processes.

Author contributions

E. A., M. T., R. R., K. A., W. L., T. W. prepared and characterized samples, A. C. and H. A. characterized the material, H. S. and J. R. characterized part of the samples with SEM. A. T. and D. H. modeled the system, C. H. supervised part of the experiments, C. D. and P. F. conceived the idea, supervised experiments, and drafted the manuscript.

Conflicts of interest

The authors confirm that there are no conflicts to declare.

Acknowledgements

This work was supported by the Australian Research Council under the Discovery Projects Scheme (DP170103531). E. A. acknowledges the Austrian Agency for International Cooperation in Education and Research (OeAD-GmbH) for the PhD scholarship. A. T. acknowledges the Australian Government for a Research Training Program Scholarship and CSIRO Materials Science and Engineering for a PhD top-up scholarship. Chaitanya Tabib is acknowledged for the support in the laboratory. K. A. and C. H. acknowledge NHMRC (APP1098867, APP1078118). P. F. acknowledges TU Graz for the Lead Project (LP-03). R. R. acknowledges the European Union's Horizon 2020 research and innovation programme under the Marie Skłodowska-Curie grant agreement #748649 (project "MNEMONIC"). The research leading to these results has received funding from the European Research Council under the European Union's Horizon 2020 Programme (FP/2014-2020)/ERC Grant Agreement no. 771834 – POPCRYSTAL. The authors acknowledge support from the European Union's Horizon 2020 FETOPEN-1-2016-2017 research and innovation program under grant agreement 801464.

Notes and references

- H. Furukawa, K. E. Cordova, M. O'Keeffe and O. M. Yaghi, *Science*, 2013, **341**, 1230444.
- J. A. Mason, M. Veenstra and J. R. Long, *Chem. Sci.*, 2014, **5**, 32–51.
- J. Gascon, A. Corma, F. Kapteijn and F. X. Llabrés i Xamena, *ACS Catal.*, 2014, **4**, 361–378.
- J.-R. Li, R. J. Kuppler and H.-C. Zhou, *Chem. Soc. Rev.*, 2009, **38**, 1477.
- Q.-L. Zhu and Q. Xu, *Chem. Soc. Rev.*, 2014, **43**, 5468–5512.
- P. Falcaro, R. Ricco, A. Yazdi, I. Imaz, S. Furukawa, D. Maspoch, R. Ameloot, J. D. Evans and C. J. Doonan, *Coord. Chem. Rev.*, 2016, **307**, Part 2, 237–254.
- C. Doonan, R. Riccò, K. Liang, D. Bradshaw and P. Falcaro, *Acc. Chem. Res.*, 2017, **50**, 1423–1432.
- R. Riccò, W. Liang, S. Li, J. J. Gassensmith, F. Caruso, C. Doonan and P. Falcaro, *ACS Nano*, 2018, **12**, 13–23.
- P. Horcajada, R. Gref, T. Baati, P. K. Allan, G. Maurin, P. Couvreur, G. Férey, R. E. Morris and C. Serre, *Chem. Rev.*, 2012, **112**, 1232–1268.
- M. Lismont, L. Dreesen and S. Wuttke, *Adv. Funct. Mater.*, 2017, **27**, 1606314.
- W. Liang, R. Ricco, N. K. Maddigan, R. P. Dickinson, H. Xu, Q. Li, C. J. Sumbly, S. G. Bell, P. Falcaro and C. J. Doonan, *Chem. Mater.*, 2018, **30**, 1069–1077.
- S. K. Alsaiani, S. Patil, M. Alyami, K. O. Alamoudi, F. A. Aleisa, J. S. Merzaban, M. Li and N. M. Khashab, *J. Am. Chem. Soc.*, 2018, **140**, 143–146.
- F. Lyu, Y. Zhang, R. N. Zare, J. Ge and Z. Liu, *Nano Lett.*, 2014, **14**, 5761–5765.
- F.-K. Shieh, S.-C. Wang, C.-I. Yen, C.-C. Wu, S. Dutta, L.-Y. Chou, J. V. Morabito, P. Hu, M.-H. Hsu, K. C.-W. Wu and C.-K. Tsung, *J. Am. Chem. Soc.*, 2015, **137**, 4276–4279.
- S. Li, M. Dharmarwardana, R. P. Welch, Y. Ren, C. M. Thompson, R. A. Smaldone and J. J. Gassensmith, *Angew. Chem., Int. Ed.*, 2016, **55**, 10691–10696.
- C. Wang, S. Tadepalli, J. Luan, K.-K. Liu, J. J. Morrissey, E. D. Kharasch, R. R. Naik and S. Singamaneni, *Adv. Mater.*, 2017, **29**, 1604433.
- C. Wang, H. Sun, J. Luan, Q. Jiang, S. Tadepalli, J. J. Morrissey, E. D. Kharasch and S. Singamaneni, *Chem. Mater.*, 2018, **30**, 1291–1300.
- K. Liang, J. J. Richardson, J. Cui, F. Caruso, C. J. Doonan and P. Falcaro, *Adv. Mater.*, 2016, **28**, 7910–7914.
- K. Liang, R. Ricco, C. M. Doherty, M. J. Styles, S. Bell, N. Kirby, S. Mudie, D. Haylock, A. J. Hill, C. J. Doonan and P. Falcaro, *Nat. Commun.*, 2015, **6**, 7240.
- A. Varki, *Glycobiology*, 2017, **27**, 3–49.
- H. H. Freeze, *Nat. Rev. Genet.*, 2006, **7**, 537–551.
- H. M. I. Osborn, P. G. Evans, N. Gemmell and S. D. Osborne, *J. Pharm. Pharmacol.*, 2004, **56**, 691–702.
- S. Mitragotri, P. A. Burke and R. Langer, *Nat. Rev. Drug Discovery*, 2014, **13**, 655–672.
- R. Duncan, *Nat. Rev. Drug Discovery*, 2003, **2**, 347–360.
- E. Maverakis, K. Kim, M. Shimoda, M. E. Gershwin, F. Patel, R. Wilken, S. Raychaudhuri, L. R. Ruhaak and C. B. Lebrilla, *J. Autoimmun.*, 2015, **57**, 1–13.
- R. J. Solá and K. Griebenow, *J. Pharm. Sci.*, 2009, **98**, 1223–1245.
- L. Zhang, S. Luo and B. Zhang, *mAbs*, 2016, **8**, 205–215.
- A. Chandrasekaran, A. Srinivasan, R. Raman, K. Viswanathan, S. Raguram, T. M. Tumpey, V. Sasisekharan and R. Sasisekharan, *Nat. Biotechnol.*, 2008, **26**, 107–113.
- K. W. Moremen, A. Ramiah, M. Stuart, J. Steel, L. Meng, F. Forouhar, H. A. Moniz, G. Gahlay, Z. Gao, D. Chapla, S. Wang, J.-Y. Yang, P. K. Prabhakar, R. Johnson, M. dela



- Rosa, C. Geisler, A. V. Nairn, J. Seetharaman, S.-C. Wu, L. Tong, H. J. Gilbert, J. LaBaer and D. L. Jarvis, *Nat. Chem. Biol.*, 2017, **14**, 156–162.
- 30 A. O. Tzianabos, *Clin. Microbiol. Rev.*, 2000, **13**, 523–533.
- 31 K. Liang, R. Wang, M. Boutter, C. M. Doherty, X. Mulet and J. J. Richardson, *Chem. Commun.*, 2017, **53**, 1249–1252.
- 32 Y. Hu, H. Kazemian, S. Rohani, Y. Huang and Y. Song, *Chem. Commun.*, 2011, **47**, 12694.
- 33 Z.-X. Low, J. Yao, Q. Liu, M. He, Z. Wang, A. K. Suresh, J. Bellare and H. Wang, *Cryst. Growth Des.*, 2014, **14**, 6589–6598.
- 34 M. Jian, B. Liu, R. Liu, J. Qu, H. Wang and X. Zhang, *RSC Adv.*, 2015, **5**, 48433–48441.
- 35 L. Huang, *Microporous Mesoporous Mater.*, 2003, **58**, 105–114.
- 36 M. J. C. Ordoñez, K. J. Balkus, J. P. Ferraris and I. H. Musselman, *J. Membr. Sci.*, 2010, **361**, 28–37.
- 37 B. K. Keitz, C. J. Yu, J. R. Long and R. Ameloot, *Angew. Chem., Int. Ed.*, 2014, **53**, 5561–5565.
- 38 A. Repko, D. Nižňanský, I. Matulková, M. Kalbáč and J. Vejpravová, *J. Nanopart. Res.*, 2013, **15**, 1767.
- 39 Y.-X. Sun, X.-Z. Zhang, H. Cheng, S.-X. Cheng and R.-X. Zhuo, *J. Biomed. Mater. Res., Part A*, 2008, **84A**, 1102–1110.
- 40 A. N. J. Heyn, *Biopolymers*, 1974, **13**, 475–506.
- 41 F. T. Wall and J. Berkowitz, *J. Chem. Phys.*, 1957, **26**, 114–122.
- 42 N. K. Maddigan, A. Tarzia, D. M. Huang, C. J. Sumby, S. G. Bell, P. Falcaro and C. J. Doonan, *Chem. Sci.*, 2018, **9**, 4217–4223.
- 43 H. Ren, L. Zhang, J. An, T. Wang, L. Li, X. Si, L. He, X. Wu, C. Wang and Z. Su, *Chem. Commun.*, 2014, **50**, 1000–1002.
- 44 T. Tsoufis, C. Tampaxis, I. Spanopoulos, T. Steriotis, F. Katsaros, G. Charalambopoulou and P. N. Trikalitis, *Microporous Mesoporous Mater.*, 2018, **262**, 68–76.
- 45 *Carbohydrate-based drug discovery*, ed. C.-H. Wong, Wiley-VCH, Weinheim, New York, 2003.
- 46 A. Dove, *Nat. Biotechnol.*, 2001, **19**, 913–917.
- 47 D. Huang, W. Wang and A. Wang, *Adsorpt. Sci. Technol.*, 2013, **31**, 611–623.
- 48 E. Blanco, H. Shen and M. Ferrari, *Nat. Biotechnol.*, 2015, **33**, 941–951.
- 49 S. D. Putney and P. A. Burke, *Nat. Biotechnol.*, 1998, **16**, 153–157.
- 50 R. A. A. Muzzarelli, F. Tanfani, M. Emanuelli and S. Mariotti, *Carbohydr. Res.*, 1982, **107**, 199–214.
- 51 S. J. Wallace, J. Li, R. L. Nation and B. J. Boyd, *Drug Delivery Transl. Res.*, 2012, **2**, 284–292.
- 52 F. O. Costa, J. J. S. Sousa, A. A. C. C. Pais and S. J. Formosinho, *J. Controlled Release*, 2003, **89**, 199–212.
- 53 K. Ghosal, A. Nanda and A. Chandra, *Pharmazie*, 2012, **67**, 147–155.
- 54 K. Zhang, R. P. Lively, C. Zhang, R. R. Chance, W. J. Koros, D. S. Sholl and S. Nair, *J. Phys. Chem. Lett.*, 2013, **4**, 3618–3622.
- 55 A. U. Ortiz, A. P. Freitas, A. Boutin, A. H. Fuchs and F.-X. Coudert, *Phys. Chem. Chem. Phys.*, 2014, **16**, 9940–9949.



Supporting Info

Carbohydrates@MOFs

Efwita Astria^{1‡}, Martin Thonhofer^{1,2‡}, Raffaele Ricco¹, Weibin Liang³, Angela Chemelli⁴, Andrew Tarzia³, Karen Alt⁵, Christoph E. Hagemeyer⁵, Johannes Rattenberger⁶, Hartmuth Schroettner⁶, Tanja Wrodnigg⁷, Heinz Amenitsch⁴, David M. Huang³, Christian J. Doonan^{3*}, Paolo Falcaro^{1,3*}

1) Institute of Physical and Theoretical Chemistry, Graz University of Technology, 8010 Graz, Austria 2) Laboratory for Characterisation and Processing of Polymer, Faculty of Mechanical Engineering, University of Maribor, SI-2000, Maribor, Slovenia 3) Department of Chemistry, The University of Adelaide, 5005 Adelaide, South Australia 4) Institute of Inorganic Chemistry, Graz University of Technology, 8010 Graz, Austria 5) Australian Centre for Blood Diseases, Monash University, Melbourne, Australia 6) Graz Centre for Electron Microscopy (ZFE), 8010 Graz, Austria 7) Institute of Organic Chemistry, Graz University of Technology, 8010 Graz, Austria.

CONTENTS:

Experimental Section

Table S1. Tested monosaccharides.

Table S2. Calculated amounts of the respective monosaccharides for the preparation of different concentrations in a 2mIM solution.

Table S3. pH-values of the respective reaction mixtures.

Table S4. Tested Polysaccharides.

Table S5. Yield of CM-dextran@ZIF-8 B recipe.

Table S6. Parameters of the ion-permeable sphere model of dextrans.

Figure S1. Schematic overview of the performed MOF-synthesis.

Figure S2. General schematic of the performed photo-series.

Figure S3. Time-dependent MOF formation induced by different carbohydrates (1.250 M in total).

Figure S4. Time-dependent MOF formation induced by different carbohydrates (0.50 M in total).

Figure S5. Time-dependent MOF formation induced by different carbohydrates (0.250 M in total).

Figure S6. Time-dependent MOF formation induced by different carbohydrates (0.050 M in total).

Figure S7. Time-dependent MOF formation induced by different carbohydrates (0.005 M in total).

Figure S8. Time-dependent MOF formation induced by different concentrations of D-Glucose (**1**) at different concentrations.

Figure S9. Time-dependent MOF formation induced by different concentrations of Methyl α -D-Glucopyranoside (**5**) at different concentrations.

- Figure S10.** Time-dependent MOF formation induced by different concentrations of D-Glucitol (**6**) at different concentrations.
- Figure S11.** Time-dependent MOF formation induced by different concentrations of D-Gluconic acid- δ -lactone (**11**) at different concentrations.
- Figure S12.** Time-dependent MOF formation induced by different concentrations of Meglumine (**7**) at different concentrations.
- Figure S13.** Time-dependent MOF formation induced by different concentrations of D-Glucosamine HCl (**9**) at different concentrations.
- Figure S14.** Time-dependent MOF formation induced by different concentrations of *N*-Acetyl-D-glucosamine (**8**) at different concentrations.
- Figure S15.** Time-dependent MOF formation induced by different concentrations of D-Xylose (**4**) at different concentrations.
- Figure S16.** Comparison of different conditions during the MOF-synthesis supported by Methyl- α -D-glucopyranoside (**5**).
- Figure S17.** Comparison of different conditions during the MOF-synthesis supported by Glucitol (**6**).
- Figure S18.** Comparison of different conditions during the MOF-synthesis supported by Meglumine (**7**).
- Figure S19.** Schematic overview of the general procedure for the preparation of zeolitic frameworks.
- Figure S20.** FTIR-spectra of the observed products.
- Figure S21.** FTIR-spectra of the respective tested monosaccharides.
- Figure S22.** FTIR-spectra of: a) Maltodextrin, compared with the obtained products b) 5 mg/mL, c) 10 mg/mL, and d) 20 mg/mL of Maltodextrin supported ZIF-8 formation.
- Figure S23.** Kinetic tests using different Dextrans at various concentrations for the investigation of their biomimetic mineralization effects.
- Figure S24.** Photographs of solutions using the polysaccharides with different molecular weights (Dextrans and Maltodextrin).
- Figure S25.** Screenshot of synthesis of ZIF-8 with the Zn^{2+} :2mIM = 1:4 at 30 second, 30 minutes and 24 hours on paper and glass plate.
- Figure S26.** SEM image of the product using Zn^{2+} :2mIM = 1:4 on glass surface after 30 second (scale bar = 25 μm).
- Figure S27.** SEM image of the product using Zn^{2+} :2mIM = 1:4 on glass surface after 30 minutes (scale bar = 25 μm).
- Figure S28.** SEM image of the product using Zn^{2+} :2mIM = 1:4 on glass surface after 24 hours (scale bar = 25 μm).
- Figure S29.** SEM image of the product using Zn^{2+} :2mIM = 1:4 on paper after 30 second (scale bar = 25 μm).
- Figure S30.** SEM image of the product using Zn^{2+} :2mIM = 1:4 on paper after 30 minutes (scale bar = 25 μm).
- Figure S31.** SEM image of the product using Zn^{2+} :2mIM = 1:4 on paper after 24 hours (scale bar = 25 μm).
- Figure S32.** FTIR Spectra of paper (S&S filter paper 110 mm) with Zn^{2+} :2mIM = 1:4 after 30 second, 30 minutes and 24 hours compared with ZIF-8.
- Figure S33.** Photographs of solutions using the polysaccharides with different molecular weights and chemical functionalizations.

Figure S34. The pH of CM-dextran (0, 0.18, 0.36, 0.72, 1.44 mg/mL) in H₂O and 2mIM solutions with total volume 2 mL.

Figure S35. FTIR spectra of CM-dextran@ZIF-8 (Zn²⁺:2mIM = 1:4)

Figure S36. Schematic of the ion-permeable spherical model of a carbohydrate chain with a radius of gyration (R_g) in an electrolyte solution. The electrostatic potential was taken to be zero at a large distance, R , from the centre of the ion-permeable sphere.

Figure S37. Volume charge density (ρ_s) of the ion-permeable spheres as a function of degree of substitution for carboxymethyl (CM) and amine (AM) functionalities.

Figure S38. Calculated Zn²⁺ ion enhancement at the center of the carbohydrate versus degree of carboxymethyl or amino functionalization.

Figure S39. XRD of the FITC-CM-dextran@ZIF-8 biocomposites obtained with different metal-to-ligand ratios (AF=1:2.52, BF=1:3.47, CF=1:4, DF=1:6, EF=1:8, FF=1:16).

Figure S40. SEM images of B sample (Zn²⁺:2mIM = 1:3.47).

Figure S41. SEM images of C sample (Zn²⁺:2mIM = 1:4).

Figure S42. Schematic illustration of sugar on the surface of ZIF-8.

Figure S43. FTIR spectra of various CM-dextran@ZIF-8 B recipes (Zn²⁺:2mIM = 1:3.47).

Figure S44. SEM image of ZIF-8 prepared using different concentrations of FITC-tagged CM-dextran: B1= 0.18, B2= 0.36, B3= 0.72 and B4= 1.44 mg mL⁻¹.

Figure S45. Release test of FITC-CM-dextran@ZIF-8 with 100 mM of citrate buffer (pH = 6).

Figure S46. The UV-VIS absorbance of FITC-CM-dextran after adding EDTA, Zn(OAc)₂·2H₂O and 2mIM.

Figure S47. Correction Factor based on 2mIM was determined by measuring the absorbance intensity of FITC-CM-dextran at different concentrations of EDTA (10, 20, 40 mM) after adding 2mIM with different volumes.

Experimental Section

Materials

D-glucose (**1**), D-mannose (**2**), D-galactose (**3**), D-xylose (**4**), methyl- β -D-glucopyranoside, (**5**) D-glucitol (**6**), meglumine (**7**), *N*-acetyl-D-glucosamine (**8**), D-glucosamine hydrochloride (**9**), sucrose (**10**), maltodextrin (**11**, approximately 20 α -1,4-D-glucose units), ethylene glycol (**12**) and *N*-methylaminoethanol (**13**), Carboxymethyl dextran (**CM-dextran**, average Mol. Wt: 10.000-20.000), FITC-tagged carboxymethyl dextran (**FITC-CM-dextran**, average Mol. Wt: 40.000, 1-8 mmol FITC/mol glucose, carboxymethyl groups content: 3-7%), and EDTA disodium salt were purchased from Sigma-Aldrich. Zinc acetate dihydrate (**Zn(OAc)₂·2H₂O**) was purchased from Merck Millipore. 2-Methylimidazole (**2mIM**) was purchased from TCI chemicals. MOFs growth on paper was performed using 589³ Blue ribbon S&S Filter paper circles ($\varnothing = 110$ mm). All solutions were prepared in deionized water (DI Water). Absolute ethanol for washings was purchased from Fisher Scientific and used without further purification. Unless otherwise specified, all reactions were conducted into 2mL plastic Eppendorf vials.

General procedure for the preparation of monosaccharides@ZIF-8

In 20 mL glass vials, compounds **1-13** were dissolved in 5 mL of aqueous solutions of 2mIM (initial concentration: 160 mM) to provide different sugar concentrations ranging from 0.01 M to 1 M. After 30 min, 5 mL of aqueous solutions of Zn(OAc)₂·2H₂O (initial concentration: 40 mM) were added at once, and the reaction mixtures left to stir at room temperature on a tube rotator at 20 rpm. After 12 h, 20 mL of EtOH were added dropwise (within 15 min), and the reaction mixtures rotated for additional 8 h. The formed particles were concentrated by centrifugation (5750 rcf, 7 minutes) and washed with water (3x 7 mL) and EtOH (3x 7 mL) respectively. The resulting white powders were dried for 24 h at ambient pressure and temperature.

Attempted synthesis of dextrans@ZIF-8

The solution of 2mIM (initial concentration 160 mM) was mixed with dextran sugars in 1 mL DI water. The separate solution of Zn(OAc)₂·2H₂O (initial concentration: 40 mM, 1 mL) was also prepared. The two solutions were mixed and left at room temperature for 24 hours without stirring. Details on the substrates used are reported in Supporting Table S4

Growth @ZIF-8 on glass and paper substrates

The aqueous solution of 2mIM (initial concentration: 160 mM, 6 mL) was mixed with Zn(OAc)₂·2H₂O (initial concentration: 40 mM, 6 mL), a glass plate (vial **a**), CM-dextran 0.36 mg/mL (vial **b**) and a piece of paper (589³ Blue ribbon S&S Filter paper circles 110 mm) (vial **c**). The video screenshots were taken at 30 second, 30 minutes and 24 hours.

Synthesis of CM-dextran@ZIF-8 (CM@ZIF-8) with different ligand/metal ratios

CM@ZIF-8 samples were synthesized by mixing aqueous stock solutions of 2mIM (initial concentration: 3.84 M) and CM-dextran (final amount: 0.36 mg/mL), adding water when necessary, according to the different final ratios of ligand and metal chosen (2mIM/Zn²⁺ = 2.52, 3.47, 4, 6, 8, 16). The solutions were stirred in vortex mixer for three seconds. Subsequently, a stock solution of Zn(OAc)₂·2H₂O (initial

concentration: 0.24 M) was added. Total final volume for each sample was 2 mL. The solutions were briefly vortex-mixed (three seconds) and left standing at room temperature (no stirring) for 24 hours. The precipitates were collected by centrifugation (9660 rcf, 5 min), washed with DI water (3x), ethanol (3x). The resulting white powders were dried for 24 h at ambient pressure and temperature.

Synthesis of CM@ZIF-8 “B series”

Samples with the ratio $Zn^{2+}:2mIM = 1:3.47$ were prepared by mixing $Zn(OAc)_2 \cdot 2H_2O$ solution (initial concentration: 105.5 mM, 1 mL) with 2mIM aqueous solution (initial concentration: 30.4 mM, 1 mL) and CM-dextran solutions (Final amount: 0.36 mg/mL reaching final amounts as follows: B1 = 0.18, B2 = 0.36, B3 = 0.72, B4 = 1.44 mg/mL). Total final volume for each sample was 2 mL. The solutions were briefly vortex-mixed (three seconds) and left standing at room temperature (no stirring) for 24 hours. The precipitates were collected by centrifugation (9660 rcf, 5 min), washed with DI water (3x), ethanol (3x). The resulting white powders were dried for 24 h at ambient pressure and temperature.

Synthesis of FITC-CM-dextran@ZIF-8 (FITC-CM@ZIF-8) “BF series”

Synthesis of FITC-CM@ZIF-8 was analogous to synthesis of CM@ZIF-8 “B series”, but using FITC-CM-dextran in place of CM-dextran, and under the same conditions. Total final volume for each sample was 2 mL. The solutions were briefly vortex-mixed (three seconds) and left standing at room temperature (no stirring) for 24 hours. The precipitates were collected by centrifugation (9660 rcf, 5 min), washed with DI water (3x), ethanol (3x) and used for the further release tests.

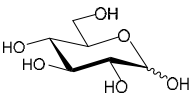
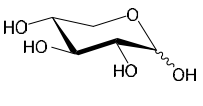
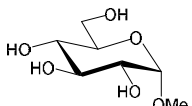
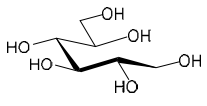
Washing Procedure Optimization

A suspension of ZIF-8 (3.4 mg/mL, 45 mL) was mixed with CM-dextran solution (36 mg/mL, 3 mL), and left at room temperature for 1 hour. 2 mL aliquots were taken and washed with water (1x, or 3x) or ethanol (3x). An additional aliquot of 30 mL was equally divided into 3 vials, and each of them was consecutively washed with water, and ethanol, and the solid residuals immersed in SDS (0.1%, 1% and 10%, respectively) for 30 minutes. After centrifugation, the supernatants were removed and the precipitates were washed 2x with MOPS (3-(*N*-morpholino)propanesulfonic acid) buffer (10 mM, pH = 7.4), and 2x with ethanol (see **Figure S42**).

Release tests of FITC-CM@ZIF-8 “BF2 sample” by different amounts of EDTA

BF2 samples were washed 3X with DI Water then mixed with 600 μ L DI water. For each BF2 samples, 600 μ L EDTA solution (initial concentrations: 20, 40, 80 mM) was added afterwards. The sample was vortex-mixed for three seconds. At regular intervals of 1 hour, the mixture was centrifuged (11337 rcf, 1 min), and 1 mL of the supernatant taken with micropipettes. The absorbance was measured by UV-VIS spectroscopy (Thermo Scientific Nano Drop One^c, λ_{max} : 490 nm).

Table S1. Tested monosaccharides.

			
D-Glucose	D-Xylose	Methyl- α -D-glucopyranoside	D-Glucitol
1	4	5	6

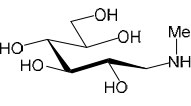
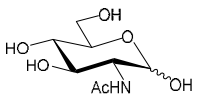
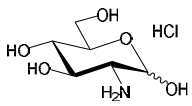
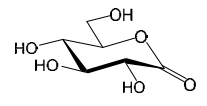
			
Meglumine	<i>N</i> -Acetyl-D-glucosamine	D-Glucosamine hydrochloride	D-Gluconic acid- δ -lactone
7	8	9	11

Table S2. Calculated amounts of the respective monosaccharides for the preparation of different concentrations in a 2mIM solution.

The concentrations of carbohydrate listed in **Table S2** are related to the 1st precursor solution (2mIM). Due to the dilution in the next step (addition of the same volume of the 2nd precursor solution (Zn(OAc)₂), the final concentration halves. These final, total concentrations are given in the following pictures and tables.

Compound	1	4	5	6	7	8	9	11	
M (g/mol)	180,16	150,13	194,18	182,17	195,21	221,21	215,63	178,14	
m (g)	0,4504	0,3753	0,4855	0,4554	0,4880	0,2765	0,2695	0,4454	A
Vol (mL)	1	1	1	1	1	1	1	1	
c (mol/L)	2,5	2,5	2,5	2,5	2,5	1,25 ¹⁾	1,25 ¹⁾	2,5	
m (g)	0,3603	0,3003	0,3884	0,3643	0,3904	0,4424	0,4313	0,3563	
Vol (mL)	2	2	2	2	2	2	2	2	B
c (mol/L)	1	1	1	1	1	1	1	1	
Vol _B (mL)	0.5	0.5	0.5	0.5	0.5	0.5	0.5	0.5	C
Vol _{2mIM} (mL)	0.5	0.5	0.5	0.5	0.5	0.5	0.5	0.5	
c (mol/L)	0.5	0.5	0.5	0.5	0.5	0.5	0.5	0.5	
Vol _B (mL)	0.1	0.1	0.1	0.1	0.1	0.1	0.1	0.1	D
Vol _{2mIM} (mL)	0.9	0.9	0.9	0.9	0.9	0.9	0.9	0.9	
c (mol/L)	0.1	0.1	0.1	0.1	0.1	0.1	0.1	0.1	
Vol _B (mL)	0.01	0.01	0.01	0.01	0.01	0.01	0.01	0.01	E
Vol _{2mIM} (mL)	0.99	0.99	0.99	0.99	0.99	0.99	0.99	0.99	
c (mol/L)	0.01	0.01	0.01	0.01	0.01	0.01	0.01	0.01	

Table S3. pH-values of the respective reaction mixtures.

	1	4	5	6	7	8	9	11	Final concentration
	D-Glucose	D-Xylose	Methyl- α -D-glucopyranoside	D-Glucitol	Meglumine	N-Acetyl-D-glucosamine	D-glucosamine hydrochloride	D-Gluconic acid δ -lactone	
A	10	10	10	10	14	10	6	1	1.250 M
B	10	10	10	10	14	10	6	2	0.500 M
C	10	10	10	10	14	10	8	3	0.250 M
D	10	10	10	10	12	10	10	8	0.050 M
E	10	10	10	10	10	10	11	10	0.005 M

The blue highlighted samples show a clear formation of precipitate after 5 min. The respective amounts were indicated visually and are indicated from dark blue (highest amount) to light blue (lowest amount).

There are different explanations on the effect of these sugars on the formation of MOF.

For substrates **1** and **4**, a possible effect would occur during the α to β anomeric mutarotation of glucose, in which the interaction between the open aldehyde intermediate and the 2-methylimidazole ligand starts to become statistically appreciable at the highest concentration studied. This also explain why the substrates **5** (blocked due to methyl group) and **6** (a polyol) does not show the same, although weak, effect.

Substrate **7** is basic due to the presence of a secondary amine, and can easily deprotonate the ligand, whereas amide substrate **8** is more basic than a normal sugar and permits deprotonation as well, although in a minor extent than **7**.

Substrate **9** has similar basic activity as **7** when freebase, however here it is present in its hydrochloride form. The more HCl sugar is added, the more the ligand is protonated, whereas at the lowest concentration the residual ligand that has not been protonated by hydrochloric acid can be deprotonated by the now freed glucosamine.

Similarly, **11** as an organic acid can easily interact with 2-methylimidazole and prevent the formation of the framework, so only at the lowest concentration studied its amount has minimal effect in the ZIF reaction.

Table S4. Tested Polysaccharides.

Video A compares the biomimetic mineralization effect of different polysaccharides. In a typical experiment, 1 mg of the respective carbohydrate (listed in **Table S4**) was dissolved in 1 mL of a freshly prepared 2mM solution (160 mM in DI water) at ambient temperature. After 30 min, the 1 mL of the 2nd precursor solution (Zn(OAc)₂, 40mM in DI water) was added at once.

Sample		MW (g/mol)	Detail	Biomimetic Mineralization
A	No polysaccharides added	-	Control sample (blank)	Control (No)
B	Maltodextrin	3.000-4.000	-	No
C	Dextran	6.000	-	No
D	Dextran	40.000	-	No
E	Dextran	70.000	-	No
F	Diethylaminoethyl dextran (DEAE-dextran)	10.000	2.5-4.5% nitrogen; (ca. one substituent on every 3 rd glucose unit)	No
G	Carboxymethyl dextran sodium salt (CM-dextran)	10.000-20.000	1.1-1.5 mmol/g; (ca. one substituent on every 3 rd glucose unit)	Yes

Table S5. Yield of CM-dextran@ZIF-8 B recipe.

Sample	Actual Yield (mg)	Theoretical Yield (mg)	Yield %
B1	0.24	7.28	3.3
B2	1.02	7.64	13.35
B3	1.14	8.36	13.64
B4	0.84	9.8	8.57

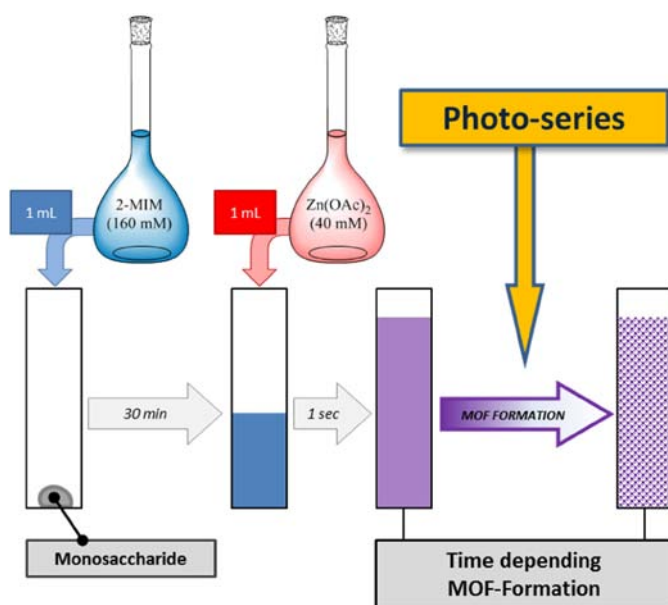


Figure S1. Schematic overview of the performed MOF-synthesis.

As indicated in **Figure S1** and according to **Table S2**, a particular amount of the respective monosaccharide (listed in **Table S1**) was dissolved in the indicated volume of a freshly prepared 2mIM solution (160 mM in DI water) at ambient temperature to provide a set of samples with different concentrations of each carbohydrate in the 1st precursor solution. Lower concentrations of the respective mixtures were achieved by diluting a particular volume the 1 M stock solution with the previously prepared 2mIM solution (160 mM in DI water) as listed in table 2. After 30 min, 1 mL of the 2nd precursor solution ($\text{Zn}(\text{OAc})_2$, 40mM in DI Water) was added at once.

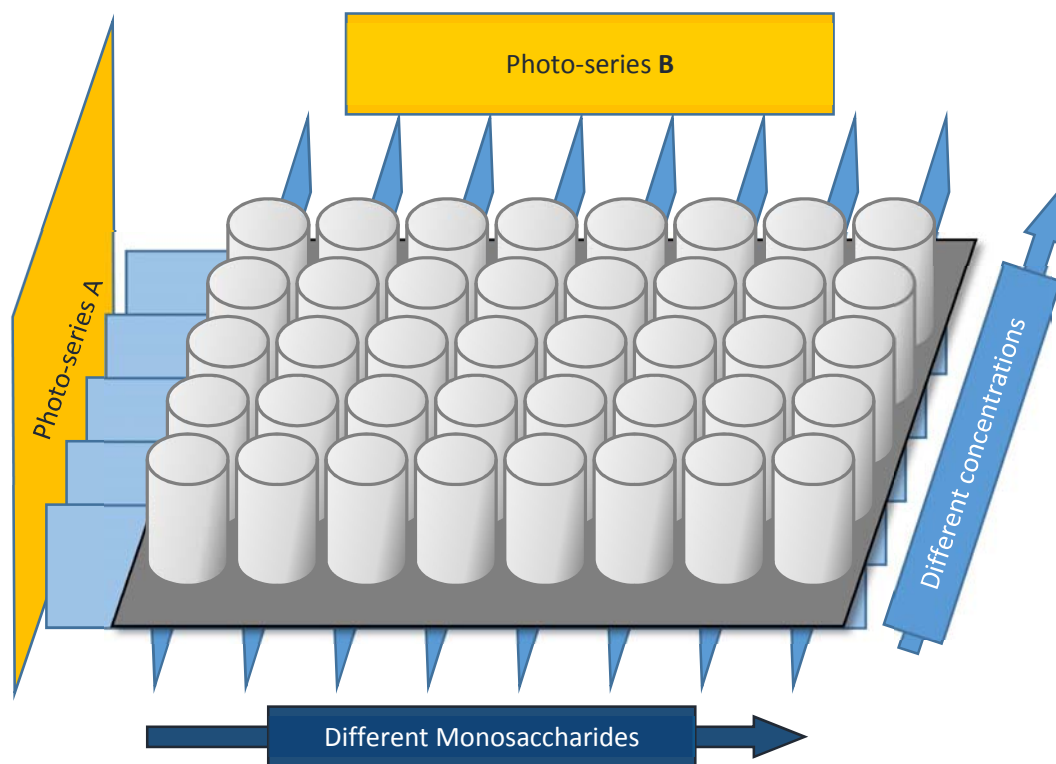


Figure S2. General schematic of the performed Photo-series.

Starting from now, time-dependent series of photos (compare **Figure S2**), comparing different carbohydrates at one concentration respectively (Photo series A) as well as each carbohydrate at different concentrations ((Photo series B), were collected. The obtained results are shown in **Figure S3-S7** and **Figure S13-S15** respectively.

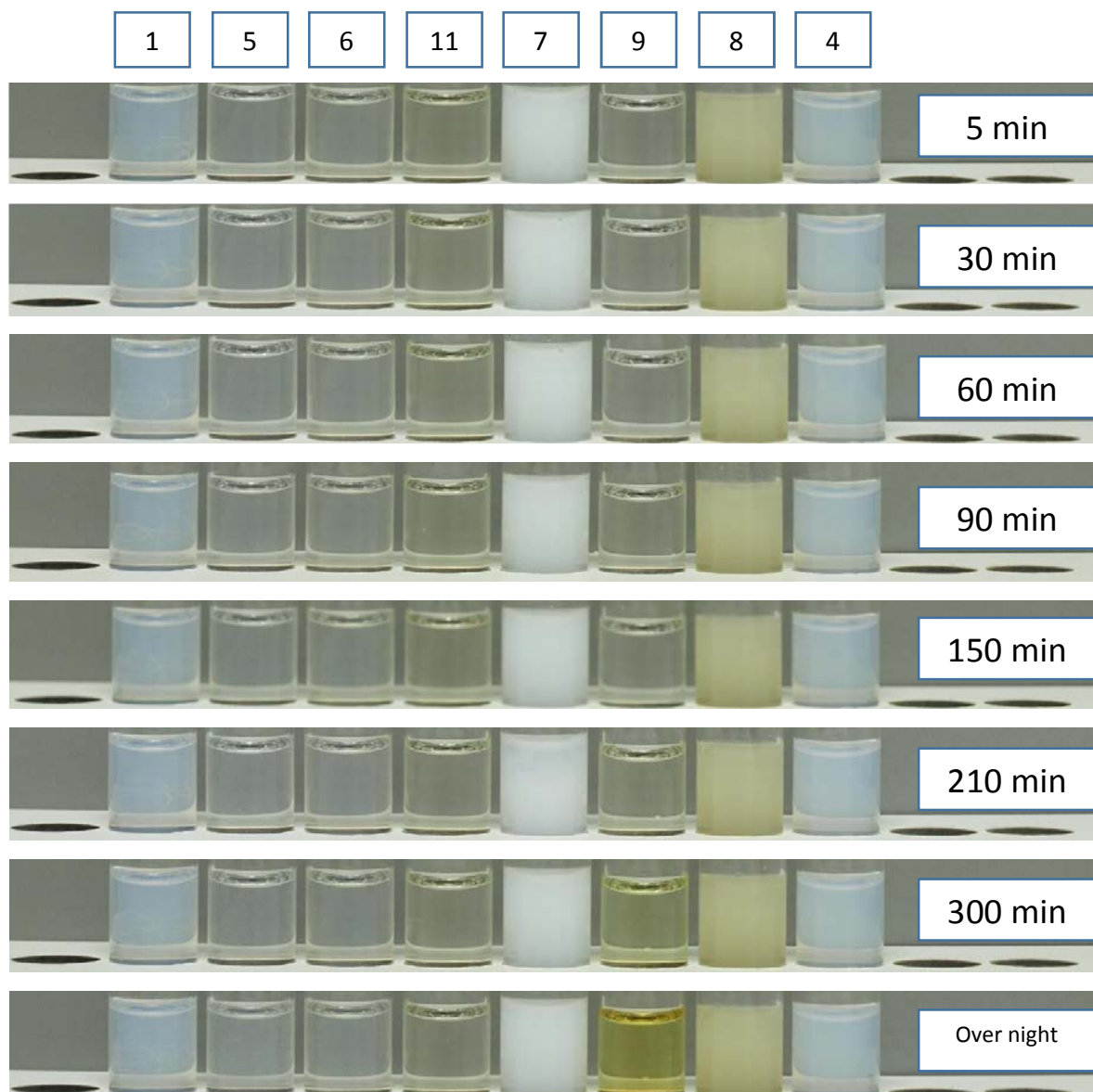


Figure S3. Time-dependent MOF formation induced by different carbohydrates (1.250 M in total).

The concentration of the corresponding monosaccharides is 1.250 M. Addition of Meglumine (**7**) clearly induces ZIF-8 formation. Although translucent solutions were obtained when with the addition of D-Glucose (**1**) and D-Xylose (**4**), it was not possible to isolate a significant amount of solid sample from a 2 mL vial. To ascertain the encapsulation of the respective carbohydrates in the final product, several vials with the same reagents were prepared (see Table S2), however the carbohydrate was never detected within the obtained solid material (see figure S3). The nitrogen containing sugars **8** and **9** show a typical colour change to yellow possibly due to various decomposition reactions, such as Amadori-rearrangements and *N*-oxide formation.¹ For GlcNH₂ (**9**), a solid product is not observed. We believe the reason is the presence and excess (1.25 M) of GlcNH₂ hydrochloride (needed in commercial samples due to the higher stability) compared to 2mIM (0.16 M), thus a basic catalysed reaction is not possible.

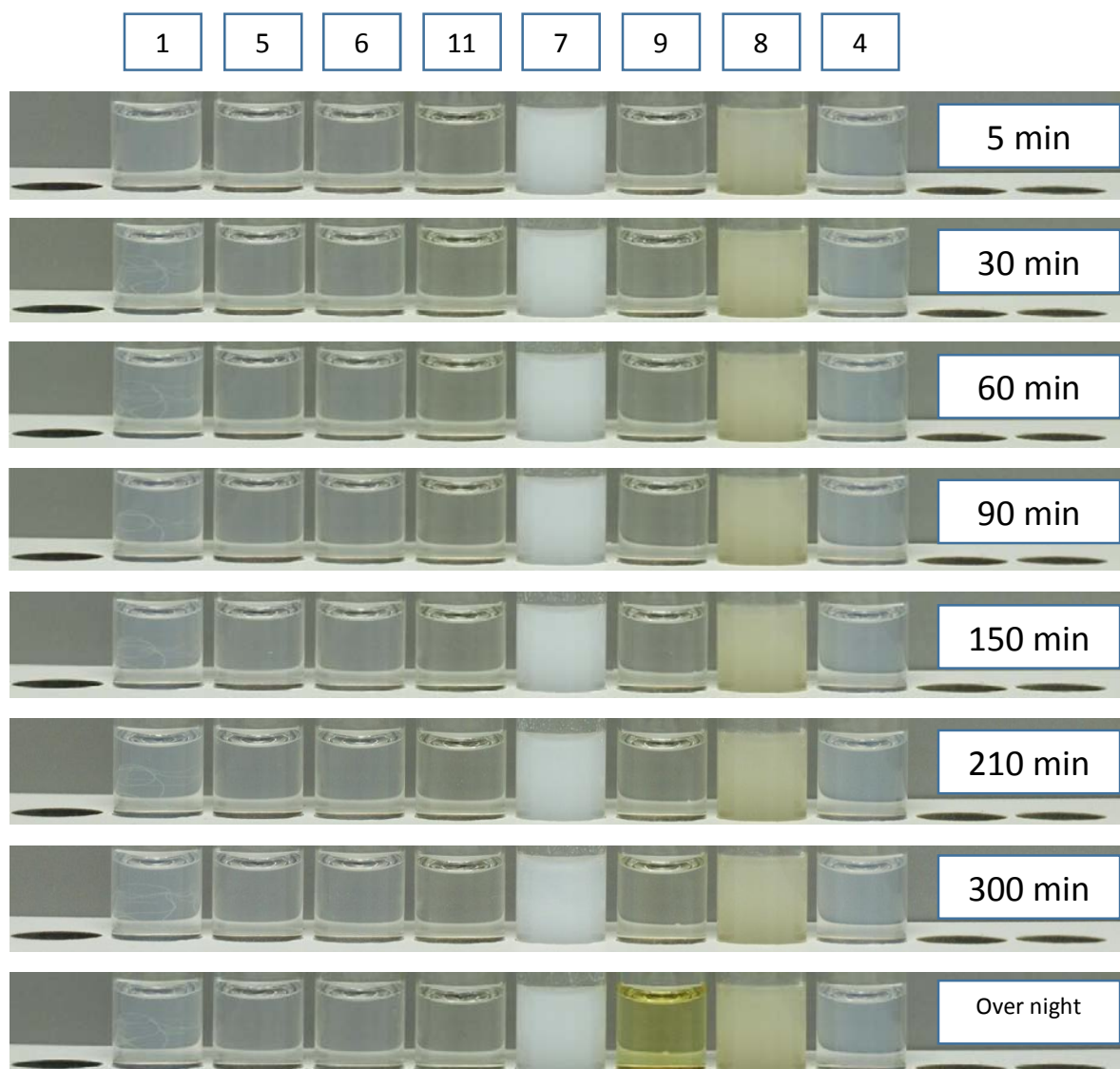


Figure S4. Time-dependent MOF formation induced by different carbohydrates (0.50 M in total).

The concentration of the corresponding monosaccharides is 0.50 M .

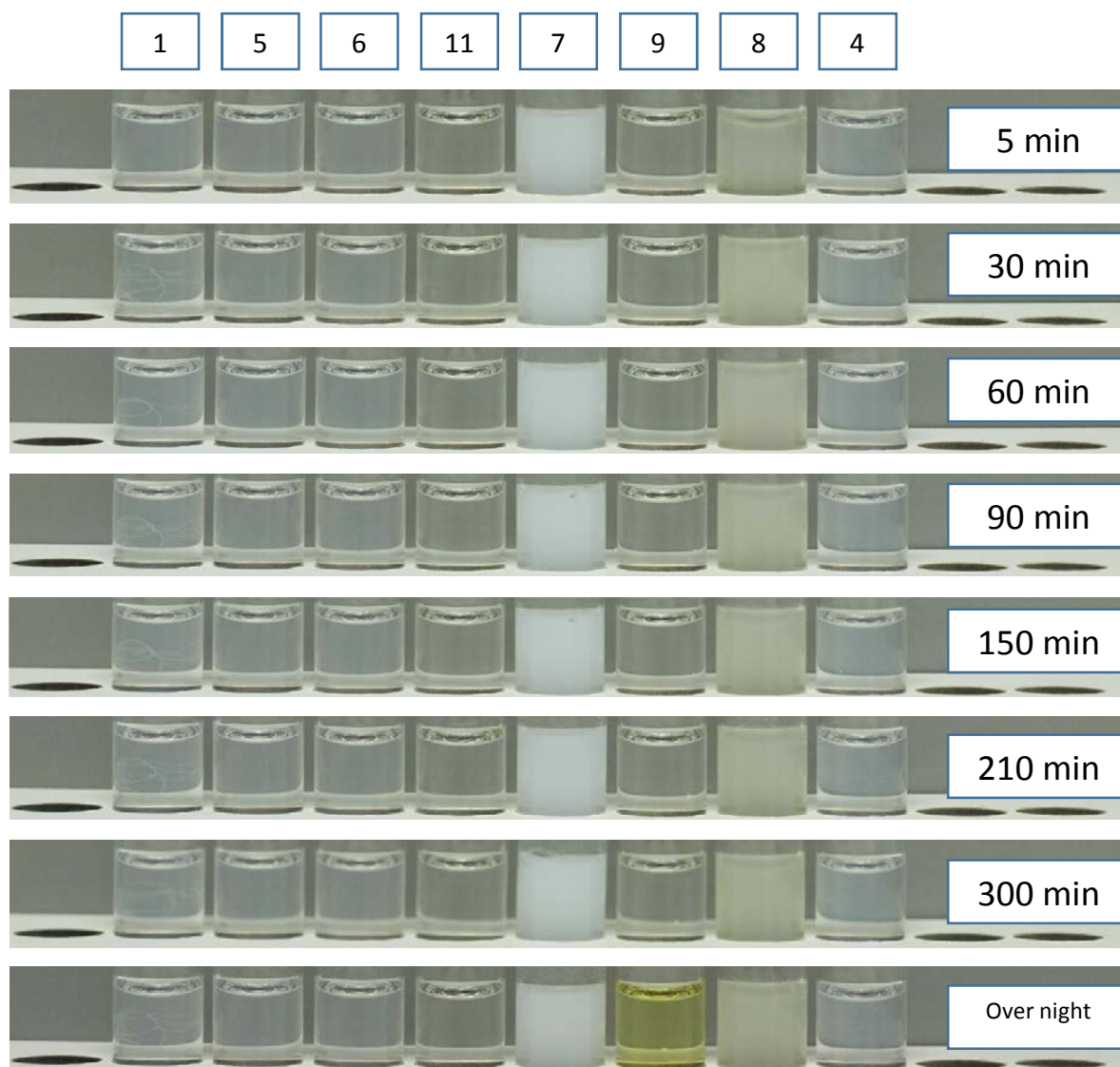


Figure S5. Time-dependent MOF formation induced by different carbohydrates (0.250 M in total).

The concentration of the corresponding monosaccharides is 0.250 M.

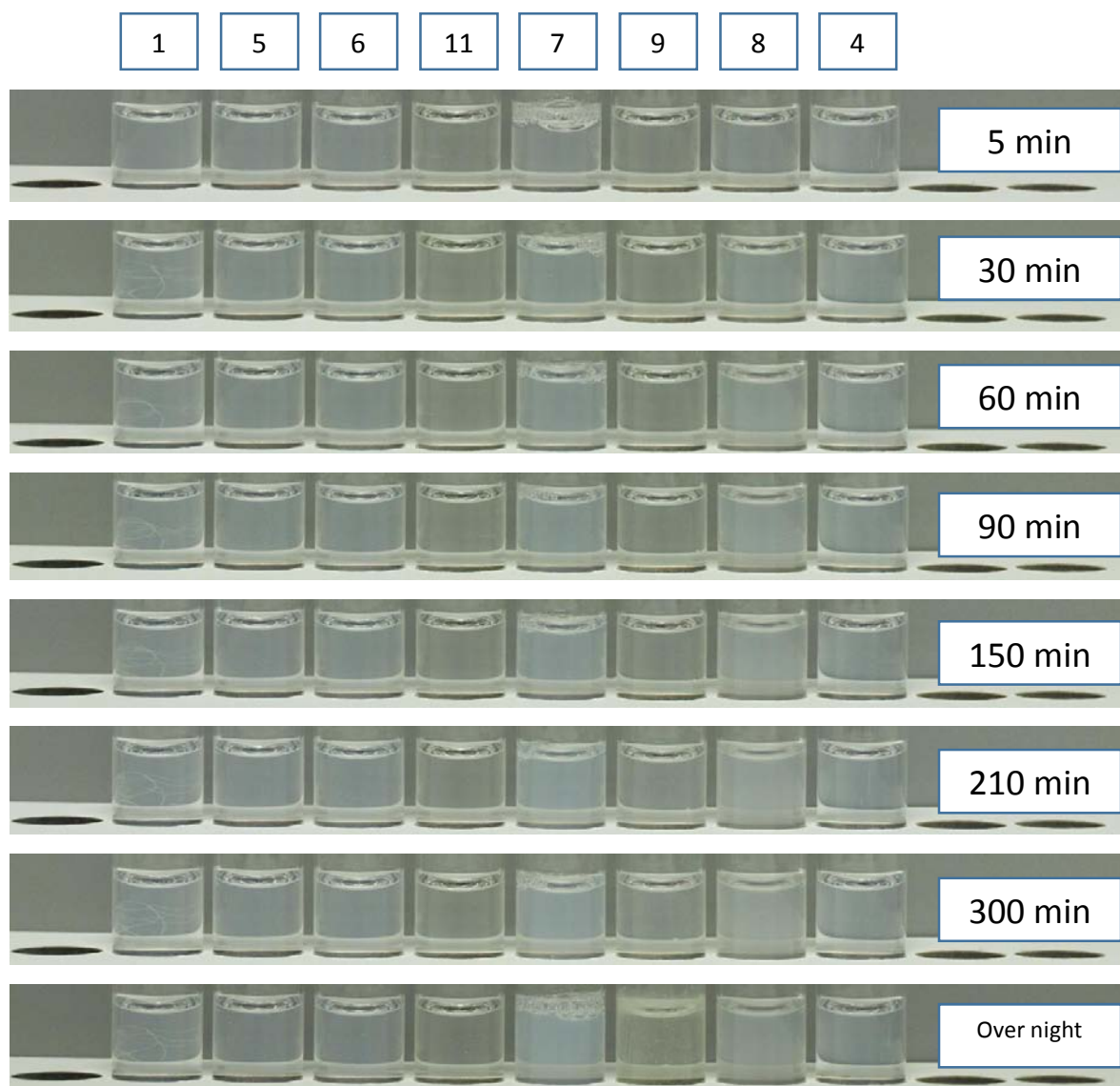


Figure S6. Time-dependent MOF formation induced by different carbohydrates (0.050 M in total).

The concentration of the corresponding monosaccharides is 0.050 M

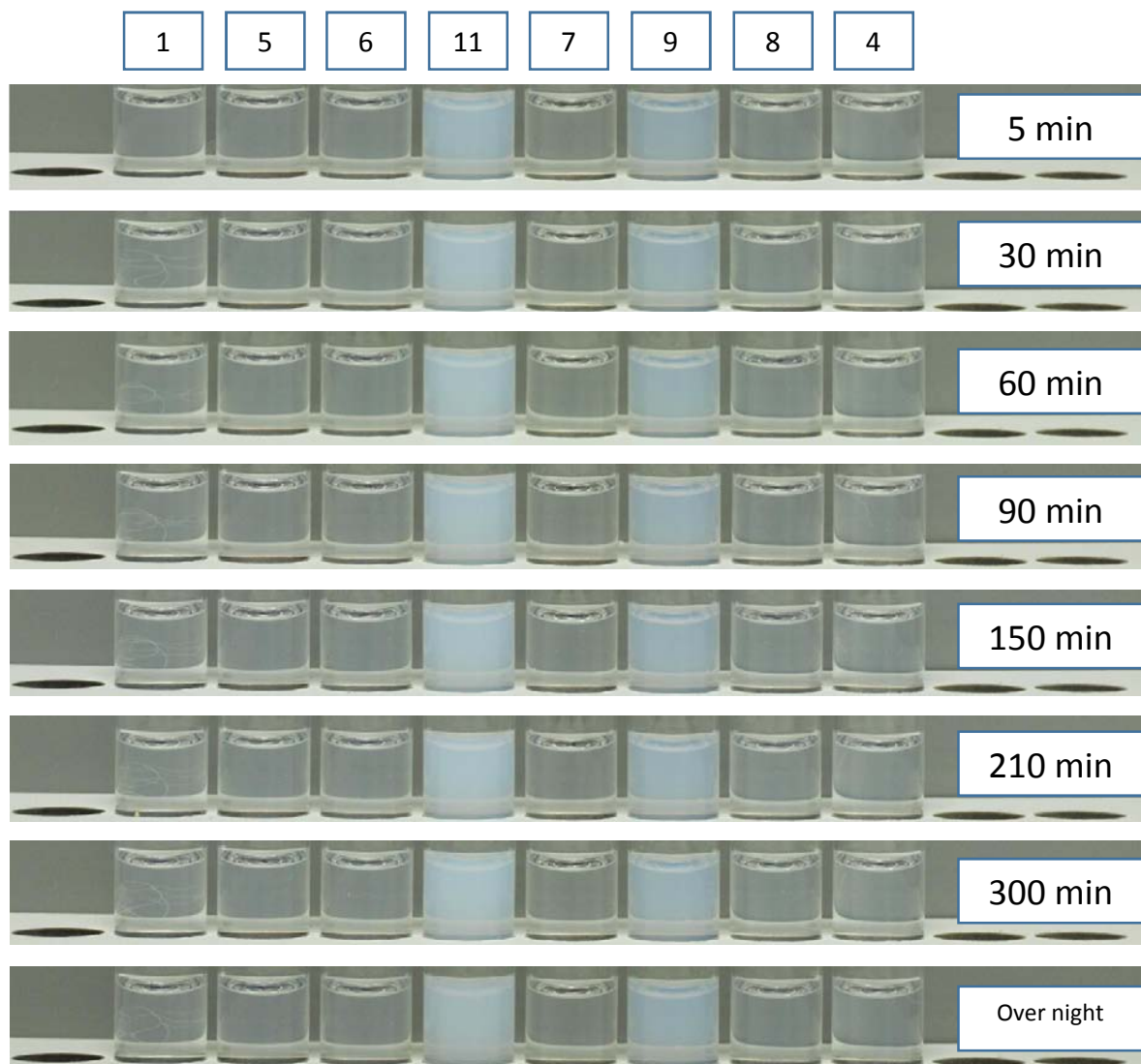


Figure S7. Time-dependent MOF formation induced by different carbohydrates (0.005 M in total).

The concentration of the corresponding monosaccharides is 0.005 M. With this concentration, GlcNH₂ (**9**) seems to trigger the formation of MOF particles. We think the low concentration of GlcNH₂ hydrochloride (0.005 M) compared to 2mIM (0.16 M) could play a role, HCl is neutralized by 2mIM and due to the liberated amino functionality the known basic catalysed reaction occurs (deprotonation of 2mIM). The same effect is observed in the sample with D-gluconic acid- δ -lactone (**11**) which might be related to the equilibrium between the lactone, carboxylic acid and carboxylate of the carbohydrate.

These hypothesis are further supported by the measured pH-values of the respective samples (see **Table S3**).

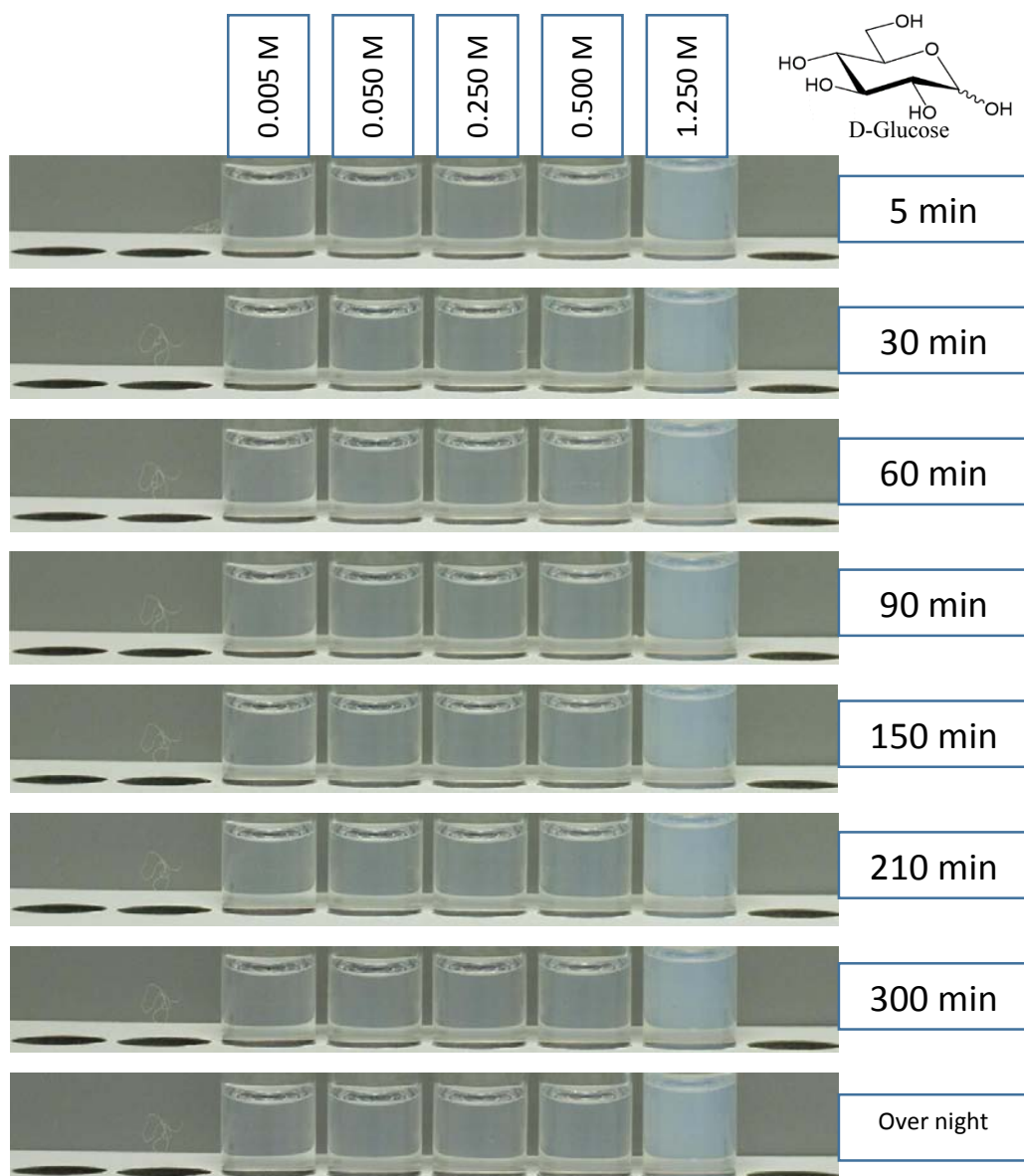


Figure S8. Time-dependent MOF formation induced by different concentrations of D-Glucose (**1**) at different concentrations.

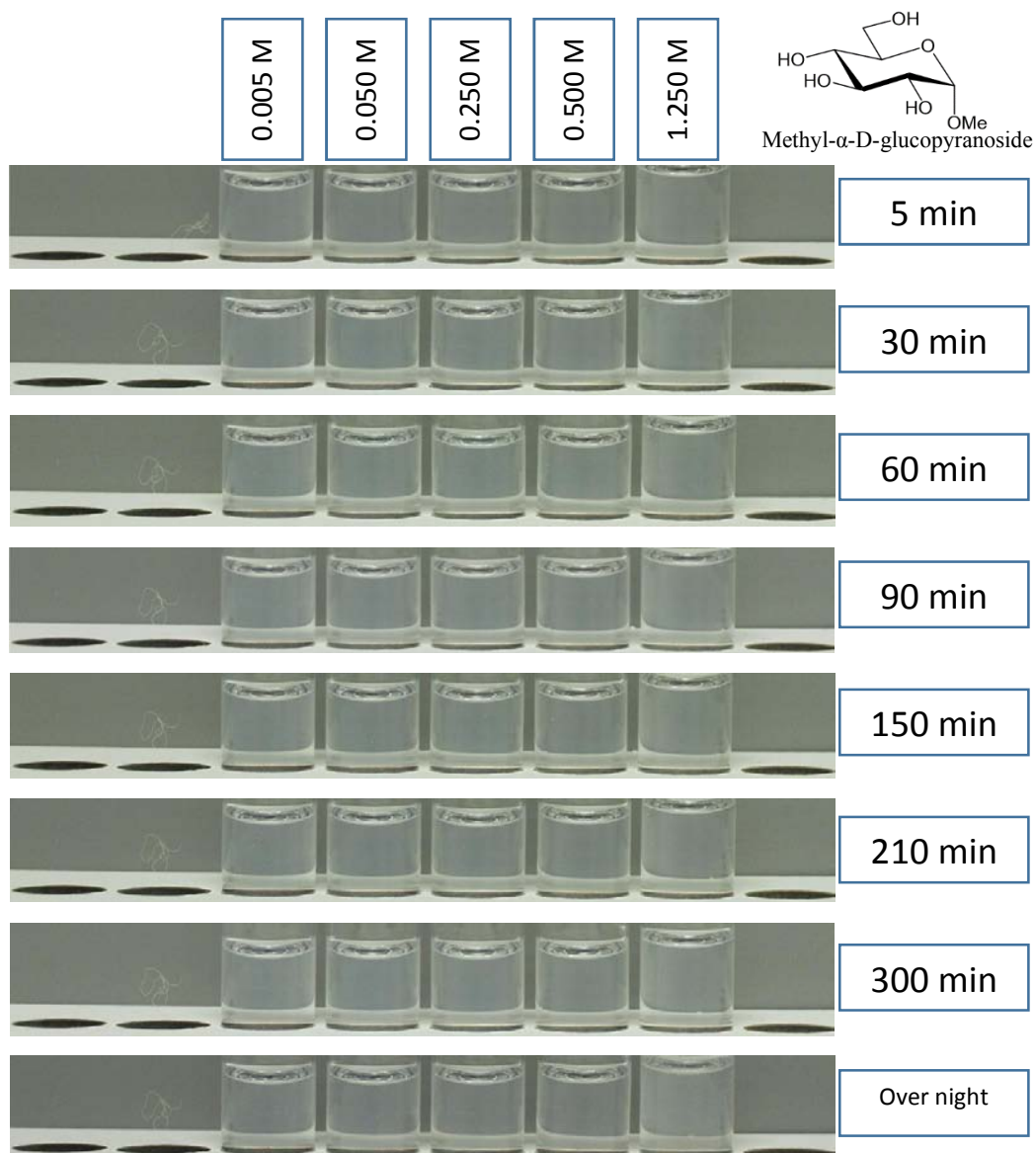


Figure S9. Time-dependent MOF formation induced by different concentrations of Methyl α -D-Glucopyranoside (5) at different concentrations.

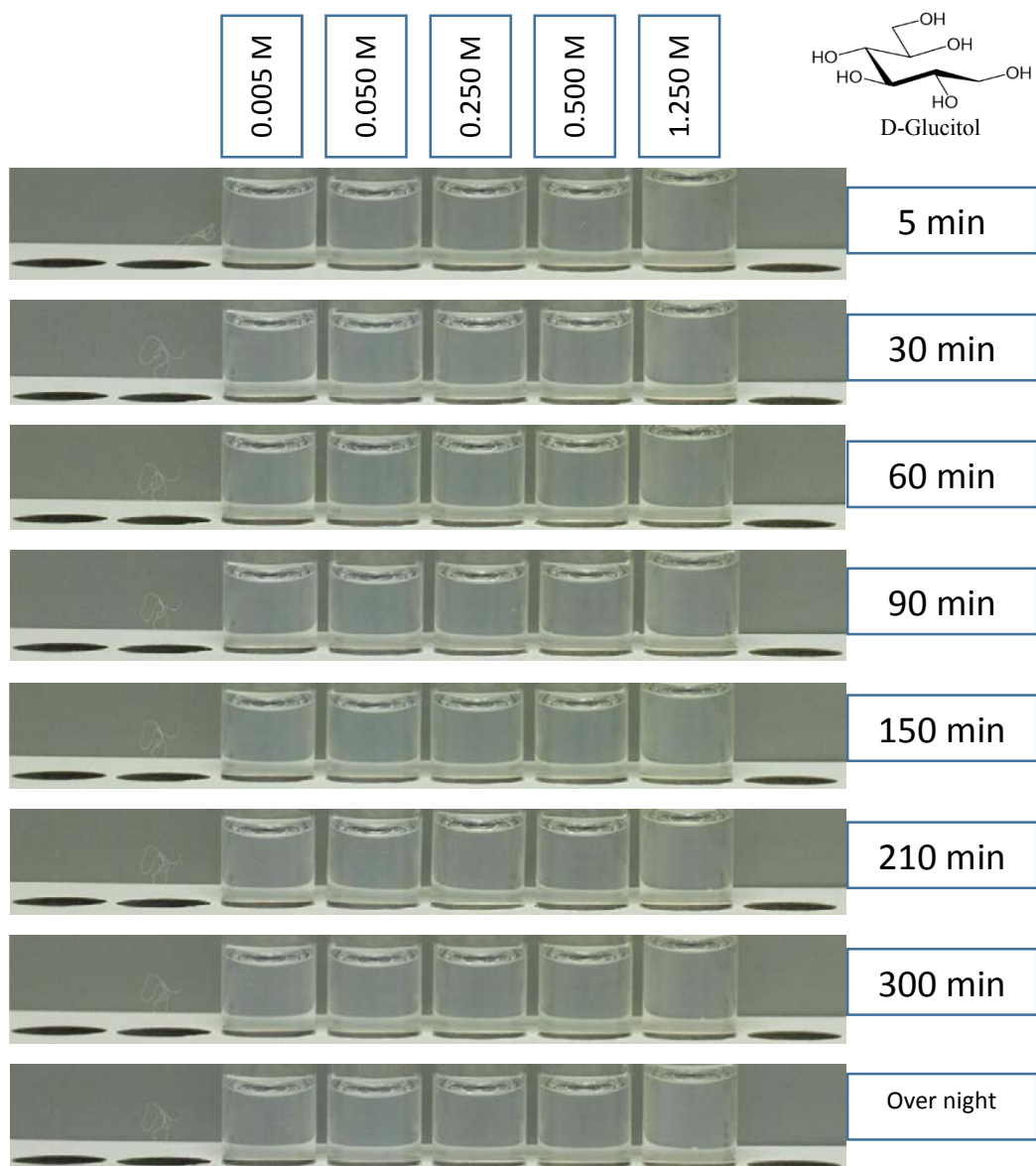


Figure S10. Time-dependent MOF formation induced by different concentrations of D-Glucitol (6) at different concentrations.

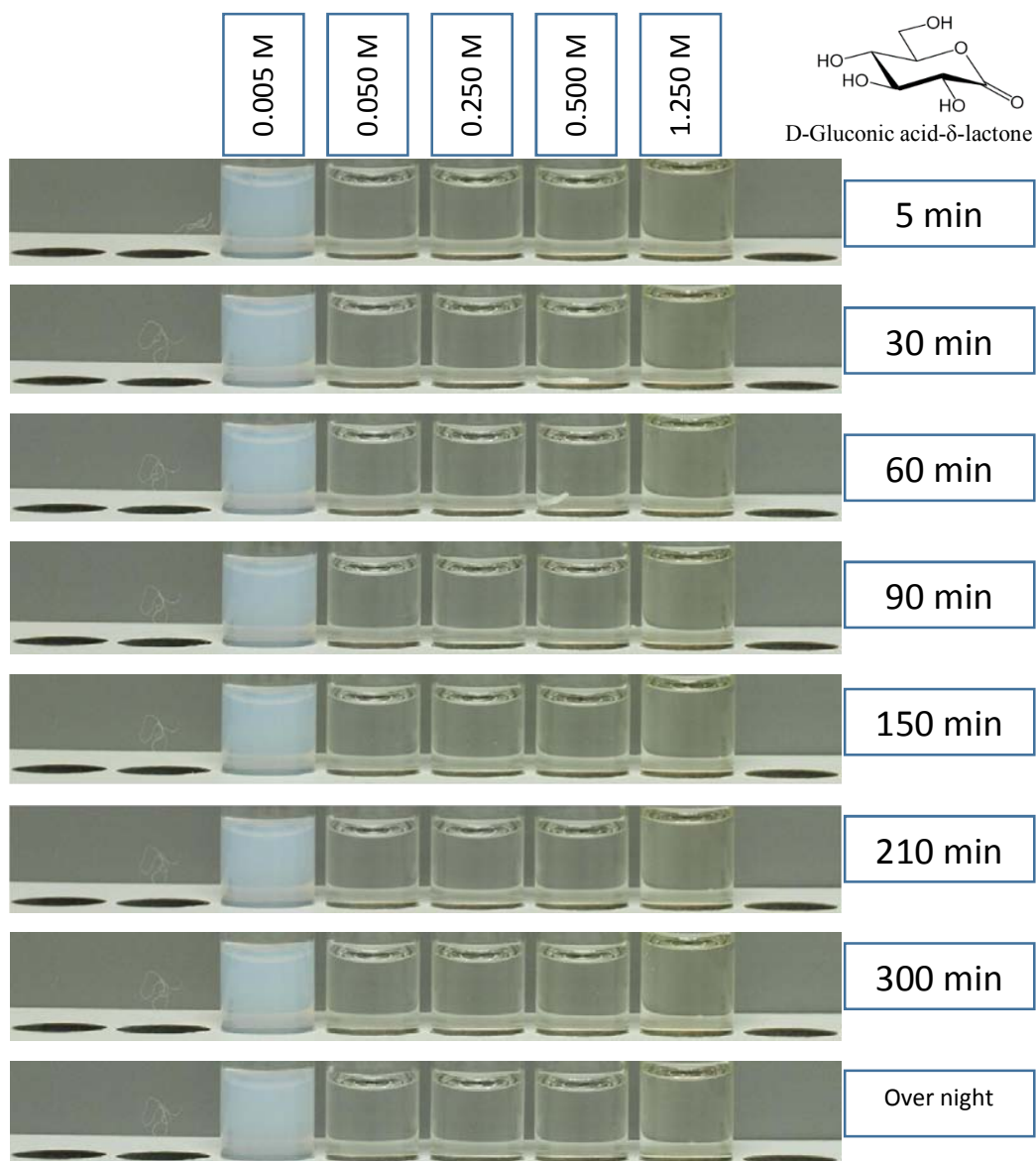


Figure S11. Time-dependent MOF formation induced by different concentrations of D-Gluconic acid- δ -lactone (**11**) at different concentrations.

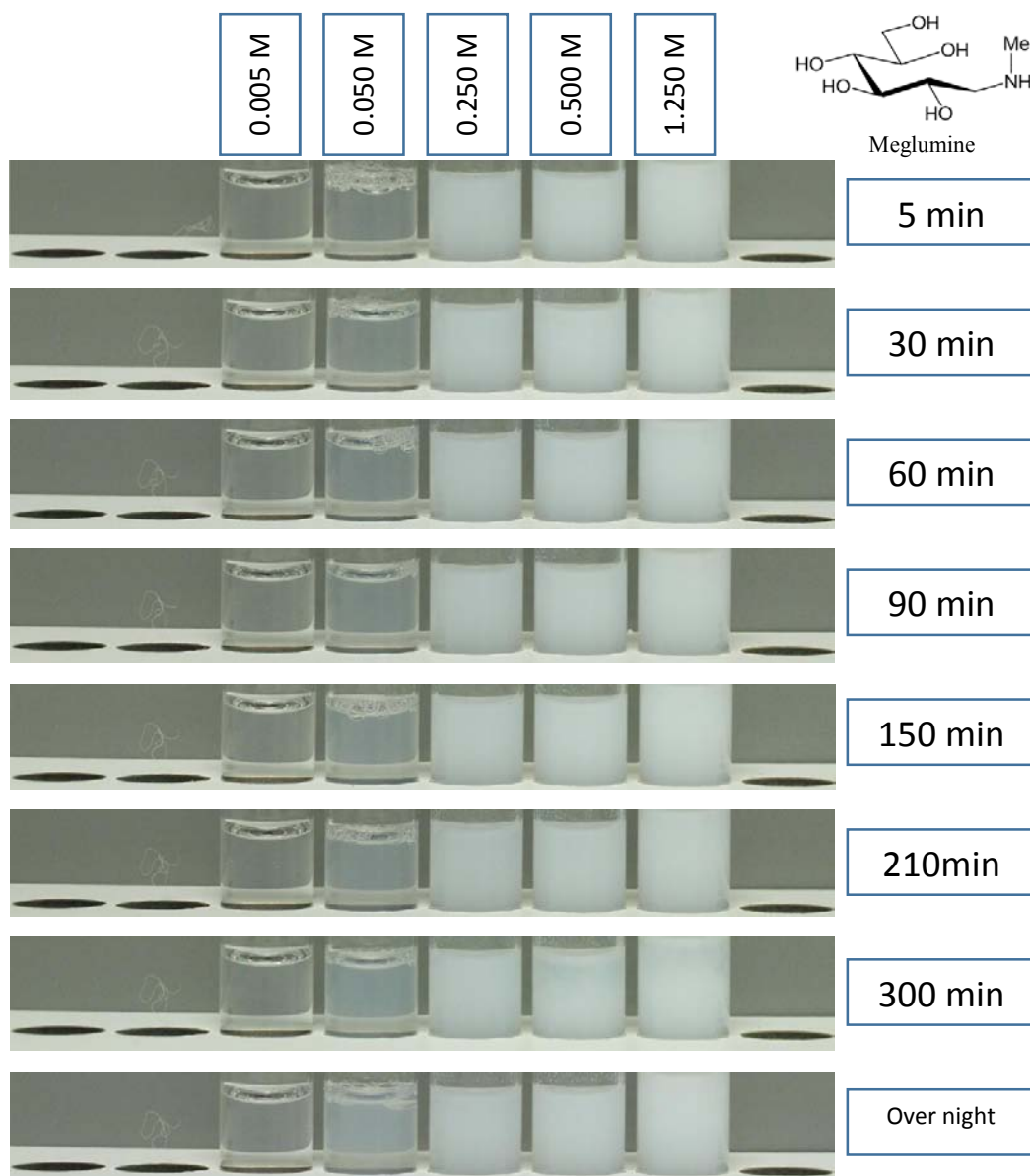


Figure S12. Time-dependent MOF formation induced by different concentrations of Meglumine (7) at different concentrations.

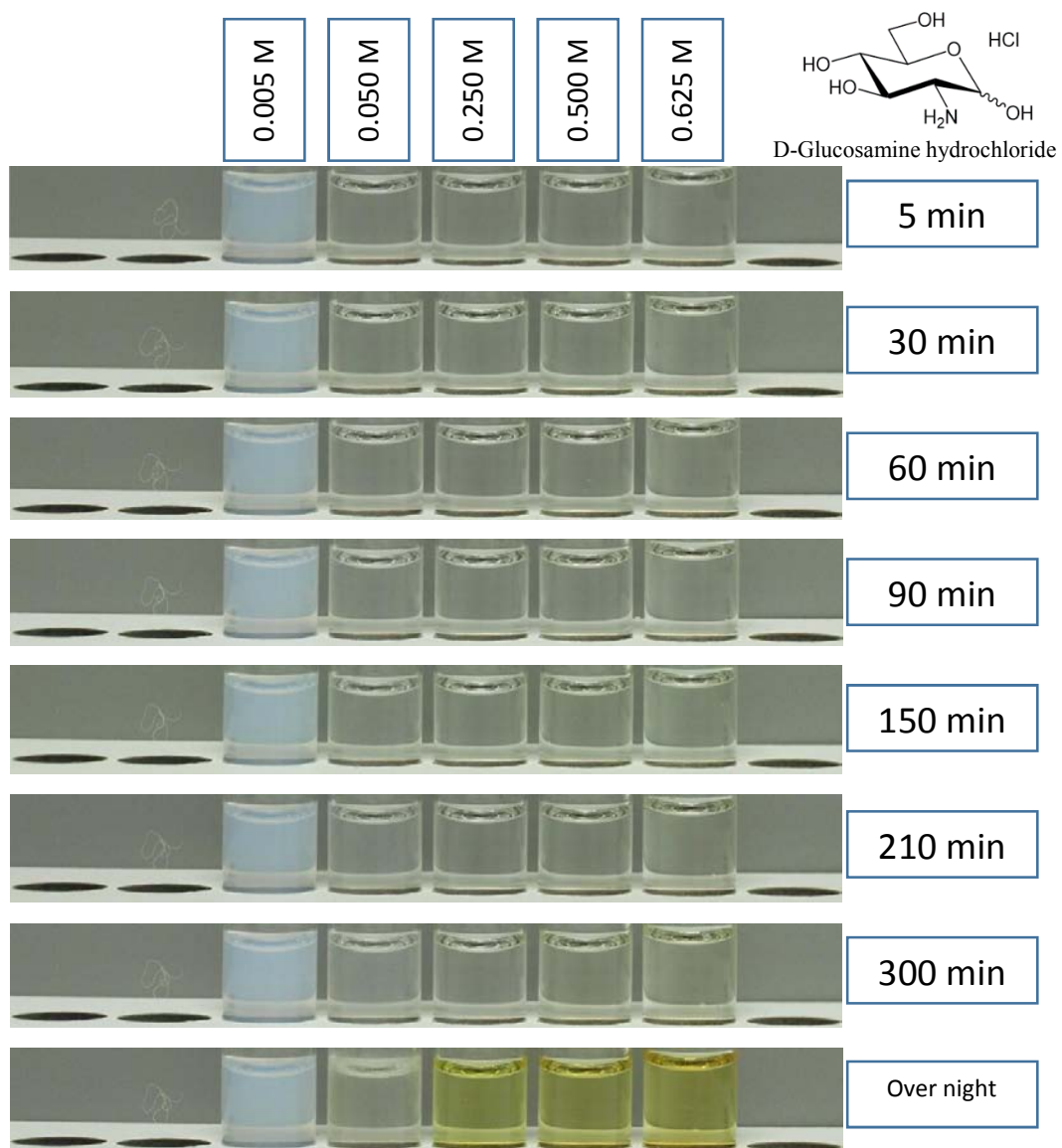


Figure S13. Time-dependent MOF formation induced by different concentrations of D-Glucosamine HCl (9) at different concentrations.

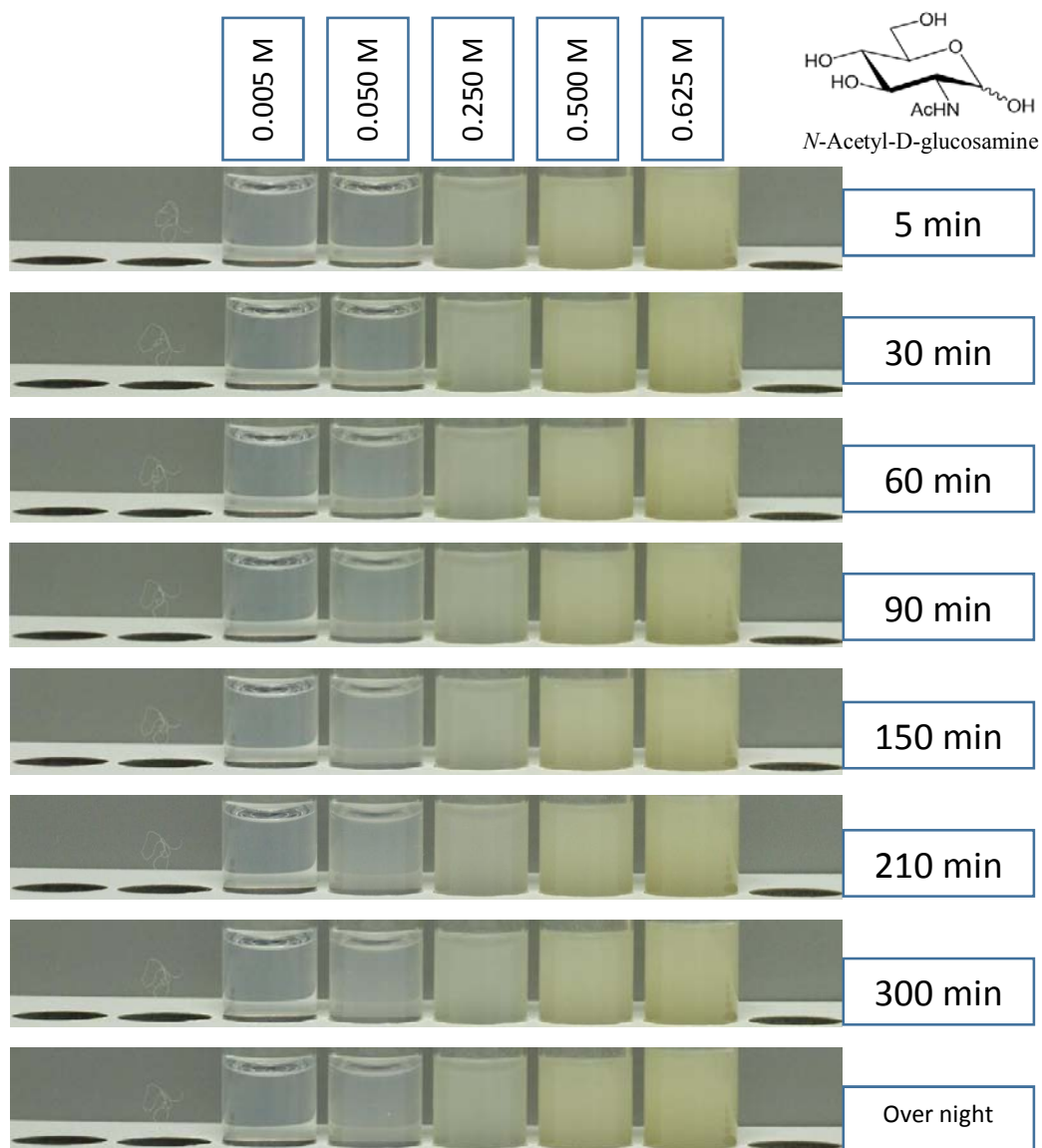


Figure S14. Time-dependent MOF formation induced by different concentrations of *N*-Acetyl-D-glucosamine (8) at different concentrations.

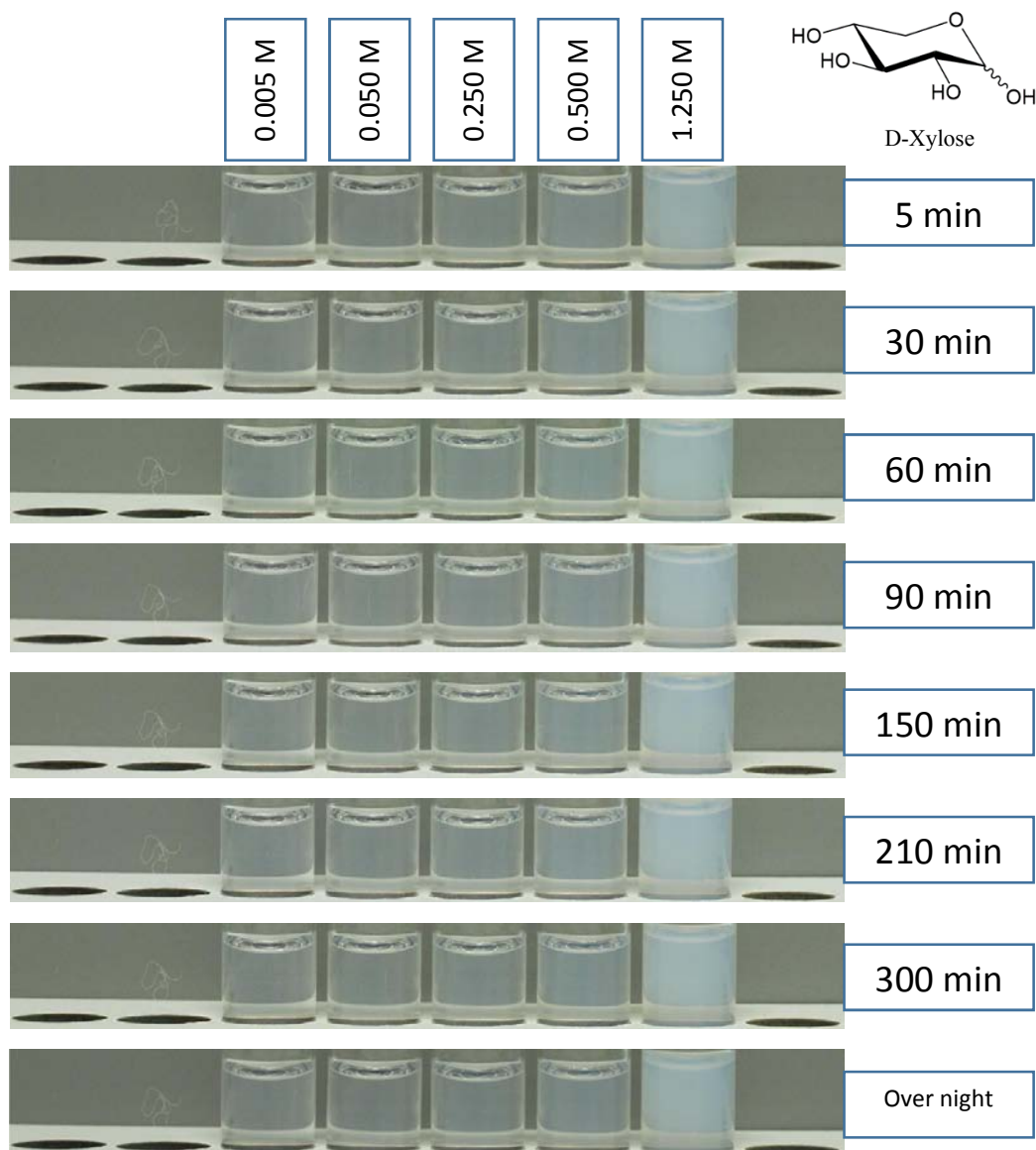


Figure S15. Time-dependent MOF formation induced by different concentrations of D-Xylose (**4**) at different concentrations.

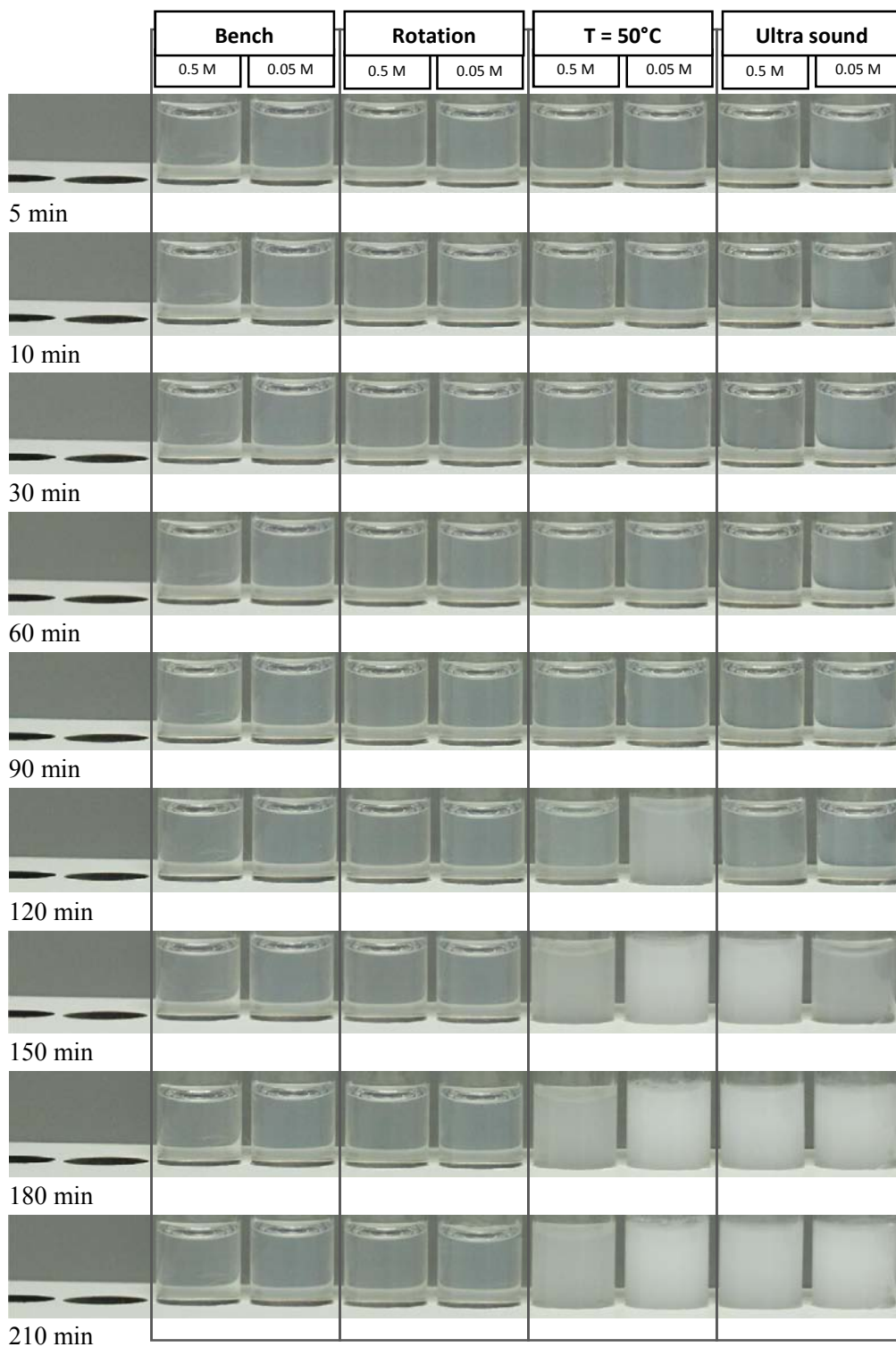


Figure S16. Comparison of different conditions during the MOF-synthesis supported by Methyl- α -D-glucopyranoside (**5**).

The influence of different conditions during the MOF-formation were also investigated. Reaction mixtures containing two different concentrations (0.5 M and 0.05 M in total) of Methyl- α -D-glucopyranoside (**5**), D-Glucitol (**6**) and Meglumine (**7**) were prepared. Samples were prepared using different conditions such as: increased reaction temperature ($T = 50^{\circ}\text{C}$); sonication, at room temperature; static conditions at room temperature; placed under rotation at room temperature. For all these conditions, the time depending appearance is summarized in **Figure S17–S18**.

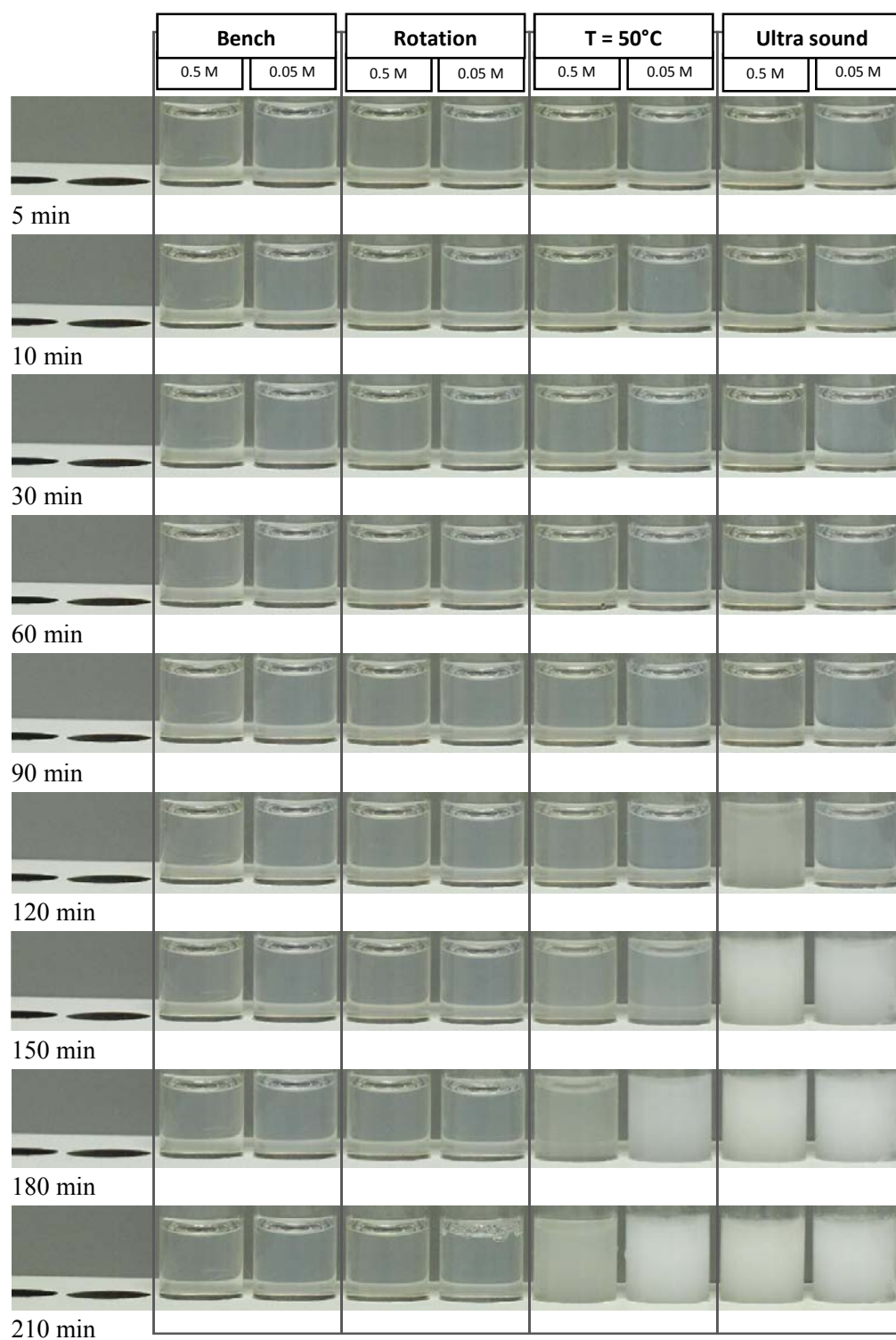


Figure S17. Comparison of different conditions during the MOF-synthesis supported by Glucitol (6).

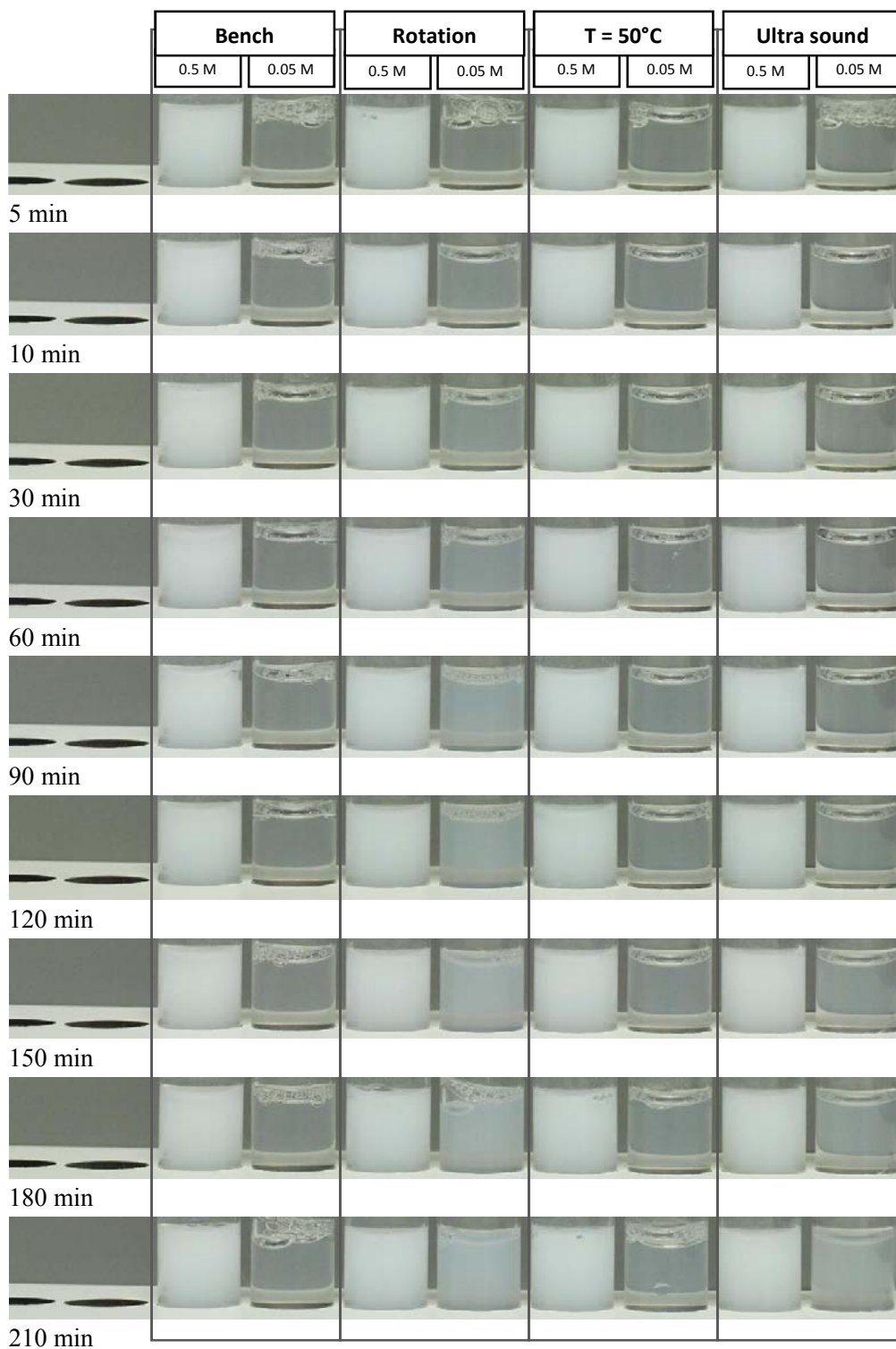


Figure S18. Comparison of different conditions during the MOF-synthesis supported by Meglumine (7).

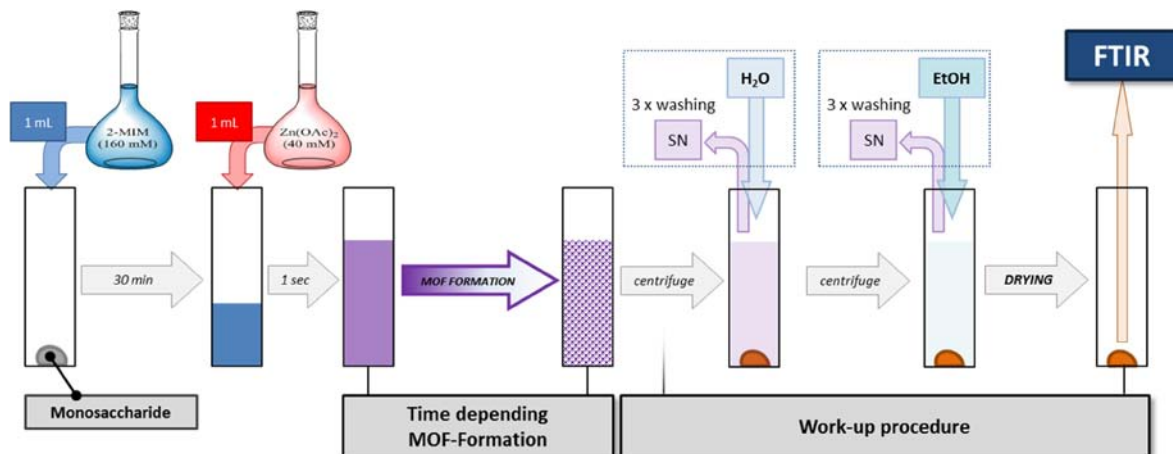


Figure S19. Schematic overview of the general procedure for the preparation of zeolitic frameworks.

For the investigations towards the encapsulation of monosaccharides, several reaction mixtures containing potential monosaccharides were prepared as described above (see **Figure S1**). After 15 hours (and under the premise, that a significant amount of precipitate was formed), the resulting reaction mixture was centrifuged (4500 rpm, 8 min). After the supernatant was removed, the remaining residue was washed with distilled water (ca. 5 min) and centrifuged again. This step was repeated three times and subsequently performed with ethanol instead of the water. Finally, the resulting product was dried at ambient conditions for 24 hours (see **Figure S19**). FTIR-spectroscopy of the obtained powders (**Figure S20-S22**) provide clear evidence that all the attempt in encapsulating saccharides failed as the vibrational modes are related to pure zeolitic Imidazolate framework materials.

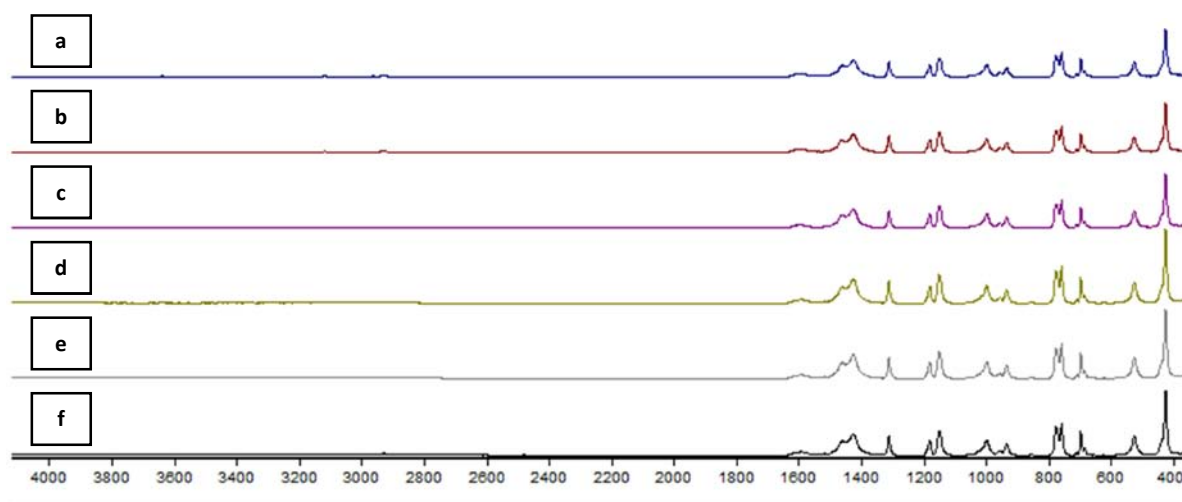


Figure S20. FTIR-spectra of the observed products.

a) D-Glucose (**1**, $c = 1.25$ M), **b)** D-Gluconic acid- δ -lactone (**11**, $c = 0.005$ M), **c)** Meglumine (**7**, $c = 1.25$ M), **d)** D-Glucosamine hydrochloride (**9**, $c = 0.005$ M), **e)** *N*-Acetyl-D-glucosamine (**8**, $c = 0.625$ M), **f)** D-Xylose (**4**, $c = 1.25$ M).

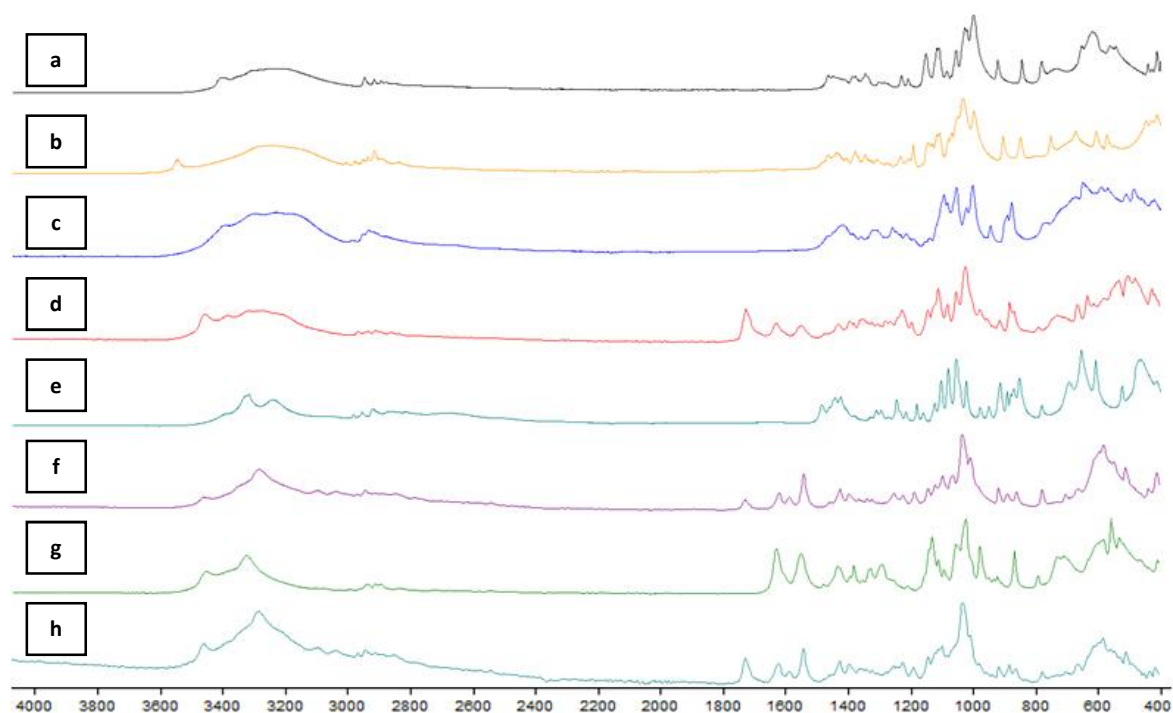


Figure S21. FTIR-spectra of the respective tested monosaccharides.

a) D-Glucose (**1**), **b)** Methyl- α -D-glucopyranoside (**5**), **c)** D-Glucitol (**6**), **d)** D-Gluconic acid- δ -lactone (**11**), **e)** Meglumine (**7**), **f)** D-Glucosamine hydrochloride (**9**), **g)** *N*-Acetyl-D-glucosamine (**8**), **h)** D-Xylose (**4**).

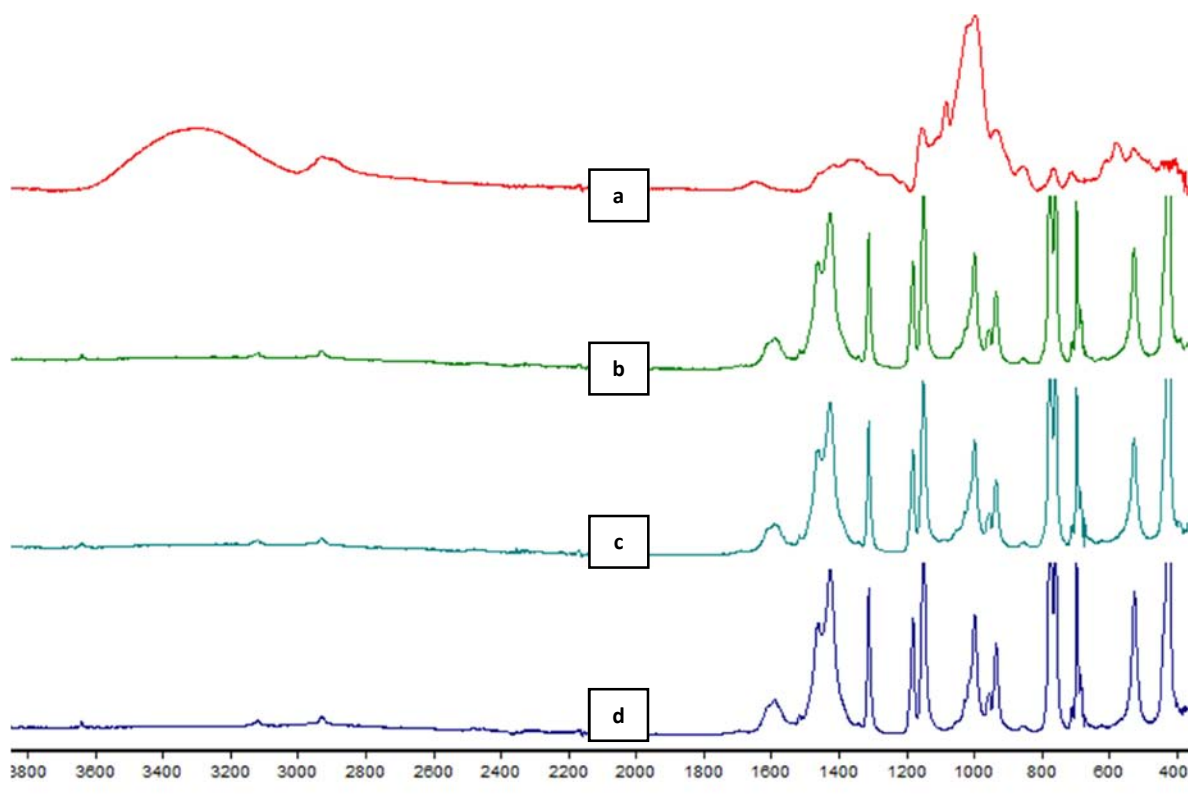


Figure S22. FTIR-spectra of: a) Maltodextrin, compared with the obtained products b) 5 mg/mL, c) 10 mg/mL, and d) 20 mg/mL of Maltodextrin supported ZIF-8 formation.

In a typical experiment Maltodextrin in the respective amount (5, 10 and 20 mg/mL) was dissolved in 7 mL 2mIM (initial concentration = 160 mM). Then aqueous solution of 7 mL Zn(OAc)₂ (initial concentration = 40 mM) was added at room temperature. The solutions were stirred overnight at room temperature. The precipitates were collected by centrifugation, washed with DI water (3X) and ethanol (3X). The resulting powders were dried for FTIR characterisation. The reaction was performed 3 times to prove its reproducibility.

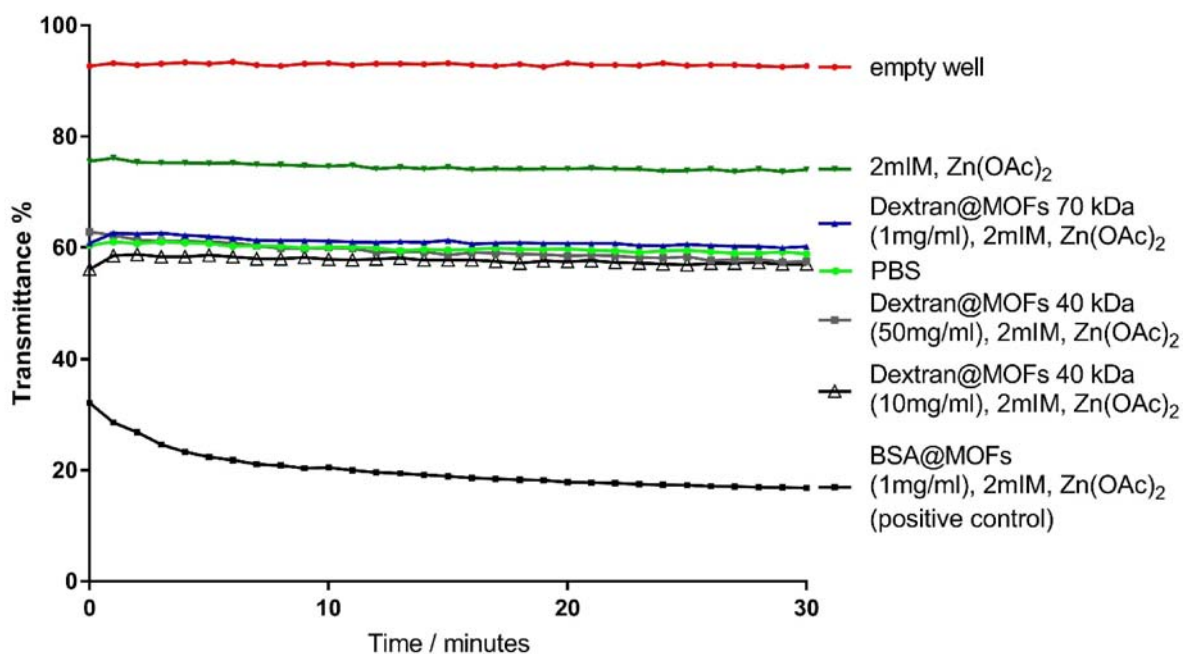
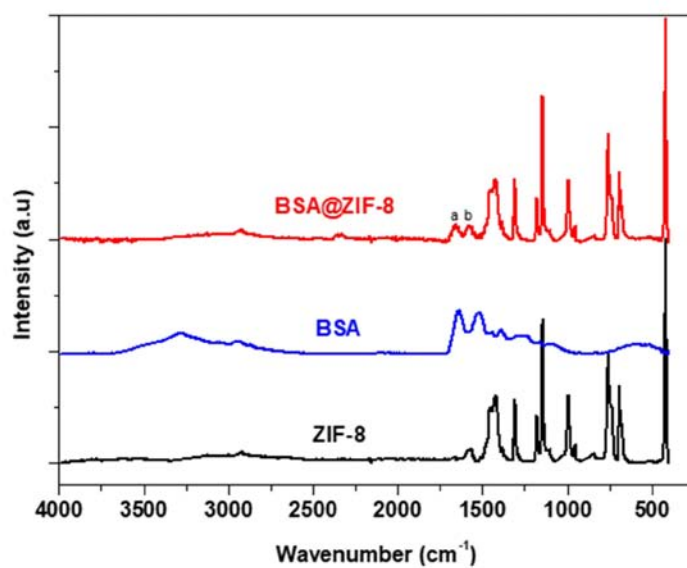


Figure S23. Kinetic tests using different Dextrans at various concentrations for the investigation of their biomimetic mineralization effects.

The test was performed adding Dextrans in an aqueous solution of 2mIM and $\text{Zn}(\text{OAc})_2 \cdot 2\text{H}_2\text{O}$. The kinetic was monitored using a plate reader (595 nm). Three negative controls were used: 1) the empty well, 2) the aqueous mixture of 2mIM and $\text{Zn}(\text{OAc})_2$ mixed in water and 3) PBS buffer solution. As a positive control BSA was used to test the biomimetic mineralization adding the protein to an aqueous solution of 2mIM and $\text{Zn}(\text{OAc})_2$. From this experiment, BSA demonstrated a significantly higher decrease in the transmittance due to the formation of BSA@MOFs.

Details of the experiment

30 μl of freshly-made 2mIM (13.1 mg/mL; 160 mM) and 30 μl of freshly-made $\text{Zn}(\text{OAc})_2 \cdot 2\text{H}_2\text{O}$ (8.8 mg/mL; 40 mM) were pre-mixed with 30 μl of either Dextran 70 kDa (1 mg/mL), Dextran 40 kDa (10 mg/mL and 50 mg/mL) or BSA (1 mg/mL). Directly after mixing, the particle formation was investigated using a plate reader (FLUOstar OTPIMA, BMG LABTECH), absorbance measurement at 595 nm for 30 min with 1 minute time frames, no shaking and at 37°C. The mean absorbance out of two independent runs was calculated and the mean absorbance was converted into % transmittance via $\text{antilog}(2 - \text{absorbance})$. The graph was plotted using GraphPad Prism 7.02 and analysed via ANOVA followed by Tukey's multiple comparisons test. BSA@MOFs showed a highly significant increase in % transmittance compared to the Dextrans ($p=0.0001$).



FTIR Spectra of BSA@MOF (1mg/mL BSA). Amide I (a) and Amide II (b).

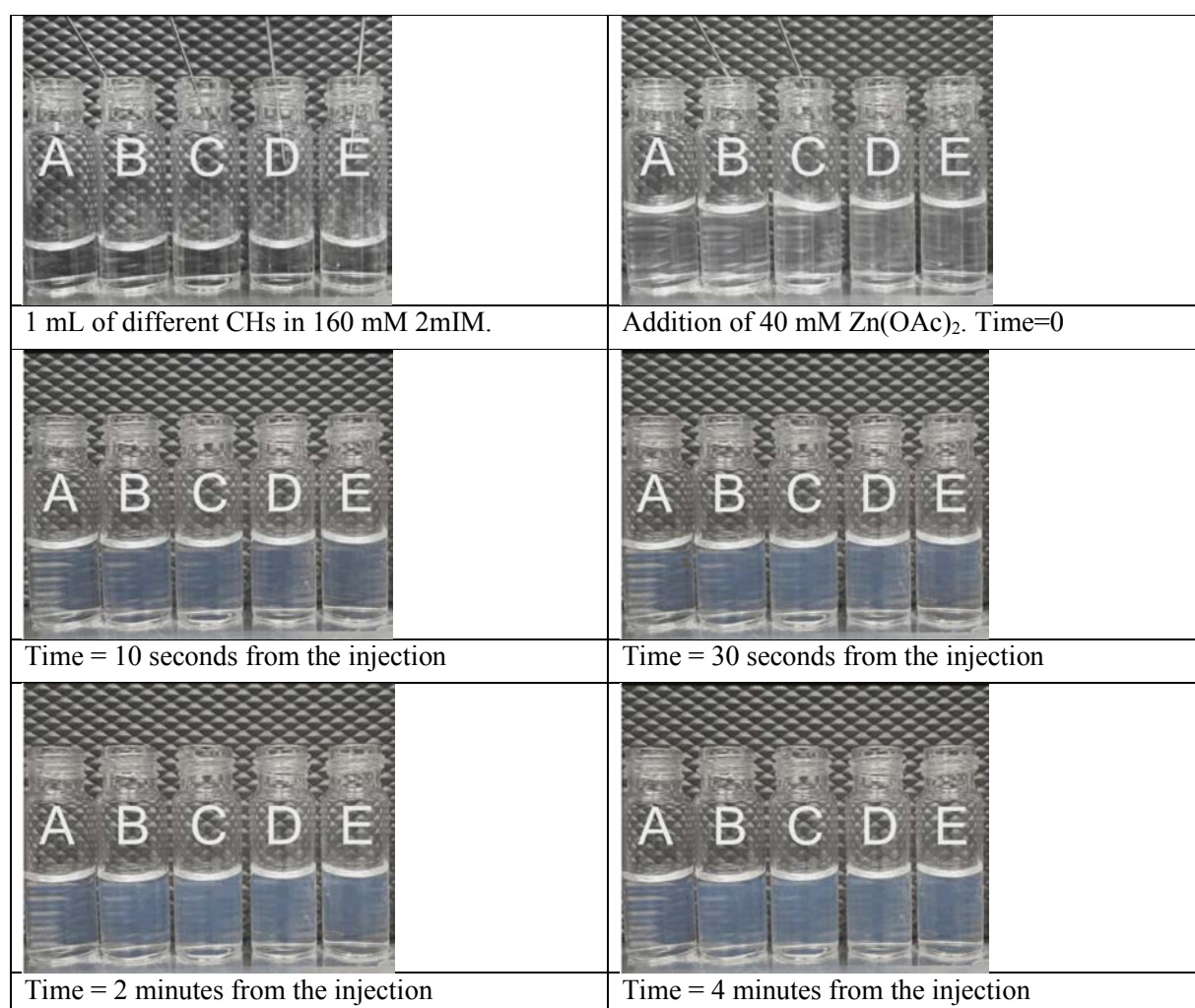


Figure S24. Photographs of solutions using the polysaccharides with different molecular weights (Dextrans and Maltodextrin).

Photographs of solutions using the polysaccharides listed in table below. Composition and procedure: 1 mg of the respective carbohydrate (listed in **Table below**) was dissolved in 1 mL of a freshly prepared 2mIM solution (160 mM in DI water) at ambient temperature (Figure S24). After 30 min, the 1 mL of the 2nd precursor solution (Zn(OAc)₂, 40mM in DI water) was added at once in all vials (Figure S24).

Table of CHs with different molecular weights (Dextrans and Maltodextrin)

Sample		MW (g/mol)	comment
A	Blank	-	NO polysaccharide added
B	Maltodextrin	3.000-4.000	-
C	Dextran	6.000	-
D	Dextran	40.000	-
E	Dextran	70.000	-

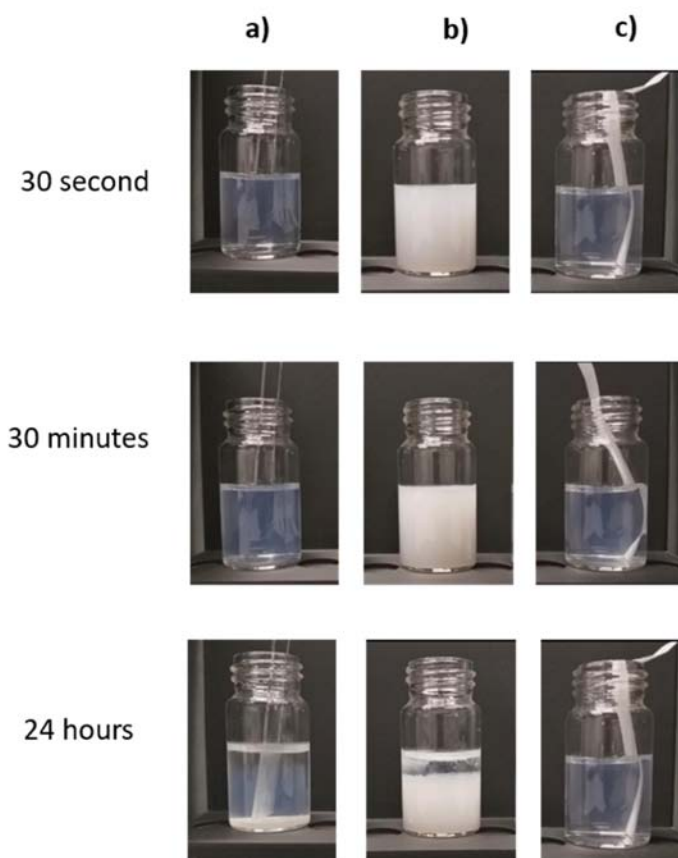


Figure S25. Screenshot of synthesis of ZIF-8 with the $\text{Zn}^{2+}:\text{2mIM} = 1:4$ at 30 second, 30 minutes and 24 hours on paper and glass plate.

The solution of 2mIM (160 mM) was mixed by $\text{Zn}(\text{OAc})_2$ (40 mM) and a glass plate **a)**, the next vial contains of 2mIM (160 mM) and CM-dextran (0.36 mg/mL) was mixed by $\text{Zn}(\text{OAc})_2$ (40 mM) **b)**, the last vial contains 2mIM solution (160 mM) was mixed by $\text{Zn}(\text{OAc})_2$ (40 mM) and a piece of paper (S&S filter paper 110 mm) **c)**.

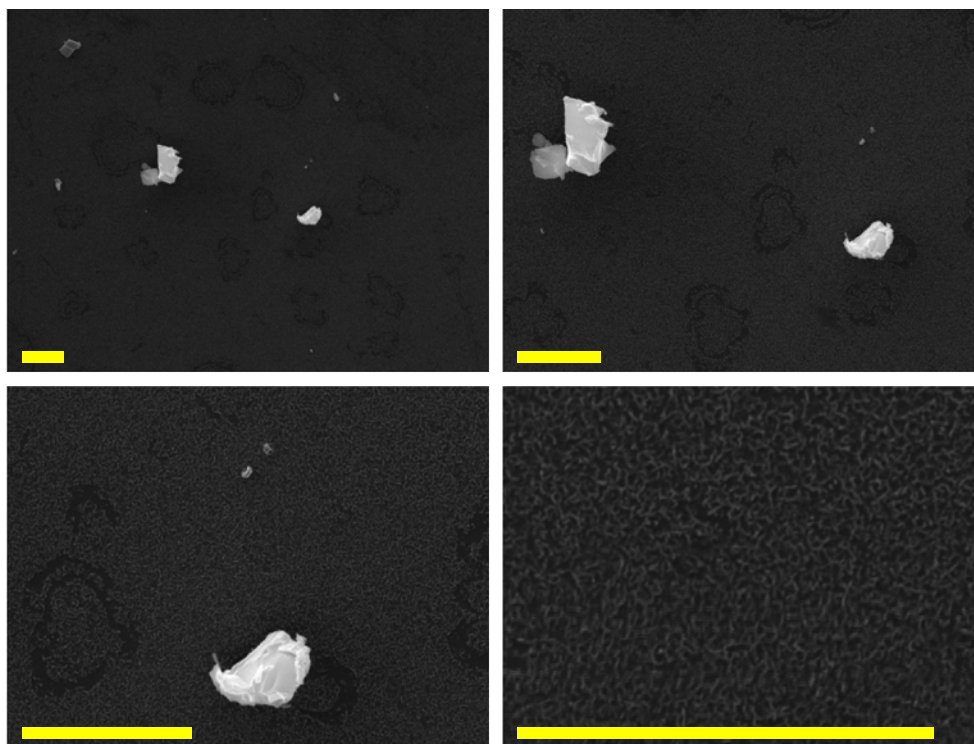


Figure S26. SEM image of the product using $\text{Zn}^{2+}:\text{2mIM} = 1:4$ on glass surface after 30 second (scale bar = 25 μm).

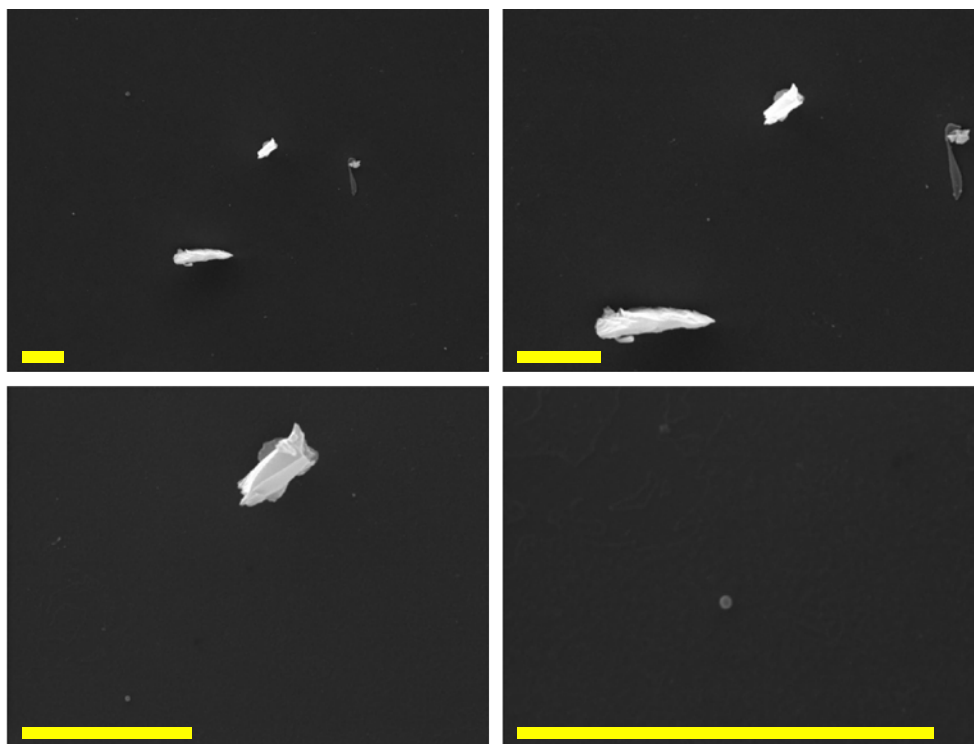


Figure S27. SEM image of the product using $\text{Zn}^{2+}:\text{2mIM} = 1:4$ on glass surface after 30 minutes (scale bar = 25 μm).

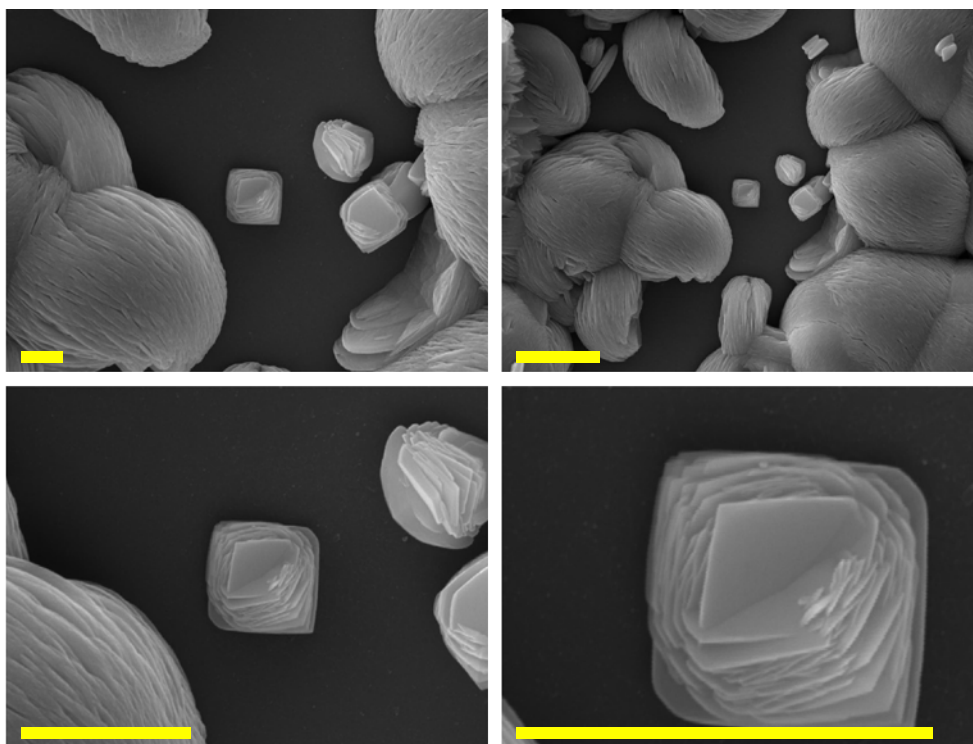


Figure S28. SEM image of the product using $\text{Zn}^{2+}:\text{2mIM} = 1:4$ on glass surface after 24 hours (scale bar = 25 μm).

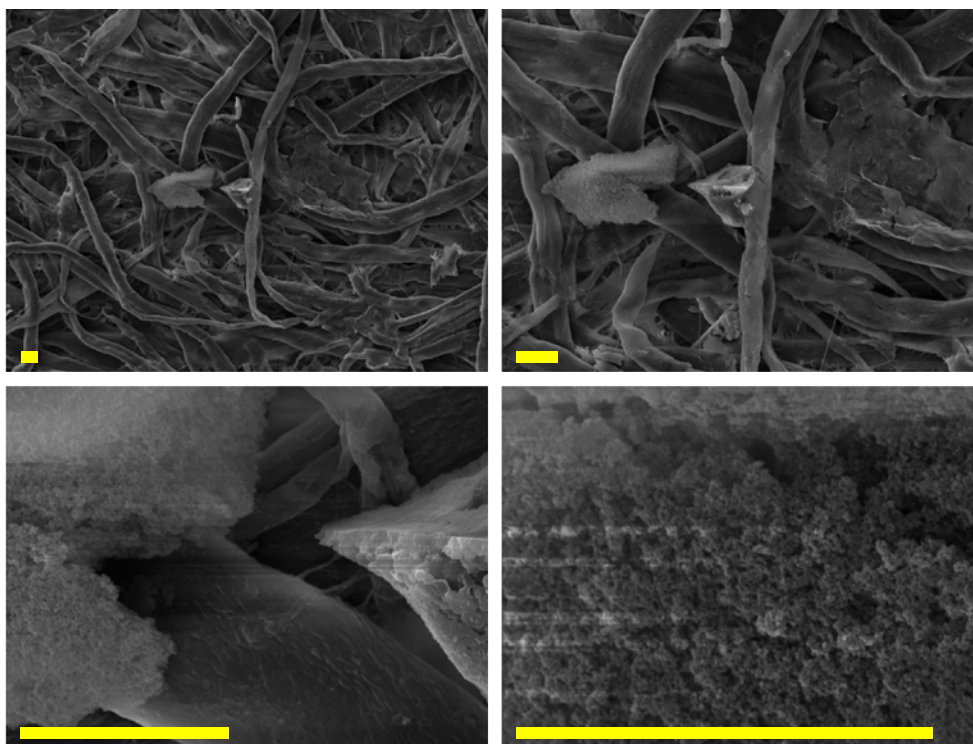


Figure S29. SEM image of the product using $\text{Zn}^{2+}:\text{2mIM} = 1:4$ on paper after 30 second (scale bar = 25 μm).

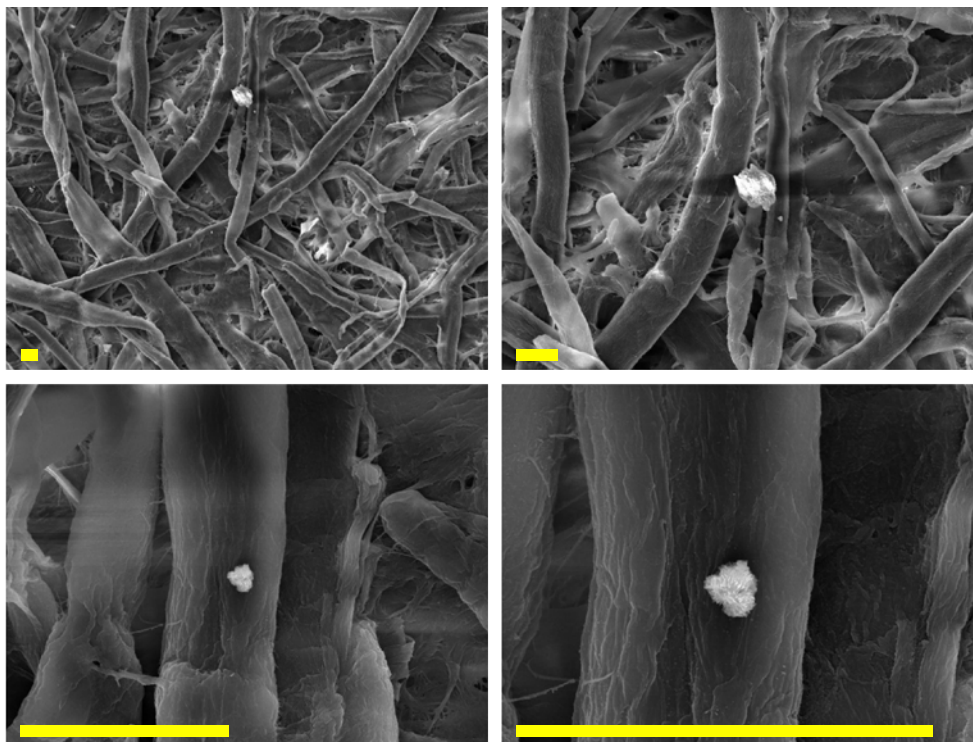


Figure S30. SEM image of the product using $\text{Zn}^{2+}:\text{2mIM} = 1:4$ on paper after 30 minutes (scale bar = 25 μm).

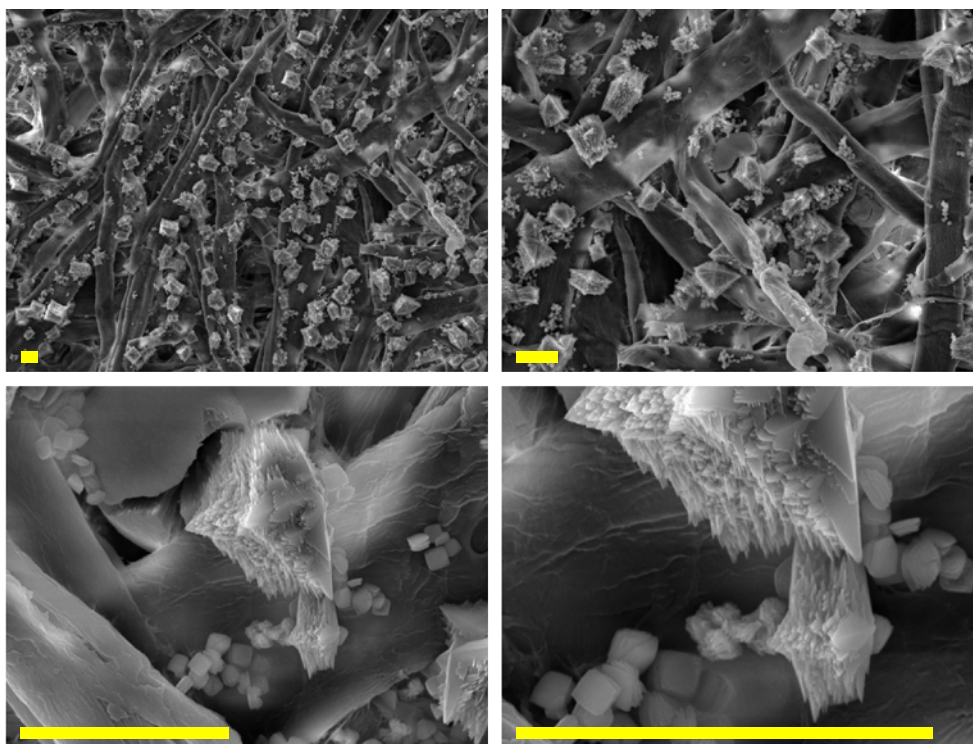


Figure S31. SEM image of the product using $\text{Zn}^{2+}:\text{2mIM} = 1:4$ on paper after 24 hours (scale bar = 25 μm).

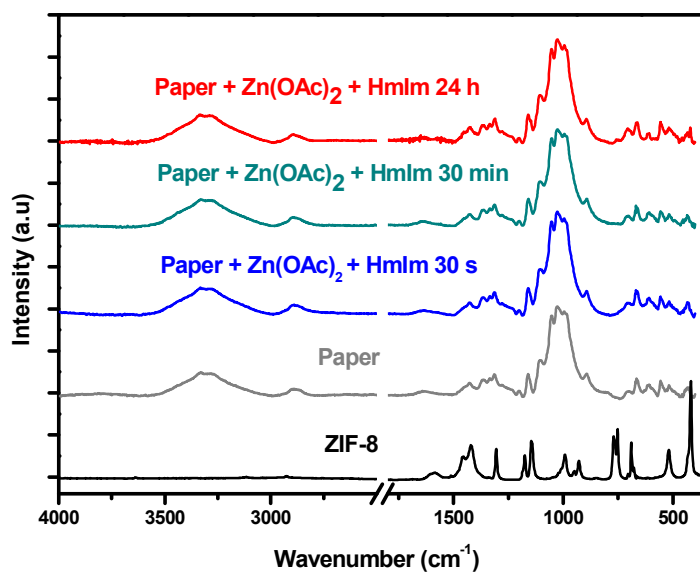


Figure S32. FTIR Spectra of paper (S&S filter paper 110 mm) with Zn²⁺:2mIM = 1:4 after 30 second, 30 minutes and 24 hours compared with ZIF-8.

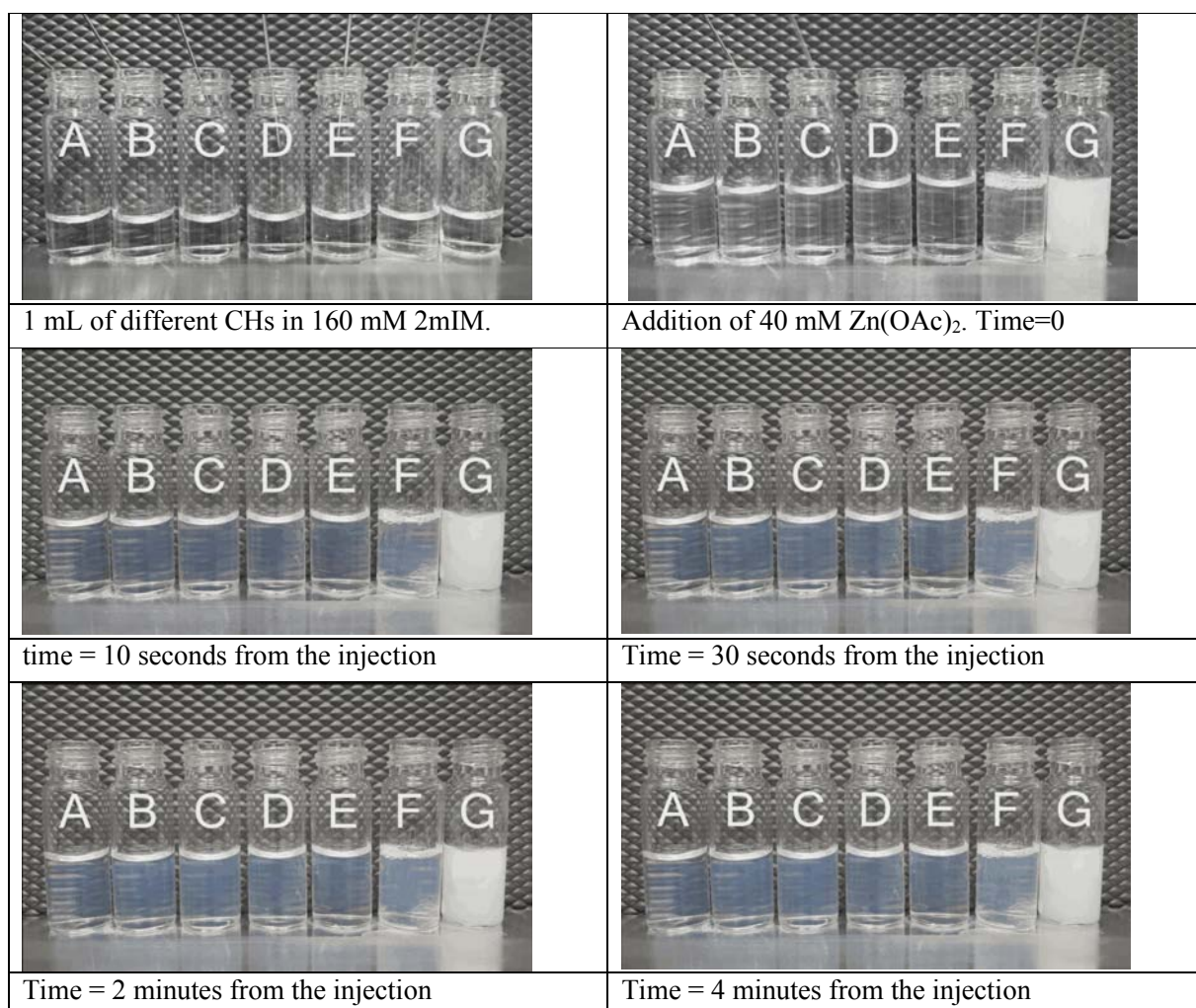


Figure S33. Photographs of solutions using the polysaccharides with different molecular weights and chemical functionalizations.

The video is available as supporting information. Photographs of solutions using the polysaccharides listed in table on the next page. Composition and procedure: 1 mg of the respective carbohydrate (listed in Table on the next page) was dissolved in 1 mL of a freshly prepared 2mIM solution (160 mM in DI Water) at ambient temperature (Figure S33). After 30 min, 1 mL of the 2nd precursor solution (Zn(OAc)₂, 40mM in DI water) was added at once in all vials (Figure S33).

Table of CHs with different molecular weights and chemical functionalizations

Sample		MW (g/mol)	comment
A	Blank	-	NO polysaccharide added
B	Maltodextrin	3.000-4.000	-
C	Dextran	6.000	-
D	Dextran	40.000	-
E	Dextran	70.000	-
F	Diethylaminoethyl dextran	10.000	2.5-4.5% nitrogen; (ca. one substituent on every 3 rd glucose unit)
G	Carboxymethyl dextran sodium salt	10.000-20.000	1.1-1.5 mmol/g; (ca. one substituent on every 3 rd glucose unit)

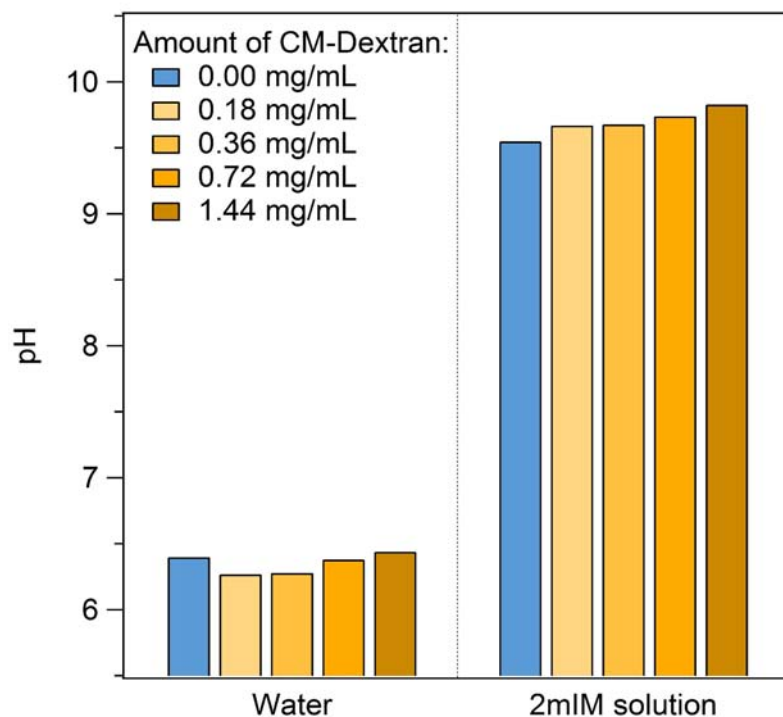


Figure S34. The pH of CM-dextran (0, 0.18, 0.36, 0.72, 1.44 mg/mL) in H₂O and 2mIM solutions with total volume 2 mL.

The pH for solutions prepared according to the volumes and the concentrations used for the synthesis of CM-dextran@ZIF-8. Based on the values of the pH measured with respect to the control samples (no CM-dextran), it does not seem that the CM-dextran plays a significant role in the deprotonation of the ligand. However, the ligand itself changes the pH from 6.4 (water) to c.a. 9.5 (mixture 2mIM in water).

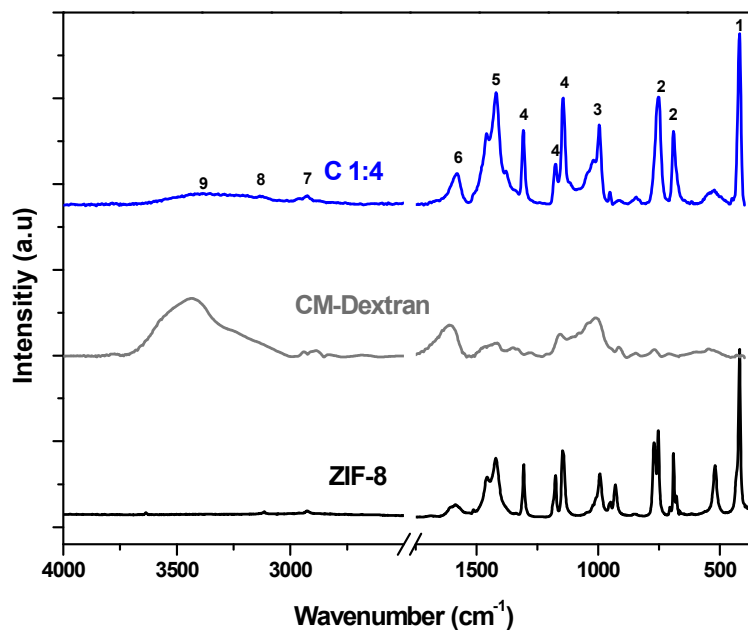


Figure S35. FTIR spectra of CM-dextran@ZIF-8 (Zn^{2+} :2mIM = 1:4)

The assignment of the vibrational modes is reported in the table below.

Table of FTIR interpretation of CM-dextran@ZIF-8

No	Characteristic Absorptions (cm^{-1})	Functional Group	References
1	421	Zn-N stretching	2
2	600-800	Out plane bending of the 2mIM ring	2 3
3	900-1350	In plane bending of the 2mIM ring	2 3
4	997	C-O stretching of CM-dextran	4
5	1420	Entire ring stretching of 2mIM	5
6	1608	COO ⁻ of CM-dextran	6 7
7	2926	Aliphatic C-H stretching of 2mIM	5
8	3120	Aromatic C-H stretching of 2mIM	5
9	2850-3600	O-H stretching	8

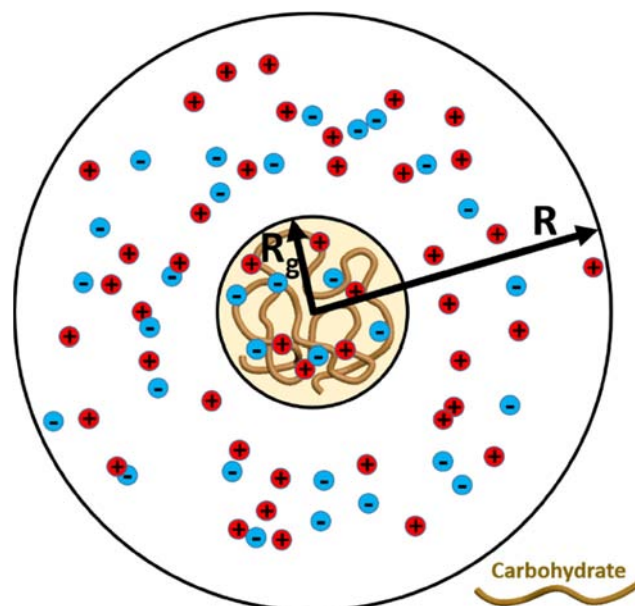


Figure S36. Schematic of the ion-permeable spherical model of a carbohydrate chain with a radius of gyration (R_g) in an electrolyte solution. The electrostatic potential was taken to be zero at a large distance, R , from the centre of the ion-permeable sphere.

We modelled a dextran chain as an ion-permeable sphere with a radius given by the radius of gyration (R_g) of a freely-jointed chain of length N segments (**Figure S36**),⁹ since single molecule AFM studies of functionalized and native dextran chains have shown from their elasticity that they can be described approximately as freely-jointed chains with Kuhn lengths equal to the length of the glucose monomer (4.4 Å).^{10,11} Therefore, the number of segments, N , was equal to the degree of polymerization (DP).⁹ Although branching is common for dextran chains, the branching density of the experimental sample was unknown, so for simplicity we assumed that the dextran chain in our model was unbranched. Nevertheless, we do not expect the conclusions from the model to change significantly if branching was considered. We applied the ion-permeable sphere model because most of the pervaded volume will be accessible to ions in solution (the average separation of monomers in the pervaded volume ≈ 5.7 Å, whereas the diameter of Zn^{2+} ion is 1.48 Å and the diameter of the acetate counter-ion is ≈ 3.72 Å)^{12,13}. Table S6 below shows the parameters used.

Table S6. Parameters of the ion-permeable sphere model of dextrans.

parameter	value
carbohydrate concentration	0.72 mg mL ⁻¹
degree of polymerisation (DP)	60
Kuhn length (l_k)	4.4 Å ¹⁰
polymer molecular weight (M)	≈ 10kDa
radius of gyration (R_g)	13.91 Å
bulk zinc concentration ($c_{+, \text{bulk}}$)	0.04 M
pK_a of CM	4.0
pK_a of AM	10.64 ¹⁴
pH	11

Under the standard ZIF-8 synthesis conditions used throughout this work, the bulk zinc ion (Zn^{2+}) concentration ($c_{+, \text{bulk}}$) is 0.04 M and the concentration of counter ions, with a valency of -1, is 0.08 M. The Debye length (λ_D) is

$$\lambda_D = \kappa^{-1} = \left(\frac{\epsilon_r \epsilon_0 k_B T}{2e^2 I} \right)^{1/2}, \quad (\text{S1})$$

where ϵ_0 is the vacuum permittivity, ϵ_r is the relative permittivity of water (80), T is temperature (298 K), k_B is the Boltzmann constant, e is the elementary charge, and I is the ionic strength of the electrolyte solution, giving $\lambda_D = 8.86$ Å.

The average number of functionalized sites per glucose monomer is given by the degree of substitution (DS), α , which can take any value from 0 to 3. DS was approximately 0.125 in the experiments presented in this paper, which corresponds to 1 functionalized group every eight monomers. We calculated the total charge (Q_{\pm}) on a dextran chain as $Q_{\pm} = \alpha N q_{\pm}$, where q_{\pm} is the average charge of a functional group on the chain, given by the Henderson-Hasselbach equation,

$$q_{\pm} = \pm \frac{10^{\mp \text{pH} \pm pK_a}}{10^{\mp \text{pH} \pm pK_a} + 1}, \quad (\text{S2})$$

where the sign of q_{\pm} is determined by the sign of the charge on the functionality (-1 for CM and +1 for AM). A range of values have been reported for pK_a of the CM functionality, but in all cases it is much smaller than the pH (≈ 11) used in the experiments. Thus, each CM functionality is expected to have a full negative charge under the experimental conditions. Furthermore, there are multiple amine species associated with the AM functionality and it is expected that each amine will have a different pK_a . For

simplicity, we have assumed a single pK_a value, representative of a tertiary amine,¹⁴ which will be partially positively charged at the pH used in the experiments. The following figure shows the volume charge density ($\rho_s = \frac{3Q_{\pm}}{4\pi R_g^3}$) as a function of DS for both functionalities with the specified parameters (**Table S6**).

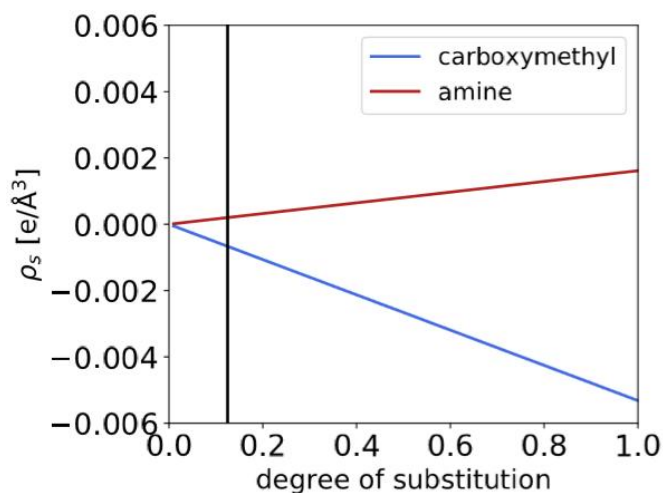


Figure S37. Volume charge density (ρ_s) of the ion-permeable spheres as a function of degree of substitution for carboxymethyl (CM) and amine (AM) functionalities. The black line represents the approximate DS used in the experiments.

We used the boundary value problem solver in the SciPy Python library¹⁵ to solve the nonlinear Poisson-Boltzmann (PB) equation around an ion-permeable sphere,¹⁶

$$\nabla^2 \psi = -\frac{e}{\epsilon_r \epsilon_0} \left[\sum_{i=\pm} c_{i, \text{bulk}} z_i \exp\left(\frac{-z_i e \psi}{k_B T}\right) \right] - \frac{\rho(r)}{\epsilon_r \epsilon_0}, \quad (\text{S3})$$

where ψ is the electrostatic potential at the radial coordinate r , $c_{\pm, \text{bulk}}$ and z_{\pm} are the bulk concentration and valency of the positive zinc ions ($c_{+, \text{bulk}} = 0.04\text{M}$ and $z_+ = +2$) and negative acetate ions ($c_{-, \text{bulk}} = 0.08\text{M}$ and $z_- = -1$) in solution, respectively, and $\rho(r)$ is the charge density due to the carbohydrate chain, given by

$$\rho(r) = \begin{cases} \rho_s, & \text{if } 0 \leq r \leq R_g \\ 0, & \text{if } r > R_g \end{cases}. \quad (\text{S4})$$

The following boundary conditions were applied to Equation S3:

$$1. \lim_{r \rightarrow 0} \frac{d\psi}{dr} = 0 \quad (\text{S5})$$

$$2. \psi(r = R) \rightarrow 0 \quad (\text{S6})$$

R was set to a large enough value (100 Å) such that its specific value did not affect the calculated potential or ion concentration near the ion-permeable sphere. We also applied the analytical solution to the linearized PB equation for an ion-permeable sphere reported by Ohshima and co-workers.¹⁷ We note that the linearized

PB equation is only applicable when $|\psi| \ll \frac{k_B T}{z_+ e} \approx 12$ mV. Therefore, numerical solutions to the nonlinear PB equation were required in general. At low DS values ($\alpha < 0.04$), where the assumptions of the linearized PB equation are expected to hold, we found good agreement between the analytical and numerical results. For numerical stability, we replaced the step-function form of $\rho(r)$ in Equation 4 by the smooth function

$$\rho(r) = -\frac{\rho_s}{2} \left[\tanh\left(\frac{r-R_g}{2w}\right) - 1 \right], \quad (\text{S7})$$

where w defines the width of the transition of $\rho(r)$ from ρ_s to 0. w was set to $0.02\lambda_D$ and the final enhancement results were found to be robust to changes in w in the range $0.01\lambda_D \leq w \leq 0.5\lambda_D$.

From the electrostatic potential calculated using the PB equation, the concentration of zinc ions, $c_+(r)$, at radial coordinate r was calculated using

$$c_+(r) = c_{+, \text{bulk}} \exp\left[\frac{-z_+ e \psi(r)}{k_B T}\right]. \quad (\text{S8})$$

The zinc ion enhancement at radial coordinate r is the ratio $\frac{c_+(r)}{c_{+, \text{bulk}}}$.

The electrostatic potential and zinc ion enhancement is reported at $r = 0$ (in Figures 2c and S37) because the approximate size of the MOF precursors (Zn^{2+} diameter = 1.48 Å and 2mIM diameter ≈ 5.2 Å) are smaller than the average separation of monomers in the pervaded volume (≈ 5.7 Å). Therefore, it is possible that ZIF formation would occur anywhere within the pervaded volume of the carbohydrate chain. Thus, it can reasonably be expected that ZIF formation will be governed by the electrostatic potential and zinc ion enhancement at the centre of the ion-permeable sphere where the zinc ion concentration is greatest, but we note that ZIF growth could be seeded at any point for $0 \leq r \leq R_g$.

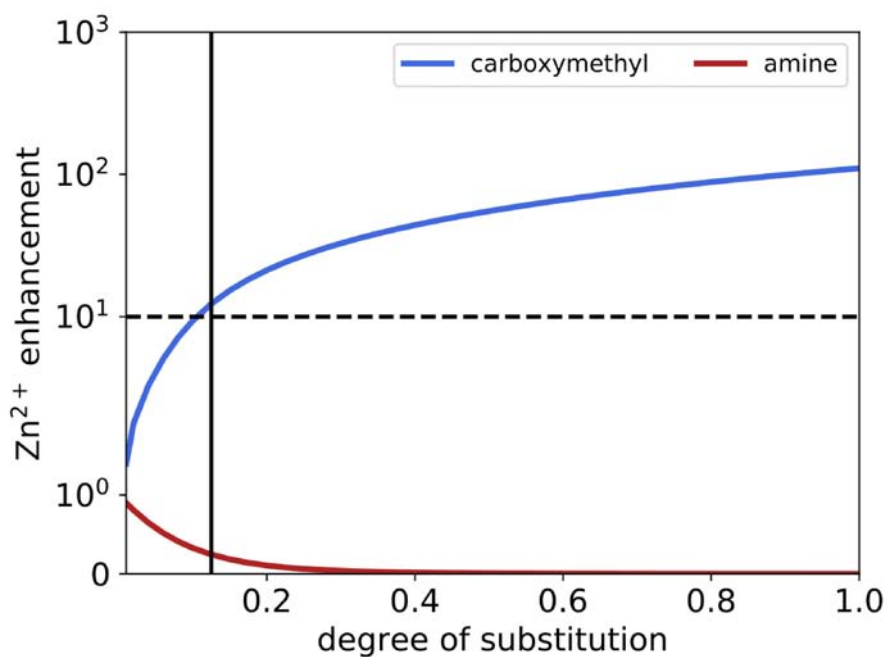


Figure S38. Calculated Zn²⁺ ion enhancement at the center of the carbohydrate versus degree of carboxymethyl or amino functionalization.

The code used for all calculations is available at https://bitbucket.org/andrewtarzia/sugar_source/

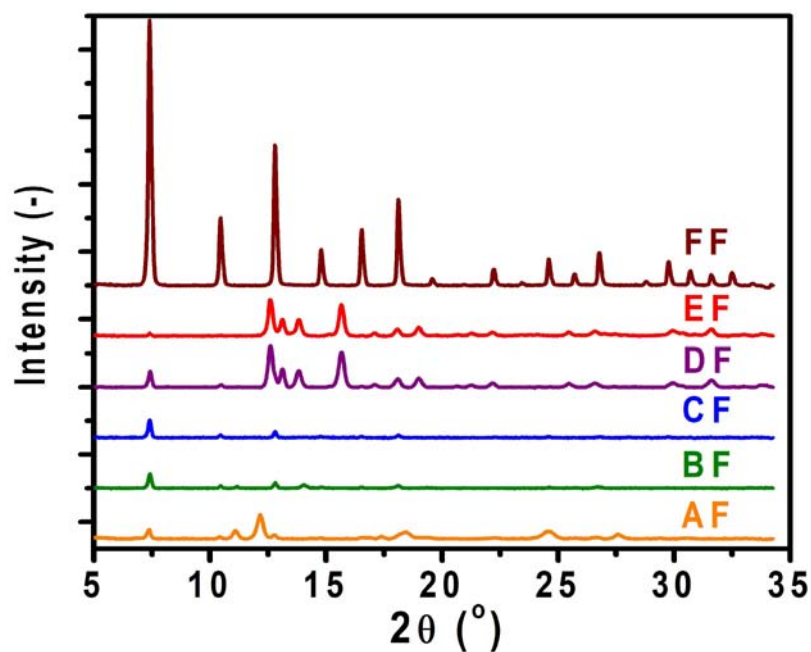


Figure S39. XRD of the FITC-CM-dextran@ZIF-8 biocomposites obtained with different metal-to-ligand ratios (AF = 1:2.52, BF = 1:3.47, CF = 1:4, DF = 1:6, EF = 1:8, FF=1:16).

The samples were synthesized analogous to synthesize CM-Dextran@ZIF-8, but using the FITC-CM-dextran in place of CM-dextran. The precipitates were collected by centrifugation and washed with H₂O and EtOH and dried in ambient temperature. AF found to be a mixture of phases, dominated by U12, BF and CF are predominantly sod, DF, and EF were a mixture of dia- and sod-Zn(mIM)₂ phases, while FF was found to be pure sod-Zn(mIM)₂.

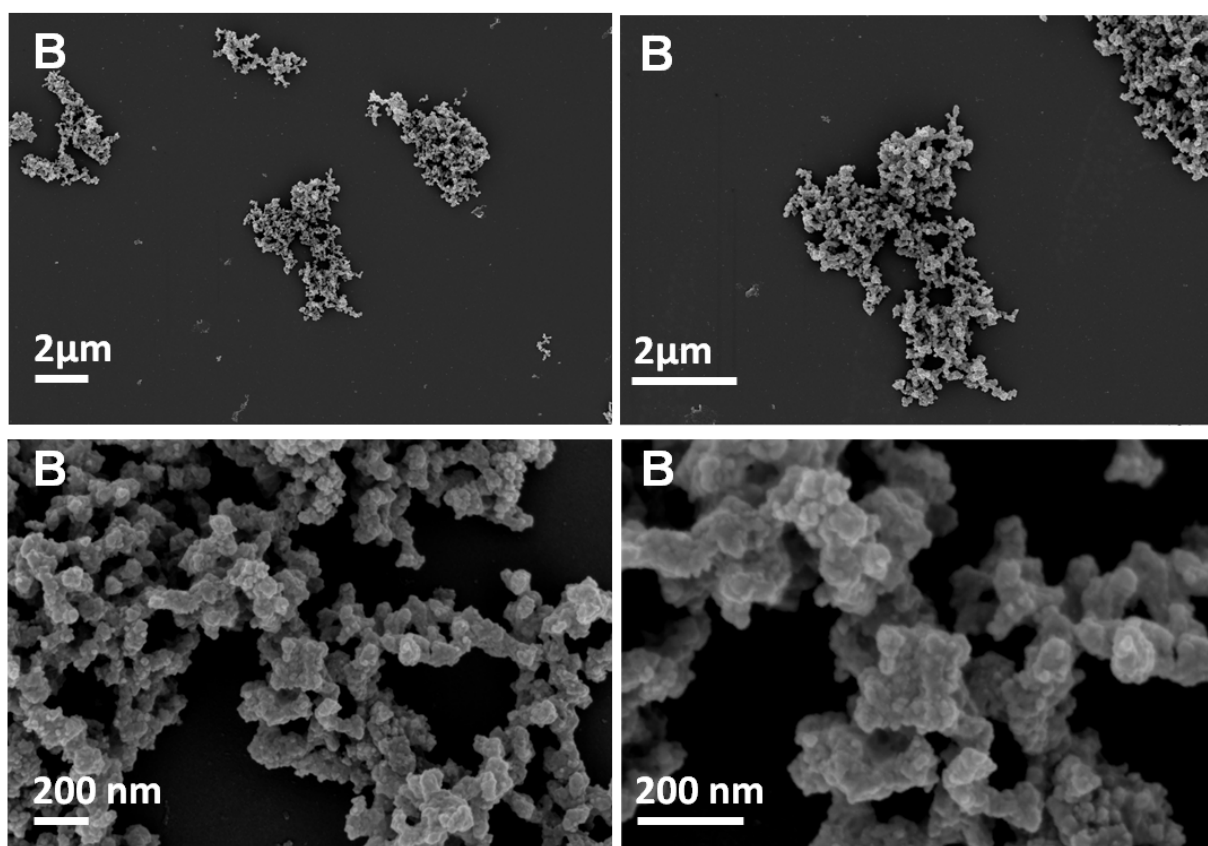


Figure S40. SEM images of B sample ($\text{Zn}^{2+}:\text{2mIM} = 1:3.47$).

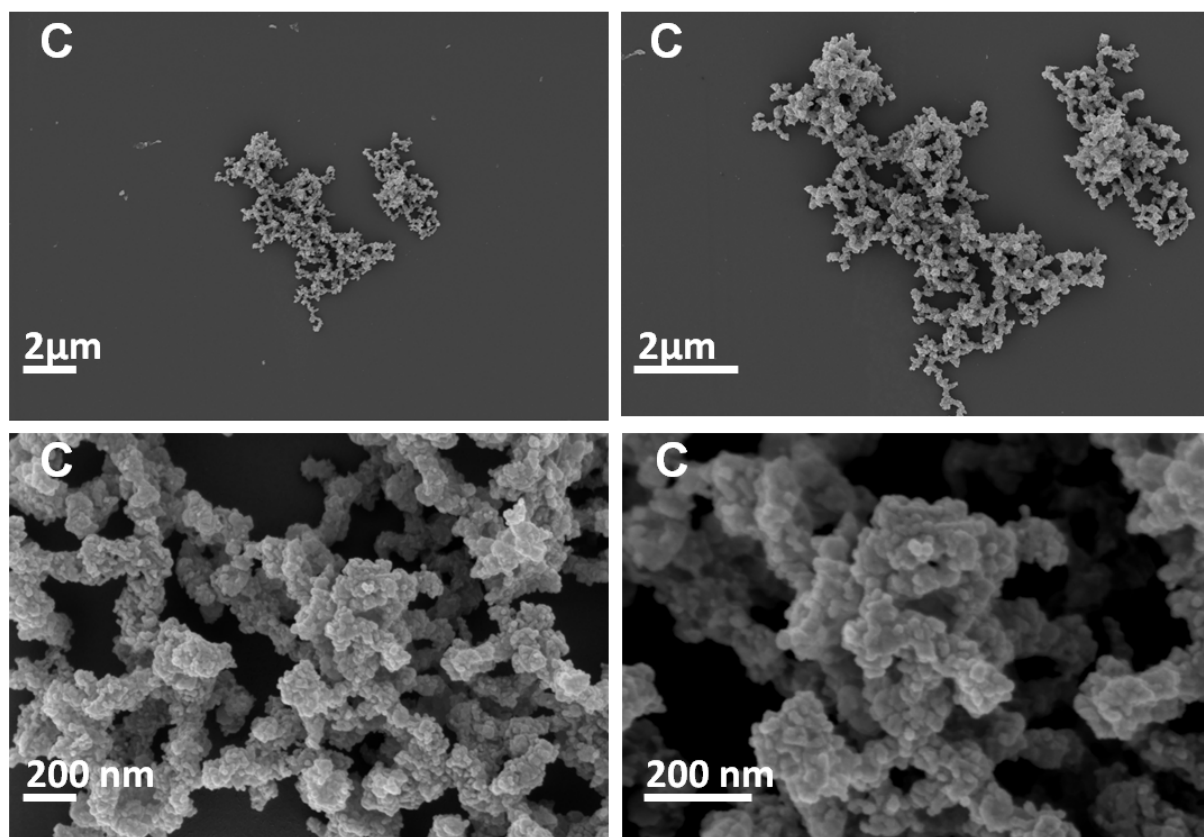


Figure S41. SEM images of C sample ($\text{Zn}^{2+}:\text{2mIM} = 1:4$).

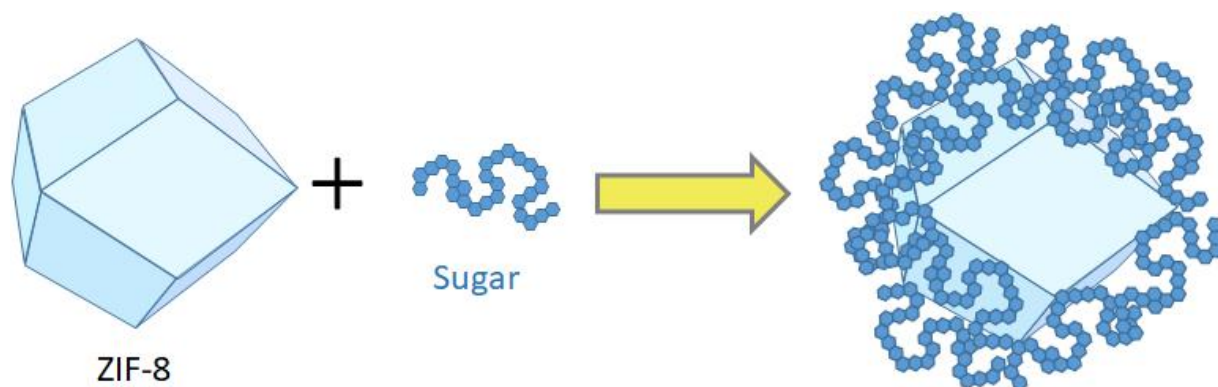
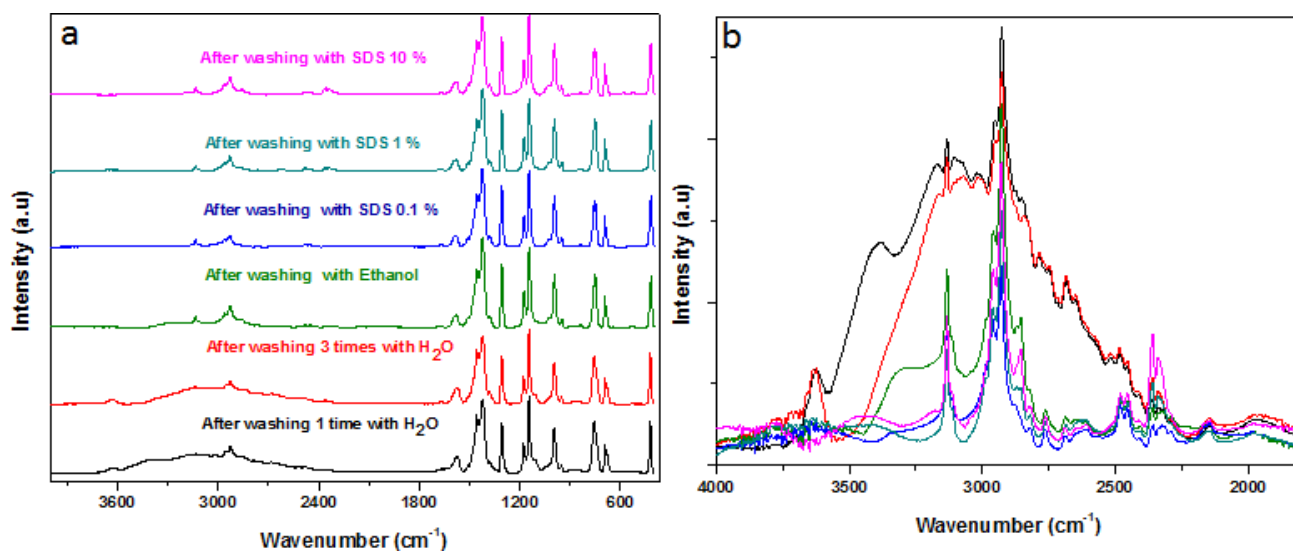


Figure S42. Schematic illustration of sugar on the surface of ZIF-8.

This was used for the optimization of the washing procedure (for the detail see page 5).



a) Pre-synthesized ZIF-8 subsequently exposed to CM-dextran. These samples were washed with H₂O one time (black), H₂O three times (red), ethanol (green), SDS 0.1 % (blue), SDS 1% (cyan) and SDS 10 % (magenta) b) Magnified spectra in the 4000-1800 cm⁻¹. The broad band between 3500 and 2500 cm⁻¹ corresponds to OH groups from CM-dextran after washing with H₂O, EtOH and SDS. Washing with EtOH removed the majority of CM-dextran, so washing with SDS was considered unnecessary.

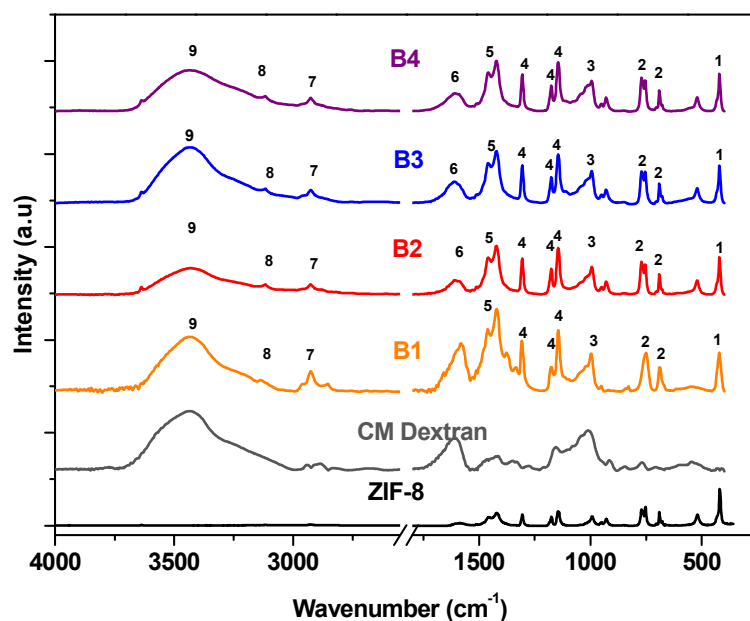


Figure S43. FTIR spectra of various CM-dextran@ZIF-8 B recipes ($\text{Zn}^{2+}:\text{2mIM} = 1:3.47$).

The assignment of the vibrational modes is reported in the table below.

Table of FTIR interpretation of CM-dextran B recipes

No	Characteristic Absorptions (cm^{-1})	Functional Group	References
1	421	Zn-N stretching	2
2	600-800	Out plane bending of the 2mIM ring	2 3
3	900-1350	In plane bending of the 2mIM ring	2 3
4	997	C-O stretching of CM-dextran	4
5	1420	Entire ring stretching of 2mIM	5
6	1608	COO ⁻ of CM-dextran	6 7
7	2926	Aliphatic C-H stretching of 2mIM	5
8	3120	Aromatic C-H stretching of 2mIM	5
9	2850-3600	O-H stretching	8

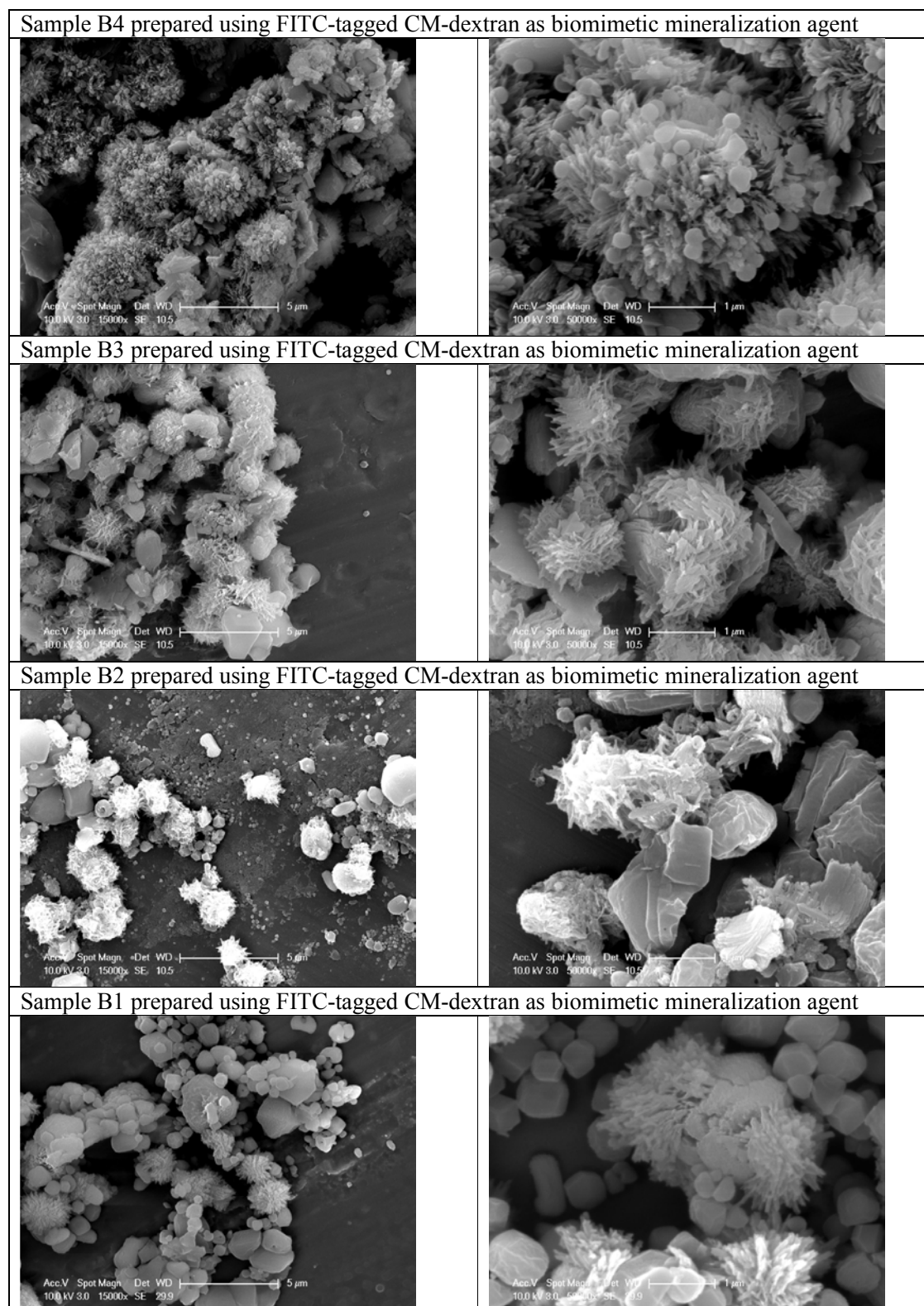


Figure S44. SEM image of ZIF-8 prepared using different concentrations of FITC-tagged CM-dextran: B1 = 0.18, B2 = 0.36, B3 = 0.72 and B4 = 1.44 mg mL⁻¹.

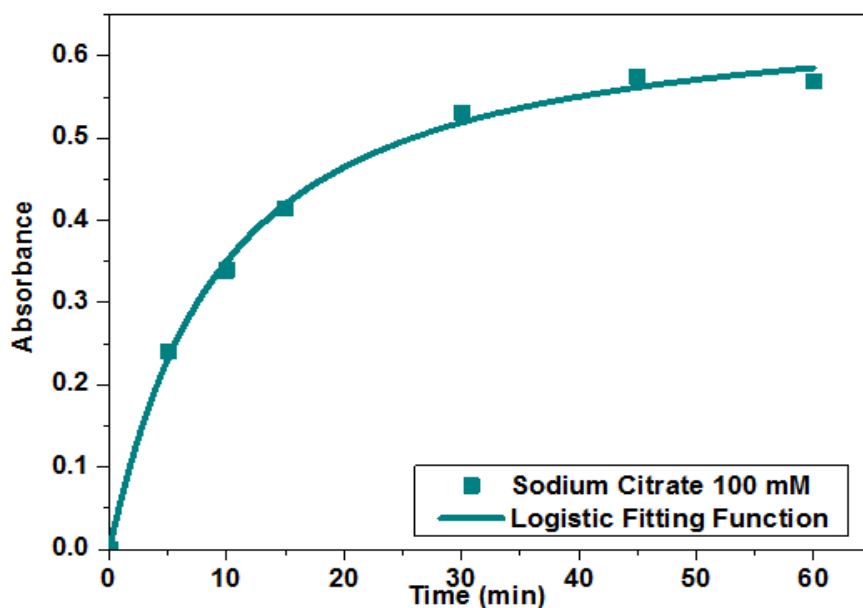


Figure S45. Release test of FITC-CM-dextran@ZIF-8 with 100 mM of sodium citrate (pH = 6).

$$Y = \frac{A2 + (A1 - A2)}{\left(1 + \left(\frac{x}{x0}\right)^p\right)}$$

Adj. R-Square 0.99375		
	Value	Standard Error
A1	0.00104	0.01655
A2	0.66336	0.05128
x0	9.02336	1.55683
p	1.06347	0.19551

The release test procedure of BF2 with sodium citrate was similar to release test with EDTA. Sample was mixed with sodium citrate solution 100 mM. The sample was vortex mixed for three second. At regular interval of 1 hour the mixture was centrifuge 1 min at 11337 ref, then 1 mL of supernatant taken with micropipettes.

Monitoring the absorbance at 490 nm with time (please see figure above), we could prove that FITC-CM-Dextran can be released from FITC-CM-Dextran@ZIF-8 exposed to the sodium citrate solution. The experimental points can be fitted using a logistic fitting function.

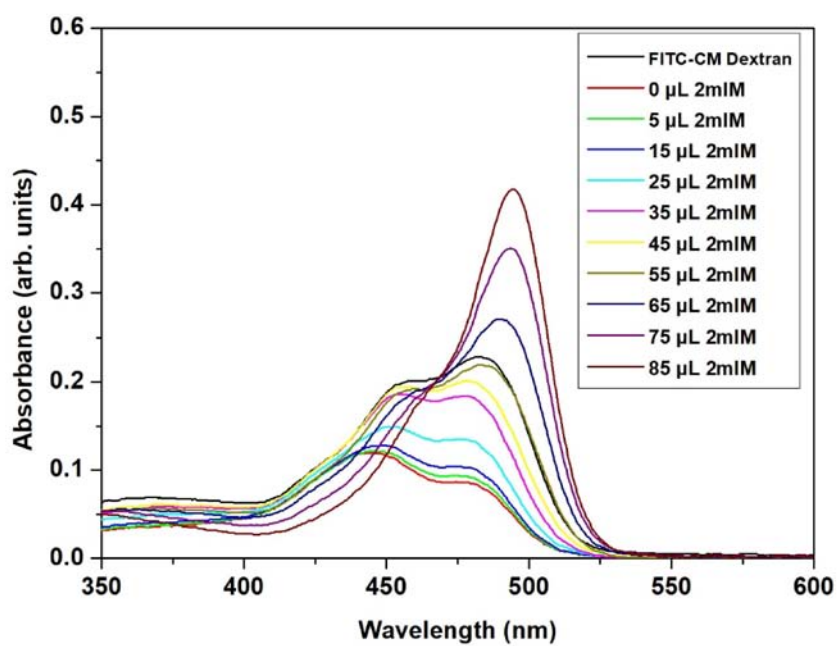
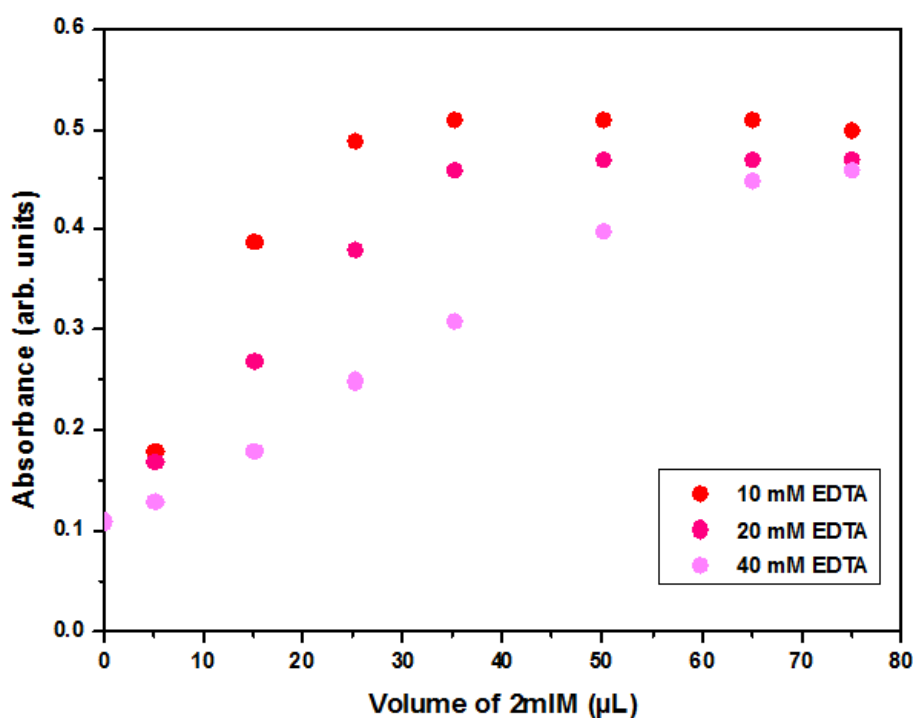


Figure S46. The UV-VIS absorbance of FITC-CM-dextran after adding EDTA, $\text{Zn}(\text{OAc})_2 \cdot 2\text{H}_2\text{O}$ and 2mIM.



B3F Solution after release test	Volume Of Final Solution (μL)	Volume of 2 mIM (μL)	Absorbance		Correction Factor $F_{2\text{mIM}} = Y/X$
			X	Y	
10 mM EDTA	600	0	0.38		1.00
	600	12.5		0.38	
20 mM EDTA	600	0	0.22		1.76
	600	17.5		0.39	
40 mM EDTA	600	0	0.17		2.24
	600	32.5		0.38	

Figure S47. Correction Factor based on 2mIM was determined by measuring the absorbance intensity of FITC-CM-dextran at different concentrations of EDTA (10, 20, 40 mM) after adding 2mIM with different volumes.

The absorbance intensity of FITC-CM-dextran becomes constant after the addition of certain amount of 2mIM. Y is determined from absorbance intensity after adding the certain amount of 2mIM to the final solutions of release test with the different EDTA, meanwhile X is the absorbance intensity of the final solution after release tests with different concentration of EDTA. Correction factor based on 2mIM ($F_{2\text{mIM}}$) = Y/X.

References

1. Hodge, J. E. & Rist, C. E. The Amadori Rearrangement under New Conditions and its Significance for Non-enzymatic Browning Reactions. *J. Am. Chem. Soc.* **75**, 316–322 (1953).
2. Low, Z. X. *et al.* Crystal transformation in zeolitic-imidazolate framework. *Cryst. Growth Des.* **14**, 6589–6598 (2014).
3. Jian, M. *et al.* Water-based synthesis of zeolitic imidazolate framework-8 with high morphology level at room temperature. *RSC Adv.* **5**, 48433–48441 (2015).
4. Glišić, S., Nikolić, G., Cakić, M. & Trutić, N. Spectroscopic study of copper(II) complexes with carboxymethyl dextran and dextran sulfate. *Russ. J. Phys. Chem. A* **89**, 1254–1262 (2015).
5. Hu, Y., Kazemian, H., Rohani, S., Huang, Y. & Song, Y. In situ high pressure study of ZIF-8 by FTIR spectroscopy. *Chem. Commun.* **47**, 12694 (2011).
6. Repko, A., Nižňanský, D., Matulková, I., Kalbáč, M. & Vejpravová, J. Hydrothermal preparation of hydrophobic and hydrophilic nanoparticles of iron oxide and a modification with CM-dextran. *J. Nanoparticle Res.* **15**, (2013).
7. Sun, Y. X., Zhang, X. Z., Cheng, H., Cheng, S. X. & Zhuo, R. X. A low-toxic and efficient gene vector: Carboxymethyl dextran-graft- polyethylenimine. *J. Biomed. Mater. Res. - Part A* **84**, 1102–1110 (2008).
8. Heyn, A. N. J. The infrared absorption spectrum of dextran and its bound water. *Biopolymers* **13**, 475–506 (1974).
9. Rubinstein, M. & Colby, R. H. *Polymer physics. Polymer International* Oxford University Press, Oxford (2003).
10. Marszalek, P. E., Oberhauser, A. F., Pang, Y. P. & Fernandez, J. M. Polysaccharide elasticity governed by chair-boat transitions of the glucopyranose ring. *Nature* **396**, 661–664 (1998).
11. Rief, M., Oesterhelt, F., Heymann, B. & Gaub, H. E. Single Molecule Force Spectroscopy on Polysaccharides by Atomic Force Microscopy. *Science*. **275**, 1295–1298 (1997).
12. Shannon, R. D. Revised effective ionic radii and systematic studies of interatomic distances in halides and chalcogenides. *Acta Crystallogr. Sect. A* **32**, 751–767 (1976).
13. Simoes, M. C., Hughes, K. J., Ingham, D. B., Ma, L. & Pourkashanian, M. Estimation of the Thermochemical Radii and Ionic Volumes of Complex Ions. *Inorg. Chem.* **56**, 7566–7573 (2017).
14. Rayer, A. V., Sumon, K. Z., Jaffari, L. & Henni, A. Dissociation constants (pKa) of tertiary and cyclic amines: Structural and temperature dependences. *J. Chem. Eng. Data* **59**, 3805–3813 (2014).

15. Oliphant, T. E. Python for scientific computing. *Comput. Sci. Eng.* **9**, 10–20 (2007).
16. Wall, F. T. & Berkowitz, J. Numerical solution to the poisson-boltzmann equation for spherical polyelectrolyte molecules. *J. Chem. Phys.* **26**, 114–122 (1957).
17. Ohshima, H. & Kondo, T. Electrostatic double-layer interaction between two charged ion-penetrable spheres: An exactly solvable model. *J. Colloid Interface Sci.* **155**, 499–505 (1993).

2.2 Modulation of metal-azolate frameworks for the tunable release of encapsulated glycosaminoglycans

ZIF-8-based biocomposites have been actively studied for various applications (e.g. DDS, biopreservation, cell and virus manipulation, and biosensing); however, only limited attention has been given to ZIF-90 and MAF-7. [10,15,17,19,23,74] Recently, it has been reported that the activity of enzymes encapsulated in ZIF-8, ZIF-90, and MAF-7 is superior for hydrophilic ZIFs (ZIF-90 and MAF-7). Conversely, hydrophobic ZIF-8 demonstrated a substantial deactivation of the encapsulated enzymes. This study highlighted the importance of hydro-phobic/-philic ZIFs for the encapsulation of biomacromolecules.^[54]

Inspired by this work, we investigated whether the different chemical properties of ZIF-8, ZIF-90, and MAF-7 could also affect their performance as drug delivery carriers. Having known that ZIF-8 precursors could be used for the encapsulation of negatively charged carbohydrates (i.e. CM-dextran), we also investigated ZIF-90 and MAF-7 as carriers for carbohydrate-based therapeutics. Thus, in this study, we tested the encapsulation, protection, and release of carbohydrate-based therapeutics (HP, HA, DS, CS, GM-1111, and HepSYL) using three aforementioned MAFs. Then, we determined the encapsulation efficiency and the release profile for each biocomposite. Finally, we investigated the biopreservation properties of these MOF shells by comparing the anticoagulant activity of free heparin and heparin released from ZIF-8, ZIF-90, and MAF-7 carriers after being exposed to lyase agent (heparinase I).

Cite this: *Chem. Sci.*, 2020, **11**, 10835

All publication charges for this article have been paid for by the Royal Society of Chemistry

Modulation of metal-azolate frameworks for the tunable release of encapsulated glycosaminoglycans†

Miriam de J. Velásquez-Hernández,^a Efwita Astria,^a Sarah Winkler,^a Weibin Liang,^b Helmar Wiltsche,^c Arpita Poddar,^d Ravi Shukla,^d Glenn Prestwich,^e John Paderi,^f Pablo Salcedo-Abraira,^g Heinz Amenitsch,^h Patricia Horcajada,^g Christian J. Doonan^{g*} and Paolo Falcaro^{g*}

Glycosaminoglycans (GAGs) are biomacromolecules necessary for the regulation of different biological functions. In medicine, GAGs are important commercial therapeutics widely used for the treatment of thrombosis, inflammation, osteoarthritis and wound healing. However, protocols for the encapsulation of GAGs in MOFs carriers are not yet available. Here, we successfully encapsulated GAG-based clinical drugs (heparin, hyaluronic acid, chondroitin sulfate, dermatan sulfate) and two new biotherapeutics in preclinical stage (GM-1111 and HepSYL proteoglycan) in three different pH-responsive metal-azolate frameworks (ZIF-8, ZIF-90, and MAF-7). The resultant GAG@MOF biocomposites present significant differences in terms of crystallinity, particle size, and spatial distribution of the cargo, which influences the drug-release kinetics upon applying an acidic stimulus. For a selected system, heparin@MOF, the released therapeutic retained its antithrombotic activity while the MOF shell effectively protects the drug from heparin lyase. By using different MOF shells, the present approach enables the preparation of GAG-based biocomposites with tunable properties such as encapsulation efficiency, protection and release.

Received 28th February 2020
Accepted 11th July 2020

DOI: 10.1039/d0sc01204a

rsc.li/chemical-science

Introduction

Metal-organic frameworks (MOFs) are a class of extended materials composed of metal nodes connected *via* multidentate organic linkers.^{1,2} The chemical mutability of these building blocks permits tailoring the properties of MOFs for applications ranging from gas storage to chemical sensing and catalysis.^{3,4} More recently, MOFs have been studied for drug delivery because of their high encapsulation efficiency, tunable release profile, high selectivity toward specific cells and tissues, and low cytotoxicity.⁵ MOFs can be loaded with different therapeutics,

including biomacromolecules and assembly of thereof (proteins, DNA, viruses and cells).^{6–8} In these cases, the MOF coating acts as a protective carrier that can be dissolved under controlled conditions to release the bioentities.^{7,9–12} The immobilisation of large biomolecules within Zn-based zeolitic imidazolate frameworks (ZIFs),^{13–16} including ZIF-8 and related topologies, ZIF-90 and MAF-7,^{17–20} is commonly achieved *via* encapsulation.^{6–8} The widespread interest in ZIFs for the encapsulation of biomacromolecules is due to their compatibility with aqueous synthetic conditions,⁶ their hydrolytic stability,²¹ and their controlled release properties (*e.g. via* acidic pH or addition of chelating agents).²² These properties have been exploited for the design of stimulus-responsive drug delivery systems.^{23–26}

Despite the versatility of the encapsulation protocol, we recently demonstrated that not all the biomacromolecules are prone to induce the spontaneous crystallisation of ZIFs.²⁷ For example, negatively charged molecules trigger the growth of biocomposites, while their positively charged counterparts prevent their spontaneous formation.²⁷ These results underscore the importance of electrostatic interactions between target biomolecules and Zn²⁺ ions, as an increased local concentrations of Zn²⁺ on the surface of the biomolecule triggers the self-assembly of the framework. We hypothesize that this approach can be applied to the design of ZIF-based drug carriers for highly-negative charged clinical biotherapeutics

^aInstitute of Physical and Theoretical Chemistry, Graz University of Technology, Stremayrgasse 9, Graz 8010, Austria. E-mail: paolo.falcaro@tugraz.at

^bSchool of Physical Sciences, Faculty of Sciences, University of Adelaide, South Australia 5005, Australia. E-mail: christian.doonan@adelaide.edu.au

^cInstitute of Analytical Chemistry and Food Chemistry, Graz University of Technology, 8010 Graz, Austria

^dSchool of Science, Nanobiotechnology Research Laboratory (NBRL), RMIT University, 3001 Melbourne, Australia

^eThe University of Utah, College of Pharmacy, Salt Lake City, Utah 84112-5820, USA

^fSymic. Bio, Inc., 1400 Pine St., #640505, San Francisco, CA 94164, USA

^gAdvanced Porous Materials Unit (APMU), IMDEA Energy, Avda. Ramón de la Sagra 3, E-28935 Móstoles, Madrid, Spain

^hInstitute of Inorganic Chemistry, Graz University of Technology, 8010 Graz, Austria

† Electronic supplementary information (ESI) available: Experimental details, and additional figures. See DOI: 10.1039/d0sc01204a



such as glycosaminoglycans,²⁸ it is worth noting that, so far, carbohydrate@ZIF composites have been prepared only with CM-dextran (a model drug) and ZIF-8.²⁹ Thus, the encapsulation of real carbohydrate-based therapeutics in azolate frameworks would progress MOF-based carriers to drug delivery applications. Glycosaminoglycans (GAGs) are unbranched high-molecular weight polysaccharides formed from disaccharide units that consist of an amino sugar (D-glucosamine or D-galactosamine), and uronic acid (D-glucuronic acid or L-iduronic acid).²⁸ The multiple carboxylate and sulfate moieties attached to the carbohydrate backbone impart the negative charge to GAGs.²⁸ The most common GAGs are heparin (HP), hyaluronic acid (HA), chondroitin sulfate (CS), and dermatan sulfate (DS).^{28,30} They naturally occur either covalently linked to proteins, forming proteoglycans, or free within the extracellular matrix.^{28,30} In living organisms, GAGs are involved in a variety of biological roles, including anti-coagulation, wound healing, lubrication of synovial joints, cell signalling, angiogenesis, and axonal growth.^{28,30–32} GAGs can be used as therapeutics to prevent the proliferation of bacteria (*e.g. Mycobacterium tuberculosis*), and viruses (*e.g. Herpes simplex*).^{28,30–33} Recently, the relevance of GAGs to vaccines, protein, and antibody modifications, and polyvalent glycan therapeutics has been highlighted by Paderi and co-workers.³⁴ Furthermore, due to the important role of proteoglycans in tumour progression and metastasis, GAGs have been applied to the design of novel anticancer therapeutics.^{28,30,32}

GAGs-based therapeutics are typically administered *via* the parenteral route as their bioavailability is compromised in the gastrointestinal tract.^{28,35,36} Dosing of GAGs, *via* the parenteral route requires careful monitoring, as an excess of the drug can lead to bleeding as result of their anticoagulant properties.^{35,36} This method of administration is not compatible with all disease treatments such as wound healing and anti-inflammatory applications that require efficient local administration.³⁷ As a consequence, novel carriers with customisable delivery properties for the administration of GAGs are desirable.

This study presents a straightforward approach to circumvent those problems through the modulation of the drug release kinetics of the resultant biocomposites by tuning the physico-chemical properties of the MOF shell. Three different Zn-based metal-azolate frameworks (ZIF-8, ZIF-90, and MAF-7), of markedly different hydro-phobicity/-philicity,^{38,39} were employed to encapsulate a selected set of GAGs-based therapeutics (HA, HP, CS, DS, GM-1111, and HepSYL, where the last two are synthetic drugs in preclinical development).^{34,40,41} The encapsulation efficiencies (EE%) and therapeutic release profiles of each biocomposite were assessed as these are crucial information for the development of drug delivery systems.²⁵

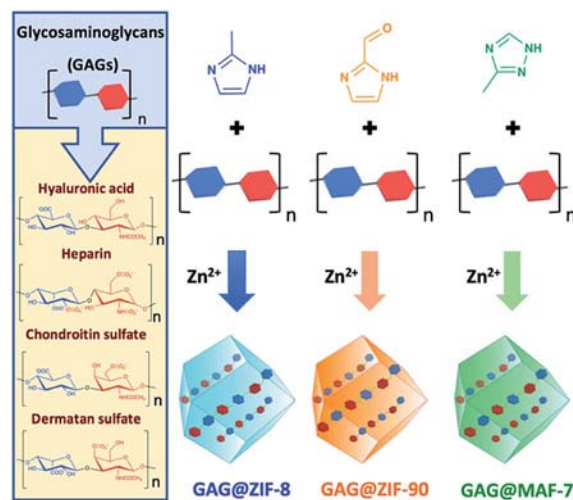
As a case study, we focused on HP, a GAG with anticoagulant activity mediated by its affinity for binding to antithrombin III (AT) leading to the inhibition of serine proteases involved in the coagulation process.⁴² However, in this process, the therapeutic activity is strongly dependent on the preservation of specific pentasaccharide sequence of HP. Thus, subtle structural modifications on the pentasaccharide sequence might alter the anticoagulant activity of HP.⁴² In this context, the current

delivery of HP is predominantly based on covalent surface immobilisation on carriers, an immobilisation method that compromises the activity of this GAG.⁴³ Thus, new protocols for encapsulation and delivery of GAGs are highly desired.⁴² Here we examine the activity of HP released by HP@ZIF-8, HP@ZIF-90, and HP@MAF-7 demonstrating that MAF-7 fully preserve HP bioactivity.

For the first time we demonstrated that the encapsulation, protection and release of pharmacologically active carbohydrate-based therapeutics can be performed using azolate-based MOF particles.

Results and discussion

ZIF-8-based biocomposites have been intensively studied for their drug release properties, however limited or no attention has been paid to ZIF-90 and MAF-7 as drug carriers.^{25,44,45} Although, ZIF-8, ZIF-90 and MAF-7 are isoreticular, they are composed of different organic linkers and possess distinct chemical properties.^{17,38,39} For example, ZIF-8 (2-methylimidazole; HmIM) is more hydrophobic than ZIF-90 (2-imidazole carboxaldehyde; HICA) and MAF-7 (3-methyl-1,2,4-triazole; Hmtz).^{38,39} We posit that the different properties of these ZIFs could influence their performance as drug delivery carriers. To verify this hypothesis, we encapsulated six different GAGs-based therapeutics (HA, HP, CS, DS, GM-1111, and HepSYL) within ZIF-8, ZIF-90, and MAF-7, respectively (Scheme 1) and examined the performance characteristics of the GAG@ZIF biocomposites as carriers for pH-responsive delivery. For each system, we determined the encapsulation efficiency (EE%) and the drug release profiles.⁴⁶ However, we first focused our attention on finding the synthetic conditions to the loading capacity and release properties of the biocomposites derived from the three different MOF systems (ZIF-8, ZIF-90, and MAF-7).



Scheme 1 Schematic representation of one-pot synthesis of GAG@-MOFs biocomposites based on three different metal-azolate frameworks.



Given that there are no previous studies describing the encapsulation of carbohydrates in ZIF-90 and MAF-7, we used carboxymethyl-dextran tagged with fluorescein isothiocyanate (FITC-CMD), as a model therapeutic to determine if carbohydrate-based biocomposites of these ZIFs could be obtained. FITC-CMD was selected as it is an inexpensive carbohydrate that closely mimics GAGs, and the fluorescein tag permits quantification of the amount of CM-dextran encapsulated (Fig. S1–S3, ESI†).²²

The synthesis of FITC-CMD@ZIF-8, FITC-CMD@ZIF-90 and FITC-CMD@MAF-7 was performed by varying the concentration of the biomolecule ([FITC-CMD] = 0 (1), 0.18 (2), 0.36 (3), 0.72 (4), 1.44 (5) mg mL⁻¹) and the metal to ligand ratio (Zn²⁺ : L = 1 : 4 (A), 1 : 3.47 (B) and 1 : 2.52 (C)) (Tables S1 and S2†). The data shows that for FITC-CMD@ZIF-8 biocomposites, the optimal encapsulation efficiencies (>90%) were reached using 0.36 and 0.72 mg mL⁻¹ of FITC-CMD and metal to ligand ratios of 1 : 4 (A) and 1 : 3.47 (B) (Fig. S1, ESI†). In the case of FITC-CMD@ZIF-90 biocomposites the higher EE% values (>90%) were observed for samples obtained from the lowest concentration of FITC-CMD (0.18 mg mL⁻¹), for both 1 : 3.47 (B) and 1 : 2.52 (C) Zn²⁺ : HICA ratios (Fig. S2, ESI†). Conversely, FITC-CMD@MAF-7 biocomposites present exceptional polysaccharide payloads regardless of the initial concentration of FITC-CMD, when using 1 : 3.47 (B) Zn²⁺ : Hmtz ratio (Fig. S3, ESI†). However, it should be pointed out that, unlike previous reports describing the synthesis of protein@MAF-7 biocomposites,^{19,38} in this work FITC-CMD@MAF-7 is synthesised in absence of ammonia, a deprotonating agent with low biocompatibility.⁴⁷ Furthermore, we note that the encapsulation efficiency of FITC-CMD increases concomitantly with a reduction in the amount of NH₃·H₂O.

The drug release kinetics of the FITC-CMD@ZIF-8, FITC-CMD@ZIF-90 and FITC-CMD@MAF-7 biocomposites were obtained upon applying an external acidic stimulus (Fig. S4–S6, ESI†). The release profiles obtained from FITC-CMD@MAF-7 biocomposites show that the higher the concentration of the FITC-CMD the faster the delivery of the cargo (Fig. S7†). Similar behaviour was observed for the samples obtained from FITC-CMD@ZIF-90 when using 1 : 3.47 metal-to-ligand ratio (90DXBn; where n = 2–5). However, for FITC-CMD@ZIF-90 biocomposites obtained from Zn²⁺ : HICA = 1 : 4 and Zn²⁺ : HICA = 1 : 2.52 ratios (90DXAn and 90DXCn, respectively; where n = 2–5), as well as for the FITC-CMD@ZIF-8 biocomposites, a clear trend is not evident (Fig. S7†). For FITC-CMD@MAF-7 and FITC-CMD@ZIF-90 biocomposites, the release rate increases as the Zn²⁺ : L ratio decreases (Fig. S4–S7†). For FITC-CMD@ZIF-8 biocomposites, this trend was observed only for the samples obtained with FITC-CMD > 0.36 mg mL⁻¹; however, the FITC-CMD@ZIF-8 samples obtained with FITC-CMD = 0.18 mg mL⁻¹ show the slowest release rate with Zn²⁺ : HmIM = 1 : 3.47 (Fig. S4–S7†).

Additionally, our stability tests in water (pH = 7.0) demonstrate that for FITC-CMD@MOF biocomposites obtained from 0.36 mg mL⁻¹ of FITC-CMD keeping the Zn²⁺ : L = 1 : 3.47 (8DXB3, 90DXB3 and 7DXB3) do not release FITC-CMD after being stored in water (pH = 7.0) for 24 h (Fig. S24, ESI†). However, for its analogues obtained from 0.72 mg mL⁻¹ and

1.44 mg mL⁻¹ of FITC-CMD we measured leaching of the model drug during the incubation of the samples in DI water for 24 h at room temperature.

Thus, the maximum concentration of FITC-CMD that afforded controlled stimulus-response drug release was 0.36 mg mL⁻¹. The stability of the samples 8DXB3, 90DXB3 and 7DXB3 was further confirmed by inductively coupled plasma-optical emission spectrometry (ICP-OES) through the determination of Zn²⁺ released upon the incubation of the samples in DI water for 24 h (Fig. S24d, ESI†).

In summary, employing FITC-CMD, as a model drug, we found that a metal to ligand ratio Zn²⁺ : L = 1 : 3.47 and a carbohydrate concentration of 0.36 mg mL⁻¹ yielded acceptable EE% and facilitates the release of the model therapeutic on demand. Accordingly, these synthetic conditions (Zn²⁺ : L = 1 : 3.47, [GAG] = 0.36 mg mL⁻¹) were employed for the encapsulation of selected GAG-based therapeutics (*i.e.* HA, HP, CS, DS, see Scheme 1).

The biocomposites derived from ZIF-8 and ZIF-90 were isolated as crystalline precipitates (HA@ZIF-*n*, HP@ZIF-*n*, CS@ZIF-*n*, and DS@ZIF-*n*, where *n* = 8 and 90; respectively). However, the MAF-7-based biocomposites formed either viscous solutions with a gel-like consistency (HP@MAF-7, CS@MAF-7, and DS@MAF-7) or non-flowing gels (HA@MAF-7). The formation of metal-organic gels has been previously explained as a result of the rapid formation of MOF nanoparticles, which aggregate through weak van der Waals interactions, H-bonding or π-π stacking.^{48–50}

After the 24 h of reaction, GAG@MOF samples were washed with water and ethanol (see ESI† for details) and the air-dried solids were analysed by powder X-ray diffraction (PXRD) (Fig. 1). The diffraction patterns show that the control sample (ZIF-8 without biotherapeutic) possess predominantly a diamondoid topology (**dia**), while the GAG@ZIF-8 biocomposites exhibit a sodalite (**sod**) topology (Fig. 1a). These data indicate that the presence of GAGs enhance the formation rate of the ZIF yielding the less thermodynamically stable **sod** topology.⁵¹ The PXRD pattern of ZIF-90, prepared in the absence of GAGs, is consistent with the **dia** polymorph. However, in presence of the biomolecule the resultant GAG@ZIF-90 biocomposites show a mixture of kinetic **sod**-ZIF-90 and the thermodynamic polymorph **dia**-ZIF-90 (Fig. 1b). Finally, the diffraction pattern of pure MAF-7 synthesised in presence of NH₃·H₂O (10%) shows the formation of a crystalline phase with **sod** topology, which is consistent with previous reports.^{19,38} Conversely, the PXRD pattern of MAF-7 prepared in absence of ammonia shows diminished crystallinity (Fig. 1c). The diffraction patterns obtained from the GAG@MAF-7 biocomposites indicate that HA@MAF-7 and HP@MAF-7 are predominantly amorphous, whereas DS@MAF-7 shows a mixture of crystalline and amorphous phase. The sample CS@MAF-7 gives rise to a PXRD pattern with broad diffraction peaks that can be attributed to the presence of nanoparticles with domain sizes between (3.3 ± 2 to 92.7 ± 5 nm) as determined by the Scherrer equation (Fig. 1c). The crystal size and the morphology of the control samples of MOFs and their corresponding GAG@MOF biocomposites were assessed by scanning electron microscopy (SEM) (Fig. 1). The micrographs obtained from the control



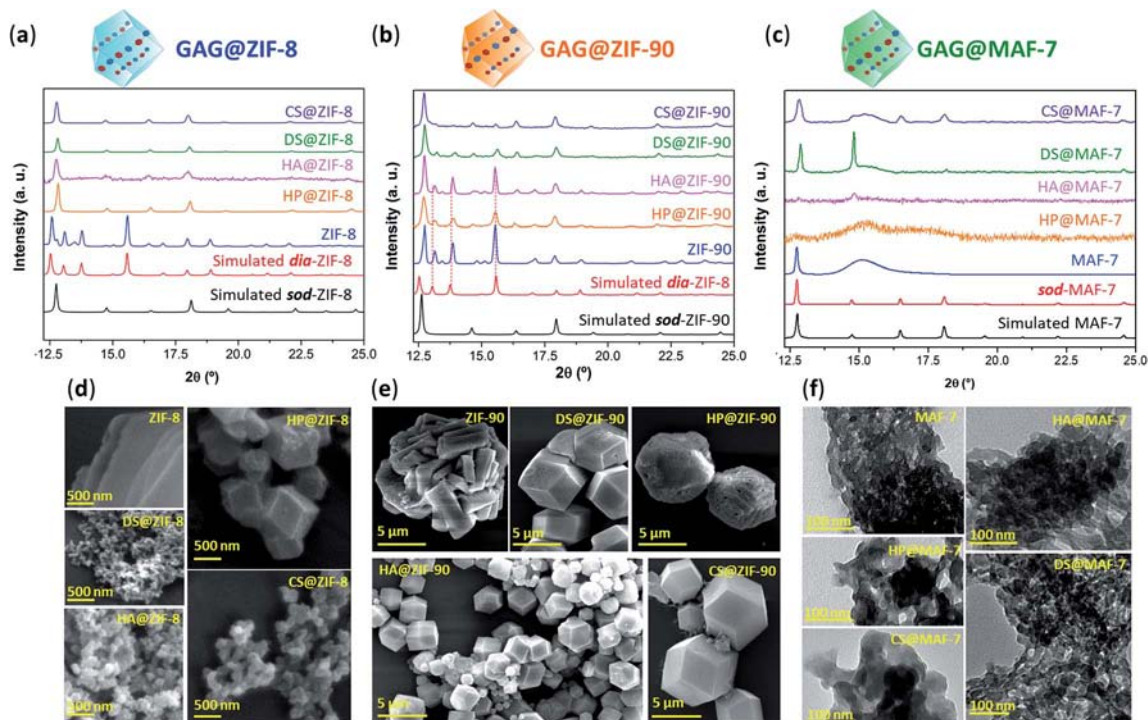


Fig. 1 (a) Comparison of the diffraction patterns of ZIF-8 and GAG@ZIF-8 biocomposites (GAGs = heparin (HP), hyaluronic acid (HA), chondroitin sulfate (CS), and dermatan sulfate (DS)). (b) Diffraction patterns obtained from ZIF-90 and GAG@ZIF-90 biocomposites. The dashed lines represent the diffraction peaks associated to the formation of *dia* phase. (c) Diffraction patterns of *sod*-MAF-7 obtained in presence of $\text{NH}_3 \cdot \text{H}_2\text{O}$ (10%), as well as the air-dried xerogel obtained from the synthesis of MAF-7 and GAG@MAF-7 biocomposites without ammonia. (d) SEM images of pure ZIF-8 and its corresponding GAG@ZIF-8 biocomposites. (e) SEM images of ZIF-90 and GAG@ZIF-90 biocomposites. (f) TEM images of MAF-7 and GAG@MAF-7 biocomposites obtained without the addition of deprotonating agents (e.g. $\text{NH}_3 \cdot \text{H}_2\text{O}$).

sample of ZIF-8 show the formation of plate-like crystals, which is the typical morphology observed in *dia*-ZIF-8 topology (Fig. S8†).^{18,20,51} For GAG@ZIF-8 (Fig. 1d), the characteristic rhombic dodecahedron morphology of *sod*-ZIF-8 topology is present.^{18,20,51} HA@ZIF-8, CS@ZIF-8, and DS@ZIF-8 have particle sizes below 500 nm, while HP@ZIF-8 shows wider size distribution up to 1 μm (Fig. 1d, S8 and S9†).

SEM images obtained from pure ZIF-90 shows spherical clusters of prismatic crystals (Fig. 1e). For all the other samples prepared in presence of GAGs (GAG@ZIF-90) a rhombic dodecahedron morphology is observed (Fig. 1e).¹⁸ The crystalline powder obtained from HP@ZIF-90, CS@ZIF-90, and DS@ZIF-90 possesses particle sizes ranging from *ca.* 5 μm to *ca.* 7 μm ; whereas HA@ZIF-90 presents a wider particle size distribution ranging from *ca.* 500 nm to *ca.* 4 μm (Fig. S10 and S11, ESI†). Furthermore, mesopores are observed on the surface of some of the GAG@ZIF-90 crystals. Although this is more evident for HP@ZIF-90, this can be seen for CS@ZIF-90, and DS@ZIF-90 (Fig. 1e and S11†). Similar textural features have been previously found in other MOFs, prepared in the presence of long-chain carboxylic acids.^{52,53} Due to the small particle sizes of the MAF-7 materials obtained without $\text{NH}_3 \cdot \text{H}_2\text{O}$ (10%), they were studied using transmission electron microscopy (TEM) (Fig. 1f). The images show that the solid materials obtained for pure MAF-7 and GAGs@MAF-7 consist of aggregated nanoparticles with an average size below 100 nm (Fig. S12 and S13†).

To ascertain the encapsulation of GAGs within the ZIF matrices, the samples were washed with water (2 mL, 3 \times) and ethanol (2 mL, 3 \times) to ensure the complete removal of GAGs loosely attached to the particle surface.²² Then the collected solids were analysed by Fourier transform infrared spectroscopy (FTIR) (Fig. S14–S18†). IR spectra obtained from GAGs@ZIFs biocomposites show the vibration bands typically attributed to the ZIF framework including the Zn–N stretching mode (421 cm^{-1}) and characteristic vibrational modes of the azolate ligands (1584 cm^{-1} ($\nu_{\text{C}=\text{N}}$), 1500–1350 cm^{-1} (ν_{ring}) and 800–650 cm^{-1} (δ_{ring})) (Fig. S14†). For each GAG used, additional bands originating from the specific pendant groups were observed.⁵⁴ For example, the vibrational bands attributed to the carboxylic groups are found around 1610–1620 cm^{-1} $\nu_{\text{as}}(\text{COO}^-)$ and 1410–1420 cm^{-1} $\nu_{\text{s}}(\text{COO}^-)$. Furthermore, all of the spectra also display a broad band around 2850–3600 cm^{-1} , that results from the stretching modes of the OH group, as well as the band attributed to C–O stretching vibration in 1020–1040 cm^{-1} .⁵⁴

Finally, those biocomposites obtained from sulfated biomacromolecules (HP, CS, and DS) present additional weak vibrational bands at 1220–1240 cm^{-1} $\nu_{\text{as}}(\text{S}=\text{O})$, and 1000–822 cm^{-1} (OSO_3^-) (Fig. S16–S18†).⁵⁴

The EE% of each GAG@MOF biocomposite was assessed using UV-vis spectroscopy using the carbazole assay; which is a direct method to quantify glycosaminoglycans by colorimetry ($\lambda_{\text{max}} = 520 \text{ nm}$) (see ESI† for details).^{55,56} The GAG@MOF



samples, were soaked, separately, in citrate buffer (2 mL, 80 mM, pH = 6) to dissolve the MOFs. Once a clear solution was obtained, a Sephadex column was used to separate the GAGs from the MOF precursors. For these clinical biotherapeutics, the MAF-7-based biocomposites present the highest EE% reaching values above 80% (Fig. 2a) and the GAG@ZIF-90 biocomposites display the lowest EE% (*ca.* 50%) (Fig. 2a). In the case of ZIF-8, the biocomposites obtained from HP and CS present exceptional EE% (*ca.* 100%); however, those derived from HA and DS show an EE% of *ca.* 60% (Fig. 2a).

The amount of the commercial GAGs (HP, CS, DS, HA) encapsulated in MOFs was confirmed by thermogravimetric analysis (TGA) (Fig. S28, ESI†) and high loading capacity of HP were calculated (*e.g.* 19 wt% HP for HP@MAF-7).

The drug-release profile studies were determined by quantifying the amount of GAG delivered in citrate buffer (80 mM, pH = 6) as a function of time (see ESI†). The citrate buffer was employed with the aim of emulating the interstitial tissue pH found in inflammatory diseases and in cancer cells.^{57,58} All the release profiles present an initial rapid release of the biotherapeutic, followed by a slower sustained delivery. Nevertheless, each MOF-system shows unique release behaviour (Fig. 2b–e). For instance, the release profiles of GAG@MAF-7 biocomposites exhibit a large initial burst release, where *ca.* 50% of the cargo was liberated within the first minute, reaching the complete delivery within 30 min (Fig. S19†). The observed burst effect for MAF-7-based biocomposites, irrespective of the GAG used, can be explained by the rapid degradation of the small nanoparticles. In the case of GAG@ZIF-8 biocomposites, the initial release rate in the burst stage varies: CS@ZIF-8 and DS@ZIF-8 present the fastest initial drug release (*ca.* 50% within the first minute), reaching the complete delivery of the cargo after 1 h (Fig. 2d and e).

HP@ZIF-8 and HA@ZIF-8 show a 50% release of the cargo within 5 min, and 100% release after 40 min (Fig. 2b and c). GAG@ZIF-90 composites display a sustained longer-term release profile. The initial burst stage is observed in 10 to 15 min, and *ca.* 50% of the loaded drug was released, followed by a gradual delivery of the cargo where the complete release ranges from 50 min (HP@ZIF-90) to 1.5 h (HA@ZIF-90, CS@ZIF-90 and DS@ZIF-90) (Fig. 2 and S19†).

In summary, by using different azolate-based MOFs we proved that we can design systems for the customised release of carbohydrate-based therapeutics from fast delivery, useful in case of infections,⁵⁹ to longer delivery desired in case of anti-coagulant administration.⁶⁰ For example, for heparin, the poor dosage control *via* intravenous administration could lead to either fast clearance from the body (under-dosage) or spontaneous haemorrhages (over-dosage).^{61,62} An initial rapid release of HP followed by a more sustained delivery is most suitable for the treatment of urgent clinical situations, such as vascular surgery, frostbite, dialysis, *etc.*^{37,43,63} Thus, the development of HP delivery systems with fast responsive rate have attracted significant attention.^{64–66} The here prepared HP@MOF composites show release profiles that are relevant for urgent medical treatments.^{37,43,63}

To test possible alteration in the biotherapeutic properties of HP due the encapsulation and recovery processes, we used a chromogenic anti-IIa assay to evaluate the anticoagulant activity of heparin before and after being encapsulated within the three different MOFs (see ESI† for details). The collected data reveals that the HP released from ZIF-8 retains $\approx 98\%$ of its initial activity, whereas the HP released from ZIF-90 and MAF-7 retains $\approx 95\%$ and $\approx 97\%$ activity, respectively (Fig. 3a and S26, ESI†). To verify the successful encapsulation of HP, we exposed the biocomposites to heparinase I, which is a heparin lyase over

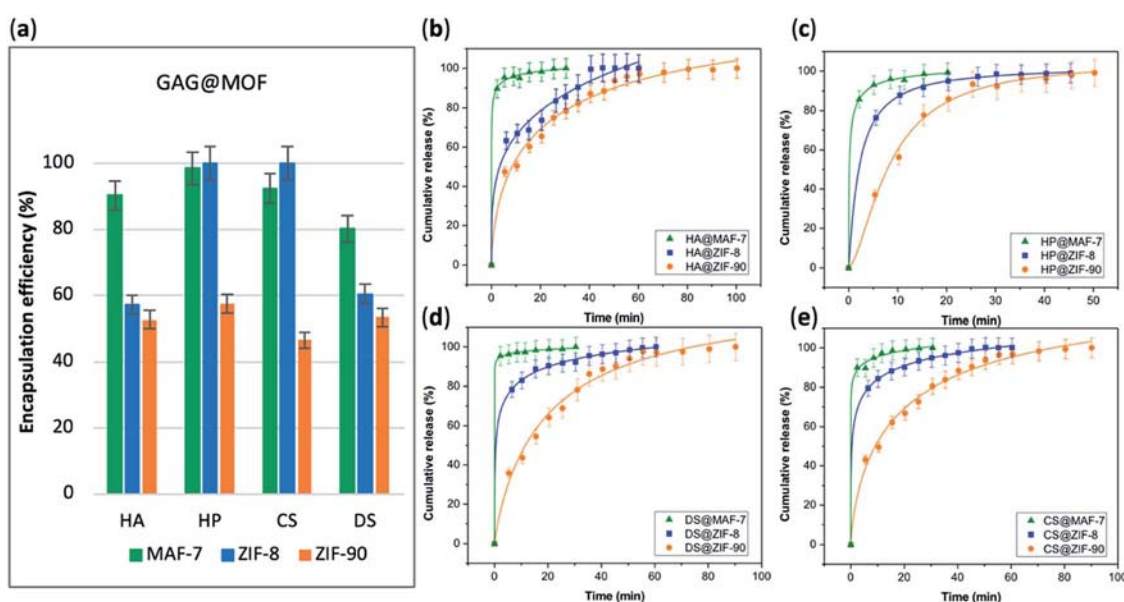


Fig. 2 (a) Encapsulation efficiency (%) of the GAGs-based biocomposites based on three different MOFs (ZIF-8, ZIF-90 and MAF-7). Comparative release profiles of the biocomposites: (b) HA@MOFs, (c) HP@MOFs, (d) DS@MOFs, and (e) CS@MOFs, upon applying an acidic stimulus (pH = 6).



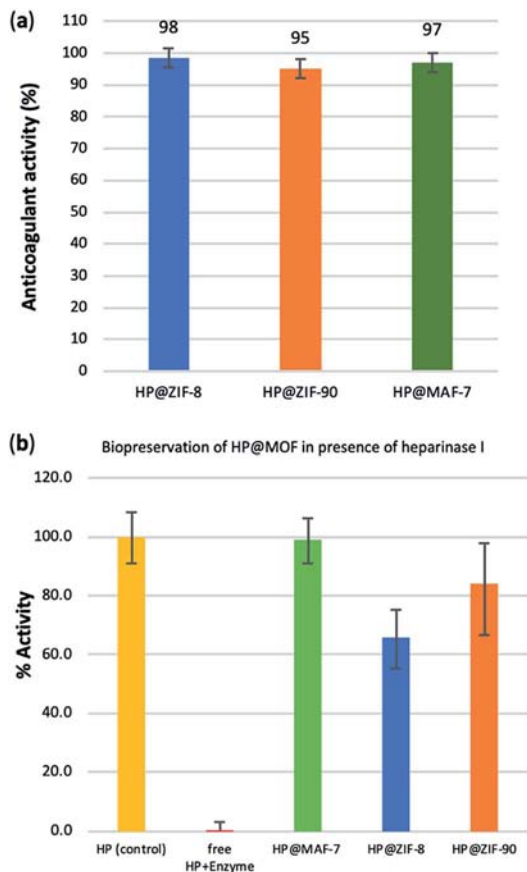


Fig. 3 (a) Determination of the remaining anticoagulant activity of the HP released from the HP@MOFs biocomposites. (b) Comparison of the anticoagulant activity of unprotected HP and HP encapsulated within the MOF particles after being exposed to heparinase I.

expressed in infected human organs and tissues.⁶⁷ Thus, herein, HP@MOFs biocomposites and the free HP were exposed to heparinase I for 1 h at 30 °C. Subsequently, the encapsulated HP was recovered from the HP@MOF biocomposites and the anticoagulant activity was determined using anti-IIa chromogenic assay and compared with the activity of unprotected heparin exposed to the enzyme and pure HP as a control (Fig. S26, ESI†). The results showed that the unprotected heparin loses completely its anticoagulant activity. In contrast, the HP released from the HP@ZIF-8 and HP@ZIF-90 partially retains the antithrombotic activity ($\approx 67\%$, $\approx 84\%$; respectively), whereas the activity HP released from MAF-7 is fully preserved ($\approx 99\%$) (Fig. 3b). These results demonstrate that HP is predominantly located within the MOF shells that protect HP from lyases.

To this point we have established that carbohydrate-based drugs can be encapsulated with high efficiency and their release can be controlled by the judicious selection of the MOF matrix (ZIF-8, ZIF-90 and MAF-7), we expanded our study to the assessment of ZIFs for the delivery of carbohydrate-based drugs in late-stage clinical trials. Thus, we employed two preclinical stage biotherapeutics: GM-1111 and HepSYL.^{34,40,41} GM-1111 is an anti-inflammatory agent engineered to treat chronic

rhinosinusitis: it inhibits multiple inflammatory mediators and requires topical intranasal administration route.⁶⁸ HepSYL is a new synthetic proteoglycan designed for oncotherapy applications. As such, a parenteral administration route is needed. GM-1111 and HepSYL were encapsulated within ZIF-8, ZIF-90 and MAF-7 following the synthetic protocol used for the GAGs based therapeutics (see ESI†). After washing and drying, the powders were examined with PXRD. The diffraction patterns indicate that GM-1111@ZIF-8 and HepSYL@ZIF-8 are a mixture of different crystalline phases, **sod**, **dia**, and **ZIF-C**,^{20,69} with **sod** as the predominant phase (Fig. 4a). By contrast, the diffraction pattern of GM-1111@ZIF-90 and HepSYL@ZIF-90 show that the samples are pure **sod** phase (Fig. 4a). GM-1111@MAF-7 and HepSYL@MAF-7 yield amorphous materials (Fig. 4a).

SEM analysis reveals that the crystalline particles of GM-1111@ZIF-8 and HepSYL@ZIF-8 are of rhombic dodecahedron morphology (Fig. 4b). For GM-1111@ZIF-8 we observed inhomogeneous particles with average size of *ca.* 500 nm; while for HepSYL@ZIF-8 the particles are homogeneous with size is below 200 nm. Likewise, the particle morphology observed in GM-1111@ZIF-90 and HepSYL@ZIF-90 samples corresponds to rhombic dodecahedron, with particle sizes of *ca.* 8 μm and *ca.* 2 μm , respectively (Fig. 4b). Due to the small particle size, GM-1111@MAF-7 and HepSYL@MAF-7 samples were analysed by TEM (Fig. 4b). The images reveal the formation of aggregates comprised of nanoparticles with an average size below 50 nm. Finally, confocal laser microscopy (CLSM) was employed to ascertain the location of HepSYL within the ZIF particles (Fig. 4c, S20, and S21†). The CLSM images show that the proteoglycan is homogeneously distributed within ZIF-8 and MAF-7 (Fig. 4c, and S20†). However, in the case of HepSYL@ZIF-90, the proteoglycan is predominantly localised towards the surface region of crystalline particles (Fig. 4c and S20†).

The EE% and the drug-release kinetics of GM-1111@MOF and HepSYL@MOF were assessed using UV-vis spectroscopy (Fig. 5a). Following the protocol previously described for GAG-based biocomposites, the amount of GM-1111 encapsulated within the MOF shell was determined using the carbazole assay ($\lambda_{\text{max}} = 520 \text{ nm}$).^{55,56}

In the case of HepSYL@ZIFs biocomposites, the EE% was determined by monitoring the absorbance of the colorant used to label the protein (CF633, $\lambda = 633 \text{ nm}$) (Fig. S22†).

The data collected reveals that the best performance, in terms of EE%, was found when using MAF-7, followed by ZIF-90 and then ZIF-8 (Fig. 5a). The EE% is also influenced by the biomacromolecule. GM-1111, that is more structurally similar to GAGs, shows a higher EE% than HepSYL, which contains positively charged peptides.

The drug release profiles of GM-1111@ZIFs reveal that GM-1111@MAF-7 and GM-1111@ZIF-8 present a rapid burst release upon applying an external acidic stimulus (pH = 6), and complete release was achieved within the first 20 min (Fig. 5b).

The release profile of GM-1111@ZIF-90 presents a long-term controlled drug delivery, with complete release observed after 2.5 h (Fig. 5b). Finally, the HepSYL@ZIF release profiles reveal that the fastest drug delivery is determined for HepSYL@MAF-7, while HepSYL@ZIF-8 and HepSYL@ZIF-90 exhibit a longer-



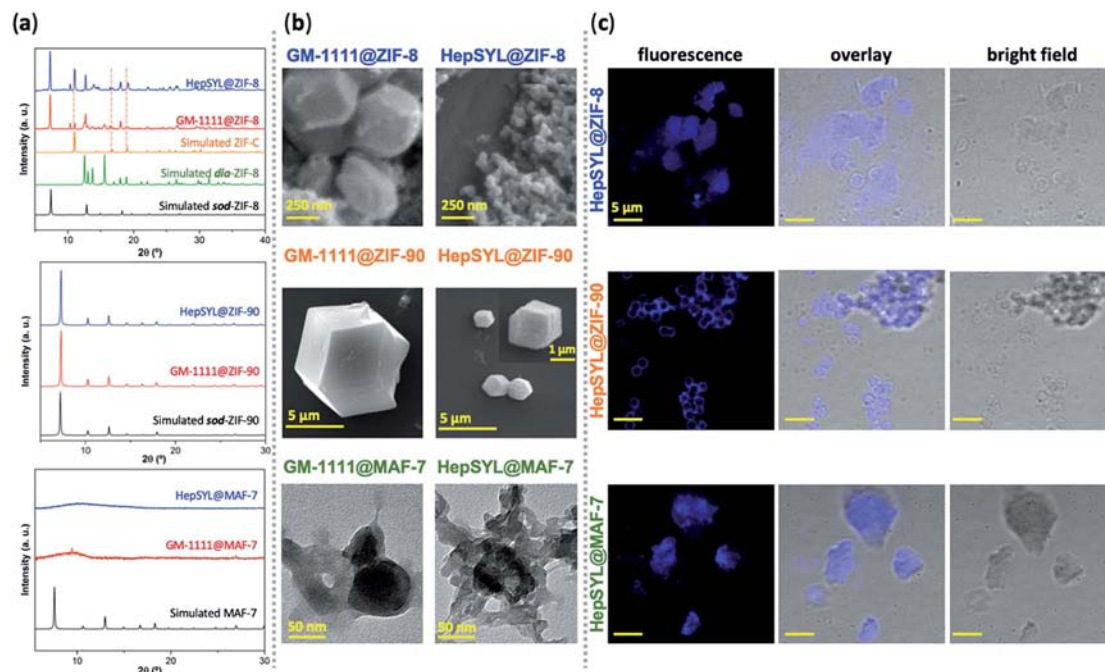


Fig. 4 (a) PXRD patterns of HepSYL@MOFs and GM-1111@MOFs based on three different MOF systems (ZIF-8, ZIF-90 and MAF-7). The dashed lines represent the diffraction peaks associated to the formation of a ZIF-C phase. (b) SEM images of HepSYL@ZIF-8, GM-1111@ZIF-8, HepSYL@ZIF-90, and GM-1111@ZIF-90 biocomposites; TEM micrographs of HepSYL@MAF-7 and GM-1111@MAF-7. (c) Confocal laser scanning micrographs showing the fluorescence, bright field, and overlay images of HepSYL@ZIF-8, HepSYL@ZIF-90, and HepSYL@MAF-7 (scale bar: 5 μm).

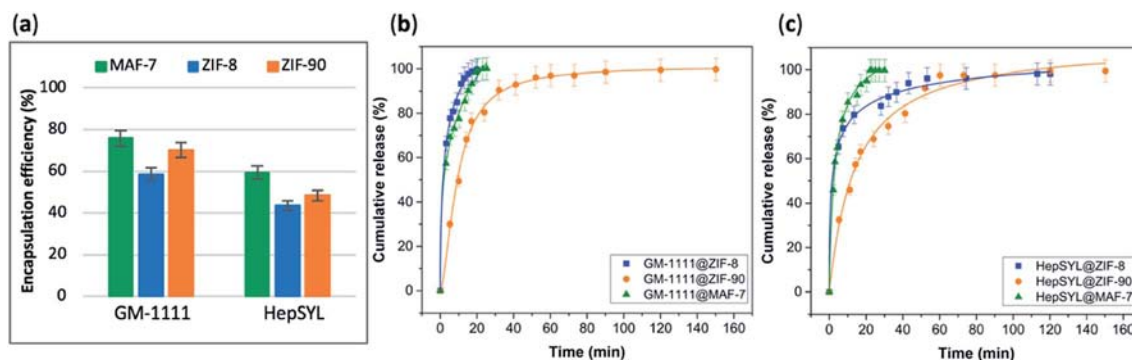


Fig. 5 (a) Encapsulation efficiency (%) of HepSYL@MOFs and GM-1111@MOFs biocomposites obtained using the three different MOF systems (ZIF-8, ZIF-90 and MAF-7). Comparative release profiles of the biocomposites: (b) GM-1111@MOFs, and (c) HepSYL@MOFs, upon applying an acidic stimulus (pH = 6).

term drug release (Fig. 5c). The complete release of the anti-carcinogenic therapeutic was observed after 2 h and 2.5 h, respectively (Fig. 5c).

Conclusions

In summary, three chemically different metal-azolate based frameworks (ZIF-8, ZIF-90, and MAF-7), were used to design pH-responsive carriers for the encapsulation and release of GAG-based biotherapeutics including heparin (HP), chondroitin sulfate (CS), dermatan sulfate (DS), and hyaluronic acid (HA). Based on the selection of the ZIF matrices, the encapsulation

efficiency varied from 50 to 100%, and the release of the clinical therapeutics could be precisely tailored. For instance, where a fast release is desired (*e.g.* in the treatment of infection-related diseases as the case of osteomyelitis,⁷⁰ in wound treatment,⁵⁹ or in pulsatile delivery processes),⁷¹ the choice could lead towards the use of GAG@ZIF-8, and GAG@MAF-7 biocomposites. However, if a controlled and sustained release of biomolecule is required to reduce the systemic side effects associated with high drug concentrations,⁵⁹ GAG@ZIF-90 biocomposites represent a desirable alternative. As a case study, we examined the encapsulation of HP in GAGs: for HP@MAF-7 we found a loading capacity of 19 wt% and the anticoagulant activity of



the released heparin was fully preserved, even after exposure to lyase agents.

Finally, the azolate-based MOF carriers were employed for the encapsulation and release of pre-clinical therapeutics used as anti-inflammatory and anticarcinogenic agents. Similar to the GAG-based biocomposites the EE% and release profiles could be tailored by the judicious selection of the MOF matrix. We anticipate that our findings will facilitate progress in the burgeoning area of MOF-based drug delivery.

Conflicts of interest

There are no conflicts to declare.

Acknowledgements

The authors acknowledge support from the European Union's Horizon 2020 FETOPEN-1-2016-2017 research and innovation program under grant agreement 801464 and LP-03. P. H. acknowledges the Spanish Ramón y Cajal Programme (2014-16823). M. J. V. H. acknowledges The National Council of Science and Technology (CONACyT, México) for the post-doctoral scholarship (CVU 419210). E. A. acknowledges Austrian Agency for International Cooperation in Education and Research (OeAD-GmbH) for the PhD scholarship. The authors acknowledge the CERIC-ERIC Consortium for the access to experimental facilities and financial support. C. J. D. and P. F. acknowledge ARC DP170103531 for financial support. A. P. acknowledge the travel scholarship support from Australian Nanotechnology Network (ANN) to visit EU and carry out experiments.

Notes and references

- O. M. Yaghi, M. O'Keeffe, N. W. Ockwig, H. K. Chae, M. Eddaoudi and J. Kim, *Nature*, 2003, **423**, 705–714.
- C. S. Diercks, M. J. Kalmutzki, N. J. Diercks and O. M. Yaghi, *ACS Cent. Sci.*, 2018, **4**, 1457–1464.
- H. Furukawa, K. E. Cordova, M. O'Keeffe and O. M. Yaghi, *Science*, 2013, **341**, 1230444.
- C. A. Trickett, A. Helal, B. A. Al-Maythaly, Z. H. Yamani, K. E. Cordova and O. M. Yaghi, *Nat. Rev. Mater.*, 2017, **2**, 17045.
- T. Simon-Yarza, A. Mielcarek, P. Couvreur and C. Serre, *Adv. Mater.*, 2018, **30**, 1707365.
- K. Liang, R. Ricco, C. M. Doherty, M. J. Styles, S. Bell, N. Kirby, S. Mudie, D. Haylock, A. J. Hill, C. J. Doonan and P. Falcaro, *Nat. Commun.*, 2015, **6**, 7240.
- X. Lian, Y. Fang, E. Joseph, Q. Wang, J. Li, S. Banerjee, C. Lollar, X. Wang and H.-C. Zhou, *Chem. Soc. Rev.*, 2017, **46**, 3386–3401.
- C. Doonan, R. Ricco, K. Liang, D. Bradshaw and P. Falcaro, *Acc. Chem. Res.*, 2017, **50**, 1423–1432.
- S. Li, M. Dharmarwardana, R. P. Welch, C. E. Benjamin, A. M. Shamir, S. O. Nielsen and J. J. Gassensmith, *ACS Appl. Mater. Interfaces*, 2018, **10**, 18161–18169.
- R. Ricco, W. Liang, S. Li, J. J. Gassensmith, F. Caruso, C. Doonan and P. Falcaro, *ACS Nano*, 2018, **12**, 13–23.
- C. Wang, H. Sun, J. Luan, Q. Jiang, S. Tadepalli, J. J. Morrissey, E. D. Kharasch and S. Singamaneni, *Chem. Mater.*, 2018, **30**, 1291–1300.
- Y. Feng, H. Wang, S. Zhang, Y. Zhao, J. Gao, Y. Zheng, P. Zhao, Z. Zhang, M. J. Zaworotko, P. Cheng, S. Ma and Y. Chen, *Adv. Mater.*, 2019, **31**, 1805148.
- B. Chen, Z. Yang, Y. Zhu and Y. Xia, *J. Mater. Chem. A*, 2014, **2**, 16811–16831.
- F. Lyu, Y. Zhang, R. N. Zare, J. Ge and Z. Liu, *Nano Lett.*, 2014, **14**, 5761–5765.
- F.-S. Liao, W.-S. Lo, Y.-S. Hsu, C.-C. Wu, S.-C. Wang, F.-K. Shieh, J. V. Morabito, L.-Y. Chou, K. C.-W. Wu and C.-K. Tsung, *J. Am. Chem. Soc.*, 2017, **139**, 6530–6533.
- C. Wang, G. Sudlow, Z. Wang, S. Cao, Q. Jiang, A. Neiner, J. J. Morrissey, E. D. Kharasch, S. Achilefu and S. Singamaneni, *Adv. Healthcare Mater.*, 2018, **7**, 1800950.
- J.-P. Zhang, Y.-B. Zhang, J.-B. Lin and X.-M. Chen, *Chem. Rev.*, 2012, **112**, 1001–1033.
- W. Liang, R. Ricco, N. K. Maddigan, R. P. Dickinson, H. Xu, Q. Li, C. J. Sumby, S. G. Bell, P. Falcaro and C. J. Doonan, *Chem. Mater.*, 2018, **30**, 1069–1077.
- W. Liang, H. Xu, F. Carraro, N. K. Maddigan, Q. Li, S. G. Bell, D. M. Huang, A. Tarzia, M. B. Solomon, H. Amenitsch, L. Vaccari, C. J. Sumby, P. Falcaro and C. J. Doonan, *J. Am. Chem. Soc.*, 2019, **141**, 2348–2355.
- F. Carraro, M. de J. Velásquez-Hernández, E. Astria, W. Liang, L. Twight, C. Parise, M. Ge, Z. Huang, R. Ricco, X. Zou, L. Villanova, C. O. Kappe, C. Doonan and P. Falcaro, *Chem. Sci.*, 2020, **11**, 3397–3404.
- K. S. Park, Z. Ni, A. P. Cote, J. Y. Choi, R. Huang, F. J. Uribe-Romo, H. K. Chae, M. O'Keeffe and O. M. Yaghi, *Proc. Natl. Acad. Sci. U. S. A.*, 2006, **103**, 10186–10191.
- E. Astria, M. Thonhofer, R. Ricco, W. Liang, A. Chemelli, A. Tarzia, K. Alt, C. E. Hagemeyer, J. Rattenberger, H. Schroettner, T. Wrodnigg, H. Amenitsch, D. M. Huang, C. J. Doonan and P. Falcaro, *Mater. Horiz.*, 2019, **6**, 969–977.
- T.-T. Chen, J.-T. Yi, Y.-Y. Zhao and X. Chu, *J. Am. Chem. Soc.*, 2018, **140**, 9912–9920.
- W.-H. Chen, G.-F. Luo, M. Vázquez-González, R. Cazelles, Y. S. Sohn, R. Nechushtai, Y. Mandel and I. Willner, *ACS Nano*, 2018, **12**, 7538–7545.
- W. Cai, J. Wang, C. Chu, W. Chen, C. Wu and G. Liu, *Adv. Sci.*, 2019, **6**, 1801526.
- M. A. Luzuriaga, R. P. Welch, M. Dharmarwardana, C. E. Benjamin, S. Li, A. Shahrivarkevishahi, S. Popal, L. H. Tuong, C. T. Creswell and J. J. Gassensmith, *ACS Appl. Mater. Interfaces*, 2019, **11**, 9740–9746.
- N. K. Maddigan, A. Tarzia, D. M. Huang, C. J. Sumby, S. G. Bell, P. Falcaro and C. J. Doonan, *Chem. Sci.*, 2018, **9**, 4217–4223.
- N. S. Gandhi and R. L. Mancera, *Chem. Biol. Drug Des.*, 2008, **72**, 455–482.
- E. Astria, M. Thonhofer, R. Ricco, W. Liang, A. Chemelli, A. Tarzia, K. Alt, C. E. Hagemeyer, J. Rattenberger,



- H. Schroettner, T. Wrodnigg, H. Amenitsch, D. M. Huang, C. J. Doonan and P. Falcaro, *Mater. Horiz.*, 2019, **6**, 969–977.
- 30 V. Pomin and B. Mulloy, *Pharmaceuticals*, 2018, **11**, 27.
- 31 A. Varki, *Glycobiology*, 2017, **27**, 3–49.
- 32 G. Ruiz-Gómez, S. Vogel, S. Möller, M. T. Pisabarro and U. Hempel, *Sci. Rep.*, 2019, **9**, 4905.
- 33 R. D. Astronomo and D. R. Burton, *Nat. Rev. Drug Discovery*, 2010, **9**, 308–324.
- 34 J. Paderi, G. D. Prestwich, A. Panitch, T. Boone and K. Stuart, *Adv. Ther.*, 2018, **1**, 1800082.
- 35 N. S. Gandhi and R. L. Mancera, *Drug Discovery Today*, 2010, **15**, 1058–1069.
- 36 A. Neves, M. Correia-da-Silva, E. Sousa and M. Pinto, *Pharmaceuticals*, 2016, **9**, 37.
- 37 K. Vaghasiya, A. Sharma, K. Kumar, E. Ray, S. Adlakha, O. P. Katare, S. K. Hota and R. K. Verma, *ACS Biomater. Sci. Eng.*, 2019, **5**, 6617–6631.
- 38 J.-P. Zhang, A.-X. Zhu, R.-B. Lin, X.-L. Qi and X.-M. Chen, *Adv. Mater.*, 2011, **23**, 1268–1271.
- 39 A. U. Ortiz, A. P. Freitas, A. Boutin, A. H. Fuchs and F.-X. Coudert, *Phys. Chem. Chem. Phys.*, 2014, **16**, 9940–9949.
- 40 J. A. Alt, W. Y. Lee, B. M. Davis, J. R. Savage, T. P. Kennedy, G. D. Prestwich and A. Pulsipher, *PLoS One*, 2018, **13**, e0204709.
- 41 J. Zhang, X. Xu, N. V. Rao, B. Argyle, L. McCoard, W. J. Rusho, T. P. Kennedy, G. D. Prestwich and G. Krueger, *PLoS One*, 2011, **6**, e16658.
- 42 T. Suzuki, A. Ishii-Watabe, N. Hashii, Y. Nakagawa, T. Takahashi, A. Ebisawa, S. Nishi, N. Fujita, A. Bando, Y. Sekimoto, K. Miyata, T. Endo, T. Otsu, S. Sugimoto, T. Kondou, Y. Fujita, N. Miyanaga, M. Mashimo, N. Shimada, H. Yoden, H. Shimamura, Y. Kurata, S. Koyama and N. Kawasaki, *Biologicals*, 2013, **41**, 415–423.
- 43 J. Rnjak-Kovacina, F. Tang, J. M. Whitelock and M. S. Lord, *Adv. Healthcare Mater.*, 2018, **7**, 1701042.
- 44 F.-M. Zhang, H. Dong, X. Zhang, X.-J. Sun, M. Liu, D.-D. Yang, X. Liu and J.-Z. Wei, *ACS Appl. Mater. Interfaces*, 2017, **9**, 27332–27337.
- 45 Z. Xie, X. Cai, C. Sun, S. Liang, S. Shao, S. Huang, Z. Cheng, M. Pang, B. Xing, A. A. Kheraif and J. Lin, *Chem. Mater.*, 2019, **31**, 483–490.
- 46 J.-W. Yoo, D. J. Irvine, D. E. Discher and S. Mitragotri, *Nat. Rev. Drug Discovery*, 2011, **10**, 521–535.
- 47 Y. K. Ip, S. F. Chew and D. J. Randall, *Fish Physiology*, Elsevier, 2001, vol. 20, pp. 109–148.
- 48 A. Mahmood, W. Xia, N. Mahmood, Q. Wang and R. Zou, *Sci. Rep.*, 2015, **5**, 10556.
- 49 B. Bueken, N. Van Velthoven, T. Willhammar, T. Stassin, I. Stassen, D. A. Keen, G. V. Baron, J. F. M. Denayer, R. Ameloot, S. Bals, D. De Vos and T. D. Bennett, *Chem. Sci.*, 2017, **8**, 3939–3948.
- 50 A. Chakraborty, P. Sutar, P. Yadav, M. Eswaremoorthy and T. K. Maji, *Inorg. Chem.*, 2018, **57**, 14480–14483.
- 51 Z. Akimbekov, A. D. Katsenis, G. P. Nagabhushana, G. Ayoub, M. Arhangelskis, A. J. Morris, T. Frišćić and A. Navrotsky, *J. Am. Chem. Soc.*, 2017, **139**, 7952–7957.
- 52 Z. Fang, B. Bueken, D. E. De Vos and R. A. Fischer, *Angew. Chem., Int. Ed.*, 2015, **54**, 7234–7254.
- 53 K. M. Choi, H. J. Jeon, J. K. Kang and O. M. Yaghi, *J. Am. Chem. Soc.*, 2011, **133**, 11920–11923.
- 54 N. Mainreck, S. Brézillon, G. D. Sockalingum, F.-X. Maquart, M. Manfait and Y. Wegrowski, *J. Pharm. Sci.*, 2011, **100**, 441–450.
- 55 S. B. Frazier, K. A. Roodhouse, D. E. Hourcade and L. Zhang, *Open Glycosci.*, 2008, **1**, 31–39.
- 56 T. M. C. C. Filisetti-Cozzi and N. C. Carpita, *Anal. Biochem.*, 1991, **197**, 157–162.
- 57 A. Riemann, A. Ihling, J. Thomas, B. Schneider, O. Thews and M. Gekle, *Biochim. Biophys. Acta, Mol. Cell Res.*, 2015, **1853**, 299–307.
- 58 G. Hao, Z. P. Xu and L. Li, *RSC Adv.*, 2018, **8**, 22182–22192.
- 59 X. Huang and C. S. Brazel, *J. Controlled Release*, 2001, **73**, 121–136.
- 60 H. Ouyang, Z. Zheng, Y. Chen, Y. Liu, C. Hong, Y. Zhu, J. Deng, X. Ding, W. Zhou and X. Wang, *J. Mater. Chem. B*, 2019, **7**, 6099–6108.
- 61 P. E. Nolan and T. C. Trujillo, in *Complications of Percutaneous Coronary Interventions*, ed. S. M. Butman, Springer, New York, NY, 2005, pp. 6–16.
- 62 P. Prandoni, A. W. A. Lensing, A. Piccioli, E. Bernardi, P. Simioni, B. Girolami, A. Marchiori, P. Sabbion, M. H. Prins, F. Noventa and A. Girolami, *Blood*, 2002, **100**, 3484–3488.
- 63 Y. Zhang, J. Yu, J. Wang, N. J. Hanne, Z. Cui, C. Qian, C. Wang, H. Xin, J. H. Cole, C. M. Gallippi, Y. Zhu and Z. Gu, *Adv. Mater.*, 2017, **29**, 1604043.
- 64 R. Bhat, À. Ribes, N. Mas, E. Aznar, F. Sancenón, M. D. Marcos, J. R. Murguía, A. Venkataraman and R. Martínez-Máñez, *Langmuir*, 2016, **32**, 1195–1200.
- 65 C. Argyo, V. Cauda, H. Engelke, J. Rädler, G. Bein and T. Bein, *Chem. – Eur. J.*, 2012, **18**, 428–432.
- 66 N. S. Jones, M. G. Glenn, L. A. Orloff and M. R. Mayberg, *Arch. Otolaryngol.*, 1990, **116**, 779–785.
- 67 P. Montalto, J. Vlachogiannakos, D. J. Cox, S. Pastacaldi, D. Patch and A. K. Burroughs, *J. Hepatol.*, 2002, **37**, 463–470.
- 68 S. Albu, *Drug Des., Dev. Ther.*, 2012, 125–132.
- 69 S. A. Basnayake, J. Su, X. Zou and K. J. Balkus, *Inorg. Chem.*, 2015, **54**, 1816–1821.
- 70 D. Puppi, D. Dinucci, C. Bartoli, C. Mota, C. Migone, F. Dini, G. Barsotti, F. Carlucci and F. Chiellini, *J. Bioact. Compat. Polym.*, 2011, **26**, 478–492.
- 71 D. Jain, R. Raturi, V. Jain, P. Bansal and R. Singh, *Biomater.*, 2011, **1**, 57–65.



Electronic Supplementary Information

Modulation of Metal-Azolate Frameworks for the Tunable Release of Encapsulated Glycosaminoglycans

Miriam de J. Velásquez-Hernández^a, Efwita Astria^a, Sarah Winkler^a, Weibin Liang^b, Helmar Wiltsche^c, Arpita Poddar^d, Ravi Shukla^d, Glenn Prestwich^e, John Paderi^f, Pablo Salcedo-Abraira^g, Heinz Amenitsch^h, Patricia Horcajada^g, Christian J. Doonan^{*b}, and Paolo Falcaro^{*a}

E-mail: paolo.falcaro@tugraz.at and christian.doonan@adelaide.edu.au

Abstract: Glycosaminoglycans (GAGs) are biomacromolecules necessary for the regulation of different biological functions. In medicine, GAGs are important commercial therapeutics widely used for the treatment of thrombosis, inflammation, osteoarthritis and wound healing. However, protocols for the encapsulation of GAGs in MOFs carriers are not yet available. Here, we successfully encapsulated GAG-based clinical drugs (heparin, hyaluronic acid, chondroitin sulfate, dermatan sulfate) and two new biotherapeutics in preclinical stage (GM-1111 and HepSYL proteoglycan) in three different pH-responsive metal-azolate frameworks (ZIF-8, ZIF-90, and MAF-7). The resultant GAG@MOF biocomposites present significant differences in terms of crystallinity, particle size, and spatial distribution of the cargo, which influences the drug-release kinetics upon applying an acidic stimulus. For a selected system, heparin@MOF, the released therapeutic retained its antithrombotic activity while the MOF shell effectively protects the drug from Heparin Lyase. By using different MOF shells, the present approach enables the preparation of GAG-based biocomposites with tunable properties such as encapsulation efficiency, protection and release.

Experimental Procedures

General Information

Heparin sodium salt from porcine intestinal mucosa, Hyaluronic acid sodium salt from *Streptococcus equi*, Dermatan sulfate sodium salt from porcine intestinal mucosa, Chondroitin sulfate sodium salt from shark cartilage, FITC-tagged carboxymethyl dextran (FITC-CM-dextran, average Mol. Wt: 40.000, 1-8 mmol FITC/mol glucose, carboxymethyl groups content: 3-7%), and Zinc nitrate hexahydrate ($\text{Zn}(\text{NO}_3)_2 \cdot 6\text{H}_2\text{O}$) were purchased from Sigma-Aldrich. 2-Methylimidazole (HmIM), Imidazole-2-carboxylaldehyde (HICA), and 3-methyl-1H-1,2,4-triazole (Hmtz) were purchased from TCI chemicals. Zinc acetate dihydrate $\text{Zn}(\text{OAc})_2 \cdot 2\text{H}_2\text{O}$ and Ammonium sulfamate were purchased from Merck Millipore. Citric acid monohydrate was purchased from Carl Roth. Tri-Sodium citrate dehydrate and Carbazole were purchased from Fluka. Sodium tetraborate was purchased from Honeywell Riedel-de Haën. All reagents and chemicals were used as received without further purification.

FT-IR spectroscopy

FT-IR spectra were recorded on a Bruker ALPHA spectrometer using the ATR accessory with a diamond window in the range of $\tilde{\nu}$ 400 – 4000 cm^{-1} , 128 of scans, resolution 2 cm^{-1} .

Powder X-ray diffraction (PXRD)

PXRD patterns of the samples (GM-1111@ZIF-8, GM-1111@ZIF-90, GM-1111@MAF-7, HepSYL@ZIF-8, HepSYL@ZIF-90 and HepSYL@MAF-7) were recorded on a Rigaku powder diffractometer equipped with D/teX Ultra 250 detector and using Cu $\text{K}\alpha$ radiation ($\lambda = 1.5406 \text{ \AA}$). The scan speed was 3 deg min^{-1} and the step 0.01°. WAXS patterns of the samples of (ZIF-8, GAGs@ZIF-8, ZIF-90, GAGs@ZIF-90, MAF-7 and GAGs@MAF-7) were collected at ELETTRA synchrotron using the Austrian SAXS beamline. Operation occurred at a photon energy of 8 keV.

Detector: Pilatus3 100K, Dectris Ltd., Baden, Switzerland; all experiments were performed at room temperature. The resulting two-dimensional images were radially integrated to obtain a 1D pattern of normalized intensity versus scattering vector q . The background was collected using kapton tape and subtracted as background.

Scanning Electron Microscopy (SEM)

SEM images of the samples were recorded by Philips XL30 FEG SEM.

Transmission electron microscopy (TEM)

TEM analysis was carried out in Philips CM100.

Confocal Laser Scanning Microscopy (CLSM)

CLSM data were recorded by Olympus FV3000 microscope, with excitation at 640 nm and emission at 650–675 nm.

Determination of Zn by Inductively Coupled plasma-optical emission spectroscopy (ICP-OES)

The Zn concentration was quantified using axially viewed ICP-OES (Ciros Vision EOP, Spectro, Germany) after dilution with 1 mol L^{-1} nitric acid. The Zn (II) 213.856 nm emission line was used.

Thermogravimetric analysis (TGA)

The amount of GAG encapsulated within different materials was assessed by TGA. The thermogravimetric analysis (TGA) was performed using a Perkin Elmer STA 6000 instrument. The program used was of under an air flow (100 mL/min) from 30 °C to 800 °C with a heating ramp of 5 °C/min.

Energy Dispersive X-ray Spectroscopy (EDS) analysis

EDS spectra were collected using Tescan VEGA 3 SEM with tungsten source filament working at 20 kV. Prior the analysis the powder samples were drop casted on a piece of Si (100) treated with a piranha solution to remove traces of organic material. Then, EDS elemental analysis was carried out over areas of 200 x 200 μm^2 . The amount of S (wt%) on the free HP was used to determine the contribution of this GAG to the elemental composition of HP@MOFs, whereas the contribution of MOF-shell to the biocomposite was estimated from N (wt%) and Zn (wt%) ratio obtained from the neat MOF.

Synthesis of GAGs@ZIF-8 and GAGs@MAF-7 biocomposites

The synthesis of GAG@ZIF-8 and GAG@MAF-7 biocomposites was carried out using a metal to ligand ratio $\text{Zn}^{2+}:\text{L} = 1:3.47$ (L = HmIM, and Hmtz; respectively), and the final concentration of the corresponding biotherapeutic was 0.36 mg mL^{-1} . The stock solution of the corresponding precursors **Zn(OAc)₂·2H₂O** (80 mM), **2-methylimidazole** (HmIM; 396.6 mM), **3-methyl-1,2,4-triazole** (Hmtz; 396.6 mM), and **GAGs** (2.4 mg mL^{-1}) were prepared in DI water at room temperature. Then, to prepare the GAGs based biocomposites **700 μL** of the required ligand stock solution was premixed with **300 μL** of the corresponding GAG stock solution (or water for control experiments). Finally, **1 mL** of zinc acetate stock solution was added to this mixture. The solutions were left standing at room temperature for 24 h. Afterwards, the solids were collected by centrifugation and washed with deionized water DI (2 mL, 3X), and EtOH (2 mL, 3X). The solids were then air dried at room temperature. Each sample was prepared by triplicate.

Synthesis of GAGs@ZIF-90 biocomposites

The synthesis of GAG@ZIF-90 biocomposites were prepared following a similar procedure described above for GAG@ZIF-8 and GAG@MAF-7 biocomposites, i.e. $\text{Zn}^{2+}:\text{HICA} = 1:3.47$; $[\text{GAG}] = 0.36 \text{ mg mL}^{-1}$. Due to the low solubility of the ligand (HICA) the preparation of the stock solutions was slightly modified. The stock solution of **HICA** (185.1 mM) was prepared in DI water at 60 °C under stirring. The stock solutions of **Zn(NO₃)₂·6H₂O** (400 mM) and the corresponding **GAG** (2.4 mg mL^{-1}) were prepared in DI water at room temperature. To synthesize the GAG@ZIF-90 biocomposites keeping the required metal to ligand ratio (1:3.47) **1.5 mL** of the HICA stock solution at 35 °C was premixed with **300 μL** of the corresponding GAG stock solution (or water for control experiments). Then, **200 μL** of **Zn(NO₃)₂·6H₂O** (400 mM) was added to this mixture. The solutions were left standing at room temperature for 24 h. Afterwards, the solids were collected by centrifugation and washed with deionized water DI (2 mL, 3X), and EtOH (2 mL, 3X). The solids were then air dried at room temperature. Each sample was prepared by triplicate.

General Procedure for Encapsulation Efficiency measurement

The encapsulation efficiency (EE%) of each GAG@MOF biocomposite was assessed using UV-vis spectroscopy and the carbazole assay, which is a direct method to quantify glycosaminoglycans by colorimetry (λ_{max} 520 nm) (*vide infra*). To determine the EE% of GAG@MOF biocomposites, each sample was soaked in citrate buffer (2 mL, 80 mM, pH = 6). The clear solution obtained was filtered through a size exclusion chromatography column to remove the ligand and Zn^{2+} ions released during the degradation

process. This improves the determination of the amount of GAG in the solution by reducing the interference of the degraded MOF components and the buffer media with the carbazole assay.

Carbazole assay

Ammonium sulfamate (20 μ L, 4 M) was added to an aliquot of sample (200 μ L) or water (blank control) and the resultant mixture was vortexed for 1 min. Then, sodium tetraborate in sulfuric acid (1 mL, 25 mM) was added and carefully mixed. The mixture was heated at 100 $^{\circ}$ C for 5 min and cooled to room temperature. Afterwards, the carbazole solution (0.1%, 40 μ L) was added and the resultant mixture was heated again at 100 $^{\circ}$ C for 15 min and then cooled down to room temperature (color develops during this step). Finally, the resultant solution was analyzed by UV-vis spectroscopy; the absorbance at 520 nm was used to quantify the amount of the analyte by comparison with the corresponding calibration curve (Fig. S23). All the experiments were performed in triplicate.

Release test of GAG@MOFs

1 mL of citrate buffer (80 mM, pH = 6) was added to a pellet of GAGs@MOF, the sample was kept under bidimensional stirring. Aliquots of 200 μ L of the supernatant were collected by centrifugation (13400 rpm, 1 min) and replaced with the same volume of fresh medium. The amount of GAG released in the incubation media was determined by UV-vis spectroscopy using carbazole assay.

Preliminary studies for determining the synthetic conditions to optimize the encapsulation efficiency (EE%)

Synthesis of FITC-CMD@ZIF-8 and FITC-CMD@MAF-7 biocomposites

The synthesis of ZIF-8 and MAF-7 based biocomposites were carried out using three different Zn^{2+} :L (L = HmIM, and Hmtz; respectively) ratios: 1:4 (A), 1:3.47 (B) and 1:2.52 (C). For each ratio, we used five different concentrations of FITC-CM-dextran (FITC-CMD) : 0 (1), 0.18 (2), 0.36 (3), 0.72 (4), 1.44 (5) mg mL⁻¹ (Table S1). The stock solution of the corresponding precursors **Zn(OAc)₂·2H₂O** (80 mM), **2-Methylimidazole** (HmIM; 800 mM), **3-methyl-1,2,4-triazole** (Hmtz; 800 mM), and **FITC-CM-dextran** (5.76 mg mL⁻¹) were prepared in DI water at room temperature. To synthesize the samples FITC-CMD@ZIF-8 (**8DXAn**, **8DXBn**, and **8DXCn**; n = 1–5) and FITC-CMD@MAF-7 (**7DXAn**, **7DXBn**, and **7DXCn**; n = 1–5), the required volume of the corresponding ligand (HmIM or Hmtz), and FITC-CMD stock solutions were premixed reaching a total volume of 1 mL, by dilution with water. Then, 1 mL of Zn(OAc)₂·2H₂O was added to this mixture (Table S1). The resultant mixtures were left standing at room temperature for 24 h. Afterwards, the solids were collected by centrifugation and washed with deionized water DI (2 mL, 3X), and EtOH (2 mL, 3X). The solids were then air-dried at room temperature. Each sample was prepared by triplicate.

Sample	Ratio M:L	Final concentration			Volume (μL)			
		L (mM)	CM-DEXT (mg mL^{-1})	Zn(OAc) $_2$ ·2H $_2$ O (mM)	L	CM-DEXT	H $_2$ O	Zn(OAc) $_2$ ·2H $_2$ O
nDXA1	1:4	160	0	40	400	0	600	1000
nDXA2	1:4	160	0.18	40	400	62.5	537.5	1000
nDXA3	1:4	160	0.36	40	400	125	475	1000
nDXA4	1:4	160	0.72	40	400	250	350	1000
nDXA5	1:4	160	1.44	40	400	500	100	1000
nDXB1	1:3.47	138.8	0	40	347	0	653	1000
nDXB2	1:3.47	138.8	0.18	40	347	62.5	590.5	1000
nDXB3	1:3.47	138.8	0.36	40	347	125	528	1000
nDXB4	1:3.47	138.8	0.72	40	347	250	403	1000
nDXB5	1:3.47	138.8	1.44	40	347	500	153	1000
nDXC1	1:2.52	100.8	0	40	252	0	748	1000
nDXC2	1:2.52	100.8	0.18	40	252	62.5	685.5	1000
nDXC3	1:2.52	100.8	0.36	40	252	125	623	1000
nDXC4	1:2.52	100.8	0.72	40	252	250	498	1000
nDXC5	1:2.52	100.8	1.44	40	252	500	248	1000

Table S1. Synthetic protocol for FITC-CMD@ZIF-8 ($n = 8$) and FITC-CMD@MAF-7 biocomposites ($n = 7$) biocomposites.

Synthesis of FITC-CMD@ZIF-90

The synthesis of ZIF-90 based biocomposites was carried out using three different Zn $^{2+}$: HICA ratios: 1:4 (**A**), 1:3.47 (**B**) and 1:2.52 (**C**). For each ratio, we used five different concentrations of FITC-CMD: 0 (**1**), 0.18 (**2**), 0.36 (**3**), 0.72 (**4**), 1.44 (**5**) mg mL^{-1} (**Table S2**). The stock solutions of **2-Imidazolecarboxaldehyde** (HICA) (213.33 mM (for ratio **A**), 185.1 mM (for ratio **B**) and 134.4 mM (for ratio **C**)) were prepared in DI water at 60 °C. Whereas the stock solutions of **Zn(NO $_3$) $_2$ ·6H $_2$ O** (320 mM) and **FITC-CM-dextran** ($S_1 = 11.52 \text{ mg mL}^{-1}$, and 2.88 mg mL^{-1}) were prepared in DI water at room temperature. To synthesize the samples **90DXAn**, **90DXBn**, and **90DXCn** ($n = 1 - 5$) the required volume of each stock solution was mixed according to **Table S2**. The resultant mixtures were left standing at room temperature for 24 h. Afterwards, the solids were collected by centrifugation and washed with deionized water DI (2 mL, 3X), and EtOH (2 mL, 3X). The solids were then air dried at room temperature. Each sample was prepared by triplicate.

Sample	Ratio M:L	Final concentration			Volume (mL)			
		HICA (mM)	FITC-CMD (mg mL^{-1})	Zn(NO $_3$) $_2$ ·6H $_2$ O (mM)	HICA	FITC-CMD	H $_2$ O	Zn(NO $_3$) $_2$ ·6H $_2$ O
90DXA1	1:4	160	0	40	1.5	0	0.25	0.25
90DXA2	1:4	160	0.18	40	1.5	0.125 (S2)	0.125	0.25
90DXA3	1:4	160	0.36	40	1.5	0.250 (S2)	0	0.25
90DXA4	1:4	160	0.72	40	1.5	0.125 (S1)	0.125	0.25
90DXA5	1:4	160	1.44	40	1.5	0.250 (S1)	0.250	0.25
90DXB1	1:3.47	138.8	0	40	1.5	0	0.25	0.25
90DXB2	1:3.47	138.8	0.18	40	1.5	0.125 (S2)	0.125	0.25
90DXB3	1:3.47	138.8	0.36	40	1.5	0.250 (S2)	0	0.25
90DXB4	1:3.47	138.8	0.72	40	1.5	0.125 (S1)	0.125	0.25
90DXB5	1:3.47	138.8	1.44	40	1.5	0.250 (S1)	0.250	0.25
90DXC1	1:2.52	100.8	0	40	1.5	0	0.25	0.25
90DXC2	1:2.52	100.8	0.18	40	1.5	0.125 (S2)	0.125	0.25
90DXC3	1:2.52	100.8	0.36	40	1.5	0.250 (S2)	0	0.25
90DXC4	1:2.52	100.8	0.72	40	1.5	0.125 (S1)	0.125	0.25
90DXC5	1:2.52	100.8	1.44	40	1.5	0.250 (S1)	0.250	0.25

Table S2. Synthetic protocol for FITC-CMD@ZIF-90 biocomposites.

Determination of the encapsulation efficiency of FITC-CMD@ZIF-8, FITC-CMD@ZIF-90, and FITC-CMD@MAF-7 biocomposites

The quantitative assessment of the cargo loaded within the biocomposites was carried out by re-dissolving the MOF matrix under acidic conditions, soaking the samples in 2 mL of citrate buffer (100 mM, pH = 6). The resultant solution was analyzed by UV-vis spectroscopy, where the absorbance at 490 nm was used to quantify the amount of the analyte by comparison with the corresponding calibration curve (Fig. S1-S3). To avoid any interference of the ligand, metal, and/or the citrate buffer during the determination process, the calibration curves were performed adding a known amount of FITC-CM-dextran to a solution of Zn²⁺ and the corresponding ligand (HICA or Hmtz) in citrate buffer media. The amount of Zn²⁺ and ligand added to this mixture depends of the amount of material formed for each metal to ligand ratio. These experiments were performed in triplicate for each sample described in the Tables S1 and S2.

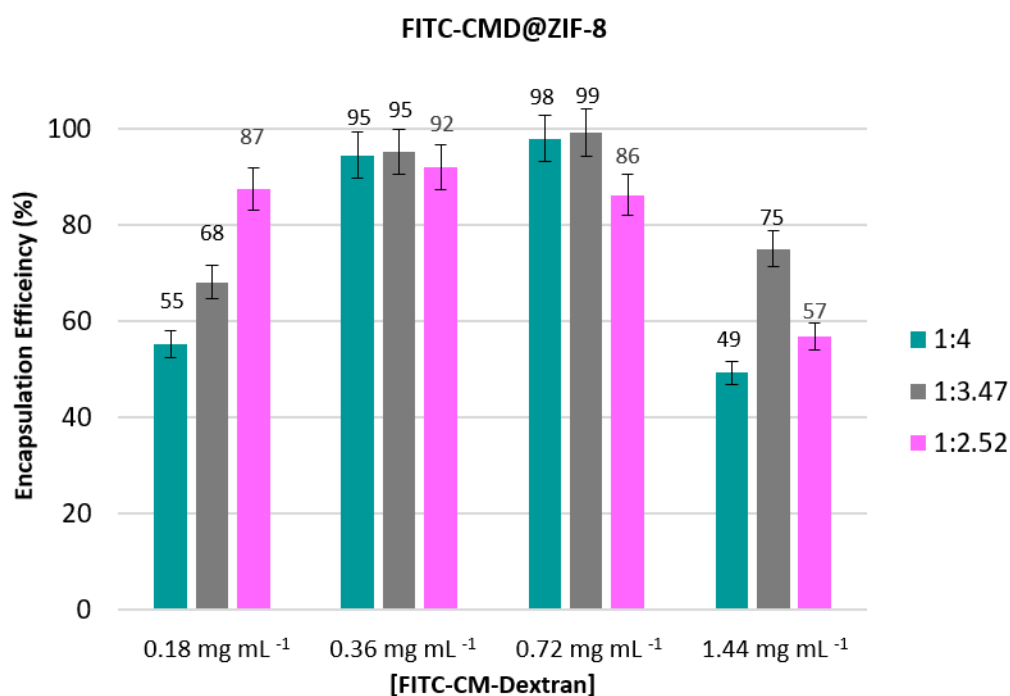


Fig. S1 Encapsulation efficiency of FITC-CMD@ZIF-8 biocomposites obtained varying the Zn²⁺:HmIM ratio and the concentration of FITC-CMD.

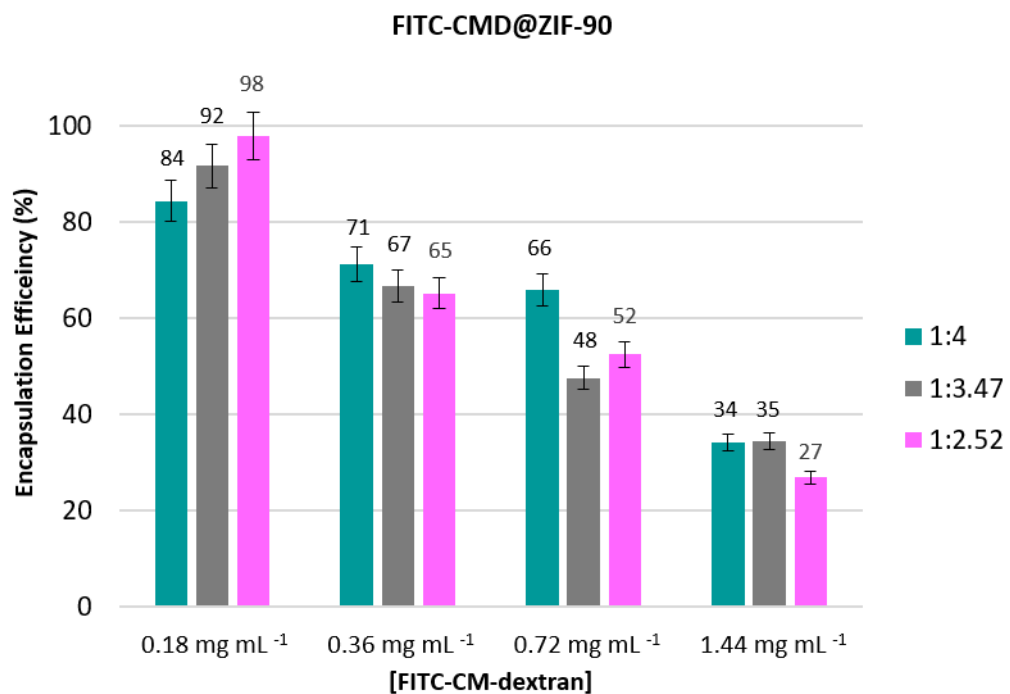


Fig. S2 Encapsulation Efficiency of FITC-CMD@ZIF-90 biocomposites obtained varying the Zn²⁺:HICA ratio and the concentration of FITC-CMD.

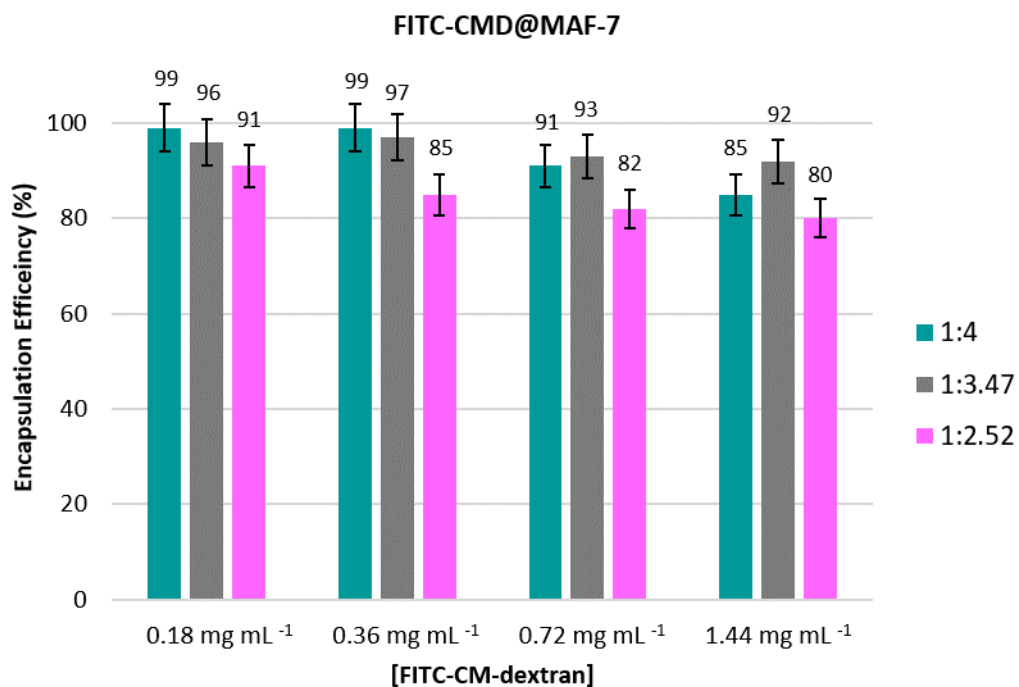


Fig. S3 Encapsulation Efficiency of FITC-CMD@MAF-7 biocomposites obtained varying the Zn²⁺:Hmtz ratio and the concentration of FITC-CMD.

Results reveal that the FITC-CMD@ZIF-8 biocomposites obtained from 0.36 (**3**) and 0.72 (**4**) mg mL⁻¹ of FITC-CMD present higher EE% than those obtained from 0.18 (**2**) and 1.44 (**5**) mg mL⁻¹ of FITC-CMD (Fig. S1). In addition, the EE% is influenced by the metal to ligand ratio: the optimal encapsulation efficiency is reached when using 0.36 (**3**) and 0.72 (**4**) mg mL⁻¹ of FITC-CMD and 1:4 and 1:3.47 metal to ligand ratio (**8DXA3**, **8DXA4**, **8DXB3**, and **8DXB4**). for FITC-CMD@ZIF-90 biocomposites (**90DXAn**; where **n = 2 – 5**), the EE% decreases drastically with the increase in the initial concentration of FITC-CMD from *ca.* 84% for **90DXA2** to *ca.* 34% for **90DXA5** (Fig. S2). Such results suggest that the EE% strongly depends on the initial concentration of the model drug.

FITC-CMD@MAF-7 biocomposites obtained from 1:4 metal to ligand ratio (**7DXAn**; where **n = 2 – 5**) present exceptional polysaccharide payloads regardless of the initial concentration of FITC-CMD. For instance, the EE% is almost quantitative for the samples prepared with low initial concentrations of FITC-CMD (EE > 90% for **7DXA2**, **7DXA3**, and **7DXA4**). The EE% decreases slightly as the concentration of FITC-CMD increases (*ca.* 85% for **7DXA5**) (Fig. S3). These findings are consistent with the previous reports about the biomineralization of carbohydrates within ZIF-8.^[1] However, such reports also declare that Zn²⁺:L ratio affects the polysaccharide payloads. Thus, in concordance with these studies, another two different metal to ligand ratios were tested (Zn²⁺:L = 1:3.47 (**B**) and 1:2.52 (**C**)) to corroborate the role of this parameter in the EE of the resultant FITC-CMD@MAF-7 and FITC-CM-dextran@ZIF-90 biocomposites (**7DXBn**, **7DXCn**, **90DXBn**, and **90DXCn**; where **n = 2 – 5**) (Table S1 and S2). The collected data indicate that high polysaccharide payloads were achieved in FITC-CMD@MAF-7 biocomposites when using a 1:3.47 ratio (EE > 90%) regardless of the concentration of FITC-CM-dextran (Fig. S3). Whereas, the biocomposites obtained from Zn²⁺:L = 1:2.52 ratio present lower EE than their analogous derived from Zn²⁺:L = 1:3.47 and 1:4 (Fig. S3). Regarding FITC-CMD@ZIF-90 biocomposites, the trend of EE because of the variations in the Zn²⁺:L ratio is not as clear as for MAF-7 biocomposites. Since for ZIF-90-based biocomposites a synergistic effect between Zn²⁺:L ratio and the initial concentration of FITC-CMD determines the final EE (Fig. S3).

Release test of FITC-CMD@ZIF-8 FITC-CMD@MAF-7 and FITC-CMD@ZIF-90

The drug release performance of the resultant MAF-7 and ZIF-90-based biocomposites (8DXAn, 8DXBn, 8DXCn, 7DXAn, 7DXBn, 7DXCn and 90DXAn, 90DXBn, and 90DXCn; where n = 2 – 5) was assessed by monitoring the amount of FITC-CM-dextran released over time upon applying an external acidic stimulus (Fig. S4–S7). Thus, the powder material was soaked in 1 mL of citrate buffer (100 mM, pH = 6) under bidimensional continuous stirring (500 rpm). At different incubation times the sample was centrifuged, and 1 mL of the supernatant was taken to be analyzed by UV-vis spectroscopy (λ_{\max} 490 nm). It is worth to mention that the samples prepared with MAF-7 keeping $Zn^{2+}:L = 1:2.52$ ratio degrades almost immediately upon the addition of citrate buffer.

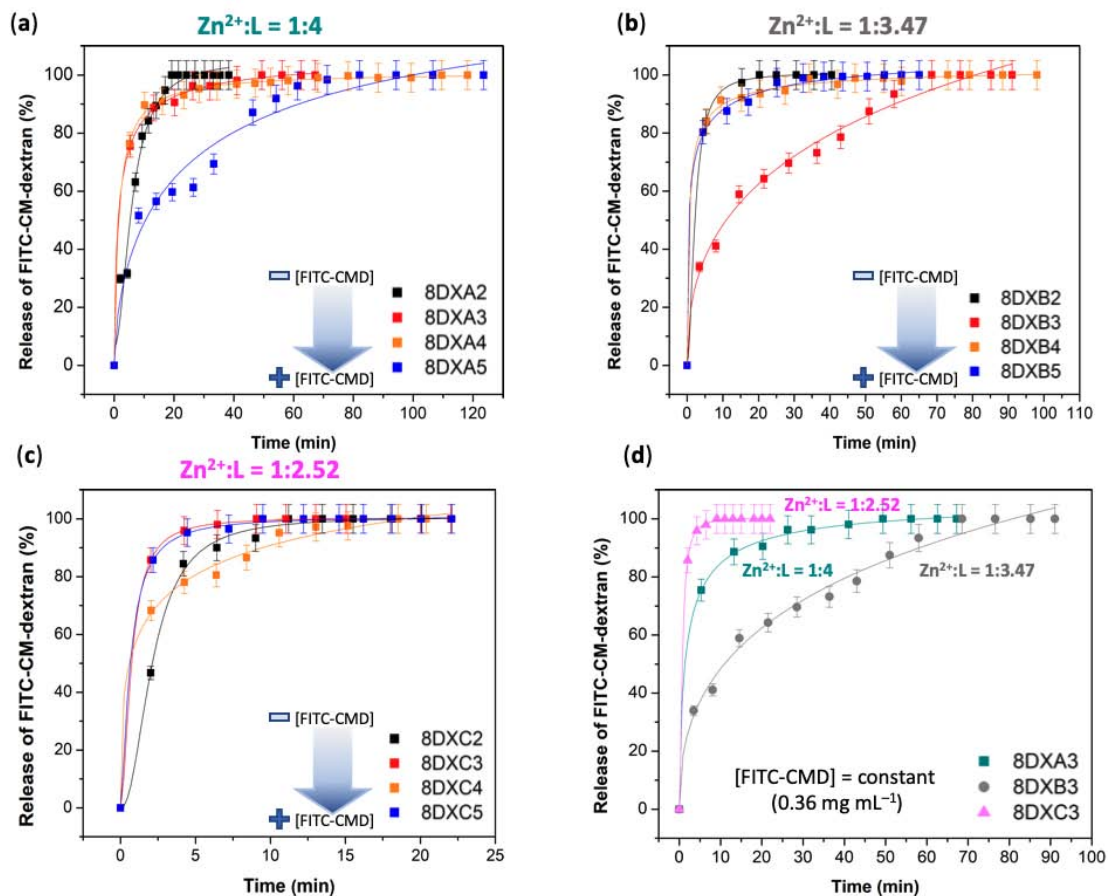


Fig. S4. Release profiles of the FITC-CMD@ZIF-8 biocomposites. from: (a) $Zn^{2+}:HmIM = 1:4$, (b) $Zn^{2+}:HmIM = 1:3.47$, (c) $Zn^{2+}:HmIM = 1:2.52$ varying the initial concentration of FITC-CMD. (d) Comparative release profiles of samples obtained from different $Zn^{2+}:HmIM$ ratios keeping constant the initial concentration of FITC-CMD (0.36 mg mL^{-1}).

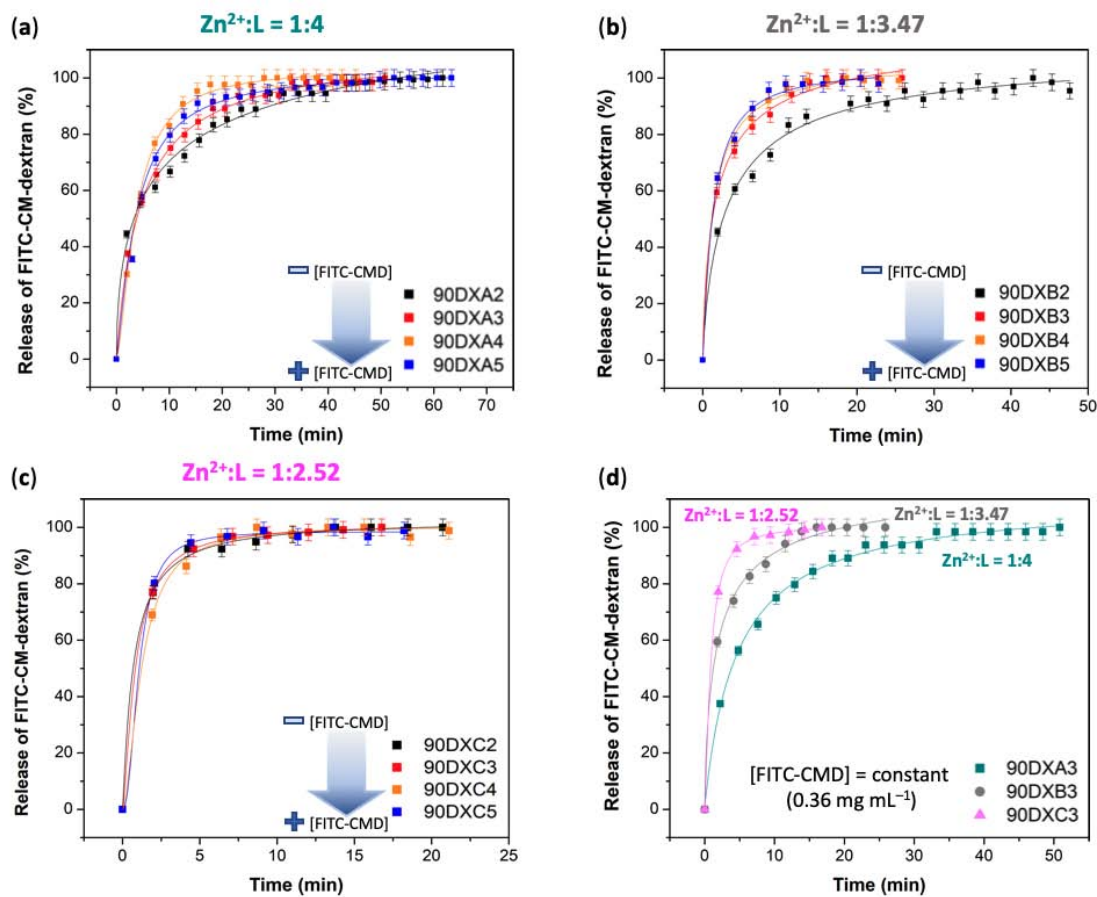


Fig. S5. Release profiles of the FITC-CMD@ZIF-90 biocomposites. from: (a) $Zn^{2+}:HICA=1:4$, (b) $Zn^{2+}:HICA=1:3.47$, (c) $Zn^{2+}:HICA=1:2.52$ varying the initial concentration of FITC-CMD. (d) Comparative release profiles of samples obtained from different $Zn^{2+}:HICA$ ratios keeping constant the initial concentration of FITC-CMD (0.36 mg mL^{-1}).

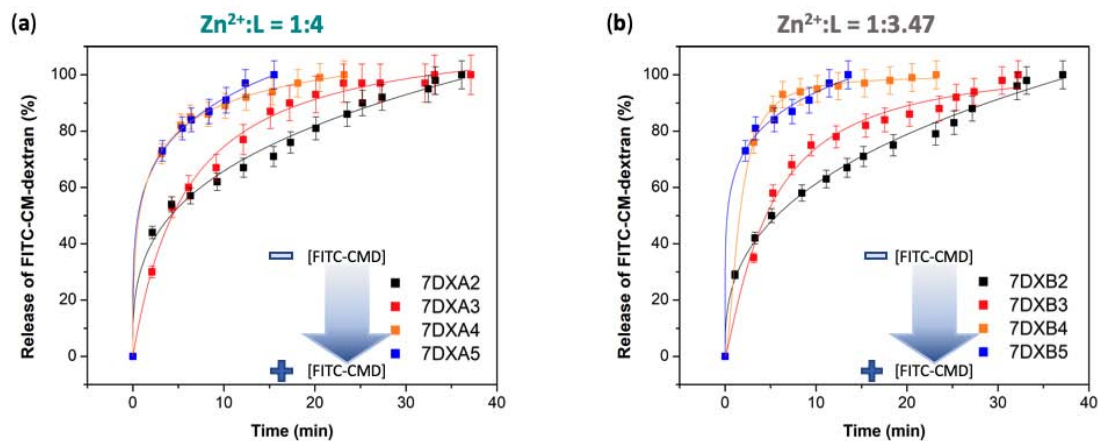


Fig. S6. Release profiles of the FITC-CMD@MAF-7 biocomposites. (a) from $Zn^{2+}:Hmtz=1:4$ ratio varying the initial concentration of FITC-CMD, and (b) from $Zn^{2+}:Hmtz=1:3.47$ varying the initial concentration of FITC-CMD.

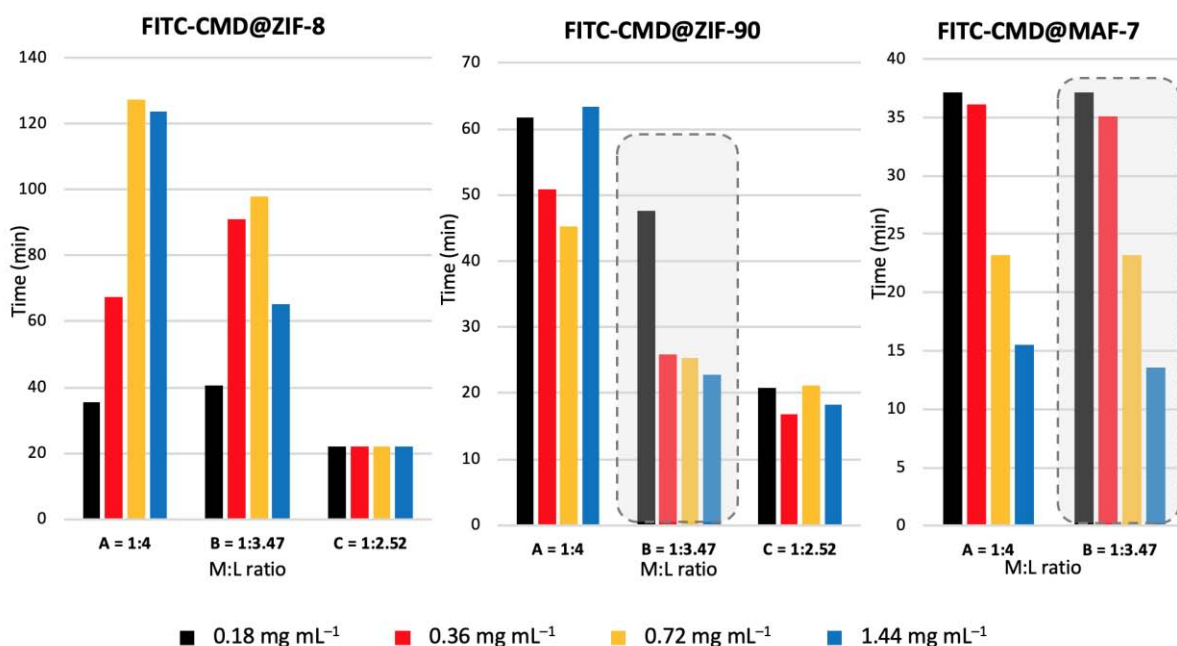


Fig. S7. Time required to release 100% of FITC-CMD from the MOF biocomposites obtained by varying the initial concentration of the model drug (FITC-CMD) and the Zn²⁺:L ratio.

In general, the release profiles of ZIF-8, ZIF-90 and MAF-7 biocomposites present an initial burst release, followed by a sustained delivery process (Fig. S4–S7).

After a close inspection of the release profiles obtained from different metal to ligand ratio, it is evident that the delivery rate increases as the Zn²⁺:L decreases. For instance, a comparative analysis of the release kinetics obtained from **90DXA3**, **90DXB3**, and **90DXC3** (Zn²⁺:L = 1:4, 1:3.47, and 1:2.52; respectively) reveals that **90DXA3** required around 50 min to achieve the full release of the model drug; whereas its analogous **90DXB3** and **90DXC3** achieved the complete release of the cargo within 25 and 15 min, respectively (Fig. S5). Similarly, for MAF-7-based biocomposites, it was observed that the samples obtained from Zn²⁺:L = 1:2.52 (**7DXCn**) degraded immediately upon soaking them into the acidic media. By contrast, for those prepared from 1:4 (A) and 1:3.47 (B) Zn²⁺:L ratio took from 15 min (**7DXA5** and **7DXB5**) to 30 min (**7DXA2**, **7DXA3**, **7DXB2** and **7DXB3**) to achieve the full release of the cargo (Fig. S6).

In light of such findings, we conclude that the optimal synthetic conditions to ensure acceptable encapsulation efficiencies and drug release kinetics, for all the three different metal-azolate systems, requires the usage of 0.36 mg mL⁻¹ of the biomacromolecule keeping the ratio Zn²⁺:L = 1:3.47.

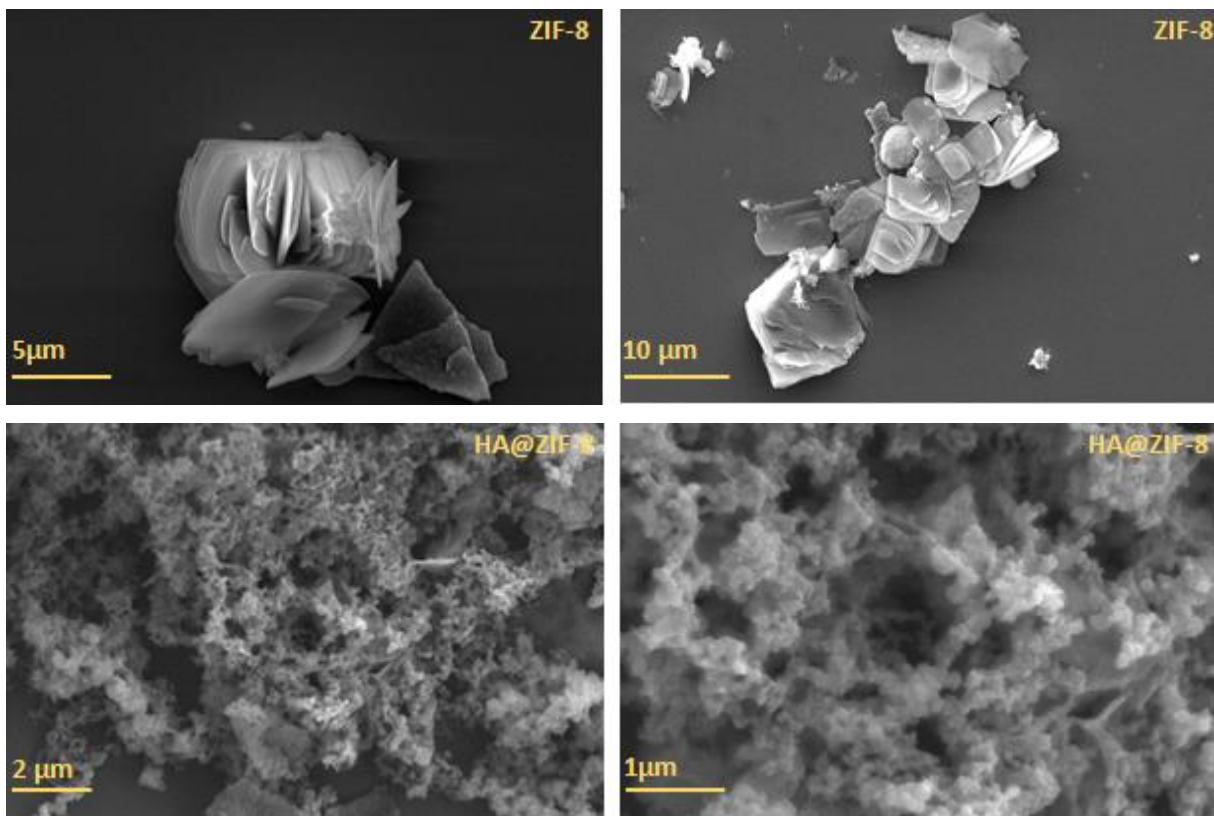


Fig. S8 SEM images for ZIF-8 and HA@ZIF-8.

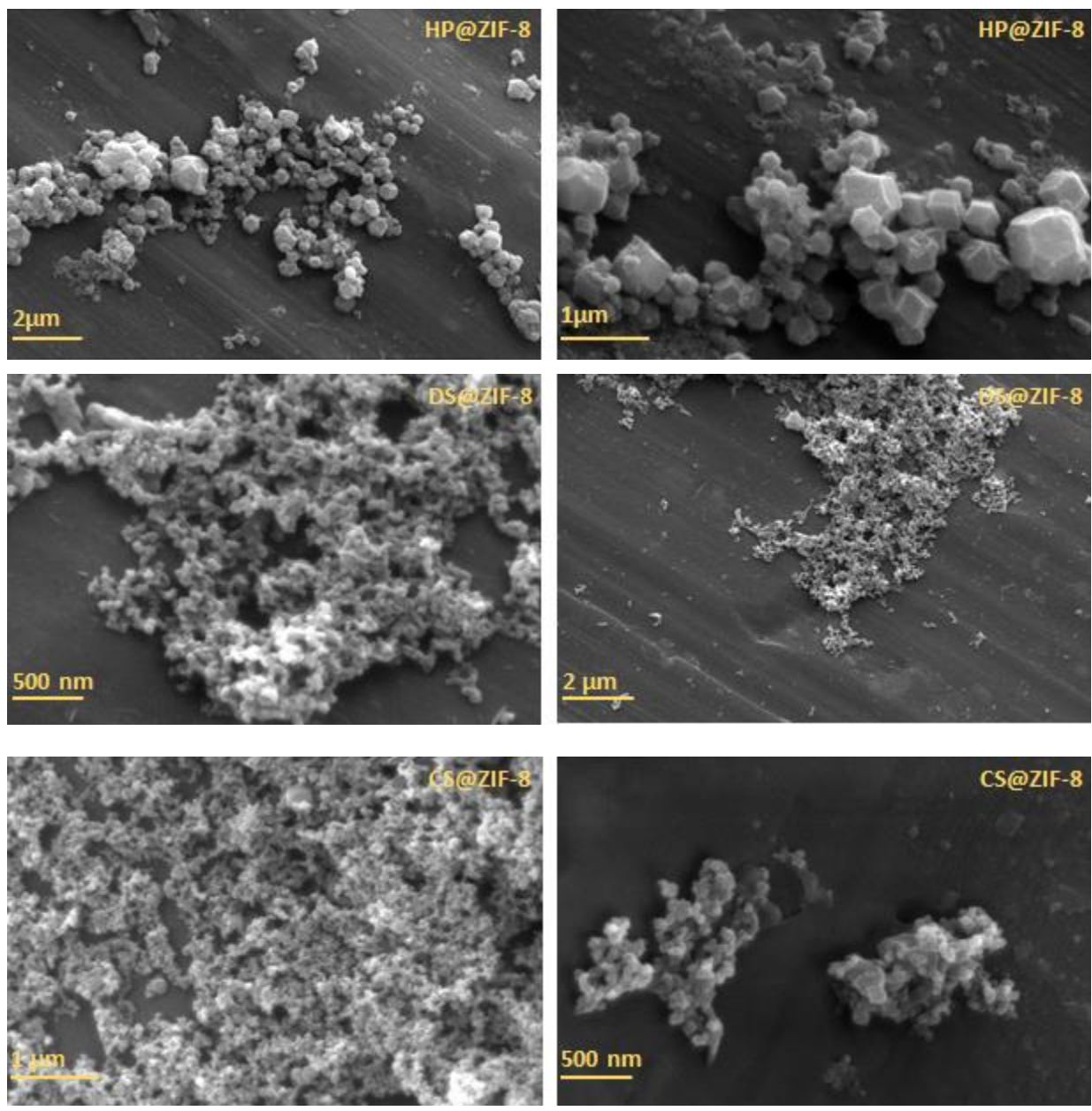


Fig. S9 SEM images for HP@ZIF-8, DS@ZIF-8, and CS@ZIF-8.

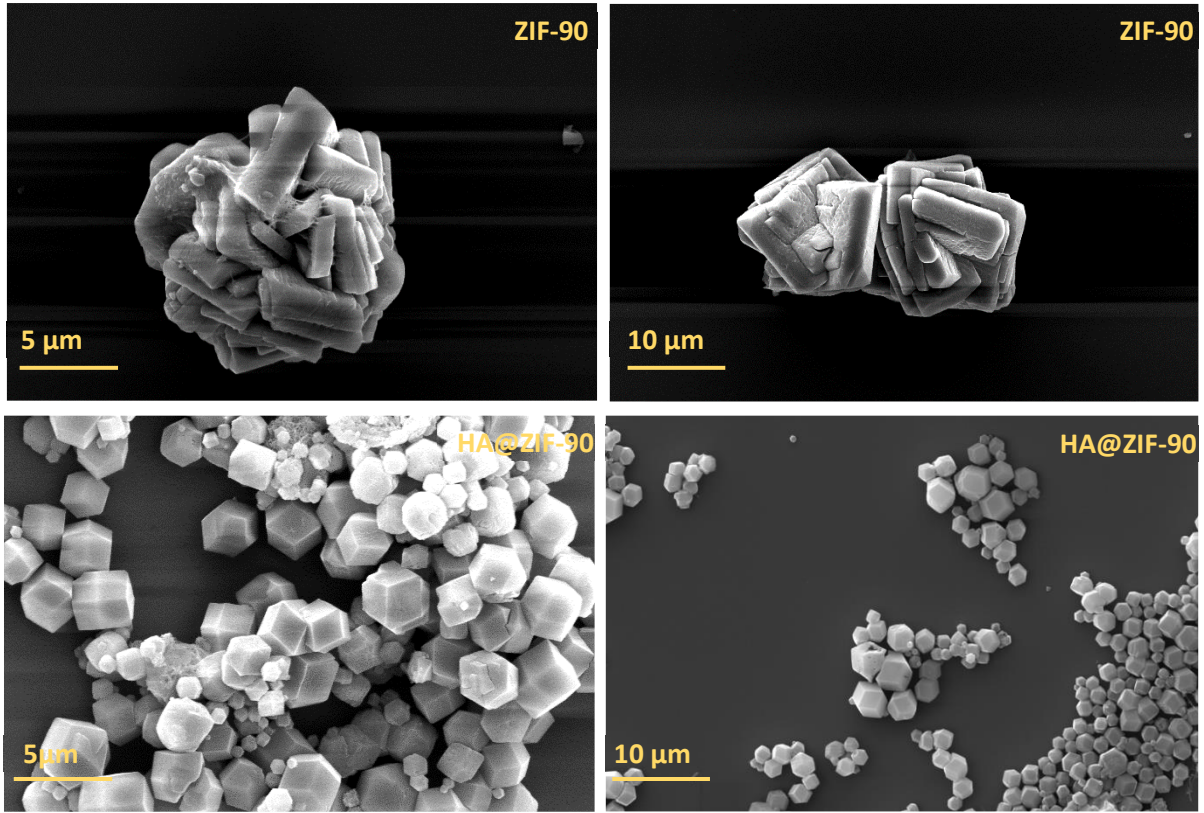


Fig. S10 SEM images of pure ZIF-90 and HA@ZIF-90.

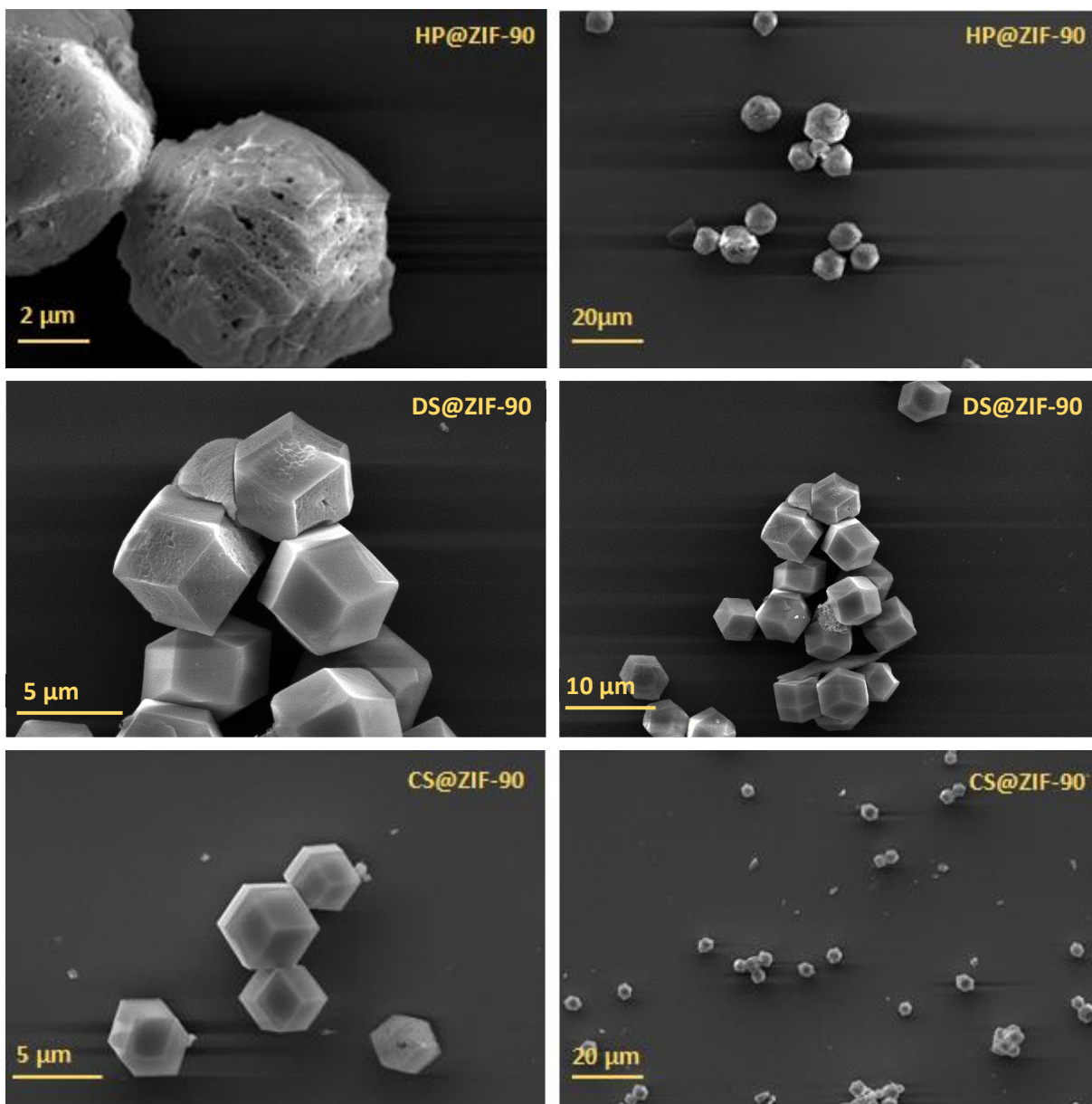


Fig. S11 SEM images for HP@ZIF-90, CS@ZIF-90, and DS@ZIF-90.

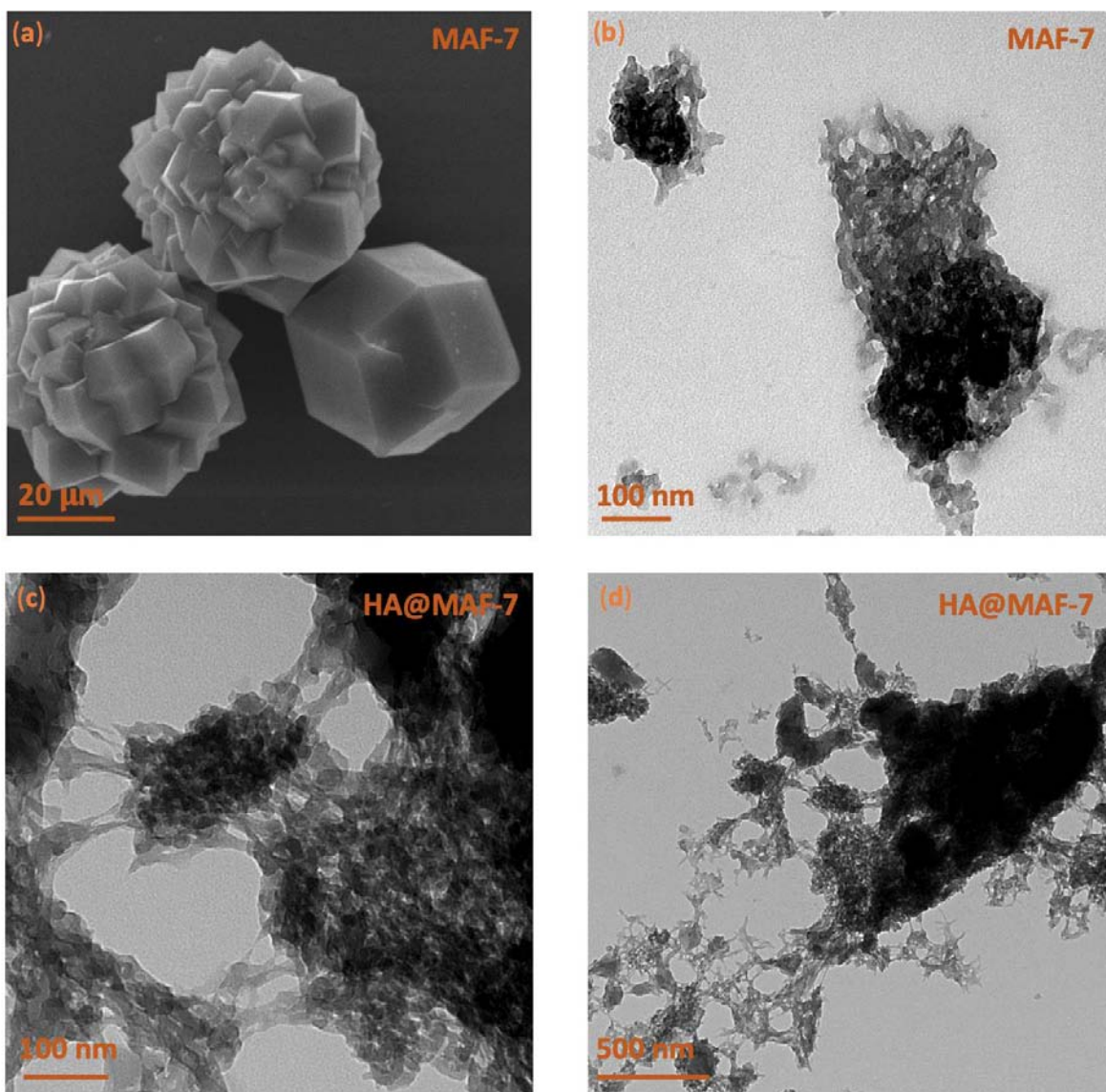


Fig. S12. (a) SEM image of MAF-7 synthesized in presence of $\text{NH}_3 \cdot \text{H}_2\text{O}$ (10 %). (b) TEM image of MAF-7 synthesized without ammonia. (c) and (d) TEM images of HA@MAF-7.

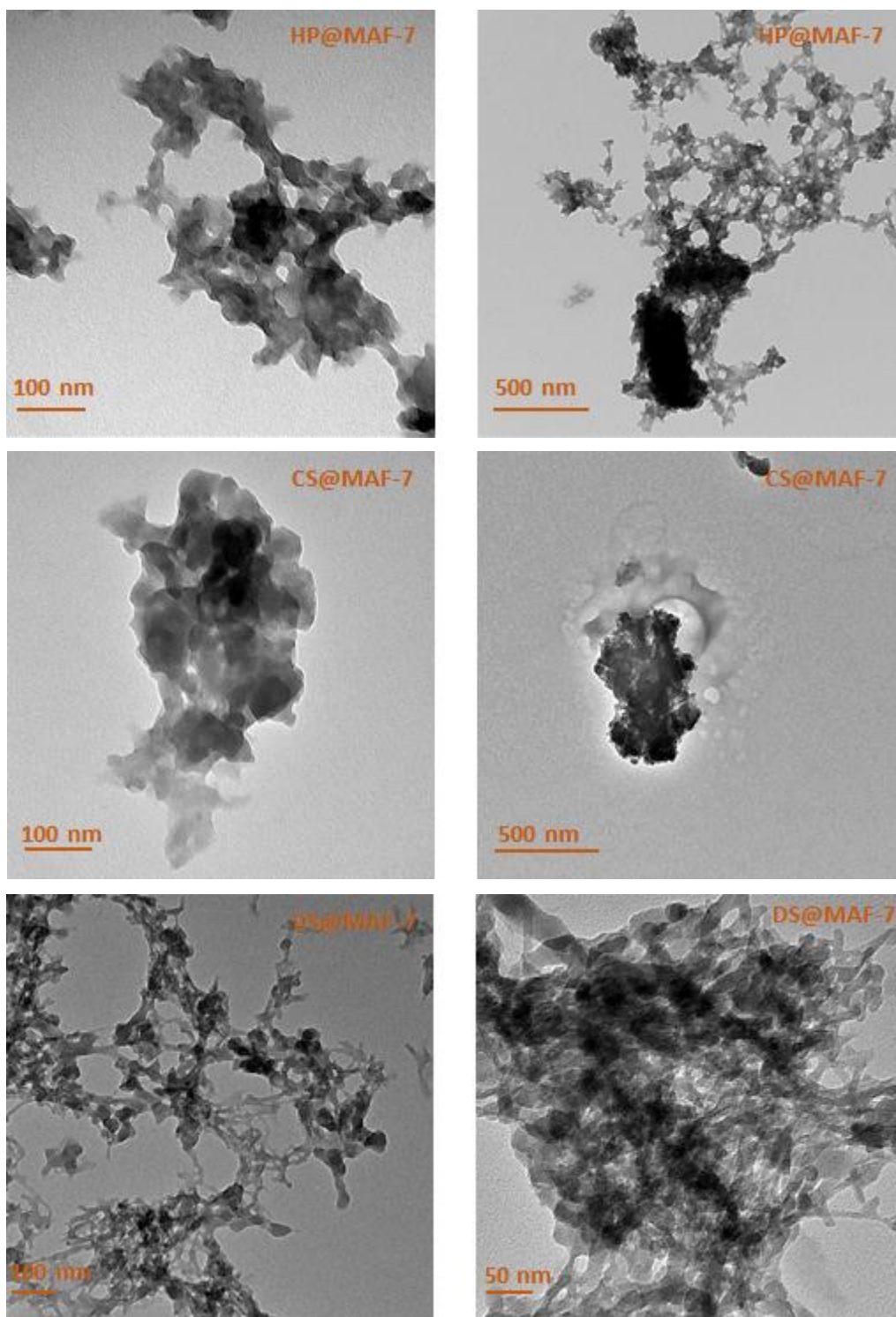


Fig. S13 TEM images for HP@MAF-7, CS@MAF-7, and DS@MAF-7.

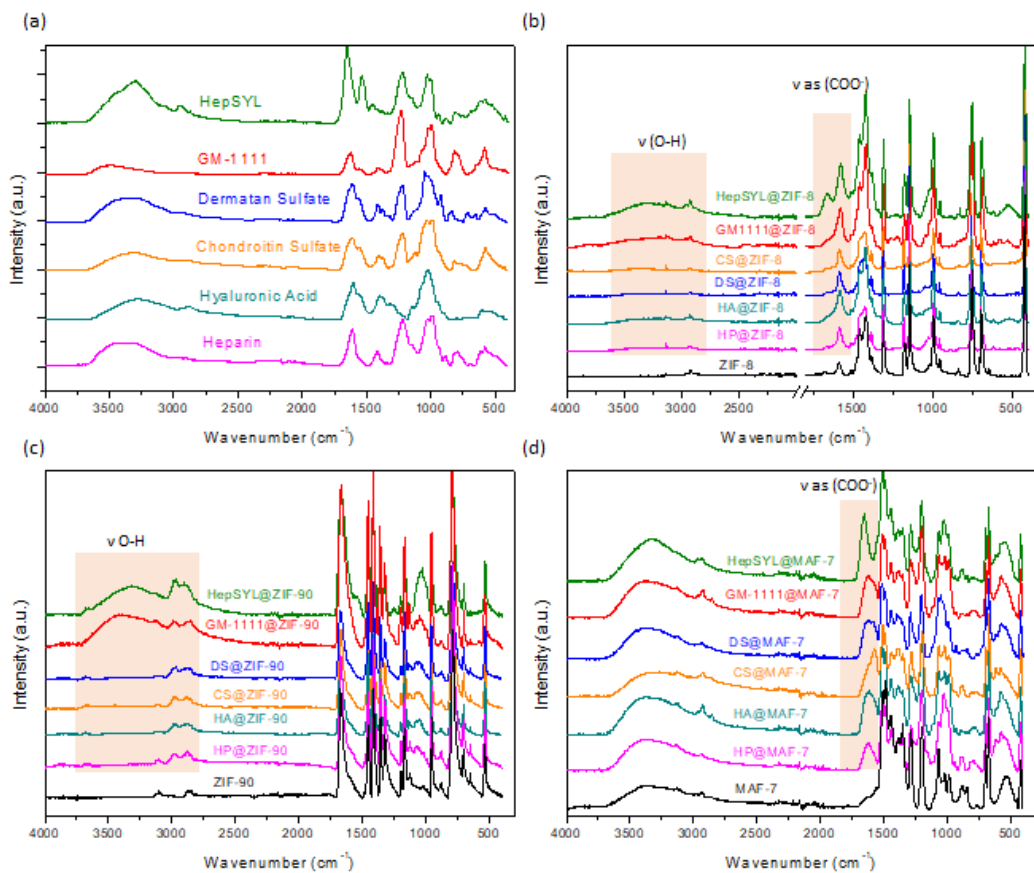


Fig. S14 FTIR spectra of GAGs and GAGs@MOFs (a) FTIR spectra of GAGs. (b) FTIR spectra of GAGs@ZIF-8. (c) FTIR spectra of GAGs@MAF-7 (d) FTIR spectra of GAGs@ZIF-90.

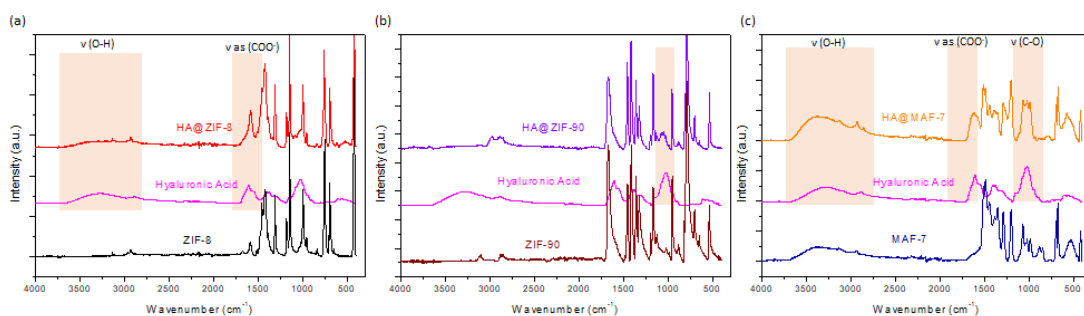


Fig. S15 FTIR spectra of HA@MOFs (a) FTIR spectra of HA@ZIF-8 (b) FTIR spectra HA@ZIF-90 of (c) FTIR spectra HA@MAF-7

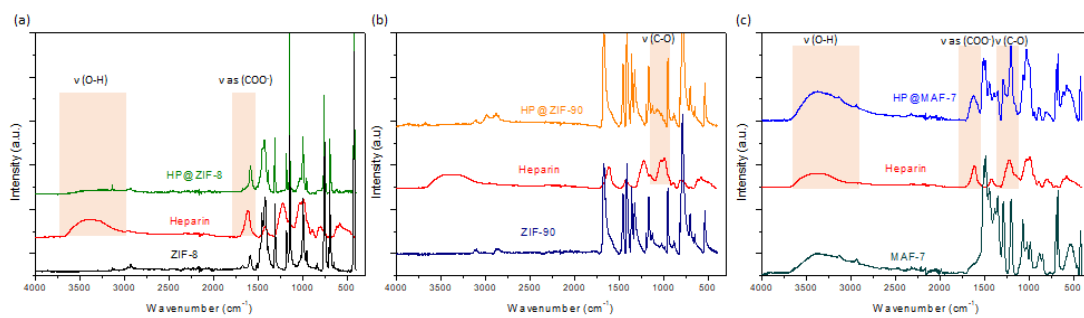


Fig. S16 FTIR spectra of HP@MOFs. (a) FTIR spectra of HP@ZIF-8. (b) FTIR spectra of HP@ZIF-90 (c) FTIR spectra HP@MAF-7.

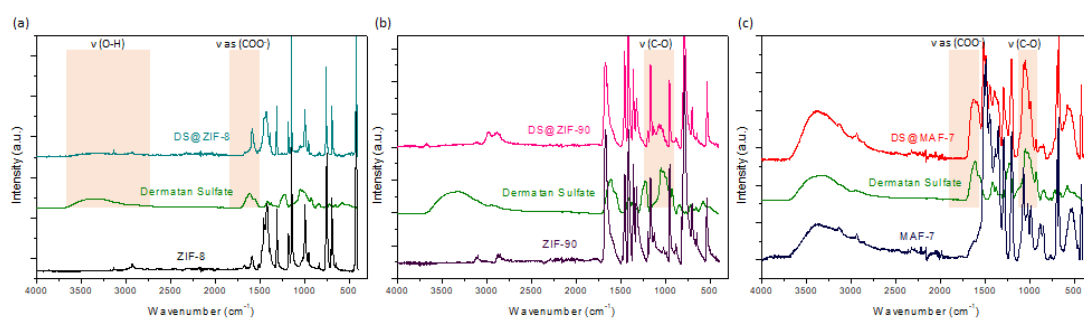


Fig. S17 FTIR spectra of DS@MOFs (a) FTIR spectra of DS@ZIF-8 (b) FTIR spectra of DS@ZIF-90 (c) FTIR spectra DS@MAF-7.

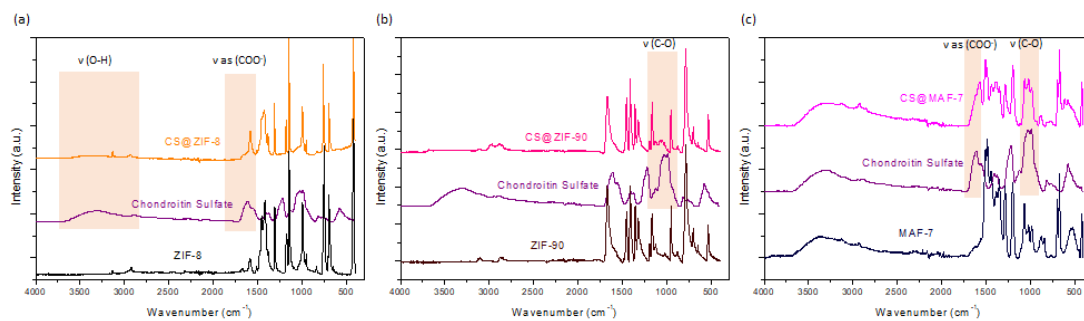


Fig. S18 FTIR spectra of CS@MOFs (a) FTIR spectra of CS@ZIF-8 (b) FTIR spectra of CS@ZIF-90 (c) FTIR spectra CS@MAF-7.

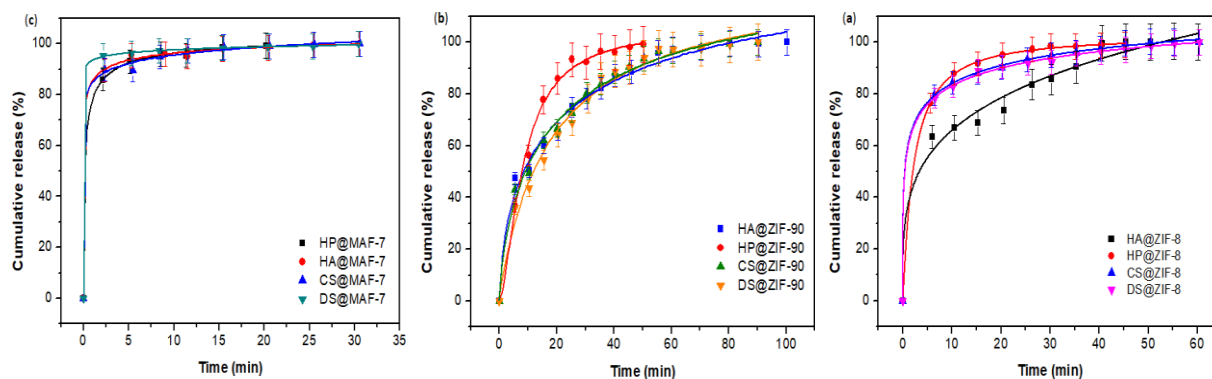


Fig. S19 Drug release kinetics of GAG@MOFs biocomposites. (a) Drug release profile of GAG@MAF-7; (b) Drug release profile of GAG@ZIF-90; (c) Drug release profile of GAG@ZIF-8.

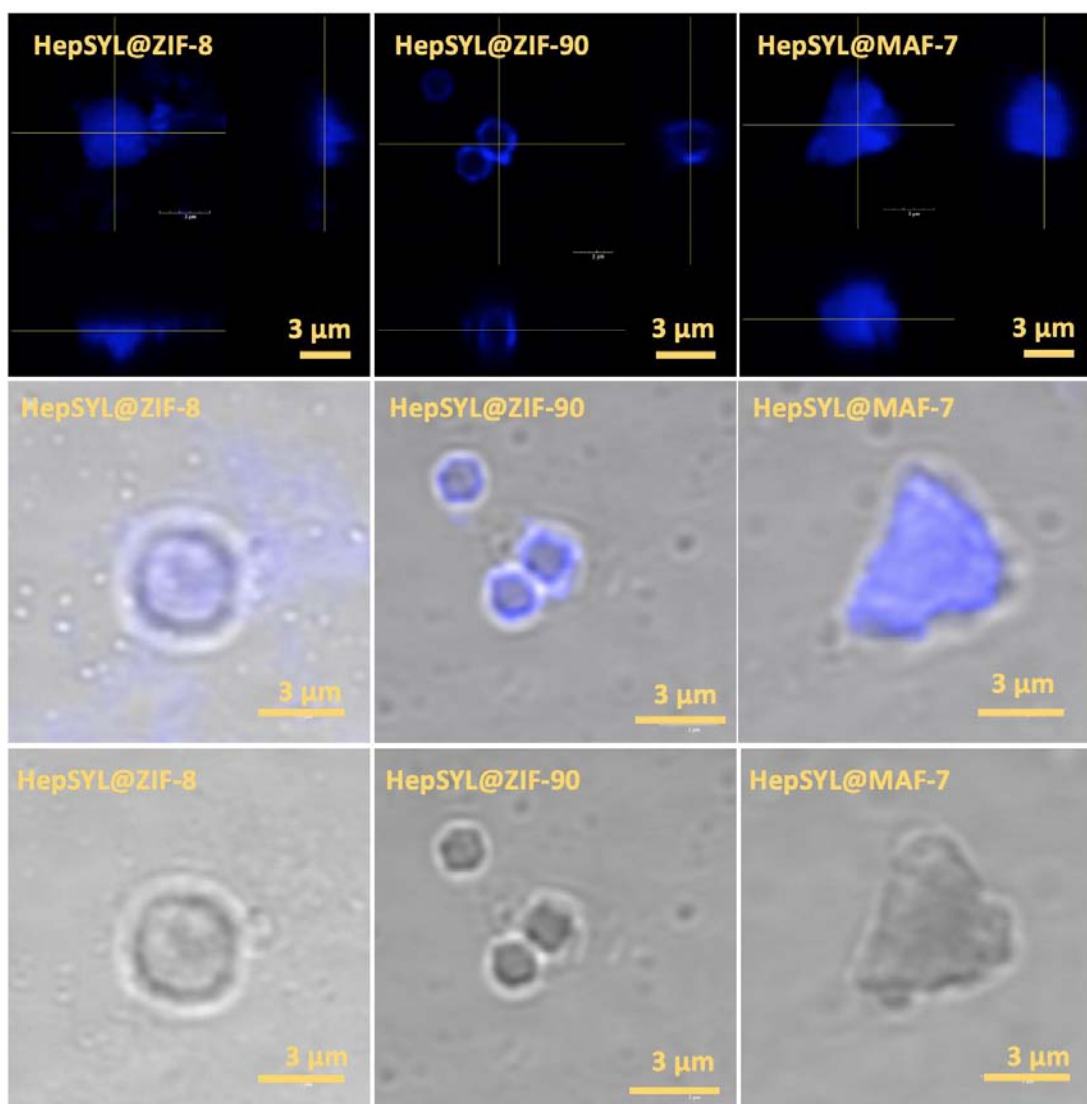


Fig. S20. Confocal laser scanning micrographs showing the fluorescence, overlay and bright field, images of HepSYL@ZIF-8, HepSYL@ZIF-90, and HepSYL@MAF-7.

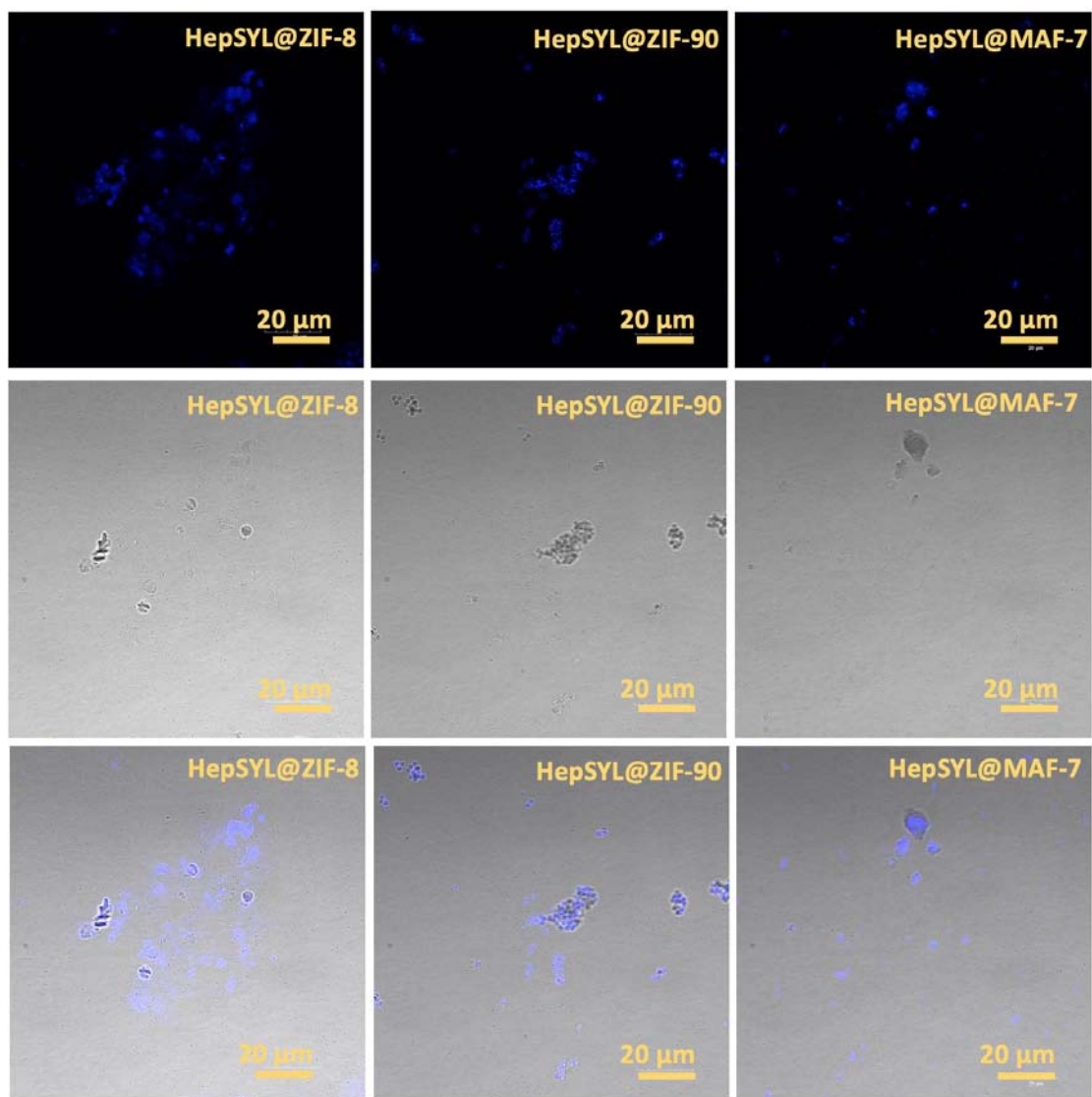


Fig. S21. Confocal laser scanning micrographs taken from the samples HepSYL@ZIF-8, HepSYL@ZIF-90, and HepSYL@MAF-7 showing the fluorescence, bright field and overlay.

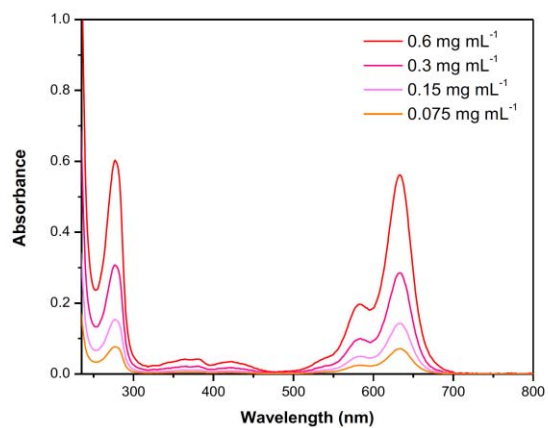


Fig. S22 The UV-Vis absorption spectra of HepSYL.

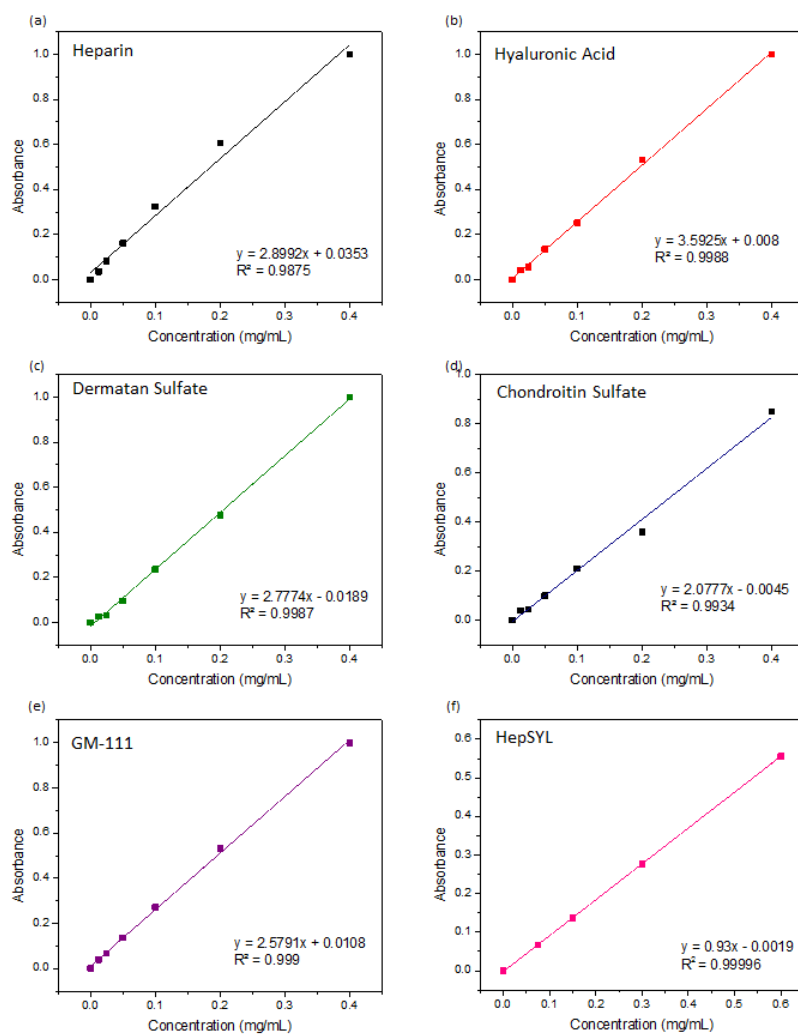


Fig. S23 Calibration curve of GAGs. Calibration curve of Heparin (a) Hyaluronic acid (b) Dermatan sulfate (c) Chondroitin sulfate (d) GM-111 (e) and HepSYL (f).

Stability of 8DXB3, 90DXB3 and 7DXB3 in SDS and water

To prove the stability of FITC-CMD@ZIF-8 (**8DXB3**), FITC-CMD@ZIF-90 (**90DXB3**), and FITC-CMD@MAF-7 (**7DXB3**) biocomposites in water at pH = 7, the MOF biocomposites were incubated in water for 1h, 5h and 24 h. Then, the supernatant was recovered by centrifugation and analyzed by UV-vis to determine the leaching of cargo ($\lambda_{\max} = 490$ nm). Additionally, the concentration of Zn^{2+} released upon 24 h of incubation in water at pH = 7 for was determined by ICP-OES.

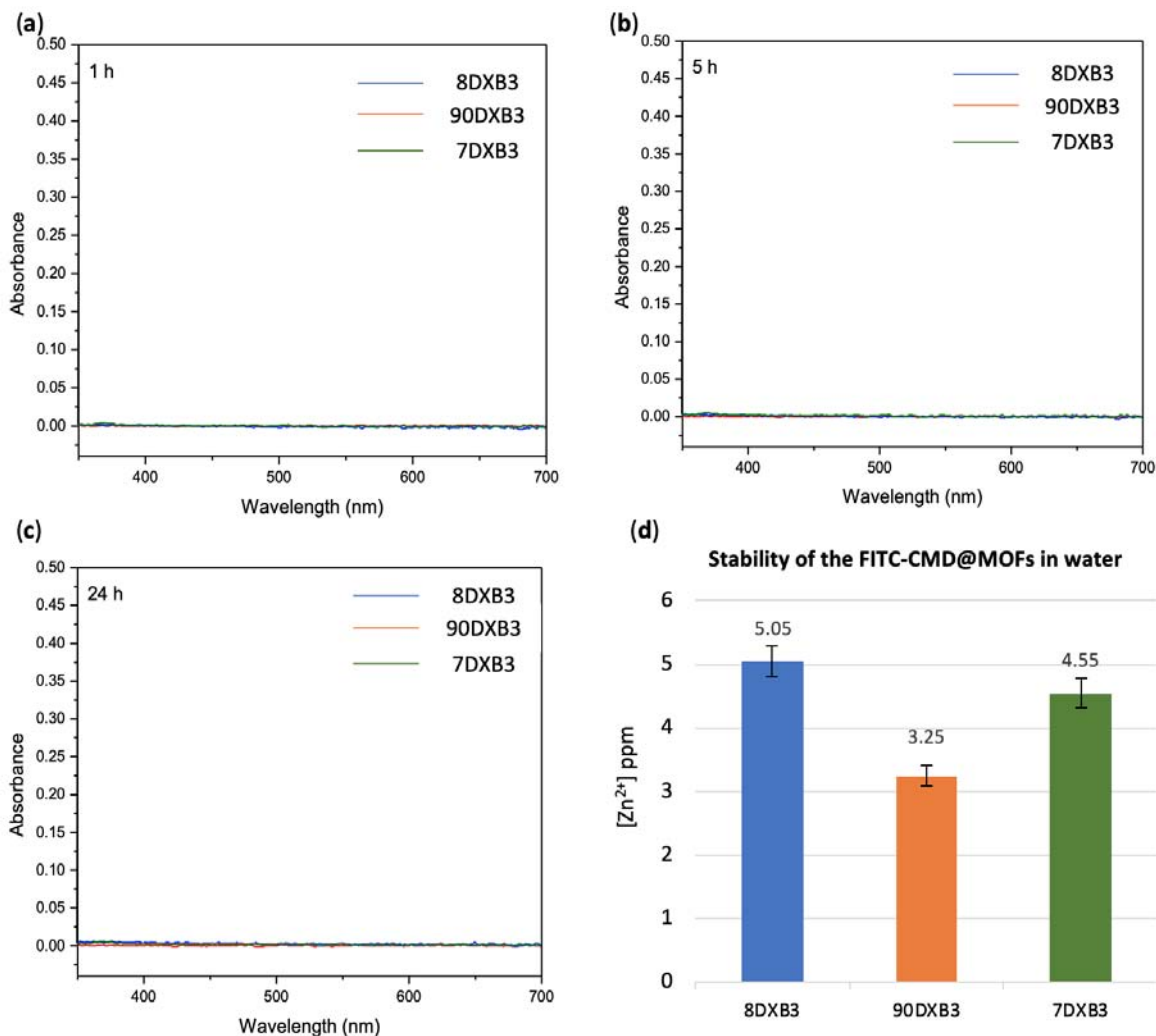


Fig S24. Stability test of FITC-CMD@ZIF-8 (**8DXB3**), FITC-CMD@ZIF-90 (**90DXB3**), and FITC-CMD@MAF-7 (**7DXB3**) biocomposites in water. The FITC-CMD@MOF samples obtained from $[\text{FITC-CMD}] = 0.36 \text{ mg mL}^{-1}$ and $\text{Zn}^{2+}:\text{L} = 1:3.47$ were washed with water and then incubated in DI water (2 mL, pH = 7), the supernatant of was analyzed by UV-vis spectroscopy ($\lambda_{\max} 490$ nm) at different incubation times (a) 1h, (b) 5h, and (c) 24h (d). ICP-OES determination of Zn in the supernatant after the incubation of **8DXB3**, **90DXB3** and **7DXB3** biocomposites in DI water for 24 h that corresponds to a decomposition of 0.37 % (wt) (**8DXB3**), 0.22 % (wt) (**90DXB3**), 0.68 % (wt) (**7DXB3**).

To prove the stability of FITC-CMD@ZIF-8 (**8DXB3**), FITC-CMD@ZIF-90 (**90DXB3**), and FITC-CMD@MAF-7 (**7DXB3**) biocomposites in SDS, the MOF biocomposites were incubated in SDS (2.5%, 5%, and 10%), for 30 min. Then, the supernatant was recovered by centrifugation and analyzed by UV-vis to determine the leaching of cargo ($\lambda_{\max} = 490$ nm). Additionally, the concentration of Zn^{2+} released in the supernatant was determined by ICP-OES.

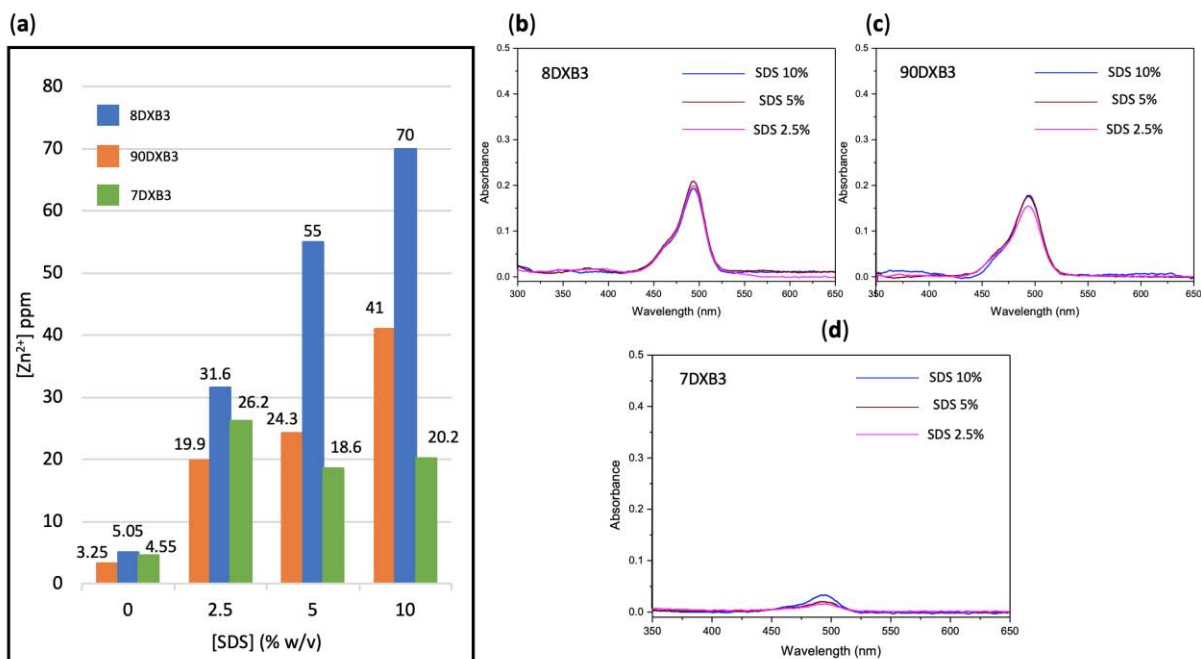


Fig. S25. Stability test of FITC-CMD@MOF biocomposites (**8DXB3**, **90DXB3** and **7DXB3**) in SDS (2.5%, 5%, and 10%). (a) ICP-OES determination of Zn in the supernatant. (b)–(d) UV-vis analysis of the supernatant to prove the release of the cargo FITC.CMD at $\lambda_{\max} = 490$ nm.

Determination of the anticoagulant activity of HP@MOFs

The anticoagulant activity of heparin was assessed by a chromogenic method for anti-IIa assay using a commercial kit (Iduron ANTI-IIA HEPARIN KIT). This assay is a two-step chromogenic method based on the inhibition of an excess of factor IIa in presence of antithrombin (AT).

Step 1: HP + AT \rightarrow [AT-HP]

Step 2: [AT-HP] + IIa_(excess) \rightarrow [AT-HP-IIa]_(inactive) + IIa_(residual)

IIa_(residual) + IIa substrate_(colorless) \rightarrow pNA_(chromophore) ($A_{405\text{ nm}}$) + peptide

The standard solutions were prepared using Heparin sodium salt from porcine intestinal mucosa (>180 USP/mg) purchased from Sigma-Aldrich. ($S_0 = 0$ IU mL⁻¹, $S_1 = 0.1$ IU mL⁻¹, $S_2 = 0.15$ IU mL⁻¹, $S_3 = 0.2$ IU mL⁻¹, $S_4 = 0.25$ IU mL⁻¹, $S_5 = 0.3$ IU mL⁻¹). The HP encapsulated within the MOF shells was released using EDTA solution (40 mM). Then resultant clear solutions were diluted to prepare two test solutions ($T_1 = 0.15$ IU mL⁻¹, $T_2 = 0.30$ IU mL⁻¹) for each biocomposite (HP@ZIF-8, HP@ZIF-90, and HP@MAF-7). The dilution factor for each solution was calculated considering: (i) the amount of HP encapsulated within each biocomposite (this value was determined by the carbazole assay), (ii) the HP activity reported by the manufacturer (> 180 USP mg⁻¹). The standard and test solutions were analyzed following the established assay protocol provided by the manufacturer. The

anticoagulant activity of HP@ZIF-8, HP@ZIF-90, and HP@MAF-7 samples was tested by triplicate. The standard curve was obtained plotting the $\log A_{\lambda_{\max}}$ against [HP] (IU mL⁻¹) the regression line of the standard samples was used to evaluate the relative anticoagulant activity of test samples (Fig. S26a).

Biopreservation experiments

The heparinase I (0.1 IU) was purchased from Iduron, and was supplied as frozen solution. A preliminary experiment was performed in order to determine the time required to complete degradation of the HP used in this work. This kinetic experiment was performed by UV spectroscopy following the formation of uronic acid ($A_{\lambda_{\max}} = 232$ nm) produced during the enzymatic degradation of the HP (Fig. S26c). The experiment was performed at 30 °C in an acetate buffer media (pH = 7, containing sodium acetate 50 mM, and calcium acetate 1mM). The assay was accomplished by mixing 0.8 mL of HP solution (750 $\mu\text{g mL}^{-1}$) with 0.2 mL of heparinase I solution (50 μmL^{-1}). The enzymatic kinetic reveals that after 1h of reaction the inactivation of HP proceeds quantitatively. Then, to evaluate the protection capabilities of the MOF materials, each HP@MOFs biocomposite and the free HP were incubated, separately, in acetate buffer media at 30 °C for 1h in presence of heparinase I. Afterwards, the samples were heated at 100 °C for 5 min to inactivate the enzyme. The biocomposite materials were washed with water (2 mL, 3X) and ethanol (2 mL, 3X), and the encapsulated HP was recovered soaking the HP@MOFs biocomposite in EDTA (40 mM) to degrade the MOF matrix. The resultant solutions were diluted to determine the antithrombotic activity of the released HP, using the chromogenic anti-IIa assay (Fig. S26d).

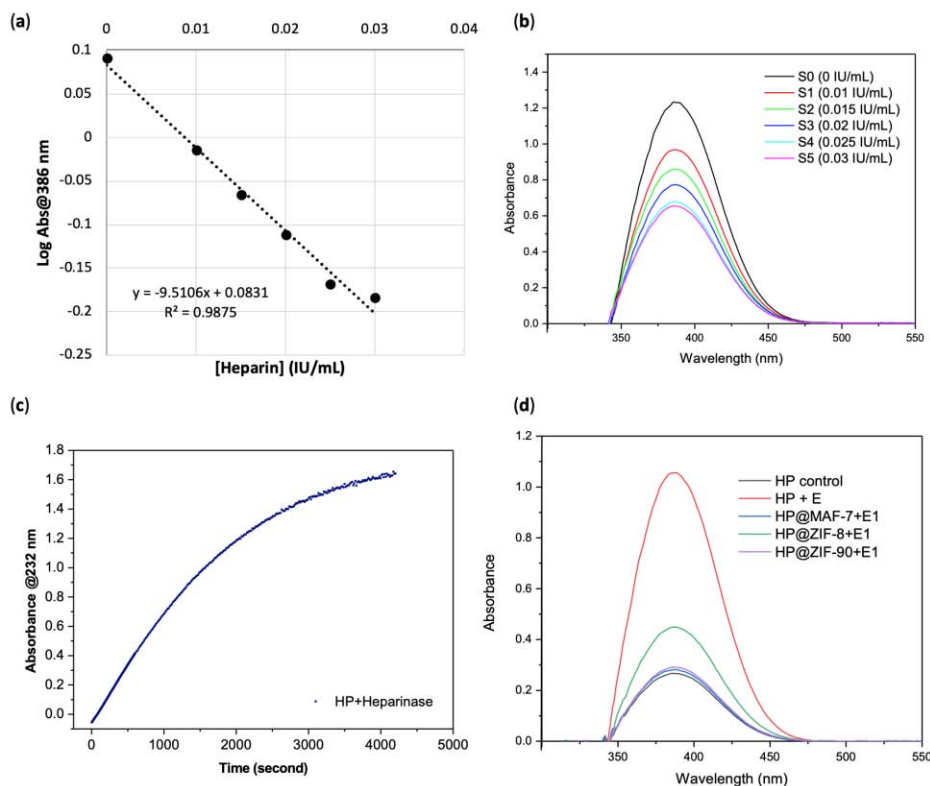


Fig. S26. Chromogenic anti-II assay to determine the anticoagulant activity of HP. (a) calibration curve. (b) Absorbance recorded at 386 nm for standard solutions. (c) Kinetic of the enzymatic degradation of heparin in presence of heparinase I. (d) Absorbance recorded at 386 nm for free HP and encapsulated HP exposed to heparinase I, and the pure HP as a control.

Gas Sorption

Gas adsorption isotherm measurements were performed on an ASAP 2020 Surface Area and Pore Size Analyzer. Samples were activated by heating in vacuum at 100 °C for 3 h under N₂ and 100 °C for 18 h under vacuum (2X10⁻⁶ mm of Hg). UHP grade (99.999%) N₂ and He were used for all measurements. The temperatures were maintained at 77 K (liquid nitrogen bath).

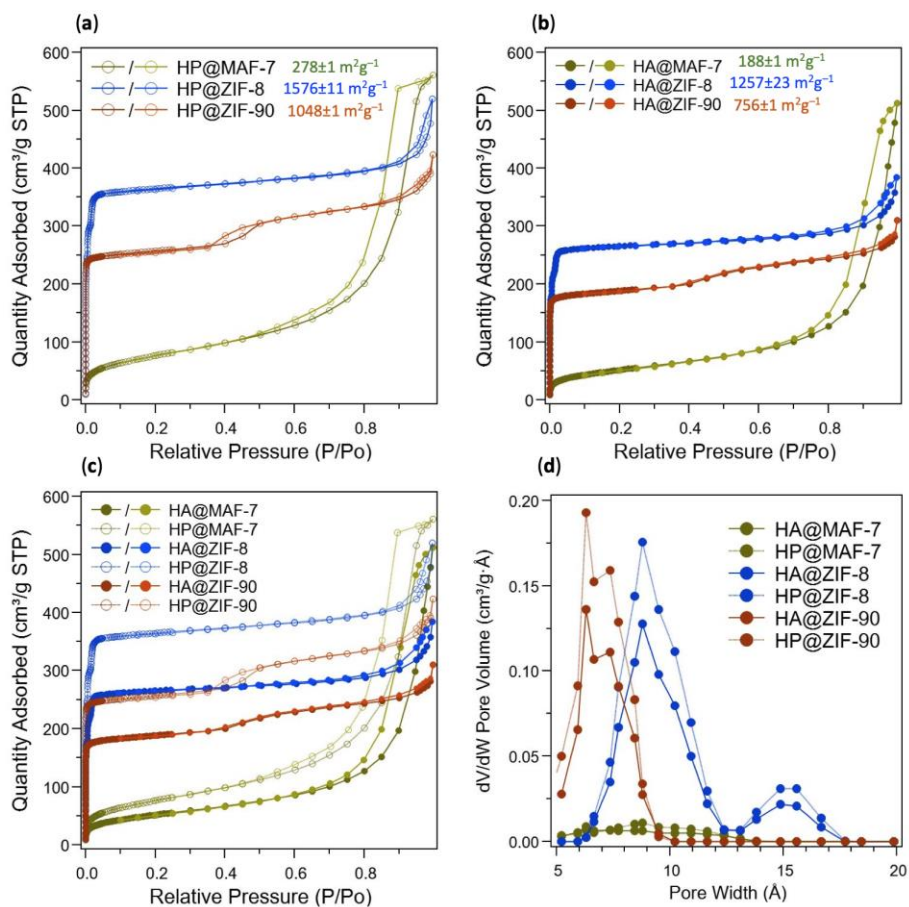


Fig. S27. 77 K N₂ adsorption and desorption isotherms for (a) HP@MOFs and (b) HA@MOFs biocomposites. The calculated BET surface areas for samples are listed in the inset. (c) Comparison of the 77 K N₂ adsorption and desorption isotherms obtained varying the biomolecules (HP and HA), and the MOF shell (ZIF-8, ZIF-90 and MAF-7). (d) Calculated pore size distribution curves for HP@MOFs and HA@MOFs biocomposites.

Sample	Calculated BET surface area (m ² g ⁻¹)
HP@ZIF-8	1576±11
HA@ZIF-8	1257±23
ZIF-8	1437±23
HP@ZIF-90	1048±1
HA@ZIF-90	756±1
ZIF-90	1589±17
HP@MAF-7	278±1
HA@MAF-7	188±1
MAF-7	1435±23

Table S3. Comparison of the calculated BET surface areas for samples HP@MOFs and HA@MOFs with respect to the neat MOFs (*sod*-ZIF-8, *sod*-ZIF-90, and *sod*-MAF-7) prepared under conventional synthetic conditions.

Thermogravimetric analysis (TGA)

TGA data confirmed the estimation made via carbazole assay (Fig. S28). However, the TGA data suggest that GAGs@MOF biocomposites possess a higher amount of zinc cations compared to the pure MOF materials (Fig. S28). This observation may be attributed to the electrostatic interactions between the Zn^{2+} and the negatively charged sulphate and carboxylate groups of the GAGs as reported by Parrish et al.² To confirm this hypothesis, we used energy dispersive X-ray spectroscopy (EDS) to determine the elemental composition of the HP@MOF biocomposites and related control samples (i.e. neat MOFs, and free HP) (Fig. S29, ESI[†]). In all the samples, as shown in plot S29 we observed an excess of Zn associated to the S assigned to sulphate groups. (Fig. S29 and Table S4–S7, ESI[†]). This excess of Zn validates the hypothesis and explain the TGA results.

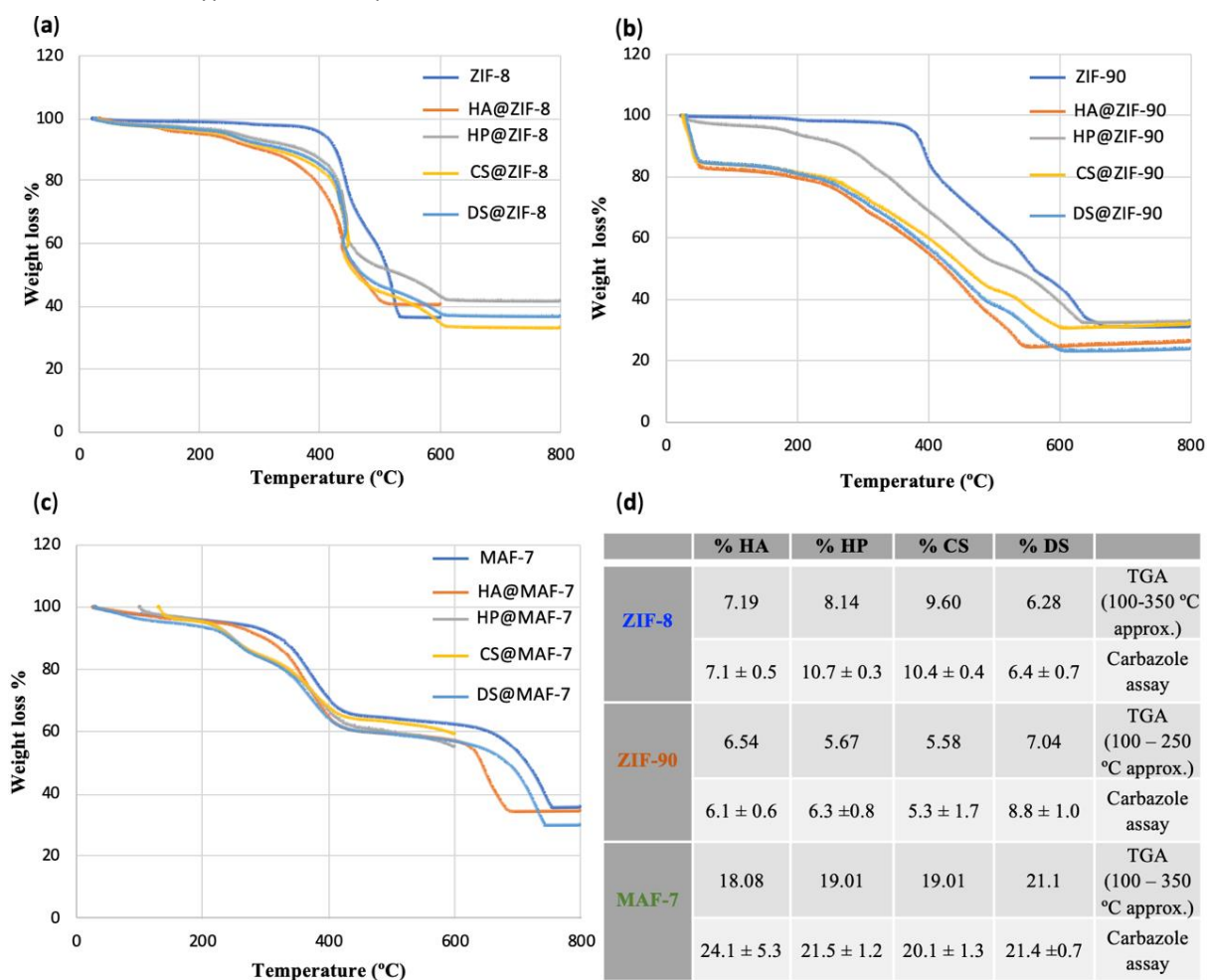


Fig. S28. Thermogravimetric analysis (TGA) of showing the thermal decomposition of (a) neat ZIF-8 and GAG@ZIF-8 biocomposites, (b) neat ZIF-90 and GAG@ZIF-90 biocomposites, (c) neat MAF-7 and GAG@MAF-7 biocomposites. (d) Estimation loading capacity using two different techniques: TGA and carbazole assay (data given in weight % referenced to the 100% of the biocomposite).

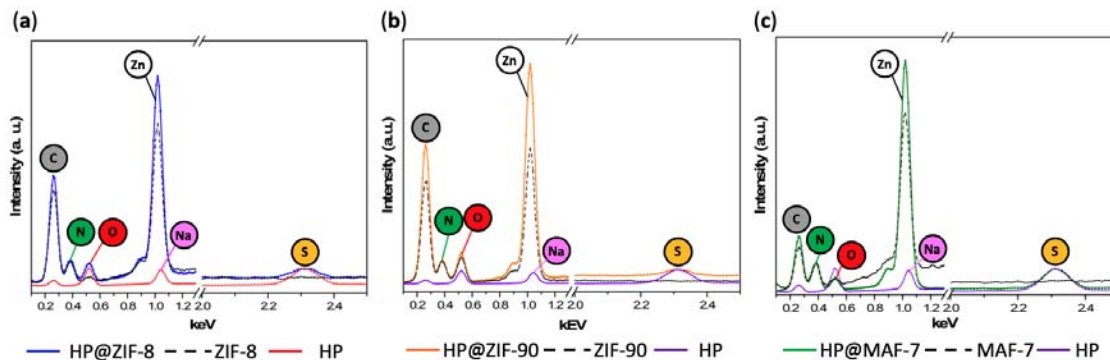


Fig. S29. EDS elemental composition of HP@MOF biocomposites and their corresponding neat MOFs. EDS spectrum of (a) HP@ZIF-8, (b) HP@ZIF-90, and (c) HP@MAF-7 and the elemental contributions of their corresponding constituents pure HP and ZIF-8, ZIF-90 and MAF-7; respectively.

Average(wt%)							
Element (wt%)	HP	HP@MAF-7	MAF-7	HP@ZIF-8	ZIF8	HP@ZIF-90	ZIF-90
C	29.64	30.39	30.01	38.87	40.76	41.73	42.210
O	47.07	10.30	5.24	11.49	3.65	13.20	17.400
Na	11.80	0.00	0.00	0.00	0.00	0.00	0.000
S	11.49	1.98	0.00	0.79	0.00	0.38	0.000
Zn	0.00	19.18	2.72	21.18	21.78	21.72	14.15
N	0.00	36.39	34.18	27.65	33.81	22.96	26.24
Cl	0.00	1.78	2.72	0	0	0	0

Table S4. Elemental composition of HP@MOFs biocomposites and their corresponding neat MOFs obtained from EDS analysis

Contribution to the elemental composition of HP@ZIF-8					
Element	(wt%) from ZIF-8	(wt%) from HP	solvent and other impurities	Excess of Zn ²⁺ (wt%)	HP@ZIF-8 total
C	33.33	2.05	3.49		38.87
O		3.25	8.24		11.49
S		0.79	0.00		0.79
Zn	17.81			3.37	21.18
N	27.65				27.65
TOTAL	78.80	6.09	11.74	3.37	100.00

Table S5. Estimation of the excess of Zn²⁺ in HP@ZIF-8, based on the elemental contribution of neat ZIF-8 and pure HP.

Contribution to the elemental composition of HP@ZIF-90					
Element	(wt%) from ZIF-90	(wt%) from HP	solvent and other impurities	Excess of Zn ²⁺ (wt%)	HP@ZIF-90 total
C	40.75	0.98	3.49		41.73
O	11.65	1.56	8.24		13.21
S		0.38	0.00		0.38
Zn	12.38			9.34	21.72
N	22.96				22.96
TOTAL	87.74	2.92	11.74	9.34	100.00

Table S6. Estimation of the excess of Zn²⁺ in HP@ZIF-90, based on the elemental contribution of neat ZIF-90 and pure HP.

Contribution to the elemental composition of HP@MAF-7					
Element	(wt%) from MAF-7	(wt%) from HP	solvent and other impurities	Excess of Zn ²⁺ (wt%)	HP@MAF-7 total
C	25.28	5.11	0.00		30.39
O		8.11	2.18		10.30
S		1.98	0.00		1.98
Zn	2.89			16.28	19.18
N	36.39				36.39
Cl			1.78		1.78
TOTAL	64.55	15.20	3.96	16.28	100.00

Table S7. Estimation of the excess of Zn²⁺ in HP@MAF-7, based on the elemental contribution of neat MAF-7 and pure HP.

Estimation of the USP units of heparin released form the maximum safe dosage of HP@MOF

Herein, we provide an estimation of the USP units of heparin released form the maximum safe dosage of HP@MOF biocomposites. Based on the cytotoxicity of ZIF-8 (30 mg L^{-1}),³ we can estimate the threshold concentration for ZIF-90 (32 mg L^{-1}), and MAF-7 (30 mg L^{-1}) to ensure the biocompatibility of those materials (IC20) (see Table S8 and Fig S30). Considering the amount of HP encapsulated in 100 mg of biocomposite, we calculated the USP units of HP released from the maximum dose of HP@MOF (Table S8, Fig. S30). According to the current dose regulations for heparin,⁴ MAF-7 seems to be a suitable carrier for intravenous injection of HP. The particle size of this biocomposite is compatible with this administration route.⁵

Sample	%HP Loading Capacity	Maximum dosage of HP@MOF (mg L^{-1})	Maximum dosage of HP@MOF (mg) ^a	USP units of heparin encapsulated in the maximum dosage ^b
HP@ZIF-8	8.14	32.7	163.3	2392.5
HP@ZIF-90	5.67	33.9	169.6	1731.1
HP@MAF-7	19.01	37.0	185.2	6337.4

Table S8. Estimation of USP units of Heparin released from the maximum safe dosage of each HP@MOF biocomposites, ^a Average body weight 70 kg equivalent to blood volume of 5 L, ^b The HP used in this work has 180 USP mg^{-1} .

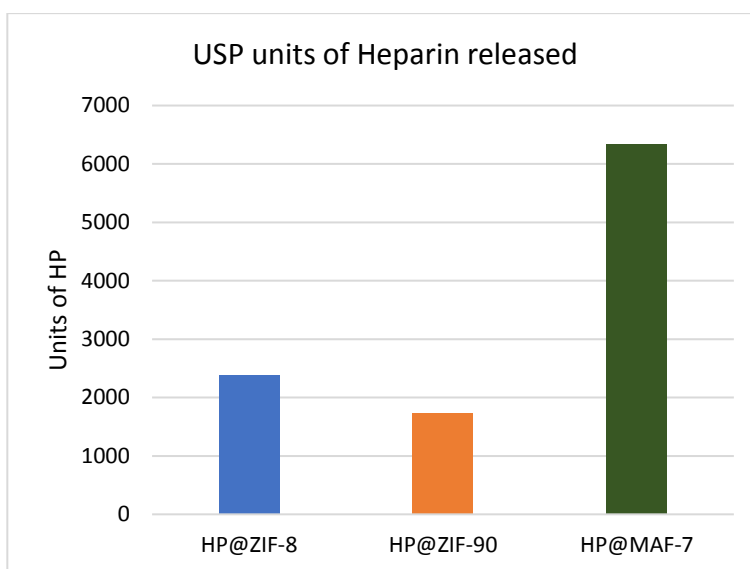


Fig. S30. Estimation of USP units of HP released from HP@MOFs

Type of system	Material	Type of immobilization	EE(%)	Loading capacity (wt%)	Protection properties	Ref
MOFs	This work ZIF-8	Encapsulation	100	8.14	Protection of heparin from Heparinase I enzyme	
	This work ZIF-90	Encapsulation	60	5.67	Protection of heparin from Heparinase I enzyme	
	This work MAF-7	Encapsulation	98	19	Protection of heparin from Heparinase I enzyme	
	MIL-101(Fe)	Adsorption	Not stated	15	Not stated	6
Silica	Mesoporous Silica nanoparticle (MSN)	Encapsulation	Not stated	Not stated	Not stated	7
	Silica Xerogel	Sol-gel	Not stated	13.6	Not stated	8
	ammoniated-hollow mesoporous silica (A-HMS)	Adsorption	Not stated	9	Not stated	9
	ammoniated-magnetic mesoporous silica (A-MMS)	Adsorption	Not stated	1.5	Not stated	9
	(PEDOT/MS/MnO ₂)	Adsorption	Not stated	5.6	Not stated	10
	PEDOT/MS	Adsorption	Not stated	5.8	Not stated	10
	PEDOT/MNO ₂	Adsorption	Not stated	0.6	Not stated	10
Polymer	Eudragit RS (RS)	Encapsulation	59	6.57	Not stated	11
	PLGA	Encapsulation	14	1.6	Not stated	11
	Poly caprolactone	Encapsulation	8	0.9	Not stated	11
	Eudragit RL (RL)	Encapsulation	97	10.8	Not stated	11
	RL/PCL	Encapsulation	53	5.9	Not stated	11
	RS/RL/PLGA	Encapsulation	38	4.2	Not stated	11
	RS/PLGA	Encapsulation	36	3.9	Not stated	11
	N-trimethyl chitosan (TCM)	Ionotropic gelation	71.9	Not stated	Protection of heparin from gastrointestinal tract pH gastric fluid (SGF, pH 1.2) and simulated intestinal fluid (SIF, pH 7.4)	12
	Chitosan (CS)	Ionotropic gelation	72.6	Not stated	Protection of heparin from SGF, pH (1.2) and SIF (pH 7.4) (lower than TCM)	12
	PMMA-b-PMAETMA	Encapsulation	98	16.4	Not stated	13
	PHB-HV/PEG	Encapsulation	59	Not stated	Not stated	14
	PCL	Encapsulation	Not stated	0.5	Not stated	15
	PCL- α -TCP	Encapsulation	Not stated	2	Not stated	16
	PLGA	Encapsulation	14.9	Not stated	Not stated	17
	RS	Encapsulation	98.1	Not stated	Not stated	18
	RS/PLGA	Encapsulation	96.9	Not stated	Not stated	18
	PLGA	Encapsulation	38.6	Not stated	Not stated	18
	PLLA-PEG-PLLA	Encapsulation	15.8	0.52	Not stated	19
	EDC/NHS-crosslinked collagen	Grafting	Not stated	5.5	Not stated	20
	Thermosensitive hydrogel (TSH)	Absorption	Not stated	15.3	Not stated	21
	Thiolated Chitosan (TCS)	Grafting	97.91	15.14	Protection of heparin from stomach acid and digestive enzyme degradation (pepsin)	22
	PLGA:E-RLPO	Encapsulation	92.1	Not stated	Not stated	23
	RL	Encapsulation	80	8.87	Not stated	24
RS/gelatin A	Encapsulation	67	7.4	Not stated	24	
PLGA/Gelatin A	Encapsulation	58	6.5	Not stated	24	
PCL/Gelatin A	Encapsulation	58	6.4	Not stated	24	
others	Liposomes	Encapsulation	48.3	Not stated	Protection of heparin from Temperature (40 °C)*	25
	Thrombin-responsive polymer	Grafting	Not stated	Not stated	Not stated	26
	Erythrocytes	Encapsulation	44	Not stated	Not stated	27

Table S9. Comparative overview of the properties reported for other drug delivery systems designed for heparin release. MS= mesoporous silica, CL=cargo loading, PEDOT = poly(3,4-ethylenedioxythiophene), PLGA = poly(lactic-co-glycolic acid), PMMA-b-PMAETMA = poly(methyl methacrylate-b-trimethyl aminoethyl methacrylate), PHB = polyhydroxybutyrate-co-hydroxyvalerate, PEG = polyethylene glycol, PCL = poly(ϵ -caprolactone), TCP = tricalcium phosphate, PLLA = poly(L-lactic acid). When needed, we used the efficacy of our heparin (180 USP/mg) for the calculation of the lading capacity.

*from Aldrich, our Heparin can be treated at 120 °C

References

- 1 E. Atria, M. Thonhofer, R. Ricco, W. Liang, A. Chemelli, A. Tarzia, K. Alt, C. E. Hagemeyer, J. Rattenberger, H. Schroettner, T. Wrodnigg, H. Amenitsch, D. M. Huang, C. J. Doonan and P. Falcaro, *Materials Horizons*, 2019, **6**, 969–977.
- 2 R. F. Parrish and W. R. Fair, *Biochem. J.*, 1981, **193**, 407–410.
- 3 M. Hoop, C. F. Walde, R. Riccò, F. Mushtaq, A. Terzopoulou, X.-Z. Chen, A. J. deMello, C. J. Doonan, P. Falcaro, B. J. Nelson, J. Puigmartí-Luis and S. Pané, *Applied Materials Today*, 2018, **11**, 13–21.
- 4 M. A. Smythe, J. Priziola, P. P. Dobesh, D. Wirth, A. Cuker and A. K. Wittkowsky, *J Thromb Thrombolysis*, 2016, **41**, 165–186.
- 5 T. Simon-Yarza, A. Mielcarek, P. Couvreur and C. Serre, *Adv. Mater.*, 2018, **30**, 1707365.
- 6 V. V. Vinogradov, A. S. Drozdov, L. R. Mingabudinova, E. M. Shabanova, N. O. Kolchina, E. I. Anastasova, A. A. Markova, A. A. Shtil, V. A. Milichko, G. L. Starova, R. L. M. Precker, A. V. Vinogradov, E. Hey-Hawkins and E. A. Pidko, *J. Mater. Chem. B*, 2018, **6**, 2450–2459.
- 7 F. Wu, T. Xu, G. Zhao, S. Meng, M. Wan, B. Chi, C. Mao and J. Shen, *Langmuir*, 2017, **33**, 5245–5252.
- 8 M. S. Ahola, E. S. Säilynoja, M. H. Raitavuo, M. M. Vaahtio, J. I. Salonen and A. U. O. Yli-Urpo, *Biomaterials*, 2001, **22**, 2163–2170.
- 9 S. Hu, S. Shao, H. Chen, J. Sun, J. Zhai, H. Zheng, M. Wan, Y. Liu, C. Mao and J. Zhao, *J. Phys. Chem. C*, 2018, **122**, 9680–9687.
- 10 Q. Wang, Y. Wang, B. Guo, S. Shao, Y. Yu, X. Zhu, M. Wan, B. Zhao, C. Bo and C. Mao, *J. Mater. Chem. B*, 2019, **7**, 2688–2695.
- 11 Y. Jiao, N. Ubrich, M. Marchand-Arvier, C. Vigneron, M. Hoffman, T. Lecompte and P. Maincent, *Circulation*, 2002, **105**, 230–235.
- 12 R. Paliwal, S. R. Paliwal, G. P. Agrawal and S. P. Vyas, *International Journal of Pharmaceutics*, 2012, **422**, 179–184.
- 13 F. Reyes-Ortega, G. Rodríguez, M. R. Aguilar, M. Lord, J. Whitelock, M. H. Stenzel and J. San Román, *J. Mater. Chem. B*, 2013, **1**, 850–860.
- 14 A. Monnier, C. Rombouts, D. Kouider, I. About, H. Fessi and N. Sheibat-Othman, *International Journal of Pharmaceutics*, 2016, **513**, 49–61.
- 15 E. Luong-Van, L. Grøndahl, K. N. Chua, K. W. Leong, V. Nurcombe and S. M. Cool, *Biomaterials*, 2006, **27**, 2042–2050.
- 16 M. Alehosseini, N. Golafshan, M. Kharaziha, M. Fathi and H. Edris, *Macromol. Biosci.*, 2018, **18**, 1800020.
- 17 Lee, Byong Taek, *Bulletin of the Korean Chemical Society*, 2011, **32**, 1465–1470.
- 18 A. Lamprecht, P. Koenig, N. Ubrich, P. Maincent and D. Neumann, *Nanotechnology*, 2006, **17**, 3673–3680.
- 19 X. Luo, D. Qiu, B. He, L. Wang and J. Luo, *Macromol. Biosci.*, 2006, **6**, 373–381.
- 20 M. J. B. Wissink, R. Beernink, J. S. Pieper, A. A. Poot, G. H. M. Engbers, T. Beugeling, W. G. van Aken and J. Feijen, *Biomaterials*, 2001, **22**, 151–163.
- 21 A. Gutowska, Y. H. Bae, J. Feijen and S. W. Kim, *Journal of Controlled Release*, 1992, **22**, 95–104.
- 22 B. Fan, Y. Xing, Y. Zheng, C. Sun and G. Liang, *Drug Delivery*, 2016, **23**, 238–247.

- 23V. Ganti, A. Mengesha, J. Marszalek and B.-B. Youan, *Acta Pharmaceutica*, 2010, **60**, 281–293.
- 24Y. Jiao, N. Ubrich, V. Hoffart, M. Marchand-Arvier, C. Vigneron, M. Hoffman and P. Maincent, *Journal of Pharmaceutical Sciences*, 2002, **91**, 760–768.
- 25K. Vaghasiya, A. Sharma, K. Kumar, E. Ray, S. Adlakha, O. P. Katare, S. K. Hota and R. K. Verma, *ACS Biomater. Sci. Eng.*, 2019, **5**, 6617–6631.
- 26Y. Zhang, J. Yu, J. Wang, N. J. Hanne, Z. Cui, C. Qian, C. Wang, H. Xin, J. H. Cole, C. M. Gallippi, Y. Zhu and Z. Gu, *Adv. Mater.*, 2017, **29**, 1604043.
- 27H. G. Eichler, W. Schneider, G. Raberger, S. Bacher and I. Pabinger, *Res. Exp. Med.*, 1986, **186**, 407–412.

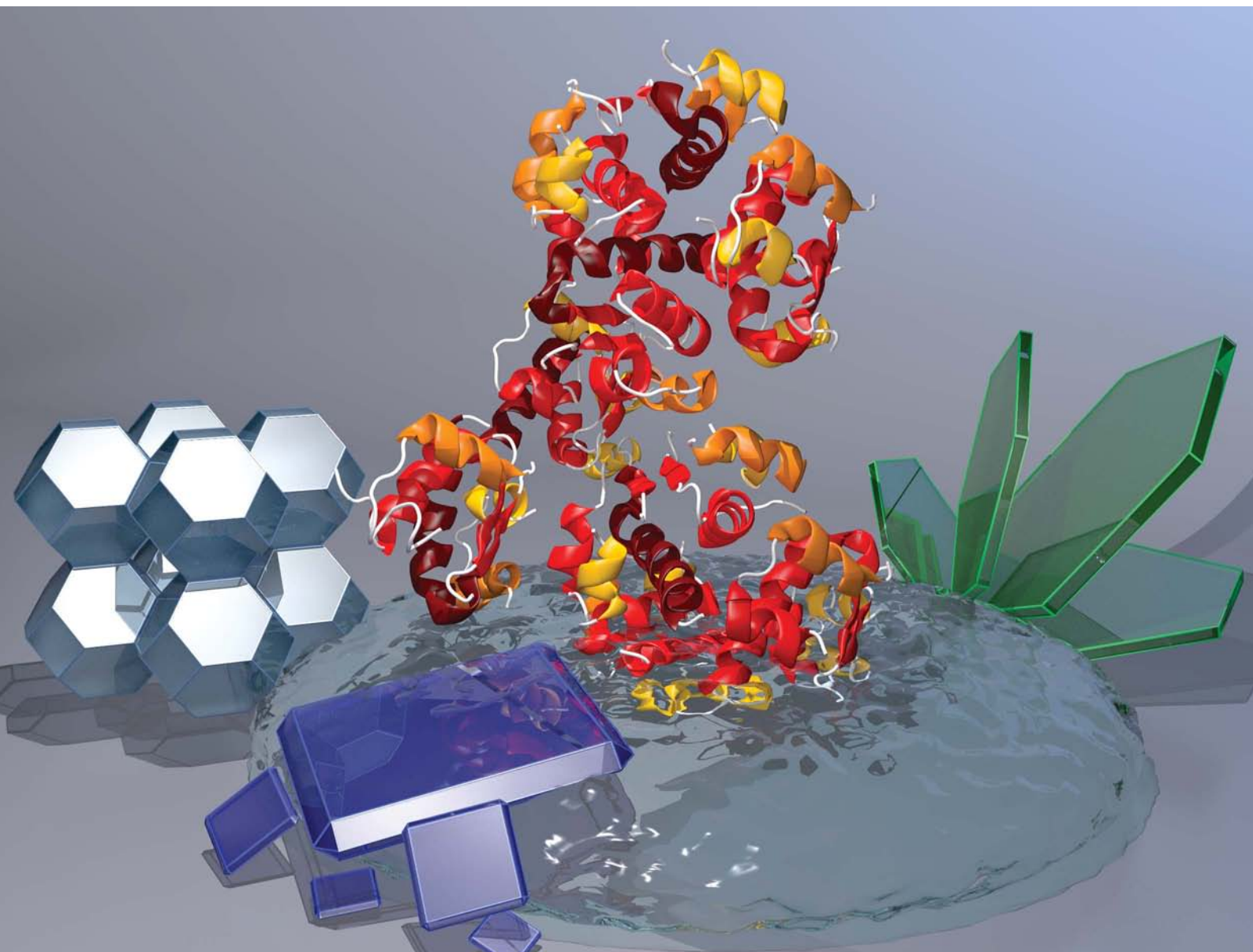
2.3 Phase dependent encapsulation and release profile of ZIF-based biocomposites

The popular crystalline phase for $\text{Zn}(\text{mIM})_2$ MOF is ZIF-8 with sodalite (*sod*) topology.^[36,41,171,172] However, recent studies have disclosed the controlled formation of other crystalline phases including diamondoid (*dia*), katsenite (*kat*), and ZIF-L.^[173–177] These topologies can be obtained simply by varying the concentration of the ZIF precursors (zinc acetate and HmIM).^[173–177] Similarly, different crystalline phases of ZIF-based biocomposites can be obtained by varying the reaction conditions.^[19,88] This motivated us to study in-depth the different phases of MOF-based biocomposites. We used bovine serum albumin (BSA), an inexpensive model molecule that has been widely used as a standard for investigating ZIFs-based biocomposites. Experimentally, we systematically varied the concentration of the main constituents (metal ion, ligand, and biomolecule) of BSA@MOF composite. Then we studied the post-synthetic washing treatments (washes with water or water & ethanol). We assessed both the encapsulation efficiency (EE) and release profile of BSA from BSA@ZIF particles. Finally, in this study, we investigated the encapsulation of insulin which is a clinical therapeutic for the treatment of diabetes. Insulin@ZIF biocomposites were successfully prepared and their properties including EE and release profile were examined.

Chemical Science

Volume 11
Number 13
7 April 2020
Pages 3381–3576

rsc.li/chemical-science



ISSN 2041-6539

EDGE ARTICLE

C. Doonan, P. Falcaro *et al.*
Phase dependent encapsulation and release profile
of ZIF-based biocomposites

Cite this: *Chem. Sci.*, 2020, **11**, 3397

All publication charges for this article have been paid for by the Royal Society of Chemistry

Phase dependent encapsulation and release profile of ZIF-based biocomposites†

F. Carraro,^a M. de J. Velásquez-Hernández,^a E. Astria,^a W. Liang,^b L. Twight,^a C. Parise,^{acd} M. Ge,^e Z. Huang,^{de} R. Ricco,^{da} X. Zou,^{de} L. Villanova,^f C. O. Kappe,^c C. Doonan^{ab*} and P. Falcaro^{ab*}

Biocomposites composed of Zeolitic Imidazolate Frameworks (ZIFs) are generating significant interest due to their facile synthesis, and capacity to protect proteins from harsh environments. Here we systematically varied the composition (*i.e.* relative amounts of ligand (2-methylimidazole), metal precursor (Zn(OAc)₂·2H₂O), and protein) and post synthetic treatments (*i.e.* washes with water or water/ethanol) to prepare a series of protein@ZIF biocomposites. These data were used to construct two ternary phase diagrams that showed the synthesis conditions employed gave rise to five different phases including, for the first time, biocomposites based on ZIF-CO₃-1. We examined the influence of the different phases on two properties relevant to drug delivery applications: encapsulation efficiency and release profile. The encapsulation efficiencies of bovine serum albumin and insulin were phase dependent and ranged from 75% to 100%. In addition, release profiles showed that 100% protein release varied between 40 and 300 minutes depending on the phase. This study provides a detailed compositional map for the targeted preparation of ZIF-based biocomposites of specific phases and a tool for the straightforward analysis of the crystalline phases of ZIF based materials (web application named “ZIF phase analysis”). These data will facilitate the progress of ZIF bio-composites in the fields of biomedicine and biotechnology.

Received 28th October 2019
Accepted 13th February 2020

DOI: 10.1039/c9sc05433b

rsc.li/chemical-science

Introduction

Metal–Organic Frameworks (MOFs) are a class of extended materials synthesized *via* a modular approach from inorganic (metal clusters or ions) and organic components that typically possess high surface areas and pore volumes.¹ By carefully selecting the framework building units and reaction conditions, the chemistry, porosity and particle size of MOFs can be precisely controlled. These properties have attracted researchers to explore MOFs, and their composites, for a variety of applications including biomedicine.² For example, MOF particles have shown unprecedented properties for the uptake

and release of synthetic drugs,^{3,4} and more recently have been integrated with fragile biotherapeutics^{5,6} to improve their stability.^{7,8}

Recently, Zeolitic Imidazolate Frameworks (ZIFs)^{9,10} were used to encapsulate biomacromolecules and to form bio-active composites.^{11–16} The most explored ZIF material for the encapsulation of bioentities is ZIF-8 which is composed of Zn²⁺ cations and 2-methylimidazole (HmIM). ZIF-8-based biocomposites form spontaneously in water around negatively charged biomacromolecules without any additives.¹⁷ This specific process has been termed *biomimetic mineralization* due to its broad similarities to naturally occurring biomineralization.^{11,18,19} The ZIF matrix has been shown to protect fragile biomacromolecules and assemblies thereof (*e.g.* viruses and living cells) from conditions that typically lead to loss of their activity and also act as a vector for *in vitro* and *in vivo* delivery.^{11,12,15,19–23} With respect to drug delivery applications, the biomimetic mineralization approach yields high encapsulation efficiencies (EE%) for biomacromolecules, typically ranging from 80% to 100%.^{11,18,21} In general, high EE% values are relevant to drug delivery applications as the therapeutic is the valuable component of the composite.¹⁸ Release of the biomolecules is achieved *via* decomposition of the ZIF-8 matrix at pH values < 6.5, in the presence of chelating agents (*e.g.* ethylenediaminetetraacetic acid, EDTA), or in specific buffer solutions (*e.g.* phosphate-buffered saline, PBS).^{18,24,25}

^aInstitute of Physical and Theoretical Chemistry, Graz University of Technology, Stremayrgasse 9, Graz 8010, Austria. E-mail: paolo.falcaro@tugraz.at

^bDepartment of Chemistry and the Centre for Advanced Nanomaterials, The University of Adelaide, Adelaide, South Australia 5005, Australia

^cInstitute of Chemistry, University of Graz, NAWI Graz, Heinrichstrasse 28, 8010 Graz, Austria

^dDipartimento di Chimica Industriale “Toso Montanari”, Università di Bologna, Viale del Risorgimento 4, Bologna, Italy

^eDepartment of Materials and Environmental Chemistry, Stockholm University, 106 91 Stockholm, Sweden

^fFaculty of Technical Chemistry, Chemical and Process Engineering, Biotechnology, Graz University of Technology, Petersgasse 10-12, 8010 Graz, Austria

† Electronic supplementary information (ESI) available: Experimental section, Tables S1–S6, Fig. S1–S9, The “ZIF phase analysis” application description. See DOI: 10.1039/c9sc05433b



ZIF-8 is a crystalline microporous material with sodalite (*sod*) topology that is synthesized by mixing aqueous solutions of HmIM and Zn^{2+} .^{26–28} However, by varying the synthetic conditions, other topologies can be obtained (e.g. diamondoid (*dia*), katsenite (*kat*), ZIF-L).^{29–33} Similarly, for ZIF-based biocomposites, a variety of topologies can be accessed by modulating the reaction conditions.^{19,34} In these studies, a fixed amount of biomacromolecule was employed while the concentrations of the ZIF components were varied. Thus, the network topology was controlled by the relative amount of ligand and cation. In a subsequent study we observed that increasing the biomolecule concentration (i.e. carbohydrates) and maintaining a fixed HmIM: Zn^{2+} ratio also led to a change in topology from *dia* to *sod*.¹⁸

This was most likely due to the dependence of sugar concentration on the pH of the reaction solution as the final solid ZIF product did not contain any carbohydrate. In addition to varying the relative concentration of the ZIF components and biomacromolecules, we have also found that post synthesis treatments (e.g. washing procedure) can trigger phase transitions.^{18,34}

Though the various ZIF topologies share the same chemical connectivity, they can exhibit vastly different physical and chemical properties. For example, ZIF (*sod*) has an accessible porosity of ca. $1800 \text{ m}^2 \text{ g}^{-1}$,²⁸ while ZIF (*dia*) is non porous to N_2 .³² In addition, each topology possesses a distinct density and surface chemistry which influences their chemical stability.^{35,36} Accordingly, for biomedical applications, such as drug delivery, we posit that the precise control of topology is critical for the design of a carrier with specific release profiles. In this present work, for the first time, we systematically explored how the combination of the ratio of ZIF components, biomolecule concentration and washing procedure determines the structural phase of the biocomposite.

Here, we screened 36 compositions varying the weight fractions of HmIM, $\text{Zn}(\text{OAc})_2 \cdot 2\text{H}_2\text{O}$, and Bovine Serum Albumin (BSA). BSA was selected as a model biomacromolecule since it has been widely employed in the literature as a standard inexpensive protein for the preparation of biocomposites.^{37–39} The washing procedure was carried out using either water only or water and ethanol. The resulting solids were analysed by X-ray diffraction (XRD) and their topologies represented in ternary phase diagrams namely *TD-H₂O* (water washed) and *TD-EtOH* (water and ethanol washed). A noteworthy result of this study is that we identified proteins encapsulated within ZIF- CO_3 -1, a ZIF previously obtained using solvothermal synthesis in absence of biomacromolecules.⁴⁰ For each distinct phase: amorphous, U13, sodalite, diamondoid, and ZIF- CO_3 -1 (here referred as *am*, *U13*, *sod*, *dia* and *ZIF-C*, respectively) we selected and characterised a representative sample using scanning electron microscopy (SEM), vibrational spectroscopy (Fourier Transformed Infrared, FTIR, and Raman), and energy-dispersive X-ray spectroscopy (EDX).

Given the potential application of these biocomposites to drug delivery, for each identified phase we determined the encapsulation and release profiles of BSA and insulin (a clinical biotherapeutic). Our results show that each biocomposite has high encapsulation efficiency EE% and a distinct release profile. These data will inform and facilitate future research in the burgeoning area of MOF-based drug delivery.

Results and discussion

To explore the entire space of the variables, we selected compositions that were equally distributed within the phase diagram (see Fig. S1 in ESI†).

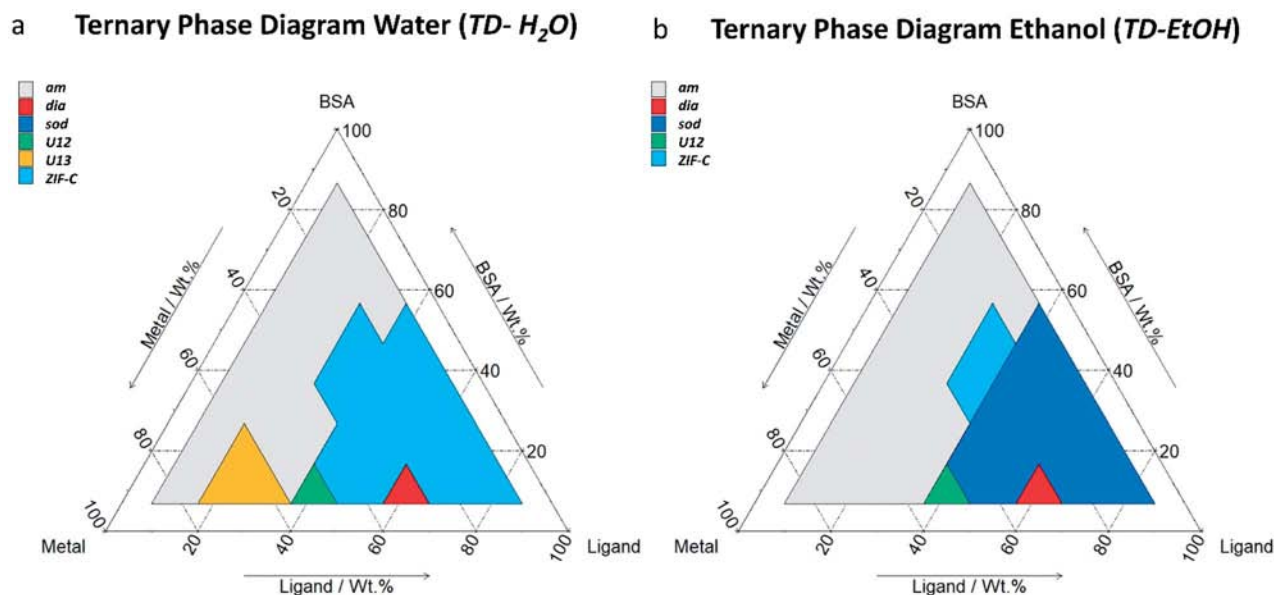


Fig. 1 Ternary diagrams (by weight fraction, see Table S1† for details) of BSA, HmIM (labelled as ligand) and $\text{Zn}(\text{OAc})_2 \cdot 2\text{H}_2\text{O}$ (labelled as metal). *TD-H₂O* (a) represents the main phases (>50% wt, see Table S2† for details) obtained by washing the sample with DI water. *TD-EtOH* (b) represents the main phases (>50% wt, see Table S3† for details) obtained by washing the sample first with DI water and then with ethanol. The total mass of the reagent was chosen by selecting a value in between those previously reported in the literature (see ESI† for further details).^{11,34}



We prepared 36 different samples by varying the composition of zinc acetate, HmIM and BSA (each restricted to a mass fraction range of 10–80%, see Fig. S1 and Table S1 in ESI†) in a fixed volume of water (2 mL, see ESI† for Experimental details) and examined their topology *via* XRD.

After mixing, the different solutions were left to stand at room temperature for 24 h. From each of the 36 vials, the solid was separated *via* centrifugation and divided in two parts. One part was washed with deionised (DI) water only and the other was washed with water and ethanol. The samples were then air dried and investigated by X-ray diffraction (XRD). The resultant phases are reported in the ternary diagrams that relate each polymorph to the relative composition of $\text{Zn}(\text{OAc})_2 \cdot 2\text{H}_2\text{O}$, HmIM, and BSA in the synthesis solution. Fig. 1a and b show the ternary diagrams of the samples washed with DI water (TD- H_2O) and with DI water and ethanol (TD-EtOH), respectively. Specific details related to the washing procedures and measurement conditions are reported in ESI.†

When powders were washed only with DI water (TD- H_2O) we observed the formation of an amorphous product (*am*) for small mass fractions of HmIM (10–20%). However, increasing HmIM to 20–30% while keeping $\text{BSA} \leq 20\%$, we found crystalline patterns dominated by a phase we have previously identified as *U13*.³⁴ Moving towards lower mass fractions of Zn^{2+} (10%), we measured amorphous diffraction patterns until BSA exceeded 50%. The remaining mass fraction ratios yielded diffraction patterns attributed to *ZIF-C* (Fig. 1a, S1 and Table S2 in ESI†). This was confirmed by continuous rotation electron diffraction (cRED, Fig. 2a, see ESI† for further details), which is

a specialized technique for the structural determination of nanocrystals.^{41,42} *ZIF-C* is a high density framework (Fig. 2b) non porous to N_2 (see Fig. S3, ESI†), that is prepared using solvothermal conditions ($\text{DMF}/\text{H}_2\text{O}$, 140°C)⁴⁰ and not observed as a component of a biocomposites until this work. In a limited number of samples, *ZIF-C* was found mixed with previously reported patterns termed *U12*, *U13*, and *dia* topology.³⁴

The TD-EtOH diagram indicates that ethanol washing gives rise to phase transitions: *U13* is no longer present and all the other samples with *ZIF-C* are partially or totally converted into *sod*, with the exception of the *dia/ZIF-C* mixed phase (TD- H_2O BSA/HmIM/ $\text{Zn}^{2+} = 10\%/60\%/30\%$) that transforms into *dia*. Furthermore, *U12* is converted to a mixture of 3 phases (*U12*, *sod*, *ZIF-C*). Lastly, for all samples with mass fraction = 10% of Zn^{2+} and $\text{HmIM} \geq 40\%$ we measured pure *sod*. We observed diffraction patterns (*i.e.* crystalline) only for *ca.* $\text{wt}_{\text{HmIM}} \geq 30\%$, thus TD-EtOH confirms the important role of HmIM for the preparation of a crystalline material.

Combined, TD- H_2O and TD-EtOH show the presence of 5 different phases (*am*, *sod*, *dia*, *U13*, *ZIF-C*) in their pure form or as compositions of phases (see Tables S2 and S3 ESI†). It is well known that the physical and chemical properties of ZIFs are dependent on their phase,^{32,43,44} thus we were motivated to examine the biomolecule encapsulation and release profiles of each biocomposite. However, first, we characterised each material by XRD, FTIR and Raman Spectroscopies, their elemental distribution *via* EDX and morphologies by SEM. In addition, given that biopharmaceuticals are the most expensive component of a drug delivery system^{45–47} we selected

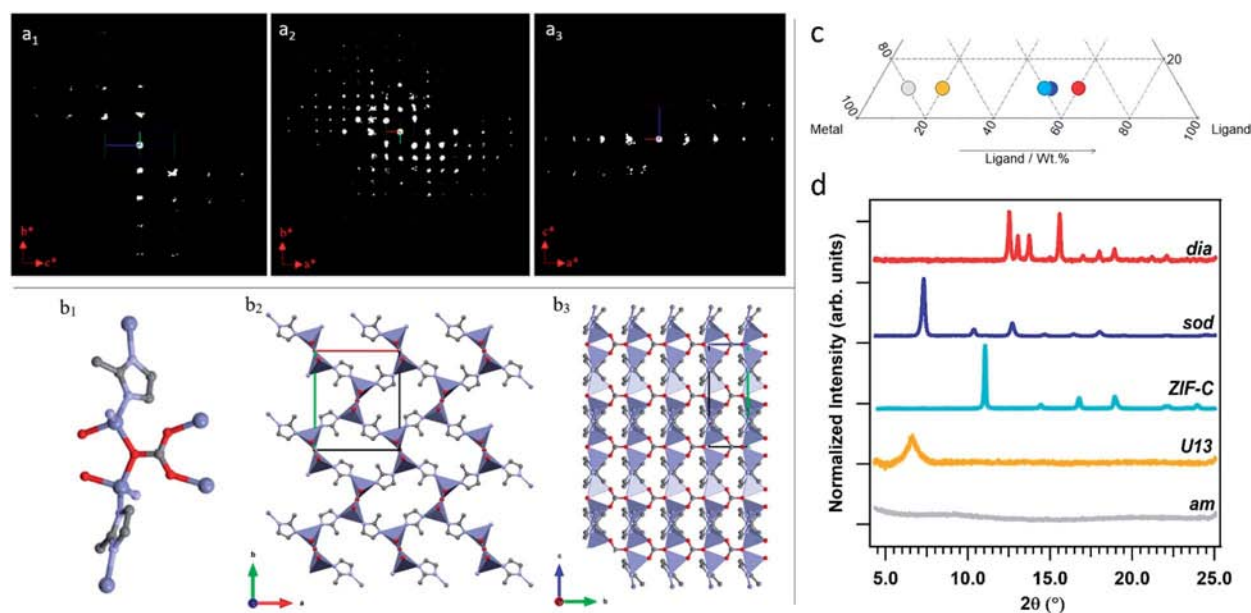


Fig. 2 2D slice cuts from the reconstructed 3D reciprocal lattice show the $0kl$ (a_1) $hk0$ (a_2) and $h0l$ (a_3) planes. The scattering background (see Fig. S2†) was removed for clarification. Structure of ZIF-CO3-1: (b_1) coordination mode of Zn; (b_2) framework viewed along the c axis; (b_3) framework structure viewed along the a axis. The Zn, O, N and C atoms are shown in blue, red, light blue and grey, respectively. (c) Section of the ternary diagram to highlight the samples selected as representative of the different phases (grey spot: amorphous biocomposite (TD- H_2O); yellow spot: *U13* (TD- H_2O); azure: *ZIF-C* (TD- H_2O); blue: *sod* (TD-EtOH); red: *dia* (TD-EtOH)). The *ZIF-C* and *sod* samples were obtained with the same protocol, but with different washing procedures (TD- H_2O and TD-EtOH, respectively). (d) XRD patterns of the amorphous biocomposite and of the biocomposites with *dia*, *sod*, *ZIF-C* topologies, and *U13*.



a biocomposite with a fixed 10 wt% of protein. Moving along this mass fraction we prepared the 5 different phases shown in Fig. 2c. The diffraction patterns plotted in Fig. 2d are univocally assigned to *dia*, *sod*, *ZIF-C* and *U13* (see Fig. S4, ESI†). For *am* the disordered state is confirmed by the absence of reflections. To facilitate the progress of Zn-mIM bio-composites towards biomedicine and biotechnology, we have developed a web application (<https://rapps.tugraz.at/apps/porousbiotech/ZIFphaseanalysis/>) named *ZIF phase analysis*. By uploading diffraction patterns collected using Cu K α radiation, this web application allows for (1) a rapid identification of the crystalline phases, and (2) a rough estimation of the relative amounts (wt%). The web application was developed using the statistical software R – shiny package.⁴⁸ Additional information can be found in ESI.†

To assess the connectivity and chemical composition of the bio-composites, we examined powder samples of *am*, *dia*, *sod*, *U13* and *ZIF-C* using vibrational spectroscopy (Fig. 3). Analysis of the FTIR data confirms the presence of characteristic modes of the peptide backbone of BSA such as the amide I (1700–1610 cm⁻¹) and amide II (1595–1480 cm⁻¹) bands.^{49,50} The spectra of *am* and *U13* did not show vibrational modes that could be attributed to the imidazolite ligand. Furthermore, the vibrational mode at ca. 420 cm⁻¹, assigned to the Zn–N stretching mode, is missing in the selected *am* and *U13* samples. This confirms that *am* and *U13* are not Zn(mIM)₂-based polymorphs. Conversely, the spectra of *sod*, *dia* and *ZIF-C* show several bands (420, 690, 752, 998, 1145, 1175, 1308, 1419, 1458, 1580 cm⁻¹) typically observed for *sod*-Zn(mIM)₂.^{31,34,51} The spectrum of *ZIF-C* shows additional bands in the 700–850 and 1300–1400 cm⁻¹ regions that can be assigned to bending and asymmetric stretching modes of CO₃²⁻.⁴⁰ Moreover, the Zn–N stretching mode is slightly shifted from 421 to 427 cm⁻¹; we posit this is due to the different Zn-mIM coordination environment with respect to *sod* or *dia* topologies. The Raman spectra (160–1800 cm⁻¹) of the same samples are reported in Fig. 3b. The *sod* and *dia* topologies show the typical Raman fingerprint of *sod*.^{52,53} For both *sod* and *dia*, the main bands are assigned to methyl bending (1459 cm⁻¹), C5–N stretching (1147 cm⁻¹), imidazole ring puckering (690 cm⁻¹) and Zn–N stretching (178 and 278 cm⁻¹).^{52,53} Comparing the Raman spectra of *ZIF-C* to *sod*, small differences can be observed at 1466 cm⁻¹ (assigned to imidazole ring puckering and to methyl bending) and 1097 cm⁻¹ (assigned to CO₃²⁻ stretching mode).^{52–54} These data support the different Zn-mIM coordination environment. In all the three crystalline Zn(mIM)₂ phases (*sod*, *dia*, *ZIF-C*) we could confirm the presence of BSA (1550–1720 cm⁻¹, amide I).⁵⁵ For *am* and *U13* the vibrational modes of BSA dominate the spectra with broad bands assigned to amide I (1600–1700 cm⁻¹), amide III (1300–1350 cm⁻¹) and –CH deformation (1445 cm⁻¹).⁵⁵ The broad band at 400 cm⁻¹ could be attributed to Zn–O stretching. This indicates potential for zinc protein interactions.⁵⁶ The elemental composition of the bio-composites estimated by EDX shows a Zn content of ca. 5 wt% in the case of *sod*. This value increases to ca. 15% for *am* and ca. 18% for *U13* (details can be found in ESI, Fig. S5 and Table

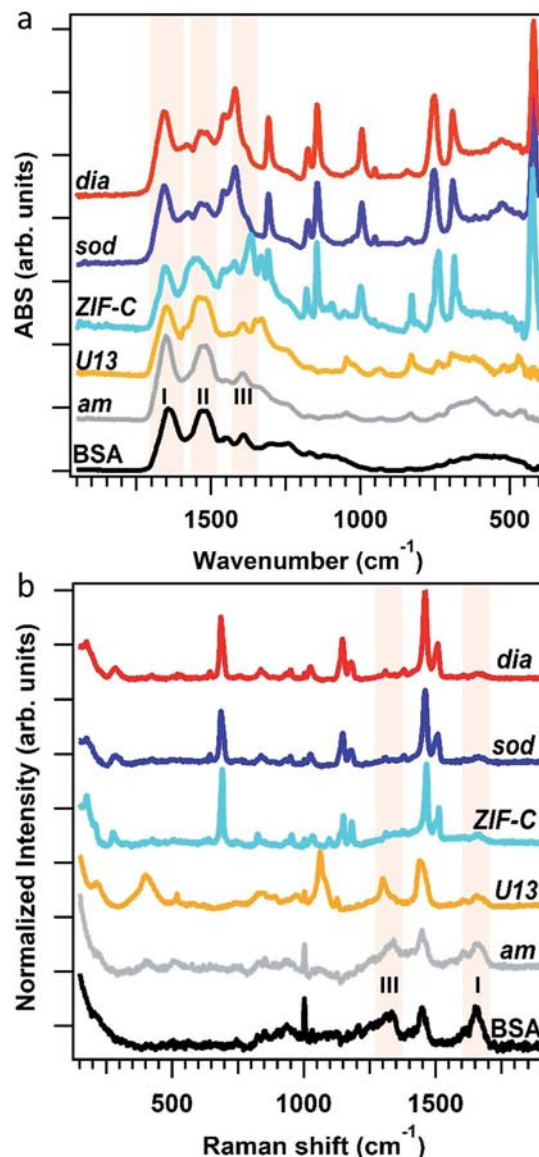


Fig. 3 FTIR (a) and Raman (b) spectra of BSA, the biocomposites with *am*, *dia*, *sod*, *U13* and *ZIF-C* phases. The spectral regions of Amide I, II and III bands of BSA are highlighted in light pink.

S5†), suggesting that *am* and *U13* are mainly composed of Zn and BSA. We note that Zn²⁺ cations and BSA have been shown to form solid particles.^{57,58} Next, we investigated the morphology of the different phases by SEM (Fig. 4). For the water washed samples, very small particles of indistinguishable morphology were observed for *am* (Fig. 4a). While for *U13* the image shows spherical particles, and for *dia*-Zn(mIM)₂ and *ZIF-C* aggregates of plates 2–3 μm in size (Fig. 4b, d and e, respectively). For the ethanol washed sample, the particle size was reduced to less than 100 nm (Fig. 4c, f and S6, ESI†), with the exception of *U13*. In this case, a similar particle morphology is observed despite the phase transition to *am* (Fig. S7, ESI†). We hypothesise that the particle size change is due to a combination of the crystalline network rearrangement



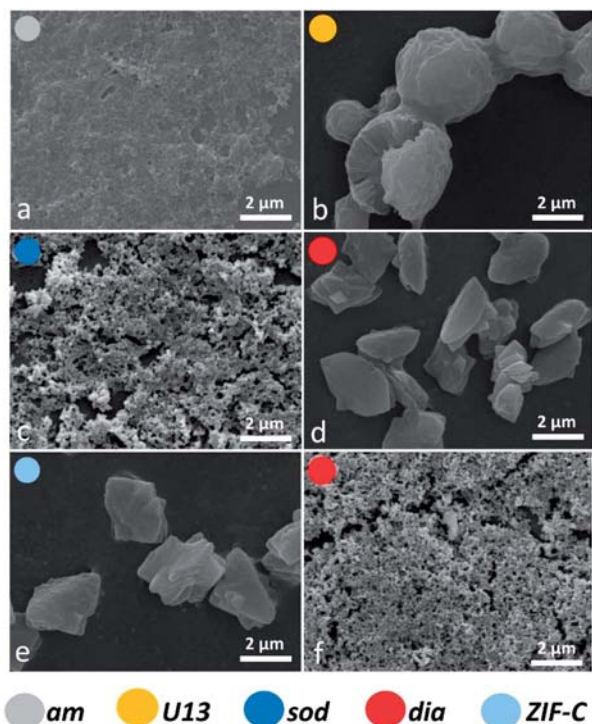


Fig. 4 SEM micrographs of the biocomposites *am* (a) and *U13* (b, from TD-H₂O), *sod* (c, from TD-EtOH), *dia* (from TD-H₂O) (d) and from TD-EtOH (f) and *ZIF-C* (e, from TD-H₂O) phases. *ZIF-C* refers to ZIF-CO₃-1.⁴⁰

and the collapse of the polycrystalline clusters induced by the different surface tension during the ethanol wash.^{59,60}

We then turned our efforts to investigate the potential of using the 5 biocomposites *am*, *U13*, *sod*, *dia*, and *ZIF-C* as drug delivery systems. Initially BSA was employed as a model biotherapeutic.^{61,62} For each sample a 10% mass fraction of BSA was employed in the synthesis (*vide supra*) and two important properties of a drug carrier were assessed: EE% and release profile.⁶³⁻⁶⁵ The estimated EE% (average of five independent analyses) for the different phases is shown in Fig. 5a. For each

phase, high EE% values were observed (EE% > 85%) and, remarkably, *dia*, *sod* and *ZIF-C* topology showed a 100% EE%. Details can be found in ESI†.

BSA release profiles were investigated to ascertain the quantity of protein released over time. As our study focuses on the examination of the crystalline phases and their properties rather than targeting a specific administration route, we examined release profiles at pH 5.5 as these conditions facilitate release of the cargo and simplifies a comparison between the different ZIF based particles. However, we note that different pH values will lead to different release profiles. The dissolution of each biocomposite was performed by exposing 1.08 mg of each phase to citric acid buffer solution (1 mL, 100 mM, pH 5.5, room temperature). We used UV-Vis and the Bradford Assay (see ESI† for details) to measure the amount of BSA in solution over time (see ESI† for details), and the release profiles are plotted in Fig. 5b and c. The experimental data points were fitted with a logistic fitting function⁶⁶ which has previously been employed in the literature for the analysis of data related to the dissolution of different hydrophobic carries, including ZIF-8.^{18,67,68} Among the biocomposites washed only with water, *am* and *U13* showed the fastest dissolution: in 20 minutes, 100% of the encapsulated BSA was released (see ESI†) and the slowest release was measured for the *dia* topology: 100% of protein release was reached after 250 minutes. Whilst *ZIF-C* released 100% of the protein in 120 min. With respect to the ethanol-washed samples, *am* showed rapid release, *ca.* 20 min, and similar to the water washed samples, the slowest release was measured for the biocomposite of *dia* topology. However, in this case the release was significantly faster; 100% was observed in 60 minutes (compared to 250 min for the water washed samples). The different dissolution times observed for biocomposites of the same phase (*e.g.* *dia*) can be attributed to particle size. However, when comparing the release profiles of topologically different particles the phase appears to play a dominant role. Thus, we can conclude that both the crystalline phase and the particle size play a crucial role in the design of MOF carriers for drug delivery applications.

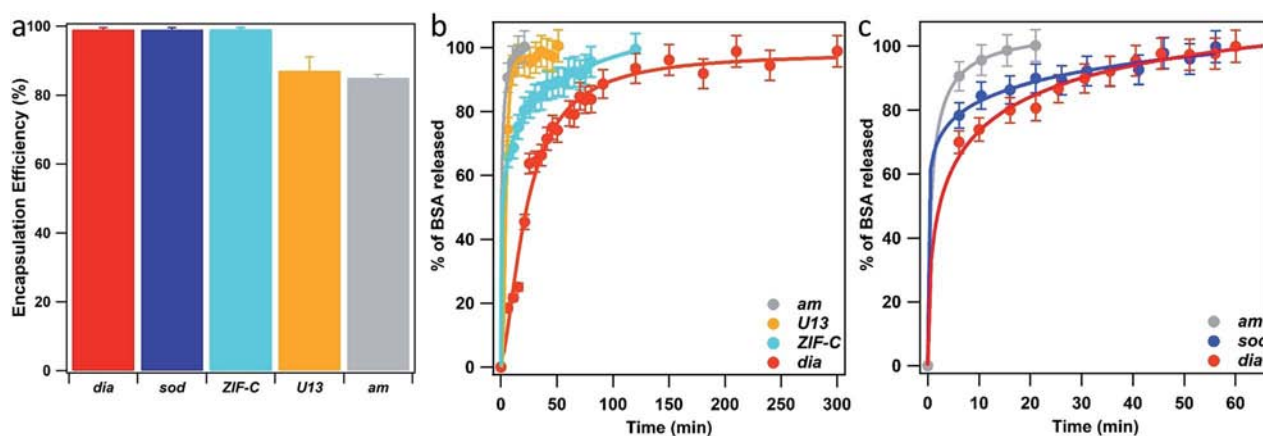


Fig. 5 BSA encapsulation efficiency (EE%) (a) and BSA release profiles (from TD-H₂O (b) and from TD-EtOH (c)) of the biocomposites with *am*, *U13*, *sod*, *dia* and *ZIF-C* phases. *ZIF-C* refers to ZIF-CO₃-1.⁴⁰



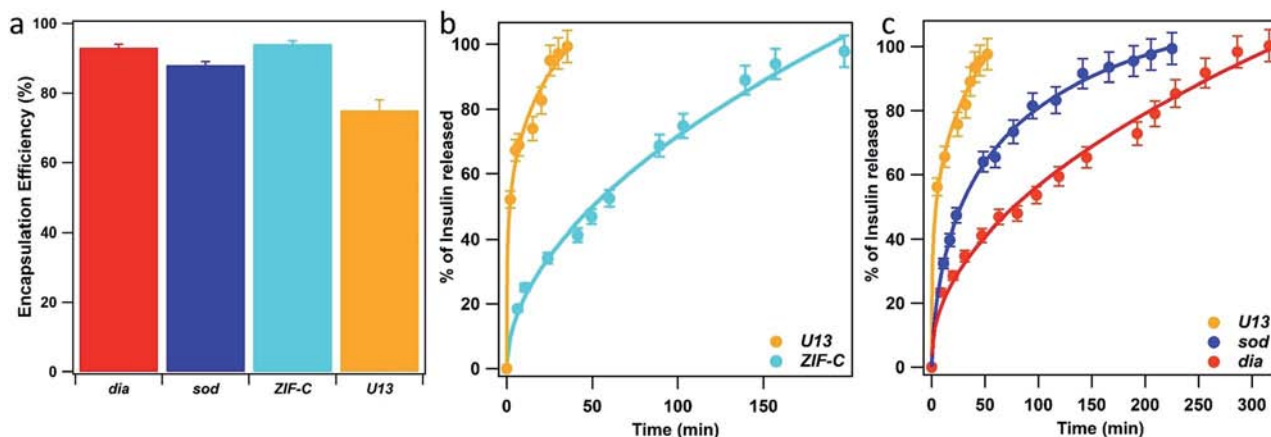


Fig. 6 Insulin encapsulation efficiency (EE%) (a) and Insulin release profiles of the biocomposites with *U13* and *ZIF-C* phases (b, water washed samples) and *U13*, *sod* and *dia* (c, EtOH washed samples) phases. *ZIF-C* refers to ZIF-CO_3 -1.⁴⁰

To explore the potential biomedical applications of these biocomposites for the delivery of therapeutics we determined the release profiles of insulin encapsulated within the same 5 phases as studied for BSA. XRD data confirmed the expected phases (see Fig. S8, ESI[†]). However, for the *dia* phase an impurity of *sod* was present (15 wt%). The morphology of insulin biocomposites were investigated *via* SEM (Fig. S9 ESI[†]). The *U13* samples formed large micrometer sized star-like aggregates. Insulin@*ZIF-C* is composed of both micrometer sized aggregates and small particles (<100 nm). We note the micrometer particles are of analogous morphology to the BSA@*ZIF-C* particles. Similar to BSA@*dia*, insulin@*dia* is composed of small particles (<100 nm). The insulin@*sod* particles are composed of aggregates of small nanoparticles (100–200 nm). As expected, the insulin-based biocomposites (Fig. S10 ESI[†]) afford similar FTIR spectra to those of the BSA. For the samples with *dia*, *sod* and *ZIF-C* topology we measured 93, 88 and 94% of insulin EE%, respectively (Fig. 6a). The lowest value was found for *U13* sample (EE% = 75%). Then, we tested the insulin release profiles (Fig. 6b and c). Among the crystalline water washed samples, the *U13* biocomposite showed the fastest release: in the first 40 minutes 100% of the encapsulated insulin was released. The slowest release was measured for the sample that possesses *ZIF-C* topology: the insulin release is 50% in 60 min and 100% in 200 min. Among the ethanol washed crystalline samples, *U13* showed the fastest release and a profile comparable to the water washed *U13* sample. The slowest release was measured for the sample that possesses *dia* topology: 100% of release was reached in 300 minutes. The sample that possesses *sod* topology showed an intermediate release profile (100% of insulin released in 220 minutes). In the context of insulin delivery systems, transdermal delivery is being explored as a less invasive method of administration.⁶⁹ The measured cargo release times from ZIF-based biocomposites are similar to previously reported transdermal delivery systems.^{70,71} The difference in the release profiles from BSA and insulin suggests that the chemical nature, charge, and size of the protein could influence defects in the biocomposites.

To further validate the relevance of BSA ternary diagrams as a guide for the synthesis of other systems, we prepared a series of horseradish peroxidase (HRP) biocomposites. Analogous to BSA and insulin-based biocomposites, XRD data confirmed the presence of *am*, *U12*, *ZIF-C* and *sod* phases for the selected compositions (Fig. S11 ESI[†]). Although analogous synthetic conditions yielded to biocomposites with the same crystalline phases for BSA, insulin, and HRP, we hypothesise that the intrinsic heterogeneity of proteins (*e.g.* isoelectric point, hydrophobicity) could lead to deviations from the here proposed trend.

Conclusion

We investigated the dependence of the crystal phases on the mass fraction of precursors (BSA or insulin, $\text{Zn}(\text{OAc})_2 \cdot 2\text{H}_2\text{O}$, HmIM) and the washing procedure (water or ethanol). For BSA we prepared 36 samples, washed only with water; the crystal phases were used to plot a ternary phase diagram (TD-H₂O). More than 40% of the samples were found to be amorphous and the remaining samples were crystalline and non-porous (*dia*, *U13*, *ZIF-C*). Then, we tested the effect of ethanol washes on the 36 samples and found that it gave rise to phase transitions. For example, *U13* became amorphous, while *ZIF-C* transformed partially or completely into *sod*. From these data we constructed a new second ternary phase diagram (TD-EtOH). Approximately 50% of the samples in TD-EtOH are amorphous; the remaining crystalline samples are dominated by the porous *sod* topology. The two ternary diagrams were used for the design of BSA-based composites with different crystallinity: starting with the same amount of protein, we could select conditions for the preparation of 5 different crystalline phases. To assess the potential of these systems for application to drug delivery, we focused our attention on determining their encapsulation efficiency and release profiles. We measured encapsulation efficiencies over 85% and a 100% release that can be tuned from 20 to 300 min depending on the selected phase. In general, we believe that the ternary diagrams can be used to design new biocomposites with



tailored functional properties for bio-catalysis, bio-banking and drug delivery. As a proof of concept, we applied the ternary diagram to synthesize insulin biocomposites and test their encapsulation and release properties. Finally, we uncovered for the first-time proteins@ZIF-C composites. For BSA@ZIF-C and insulin@ZIF-C, we measured $EE_{BSA}\% = 99\%$ and $EE_{insulin}\% = 94\%$, and 100% release was achieved in 120 and 200 min, respectively. This new bioMOF composite is an appealing crystalline structure alternative to *sod* and *dia* with potentially useful properties for encapsulation and release of biotherapeutics.

Conflicts of interest

There are no conflicts to declare.

Acknowledgements

The research leading to these results has received funding from the European Research Council under the European Union's Horizon 2020 Programme (FP/2014-2020)/ERC Grant Agreement no. 771834 – POPCRYSTAL. The authors acknowledge support from the European Union's Horizon 2020 FETOPEN-1-2016-2017 Research and Innovation Program under grant agreement 801464. This work was supported by the Australian Research Council Discovery Project (DP170103531). P. F. acknowledges TU Graz for the Lead Project (LP-03). M. J. V. H. acknowledges The National Council of Science and Technology (CONACyT, México) for the postdoctoral scholarship (CVU 419210). R. R. acknowledges the European Union's Horizon 2020 Research and Innovation Programme under the Marie Skłodowska-Curie grant agreement #748649 (project "MNEMONIC"). Financial support from the Swedish Research Council (2017-0432) and the Knut and Alice Wallenberg Foundation (KAW 2016.0072) are gratefully acknowledged. E. A. acknowledges the Austrian Agency for International Cooperation in Education and Research (OeAD-GmbH) for the PhD scholarship.

Notes and references

- H. Furukawa, K. E. Cordova, M. O'Keeffe and O. M. Yaghi, *Science*, 2013, **341**, 1230444.
- A. C. McKinlay, R. E. Morris, P. Horcajada, G. Férey, R. Gref, P. Couvreur and C. Serre, *Angew. Chem., Int. Ed.*, 2010, **49**, 6260–6266.
- P. Horcajada, C. Serre, M. Vallet-Regí, M. Sebban, F. Taulelle and G. Férey, *Angew. Chem., Int. Ed.*, 2006, **45**, 5974–5978.
- S. Wuttke, A. Zimpel, T. Bein, S. Braig, K. Stoiber, A. Vollmar, D. Müller, K. Haastert-Talini, J. Schaeske, M. Stiesch, G. Zahn, A. Mohmeyer, P. Behrens, O. Eickelberg, D. A. Bölükbas and S. Meiners, *Adv. Healthcare Mater.*, 2017, **6**, 1600818.
- C. Doonan, R. Riccò, K. Liang, D. Bradshaw and P. Falcaro, *Acc. Chem. Res.*, 2017, **50**, 1423–1432.
- D. A. LaVan, D. M. Lynn and R. Langer, *Nat. Rev. Drug Discovery*, 2002, **1**, 77–84.
- Y. Chen, P. Li, J. A. Modica, R. J. Drout and O. K. Farha, *J. Am. Chem. Soc.*, 2018, **140**, 5678–5681.
- Y. Feng, H. Wang, S. Zhang, Y. Zhao, J. Gao, Y. Zheng, P. Zhao, Z. Zhang, M. J. Zaworotko, P. Cheng, S. Ma and Y. Chen, *Adv. Mater.*, 2019, **31**, 1805148.
- J. Yao and H. Wang, *Chem. Soc. Rev.*, 2014, **43**, 4470–4493.
- B. Chen, Z. Yang, Y. Zhu and Y. Xia, *J. Mater. Chem. A*, 2014, **2**, 16811–16831.
- K. Liang, R. Ricco, C. M. Doherty, M. J. Styles, S. Bell, N. Kirby, S. Mudie, D. Haylock, A. J. Hill, C. J. Doonan and P. Falcaro, *Nat. Commun.*, 2015, **6**, 7240.
- W. Liang, H. Xu, F. Carraro, N. K. Maddigan, Q. Li, S. G. Bell, D. M. Huang, A. Tarzia, M. B. Solomon, H. Amenitsch, L. Vaccari, C. J. Sumbly, P. Falcaro and C. J. Doonan, *J. Am. Chem. Soc.*, 2019, **141**, 2348–2355.
- F. Lyu, Y. Zhang, R. N. Zare, J. Ge and Z. Liu, *Nano Lett.*, 2014, **14**, 5761–5765.
- X. Wu, M. Hou and J. Ge, *Catal. Sci. Technol.*, 2015, **5**, 5077–5085.
- X. Wu, J. Ge, C. Yang, M. Hou and Z. Liu, *Chem. Commun.*, 2015, **51**, 13408–13411.
- F.-K. Shieh, S.-C. Wang, C.-I. Yen, C.-C. Wu, S. Dutta, L.-Y. Chou, J. V. Morabito, P. Hu, M.-H. Hsu, K. C.-W. Wu and C.-K. Tsung, *J. Am. Chem. Soc.*, 2015, **137**, 4276–4279.
- N. K. Maddigan, A. Tarzia, D. M. Huang, C. J. Sumbly, S. G. Bell, P. Falcaro and C. J. Doonan, *Chem. Sci.*, 2018, **9**, 4217–4223.
- E. Astria, M. Thonhofer, R. Ricco, W. Liang, A. Chemelli, A. Tarzia, K. Alt, C. E. Hagemeyer, J. Rattenberger, H. Schroettner, T. Wrodnigg, H. Amenitsch, D. M. Huang, C. J. Doonan and P. Falcaro, *Mater. Horiz.*, 2019, **6**(5), 969–977.
- S. Li, M. Dharmawardana, R. P. Welch, C. E. Benjamin, A. M. Shamir, S. O. Nielsen and J. J. Gassensmith, *ACS Appl. Mater. Interfaces*, 2018, **10**, 18161–18169.
- M. Hoop, C. F. Walde, R. Riccò, F. Mushtaq, A. Terzopoulou, X.-Z. Chen, A. J. deMello, C. J. Doonan, P. Falcaro, B. J. Nelson, J. Puigmartí-Luis and S. Pané, *Appl. Mater. Today*, 2018, **11**, 13–21.
- T.-T. Chen, J.-T. Yi, Y.-Y. Zhao and X. Chu, *J. Am. Chem. Soc.*, 2018, **140**, 9912–9920.
- W. Chen and C. Wu, *Dalton Trans.*, 2018, **47**, 2114–2133.
- X. Wu, C. Yang and J. Ge, *Bioresour. Bioprocess.*, 2017, **4**, 24.
- M. de J. Velásquez-Hernández, R. Ricco, F. Carraro, F. T. Limpoco, M. Linares-Moreau, E. Leitner, H. Wiltsche, J. Rattenberger, H. Schröttner, P. Frühwirt, E. M. Stadler, G. Gescheidt, H. Amenitsch, C. J. Doonan and P. Falcaro, *CrystEngComm*, 2019, **21**, 4538–4544.
- M. A. Luzuriaga, C. E. Benjamin, M. W. Gaertner, H. Lee, F. C. Herbert, S. Mallick and J. J. Gassensmith, *Supramol. Chem.*, 2019, **0**, 1–6.
- O. Karagiari, M. B. Lalonde, W. Bury, A. A. Sarjeant, O. K. Farha and J. T. Hupp, *J. Am. Chem. Soc.*, 2012, **134**, 18790–18796.
- Q. Bao, Y. Lou, T. Xing and J. Chen, *Inorg. Chem. Commun.*, 2013, **37**, 170–173.



- 28 K. Kida, M. Okita, K. Fujita, S. Tanaka and Y. Miyake, *CrystEngComm*, 2013, **15**, 1794.
- 29 M. Jian, B. Liu, R. Liu, J. Qu, H. Wang and X. Zhang, *RSC Adv.*, 2015, **5**, 48433–48441.
- 30 A. D. Katsenis, A. Puškarić, V. Štrukil, C. Mottillo, P. A. Julien, K. Užarević, M.-H. Pham, T.-O. Do, S. A. J. Kimber, P. Lazić, O. Magdysyuk, R. E. Dinnebier, I. Halasz and T. Friščić, *Nat. Commun.*, 2015, **6**, 6662.
- 31 M. He, J. Yao, Q. Liu, K. Wang, F. Chen and H. Wang, *Microporous Mesoporous Mater.*, 2014, **184**, 55–60.
- 32 Z. Akimbekov, A. D. Katsenis, G. P. Nagabhushana, G. Ayoub, M. Arhangelskis, A. J. Morris, T. Friščić and A. Navrotsky, *J. Am. Chem. Soc.*, 2017, **139**, 7952–7957.
- 33 R. Chen, J. Yao, Q. Gu, S. Smeets, C. Baerlocher, H. Gu, D. Zhu, W. Morris, O. M. Yaghi and H. Wang, *Chem. Commun.*, 2013, **49**, 9500–9502.
- 34 W. Liang, R. Ricco, N. K. Maddigan, R. P. Dickinson, H. Xu, Q. Li, C. J. Sumby, S. G. Bell, P. Falcaro and C. J. Doonan, *Chem. Mater.*, 2018, **30**, 1069–1077.
- 35 S. Cao, T. D. Bennett, D. A. Keen, A. L. Goodwin and A. K. Cheetham, *Chem. Commun.*, 2012, **48**, 7805–7807.
- 36 C. Avci, J. Ariñez-Soriano, A. Carné-Sánchez, V. Guillerme, C. Carbonell, I. Imaz and D. MasPOCH, *Angew. Chem., Int. Ed.*, 2015, **54**, 14417–14421.
- 37 D. J. Connell, A. Gebril, M. A. H. Khan, S. V. Patwardhan, K. Kubiak-Ossowska, V. A. Ferro and P. A. Mulheran, *Sci. Rep.*, 2018, **8**, 17115.
- 38 K. A. Majorek, P. J. Porebski, A. Dayal, M. D. Zimmerman, K. Jablonska, A. J. Stewart, M. Chruszcz and W. Minor, *Mol. Immunol.*, 2012, **52**, 174–182.
- 39 W. Liang, F. Carraro, M. B. Solomon, S. G. Bell, H. Amenitsch, C. J. Sumby, N. G. White, P. Falcaro and C. J. Doonan, *J. Am. Chem. Soc.*, 2019, **141**, 14298–14305.
- 40 S. A. Basnayake, J. Su, X. Zou and K. J. Balkus, *Inorg. Chem.*, 2015, **54**, 1816–1821.
- 41 M. O. Cichocka, J. Ångström, B. Wang, X. Zou and S. Smeets, *J. Appl. Crystallogr.*, 2018, **51**, 1652–1661.
- 42 S. Yuan, J.-S. Qin, H.-Q. Xu, J. Su, D. Rossi, Y. Chen, L. Zhang, C. Lollar, Q. Wang, H.-L. Jiang, D. H. Son, H. Xu, Z. Huang, X. Zou and H.-C. Zhou, *ACS Cent. Sci.*, 2018, **4**, 105–111.
- 43 Y. Lo, C. H. Lam, C.-W. Chang, A.-C. Yang and D.-Y. Kang, *RSC Adv.*, 2016, **6**, 89148–89156.
- 44 L. Bouëssel du Bourg, A. U. Ortiz, A. Boutin and F.-X. Coudert, *APL Mater.*, 2014, **2**, 124110.
- 45 M. Baker, *Nat. Biotechnol.*, 2005, **23**, 1065–1072.
- 46 T. W. Overton, *Drug Discovery Today*, 2014, **19**, 590–601.
- 47 G. Walsh, *Nat. Biotechnol.*, 2010, **28**, 917–924.
- 48 W. Chang, J. Cheng, J. J. Allaire, Y. Xie, J. McPherson, RStudio, jQuery F. (jQuery library and jQuery U. library), jQuery contributors (jQuery library; authors listed in inst/www/shared/jquery-AUTHORS.txt), jQuery U. contributors (jQuery U. library; authors listed in inst/www/shared/jqueryui/AUTHORS.txt), M. O. (Bootstrap library), J. T. (Bootstrap library), B. contributors (Bootstrap library), Twitter, I. (Bootstrap library), A. F. (html5shiv library), S. J. (Respond js library), S. P. (Bootstrap-datepicker library), A. R. (Bootstrap-datepicker library), D. G. (Font-A. font), B. R. (selectize js library), K. M. K. (es5-shim library), es5-shim contributors (es5-shim library), D. I. (ion rangeSlider library), S. S. (Javascript strftime library), S. L. (DataTables library), J. F. (showdown js library), J. G. (showdown js library), I. S. (highlight js library) and R. C. T. (tar implementation from R), shiny: Web Application Framework for R, 2019.
- 49 A. Barth, *Biochim. Biophys. Acta, Bioenerg.*, 2007, **1767**, 1073–1101.
- 50 M. Jackson and H. H. Mantsch, *Crit. Rev. Biochem. Mol. Biol.*, 1995, **30**, 95–120.
- 51 Y. Hu, H. Kazemian, S. Rohani, Y. Huang and Y. Song, *Chem. Commun.*, 2011, **47**, 12694–12696.
- 52 G. Kumari, K. Jayaramulu, T. K. Maji and C. Narayana, *J. Phys. Chem. A*, 2013, **117**, 11006–11012.
- 53 J. Ethiraj, F. Bonino, C. Lamberti and S. Bordiga, *Microporous Mesoporous Mater.*, 2015, **207**, 90–94.
- 54 G. Socrates, *Infrared and Raman Characteristic Group Frequencies: Tables and Charts*, John Wiley & Sons, 2004.
- 55 N. Kuhar, S. Sil, T. Verma and S. Umapathy, *RSC Adv.*, 2018, **8**, 25888–25908.
- 56 M. Wang, L. Jiang, E. J. Kim and S. H. Hahn, *RSC Adv.*, 2015, **5**, 87496–87503.
- 57 C. Li, L. Xing and S. Che, *Dalton Trans.*, 2012, **41**, 3714–3719.
- 58 H. Qing, H. Yanlin, S. Fenlin and T. Zuyi, *Spectrochim. Acta, Part A*, 1996, **52**, 1795–1800.
- 59 Z.-X. Low, J. Yao, Q. Liu, M. He, Z. Wang, A. K. Suresh, J. Bellare and H. Wang, *Cryst. Growth Des.*, 2014, **14**, 6589–6598.
- 60 A. P. Nelson, O. K. Farha, K. L. Mulfort and J. T. Hupp, *J. Am. Chem. Soc.*, 2009, **131**, 458–460.
- 61 A. S. Determan, B. G. Trewyn, V. S.-Y. Lin, M. Nilsen-Hamilton and B. Narasimhan, *J. Controlled Release*, 2004, **100**, 97–109.
- 62 K. N. Clayton, D. Lee, S. T. Wereley and T. L. Kinzer-Ursem, *Lab Chip*, 2017, **17**, 4148–4159.
- 63 M. Mishra, *Handbook of Encapsulation and Controlled Release*, CRC Press, 2015.
- 64 M. L. Hans and A. M. Lowman, *Curr. Opin. Solid State Mater. Sci.*, 2002, **6**, 319–327.
- 65 C.-Y. Sun, C. Qin, X.-L. Wang and Z.-M. Su, *Expert Opin. Drug Delivery*, 2013, **10**, 89–101.
- 66 F. O. Costa, J. J. S. Sousa, A. A. C. C. Pais and S. J. Formosinho, *J. Controlled Release*, 2003, **89**, 199–212.
- 67 K. Zhang, R. P. Lively, C. Zhang, R. R. Chance, W. J. Koros, D. S. Sholl and S. Nair, *J. Phys. Chem. Lett.*, 2013, **4**, 3618–3622.
- 68 K. Ghosal, A. Chandra, R. Rajabalaya, S. Chakraborty and A. Nanda, *Pharmazie*, 2012, **67**(2), 147–155.
- 69 Y. Zhang, J. Yu, A. R. Kahkoska, J. Wang, J. B. Buse and Z. Gu, *Adv. Drug Delivery Rev.*, 2019, **139**, 51–70.
- 70 C.-J. Ke, Y.-J. Lin, Y.-C. Hu, W.-L. Chiang, K.-J. Chen, W.-C. Yang, H.-L. Liu, C.-C. Fu and H.-W. Sung, *Biomaterials*, 2012, **33**, 5156–5165.
- 71 X. Jin, D. D. Zhu, B. Z. Chen, M. Ashfaq and X. D. Guo, *Adv. Drug Delivery Rev.*, 2018, **127**, 119–137.



Supporting Information

Phase dependent encapsulation and release profile of ZIF-based biocomposites

*F. Carraro,^a M. de J. Velasquez-Hernandez,^a E. Astria,^a W. Liang,^b L. Twight,^a C. Parise,^{a,c,d} M. Ge,^e Z. Huang,^e R. Ricco,^a X. Zou,^e L. Villanova,^f C. Oliver Kappe,^c C. Doonan^{*b}, P. Falcaro^{*a,b}*

a) Institute of Physical and Theoretical Chemistry, Graz University of Technology, Stremayrgasse 9, Graz 8010, Austria

b) Department of Chemistry and the Centre for Advanced Nanomaterials, The University of Adelaide, Adelaide, South Australia 5005, Australia

c) Institute of Chemistry, University of Graz, NAWI Graz, Heinrichstrasse 28, 8010 Graz, Austria

d) Dipartimento di Chimica Industriale "Toso Montanari", Università di Bologna, Viale del Risorgimento 4, Bologna

e) Department of Materials and Environmental Chemistry, Stockholm University, 106 91 Stockholm, Sweden

f) Faculty of Technical Chemistry, Chemical and Process Engineering, Biotechnology, Graz University of Technology, Petersgasse 10-12, 8010 Graz, Austria

Contents:

Experimental section. Pages 3-5

Table S1: List of the synthesized samples for each Ternary Diagram, together with the details about the weight percentages of the different components and the ligand/metal weight and molar ratios in the starting solution mixture. Page 6.

Table S2: List of the weight % of the different phases calculated from the diffraction patterns of the samples of the TD-H₂O. The data were analyzed using the “ZIF phase analysis” application. Page 7.

Table S3: List of the weight % of the different phases calculated from the diffraction patterns of the samples of the TD-EtOH. The data were analyzed using the “ZIF phase analysis” application. Page 8.

Figure S1: Ternary diagrams (TD, by weight fraction) of BSA, HmIM (labelled as Ligand) and Zn(OAc)₂·2(H₂O) (labelled as Metal) with the 36 investigated points. Page 9.

Figure S2: The Reconstructed 3D reciprocal lattice from the cRED data. Page 9.

Table S4: Experimental parameters for cRED data collection and crystallographic data. Page 10

Figure S3: N₂ 77K isotherms of the ZIF-C biocomposite (Sample #29 of Table S1), the sod biocomposite obtained by washing with ethanol the ZIF-C sample and the sod biocomposite treated at 325°C for 2h. Page 10.

Figure S4: XRD patterns of dia, sod and ZIF-C biocomposites and of the calculated pure MOFs. Page 11.

Figure S5: EDX spectra of patterns of BSA, of the amorphous biocomposite and of the biocomposites with dia, sod, ZIF-C, and U13 topology. Page 11.

Table S5: Atomic % calculated from EXD spectra. Page 12.

Figure S6: SEM micrographs of the dia (left) and sod(right) samples obtained by washing the samples with ethanol (TD-EtOH). Page 12.

Figure S7: SEM micrograph of the am sample obtained by washing with ethanol the U13 sample. Page 13.

Figure S8: XRD patterns of the different phases of the Insulin biocomposites. Page 13

The “ZIF phase analysis” application – Version 1.0.0 Pages 14-23.

Figure S9. Example of accepted data file of the “ZIF phase analysis” application – Version 1.0.0. Page 14.

Table S6. 2θ values and RIR factors of selected peaks used for the identification of five ZIF phases, biocomposites with U12 and U13 structure and two references (ZnO and ZrO₂). Page 23.

Experimental section

Synthesis

In a typical experiment for ZIF polymorph synthesis, 1 mL of an aqueous solution of $\text{Zn}(\text{OAc})_2 \cdot 2(\text{H}_2\text{O})$ (EMSURE, Merck) was added to a 1 mL of an aqueous solution of HmIM (TCI Chemicals) and Bovine Serum Albumin (BSA, lyophilized powder, Sigma-Aldrich). The total volume of each synthesis was 2 mL. Deionized (DI) water was used for all the experiments. The relative weight percentage of the three components ($\text{Zn}(\text{OAc})_2 \cdot 2(\text{H}_2\text{O})$, BSA, HmIM) were systematically varied from 10 to 80 wt%, starting from the following aqueous stock solutions: 80 mM $\text{Zn}(\text{OAc})_2 \cdot 2(\text{H}_2\text{O})$, 440 mM HmIM and 36 mg/mL of BSA. For all the investigated samples, the total mass of the reagents is 43.8 mg (21.9 mg/ml). This value was chosen selecting a value in between the those of previous reported in the literature for the synthesis via the biomimetic mineralization method of BSA@ZIF-8 biocomposites.^{i,ii} The detailed composition of each investigated point of the ternary diagram is summarized in Table S1. The reaction mixture was left under static conditions at RT for 24 h. Each sample was synthesized in a 2 mL Eppendorf Tube. After 24 hours the solid product was separated via centrifugation (13000 rpm for 5 min; centrifuge used: Eppendorf 5425) and the supernatant was discarded. Depending on the phase diagram (TD- H_2O , or TD-EtOH), the obtained powder pellet was then washed using one of two different protocols (see also [Washing_Procedure.mp4](#)):

TD- H_2O - Water washed materials:

The pellet was re-suspended in deionized water (1.5 mL) using a vortex mixer (3000 rpm for 1 minute, VELP Scientifica ZX3). The suspension was centrifuged (13000 rpm for 5 min) to yield a pellet and the supernatant was discarded. This washing procedure was repeated 6 times. Finally, the recovered powders were air-dried for 48 h at 25 °C.

TD-EtOH - Water and Ethanol washed materials:

The pellet was re-suspended in deionized water (1.5 mL) using a vortex mixer (3000 rpm for 1 minute, VELP Scientifica ZX3). The suspension was centrifuged (13000 rpm for 5 min) to yield a pellet (13000 rpm for 5 min) and the supernatant was discarded. This deionized water washing procedure was repeated 3 times. Then, the pellet was re-suspended in ethanol (1.5 mL) using a vortex mixer (3000 rpm for 1 minute, VELP Scientifica ZX3). The suspension was centrifuged (13000 rpm for 5 min) to yield a pellet and the supernatant was discarded. This ethanol washing procedure was repeated 3 times. Finally, the recovered powders were air-dried for 48 h at 25°C.

The mass percentages of the different phases calculated from the diffraction patterns of each investigated sample are summarized in Table S2 and S3 and in Figure S1.

Characterization

XRD

XRD patterns were acquired using a Rigaku SmartLab II equipped with a Cu anode ($\lambda=1.5406 \text{ \AA}$) and operating at 9 kW.

SEM-EDX

SEM micrographs and EDX spectra were collected using Tescan VEGA 3 SEM with tungsten source filament working at 20 kV. Prior the analysis the powder samples were dropcasted on a piece of Si (100) and sputter-coated with Gold.

ATR

FT-IR spectra were recorded on a Bruker ALPHA spectrometer using the ATR accessory with a diamond window in the range 400 – 4000 cm^{-1} .

RAMAN

Raman spectra were recorded on a Thermo Fisher DXR2 Microscope equipped with a 785 nm laser operating at 35 mW and a 10x objective.

Gas Sorption

Gas adsorption isotherm measurements were performed on an ASAP 2020 Surface Area and Pore Size Analyser. Samples were activated by heating in vacuum at 120 °C for 12 hours. UHP grade (99.999%) N_2 and He were used for all measurements. The temperatures were maintained at 77 K (liquid nitrogen bath).

Evaluation of Encapsulation Efficiency

Encapsulation Efficiency measurement from supernatant: the samples after synthesis (24 hours) were centrifuged 5 minutes 13000 rpm. The supernatant (1 mL) was recovered by micropipette. 50 μL of supernatant was mixed with 1500 μL of Bradford solution (Sigma-Aldrich, sample-to-Bradford ratio 1:30). The solution was left for 5 minutes at room temperature. Afterwards, this mixture was analyzed by UV-VIS (595 nm). All the experiments were performed in triplicates.

Encapsulation Efficiency measurement from destroyed MOFs: samples were washed 3X with water and 3X with ethanol (TD-EtOH) or 6X with water (TD- H_2O). The MOF was destroyed under acidic conditions using Citrate Buffer (2 mL, 100 mM pH 5.5). Then, 50 μL of the resultant clear solution was mixed with 1500 μL of Bradford solution (Sigma-Aldrich, sample-to-Bradford ratio 1:30). The solution was left for 5 minutes at room temperature. Afterwards, this mixture was analyzed by UV-VIS (595 nm). All the experiments were performed in triplicates.

This overall amount of BSA part of the biocomposite was then compared to the amount of BSA obtained by the dissolution (0.1 M citric acid aqueous solution at pH 5.5) of the washed biocomposites. This was useful for the evaluation of the effect of the washing procedure on the surface-adsorbed protein. Only in the case of **am** (72%) and **U13** (76%) we noticed a significant difference (>5%) in the calculated EE%. These results excluded release of a significant amount of protein from the **sod**, **dia**, ZIF-C biocomposites particles once exposed to ethanol.

Evaluation of BSA-release profile

Release test was performed using cumulative release method. The samples were mixed with 1 mL Citrate Buffer (100 mM pH = 5.5, room temperature). The samples were shaken using an orbital mixer. At regular intervals, the mixture was vortexed for 3 s and centrifuged 1 min. Then, 50 μL of the supernatant was taken and replaced with the same volume of fresh Citrate buffer. Then, the 50 μL of the supernatant was mixed with 1500 μL of Bradford solution (Sigma-Aldrich, sample-to-Bradford ratio 1:30). The solution was

left for 5 minutes at room temperature. Afterwards, this mixture was analyzed by UV-VIS (595 nm). All the experiments were performed in triplicates.

Transmission electron microscopic (TEM) analysis.

Samples for transmission electron microscopy observation were dispersed in deionized water. A droplet of the suspension was transferred onto a carbon-coated copper grid for each sample. Observation was performed on a JEOL JEM2100 microscope, and operated at 200 kV (Cs 1.0 mm, point resolution 0.23 nm). Images were recorded with a Gatan Orius 833 CCD camera (resolution 2048 x 2048 pixels, pixel size 7.4 μm) under low dose conditions. Electron diffraction patterns were recorded with a Timepix pixel detector QTPX-262k (512 x 512 pixels, pixel size 55 μm , Amsterdam Sci. Ins.).

Continuous Rotation electron diffraction (cRED) collection.

The data were collected using the software Instamatic1-3. A single-tilt holder was used for the data collection, which could tilt from -60° to $+60^\circ$ in the TEM. The area used for cRED data collection was about 1.0 μm in diameter. The speed of goniometer tilt was $0.45^\circ \text{ s}^{-1}$. The exposure time was 0.5 s per frame. Data was collected at room temperature within 4 min. The covered tilt angle was 93.91° .

As shown in the Inset of Figure S2, the size of the crystal is in the range of nanometers. Due to the tiny crystal size, the structural determination was conducted using cRED data. Figure S2 shows the reconstructed 3D reciprocal lattices from the cRED data. Unit cell parameters were determined to be $a = 10.3 \text{ \AA}$, $b = 12.5 \text{ \AA}$, $c = 4.7 \text{ \AA}$, $\alpha = 88.9^\circ$, $\beta = 89.6^\circ$, and $\gamma = 89.6^\circ$. As the lattice parameters α , β and γ are near 90° , it indicates that the possible crystal system could be orthorhombic. From 3D projections and two-dimensional (2D) slice cuts of the 3D reciprocal lattice at $0kl$, $hk0$ and $h0l$ planes (Figure 2a, main text), the reflection conditions are $0kl: k=2n$, $h0l: h=2n$, $h00: h=2n$, and $0k0: k=2n$. Thus, the possible space groups are $Pba2$ (No. 32), and $Pbam$ (No. 55). The space group $Pba2$ was chosen for further structural determination. These results are summarized in Table S4.

We investigated also the **U13** sample with cRED. However, in case of **U13**, the limited crystallinity of the sample (only 1 broad peak at 6.6°) does not allow for the identification of the unit cell.

Table S1: List of the synthesized samples for each Ternary Diagram, together with the details about the weight percentages of the different components and the ligand/metal weight and molar ratios in the starting solution mixture.

SAMPLE #	Weight Percentage (%)			Ligand/Metal	Ligand/Metal
	Zn(OAc) ₂ ·2(H ₂ O)	HmIM	BSA	weight ratio	molar ratio
1	10	10	80	1.00	2.70
2	20	10	70	0.50	1.35
3	30	10	60	0.33	0.90
4	40	10	50	0.25	0.68
5	50	10	40	0.20	0.54
6	60	10	30	0.17	0.45
7	70	10	20	0.14	0.39
8	10	20	70	2.00	5.30
9	20	20	60	1.00	2.65
10	30	20	50	0.67	1.77
11	40	20	40	0.50	1.33
12	50	20	30	0.40	1.06
13	60	20	20	0.33	0.88
14	70	20	10	0.29	0.76
15	10	30	60	3.00	8.00
16	20	30	50	1.50	4.00
17	30	30	40	1.00	2.67
18	40	30	30	0.75	2.00
19	50	30	20	0.60	1.60
20	60	30	10	0.50	1.33
21	10	40	50	4.00	10.70
22	20	40	40	2.00	5.35
23	30	40	30	1.33	3.57
24	40	40	20	1.00	2.68
25	50	40	10	0.80	2.14
26	10	50	40	5.00	13.30
27	20	50	30	2.50	6.65
28	30	50	20	1.67	4.43
29	40	50	10	1.25	3.33
30	10	60	30	6.00	16.00
31	20	60	20	3.00	8.00
32	30	60	10	2.00	5.33
33	10	70	20	7.00	18.70
34	20	70	10	3.50	9.35
35	10	80	10	8.00	21.30
36	80	10	10	0.13	0.34

Table S2: List of the weight % of the different phases calculated from the diffraction patterns of the samples of the TD-H₂O. The data were analyzed using the “ZIF phase analysis” application. The rows highlighted in gray represent amorphous samples.

TD-H ₂ O	Weight Percentage (%)					
	SAMPLE #	sod	dia	ZIF-C	U13	U12
	1					
	2					
	3					
	4					
	5					
	6					
	7					
	8					
	9					
	10					
	11					
	12					
	13				100	
	14				100	
	15					
	16			100		
	17			100		
	18					
	19					
	20				100	
	21			100		
	22			100		
	23			100		
	24			100		
	25			40		60
	26			100		
	27			100		
	28			100		
	29			100		
	30			100		
	31			100		
	32		89	11		
	33			100		
	34			100		
	35			100		
	36					

Table S3: List of the weight % of the different phases calculated from the diffraction patterns of the samples of the TD-EtOH. The data were analyzed using the "ZIF phase analysis" application. The rows highlighted in gray represent amorphous samples.

TD-EtOH SAMPLE #	Weight Percentage (%)				
	sod	dia	ZIF-C	U13	U12
1					
2					
3					
4					
5					
6					
7					
8					
9					
10					
11					
12					
13					
14					
15					
16	31		69		
17	5		95		
18					
19					
20					
21	59		41		
22	100				
23	97		3		
24	100				
25	28		21		51
26	100				
27	87		11		
28	92		8		
29	100				
30	100				
31	100				
32		100			
33	100				
34	100				
35	100				
36					

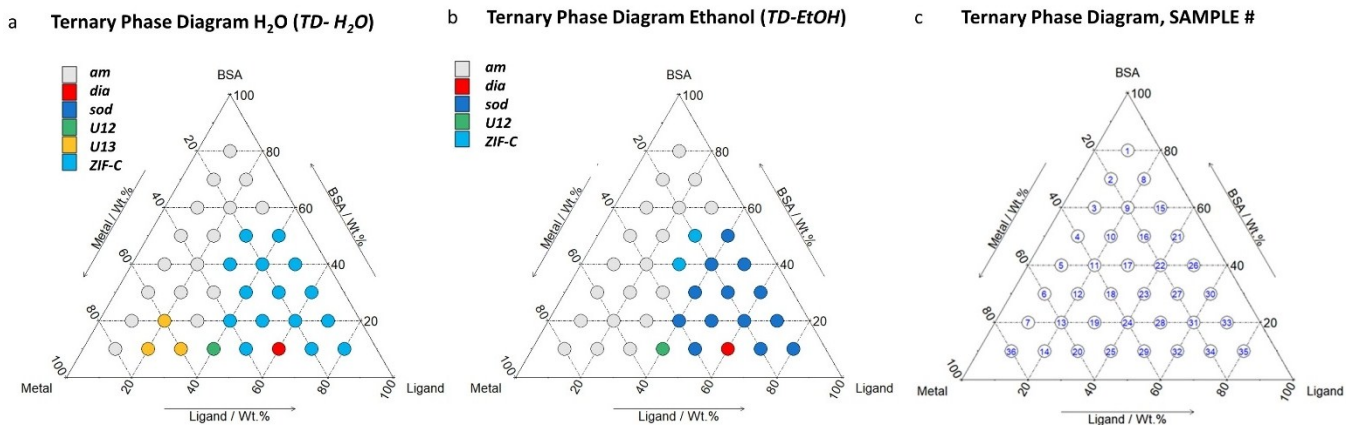


Figure S1: Ternary diagrams (TD, by weight fraction) of BSA, HmIM (labelled as Ligand) and $Zn(OAc)_2 \cdot 2(H_2O)$ (labelled as Metal) with the 36 investigated points. The colour of the points of TD- H_2O (a) represents the main phases obtained by washing the sample with DI water. The colour of the points of TD-EtOH (b) represents the main phases obtained by washing the sample first with DI water and then with ethanol. The TD in (c) highlights the sample # reported in Table S1, S2 and S3. For further details, see Tables S1, S2 and S3.

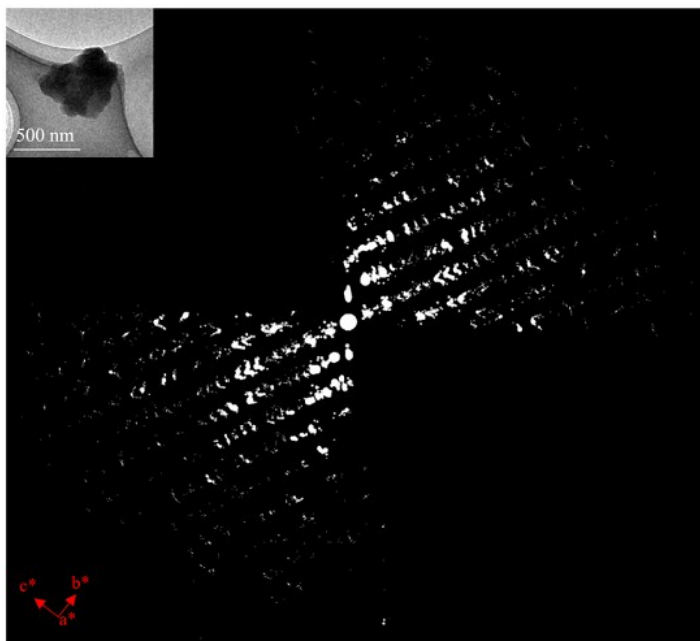


Figure S2: The Reconstructed 3D reciprocal lattice from the cRED data. The TEM micrograph of the investigated crystal is shown as an inset.

Table S4: Experimental parameters for cRED data collection and crystallographic data.

Tilt range (°)	-53.60° to 40.31°
Tilt rate (°/s)	0.45
Chemical formula	C ₉ H ₁₀ N ₄ O ₃ Zn ₂
Z	2
Exposure time/frame (s)	0.5
Total number of frames	365
Data collection time (min)	3.46
Completeness (%)	0.766

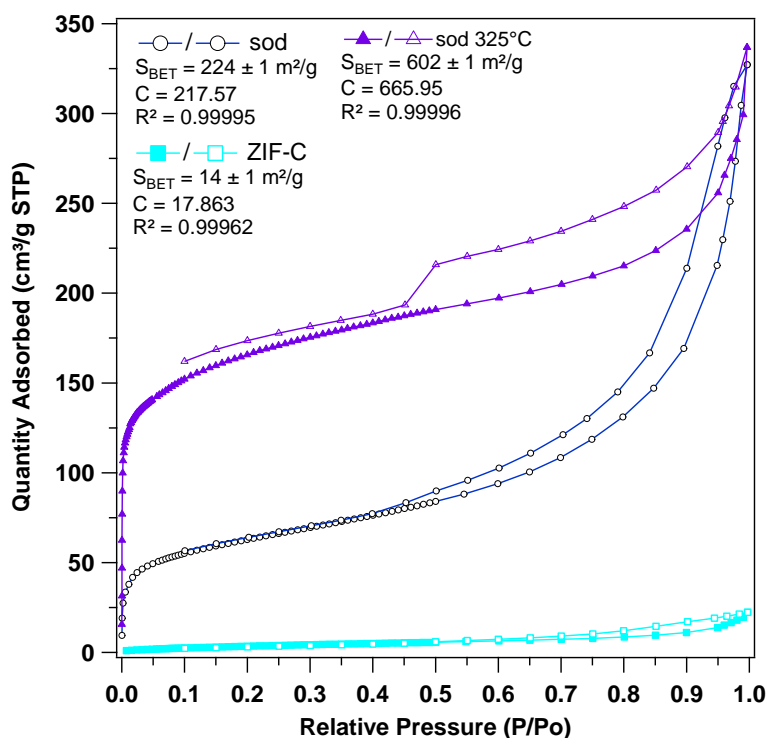


Figure S3: N₂ 77K isotherms of the ZIF-C biocomposite (Sample #29 of Table S1), the sod biocomposite obtained by washing with ethanol the ZIF-C sample and the sod biocomposite treated at 325°C for 2h. To confirm that ZIF-C obtained in presence of BSA, we characterized this sample with nitrogen adsorption and desorption experiments at 77 K (Fig SX, ESI[†]). The calculated BET surface area was 14 m²/g, confirming that ZIF-C is a non-porous material, similarly to U12, U13 and dia-Zn(mIM)₂.ⁱ Motivated by the phase transition triggered by ethanol washes, the sample originally prepared as ZIF-C and then transformed into sod was investigated with the same N₂ physisorption setup. The N₂ sorption profiles and the calculated BET surface areas confirmed the presence of permanent microporosity (BET surface area: 224 m²/g). We exposed the sample to thermal treatment to decompose the encapsulated BSA (325°C, 2h). In this case, the measured surface area was raised to 602 m²/g indicating the gravimetric contribution of the protein prior thermal decomposition.

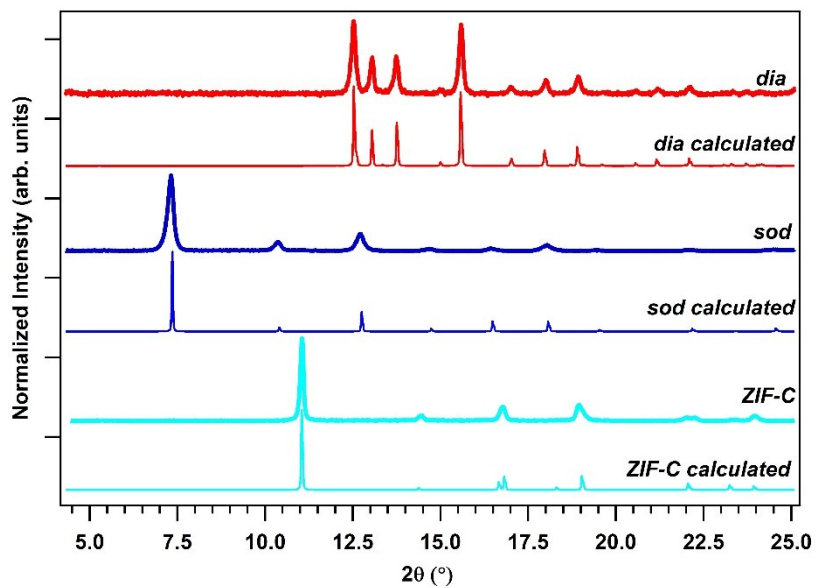


Figure S4: XRD patterns of *dia*, *sod* and ZIF-C biocomposites and of the calculated pure MOFs.

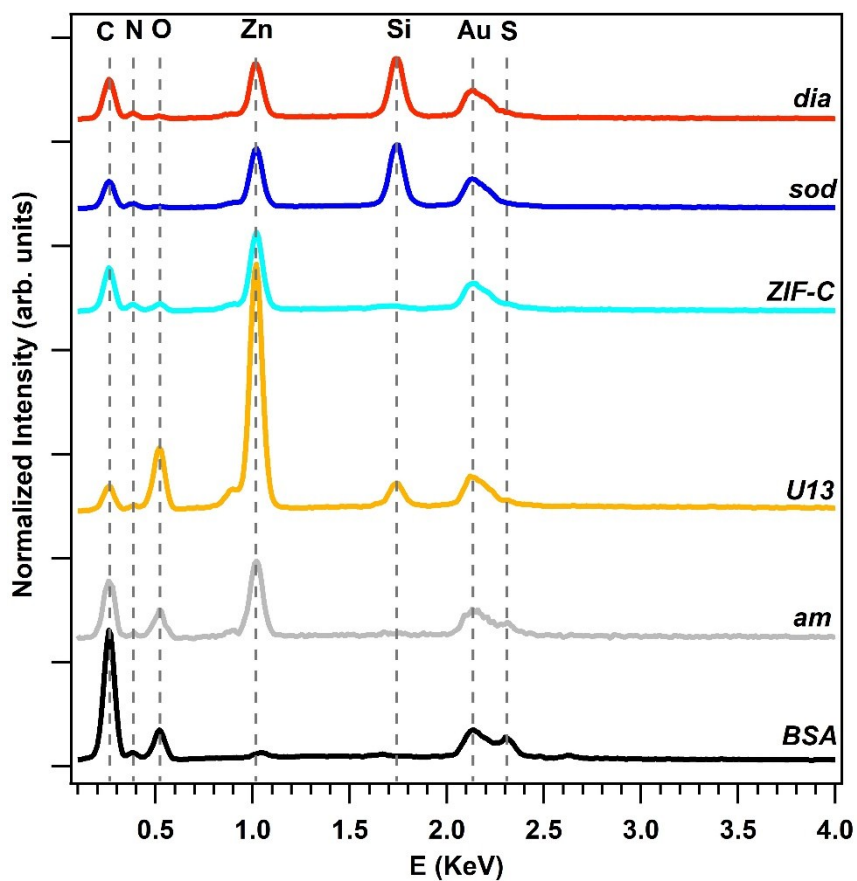


Figure S5: EDX spectra of patterns of BSA, of the amorphous biocomposite and of the biocomposites with *dia*, *sod*, ZIF-C, and U13 topology.

Table S5: Atomic % calculated from EXD spectra. The contribution from Au (coating) and Si (substrate) was not considered. For BSA, the remaining 2% was due to Na, Cl and S.

	BSA	am	U13	U15	sod	dia
C	61%	53%	40%	59%	66%	64%
N	16%	9%	6%	25%	24%	27%
Zn	0%	15%	18%	6%	5%	5%
O	21%	23%	36%	10%	4%	5%

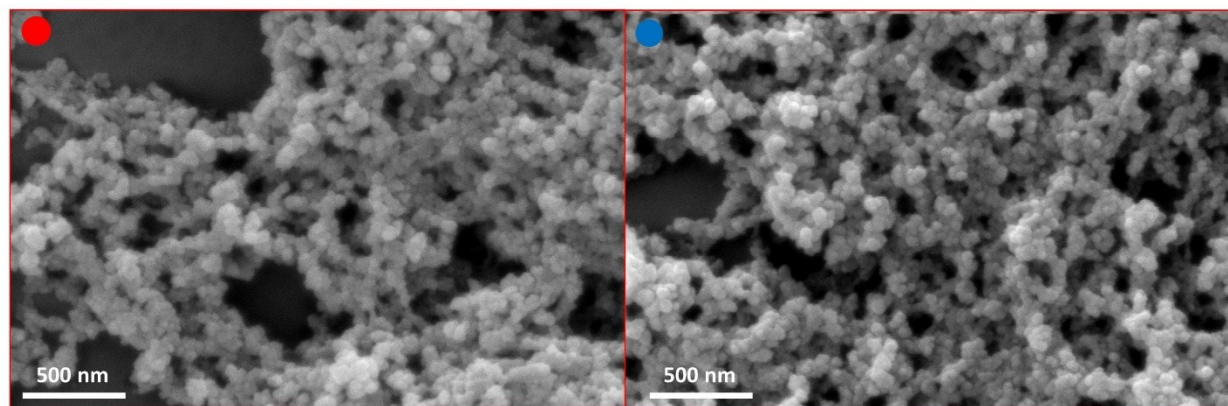


Figure S6: SEM micrographs of the dia (left) and sod(right) samples obtained by washing the samples with ethanol (TD-EtOH).

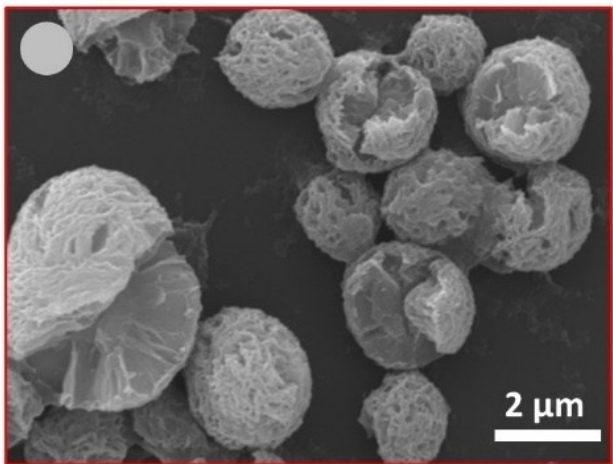


Figure S7: SEM micrograph of the am sample obtained by washing with ethanol the U13 sample.

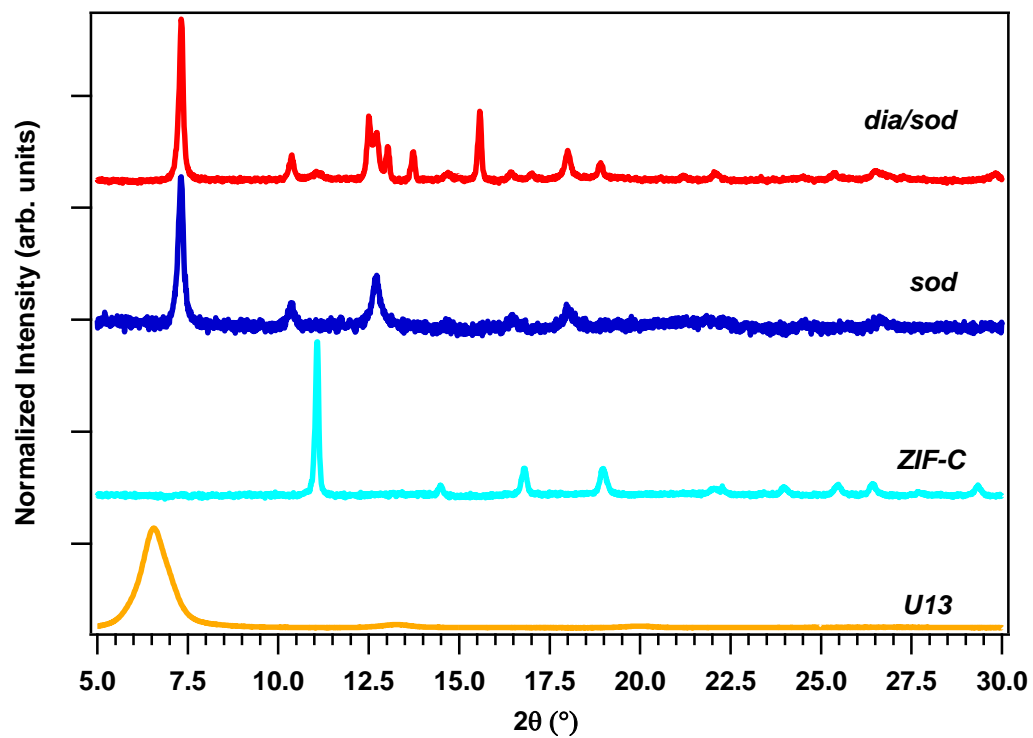
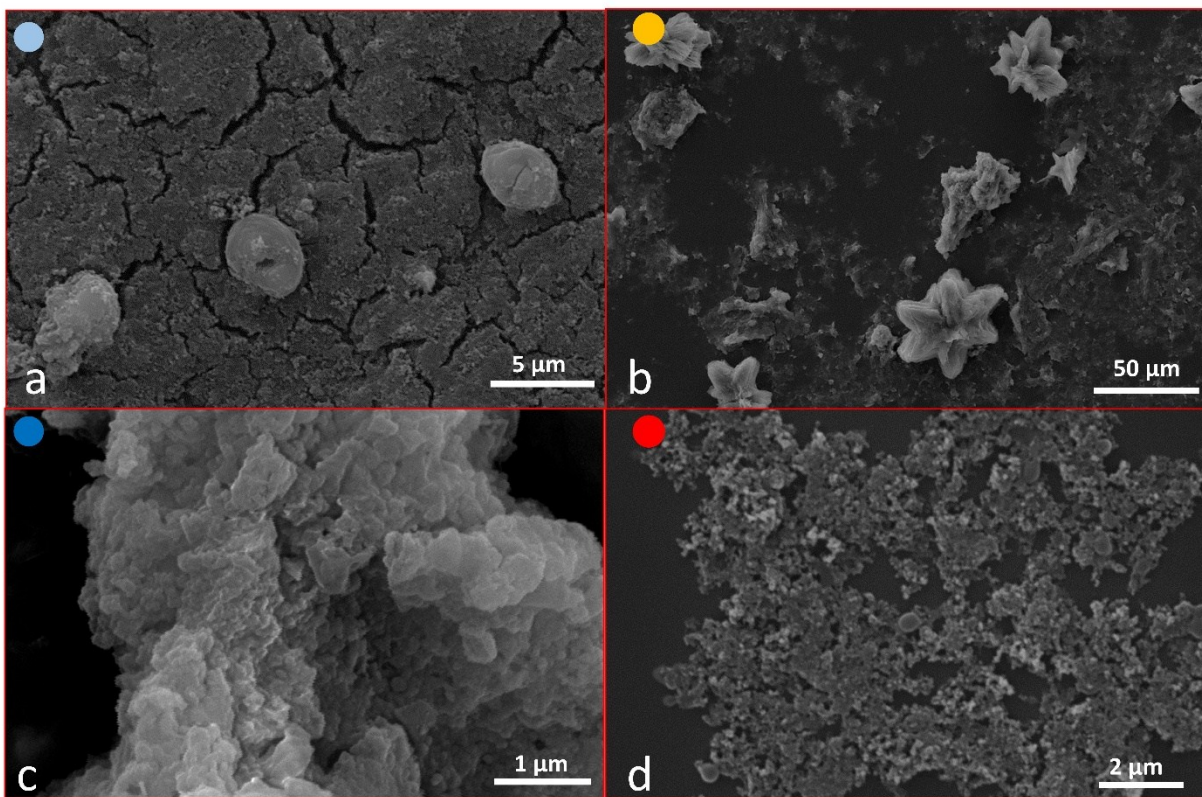


Figure S8: XRD patterns of the different phases of the Insulin biocomposites.



● ZIF-C ● U13 ● sod ● dia

Figure S9: SEM micrographs of the insulin biocomposites with ZIF-C (a, from TD-H₂O), U13 (b, from TD-H₂O), sod (c, from TD-EtOH) and dia (d, from TD-EtOH) phases.

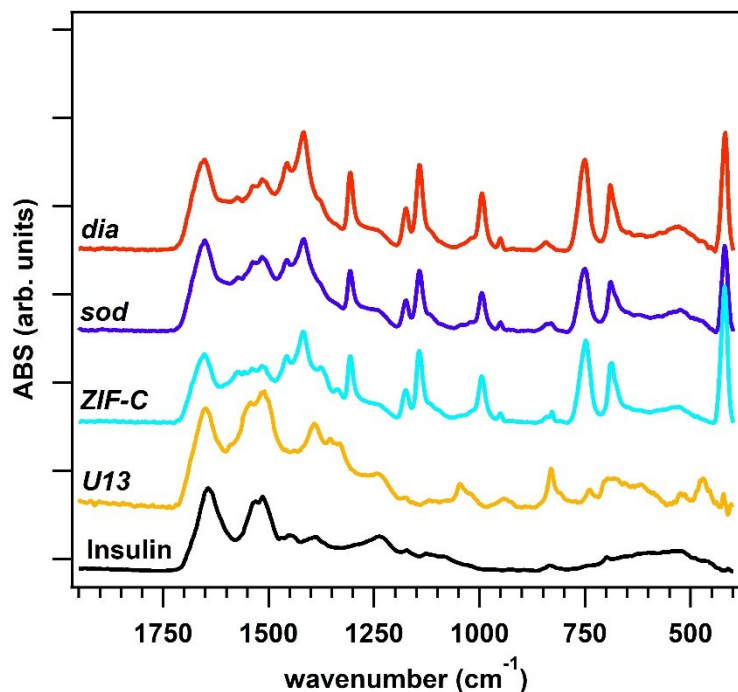


Figure S10: FTIR spectra of insulin and of the insulin-based biocomposites with dia, sod, U13 and ZIF-C phases. The analysis of the FTIR data confirms the presence of characteristic modes of the peptide backbone of insulin such as the Amide I ($1700-1610\text{ cm}^{-1}$) and Amide II ($1595-1480\text{ cm}^{-1}$) bands in all the examined polymorphs. As in the case of BSA@U13, the spectrum of insulin@U13 did not show vibrational modes that could be attributed to the imidazolate ligand and to the Zn–N bond. For insulin encapsulated in sod, dia and ZIF-C we detected several vibrational modes ($420, 690, 752, 998, 1145, 1175, 1308, 1419, 1458, 1580\text{ cm}^{-1}$) typically observed for sod-Zn(mIM)₂. Moreover, it is possible to identify the ZIF-C additional bands in the $700-850$ and $1300-1400\text{ cm}^{-1}$ regions, assigned to weak bending and asymmetric stretching modes of CO₃²⁻.

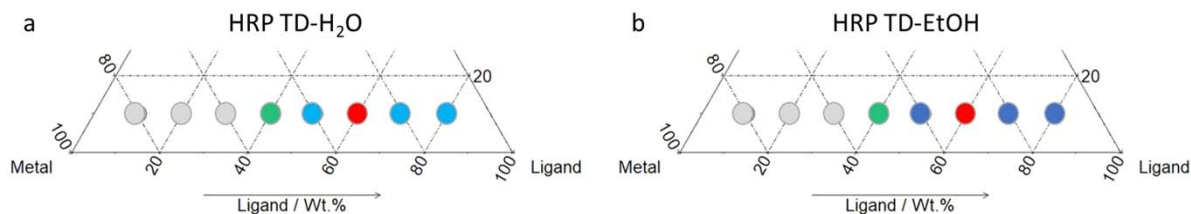


Figure S11: Investigated section of the HRP-based biocomposites ternary diagram (HRP wt%= 10%) of water (a) or ethanol (b) washed samples highlighting the obtained crystal phases (grey spot: amorphous biocomposite; azure: ZIF-C; blue: sod; red: dia; green: U12). We prepared the samples according to the protocols used to prepare the BSA biocomposites with an initial wt% of protein of 10%. According to the XRD results, we obtained am, U12, ZIF-C and sod biocomposites. U12 is obtained always in combination with ZIF-C (for the water washed samples) or ZIF-C and sod (for the ethanol washed samples) In general, the HRP samples followed the results obtained for BSA samples.

The “ZIF phase analysis“ application – Version 1.0.0

“ZIF phase analysis“ is an interactive web application built using Rⁱⁱⁱ 3.5.3, RStudio^{iv} 1.1.463 and the packages *shiny*^v, *shinydashboard*^{vi}, and *shinyalert*^{vii}. The application is hosted at the Technical University of Graz and deployed on-premises using Shiny-Server.

The application is open worldwide and can be accessed with no restrictions via the URL <https://rapps.tugraz.at/apps/porousbiotech/ZIFphaseanalysis/>. A user can upload his/her own data file consisting of the diffraction pattern obtained via X-ray measurement of powders. The application processes the uploaded data file and returns the ZIF phase(s) identified in the investigated diffraction pattern.

The “ZIF phase analysis“ application comprises of the “Data“ tab and the “Analysis“ tab, both listed in the black sidebar on the left of the screen. The “Data“ tab is used to upload the data, whereas the “Analysis“ tab is used to perform the analysis and present the results.

The following sections provide details about i) accepted data file format, ii) use of the application for data upload and analysis, and iii) underlying statistical analysis.

Accepted data file format

The data file must consist of a first column indicating the angle 2θ in degrees ($^{\circ}$) and a second column indicating the intensity (e.g. photon counts or photons/second). Columns headers are accepted; however, any other line of text must be removed from the data file. Various file formats (e.g. .txt, .dat) and column/decimal separators are accepted; additional details are reported in the section “Data file upload“. An example of accepted data file format is shown in **Figure S10**.

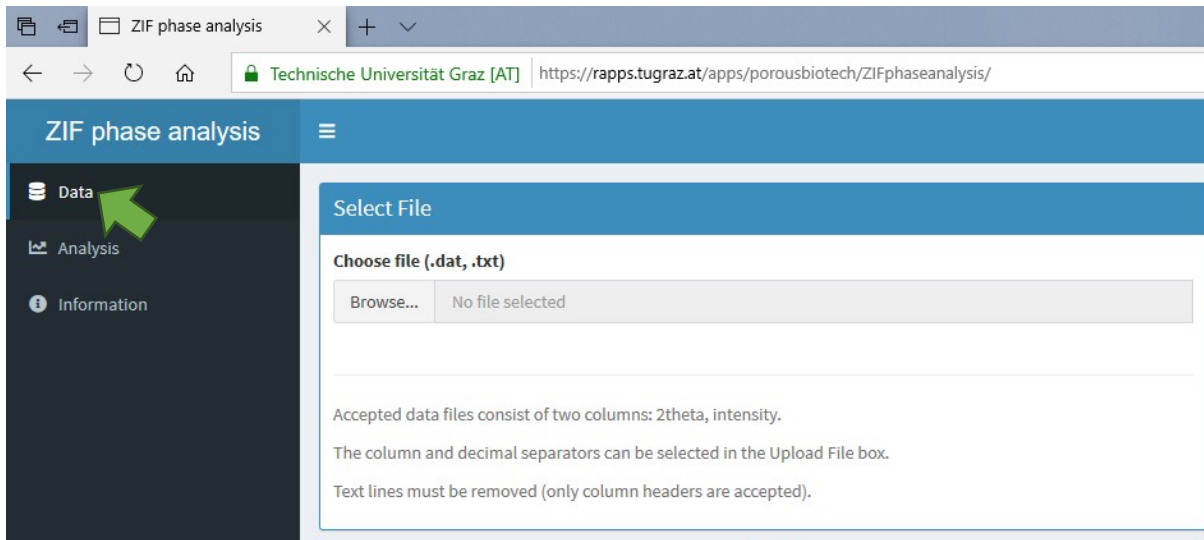


```
32W - Editor
Datei Bearbeiten Format Ansicht Hilfe
2.000 3532
2.013 3556
2.026 3401
2.040 3360
2.053 3234
2.066 3197
2.079 3176
2.093 3244
2.106 3153
2.119 3039
2.132 3078
2.146 2990
2.159 2956
```

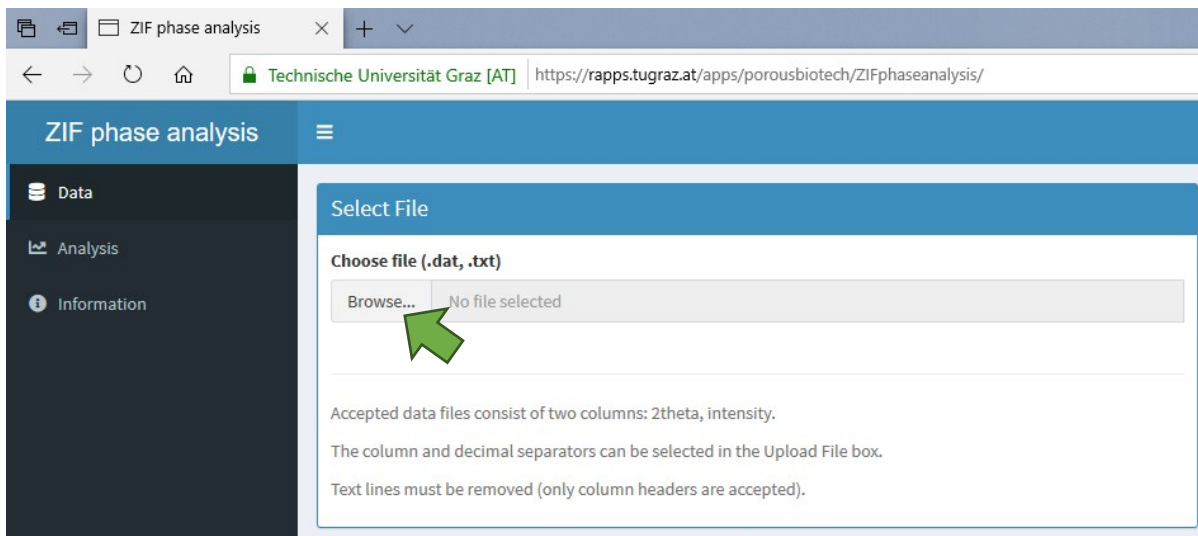
Figure S12. Example of accepted data file. The file is named “32W.dat“. It has no header (i.e. column title) and comprises of two columns of numeric values indicating 2θ angles (first column) at which the intensity (second column) is measured. The columns are separated by a white space (column separator). A point decimal separator is used.

Data file upload

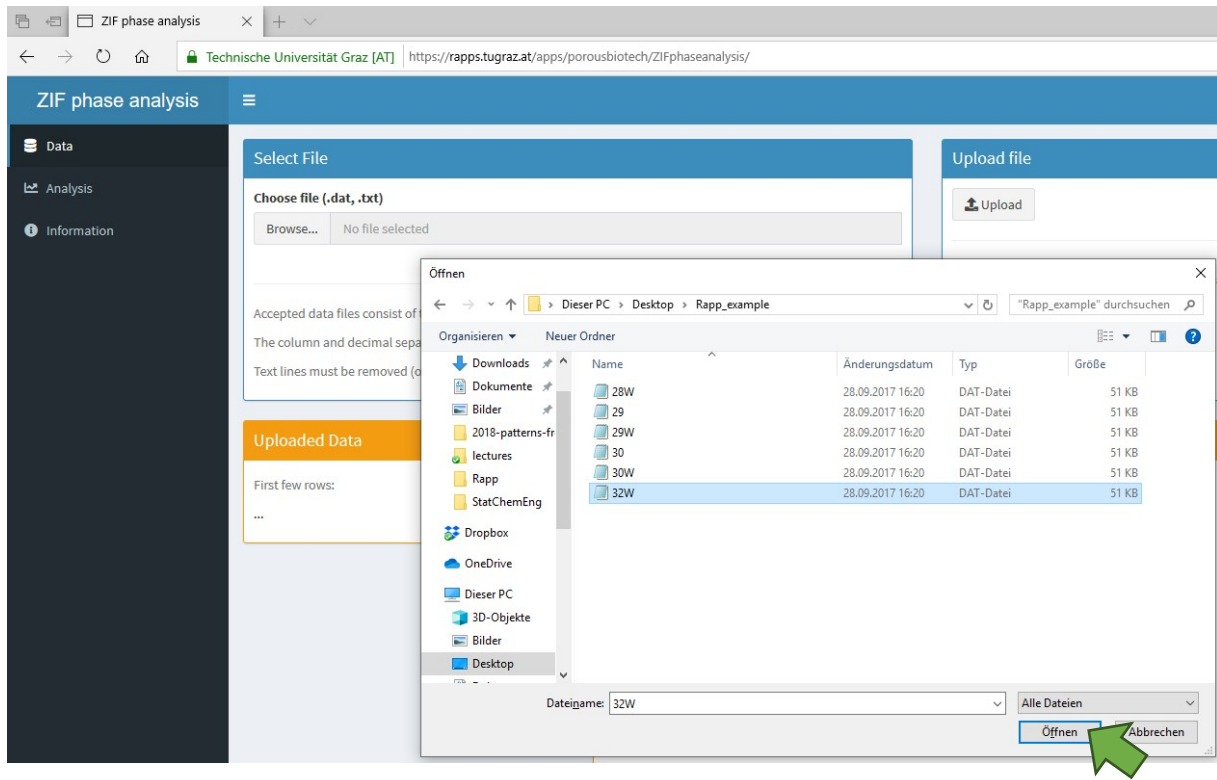
To visualize the content of the “Data” tab, click on “Data” in the sidebar (top left of screen).



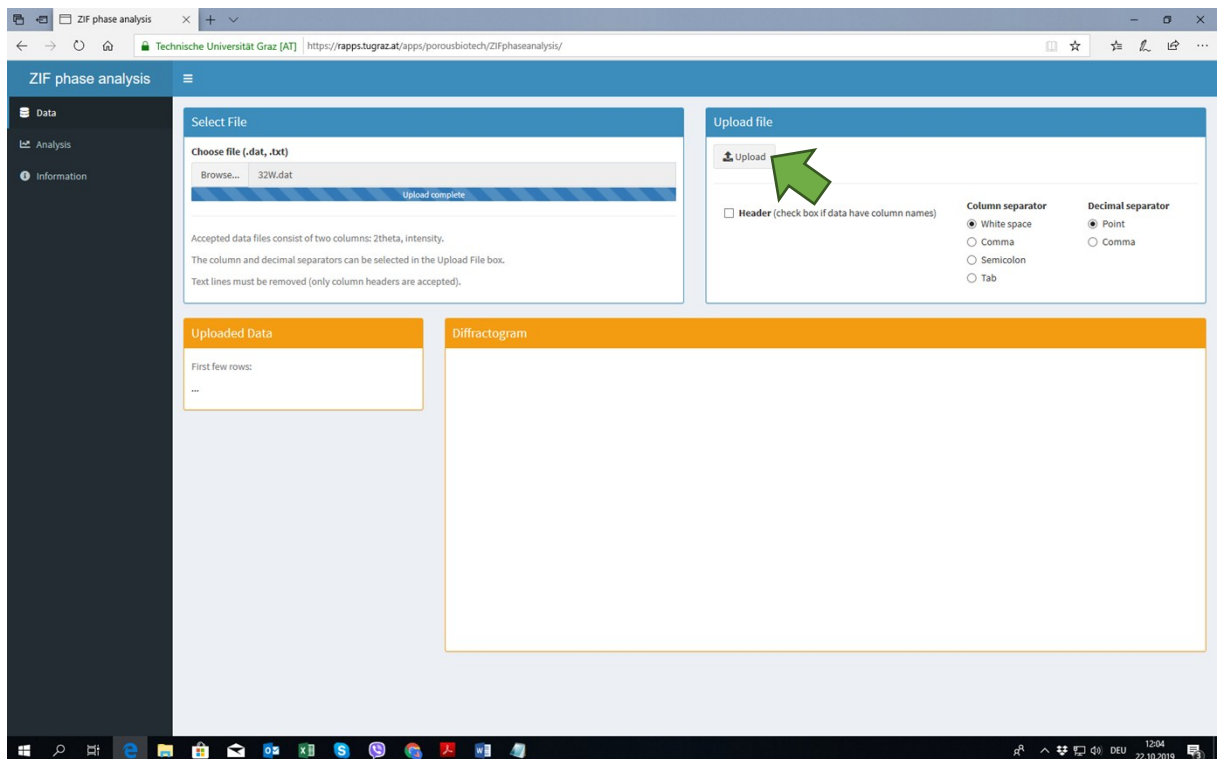
In the “Select File” box click on the “Browse” button and choose the data file to be analysed.



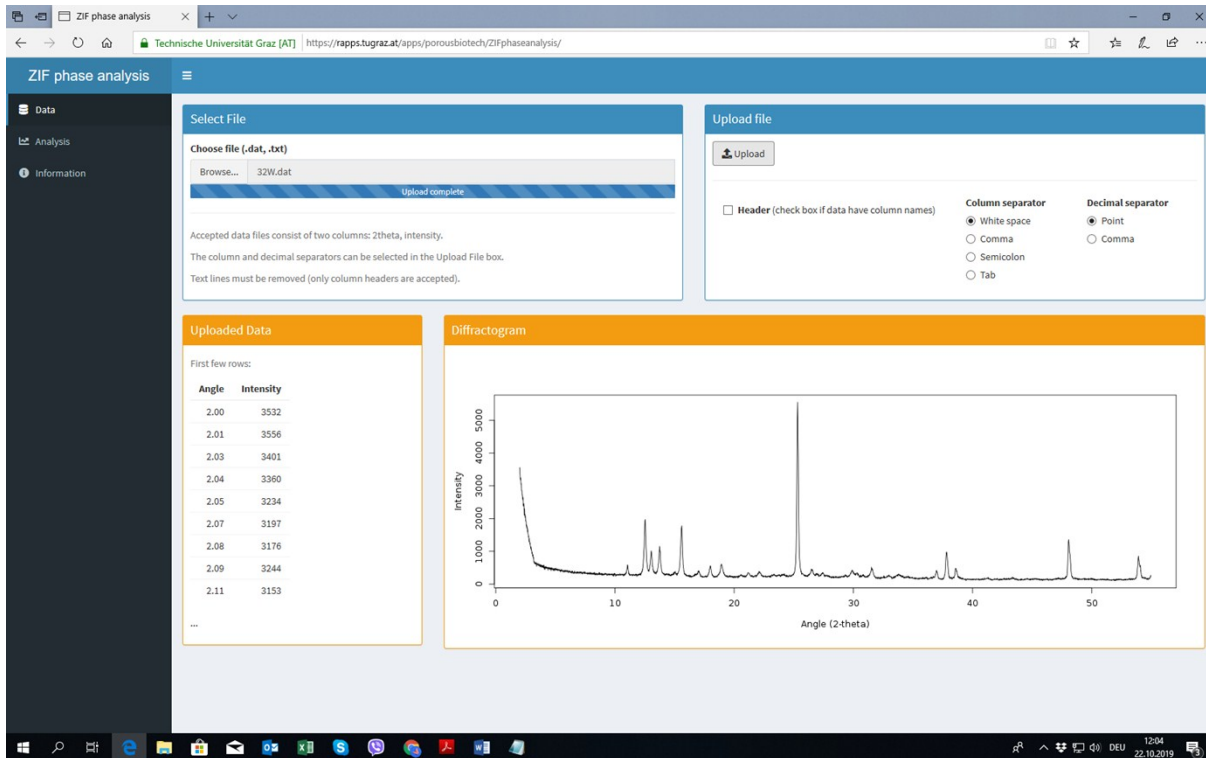
Click “Open” to confirm.



In the “Upload File” box, click on the header check box if column headers are present (default: no header). Then, choose the column separator (default: white space) and the decimal separator (default: point) used in the data file. Finally, click on the “Upload” bottom.



The application runs a series of checks on the file format. In case of problems an error message is returned along with a hint on how to fix the problem. Otherwise, the application visualizes the first few rows of the data file in the “Uploaded Data” box and the diffraction pattern in the “Diffractiongram” box.



The screenshot shows the ZIF phase analysis web application interface. The browser address bar indicates the URL is <https://rapps.tugraz.at/apps/porousbiotech/ZIFphaseanalysis/>. The application has a dark sidebar with navigation options: Data, Analysis, and Information.

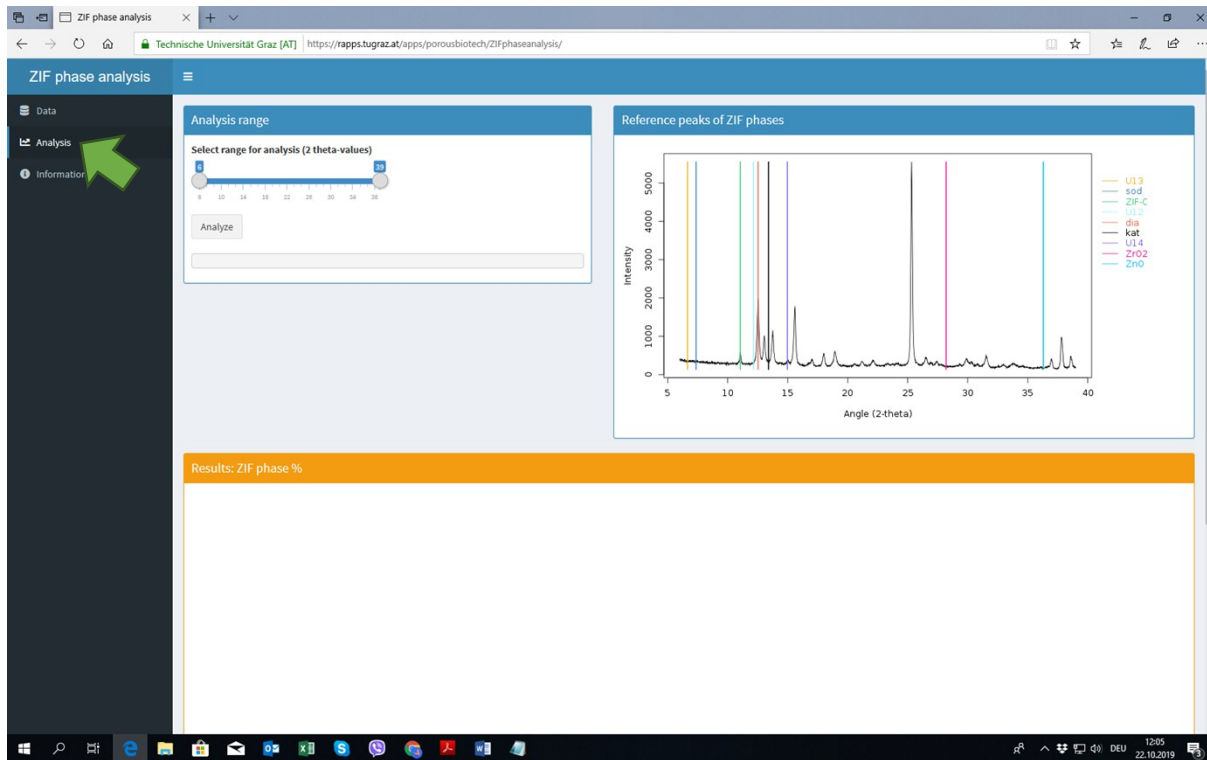
The main content area is divided into four sections:

- Select File:** Shows a file named "32W.dat" has been uploaded. Below the file list, it states: "Accepted data files consist of two columns: 2theta, intensity. The column and decimal separators can be selected in the Upload File box. Text lines must be removed (only column headers are accepted)." There is an "Upload complete" button.
- Upload file:** Contains an "Upload" button and configuration options:
 - Header (check box if data have column names)
 - Column separator:** White space, Comma, Semicolon, Tab
 - Decimal separator:** Point, Comma
- Uploaded Data:** Displays the first few rows of the data file in a table:

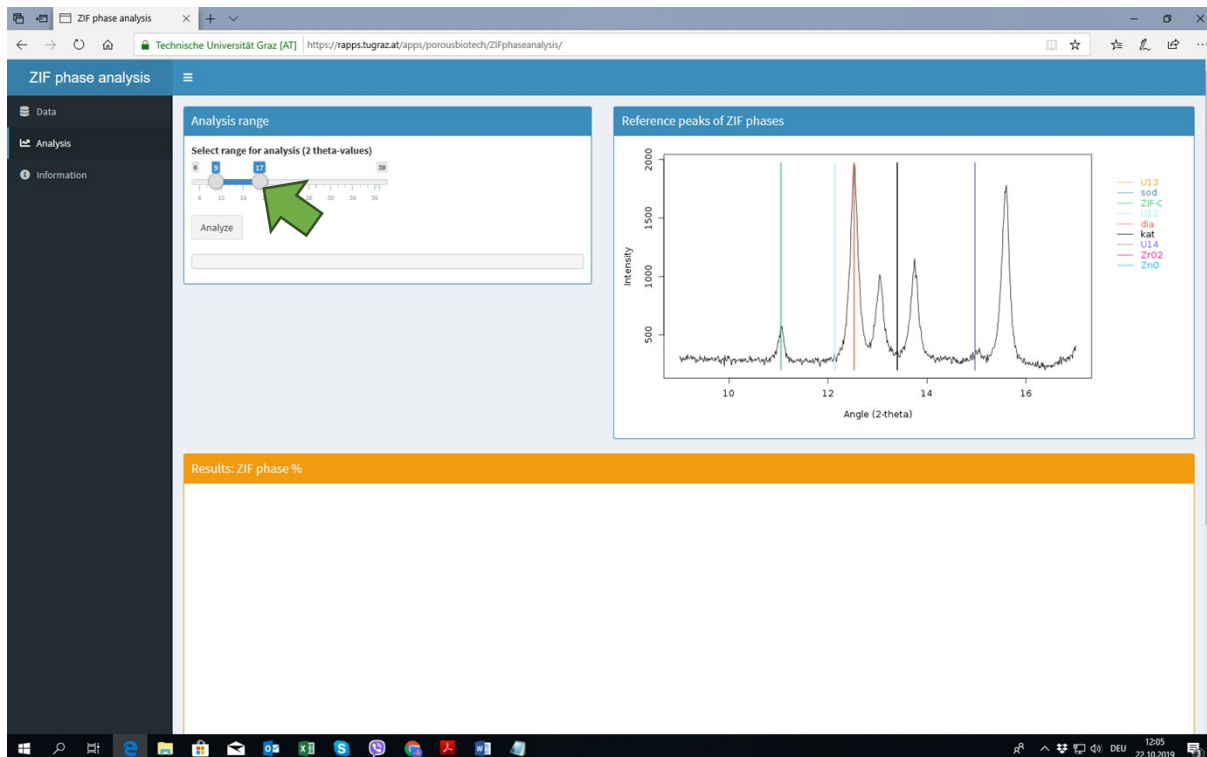
Angle	Intensity
2.00	3532
2.01	3556
2.03	3401
2.04	3360
2.05	3234
2.07	3197
2.08	3176
2.09	3244
2.11	3153
...	...
- Diffractiongram:** Shows a plot of Intensity versus Angle (2-theta). The x-axis ranges from 0 to 50, and the y-axis ranges from 0 to 5000. The plot displays a series of peaks, with the most prominent peak at approximately 2.0 degrees.

Data file analysis

To visualize the content of the “Analysis” tab, click on “Analysis” in the sidebar (top left of screen).

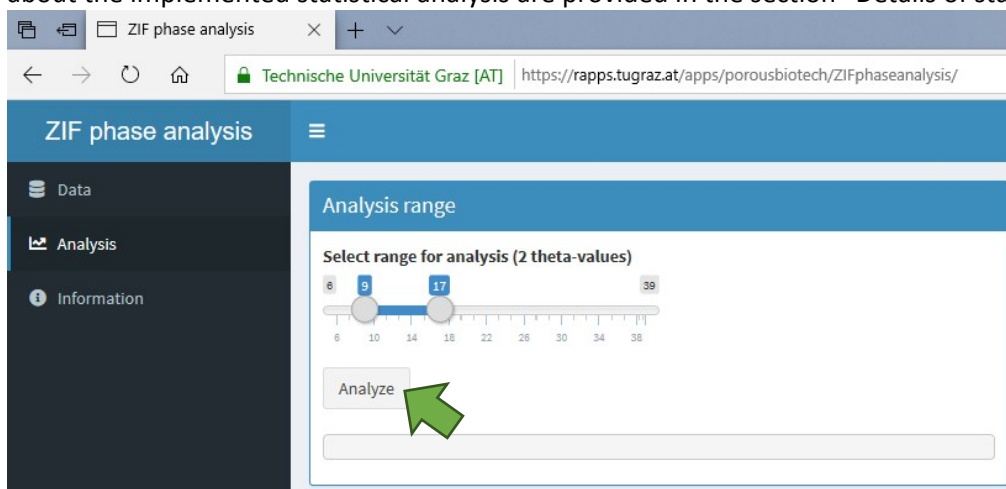


In the “Analysis range” box it is possible to select the range of 2θ values (default: 6-39) to investigate. The range of 2θ values can be varied by dragging the grey circles in the sidebar.

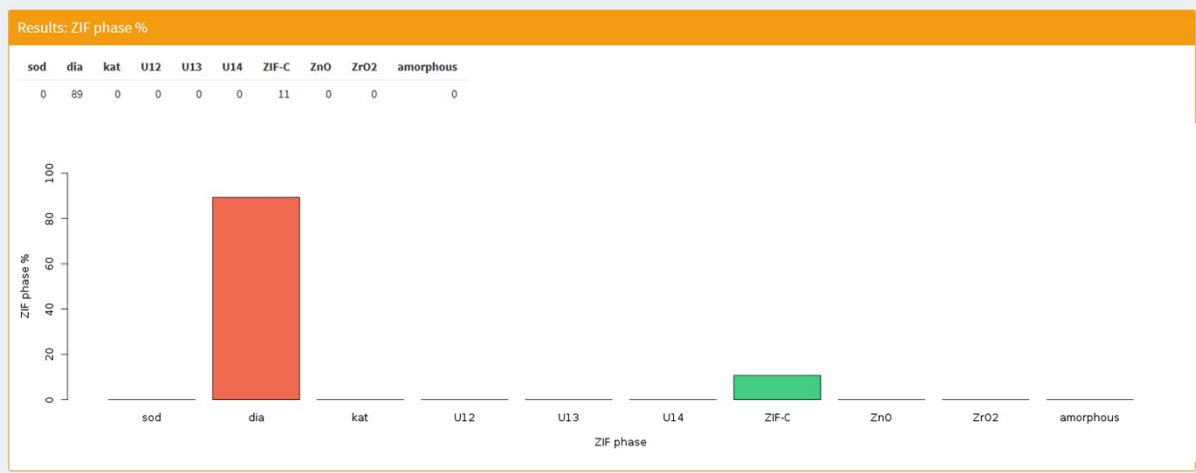


The box “Reference peaks of ZIF phases” (top right of screen) depicts the diffraction pattern in the desired analysis range. It highlights the reference peaks used for the identification of the ZIF phases, thus providing a preliminary idea of the phase(s) that are present in the analyzed pattern.

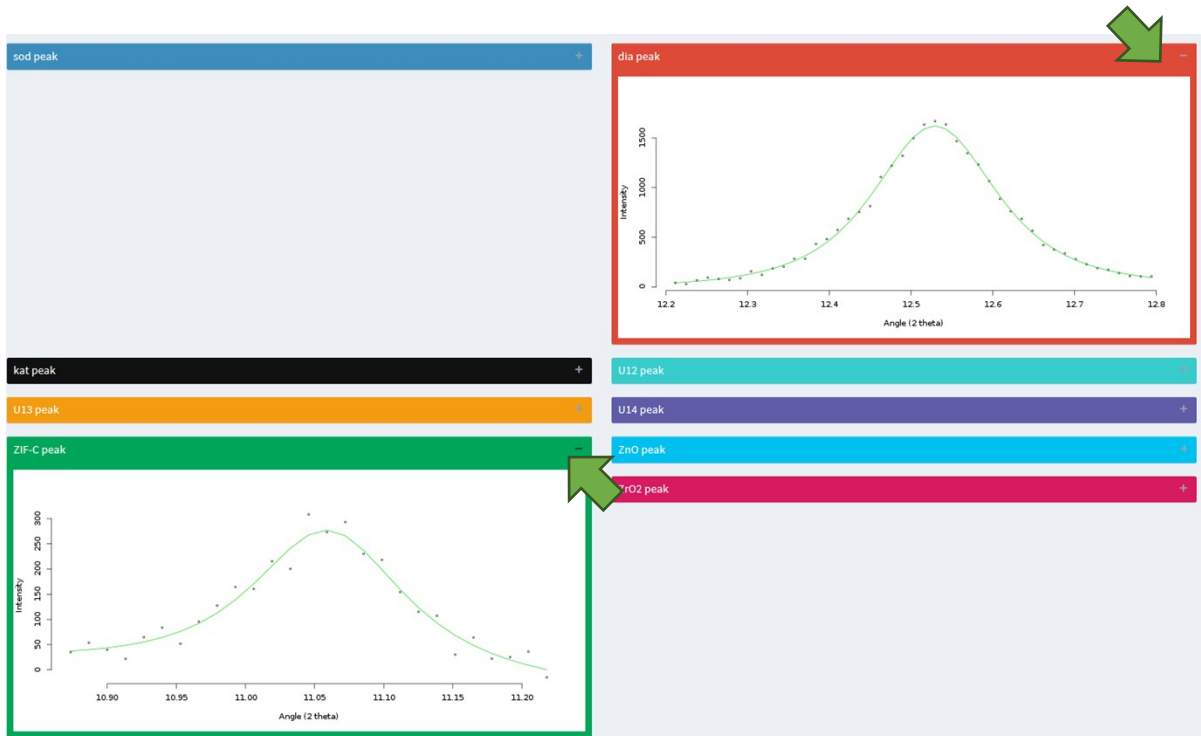
To proceed with the analysis, click on the “Analyze” button in the “Analysis range” box. As the analysis progresses the current step is listed; an alert message appears when the analysis is completed. Details about the implemented statistical analysis are provided in the section “Details of statistical analysis”.



The box “Results: ZIF phase %” shows the analysis output reporting the identified ZIF phases and their relative intensity. The percentage values of the identified ZIF phases are summarized in a table and visualized in a bar plot.



Finally, a series of collapsed boxes depict the estimates of the peaks associated to the identified ZIF phases. To visualize a specific peak estimate, the user must uncollapse the box by clicking on the “+” sign on the right-hand side of the box.



Details of statistical analysis

The statistical analysis of the diffraction pattern is implemented through a customized algorithm consisting of the following main steps:

1. estimate the peaks present in the diffraction pattern;
2. select peaks associated to the ZIF phase(s) of interest;
3. quantify the relative integrated intensity of the identified ZIF phase(s).

1. Peaks estimation

The algorithm makes use of the R package *diffraction*^{viii} to decompose the diffractogram data into baseline, peaks and noise components.^{ix} Firstly, the `baselinefit` function is used to identify the approximate peaks positions and the baseline. Secondly, the `pkdecomp` function is used to obtain accurate estimates of the peaks after baseline subtraction.

Both functions depend on a set of parameters. The first set of parameters regulates the desired accuracy of the peaks approximation; these parameters are set to their default values (i.e. $\tau = 2.5$, $\text{scl.factor} = 2$, $\alpha = 0.1$). The second set of parameters regulates the characteristics of the estimated peaks; these parameters are adjusted using information from diffraction patterns of in-house samples. In particular, we set the maximum peak width to $\text{maxwidth} = 1$ as no peak wider than one was observed. We increase the value of the parameter regulating the baseline-peak separation from its default value $\text{gam} = 1$ to $\text{gam} = 5$, as this allows us to identify the peak at 6.65 degrees corresponding to the U13 phase (when using the default value, such a peak was considered to be part of the baseline component). Finally, we reduce the values of the parameters related to the maximum number of attempts to find a good peak approximation ($\text{maxiter} = 100$; default is 10 000) and the number of searched solutions ($\text{maxsolutions} = 1$; default is 3) as this reduces the computational cost of the procedure without affecting the results quality. The output is a list of all the identified peaks (N) carrying information about the estimated peaks position and intensity.

2. Peaks selection

Not all the N identified peaks are of interest for the current study. The aim of the statistical analysis is to identify if a diffraction pattern presents one or more of the peaks in **Table 1**. The peaks in **Table 1** are expert-selected peaks (reference peaks) referring to five ZIF phases of interest (*sod*, *dia*, *kat*, *U14*, *ZIF-C*), the *U12* and *U13* phases and two references (ZnO, ZrO₂). Each ZIF phase has three to four reference peaks, one of which (highlighted in bold) is more intense than the others.

To identify the relevant peaks, the algorithm compares each of the N identified peaks with each peak in **Table 1** using a distance metric between peaks positions. The distance metric is defined by

$$D_{i,p,j} = \min_{i,p,j} |x_i - x_{p,j}^{ref}| \quad (1)$$

where:

- x_i is the 2θ value for the maximum estimated intensity of peak $i = 1, \dots, N$;
- $x_{p,j}^{ref}$ is the 2θ value of the j th reference peak for phase $p = \{sod, dia, kat, U12, U13, U14, ZIF-C, ZnO, ZrO2\}$, with $j = 1, \dots, 4$.

If

$$D_{i,p,j} < \tau \quad (2)$$

the i th peak is considered to correspond to the j th reference peak of phase p . Currently, the algorithm uses $\tau = 0.1$, as this provides with the highest correspondence between the ZIF phases identified with the algorithm and the ZIF phases identified using our expert knowledge. Those peaks for which condition (2) holds are selected.

3. ZIF phase quantification

The algorithm further selects only those peaks that correspond to the most intense reference peaks highlighted in bold in **Table 1**. Thus, at most one peak is retained per ZIF phase. We refer to these peaks as shortlisted peaks.

We quantify the magnitude of each shortlisted peak as the area under the peak approximation derived in step 1. *Peaks estimation*. To calculate the integral, we use the auc function of the R package MASS^x. Let A_p be the integral value calculated for the ZIF phase p and let RIR_p be the RIR factor^{xi} (**Table 1**) for phase p . We quantify the relative amount of an identified ZIF phase with the metric defined by

$$RI_p = \frac{(A_p/RIR_p)}{\sum_{k=1}^9 (A_k/RIR_k)} \quad (3)$$

Thus $0 \leq RI_p \leq 1$, with $RI_p = 0$ indicating that phase p is not present and $RI_p = 1$ indicating that p is the only phase present in the investigated sample. Values different from 0 or 1 indicate the presence of multiple phases in the same sample. Instead, if none of the selected phases is identified the algorithms assigns the Amorphous phase.

Phase	reference peaks (2θ , °)				RIR factor
	1	2	3	4	
sod	7,36	10,45	12,75	18,12	10,67
dia	12,53	13,05	13,76	15,57	1,614
kat	12,15	12,25	13,4	16,38	2,329
U12	12,18	18,43	24,46	24,7	1,614
U13	6,65	13,35	20		1,614
U14	9,61	13,98	14,97	17,94	1,614
ZIF-C	11,05	12,15	13,88	17,87	1,614
ZnO	31,8	34,4	36,3		4,875
ZrO ₂	28,2	31,5	34,2		4,7

Table S6. 2θ values and RIR factors of selected peaks used for the identification of five ZIF phases, biocomposites with U12 and U13 structure and two references (ZnO and ZrO₂). Each ZIF phase is identified by the presence of three to four selected peaks. The algorithm uses the most intense peak (highlighted in bold) to define if the associated phase is observed in the investigated diffraction pattern. The RIR factors are used in the quantification of the relative peaks integrated intensity. The RIR values for sod (CCDC 963856), dia (CCDC 783838), kat (CCDC 989593), ZnO (COD 9004179) and ZrO₂ (COD 9007485) were obtained from CIF files reported in crystallographic databases (CCDC: Cambridge Crystallographic Data Centre; COD: Crystallographic Open Database). Due to the non-porous nature of U12, U13, U14 and ZIF-C, the RIR factors were assumed to be the same as dia.

References

- ⁱ W. Liang, R. Ricco, N. K. Maddigan, R. P. Dickinson, H. Xu, Q. Li, C. J. Sumby, S. G. Bell, P. Falcaro and C. J. Doonan, *Chem. Mater.*, 2018, 30, 1069–1077.
- ⁱⁱ K. Liang, R. Ricco, C. M. Doherty, M. J. Styles, S. Bell, N. Kirby, S. Mudie, D. Haylock, A. J. Hill, C. J. Doonan and P. Falcaro, *Nat. Commun.*, 2015, 6, Article number: 7240
- ⁱⁱⁱ R Core Team (2019). R: A language and environment for statistical computing. R Foundation for Statistical Computing, Vienna, Austria. URL <https://www.R-project.org/>
- ^{iv} RStudio Team (2016). RStudio: Integrated Development for R. RStudio, Inc., Boston, MA URL <http://www.rstudio.com/>
- ^v Winston Chang, Joe Cheng, JJ Allaire, Yihui Xie and Jonathan McPherson (2019). shiny: Web Application Framework for R. R package version 1.3.2. <https://CRAN.R-project.org/package=shiny>
- ^{vi} Winston Chang and Barbara Borges Ribeiro (2018). shinydashboard: Create Dashboards with 'Shiny'. R package version 0.7.1. <https://CRAN.R-project.org/package=shinydashboard>
- ^{vii} Dean Attali and Tristan Edwards (2018). shinyalert: Easily Create Pretty Popup Messages (Modals) in 'Shiny'. R package version 1.0. <https://CRAN.R-project.org/package=shinyalert>
- ^{viii} P.L. Davies, U. Gather, M. Meise, D. Mergel, T. Mildenerger. Additional Code by T. Bernholt and T. Hofmeister (2018). diffractometry: Baseline Identification and Peak Decomposition for x-Ray Diffractograms. R package version 0.1-10. <https://CRAN.R-project.org/package=diffractometry>
- ^{ix} P.L. Davies, U. Gather, M. Meise, D. Mergel, T. Mildenerger (2008): "Residual based localization and quantification of peaks in x-ray diffractograms", *Annals of Applied Statistics*, Vol. 2, No. 3, 861-886
- ^x Venables, W. N. & Ripley, B. D. (2002) *Modern Applied Statistics with S*. Fourth Edition. Springer, New York. ISBN 0-387-95457-0
- ^{xi} Hubbard, C., & Snyder, R. (1988). RIR - Measurement and Use in Quantitative XRD. *Powder Diffraction*, 3(2), 74-77. doi:10.1017/S0885715600013257

2.4 Towards applications of bioentities@MOFs in biomedicine

This literature review aims to fully understand the progress of MOFs and related biocomposites in biotechnology applications, as well as their current advantages and limitations. This review outlines the progress of major classes of biomacromolecules (proteins, carbohydrates, nucleic acids) and complex biological entities including viruses and cells incorporated in MOFs. Additionally, we discuss the post functionalization of MOF-based drug carriers with lipids as potential platforms to improve the biocompatibility and bioavailability of MOFs as DDS. Thus, we summarize the applications of such biocomposites in terms of drug delivery, biosensing, biospecimen preservation, and cell and virus manipulation.

Specifically, I designed and wrote the section that describes the integration of carbohydrates with MOFs (section 4. Carbohydrates and MOFs as DDS). The application of MOFs for the delivery of CH-based therapeutics is addressed in-depth in section 4.1. Additionally, recent applications of CHs as coatings for MOF-based DDS are included in subsection 4.2. Finally, in the last subsection, the function of carbohydrates in living cells the encapsulation process is described in detail.



Contents lists available at ScienceDirect

Coordination Chemistry Reviews

journal homepage: www.elsevier.com/locate/ccr

Review

Towards applications of bioentities@MOFs in biomedicine

Miriam de J. Velásquez-Hernández^{a,1}, Mercedes Linares-Moreau^{a,1}, Efwita Astria^a, Francesco Carraro^a, Mram Z. Alyami^b, Niveen M. Khashab^b, Christopher J. Sumby^{c,*}, Christian J. Doonan^{c,*}, Paolo Falcaro^{a,*}

^aInstitute of Physical and Theoretical Chemistry, Graz University of Technology, Stremayrgasse 9, Graz 8010, Austria

^bSmart Hybrid Materials (SHMs) Laboratory, Advanced Membranes and Porous Materials Center, King Abdullah University of Science and Technology (KAUST), Thuwal 23955-6900, Saudi Arabia

^cDepartment of Chemistry and the Centre of Advanced Nanomaterials, University of Adelaide, South Australia 5005, Australia

ARTICLE INFO

Article history:

Received 12 July 2020

Received in revised form 8 October 2020

Accepted 9 October 2020

Available online xxx

Keywords:

MOFs

Biomacromolecules

Biocomposites

Drug delivery

Biosensing

Biobanking

ABSTRACT

Metal–organic frameworks (MOFs) combined with biomacromolecules, viruses and cells have emerged as novel biocomposites for application to drug delivery, biosensing, biospecimen preservation, and cell and virus manipulation. The integration of biological entities into MOF matrices generates MOF biocomposites with functional characteristics that cannot be observed in the separate components, such as enhanced chemical and thermal stability, resistance to proteases, MOF-conferred selectivity, and controlled release. In this review, we will discuss these functional properties and applications of the biocomposites obtained by the encapsulation of (i) proteins, (ii) carbohydrates, (iii) nucleic acids, and (iv) viruses or cells in a MOF matrix. Finally, we review the post functionalization of MOF-based drug carriers with lipids as a potential route to enhance the dispersion, stability in biological fluids, and blood circulation time of MOF-based drug delivery systems.

© 2020 The Authors. Published by Elsevier B.V. This is an open access article under the CC BY license (<http://creativecommons.org/licenses/by/4.0/>).

Abbreviations: AAOPE, Amino-acid-boosted one-pot embedding; AAP, 4-aminoantipyrine; ABTS, 2,2'-azino-bis(3-ethylbenzothiazoline-6-sulphonic acid); AC, Activated carbon; AFM, Atomic force microscope; AFP, Alfa-fetoprotein; cTnI, Cardiac troponin; ALP, Alkaline phosphatase; AlPcS₄, Al(III) phthalocyanine chloride tetrasulfonic acid; ALV-J, Avian leukosis virus subgroup J; APIs, Active pharmaceutical ingredients; ATP, Adenosine triphosphate; AuNRs, Au nanorods; BHb, Bovine hemoglobin; BPNSs, phosphorous nanosheets; BSA, Bovine serum albumin; BTB, 1,3,5-benzenetribenzoate; BTC, 1,3,5-benzenetricarboxylic acid; CAT, Catalase; CDs, Carbon dots; CH, Carbohydrates; CLSM, Confocal laser scanning microscopy; CMC, carboxymethylcellulose; CMD, Carboxymethyl dextran; COFs, covalent organic frameworks; CRP, C-reactive protein; COU, Coumarin; CPBA, Carboxyphenylboronic acid; CpG ODNs, Cytosine-phosphate-guanine oligodeoxynucleotides; CQ, Chloroquine diphosphate; CS, Chondroitin Sulfate; CSBN, Core-shell bionanoparticles; Cys, Cysteine; Cyt c, Cytochrome c; DAP, Meso-2,6-diaminopimelic acid; DDS, Drug delivery system; DFT, Density-functional theory; dia, Diamondoid; DL, Drug loading; DLS, Dynamic light scattering; DNA, Deoxyribonucleic acid; DS, Dermatan Sulfate; ECL, electrochemiluminescence; EDC, 1-ethyl-3-(3-dimethylaminopropyl) carbodiimide hydrochloride; EE, Encapsulation efficiency; ELISA, Enzyme-linked immunosorbent assay; FA-PEG, Poly(ethylene glycol)-folate; Fc, Ferrocene; GA, Glutaraldehyde; GAG, Glycosaminoglycan; GCE, Glassy carbon electrode; GDH, Glucose dehydrogenase; GMP, Guanine monophosphate; GO, Graphene oxide; GOx, Glucose oxidase; HA, Hyaluronic Acid; HBsAg, Hepatitis B virus antigen; PSA, Prostate-specific antigen detection; HICA, Imidazole-2-carboxaldehyde; HIF, Hypoxia inducible factor; HmlM, 2-methyl imidazole; HP, Heparin; HRP, Horseradish peroxidase; ICG, Indocyanine green; IgG, Immunoglobulin G; ITO, Indium tin oxide; LD50, Median lethal dose; LOD, Limit of detection; MB, Myoglobin; MEKP, Methyl ethyl ketone peroxide; MG, Methylene green; mlgG, Mouse immunoglobulin G antigen; MIL, Materials Institute Lavoisier; MOFs, Metal-organic frameworks; MPDA, Metal-polydopamine Frameworks; MR, Magnetic resonance; MY, Methyl yellow; CEA, Carcinoembryonic antigen; NaDC, Sodium deoxycholate; NGAL, Gelatinase-associated lipocalin; NHS, N-hydroxysuccinimide; NIR, Near-infrared; NPs, Nanoparticles; OVA, Ovalbumin; PBS, Phosphate buffered saline; PDA, Polydopamine; PDT, Photodynamic therapy; PEI, Polyethyleneimine; POC, Point-of-care; PSA, Prostate-specific antigen; PTT, Photothermal therapy; PVP, Polyvinylpyrrolidone; RES, Reticuloendothelial system; RET, resonance energy transfer; RlgG, Rabbit antimouse immunoglobulin G antibody.

* Corresponding authors.

E-mail addresses: christopher.sumby@adelaide.edu.au (C.J. Sumby), christian.doonan@adelaide.edu.au (C.J. Doonan), paolo.falcaro@tugraz.at (P. Falcaro).

¹ These authors contributed equally.

<https://doi.org/10.1016/j.ccr.2020.213651>

0010-8545/© 2020 The Authors. Published by Elsevier B.V.

This is an open access article under the CC BY license (<http://creativecommons.org/licenses/by/4.0/>).

Contents

1. Introduction	2
2. Properties and relevant concepts	3
2.1. Encapsulation efficiency and drug loading	3
2.2. Protection	4
2.3. Release	4
2.4. Compatibility	5
2.5. Particle size	5
2.6. Material cost	7
3. Protein@MOFs for biomedical applications	7
3.1. One-pot encapsulation strategies for Protein@MOF biocomposites	7
3.2. Protein@MOFs as DDS	9
3.2.1. Summary and future outlook	13
3.3. Protein@MOFs for biopreservation	13
3.3.1. Summary and future outlook	14
3.4. Protein@MOFs and Protein-on-MOFs for biosensing	15
3.4.1. Applications of protein@MOF biocomposites for small molecule detection	15
3.4.2. Protein@MOF and protein-on-MOF biocomposites in immunoassays	18
3.4.3. Summary and future outlook	21
4. Carbohydrates and MOFs as DDS	21
4.1. MOF composites as DDS for carbohydrate-based therapeutics	22
4.2. Carbohydrates as protective coatings of MOF composites for DDS	23
4.3. The role of carbohydrates in living cell encapsulation processes to form MOF biocomposites	26
4.4. Summary and future outlook	26
5. Nucleic acids@MOF composites	26
5.1. Summary and future outlook	29
6. Encapsulation of cells and viruses in MOFs	29
6.1. Encapsulation of live cells within MOFs	30
6.2. Encapsulation of viruses within MOFs	34
6.3. Summary and future outlook	35
7. Lipids-on-MOFs: A surface functionalization approach for MOFs-based DDS	36
8. Conclusions and perspectives	38
Declaration of Competing Interest	38
Acknowledgements	39
References	39

1. Introduction

The development of new biocomposites is an area of current research interest at the intersection of material science, biology and biochemistry. Ideally a biocomposite will combine characteristics of the non-biological and biological components to access improved or new properties not observed for the individual entities [1]. This synergistic effect gives rise to novel properties that make biocomposites particularly interesting for application to biomedicine and biotechnology. Hitherto, biocomposites have been prepared using a variety of synthetic materials (i.e. liposomes, dendrimers, mesoporous silica, and nanoparticles) which act as hosts for biological guests [1–4]. Metal-organic Frameworks (MOFs), a class of porous, open framework materials synthesized via a building block approach, have emerged as a versatile platform for the integration of wide range of biological entities (i.e. proteins, carbohydrates, nucleic acids, cells and viruses) [5,6]. The chemical mutability of the MOF building blocks enables molecular level control of their properties [7–9]. Moreover, both the pores and the outer surface of the MOF crystals can be post-synthetically modified [10]. For example, MOFs with high surface areas and large accessible pore volumes have been used for the uptake and release of significant amounts of therapeutic molecules [11–13], whereas MOFs with narrow pore size distributions can be used for size-selective detection of analytes [14]. Furthermore, external chemical stimuli, such as pH, can be used to dissolve MOFs allowing for triggered-release applications [15]. These selected examples show the properties of MOF-based biocomposites can be designed for wide range of potential applications including: drug delivery, biospecimen preservation, biosensing, and cell and virus manipula-

tion. Specifically, the integration of active pharmaceutical ingredients (APIs) within MOF materials allows common issues associated with the administration of free drugs to be overcome, including rapid biodegradation, systemic side effects, low specificity, poor solubility, and the inability of some biotherapeutics to cross cell membranes [11,12]. The use of MOFs to encapsulate bioentities such as vaccines, proteins, cells, and others, enhances their robustness when subjected to hostile environments during transport, handling, and storage (e.g. temperature) that can compromise their potency [16]. Finally, in the biosensing field, there have been extensive efforts to integrate MOF biocomposites in the design of diagnostic devices. In this respect, MOF-based biocomposites are typically employed as probe systems, as such materials are capable of carrying in one single particle both the biorecognition unit (enzymes, antibodies, etc) and large amount of signal molecules, which can be easily infiltrated within the porous network. This arrangement enhances the selectivity and sensitivity of detection of the target biomarker, which is attractive for the fabrication of new diagnostic technologies such as point-of-care (POC) tests [17–21]. The development of these technologies could afford the early clinical diagnosis and prompt treatment of several diseases.

The integration of biomacromolecules and other bioentities (cells and virus) with MOFs to yield the corresponding biocomposite is typically achieved following three basic strategies: (i) bioconjugation, (ii) infiltration, and (iii) encapsulation [5,6,22–24]. The bioconjugation strategy involves the immobilization of biomacromolecules on the outer surface of MOFs either by a covalent attachment or through the adsorption induced by the electrostatic interactions [25]. Infiltration refers to the immobilization of



Fig. 1. Bioentities@MOFs and their applications. A schematic representation of MOF-based biocomposites obtained by one-pot encapsulation strategy. The resultant biocomposites were classified in four different classes according to the encapsulated bioentity (proteins, carbohydrates, live cells & viruses, and nucleic acids – clockwise from bottom right) and their applications including: biosensing, drug delivery, cell and virus manipulation and biopreservation, also clockwise from bottom right.

biomacromolecules within the pore network of the material via diffusion processes [22–24,26].

Encapsulation strategies involve the growth of a MOF shell around a target bioentity and this methodology is the focus of the current review. A variety of bioentities that encompass a wide range in size from small proteins to larger cells and viruses have been successfully encapsulated by a MOF shell. This is because the encapsulation method is not limited by the pore size of the MOF [5,6,26–28], as the MOF grows around the bioentity. The integration of biomacromolecules within a MOF shell can be accomplished either by templating methods or *via* the one-pot synthesis of the MOF in presence of the biomolecule [5,29]. Typically, hard-templating and soft-templating strategies result in the biomacromolecules confined in a micrometric hollow MOF capsule [5,29]. For the hard-templating method the MOF shell is formed around a rigid material (i.e. silica nanoparticles) that could act as a sacrificial template; whereas in the soft-templating approach, the MOF shell grows at the interface of vesicles, droplets, emulsions and cell walls [5,30–32]. The soft-template provides less control over the particle size and uniformity than the hard-templating strategy. Alternatively, *one-pot* encapsulation strategies are based on the heterogeneous nucleation of MOF crystallites around the target bioentity. This strategy will be discussed in detail in the following sections [5,6,26–28]. Indeed, we intend to provide a thorough overview of state-of-the-art applications of MOF-based biocomposites obtained by the one-pot encapsulation of biomacromolecules (proteins, polysaccharides and DNA), as well as complex bioentities (cells and viruses). When possible, we will include examples of biocomposites obtained through bioconjugation strategy for a comparison. Herein, we examine a wide variety of MOF-based composites classified in four different areas depending on the corresponding biological entity: (1) protein@MOFs, (2) carbohydrate@MOFs, (3) DNA@MOFs (4) cell&virus@MOFs. In each section we will discuss the potential applications of such biocomposites in different fields including drug delivery, biosensing and biobanking (Fig. 1). In Section 2 we discuss properties and relevant concepts to assess the suitability of these biocomposites for biomedical and biotechnological applications. Additionally, we include the post functionalization of MOF-based drug carriers with lipids (Section 7) as a potential route to enhance the colloidal stability in biological fluids and blood circulation time of MOF-based drug delivery systems. Finally, we conclude with perspectives and future opportunities related to each system.

2. Properties and relevant concepts

It is important to outline some key concepts of MOF biocomposite chemistry such as encapsulation efficiency (loading potential), protective capacity and residual activity, delivery/release processes, compatibility, and particle size. These criteria are often used to assess the properties and performance of biocomposites in the field of biomedicine. Some of these criteria are common to bioentity encapsulation more generally, while others are specifically relevant to using encapsulated biomacromolecules in drug or vaccine delivery.

2.1. Encapsulation efficiency and drug loading

Encapsulation efficiency is a crucial aspect of drug delivery systems used to ascertain the potential of carriers to deliver an API [33,34]. Given a certain amount of drug involved in a preparation method, the encapsulation efficiency provides quantitative information about the amount of drug successfully transferred into a particular carrier [35]. Moreover, it is a relevant parameter to consider when a specific dose of therapeutic must be delivered precisely to the site of action [36]. Finally, from an economic point of view, as many drugs are costly, it can determine whether a system will be commercialized or not [34,36] (see Section 2.6). It is also important in biosensing and biopreservation to understand the sensing performance or uptake of biotherapeutics.

The encapsulation efficiency (EE%) is the percentage obtained by taking the ratio between the mass of active ingredient (i.e. drugs, fragrances, proteins, pesticides, antimicrobial agents, etc.) integrated in a carrier (M_i) over its total mass used in the preparation of the composite (M_t) [35,37,38],

$$EE\% = \left(\frac{M_i}{M_t} \right) \times 100\%.$$

Another important parameter to determine the capacity of the system to carry active pharmaceutical ingredients as a cargo is the drug loading (DL) [35]. The DL provides information about the ratio of the mass of drug (M_d) and the mass of the vessel (M_v). This is an essential aspect to take into consideration in drug delivery systems as the use of excessive amounts of carrier could potentially increase side effects, such as toxicity and immune responses against the carrier [39]. Thus, DL can be calculated as

$$DL\% = \left(\frac{Md}{Mv} \right) \times 100\%,$$

where Md is the mass of encapsulated active ingredient (e.g. drug molecule) and Mv is the mass of encapsulating carrier.

While EE% can be used to study the effect of a preparation step for the composite on encapsulation of the active ingredient, DL% helps identify if an encapsulation method is effective for a specific application [35,40]. Both parameters, DL% and EE%, depend on the selected system and encapsulation method. However, we note that in drug delivery systems, the relevance of EE% or DL% is related on the aim of the study. For instance, the measurement of EE% should be the important criterion if the aim is to determine either the efficiency of an overall method or the optimization of the system [35]. Alternatively, DL% should be a central focus if the goal of the study is to evaluate a dosage of drug with respect to a desired pharmacokinetic profile [35,40].

2.2. Protection

The fragile nature of biomacromolecules and complex bioentities typically requires their manipulation under careful conditions, as when treatment conditions deviate from their ideal environment (e.g. increased temperature) conformational changes or disintegration can occur. A central challenge to preserve bioentity activity during handling, transport, and storage is the need for refrigeration, the so-called “cold chain” [6,41]. For example, protein-based therapeutics are prone to losing their effectivity when handled outside of the temperature window where they are stable (typically 2–8 °C) [16,42]. The same applies to vaccines and virus-based therapeutics which require constant refrigeration to retain efficacy [6]. Similarly, the molecular conformation of enzymes is altered after exposure to high temperatures, organic solvents and mechanical stressors [43–45]. This unfolding process results in a considerable drop of the biocatalytic performance [44]. In the case of cells, additional aspects compromising their bioactivity include environmental factors such as cytotoxic compounds and radiation [46].

To overcome the fragile nature of bioentities including proteins, viruses and cells, researchers have focused on different approaches. For example, in the case of proteinaceous drugs, vaccine adjuvants or vaccines the application of a protective synthetic coating could provide a new tool for storage, handling and transportation [6,47]. In the case of living organisms such as cells, the fabrication of a tailored artificial exoskeleton can provide effective protection from environmental cytotoxic compounds, mechanical stress and radiation damage, thus facilitating storage, manipulation and transportation of cells for application in biomedicine and biotechnology [46].

Protection of bioentities is an important technological challenge and has motivated researchers to investigate different classes of materials for the fabrication of robust artificial biocomposites. Porous nanomaterials, in particular MOFs, are widely studied because of their high surface area, tunable morphology, and high affinity for protein conjugation [45]. In particular, MOFs have been considered attractive candidates as their structure, chemical properties, pore size and shape can be precisely tuned [48]. Additionally, there are an increasing number of MOFs that can be synthesized under biocompatible conditions, and moreover the encapsulated bioentity can be readily recovered upon applying external stimuli [15].

Although prior reports disclose biomolecule encapsulation in MOFs [26,28], the first systematic study comparing the biopreservation properties conferred by encapsulation was communicated by Falcaro and co-workers [27]. In that work, the authors compared the protection properties of ZIF-8 (sodalite, **sod**) versus other

inorganic exoskeletons, including mesoporous SiO₂ and CaCO₃. To provide this comparison, the authors monitored the catalytic performance of horseradish peroxidase (HRP) upon exposure to denaturing conditions (e.g. boiling water or DMF). Unlike inorganic carriers, HRP@ZIF-8 retained most of the enzymatic activity. This study also experimentally correlated the pore size of a carrier with its protective properties (the smaller the pore the higher the protection) thus suggesting the tight encapsulation of the biomacromolecule within ZIF-8 yields superior protection (see Section 3.3). Additionally, the authors demonstrated that active proteins can be released from the MOF biocomposite under mildly acidic conditions. These data suggested the further investigation of MOFs for protection against physical and chemical stress (e.g. exposure of biocomposites to mechanical forces, organic solvents, chaotropic agents and temperature) [49]. Examples of these studies will be discussed in detail below, categorized for each type of bioentity [16,44,45].

2.3. Release

Pharmacokinetics describes the process of the uptake of drugs by the body, their biotransformation, distribution in the tissues, and elimination from the organism following a period of time after administration [50]. Pharmacokinetics is critical for the understanding of the therapeutic properties of a specific drug. Biodistribution refers to the distribution of chemicals to specific locations within the body [51]. This can be also associated to the spatial localization of a biocomposite (or a carrier) overtime within an animal or human body; thus, biodistribution is fundamental to identifying target organs and anticipating safety and efficacy [52]. By using nanocarriers, aspects of pharmacokinetics and biodistribution (e.g. the release profile of the drug, their accumulation in different tissues and the biocompatibility) can be precisely controlled by tuning the properties of the carrier material.

The release is characterized by a profile that determines the amount of drug that diffuses from the carrier into the surrounding environment as a function of time. Importantly, the release time can drastically influence the therapeutic effect of the same drug [53]. Depending on the therapeutic and the treatment, different release profiles are preferred. For example analgesics and anticoagulants typically require fast release [54]. Conversely, a slow release can be favoured in prolonged treatments as a replacement to administration via parenteral (non-oral) route which can be painful and problematic [8,55,56]. This is the case for protein-based treatments such as insulin, growth hormones or oxytocin, which require multiple injections causing the patients pain and discomfort [56,57]. An example of a successful commercial product is an injectable drug delivery system based on leuprolide hormone encapsulated in PLGA microspheres (Lupron Depot[®]) which provide prolonged release [58].

Although, drug release profiles of conventional macro-sized drug delivery systems are typically assessed by standard United States Pharmacopoeia (USP) methods, for micro- and nanoparticulate systems, standard tests are not available [59]. Thus, each micro- and nanoparticle-based drug carriers system requires an *ad hoc* testing regime for the evaluation of its specific drug release profile [59–62]. Examples of methods used are side-by-side diffusion cells with artificial or biological membranes, dialysis bag diffusion techniques, and agitation followed by centrifugation [59]. The latter is the most commonly employed for its simplicity and it can be combined with a dialysis technique using synthetic membranes for the separation of the nanoparticles from the release media. Typically, the collected release profiles show a biphasic behavior with an initial burst followed by a slower sustained release of the drug [59,63]. By tuning the material structure,

chemistry and drug location in the carrier, the burst effect can be minimized and a steady sustained drug release is obtained [59].

Following preliminary testing, deeper insight can be obtained by conducting preclinical studies, which are either carried out *in vitro* or *in vivo* on biological systems. For *in vitro* systems, drugs are tested in microorganisms, cells, tissues, or isolated organs in conditions that mimic their normal biological context [64]. In drug delivery, *in vitro* systems are interesting for early phase research studies [64]. Alternatively, *in vivo* systems require whole living animals to investigate the effect of selected therapeutics and administration methods. *In vivo* studies are considered crucial to determine the absence of side effects that cannot be observed or predicted by *in vitro* experiments [64].

Recent research has moved from regular drug delivery systems (DDS) [65] that exploit non-specific Fickian diffusion to stimuli-responsive materials using nanomaterials that can release therapeutics with simultaneous control over carrier localization, release time and dosage [65]. The release could be triggered by the local environment of the target cells/tissues (example of stimuli are pH, chemical environment, temperature), or it could be regulated using external controls (example of stimuli are light, magnetic field, temperature, ions, pressure) [15]. Within the broad range of nanomaterials, MOFs are ideal candidates as carriers: by selecting the proper building blocks and structure, it is possible to impart either regular DDS properties, or triggered-release responses either from local environments or from external controls. Indeed MOF-based systems can undergo structural modifications that release a payload under specific conditions including acidic pH [15,66], presence of certain anions [67–69], and irradiation with light [70–72].

2.4. Compatibility

When a MOF is used as a carrier to deliver a drug in the body, it can undergo a degradation process that will release not only the drug, but also the constituent building blocks (i.e. cations, ligands). Therefore, it is important to evaluate the toxicity of MOF components. An interesting approach was suggested by Horcajada et al. that recommended the selection of naturally occurring building blocks for the synthesis of biocompatible MOF (aka bioMOFs) [11,73]. For the choice of the ligand, endogenous biomolecules (amino acids, peptides, proteins, nucleobases, carbohydrates, porphyrins) or exogenous bioactive ingredients (nicotinic acid, curcumin, olsalazine and some dicarboxylic acids, including fumaric acid) have been recommended as ideal candidates [11]. For the choice of metal for the nodes, it is preferable to use those cations that are part of the daily requirement of the human body [74]. However, each cation possesses its own degree of toxicity, therefore the median lethal dose (LD50) has been proposed as criteria to assess the compatibility of the specific cation. LD50 is the amount of compound that kills 50% of a given population within a selected time [74]. Based on this, the preferable metals for the construction of biocompatible MOFs are Mg^{2+} (LD50 $\text{MgSO}_4 = 5000$) > Ca^{2+} (LD50 $\text{CaCl}_2 = 1940$) > Fe^{2+} (LD50 $\text{FeCl}_2 = 984$) > Fe^{3+} (LD50 $\text{FeCl}_3 = 450$) > Zn^{2+} (LD50 $\text{Zn}(\text{OAc})_2 = 100\text{--}600$) [11,13].

Although a preliminary assessment can be conducted by considering the amount of MOF byproducts with respect to published cytotoxic values, it is relevant to stress that reports on MOF biocomposites for biomedical aspects should involve *in vitro* and *in vivo* studies. While *in vitro* experiments can provide information on some cytotoxic aspects; however, it is not enough to simply assess the biocompatibility of the materials, since the behavior inside a living system can involve several important aspects including interferences, permanence in the circulatory system, accumulation in organs, immune response, etc. [75]. For this reason, a thorough investigation of the compatibility of the MOF-

based biocomposites involving both *in vivo* and *in vitro* studies should be conducted.

2.5. Particle size

An appealing property of particulate DDS is their versatile administration that can include parenteral injection [75] and inhalation [76]. However, extensive studies have revealed the importance of the particle size and shape for blood circulation time, biodistribution, cellular internalization and compatibility [77]. For example the different mechanisms (phagocytosis, macropinocytosis, caveolar-mediated endocytosis or clathrin-mediated) of cellular internalization processes are particle size-dependent [78,79]. Particle size is also known to influence the efficiency of tumor-targeted drug delivery for cancer treatments, affecting circulation, biodistribution, tumor accumulation and penetration, cellular uptake and subcellular distribution. Studies have shown larger nanoparticles tend to be more capable of retention in tumor tissue when compared with smaller nanoparticles, but smaller particles present higher penetration efficiency in tumor tissues [80]. However, small particles (<5 nm) are quickly cleared from circulation through extravasation or renal clearance [77]. As size increases, particles seem to accumulate primarily in the liver, spleen and bone marrow. Typically, particles with dimensions in the 10 nm to 15 μm range are trapped by the spleen and then removed from circulation by cells of the reticuloendothelial system (RES). Additionally, when administered *in vivo*, specific proteins adsorb to surface of particles and this influences the accumulation in the RES. Particles larger than $\sim 15 \mu\text{m}$ are typically removed from circulation by mechanical filtration in capillaries, and a high dose can be lethal [77].

The size range between 50 and 300 nm has been found to provide an optimal circulation half-life for the parenteral administration route [11,81,82]. Nanoparticles of sizes <150 nm can exit the blood vessels through openings (fenestrations) in the endothelial lining, potentially entering organs and tissues [83,84]. Based on this, MOF nanoparticles from tens to hundreds of nanometers are ideal nanocarriers for imaging agents and drug molecules [12,85], especially when administered with intravenous/subcutaneous injection methods [75]. However, “small” nanoparticles are not suitable for every application. For example, studies have shown that nanoparticles with sizes < 10 nm in diameter, when administered trans-dermally will not penetrate through the *stratum corneum* into viable human skin and will likely accumulate in the hair follicle openings [86]. Rather, it has been shown that bigger particles on the scale of 300 nm to 1.5 μm are effective for transdermal drug delivery [87]. Biodegradable microparticles (with sizes between 300 nm and 2 μm) have been shown to offer important advantages in the area of vaccine delivery and some formulations are in clinical trials [84,85,88]. Additional benefits can arise from having larger particles, such as an increased stability in buffer and reduced aggregation, [67,76,89,90] so there are tradeoffs required to produce an optimal DDS. Relevant considerations on the influence of particle size for DDS applications discussed in this section are schematized in Fig. 2, which shows different size-dependent processes and suggested DDS administration routes.

Although we have focused the discussion specifically on particle size, the particle's shape and density can influence the retention and circulation time, biodistribution and mechanism of internalization [77,80,84]. For example, by controlling the aggregation of nanoparticles, clusters with inter-particle voids can be prepared. This strategy allows to modify the density of carriers and affords a deeper penetration (in the case of administration to the lungs) [84] and a higher retention in tumor tissues [80].

Different strategies have been employed to tune the MOF particle size [91,92]; for example, the crystal growth kinetics can be

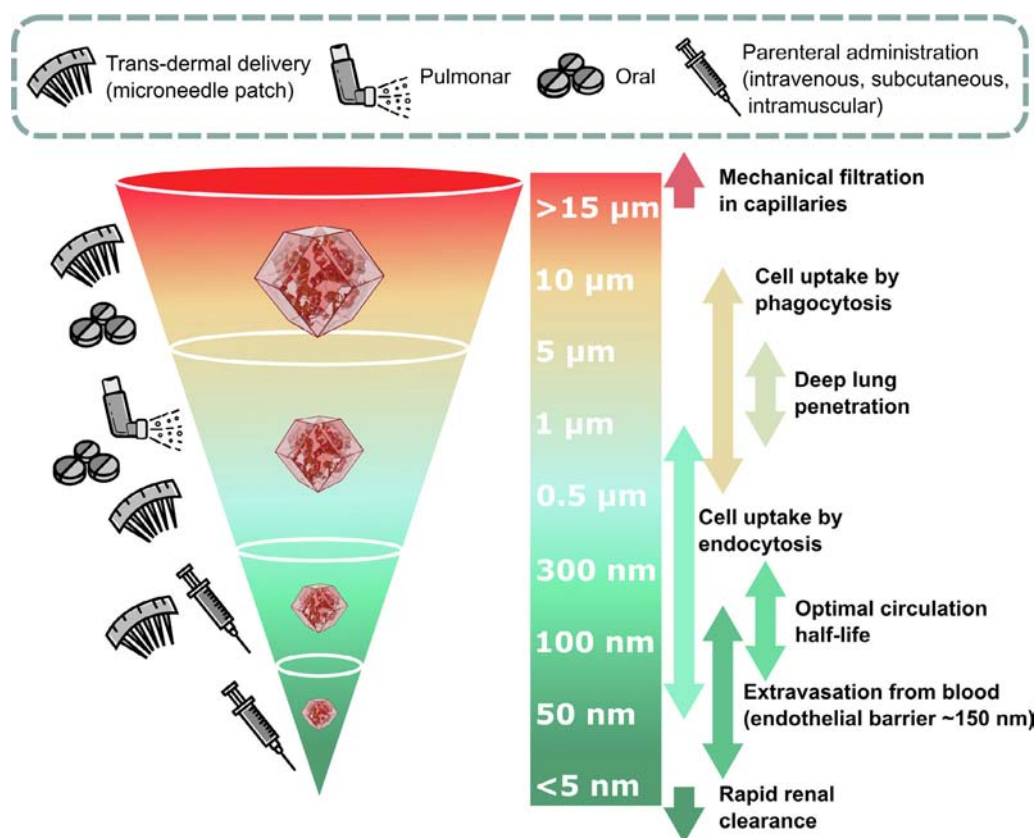


Fig. 2. Considerations of particle size for DDS applications. On the righthand-side different size-dependent processes are indicated (mechanism of internalization, penetration in the lungs, extravasation from endothelial fenestrations, etc). On the left side suggested DDS administration routes are represented, based on the available studies. Information collected from several sources [69,70,76,81,83–86] for studies performed on particulate systems for drug delivery and biomedical use, based on different compositions (polymeric particles, liposomes, Au NP and MOF NPs). These studies were typically conducted on spherical particles. We note that this schematic is to be considered only as a general guide to the influence of particle size on the design of the carrier and not as a strict rule, since these processes are also affected by particle shape, density, composition and surface functionalization.

Table 1

Estimated material cost² for selected biotherapeutics@MOF (for ZIF-8, ZIF-90 and MAF-7) and relative impact of the MOF on the total cost of the biocomposite (considered as MOF component + biomacromolecule component).

Biotherapeutic	MOF	Biotherapeutic wt%	Biotherapeutic/MOF cost ratio	Cost of MOF/total (%)	Refs.
HA	ZIF-8	7.1	30	3.2	[103]
CS	ZIF-8	10.9	28	3.4	[103]
Insulin	ZIF-8	5.2	245	0.4	[100]
DS	ZIF-8	6.5	832	0.1	[103]
Insulin	ZIF-8	20.73	1168	0.09	[101]
antitrypsin	ZIF-8	4.2	1195	0.08	[97]
H-IgG	ZIF-8	37	15433	0.007	[45]
Gelonin	ZIF-8	41.0	751116	0.0001	[102]
CS	ZIF-90	4.0	0.3	79	[103]
HA	ZIF-90	4.7	0.4	72	[103]
DS	ZIF-90	5.4	19	5	[103]
H-IgG	ZIF-90	53	827	0.1	[45]
CS	MAF-7	20.1	0.7	60	[103]
HA	MAF-7	26.0	0.9	52	[103]
DS	MAF-7	23.1	41	2.4	[103]
Drug	MOF	Drug wt%	Drug/MOF cost ratio	Cost of MOF/total (%)	Refs.
5-FU	ZIF-8	45.5	55	1.8	[104]
DOXO	ZIF-8	4.9	4702	0.02	[103]
5-FU	ZIF-90	36.35	1.0	49	[105]
DOXO	ZIF-90	13.5	398	0.3	[105]

² Aspects disregarded in this preliminary material assessment costs include: the yield of the MOF synthesis, the excess of precursors often used (e.g. ligand), the energy involved of the process, solvents used in the synthesis, cleaning procedures, the operator and equipment cost, and the disposal of waste.

influenced by adjusting the reaction parameters (e.g. type and amount of solvents, reagent concentrations, temperature, pH) [67,93], or the introduction of auxiliary additives (coordination modulators, surfactant-mediated synthesis, etc) [12,75,94–96]. These methods can be used to prepare MOF particles that can be post-

functionalized and post-infiltrated with biomacromolecules. However, for the control over the particle size of bioentities@MOF prepared via one-pot methods (e.g. encapsulation), the research is in its infancy. Pioneering work by Carraro et al. [97], used flow setup for the continuous production of BSA@ZIF-8 nanoparticles in the 40–100 nm range. The fluidic system was also used to control the particle size of antitrypsin@ZIF-8 composites. However, this flow setup uses ethanol as a quenching agent which might prevent using the approach for a number of clinical biotherapeutics. Indeed, the exposure of fragile biomacromolecules to non-native conditions (e.g. presence of organic solvents, high temperature, pH changes), can result in a drastic activity loss [27]. Thus, biocompatible synthetic approaches for the precise engineering of bioentities@MOF particles, including particle size, morphology and crystallinity, would significantly progress the use of MOFs in biomedicine.

2.6. Material cost

As active pharmaceutical ingredients can be expensive, DDSs aim to increase efficiency by enhancing the bioavailability and efficacy of therapeutics thus reducing the amount of drug used [98]. The cost-effectiveness of nanoparticle-based DDS also requires careful assessment prior to commercialization [99]. With the purpose of stimulating advances in the area of MOF bio-composites as DDSs, in this section we propose preliminary considerations on the costs of the material components.

Considering selected biocomposites reported in the literature, we will limit our discussion to the ratio between the cost of the MOF carrier to the value of the biomacromolecule-based therapeutic guest per gram of biocomposite (i.e. MOF component + biomacromolecule component²). In one gram of biocomposite, the amount of biomacromolecule was calculated based on the reported loading (wt%) while the cost of the components are the prices reported in the supplier website. In the case of the MOF component, for the sake of simplicity, we used the chemical formula of the MOF to calculate the stoichiometric amount of the MOF precursors (e.g. ligand and metal salt). We selected examples based on three different MOFs: ZIF-8, ZIF-90 and MAF-7, due to their widespread use, and list the results in Table 1.

Currently, the most widely used azolate based framework for the encapsulation of protein is ZIF-8; this is considerably cheaper than ZIF-90 (36 times) and MAF-7 (87 times) because of the higher cost of imidazole-2-carboxaldehyde (ZIF-90) and 3-methyl-1,2,4-triazole (MAF-7) when compared to 2-methylimidazole (ZIF-8). Using ZIF-8, Carraro et al. encapsulated α 1-antitrypsin with a loading of 4.2 wt% [97]. For this DDS, the therapeutic cost is 1195 times the cost of ZIF-8 matrix. Chen et al. and Hoop et al. prepared insulin@ZIF-8 with a protein loading of 5.2 and 20.7 wt%, providing a therapeutic cost that can be estimated as 245 and 1168 times the cost of ZIF-8, respectively [100,101]. Cheng et al. encapsulated gelonin into ZIF-8 with a 41 wt% thus, in this case the ratio of the therapeutic cost to that of ZIF-8 is 751,116 [102]. This observation highlights that, when a high-value protein is used, the cost of ZIF-8 biocomposites depends almost entirely on the cost of the encapsulated therapeutic.

Feng et al. have reported the encapsulation of polyclonal antibodies into ZIF-8 and ZIF-90 particles, allowing for a cost comparison of the respective ZIFs [45]. In the case of the encapsulation of Human immunoglobulin G (H-IgG) into ZIF-8, the loading was 37 wt% and the antibody cost 15,433 times the ZIF-8 component price. Using ZIF-90 as matrix, the H-IgG loading was 53 wt% and the antibody cost to ZIF-90 cost ratio is 827. From this comparison it is evident that the ZIF-90 matrix, even if more expensive than ZIF-8, accounts for only 0.1% of the final cost of the biocomposite.

A study by Velázquez et al allows the comparison of the three different ZIFs with a different class of therapeutics (carbohydrates). In this work hyaluronic (HA) acid and dermatan sulfate (DS) were encapsulated in ZIF-8, ZIF-90 and MAF-7 [103]. In the case of ZIF-8, the HA loading was 7.1 wt% and the DS loading was 6.5 wt%. In the final biocomposites, the cost of HA and DS are 30 and 832 times the cost of ZIF-8, respectively. We note that even with for an inexpensive therapeutic (HA is ca. 50 times cheaper than DS), the cost-effectiveness of ZIF-8 as carrier could be attractive given that it shows appropriate release properties. For ZIF-90 and MAF-7, we observe that the cost-effectiveness of the MOF is more reasonable only when the more expensive therapeutic (DS) is encapsulated. In this case, the therapeutic cost is 19 and 41 times the cost of ZIF-90 and MAF-7, respectively. Conversely, in the case of HA biocomposites, the costs of ZIF-90 and MAF-7 matrices are comparable to or higher than the cost of the therapeutic component which is driven by the lower biotherapeutic costs and the lower loading levels with respect to other examples.

For comparison, we report in Table 1 some examples of the encapsulation of small molecule therapeutics (e.g. Doxorubicin [DOXO] and 5-fluorouracil [5-FU]) into ZIF-8 and ZIF-90 [104,105]. As in the previous cases, the cost-effectiveness of ZIF-8 is higher than ZIF-90 and it is more evident in the case of the encapsulation of high-value therapeutics (e.g. DOXO is 1400 times more expensive than 5-FU).

Overall, this summary highlights that ZIF-8 can be considered as a cheap carrier and, even with a low loading of therapeutics, the cost ZIF-8 will only marginally affect the overall cost of the biocomposite. For ZIF-90 and MAF-7 this cost evaluation should be assessed on a case by case basis.

3. Protein@MOFs for biomedical applications

3.1. One-pot encapsulation strategies for Protein@MOF biocomposites

Proteins have been shown to trigger the rapid growth of a MOF shell around their surface leading to the formation of protein@MOF biocomposites [5]. The main advantage of this method is that proteins of any size and shape can be integrated into MOFs as the pore network dimensions do not place a restriction on the size of the guest biomacromolecule. The first report describing the one-pot encapsulation of proteins within a MOF was published by Ge and co-workers [26]. The authors demonstrated the successful encapsulation of cytochrome *c* (Cyt *c*) within two different zinc-based zeolitic imidazolate frameworks **sod**-ZIF-8 and **sod**-ZIF-10 (**sod** = sodalite). Polyvinylpyrrolidone (PVP) was employed as a coprecipitating agent as it has a strong affinity for proteins [106], and facilitated the dispersion and stabilization of the protein in methanol. Furthermore, PVP is known to attract and coordinate metal cations [107,108], increasing their local concentration around the target protein. As concentration of Zn²⁺ promotes the formation ZIF-8 [109–111], PVP can act a crystallization facilitator [107,108]. This was supported by previous reports where PVP was used to control the encapsulation of inorganic nanoparticles within ZIFs shells [109–111]. Thus, in the formation of MOF biocomposites, when PVP and Cyt *c* was added to a solution of 2-methyl imidazole (HmIM) and Zn²⁺ in methanol, the rapid formation of a Cyt *c*@ZIF-8 biocomposite was observed. This *co-precipitation* method, was improved by Tsung and co-workers who used PVP to induce the encapsulation of catalase (CAT) within ZIF-8 and ZIF-90 in aqueous media, demonstrating that organic solvents are not needed (this strategy is termed *de novo approach*) [28,112].

Then, Falcaro, Doonan, and co-workers demonstrated that additives (e.g. PVP) are not required as biomacromolecules (e.g. HRP,

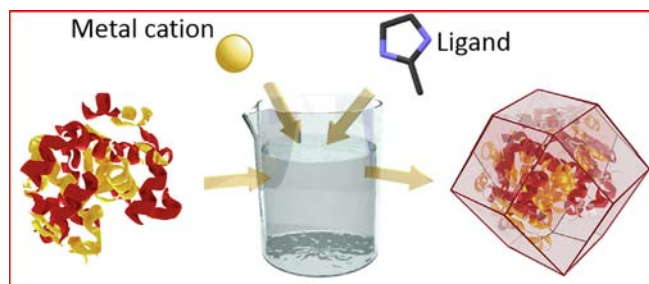


Fig. 3. Biomimetic mineralization strategy for the encapsulation of proteins within a ZIF-8 matrix.

BSA and DNA) can act as heterogeneous nucleation seeds and trigger the MOF formation in aqueous media [27,113]. This additive-free approach is termed *biomimetic mineralization* due to its similarity to natural biomineralization processes in which proteins spontaneously induce the formation of minerals (Fig. 3).

More recently, researchers demonstrated that the kinetics of the MOFs-shell formation is protein-dependent [114]. Under identical conditions, the time required for the formation of the biocomposite with a target protein varies from seconds to hours, and, in case of certain proteins, encapsulation does not occur. The authors analyzed the electrostatic (isoelectric point and zeta potential) and

hydrophobicity properties of several proteins (Fig. 4a). This work revealed that only negatively charged molecules (isoelectric point (pI) < c.a. 7) triggered the spontaneous formation of ZIF-8 biocomposites. The related computational investigation disclosed how negative charges can increase the local density of Zn^{2+} around the target biomolecule; this was considered the reason for the subsequent growth of the MOF-shell (Fig. 4a). The authors showed that positively charged proteins, that did not trigger the spontaneous biomineralization (e.g. hemoglobin), became effective MOF seeds when surface functionalized (e.g. succinylation) with negatively charged chemical groups (Fig. 4b). This fact underscores the importance of the electrostatic interactions between the target biomolecule and Zn^{2+} ions to induce the growth of the MOF-shell.

Inspired by studies that demonstrate the role of cysteine (Cys) in the accumulation of metal cations around metalloproteins [115–117], Ouyang and co-workers [118] used a PVP/cysteine-based approach for the one-pot encapsulation of biomolecules with positive surface charges such as myoglobin (MB, pI = 7.6). In this water-based synthesis, the local concentration of Cys around the PVP-protein complex depends on the hydrogen-bonding interactions between Cys and the amido groups of PVP. Then, as for metalloproteins, the abundance of Cys around the PVP-protein complex enhanced the concentration of Zn^{2+} ions via mercaptide bond formation, leading to the rapid crystallization of ZIF-8 around PVP/cysteine modified-MB.

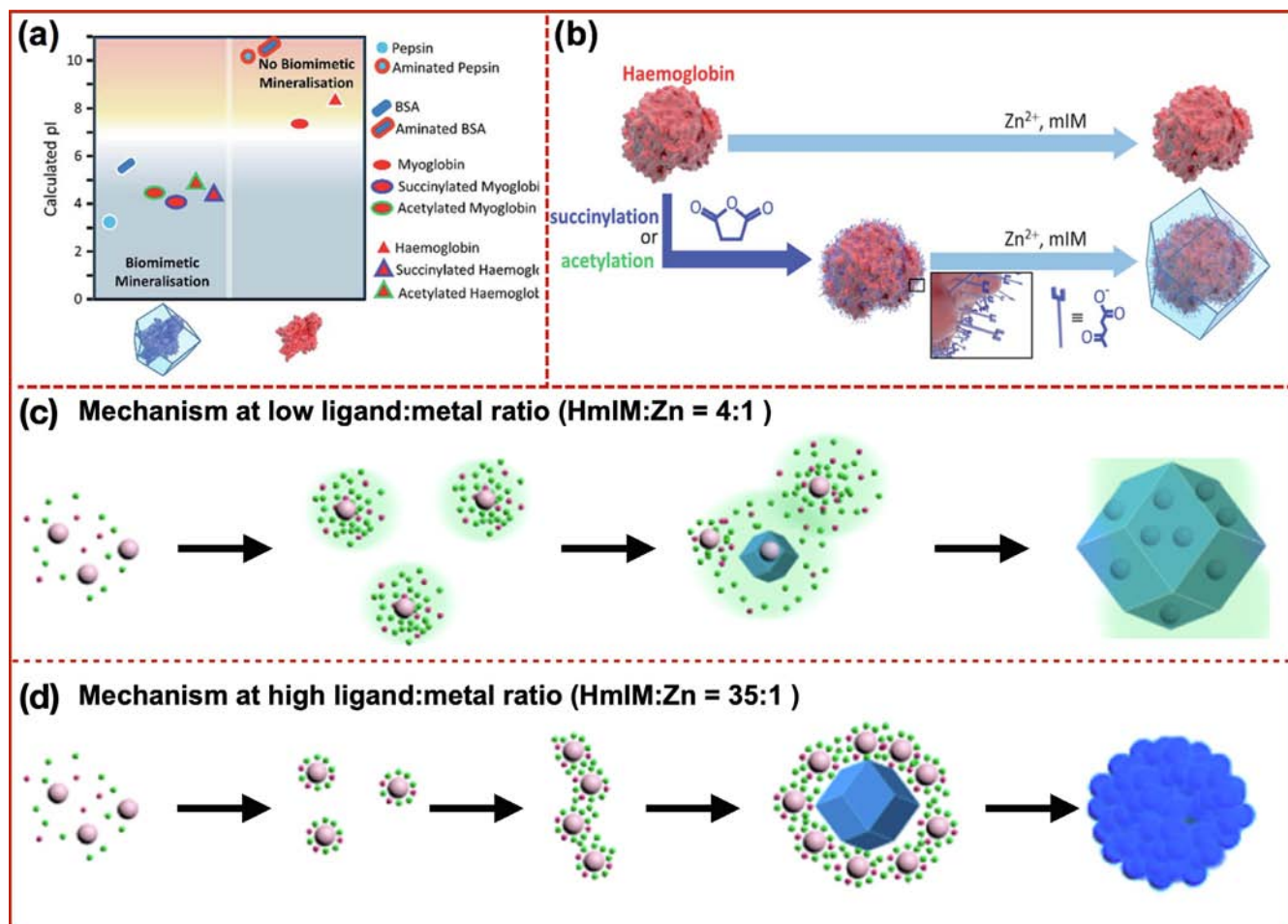


Fig. 4. (a) plot of the calculated isoelectric point for different proteins (BSA, pepsin, Hb, and Mb) before and after the surface modification. (b) Schematic representation of the biomimetic mineralization of haemoglobin (Hb). The native Hb does not undergo biomimetic mineralization under standard conditions, but after being chemically modified via acetylation or succinylation process the encapsulation process take place due to the increase of the negative charge on the protein surface. Adapted with permission from ref. [114] Copyright 2018 Royal Society of Chemistry. Mechanisms of nucleation and growth of BSA@ZIF-8 biocomposites obtained varying the ligand:metal ratios: (c) HmIM: Zn = 4:1, (d) HmIM:Zn = 35:1. Reprinted with permission from ref. [119]. Copyright 2020 American Chemical Society.

Cui and co-workers demonstrated that positively charged biomacromolecules (ovalbumin OVA, Poly-L-lysine, PLL; lysozyme, Lyz) were successfully encapsulated within ZIF-8, when poly(ethylene glycol) is present during the mineralization process [96]. By changing the amount of PEG (40 kDa), the process yielded the formation of OVA&PEG@ZIF-8, PLL&PEG@ZIF-8 and Lyz&PEG@ZIF-8 with average particle sizes of 400, 360 and 200 nm, respectively. The authors attribute the successful encapsulation of positively charged biomacromolecules to the hydrogen-bonding interaction between PEG and proteins. Moreover, the presence of this additive permits the re-dispersion of the resultant nanoparticles in aqueous media and enhances the colloidal dispersity and stability of the biocomposites in cell media [96]. The PEG-based strategy affords the encapsulation of proteins with isoelectric point < 7 , [114] providing a versatile method for the preparation of protein@ZIF-8 composites.

The mechanism of the encapsulation of BSA within ZIF-8 was revealed by Patterson and co-workers [119], who used cryo-transmission electron microscopy (cryo TEM) to monitor the structural evolution of the biocomposite. This study reveals that the encapsulation of proteins within ZIF-8 follows a nonclassical crystallization pathway which is characterized by aggregation of highly hydrated amorphous particles comprised of: (1) Zn^{2+} -mIM and (2) Zn^{2+} -mIM-BSA (Fig. 4). Aggregation of these two types of amorphous particles is largely dependent on their electrostatic interactions that control the ZIF-8 nucleation and growth mechanisms. The authors suggested that the mechanism of BSA@ZIF-8 formation depends on the ligand:metal ratio and for the 4:1 ratio, the protein promotes the crystallization of ZIF-8 (sod) analogously to natural biomineralization processes (Fig. 4c). Indeed, for 4:1 ligand:metal ratio the Zn^{2+} -mIM does not spontaneously self-assemble; however, when BSA is added to the MOF precursor solution, the protein, concentrates cations to the protein surface, thus the local supersaturation favors ZIF-8 (sod) crystallization around protein particles (Fig. 4c). As a result, BSA@ZIF-8 (sod) crystalline particles are formed. Conversely, for high ligand:metal ratios (35:1) amorphous aggregates interact with crystalline ZIF (sod); then large aggregates undergo dissolution–recrystallization to form BSA@ZIF-8 (Fig. 4d).

Finally, a recent report published by Hu et al. [120] demonstrated that the mIM: Zn^{2+} ratio can be easily adjusted when using a microfluidic flow reactor to synthesise ZIF-8-based biocomposites. This approach allows for fine control over the number of structural defects in the resultant material (see Section 3.4.1) and thus influences the mass transfer within the porous MOF bio-composite. When compared with a Cyt c@ZIF-8 biocomposite obtained via a batch procedure, the PXRD pattern of the Cyt c@ZIF-8 biocomposite prepared using the microfluidic device reveals a reduction on the crystallinity with peaks shifted to low angles. This increase in the cell parameters was attributed to the defects generated during the synthesis.

In the following sections we discuss the current applications of protein@MOF in biomedicine for drug delivery, biobanking and biosensing (Fig. 5). For clarity, we include selected examples of protein-on-MOF biocomposites.

3.2. Protein@MOFs as DDS

Proteins play a key role in the metabolic functions of the cells, including gene regulation, signaling, and immune response. The malfunction or deficiency of specific proteins can lead to the development of chronic diseases such as diabetes mellitus, Parkinson and Alzheimer [121,122]. One possible treatment for such diseases is the administration of protein therapeutics. For example, insulin administration is one of the most effective therapies for the treatment of diabetes mellitus type I and type II [55]. Compared to

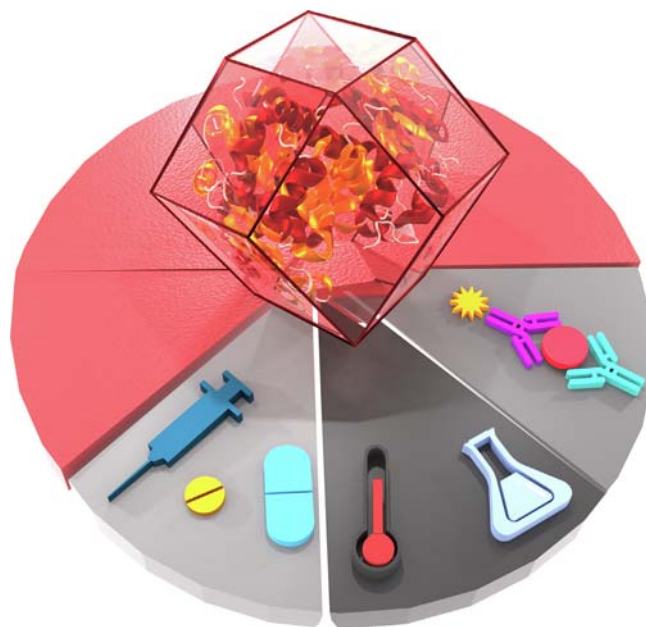


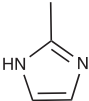
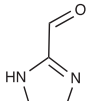
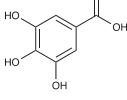
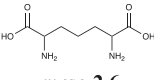
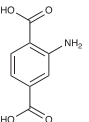
Fig. 5. Protein@MOF biocomposites and their applications as drug delivery systems, in biopreservation, and biosensing.

smaller synthetic drugs, proteins present unique properties including high specificity and potency, and reduced side effects (e.g. low toxicity) [123,124]; however, their use as therapeutics is limited. A significant reason for this is that native proteins can decompose upon exposure to mechanical stress and mild temperatures [123,124]. Furthermore, once introduced in a biological systems, therapeutics can lose their theoretical efficacy because of fast renal clearance, difficulties in crossing cell membranes and instability in serum [125], where the decomposition is carried out by proteolytic agents [55].

A promising strategy to enhance protein stability and tissue penetration/intracellular delivery is to integrate them within MOF carriers (Table 2). Indeed it has been shown that the on-demand release of encapsulated species from MOFs can be regulated by the application of specific internal or external stimuli, such as changes in the pH, or coordinating ions [15]. ZIFs have been widely investigated for drug delivery systems because: 1) they can be easily synthesized at room temperature in aqueous media, which are ideal synthetic conditions for the encapsulation of a variety of drugs (from small synthetic drugs to large biomacromolecule-based therapeutics) [15,103]; 2) the coordination bonds between Zn^{2+} and azolate linkers can be cleaved at slightly acidic pH, via chelating agents or anions with high affinity for Zn^{2+} , thus chemical-stimuli responsive drug carriers can be designed (e.g. pH responsive ZIF carriers for intracellular delivery) [15]; 3) the low cytotoxicity of ZIFs allows for the delivery of therapeutic doses sufficient to treat some diseases [11,13,74,101].

A pioneering study by Qu and co-workers [126] demonstrated the feasibility of ZIF-8-based nanocarriers for intracellular delivery of a model vaccine. The authors encapsulated ovalbumin (OVA, a protein antigen capable of inducing a humoral and cellular immune response) within ZIF-8 via the *de novo* approach. The resultant OVA@ZIF-8 biocomposite was further functionalized by the adsorption of an immune adjuvant (cytosine-phosphate-guanine oligodeoxynucleotides, CpG ODNs) to afford a core-shell composite OVA@ZIF-8-CpG with average particle size of 200 nm (Table 2). This design permits the co-delivery of the antigen and the immune adjuvants within the cell. Thus, once the OVA@ZIF-8-CpG are internalized in the cell, the acidic environment of lyso-

Table 2
Protein@MOFs as DDS.

Ligand	Cation	MOF	Biotherapeutic	Particle size	Application	Ref
 HmIM	Zn ²⁺	ZIF-8	OVA	200 nm	intracellular delivery of antigens	[126]
	Zn ²⁺	ZIF-8	CAT	110 nm	photodynamic therapy (PDT)	[130]
	Zn ²⁺	ZIF-8	GOx&TPZ	120 nm	colon cancer therapy	[131]
	Zn ²⁺	ZIF-8	BSA/caspase3 /HSA	92 nm	intracellular delivery of proteins.	[127]
	Zn ²⁺	ZIF-8	gelonin	94.6 nm	systemic and intracellular delivery of proteins	[102]
	Zn ²⁺	ZIF-8	chlorine diphosphate	250 nm	intracellular delivery of autophagy inhibitors	[128]
	Zn ²⁺	ZIF-8	insulin	300–350 nm	glucose-responsive insulin release	[100]
	Co ²⁺ /Zn ²⁺	Co-ZIF-8	insulin	0.5–1.5 μm	transdermal delivery of insulin	[87]
	Zn ²⁺	sod-ZIF-8	insulin	100–200 nm	insulin delivery	[89]
			ZIF-C	insulin	<100 nm	
		U13	insulin	>10 μm		
		dia-ZIF-8	insulin	<100 nm		
 Guanine monophosphate (GMP)	Eu ³⁺	Eu-GMP	OVA	30 nm	cancer immunotherapy	[138]
 HICA	Zn ²⁺	ZIF-90	CRISP/CAS-9	146 nm–1 μm	cytosolic protein delivery for genome editing	[134]
 Gallic acid (GA)	Fe ³⁺	Fe-GA	BSA OVA HSA	193.5 nm 233.1 nm 196.5 nm	localized photothermal therapy	[136]
 meso-2,6-diaminopimelic acid (DAP)	Mn ²⁺	Mn-DAP	OVA	150 nm	cancer immunotherapy	[137]
 2-aminoterephthalic acid	Al ³⁺	MIL-53(Al)-NH ₂	OVA	65.2 nm	oral administration of antigens	[139]

endosomes triggers the cytosolic release of OVA. This study demonstrated that the formation of a MOF-shell around OVA enhanced the *in vivo* protection against blood proteases and the on-demand release of OVA triggers a systemic immune response.

Other studies on MOF-based drug carriers have focused on improving the cell uptake and enhancing the stability of MOF biocomposites in cell media. For instance, Chu and co-workers [127] prepared BSA@ZIF-8 nanoparticles (92 nm) post-functionalized with a polyvinylpyrrolidone (PVP) coating. Live-cell studies confirmed the rapid cellular uptake of PVP-coated BSA@ZIF-8 NPs, where the nano-carriers were successfully transported from endo-lysosomes into the cytosol affording an efficient intracellular co-delivery of multiple active proteins. Similarly, Fang and co-workers [128] reported the encapsulation of chloroquine diphosphate (CQ, an autophagy inhibitor), within ZIF-8 nanoparticles dec-

orated with poly(ethylene glycol)-folate (FA-PEG). The collected data demonstrated that ZIF-8 NPs coated with FA-PEG are more effectively internalized by human cervical cancer cells (HeLa, cancer cells) than embryonic kidney cells (HEK293, healthy cells). The authors suggested that this specificity can be attributed to the presence of folic acid and folate receptors on the surface of HeLa cells.

Alternative methods for the regulation of cellular uptake and target efficacy include embedding of drug carrier NPs in extracellular vesicles or membranes [129]. In this regard, Zheng and co-workers [102] reported the encapsulation of gelonin (a ribosome-inactivating polypeptide used as apoptotic agent), within ZIF-8 nanoparticles (ca. 80 nm). The resultant biocomposites were embedded within an extracellular vesicle to enhance the specific endocytosis by homotypic cells. Vesicle gelonin@ZIF-

8 biocomposites improves the specificity of the treatment and allowed for a systemic drug administration without compromising the integrity of toxin gelonin. This strategy has been further applied for the localized treatment of malignant tumors by bioactive MOF composites capable of producing cytotoxic agents on demand (Table 2). For instance, Cheng et al. [130] designed a MOF nano-biocomposites for the spatio-temporally controlled production of cytotoxic $^1\text{O}_2$ species under near-infrared irradiation (NIR) regardless the hypoxia environment of tumor tissues. The bioactive composite was obtained by the co-encapsulation of catalase (CAT) and Al(III) phthalocyanine chloride tetrasulfonic acid (AlPcS₄), which acts as photosensitizer (PS), within a ZIF-8 shell. Subsequently, the resultant MOF biocomposites were coated with a cancer cell membrane (Mem) leading to Mem-on-CAT&PS@ZIF-8 NPs of ca. 110 nm. The Mem coating on CAT&PS@ZIF-8 possessed adhesion properties towards tumor cells, which is beneficial for targeting cancer cells. Thus, once the nanocarrier was internalized, CAT catalyzed the decomposition of endogenous intracellular H_2O_2 into H_2O and O_2 , which increased the level of O_2 within the hypoxic tumor cells. Then, the resultant O_2 was transformed by the PS into $^1\text{O}_2$ upon NIR irradiation, this highly reactive species reacts with biological molecules causing lethal damage to the cells. By contrast, Qu and co-workers [131] designed a bioactive MOF biocomposite for starvation-activated cancer therapy capable of aggravating hypoxia in tumor microenvironments (Table 2). Glucose oxidase (GOx) and tirapazamine (TPZ), which is an anticancer prodrug that can be transformed into a cytotoxic radical only under hypoxia conditions [132], were co-encapsulated in ZIF-8 and the resultant particles were coated with an erythrocyte membrane. The 120 nm membrane-coated GOx&TPZ@ZIF-8 particles were used for their synergistic actions against tumor cells: GOx was used to consume glucose (nutrient for cells) and intratumorally O_2 (enhance hypoxia), then the simultaneous production of gluconic acid promote the MOF dissolution, leading to the release of TPZ, which is transformed into a highly cytotoxic radical under the aggravated hypoxic microenvironment.

Up to now, we have examined selected examples for cancer treatment; however, MOF-biocomposites can be applied to other

pathologies, including protein disorder-related diseases. Willner's group [100], developed a MOF-based glucose-responsive carrier for the controlled release of insulin for diabetic treatments. Glucose-responsive properties were obtained by co-encapsulation of insulin and GOx in ZIF-8 (In&GOx@ZIF-8). GOx was used to catalyze the transformation of glucose and O_2 into gluconic acid and H_2O_2 . The acidified microenvironment induced the degradation of the ZIF-8 matrix, thus liberating insulin (Fig. 6a). As H_2O_2 could inhibit the enzymatic function of GOx and acts as a cytotoxic agent, catalase (CAT) was co-embedded in ZIF-8 to decompose H_2O_2 into H_2O and O_2 . By varying the concentration of glucose, it was shown that enzymatic cascade GOx/CAT could be activated or inhibited, thus controlling the insulin release on-demand (Fig. 6b, c). More recently, Tang and co-workers [87] used In&GOx@Co-ZIF-8 (Co-ZIF-8 = ZIF-8 doped with Co^{2+} ions) for the fabrication of a stimuli-responsive transdermal insulin delivery system. However, in this case the MOF matrix presents catalase-like activity due to the presence of Co^{2+} ions as inorganic nodes, thus, the Co-ZIF-8 served as the catalase substituent in the multi-enzyme cascade process to achieve the controlled release of insulin and the simultaneous decomposition of H_2O_2 (Fig. 6d). Falcaro and Doonan reported a systematic study on the effect of the crystalline phase on the insulin release properties [89]. In this work, the authors showed that different Zn-2mIM-based crystals (**dia** = diamondoid, **sod** = sodalite, U13, and ZIF- CO_3 -1) can be prepared by varying the relative amount of ligand, metal, and biomacromolecule. Surprisingly, for certain synthetic conditions, the CO_3^{2-} dissolved in water was co-assembled into a MOF structure named ZIF- CO_3 -1 (aka ZIF-C) [133]. The author examined encapsulation efficiency (EE%) and drug release kinetic of selected In@ZIFs composites upon applying an acidic stimuli (pH 5.5). A phase-dependent release profile was observed and the complete release of insulin under acidic conditions (pH 5.5) was achieved between 40 and 300 min depending on the crystalline phase of the MOF.

The stimuli-responsive release properties of ZIFs are not limited to pH-changes. Recent studies have demonstrated that ZIF-8 can be slowly degraded in phosphate buffered saline media (PBS) (Fig. 7a, b) [67]. The degradation takes place due to the affinity of the phos-

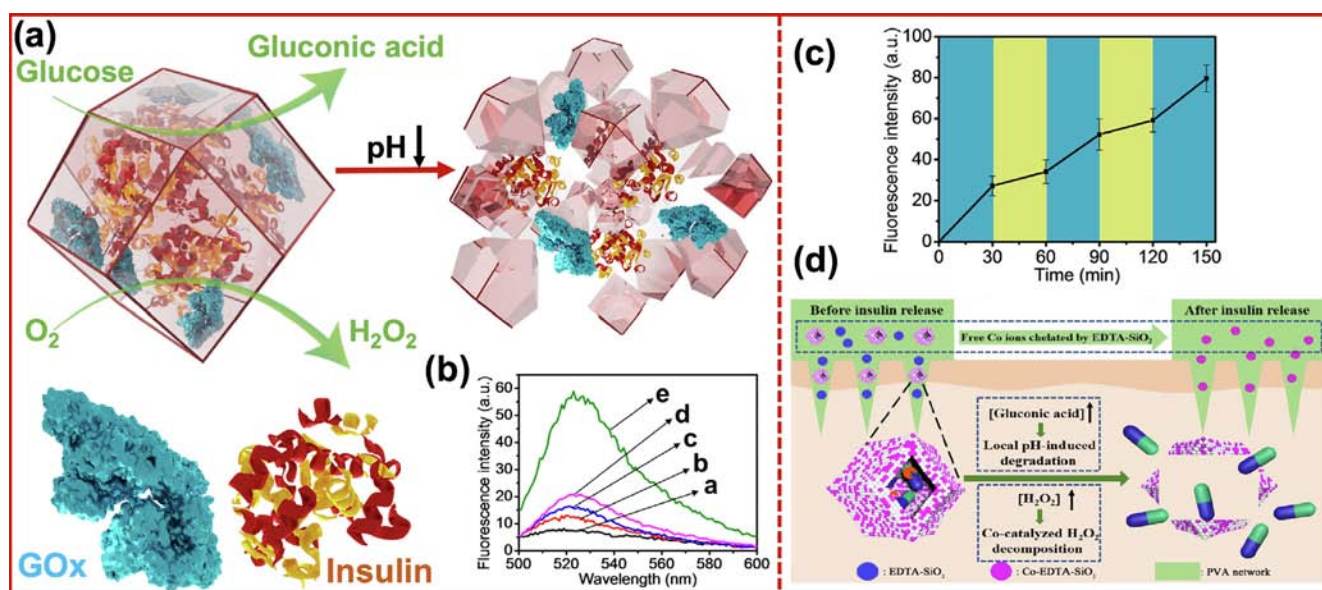


Fig. 6. (a) Schematic synthesis of the In&GOx@ZIF-8 composites and the stimuli release of the cargo triggered by the enzymatic oxidation of glucose. (b) Fluorescence spectra of FITC-labeled insulin released upon subjecting the FITC-In&GOx@ZIF-8 NMOFs to different concentrations of glucose for a fixed time interval of 1 h: (a) 0 mM, (b) 1 mM, (c) 5 mM, (d) 10 mM, (e) 50 mM. (c) Switchable time-dependent release of insulin in presence of high (15 mM, blue) and low (5 mM, yellow) concentrations of glucose. Adapted with permission from ref. [100] Copyright 2018 American Chemical Society. (d) Schematic representation of the transdermal delivery of insulin encapsulated within In&GOx@Co-ZIF-8 biocomposite. Reprinted with permission from ref. [87]. Copyright 2020 American Chemical Society.

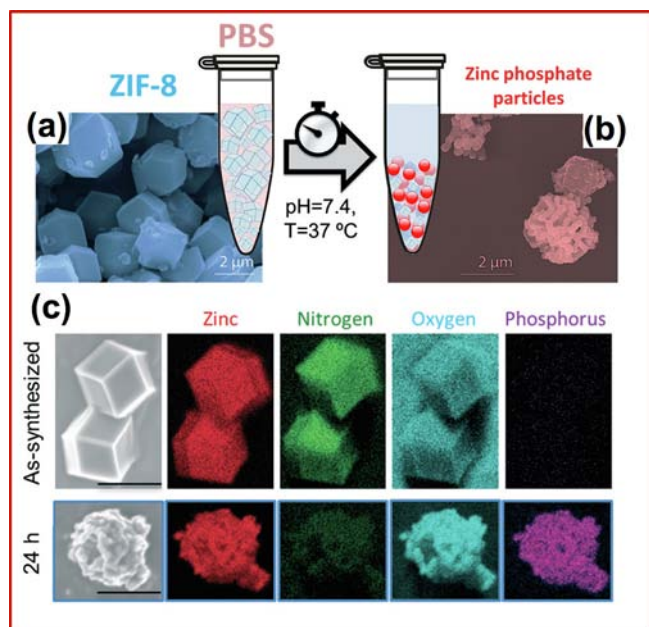


Fig. 7. Study of the stability of ZIF-8 particles in phosphate buffered saline media (PBS) under physiological conditions of pH (7.4) and temperature (37 °C). (a) SEM image of as-synthesized micro-ZIF-8 particles. (b) SEM image of micro-ZIF-8 particles after being soaked in PBS for 24 h. (c) EDX elemental maps of the as-synthesized ZIF-8 and the powder recovered after the incubation process in PBS for 24 h. Adapted with permission from ref. [67] Copyright 2019 Royal Society of Chemistry.

phate groups for the Zn^{2+} cations, which leads to the formation of amorphous zinc phosphate (Fig. 7c). The biodegradability of ZIFs in presence of phosphate groups has inspired the development of ATP-responsive carriers based on ZIF-90 for the cytosolic delivery of Cas9, which is a RNA-guided endonuclease protein used to edit the genome of mammalian cells [134]. ZIF-90 is structurally analogous to ZIF-8; however, it is composed of Zn^{2+} ions interconnected by imidazole-2-carboxaldehyde (HICA). This material was used by Mao and co-workers [134] for the encapsulation of RNase A and genome-editing Cas9 nuclease (protein) CRISPR/Cas9 (Fig. 8a). The competitive coordination of ATP towards Zn^{2+} cations

triggers the release of the cargo, where the RNase A and CRISPR/Cas9 genome editing is selectively delivered within the cells, due to the higher concentration of ATP in the cytosol (1–10 mM) than in the extracellular environment (<0.4 mM) (Fig. 8b).

Recent studies have demonstrated that the one-pot encapsulation of biomacromolecules within hybrid matrices can be extended to carboxylated-ligand based MOFs. To overcome the low solubility of this class of ligands, pioneering studies have focused on small carboxylic acids. For instance, Yang and Sun used gallic acid (GA) and Fe^{3+} ions for the encapsulation of model proteins (BSA-Paclitaxel, OVA) in Fe-GA network [135,136]. The resultant nanobiocomposites were applied to localized photothermal therapy for tumor cell treatment (Table 2).

Liu and co-workers [137] developed a drug carrier comprised of meso-2,6-diaminopimelic acid (DAP) interconnected by Mn^{2+} ions for targeted drug delivery of OVA. It is worth to mention that in this material, the DAP functioned as both ligand and adjuvant. Thus, the resultant nanoparticles OVA@Mn-DAP (ca. 150 nm) ensured the administration of an antigen protein and permitted the co-delivery of the adjuvant, which improved the cancer immunotherapy preventing the growth of melanoma tumors (Fig. 8c). The *in vivo* bioaccumulation of the biotherapeutics was tracked over time by magnetic resonance (MR) and fluorescence imaging. This study demonstrated that the retention of the biotherapeutics (OVA and DAP) in the lymph nodes increases when using OVA@Mn-DAP as a drug vehicle, in comparison to the administration of the free species (OVA and DAP) (Fig. 8d).

Similarly, Zhang and co-workers [138] reported the use of a lanthanide-based MOF carrier, obtained by guanine monophosphate (GMP) interconnected through Eu^{3+} nodes, for the encapsulation of OVA (Table 2). The resultant biocomposite was coated with an oligonucleotide capable of inducing a strong cellular immune response in cancer cells, enabling the intracellular co-delivery of OVA and tumor-associated antigens (TAAS). A further interesting example was reported by Sung, Chang, and co-workers who encapsulated OVA within MIL-53(Al)- NH_2 studying the system for oral administration of vaccines [139]. The MIL-53 (Al)- NH_2 shell was found to protect the protein antigen against the harsh conditions of the intestinal tract, and, at the same time, was acting as an adjuvant for a long-lasting immune response. Next, to facilitate the permeation of the biocomposite through the mucosa barrier, the authors embedded OVA@Al-MOF particles

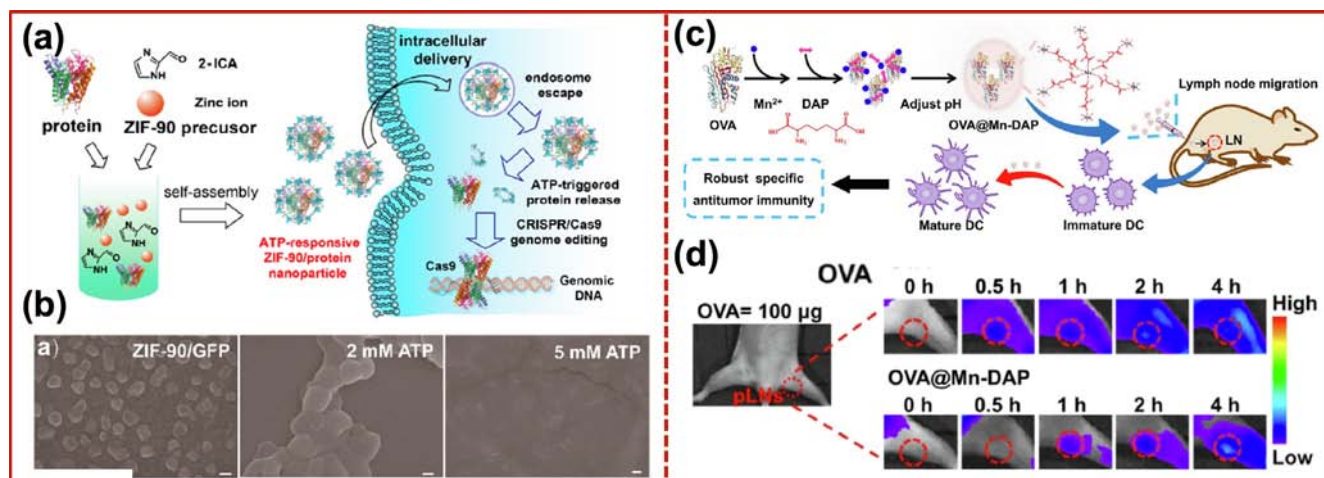


Fig. 8. (a) Schematic representation of the synthesis of protein@ZIF-90 biocomposite and ATP-triggered protein release from ZIF-90 nanoparticle inside cells. (b) SEM images of protein@ZIF-90 nanoparticles without and with ATP (2 mM and 5 mM) Scale bar: 100 nm. Adapted with permission from ref. [134]. Copyright 2019 American Chemical Society. (c) Schematic synthesis of OVA@Mn-DAP nanoparticles. (d) *In vivo* fluorescence images at the popliteal lymph nodes (pLNs). Adapted with permission from ref. [137] Copyright 2019 American Chemical Society.

within yeast-derived capsules. *In vivo* studies revealed that this co-enssembled arrangement functioned as “Trojan Horse”-like platform, allowing for the transepithelial transport of OVA@Al-MOF.

3.2.1. Summary and future outlook

MOFs have emerged as a new tunable platform for the design of protein-based drug delivery systems (DDS). One-pot encapsulation methods typically result in high EE% of model and clinical biotherapeutics in MOFs. By carefully choosing the target biological system (e.g. cancer cells) and the MOF (e.g. ZIFs), the DDS can be engineered toward its selective degradation (e.g. acidic pH in proximity of cancer tissues). In case of proteins@ZIFs, it was shown how these systems are responsive to specific chemical stimuli (e.g. presence of glucose for insulin release). Furthermore, the particle size of protein@MOF biocomposites are in the nano- to micro-meter range, which is suitable for administration routes ranging from intravenous injection to transdermal delivery (e.g. microneedles). Functionalisation of the MOF surface can improve the targeting properties or the circulation time of the DDS. Thus, by controlling degradation conditions, particle size, and surface chemistry both delivery and biodistribution can be optimized. In addition, the typical cost of the MOF material is marginal with respect to the price of the encapsulated biotherapeutic.

3.3. Protein@MOFs for biopreservation

Proteins are prone to denaturation and bioactivity loss upon their exposure to environmental stressors. Indeed the relatively “fragile” nature of biomacromolecules is the major issue that hampers the extended use of proteins as biotherapeutics, as well as in the development of new biosensing devices [123]. For example, after the production of protein-based therapeutics their storage, packaging, and transportation is needed before reaching the patient [16], and the bioactivity of the therapeutic has to be preserved along this journey. Lyophilization, or freeze-drying, is one of the most used strategies to preserve proteins in solid state [16]. However, a considerable amount of therapeutic proteins are formulated as aqueous solutions, which typically requires storage and transportation at low temperatures (aka “cold chain”) to improve their shelf-life. With respect to vaccines, the World Health Organization (WHO) suggest their storage at a temperature that ranges from 2 °C to 8 °C [16,42]. Thus, infrastructure required for the cold-chain increases the shipping costs, hampers the distribution of vaccines to geographically remote places and their storage in the absence of dedicated facility. Several strategies have been reported to address those problems, including lyophilization, spray-drying, vacuum foam, and protein immobilization using polymers or hydrogels [16]. An emerging protocol is the encapsulation of proteins within MOFs as this was shown to enhance the stability of the biomolecule against harsh conditions including high temperatures, organic solvents, mechanical stress, and presence of proteolytic/chaotropic agents. In this section, we highlight the recent progress of MOF-based biocomposites for biobanking.

The pioneering work by Falcaro's group [27], demonstrated the bio-preservation capabilities of MOF-based biocomposites obtained *via* the biomimetic mineralization approach. In this study, the authors compared the enzymatic activity of free HRP and HRP@ZIF-8 upon exposure to inhospitable environments, including the presence of a proteolytic agent (trypsin), and boiling solvents (water and DMF) (Fig. 9a). According to this study, in presence of trypsin, HRP encapsulated within a ZIF-8 exoskeleton retained 88% of its enzymatic activity for the conversion of pyrogallol to purpurogallin, whilst the free enzyme exhibited only a 20% conversion. The protective properties of ZIF-8 were compared to other porous carriers such as CaCO₃ and mesoporous SiO₂. For this purpose, the authors incubated free HRP, HRP@ZIF-8, HRP@CaCO₃,

and HRP@SiO₂ in boiling water for 1 h. The free enzyme lost its enzymatic activity, while HRP@CaCO₃ and HRP@SiO₂ only retained 39% and 65% of the bioactivity, respectively. By contrast, the HRP encapsulated within ZIF-8 preserved an 88% initial activity (Fig. 9a). The authors stated that the superior stability afforded by the ZIF-8 exoskeleton compared with CaCO₃ and SiO₂ is directly related to the tight encapsulation of the enzyme within the MOF architecture, where the biomolecules are enclosed in pockets slightly larger than the macromolecule's size. This fact was corroborated by the SAXS analysis on ZIF-8-based biocomposites, where the results revealed the presence of pocket in the MOF matrix that is 10–30% larger than the radius gyration of the encapsulated biomacromolecule. This arrangement inhibits the unfolding of the enzyme allowing bioactivity preservation [140].

More recently, Singamaneni and co-workers [44] demonstrated the practical use of ZIF-8 biocomposites for the preservation of biomarkers to improve their stability during transport, storage, and handling. In this study neutrophil gelatinase-associated lipocalin (NGAL, a protein present in blood after acute kidney injury) [141] and serum/plasma CA-125 (a tumor marker from ovarian cancer cells) [142] were used as biospecimens. The preparation of biomarkers@ZIF-8 was successfully conducted in different biological fluids such as urine, serum, plasma, and blood. Subsequently, the samples were supported on paper substrates and stored in a dry state. The samples were shipped from Missouri to California and sent back to test bioactivity of the encapsulated biospecimen (Fig. 9b). This study demonstrated that the biomacromolecules conformation is preserved at room temperature and 40 °C.

The same research group demonstrated that this strategy could be applied to preserve the biological activity of insulin (In). [143] In this study, the authors compared the biological activity of free In and In@ZIF-8 after being exposed to various stressors, including high temperatures (25, 40 and 60 °C) for one week, mechanical agitation (200 rpm for 48 h), and the incubation in organic solvents (ethyl acetate) (Fig. 9c). The immunoassay and the spectroscopic analysis demonstrated the preservation of the biological activity of the In released from the ZIF-8 biocomposite after being stored in dry state at high temperatures (>95% at 25 °C and 40 °C, >80% at 60 °C). By contrast, free In stored under the same temperatures exhibited a decrease in its biological activity (≈70%, ≈60% and ≈50% at 25 °C, 40 °C and 60 °C; respectively). A similar approach was employed by Chen and co-workers [45] who tested the stability of polyclonal antibodies including human immunoglobulin G (IgG), polyclonal antibody (H-IgG) and goat anti BSA IgG (G-IgG) encapsulated within two different MOF matrices (ZIF-8 and ZIF-90). To evaluate the protection effect of the MOF matrix on G-IgG@ZIF-90 and G-IgG@ZIF-8 biocomposites, the samples were exposed to a series of perturbation environments that would typically lead to denaturation of proteins (i.e. high temperatures, organic solvents, and mechanical pressure). Subsequently, the bioactivity of the encapsulated and free G-IgG was assessed by enzyme-linked immunosorbent assay (ELISA) test. The results showed that G-IgG released from the MOF matrix retained its binding capability (>90%), and showed low aggregation (13–25%) after being exposed at 75 °C for 20 min. By contrast, the free antibody, stored under the same conditions (75 °C), lost its initial binding activity (<10%) and presented severe aggregation (88%) (Fig. 9d). These results highlight the thermal protection of MOF matrices for antibodies.

The versatility of ZIFs was further confirmed by Ouyang and co-workers [118] who encapsulated HRP, Cyt c, ribonuclease A (RNase A), Ribonuclease B (RNase B) and trypsin, using PVP and cysteine as additives (*vide supra*). Then, the protection capabilities of the MOF shell were verified by exposing the resultant biocomposites to high temperatures, high concentrations of urea, and proteases.

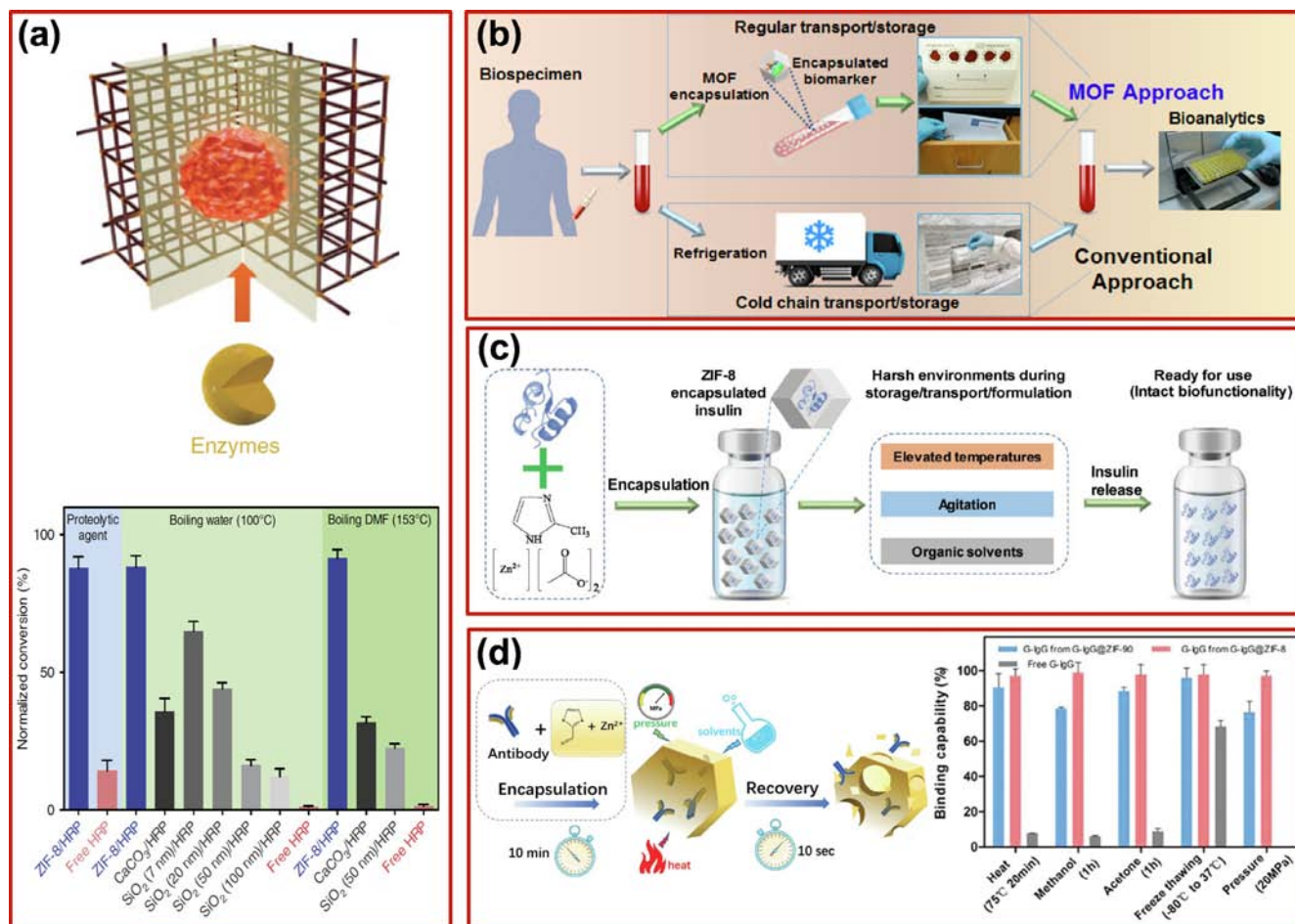


Fig. 9. (a) Schematic illustration of the biomimetic mineralization of HRP within ZIF-8. Biopreservation performance of different biocomposite materials upon exposed to drastic conditions. Adapted with permission from ref. [27] Copyright 2015 Nature communications. (b) Schematic representation of the cold-chain-based biospecimen preservation. Reprinted with permission from ref. [44] Copyright 2018 American Chemical Society. Biopreservation efficacy of insulin (c) and antibodies (d) encapsulated within different MOF shells upon being exposed under various environmental stressors. Reprinted with permission from refs [143,45] respectively. Copyright 2018 and 2019 John Wiley and Sons.

The bioactivity preservation of proteins through encapsulation within MOFs is not limited to drug delivery applications. Recent studies have demonstrated that this approach can be easily integrated in the design of protein-based nanodevices, where the biorecognition capabilities or biocatalytic activity are threatened by the operating conditions. For instance, the development of technologies based on enzymes immobilized on plasmonic nanostructures opens the possibility of using the photothermal effect of the nanomaterial to enhance the catalytic activity of conventional enzymes by controlling the local temperature close the biomolecule [144]. However, most of the enzymes present low thermostability. Thus, to overcome this issue, Singamaneni and co-workers showed that the stability of thermophilic enzymes (i.e. HRP) supported on Au nanorods (AuNRs) can be improved by encapsulation within a ZIF-8 shell [144]. The catalytic activity of the AuNR-HRP@ZIF-8 biocomposite was evaluated before and after the exposure to denaturing conditions, including high temperatures, toluene, and the presence of proteases. Some of the results indicate that the non-encapsulated system AuNR-HRP presents a catalytic activity below 5% after exposure to high temperatures. Conversely, AuNR-HRP@ZIF-8 preserves 85% of the original biological activity after exposure to 55 °C for 7 days.

More recently, Wang and co-workers [145] employed ZIF-8-based biocomposites to maintain the biorecognition capabilities of the anti-CD-146 antibody supported on an atomic force micro-

scope (AFM) tip. This antibody-conjugated nanostructure (AFM tip/anti-CD-146) serves as a nanoscale test to study the recognition capabilities of anti-CD-146 towards CD-146, which is an antigen typically expressed on the surface of melanoma cells. To this end, the authors monitored the binding force and binding frequency of AFM tip/anti-CD-146 before and after being exposed to harsh reaction conditions. The results showed that the AFM tip functionalized with anti-CD-146 does not recognise CD-146 after being stored at 50 °C for 3 days. The binding capacity of the AFM tip/anti-CD-146 coated with a ZIF-8, exposed to the same conditions (50 °C/3 days), were tested after the removal of ZIF-8 exoskeleton by rinsing the tip with an acid solution. The collected data demonstrated that the ZIF-8 exoskeleton preserves the recognition capabilities of anti-CD-146 under denaturing conditions. Moreover, such results demonstrate that the encapsulation in ZIFs and the subsequent degradation MOF shell do not affect the antibody conformation.

3.3.1. Summary and future outlook

MOFs represent a promising material for biospecimen preservation due to their unique protection properties and on-demand degradability. In particular, biomacromolecules@MOF was found to be an effective strategy for rapid encapsulation at room temperature by adding the MOF precursors to a water-based solution of the biospecimen. Hormones, enzymes, biomarkers, vaccines, anti-

bodies have been encapsulated in ZIF-8 and protected from temperature, solvents, and mechanical stress. After their release from the ZIF matrix, their activity was consistently superior to the free biomacromolecules. Indeed, it has been shown that MOF coatings present superior protective properties than other inorganic coatings such as CaCO_3 and SiO_2 . The remarkable biopreservation capabilities of MOF biocomposites have been applied in the cold-chain-free transport of biotherapeutics, this permits the handling, transport, and storage of biospecimens without the need for refrigeration, thereby reducing the shipping costs. Additionally, recent studies have demonstrated that the protective properties of MOF biocomposites can be easily applied in the design of protein-based nanodevices, where the biorecognition capabilities or biocatalytic activity of the macromolecule are threatened by the operating conditions.

3.4. Protein@MOFs and Protein-on-MOFs for biosensing

As defined by IUPAC, a biosensor is a self-contained integrated device which provides selective quantitative or semiquantitative analytical information by using a biological recognition element in direct spatial contact with a signal transducer [146]. A biosensor can use a biological response mediated by enzymes, immunosystems, or cells into a quantified processable signal. The biological recognition unit acts as a chemical receptor that responds to a target analyte; this response is transformed by the transducer into a processable electrochemical, colorimetric or optical signal [145–149].

Although different sensing, transduction and integration methods are available, sensitivity and reproducibility remains the major challenges in current diagnostic technologies [145–149]. This stimulates research in different directions, including new sensing technologies, where the main goals are fast, accurate, precise, and reproducible responses [147–151]. Improved biosensors will facilitate early diagnoses and prompt treatments. To this end, protein-based MOF biocomposites have emerged as alternative materials for the design of new, highly sensitive, and cost-effective biosensors [17–21]. The protein, which acts as a biorecognition element, can be found either embedded (protein@MOFs) in or bioconjugated to MOFs (protein-on-MOFs) [18]; whilst the signal molecules can be located within the pore network of the MOF. Therefore, the use of MOF-based composites as detection probes permits the colocalization, of the biorecognition element and a large number of signaling elements in one single particle. So far, MOF biocomposites have been extensively studied for sensing a wide variety of analytes ranging from small molecules (glucose, H_2O_2 , phenol, etc.), to large biomolecules such as antigens, biomarker, infectious agents and exosomes [17–21].

3.4.1. Applications of protein@MOF biocomposites for small molecule detection

In biochemistry, an analyte with molecular weight below 1000 Da is classified as a small molecule [148]. In particular, most of the available studies report the use of protein@MOF composites for the detection of small molecules such as H_2O_2 and glucose.

Protein@MOFs as H_2O_2 sensors

Hydrogen peroxide H_2O_2 is a major biological reactive oxygen species obtained as a by-product of numerous metabolic reactions. Although H_2O_2 plays an important role in cellular signaling processes, H_2O_2 is prone to produce hydroxyl radicals, which are strong oxidants capable of reacting with many biological molecules causing cell and tissue damaging. Therefore, it is important to develop adequate analytic techniques able to detect H_2O_2 in living organisms [152].

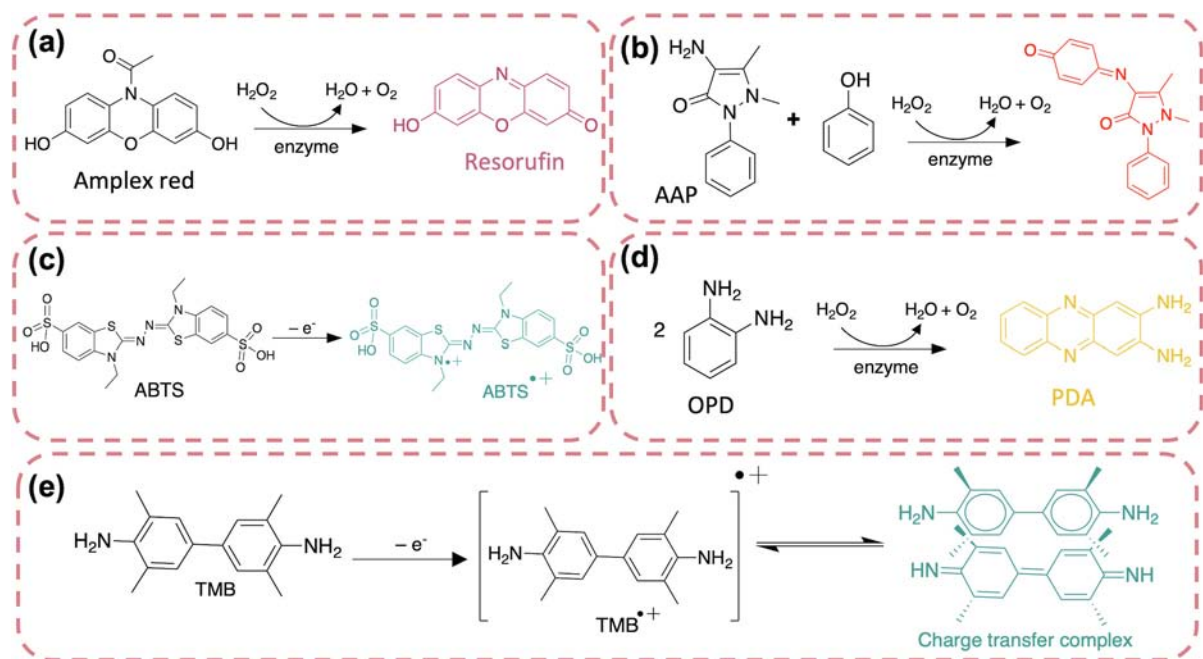
A pioneering report by Ge and Liu and co-workers [26] in 2014 suggested the use protein@MOF biocomposites in biosensing by demonstrating that the biocomposite obtained from the encapsulation of Cyt *c* within ZIF-8 crystals can be used as a fluorometric sensor to detect H_2O_2 , methyl ethyl ketone peroxide (MEKP), and *tert*-butyl hydroperoxide (TBHP) in solution. The authors used *N*-acetyl-3,7-dihydroxyphenoxazine (Amplex Red, fluorogenic probe) as a signal molecule, since in presence of the target peroxides the Cyt *c* catalyzes the oxidation of Amplex Red to yield a fluorescent phenoxazine (i.e. resorufin) [153] (Scheme 1a).

This work inspired the development of other protein@MOF biosensors for the detection of H_2O_2 . For instance, Yang and co-workers [154] designed a colorimetric biosensor encapsulating bovine hemoglobin (Bhb) in ZIF-8 particles: H_2O_2 was detected by using 4-aminoantipyrine (AAP) as signal molecules, where the peroxidase-like activity of Bhb@ZIF-8 was used to perform the catalytic co-oxidation of phenol and AAP in presence of H_2O_2 (Scheme 1b) [155]. According to the reported results, the catalytic activity of this system was 423% higher than that observed in the free Bhb. A possible explanation could be the ability of most MOFs to uptake/concentrate hydrophobic molecules [156]. The Bhb@ZIF-8 sensor showed faster catalytic response (4 min), than the free enzyme (15 min), and a wide linear range (0–800 μM) for H_2O_2 , with a limit of detection (LOD) of 1 μM (Table 3). This example confirms the importance of both protein and MOF matrix as a strategy to prepare biosensors with enhanced properties (i.e. response time and LOD). The applications of MOF biocomposites for the detection of H_2O_2 have been extended to the development of electrochemically-based sensors. Liu and co-workers [157] reported the electrochemical detection of H_2O_2 , using HRP@ZIFs nanocomposites supported on graphene oxide (GO). This HRP@ZIFs-on-GO multicomposite material was immobilized on ITO electrode using polyethyleneimine. This arrangement provides to the electrode a high sensitivity towards the target analyte (Table 3).

Protein@MOFs as glucose sensors

Glucose is a biomarker for diabetes and thus the development of novel sensors is an active field of research. Diabetes disease causes abnormal levels of insulin in the body, due to either a malfunction of the pancreas (diabetes type 1) or the ineffective use of insulin by cells (diabetes type 2). Insulin is the hormone that regulates the level of glucose in the blood, thus mild alterations in insulin levels or action will lead to hypoglycemia or hyperglycemia conditions, which can cause severe health issues including tissue damage, kidney failure, blindness, among others [158]. Consequently, regular glucose monitoring in diabetic patients is important to avoid further health complications [158]. The use of MOF-based biocomposites for the enzymatic detection of glucose has been extensively explored mostly as colorimetric or electrochemical sensors [21].

Liu and co-workers reported the first example of a colorimetric glucose biosensor based on the co-encapsulation of multiple enzymes (GOx and HRP) in ZIF-8 particles [159]. This multi-enzyme system (GOx&HRP@ZIF-8) operates via a biocatalytic cascade process: 1) GOx, in presence of O_2 oxidase glucose to yield gluconic acid and H_2O_2 ; 2) HRP consumes H_2O_2 for the oxidation of ABTS (2,2'-azino-bis(3-ethylbenzothiazoline-6-sulphonic acid)) into ABTS^{•+} (Scheme 1c) [160]. The latter is a chromogenic agent that absorbs light at 415 nm and thus the production can be monitored via UV-vis spectroscopy (Fig. 10a). The reported LOD was 0.5 μM , demonstrating higher sensitivity than the other colorimetric glucose sensors reported in the literature. Additionally, irrespective of interfering compounds (e.g. fructose, maltose) GOx&HRP@ZIF-8 showed specificity towards glucose detection



Scheme 1. Colorimetric reaction of HRP and peroxidase-like catalysts with different chromogenic substrates: (a) Amplex red, (b) 4-aminoantipyrine (AAP), (c) 2,2'-azino-bis(3-ethylbenzothiazoline-6-sulphonic acid) (ABTS), (d) o-phenyldiamine (OPD), (e) 3,3',5,5'-tetramethylbenzidine (TMB).

Table 3

Comparative overview of Protein@MOF and Protein-on-MOF biocomposites for small molecules detection.

Detection method	Molecule target	Biorecognition element	MOF	Synthetic strategy	Linear range	Detection limit	Refs
Fluorometric	H_2O_2	Cyt c	ZIF-8	encapsulation	5 nM to 1 μM	3 nM	[26]
Electrochemical sensor	H_2O_2	HRP	ZIF-8	encapsulation	0.02–6 mM	3.4 μM	[157]
Colorimetric	H_2O_2	BHb	ZIF-8	encapsulation	0–800 μM	1 μM	[154]
Colorimetric	glucose	GOx/HRP	ZIF-8	encapsulation	0–100 μM	0.5 μM	[159]
Colorimetric	glucose	GOx/HRP	ZIF-8	encapsulation	0–150 μM	0.4457 μM	[163]
Colorimetric	glucose	GOx	ZIF-8/Fe-PDA	encapsulation	0.5–100 μM	1.1 μM	[166]
Colorimetric	glucose	GOx/HRP	ZIF-8	encapsulation	8 μM to 5 mM	8 μM	[164]
Colorimetric	glucose	GOx	amph-ZIF-8	encapsulation			[165]
Fluorometric	glucose	GOx	Tb^{3+} /AMP	encapsulation	0.5–300 μM	80 nM	[168]
Fluorometric	glucose	GOx	Eu^{3+} @UIO-76	grafting	0.1 μM to 10 mM	0.23 μM	[184]
Colorimetric	glucose	GOx	Fe-MIL-88B-NH ₂	grafting	1–500 μM	0.487 μM	[161]
Colorimetric	glucose	GOx	Fe-MIL-88B-NH ₂	grafting	2–100 μM	0.98 μM	[167]
Electrochemical sensor	glucose	GDH	ZIF-70	not clear	0.1–2 mM	not clear	[169]
colorimetric	glucose	GOx	ZIF-8	encapsulation	0.01–0.3 mM	9.2 μM	[171]
Electrochemical sensor	glucose	GOx	ZIF-8	encapsulation	0.1 to 1.7 mM	not clear	[171]
Electrochemical sensor	glucose	GOx	MIL-100(Fe)	grafting	5–1400 μM	5 μM	[170]

(Fig. 10b). It is worth mentioning that the close spatial location of GOx and HRP in a porous microenvironment can facilitate the molecular diffusion enhancing the efficiency of the enzymatic cascade reaction.

Recent studies further supported the importance of the spatial distribution of the enzymes within the MOF for enhanced multi-enzyme cascade catalysis [162]. To this end, Jiang and co-workers [163] demonstrated that the compartmentalization of GOx&HRP multi-catalytic system within ZIF-8 is an effective strategy to improve the sensitivity and increase the linear range of colorimetric biosensors for glucose detection (Table 3). The compartmentalization of the enzymes was achieved by mixing sodium deoxycholate (NaDC), HRP, and the Zn^{2+} precursor. This mixture resulted in HRP encapsulated in a hydrogel coating. Then, a second solution containing both HmIM and GOx was added to this mixture. The authors suggested that the hydrogel allowed for the spatial separation between enzymes and served as a soft template to form hollow ZIF-8 spheres denoted as H-ZIF-8. These

H-ZIF-8 capsules serve to separate the enzymes in different compartments, where the HRP is located within the central cavity, whilst the GOx is supported onto the outer region of the H-ZIF-8 sphere. As a consequence, the controlled spatial localization of enzymes promotes the efficient diffusion of products from HRP to GOx pulling the equilibrium towards the product formation. The authors demonstrated the feasibility of this compartmentalized system GOx-on-HRP@H-ZIF-8 as a glucose colorimetric biosensor for point-of-care (POC) testing devices.

Similarly, Chen and co-workers [164] showed that the combined immobilization of GOx&HRP within ZIF-8 can be applied in the design of a portable lab-on-chip device for glucose detection. The colorimetric biosensor was fabricated using a polypropylene membrane as support and polydopamine/polyethyleneimine (PDA/PEI) to fix composite in microfluidic channels (Table 3).

Although, most of the GOx@Zn(mIM)₂ biocomposites used for glucose detection focused on crystalline *sod*-ZIF-8, Ge and co-workers [165] prepared amorphous *am*-GOx@Zn(mIM)₂ biocom-

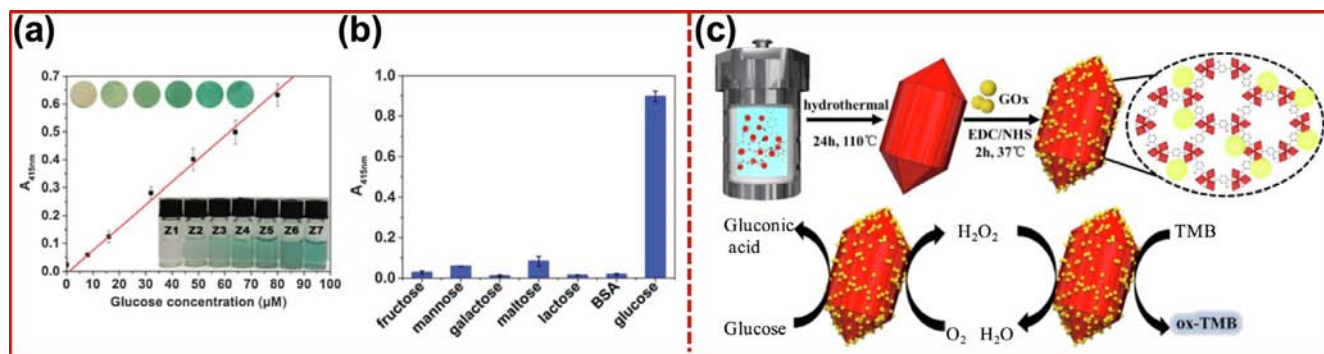


Fig. 10. (a) Application of GOx&HRP@ZIF-8 composite for the colorimetric detection of glucose in solution at concentrations of 0–100 mM inset: photographs showing visible detection of glucose by enzyme-containing paper strips and in solution. (b) Selectivity study of the multi-enzyme composite sensor in presence of various interfering compounds. Adapted with permission from ref. [159] Copyright 2015 Royal Society of Chemistry. (c) Schematic synthesis of GOx-on-Fe-MOF biocomposite, and the catalytic cascade process employed for glucose determination. Reprinted with permission from ref. [161] Copyright 2019 American Chemical Society.

posite and compared the performance of *am*-GOx@Zn(mIM)₂ with *sod*-GOx@Zn(mIM)₂ for glucose detection. The authors found that the *am*-GOx@Zn(mIM)₂ nanocomposites (particle size 150 nm) are 20 times more active than its crystalline counterpart (GOx@ZIF-8) and as active as the free GOx in solution. The authors attribute the remarkable enzymatic activity to the presence of coordination defects in *am*-Zn(mIM)₂ created during the encapsulation process. This was supported by the presence of mesopores (1–10 nm) in the *am*-Zn(mIM)₂, which significantly improved the mass transfer towards the embedded enzyme and, thereby enhancing the enzymatic response. The *am*-GOx@Zn(mIM)₂ particles were used as a probe for the *in situ* determination of glucose within living cells, and the results demonstrated a high fluorescence sensitivity for the determination of intracellular glucose (Table 3). In fact, this technique was able to discriminate among different cell types based on their glucose uptake capabilities. The determination of this cellular metabolite permits the distinction between cancerous and normal cells, providing an attractive platform for applications on early diagnosis of tumors. Such results are in agreement with a recent study published by Hu et al. [120], who reported the synthesis of different enzyme@ZIF-8 based biocomposites (enzyme = Cyt c, HRP, and GOx) using a microfluidic flow reactor. The authors demonstrated that this synthetic procedure allows for the continuous change in the concentration of ZIF-8 precursors, which modifies the mIM:Zn²⁺ ratio in the laminar flow and leads to the formation of coordination defects. These defects create mesopores that facilitate the mass transport through the MOF shell, which improves the enzymatic activity of the biocomposites in comparison with their analogues obtained by batch synthesis. It should be noted that all multi-enzyme biosensors based on the catalytic oxidation of glucose by GOx give rise to an acidic microenvironment within the MOF biocomposite that could affect the stability MOFs. This is the case for ZIF-8, which degrades under acidic conditions [103]. This aspect is a limit for the reusability of GOx@ZIF-8 biosensors. Alternatively, Zhao et al. [166] described the preparation of GOx@ZIF-8 coated with Fe-polydopamine (Fe-PDA) to afford an Fe-PDA-on-GOx@ZIF-8 composite. The Fe-PDA coating enhances the stability of the nanoreactor under acidic conditions, and mimicked the peroxidase activity, acting as H₂O₂ scavenger. The recyclability test performed on Fe-PDA-on-GOx@ZIF-8 demonstrated that this system maintained 85% initial activity after being reused 4 times.

So far, we have been discussing systems based on Zn(mIM)₂; however, recent reports have showed that the enzymatic detection of glucose can be achieved by immobilization of a biorecognition element on the outer surface of a preformed MOF with

peroxidase-mimicking activity. This approach could exploit the MOF to reduce issues related to the production of intermediates during multi-enzyme cascade reactions. To prove this hypothesis, Zhu and co-workers [161] reported the fabrication of colorimetric glucose biosensor based on grafting (covalent immobilization) of GOx onto Fe-MIL-88B-NH₂, a MOF that shows a peroxidase-like activity (Fig. 10c). In this catalytic process, first GOx catalyzes the glucose oxidation to yield gluconic acid and H₂O₂, then Fe-MIL-88B-NH₂ consumes H₂O₂ to produce ·OH, which oxidized the chromogenic substrate 3,3',5,5'-tetramethylbenzidine (TMB), into a green-blue colored ox-TMB intermediate (λ_{max} 652 nm) (see Scheme 1e). This GOx-on-Fe-MIL-88B-NH₂ biosensor displayed a linear response range of 1–500 μM, with a LOD of 0.478 μM (Table 3). When compared with the free enzyme system, GOx-on-Fe-MIL-88B-NH₂ showed higher tolerance to temperature, pH changes, and reusability (tested up to five cycles). Fe-MIL-88B was also employed by Zhao et al. [167] for the fabrication of enzymatic glucose sensor. In that work, the synthesis of Fe-MIL-88B was performed in the presence of lauric acid, to induce the formation of hierarchical porous material HP-Fe-MIL-88B (pore size distribution centered at 2, 4 and 8 nm). Then, the MOF matrix was post functionalized with boronic acid (BA) to facilitate the grafting GOx on the Fe-MOF surface. The glucose response of the hierarchical porous biocomposite GOx-on-HP-Fe-MIL-88B-BA (PSD centered at 4 and 8 nm; PSD = pore size distribution) and microporous GOx-on-Fe-MIL-88B-BA (PSD < 2 nm) was assessed by UV-vis spectroscopy using TMB as chromogenic substrate (Scheme 1e). The results indicated that hierarchically porous GOx-on-HP-Fe-MIL-88B-BA provides a 10-times faster catalytic response to glucose than GOx-on-Fe-MIL-88B-BA. The authors suggested that this difference can be attributed to the improved mass transfer in hierarchical porous systems.

Other MOFs that have been explored for the development of enzymatic glucose sensors are lanthanide-based coordination polymers. The fluorescence properties of such MOF materials together with the quenching effect of H₂O₂ released during the enzymatic oxidation of glucose is attractive for the fabrication of all-in-one fluorescent probes. For instance, Gao et al. [168] used fluorescent properties of lanthanide-based coordination polymers and carbon dots (CDs) to prepare a ratiometric biosensor for glucose detection in serum. This biosensor was obtained via co-encapsulation of GOx and CDs within a coordination polymer (CP) comprised of Tb³⁺ ions interconnected by adenosine monophosphate linkers (Fig. 11a). Then biocomposite was further functionalized with carboxyphenylboronic acid (CPBA). The complexation of this compound to the free coordination sites of Tb³⁺-

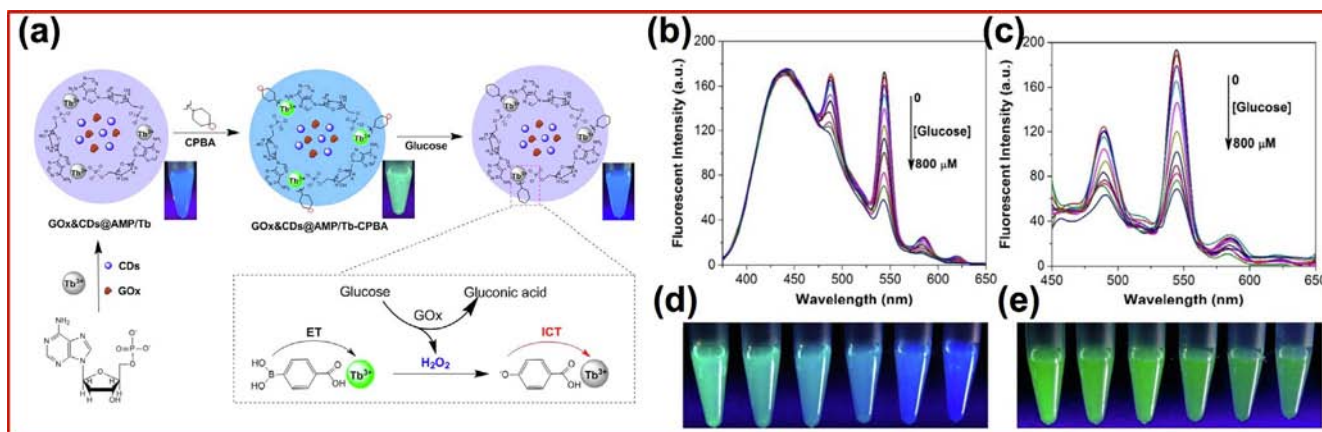


Fig. 11. (a) Schematic illustration of the synthesis of dual-emissive GOx&CDs@Tb-AMP/CPBA particles and their application in the ratiometric sensing of glucose. Emission spectra of GOx&CDs@Tb-AMP/CPBA (b) and Tb-AMP/CPBA + GOx (c) in the presence of different concentrations of glucose (0–800 μM). Fluorescence response of GOx&CDs@Tb-AMP/CPBA (d), and Tb-AMP/CPBA + GOx (e) upon the addition of different concentration of glucose (from left to right 0, 2, 5, 10, 30, 50 μM). Adapted with permission from ref. [168] Copyright 2017 Royal Society of Chemistry.

enhances the fluorescence of this lanthanide inhibiting the quenching effect of water molecules (Fig. 11a). Interestingly, the H₂O₂ released during the glucose oxidation induced the deboronation of CPBA, leading to quenching of Tb³⁺ fluorescence (Fig. 11b–e). Importantly, this process did not influence the fluorescent response of CDs, that could be employed as a reference for the ratiometric sensing of glucose. The simultaneous readings of two different wavelengths, the constant fluorescence of the internal standard (CDs response) and MOF response on glucose concentration (Tb³⁺ emission), was shown to minimize the effect of external interferences derived from the instrument, background, and environment. For this glucose sensor, the authors reported a linear response range of 0.5–300 μM and LOD of 80 nM.

The use of MOF biocomposites for glucose detection has been extended in electrochemical biosensing (Tables 3 and 4). In 2013, Mao and co-workers [169] screened different zeolitic imidazolate frameworks (ZIF-7, ZIF-8, ZIF-67, ZIF-68, and ZIF-70) as MOF supports to co-immobilize methylene green (MG) and glucose dehydrogenase (GDH) via bio-conjugation approach. Since ZIF-70 exhibited the highest loading capacity, the dehydrogenase-based electrochemical sensor was fabricated by depositing MG-on-ZIF-70 and GDH-on-ZIF-70 onto glassy carbon electrodes. According to the reported data, this biosensor was highly specific towards glucose with a linear response range within 0.1–2 mM. Similarly, Patra et al. reported the development of glucose amperometric biosensor based on GOx-on-MIL-100(Fe) supported on a carbon electrode functionalized with PtNPs [170]. The sensitivity reported for this system is 71 mA M⁻¹cm⁻² with a limit of detection of 5 μM, and response time <5 s. More recently, Dong and co-workers [171] reported a glucose biosensor fabricated by the co-encapsulation of NiPd NPs and GOx within ZIF-8 nanoflowers. The resultant GOx&NiPd@ZIF-8 biocomposite combined the peroxidase-like activity of NiPd NPs with the enzymatic activity of GOx. The authors demonstrate the applicability of GOx&NiPd@ZIF-8 for both colorimetric and electrochemical detection of glucose. The performance of this GOx&NiPd@ZIF-8 biocomposite as a colorimetric glucose sensor was assessed using *o*-phenylenediamine (OPD) as chromogenic substrate, which in presence of H₂O₂ is catalytically oxidized to yield a 2,3-diaminophenazine (PDA, λ_{max} = 417 nm) (Scheme 1d). This system presents a linear response within the range of 0.01–0.3 mM. Based on the competitive reactions of oxygen reduction and glucose oxidation, GOx&NiPd@ZIF-8 was tested for the electrochemical detection of glucose. In this case, the authors detected an increment in the cathodic peak centered at

–0.45 V when the concentration of H₂O₂ rose from 0 to 10 mM. However, the linear response reported for this electrochemical sensor is in the 0.01–0.3 mM range.

3.4.2. Protein@MOF and protein-on-MOF biocomposites in immunoassays

Early detection of specific biomarkers in biological fluids is crucial for a prompt medical diagnosis and successful therapeutic process. Immuno-diagnostic tests are attractive systems for early detection. In particular the enzyme-linked immunosorbent assay (ELISA), which is a biochemical method designed to detect and quantify targeted biomacromolecules (examples of antigens are proteins, carbohydrates, nucleic acids, viruses). ELISA uses antibodies as biorecognition elements, and an enzyme, that can be either directly or indirectly coupled to the antibody, provides the signal response when the antigen–antibody complex is formed [149] (Fig. 12a). Due to the extraordinary specificity of the antibodies, this analytical method has been extensively applied in food and environmental analysis, and medical diagnosis. [149] Nevertheless, the synthesis and purification of enzyme–antibodies conjugates requires laborious protocols. As result, a loss of biorecognition properties (antibody) and catalytic activity of the tag (enzyme) can be observed, and the sensitivity can be compromised [172,173]. These issues, combined with the low concentration of biomarkers and infection agents, limit the practical application ELISA tests at the POC tests [147–151]. A strategy to improve the sensitivity of immune-diagnostic tests is to increase either the antibody concentration or the number of signaling elements attached to the antibody. However, these changes can affect the background and the specificity of the method. An emerging strategy to improve sensitivity, stability, and selectivity is the immobilization of antibodies on MOFs, where the resulting antibody-on-MOF biocomposites can be used as probes (Fig. 12b). Indeed, both signaling and bio-recognition components can be co-localized in the same MOF-based particle. These systems as are further discussed in the next sections.

Colorimetric and fluorometric immunoassays

Tan and co-workers [174] reported the integration of a rabbit anti-mouse immunoglobulin G antibody (RlgG) on a Cu-MOF. The Cu-MOF network not only preserved the bioactivity of the antibody under operational conditions, but also due to its peroxidase-like activity, this material replaced the natural enzyme and acted as

Table 4

Comparison of the key features of commercially available glucose biosensors. The data listed in this table was taken from the manufacturer's specifications and complemented by additional references [185,186].

Manufacturer	Commercial name	Assay method	Minimal sample volume (μL)	Test time(s)	Detection range (mg/mL)
Arkray Global Business Inc.	GlucoCard X-Meter	GDH	0.3	5	10–600
BAYER	Acencia [®] Contour [™]	GDH	0.6	5	10–600
Roche	Accu-Chek [®] Aviva	hexokinase	0.6	5	10–600
Bionime	Rightest GM300	GOx	1.4	8	10–600
Nova Biomedical	Nova Max Plus	GOx	0.3	5	20–600
LifeScan	OneTouch UltraLink	GOx	drop of blood	5	20–600
AgaMatrix	WaveSense Presto [™]	GOx	0.5	6	20–600
Prodigy Diabetes Care	Prodigy AutoCode [®]	GOx	0.7	7	20–600
Abbott	FreeStyle Freedom Lite [®]	GDH	0.3	5	20–500

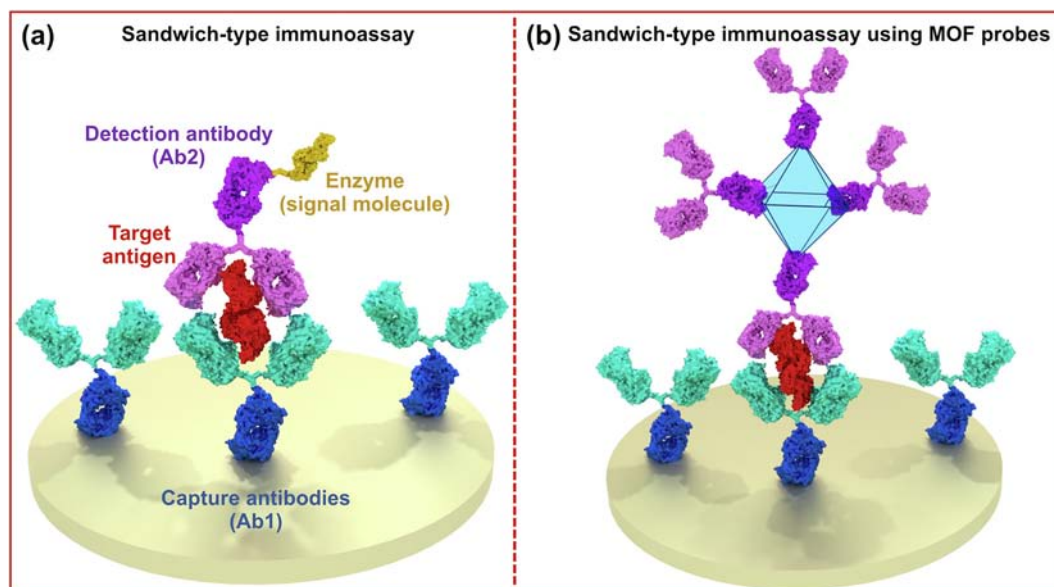


Fig. 12. (a) Schematic representation of classical sandwich-type enzyme-linked immunosorbent assay (ELISA). (b) Conceptual sandwich-type method for immunodetection of antigens using MOF probes.

the signal amplification unit. The RlgG-on-Cu-MOF system responded selectively towards mIgG, even in the presence of interfering proteins (GOx, BSA, HRP, etc.). The authors suggest that the lack of enzyme-antibody conjugate enhances the capture efficiency of the biosensor RlgG-on-Cu-MOF towards the antigen mIgG, thereby improving the detection sensitivity of immune-assay (reported of 0.34 ng/mL) (Table 5). This work demonstrates the feasibility of MOF composites with enzyme-like properties as replacements of natural enzyme-antibody conjugates. As, unlike traditional ELISA tests, this RlgG-on-Cu-MOF biosensor offers an easier and less costly detecting procedure.

Li and co-workers [175] reported the bioconjugation of secondary antibodies (Ab2) on the outer surface of HKUST-1 (Cu-BTC; BTC = 1,3,5-benzenetricarboxylic acid), to develop a fluorogenic click immunoassay for the detection of hepatitis B virus antigen (HBsAg) in clinical serum samples. This sandwich-type assay is composed of a microplate with immobilized antibodies (Ab1) that can create a complex with biomarker antigen (HBsAg); then the secondary antibodies attached to the MOF surface particles (Ab2-on-HKUST-1) will selectively bind to the immobilized HBsAg (Fig. 13a). In this system, HKUST-1 acts as an Ab2 carrier and as signal probe. Finally, Cu(II) in HKUST-1 can be reduced to Cu(I), which can catalyze the azide-alkyne cycloaddition reaction between an alkyne and fluorogenic molecules of azide to yield the corresponding triazole, and produce a fluorescence signal. The formation of multiple triazole molecules within the porous

MOF network produced such a strong fluorescence signal with a reported detection limit below 11.2 pg mL^{-1} (Fig. 13b,c). Wang et al. [176] also reported a MOF-based probe for the design of a sandwich-type colorimetric immunoassay for prostate-specific antigen detection (PSA). The MOF-probe was prepared through the co-immobilization of: (i) Ab2 (biorecognition element) and (ii) methyl yellow (MY; signal molecule) on ZIF-8 nanoparticles. The resultant system Ab2&MY-on-ZIF-8 acts as signal tag for the specific recognition of PSA. The latter can be quantified by the colorimetric signal generated by the allochroic MY molecules released from the biocomposite of upon applying acidic conditions (λ_{max} 510 nm). According to the authors the encapsulation of the ZIF-8 probe reduces the leakage of the signal molecules, which permits the signal amplification (Table 5). The overexpression of carcinoembryonic antigen (CEA) is closely associated with colorectal cancer and it serves as tumor biomarker. Therefore, it is highly important the development of sensitive analytic techniques capable of detecting low concentrations of CEA in body fluids. With this aim in mind, Tan and co-workers [177] reported the one-pot co-immobilization of alkaline phosphatase (ALP) and anti-CEA antibody in a Zn^{2+} -adenine coordination polymer (ZnCPs). The role of ALP in the resultant anti-CEA-on-ALP@ZnCPs biocomposite was to induce a catalytic cascade reaction to yield a colored product. This process take place in presence of ascorbic acid 2-phosphate (AAP), Fe^{3+} , and 1,10-phenantroline (Phen) in 2 steps: first the ALP hydrolyses AAP producing ascorbic acid (AA); second, AA

Table 5
Comparative overview of protein@MOF and protein-on-MOF biocomposites for biomacromolecules detection.

Detection method	Molecule target	Biorecognition element	MOF	Synthetic strategy	Linear range	Detection limit	Ref
SPR colorimetric	anti-IgG mlgG	rabbit IgG RlgG	ZIF-8 Cu-MOF	Encapsulation One-pot immobilization	not clear 1–100 ng/mL	not clear 0.34 ng/mL	[187] [174]
sense-and-treat ELISA Fluorometric	CEA hep-B virus antigen (HBsAg)	CEA Ab2 Ab2	ZIF-8 HKUST-1	Grafting Grafting	10–500 pg/mL 0.03–2.0 ng/mL	10 pg/mL 11.2 pg/mL	[188] [175]
colorimetric Electrochemical	PSA antigen ALV-J	Ab2 Ab2	ZIF-8 ZIF-8	Grafting Grafting	0.001–1 ng/mL 152–10,000 TCID ₅₀ mL ⁻¹	0.67 pg/mL 140 TCID ₅₀ mL ⁻¹	[176] [179]
Electrochemical	PSA antigen	Ab2	Fe-MIL-88B-NH ₂	Grafting	0.001–100 ng/mL	0.13 pg/mL	[180]
Electrochemical	CRP	Ab2	HKUST-1	Grafting	1–400 ng/mL	0.2 ng/mL	[181]
Electrochemical	exosomes	single-strand DNA aptamer	ZIF-67	Grafting	1.3X10 ² to 2.6X10 ⁵ particles mL ⁻¹	100 particles mL ⁻¹	[183]
Electrochemi-luminescence colorimetric	insulin AFP	Ab1 Ab2	UiO-67 MPDA	Grafting Grafting	0.0025 to 50 ng mL ⁻¹ 10–1000 pg/mL	0.001 ng mL ⁻¹ 2.3 pg/mL	[189] [178]
Fluorometric colorimetric	cTnl CEA	Ab2 CEA Ab2	ZIF-8 ZnCPs	Grafting Encapsulation	11.1 fM to 35.6 pM 0.05–100 ng/mL	4.4 fM 21.1 pg/mL	[190] [177]

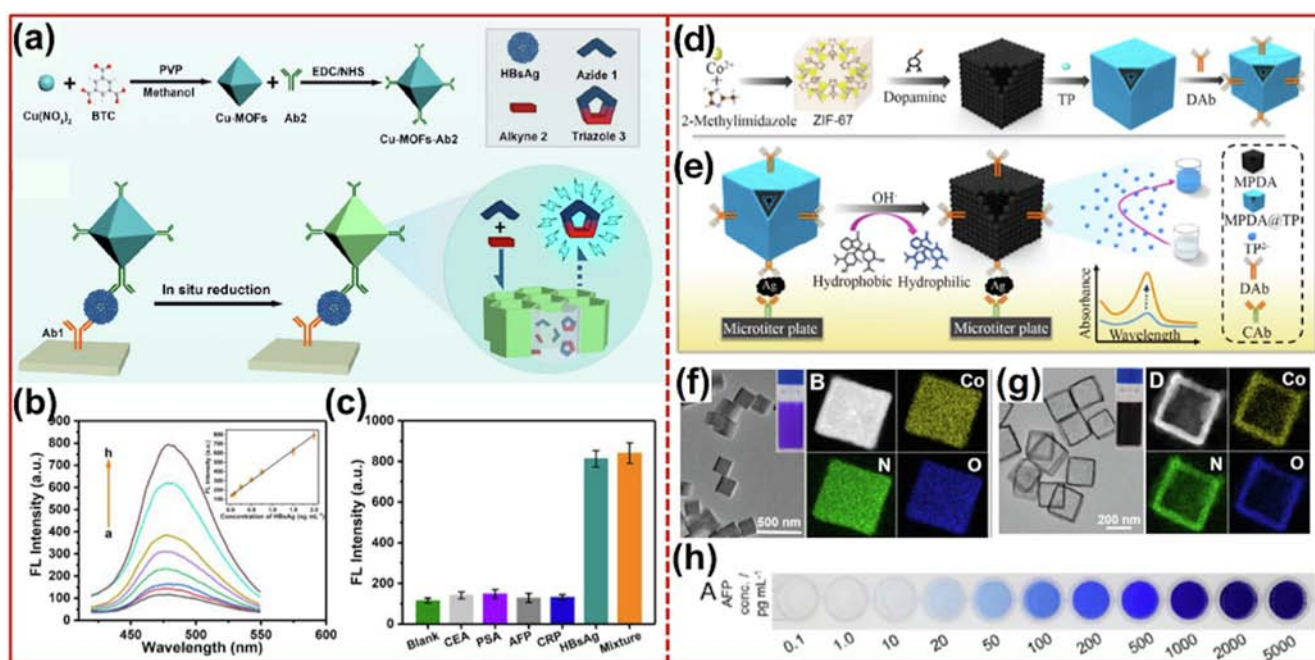


Fig. 13. (a) Schematic representation of the synthesis of Ab2 immobilized onto a Cu-MOF, and the conceptual sandwich-type method for immunodetection of HBSAG. A fluorescence signal is detected at 395 nm due to the CuAAC click reaction catalyzed by the Cu-MOF. (b) Fluorescence emission spectra upon addition of different concentrations of HBSAg. (c) Selectivity response of the immunoassay against different protein biomarkers. Adapted with permission from ref. [175] Copyright 2020 American Chemical Society. (d,e) Schematic representation of the preparation procedure of MPDA@TP-Dab and MPDA@TP-linked immunoassay (MLISA) for alpha-fetoprotein (AFP) detection. (f) TEM image and HAADF-STEM image and elemental mapping for Co, N, and O of ZIF-67. (g) TEM image and photograph and HAADF-STEM image and elemental mapping for Co, N, and O of MPDA. (h) Photographs taken from the MLISA-based visual assay using different concentrations of AFP standards. Adapted with permission from ref. [178] Copyright 2018 American Chemical Society.

reduces Fe³⁺ into Fe²⁺, which is then coordinated by Phen forming the orange-colored complex [Fe(Phen)₃]²⁺. The CEA concentration was determined by monitoring the intensity of this colored complex in a sandwich-assay configuration. The reported detection limit for this system is 21.1 pg/mL. The authors claimed that this biosensor is more cost-effective than traditional enzyme-labeled antibody immunoassays. Moreover, the integration of ALP&anti-CEA within the ZnCPs enhanced the stability of the biorecognition element. An alternative strategy to improve the sensitivity of immunoassays was reported by Tang and co-workers [178] for the colorimetric detecting alfa-fetoprotein (AFP, tumor biomarker). The authors used ZIF-67 as a MOF template for the construction of

hollow metal-polydopamine framework (MPDA) particles as an efficient material for the surface adsorption of secondary antibodies (Ab2) and large amount of the signal molecules (thymolphthalein dye; TP) (Fig. 13d–h). According to the authors, this configuration enhanced the signal amplification when compared with conventional colorimetric immunoassays (Table 5).

Electrochemical immunoassays

Electrochemical biosensors operate by converting a biological event into an electronic signal. These devices merge biological materials as sensitive components with electrodes as conversion

components. Hitherto, several reports have demonstrated the implementation of MOF biocomposites in the fabrication of electrochemical sensors for diagnostic applications due to their robustness, facile miniaturization, and high sensitivity (Table 5).

Ai and co-workers [179] reported the fabrication of a sandwich-type electrochemical immunosensor for the detection of a specific avian retrovirus known as ALV-J (avian leukosis virus subgroup J). This immunosensor was comprised of two principal components: (1) the probe, which was made with hollow ZIF-8 structures, where the outer surface was functionalized with secondary antibodies (Ab2) and HRP. (2) The electrochemical-responsive interface fabricated using a glassy carbon electrode (GCE) functionalized with tannic acid (TA), Fe₃O₄ nanoparticles, and primary antibodies (Ab1). Here, tannic acid allowed for the *in-situ* reduction of graphene oxide to conductive graphene. The presence of reactive cis-diols in tannic acid were used for the grafting of Ab1 onto the GCE. The Fe₃O₄ nanoparticles mimicked the oxidation properties of HRP, which enhances the LOD of the immunosensor. The authors stated that the use of hollow ZIF-8 improved the electron transfer properties of the material, which enhanced the response of the immunosensor platform. The reported detection range was 152–10,000 TCID₅₀ mL⁻¹ (TCID₅₀ is the tissue culture infective dose), with a LOD = 140 TCID₅₀ mL⁻¹.

More recently, Ma and co-workers [180] reported the design of a sandwich electrochemical immunosensor based on Fe-MIL-88B-NH₂ decorated with gold nanoparticles and functionalized with secondary antibodies. This sensor was used for the detection of prostate-specific antigen (PSA) (Table 5).

Yang and co-workers [181] reported a simple electrochemical immunoassay for the detection of C-reactive protein which is a biomarker typically associate to coronary heart diseases. In this work, HKUST-1 particles were immobilized onto the surface of Au NPs. Subsequently, the resultant MOF-on-Au particles were used to immobilized signal antibodies (Ab2) onto the HKUST-1 surface, where the immobilization process was achieved by an adsorption strategy. The authors claimed that in this system, the Cu²⁺ ions from the HKUST-1 can be used to produce a signal transduction which allows the detection of the analyte. Furthermore, the authors reported the use of covalent organic frameworks (COFs) functionalized with platinum nanoparticles as a substrate to further increase the electronic conductivity. This strategy offers an excellent signal transduction platform for the detection of CRP. Indeed, under optimized experimental conditions this biosensor presented a linear detection range from 1 to 400 ng/mL and a LOD of 0.2 ng/mL.

Electrochemical biocomposite devices can be even extended to the detection of complex biomarkers such as exosomes (extracellular vesicles implicated in the transmission of disease states) [182]. In this regard, Gui and co-workers [183] developed an electrochemical sensor for early cancer diagnosis. To fabricate this sensor, ZIF-67 doped with ferrocene (Fc) was electrodeposited on an indium tin oxide (ITO) support. The resultant electrode was further functionalized with black phosphorous nanosheets (BPNs) and a single-strand DNA aptamer labeled with methylene blue (MB). The latter presents high selectivity towards CD63 protein expressed on breast cancer MCF-7 cells. This aptasensor presents a dual redox signal response. The first one originates from the MB labeled on aptamer, hence, it changes in the presence of exosomes. The second one, that comes from the Fc, hardly changes, which allows the intrinsic self-calibration of the biosensor. The resultant device exhibits rapid response and high specificity towards breast cancer exosomes detecting from 1.3×10^2 to 2.6×10^5 particles mL⁻¹, with a LOD of 100 particles mL⁻¹.

3.4.3. Summary and future outlook

Protein-based MOF biocomposites are emerging materials as recognition elements for the preparation of cost-effective biosen-

sors with sensitivity and selectivity towards a variety of analytes ranging from small molecules such as H₂O₂ and glucose to large biomacromolecules such as protein biomarkers. Both protein@MOF and protein-on-MOF configurations can be exploited for colorimetric, electrochemical and fluorometric biosensors. An important aspect of this class of composites is the facile co-immobilization of the biorecognition element and the signaling components within the same MOF matrix; this aspect is expected to facilitate the implementation of the assay in miniaturized biochips, reduce the time involved in the detection process, and enhance the LOD (Tables 3–5). Accordingly, the discussed strategies lay the foundation for the progress of MOF-based sensors for POC testing devices for real-time diagnostic analyses.

4. Carbohydrates and MOFs as drug delivery systems

Carbohydrates (CHs) are a class of biomolecules which provide several biological functions, including cellular and intracellular interactions in the form of cell surface receptors, signaling molecules, and bacterial adhesives [191]. In biomedicine, carbohydrate-based drugs have recently gained attention as potential treatments for cancer, diabetes, AIDS, influenza, bacterial infections, and rheumatoid arthritis [192–194]. Among the CH subset used in biotechnology and medicine, the most commercially important ones are glycosaminoglycans (GAGs) [195]. GAGs are unbranched high molecular weight polysaccharides constructed from amino sugars (D-glucosamine or D-galactosamine) and uronic acid (D-glucuronic or L-iduronic acid) [196]. GAGs and proteoglycans regulate important biological activities. For instance, they contribute significantly to the extracellular matrix organization, cellular signaling, as well as the regulation of cell growth and tissue maturation [197]. The application of GAGs in biomedicine includes their use as anticoagulant and anti-inflammatory agents, as well as in wound healing therapy. Moreover, GAGs-based therapeutics have been explored for the treatment of osteoarthritis, diabetes, viral and bacterial infections and more recently for cancer treatment, as tumor progression inhibitors [195–197].

However, the targeted-delivery of GAGs-based therapeutics presents challenges including structural fragility and low bioavailability because of their high molecular weight and charge [197]. For instance, Heparin (HP), which is the most employed carbohydrate-based drug for the treatment of thromboembolic and anti-inflammatory angiogenesis, suffers from pharmacokinetics issues such as poor bioavailability, fast serum clearance, and rapid degradation [195,197–199]. Another example is Hyaluronic acid (HA) that can be used for wound healing applications. HA is prone to lose its therapeutic properties due to the presence of hydrolytic enzymes (hyaluronidase) and reactive oxygen species (ROS) [200,201]. Thus, from an administration perspective, having access to a carrier that provides protection and tunable release profiles would enhance the efficacy of the therapies [202]. Both of these are desired properties for GAGs when used as wound healing agents (e.g. HA requires controlled and local delivery), and as an anticoagulant (e.g. HP if administrated via the parenteral route could result in bleeding-related complications due to burst release) [203].

In this context, MOFs have the potential to become suitable carriers for carbohydrate-based drug therapeutics as: 1) MOFs have demonstrated protective properties for other biotherapeutics; and, 2) the encapsulation of CH-based drugs in MOFs can enhance the pharmacokinetics and bioavailability properties of these therapeutics [103,204,205]. However, research devoted to CHs@MOFs is in its infancy; thus, further exploratory and systematic studies about protective properties of CHs@MOFs and CHs-on-MOFs are required.

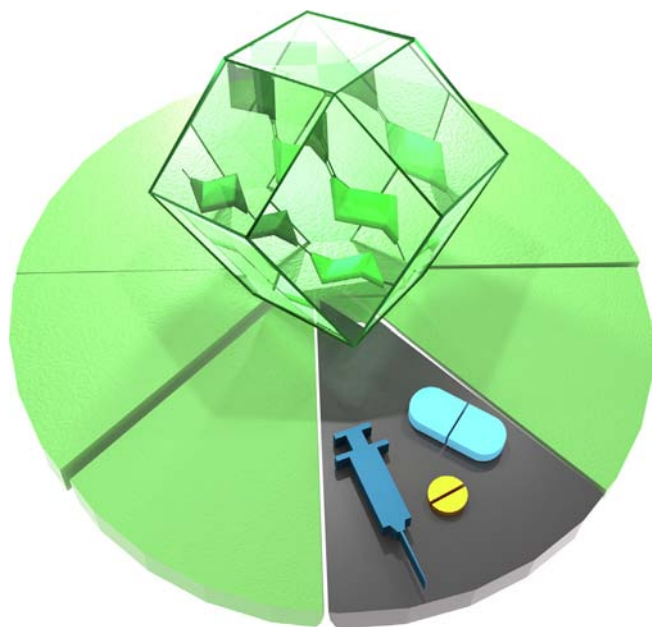


Fig. 14. CH@MOF and CH-on-MOF biocomposites and their applications in drug delivery systems. CH=carbohydrate

In this section, we will focus on the application of MOFs as drug delivery systems (DDS) for the delivery of CH-based therapeutics (Fig. 14). Additionally, there are several interesting studies where CHs are used as coatings for MOF carriers to improve the targeting ability and stability. Indeed, the CHs-on-MOF particles have shown interesting properties as stealth drug carriers for DDS. Thus, selected examples are included in this section.

4.1. MOF composites as DDS for carbohydrate-based therapeutics

As is the case for formation of protein biocomposites, the integration of a CH-based therapeutic in a MOF carrier can be achieved through a bioconjugation approach (adsorption, grafting) or via one-pot embedding strategy. Regarding formation of CH-on-MOFs biocomposites for use as DDS, Vinogradov and co-workers [205] reported the adsorption of heparin on MIL-101(Fe). The biocomposite was prepared by adding MIL-101(Fe) into a heparin solution to yield HP-on-MIL-101(Fe). Subsequently, to extend the bioactivity of the composite, HP-on-MIL-101(Fe) was mixed with an alumina sol-gel matrix and streptokinase (SK, a protein-based thrombolytic medication) solution to create HP-on-MIL-101(Fe) + SK@alumina hybrid. The resulting material was applied to polytetrafluoroethylene (PTFE) vein implants (Fig. 15). The heparin adsorption occurred due to partial ligand loss from MIL-101(Fe) followed by heparin sulfate group chelation on iron at defect sites in the MIL-101(Fe) to give a declared encapsulation efficiency of 90% (average particle size was 163 nm). The cytotoxicity of HP-on-MIL-101(Fe) was found negligible up to 40 μ M on HCT116 cells. Moreover, an anticoagulant test was carried out by immersing the composites in blood plasma which lead to the degradation of the MOF structure resulting in HP release, and providing good anticoagulant activity which was comparable to free HP. In addition, HP-on-MIL-101(Fe) coated with alumina-based sol-gel matrices (HP-on-MIL-101(Fe) + SK@alumina) could enhance the bioactivity of HP-on-MIL-101(Fe) and prevent the premature clogging of the thrombolytic coating. The authors suggested this bioactive nanocoating as a useful approach to reduce complications in PTFE vein implants [205].

Another bioconjugation approach for the preparation of CH-on-MOF biocomposites exploits a grafting strategy, which involves the formation of covalent bonds between a reactive group on the outer surface of the MOF and targeted biomolecule, (*vide supra*). For instance, Ghaee and co-workers [204] grafted HA to the outer surface of a carboxylated ZIF (FZIF) constructed from zinc ions and 2-methyl-1H-imidazole-4,5-dicarboxylic acid (2MtImDC). HA was cross-linked with 1-ethyl-3-(3-dimethylaminopropyl) carbodiimide hydrochloride and N-hydroxysuccinimide (EDC/NHS). The average particle size of HA-on-FZIF was c.a. 45 nm (drug loading not disclosed). The solution was freeze-dried and a film of 300 μ m thickness was obtained. The MOF-biocomposite film demonstrated superior mechanical properties when compared with a film made with pure MOF and this was attributed to the affinity of HA for the ZIF particles. The degradation tests for HA and HA-on-FZIF films were investigated by exposing the biocomposites to PBS solution, with and without hyaluronidase to promote the hydrolytic degradation of HA. The authors showed that the films degraded after 11 days; however, the contribution of phosphate ions to the MOF degradation was not disclosed. The MOF biocomposite films showed antibacterial properties and promoted fibroblast migration and proliferation. [204]

Recently, Astria et al. [206] encapsulated carbohydrates into MOFs using the *biomimetic mineralization* approach. The potential biomimetic mineralization of different carbohydrates in ZIF-8 (CHs@ZIF-8) was assessed by testing mono, di, oligo, and polysaccharides such as D-glucose, D-galactose, D-mannose D-xylose, D-glucitol, meglumine, methyl- β -D-glucopyranoside, N-acetyl-D-glucosamine, D-glucosamine, sucrose, maltodextrin, D-gluconic acid- δ -lactone, dextran, diethylaminoethyl dextran (DEAE-dextran), carboxymethyl dextran (CM-dextran) and cellulose as seeding agents for ZIF-8. To achieve this, each specific CH was mixed with HmIM and zinc acetate at room temperature (Fig. 16a) and the results showed that only negatively charged carbohydrates (i.e. CM-dextran, a dextran backbone substituted with carboxymethyl substituents imparting a polyanionic character) led to a MOF biocomposite (i.e. CM-dextran@ZIF-8), thus contradicting a previous finding [207]. A computational study supported the enrichment of Zn²⁺ around CM-dextran because of the COO⁻ groups, thus providing the local conditions for triggering the self-assembly of the MOF around these CHs. [206]. The observations of the biomimetic mineralization role triggered by negatively charged biomacromolecules, and assembly of thereof, is in agreement with previous studies that investigated the relevance of electrostatics in the biomimetic mineralization process [114,208]. By optimizing the synthetic protocol, the CM-dextran@ZIF-8 biocomposite was obtained with a 100% encapsulation efficiency. By changing the concentration of a chelating agent (EDTA) in solution, tunable release profiles were measured for particles with 25 nm diameter. As CM-dextran is considered an inexpensive carbohydrate that closely mimics glycosaminoglycans (GAGs), CM-dextran has been widely used as a model GAG in drug delivery systems [209]. The study considered GAGs-based therapeutics; because of the negative charge of these carbohydrates, they were considered promising biomimetic mineralization agents [103]. In particular, the encapsulation of heparin (HP), hyaluronic acid (HA), chondroitin sulfate (CS), and dermatan sulfate (DS) within three different pH-responsive metal-azolate frameworks: ZIF-8, ZIF-90, and MAF-7 (Fig. 16b) was investigated. To further demonstrate the versatility of CHs@MOFs as DDS, two preclinical drugs based on GAGs and proteoglycans (GM-1111 and HepSyl) were also encapsulated in the metal azolate frameworks. GM-1111 is an anti-inflammatory drug designed for chronic rhinosinusitis and HepSyl is a synthetic proteoglycan for oncotherapy. The resultant GAG@MOFs present different properties in terms of crys-

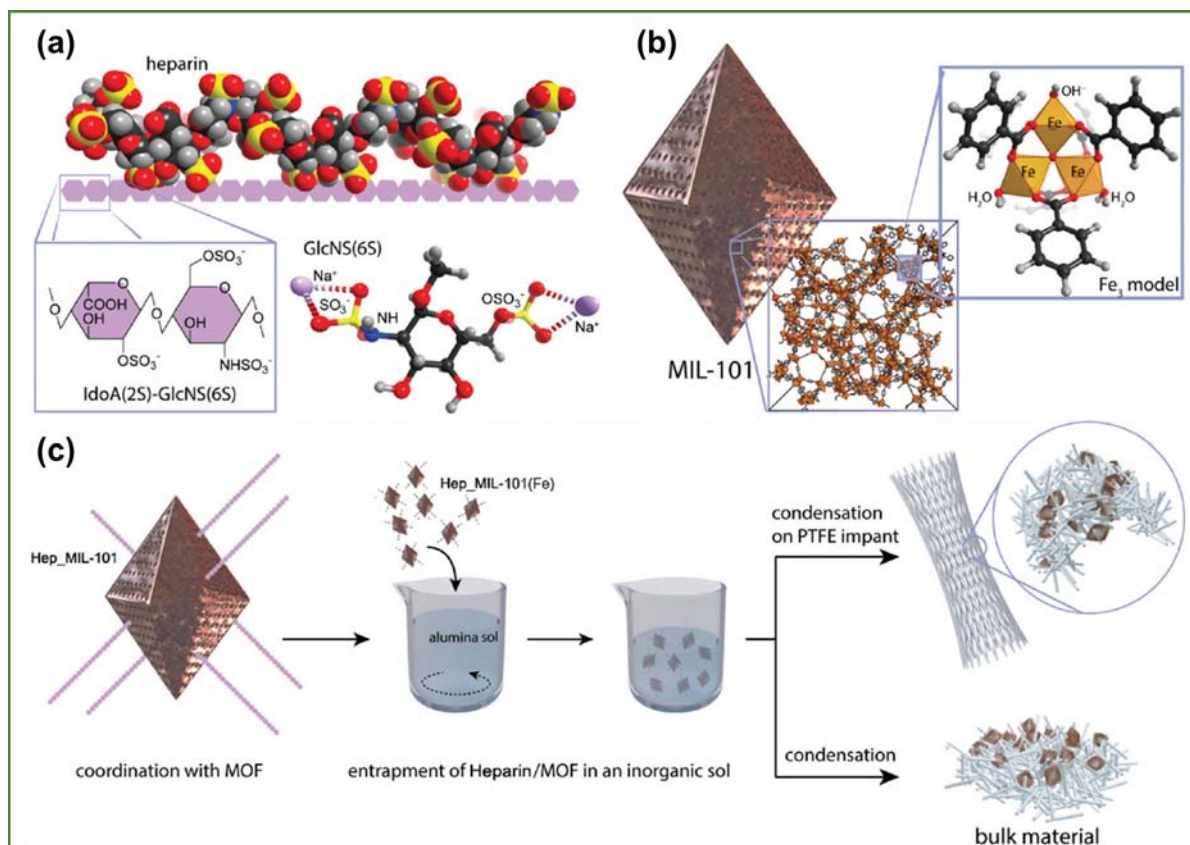


Fig. 15. Illustration showing the synthetic strategy used for preparation of HP-on-MIL-101(Fe) composites. (a) Heparin (b) metal sites of MIL-101(Fe) (c) Heparin was complexed with MIL-101(Fe) and then co-entrapped with streptokinase within sol-gel matrix for anticoagulant treatment. Adapted with permission from ref. [205] Copyright 2018 Royal Society of Chemistry.

tallinity, particle size, and spatial distribution of the cargo (Table 6). For instance, a crystalline powder was obtained from GAGs@ZIF-8 and GAGs@ZIF-90, whereas a gel was found in GAGs@MAF-7 [103]. The formation of metal-organic gels (MOG), as seen for the latter example, is typically attributed to the rapid formation of MOF nanoparticles (NPs) that aggregate through van der Waals interactions [210,211]. The EE% of GAG@MOF was evaluated using a carbazole assay and UV-vis spectroscopy (Fig. 16c, Table 6). The release profiles of each GAG@MOFs were studied in citrate buffer, showing that the release kinetics are system dependent (Fig. 16d, Table 6). To further understand the distribution of HepSyl in the MOF shell, samples were assessed by confocal laser scanning microscopy (CLSM) and the results showed that while the proteoglycan is homogeneously distributed within ZIF-8 and MAF-7; in ZIF-90, HepSyl is located on the surface of the MOF particles. These observations showed that azolate-based MOFs could be employed for the encapsulation of GAGs and proteoglycan-based therapeutics, and furthermore that specific drug release properties could be designed by selecting the proper MOF matrix. These findings could pave the way for the delivery of clinical carbohydrate-based therapeutics by using MOF carriers [103].

4.2. Carbohydrates as protective coatings of MOF composites for DDS

Despite the advantageous properties MOFs as DDS, there are still some limitations that could restrict their applications, including rapid degradation, short circulation time, and poor colloidal stability in aqueous media [11,212]. To address these issues, MOF crystals have been coated with different materials such as polymers, proteins, lipids, cyclodextrins, and high molecular weight CHs [29,212–216]. The surface modification of MOFs with CHs

can impart targeting delivery abilities and improve both the biodistribution and stimuli-responsive properties [217,218]. For example, it has been demonstrated that the use of HP improved the colloidal stability of the drug carrier, [218,219] while HA enhanced the protection of the MOF and improved the targeting properties of the carrier [212,217]. Moreover, as HA can be enzymatically degraded by hyaluronidase enzyme, the HA-based coating can be removed on demand once internalized within environments with high concentrations of hydrolytic enzymes (e.g. tumor cells) [212].

In 2015, Horcajada and co-workers [218] employed heparin as a coating agent to modify the outer surface of MIL-100(Fe) nanocarriers for the release of two model drugs (i) caffeine and (ii) furazan. Heparin was chosen as a coating agent due to its specific interaction with the surface of the MOF particle for the preparation of the HP-on-MIL-100(Fe) biocomposite. HP-on-MIL-100(Fe) DDS were prepared using two different approaches: 1) HP solution was added to a colloidal solution of MIL-100(Fe) NPs in ethanol, and then the HP-on-MIL-100(Fe) was loaded with a model drug (caffeine); or, 2) MIL-100(Fe) NPs were preloaded with furazan and then the resultant furazan@MIL-100(Fe) NPs were coated with rhodamine-labeled-heparin (Fig. 17a). The HP-on-MIL-100(Fe) coating preserved the crystallinity and porosity of the starting MIL-100(Fe), and enhanced the colloidal stability in different media such as water, PBS, PBS containing albumin 5.4% w/v and Roswell Park Memorial Institute (RPMI) medium. When infiltrating caffeine, HP-on-MIL-100(Fe) showed a drug loading up to 42 wt% and release profile data showed only 20% of caffeine was released from HP-on-MIL-100(Fe) compared to uncoated MIL-100(Fe) (56%) in the first hour in PBS solution. Thus, this study demonstrated how the surface modification of MOF NPs with GAGs can improve

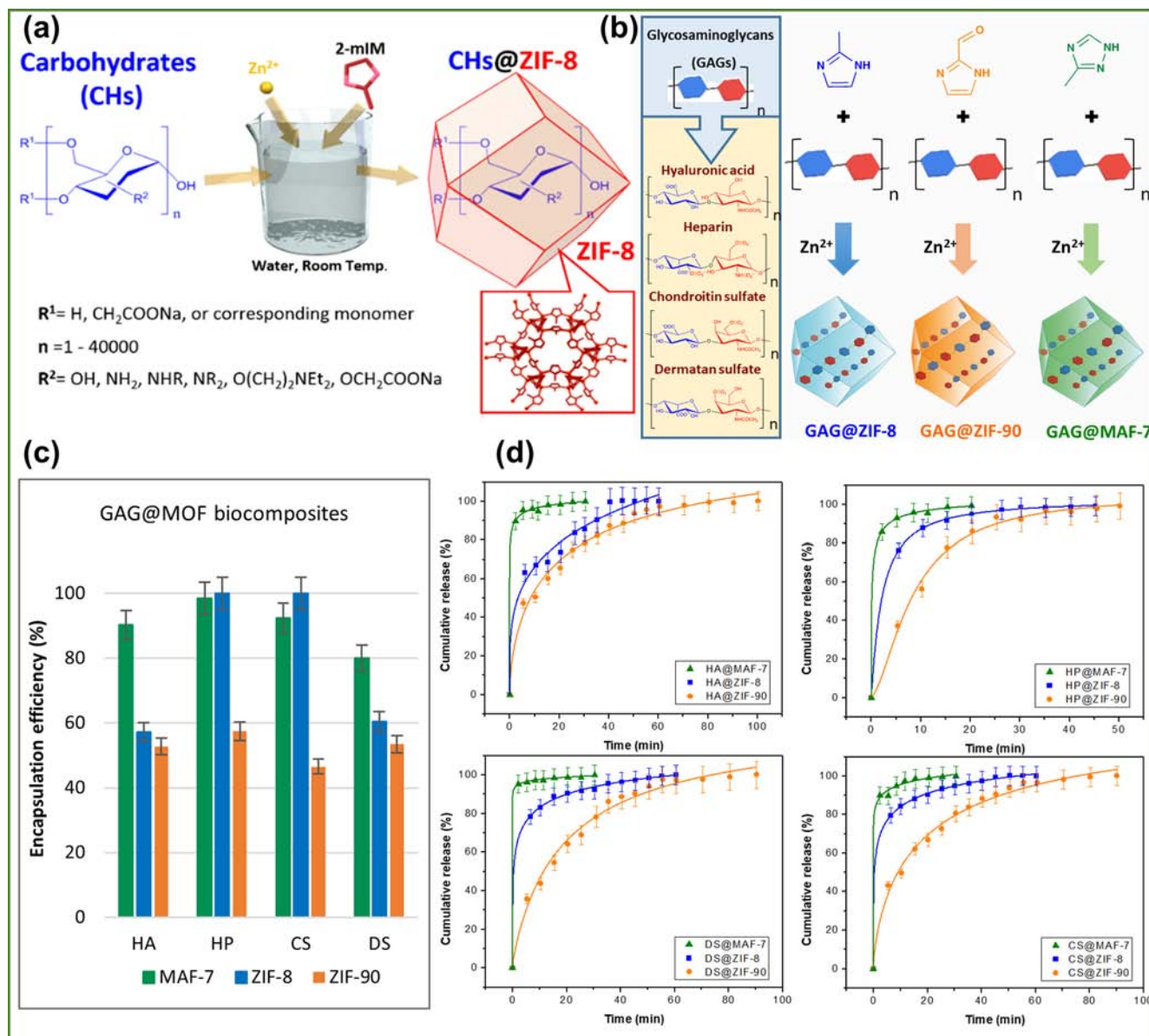


Fig. 16. (a) Schematic illustration of CH@ZIF-8 preparation. Carbohydrate combination with ZIF-8 precursors trigger biomimetic mineralization which encapsulates the carbohydrates in ZIF-8. Reprinted with permission from ref. [206]. Copyright 2019 Royal Society of Chemistry. (b) Schematic of one-pot synthesis of GAG@MOF biocomposites, by using three different metal azolate framework (ZIF-8, ZIF-90 and MAF-7). (c) Encapsulation efficiency of GAG@MOFs in the three different MOF platforms and (d) the comparative release profile of GAG@MOFs by an acidic stimulus (pH = 6). Reprinted with permission from ref. [103]

the properties of MOF-based DDS for biomedical applications [218].

Another carbohydrate that could be employed as a coating agent for MOF carriers is CM-dextran. In this realm, Nikitin and co-workers [220] described the use of a CM-dextran coating for antibody-on-MOF DDS in cancer therapy. The biocomposite was prepared by adding CM-dextran to a suspension of $Fe_3O_4@MIL-100(Fe)$, a magnetic framework composites (MFC) [221] that possess dynamic localization properties [156,222] using an external magnetic field. Following coating doxorubicin/daunorubicin was loaded into the platform and coupled with an antibody. The CM-dextran coating avoided the aggregation of magnetic MOF particles, while providing a sustained release profile and maintaining the antibody specificity [220].

CH-coated MOFs were also tested for oral drug administration. Namazi and co-workers [223] used a pH-sensitive biopolymer, carboxymethylcellulose (CMC), to protect and control the release

of ibuprofen encapsulated in Cu-MOF (IBU@Cu-MOF) for oral delivery. The CMC-coated IBU@Cu-MOF composite was prepared by mixing the dispersed IBU@Cu-MOF in water with CMC. The CMC-on-IBU@Cu-MOF biocomposite demonstrated better protection than uncoated Cu-IBU@MOF under simulated gastrointestinal conditions. In addition, CMC-on-IBU@Cu-MOF was reported to have low cytotoxicity and extended stability of drug dosing that leads to a controlled release in the gastrointestinal tract [223].

In terms of targeting properties, HA has been reported as a good targeting agent for cancer cells which over-express CD44 [224]. CD44 is a transmembrane glycoprotein that is highly expressed in cancer cells and which plays an essential role in cancer development and metastasis progression. [225]. Post-modification of MOF-based DDS with HA has been widely investigated to enhance the efficacy of cancer therapies [226]. For instance, a new promising phototheranostic platform HA-on-MIL-100(Fe) NPs infiltrated with

Table 6
Properties of GAG@MOF biocomposites formed with different metal-azolate framework.

Samples	Topology	Particle size	EE %	Time elapsed for 100% drug release
HA@ZIF-8	<i>sod</i>	<500 nm	60	40 min
HP@ZIF-8	<i>sod</i>	1 μm	100	40 min
CS@ZIF-8	<i>sod</i>	<500 nm	100	1 h
DS@ZIF-8	<i>sod</i>	<500 nm	60	1 h
GM-1111@ZIF-8	predominantly <i>sod</i>	500 nm	60	20 min
HepSYL@ZIF-8	predominantly <i>sod</i>	<200 nm	45	2 h
HA@ZIF-90	mix of <i>sod</i> and <i>dia</i>	500 nm–4 μm	50	1.5 h
HP@ZIF-90	mix of <i>sod</i> and <i>dia</i>	5 μm –7 μm	60	50 min
CS@ZIF-90	mix of <i>sod</i> and <i>dia</i>	5 μm –7 μm	50	1.5 h
DS@ZIF-90	mix of <i>sod</i> and <i>dia</i>	5 μm –7 μm	50	1.5 h
GM-1111@ZIF-90	<i>sod</i>	8 μm	70	2.5 h
HepSYL@ZIF-90	<i>sod</i>	2 μm	50	2.5 h
HA@MAF-7	amorphous	<100 nm	90	30 min
HP@MAF-7	amorphous	<100 nm	98	30 min
CS@MAF-7	predominantly amorphous	<100 nm	90	30 min
DS@MAF-7	predominantly amorphous	<100 nm	80	30 min
GM-1111@MAF-7	amorphous	<50 nm	75	20 min
HepSYL@MAF-7	amorphous	<50 nm	60	30 min

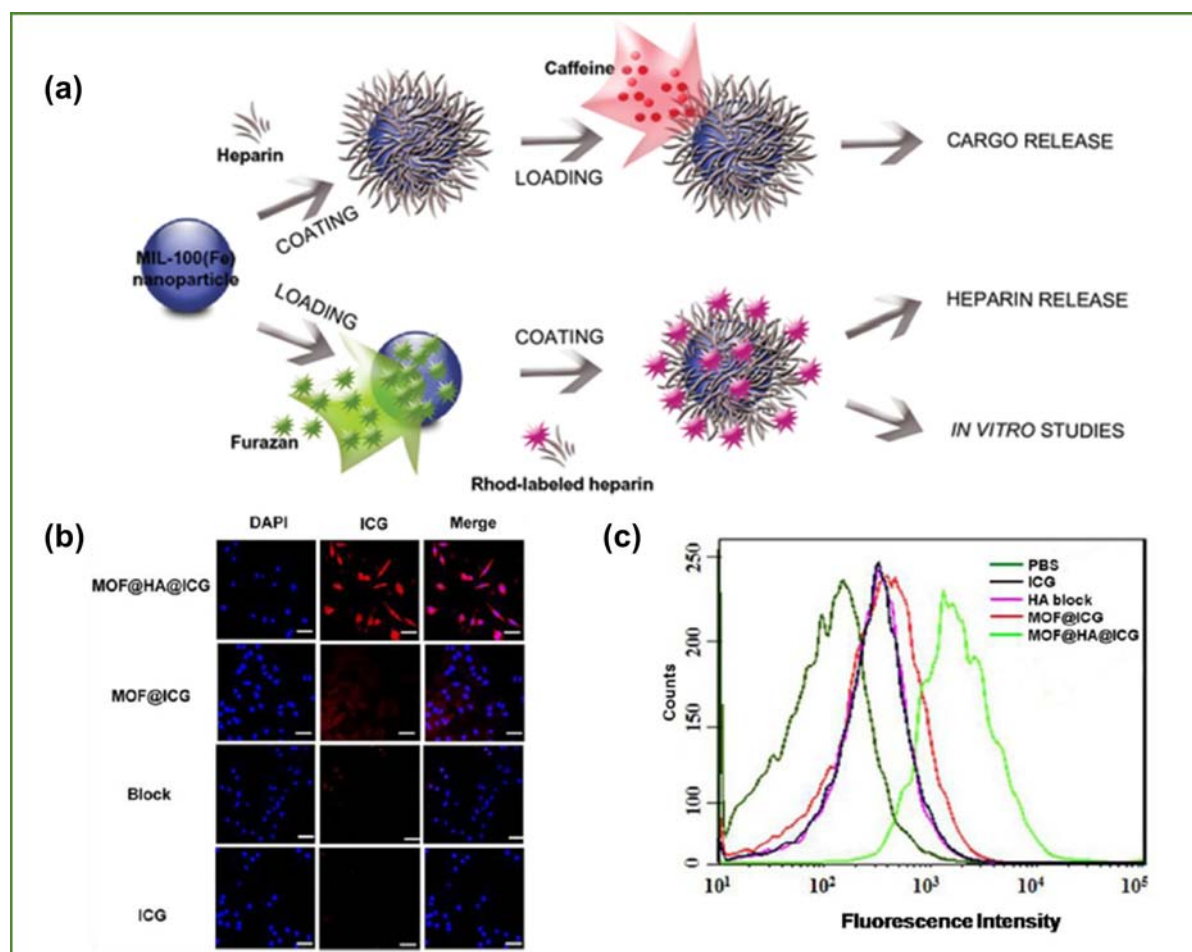


Fig. 17. (a) A schematic illustration of the external surface modifications of MIL-100(Fe) NPs with heparin. Reprinted with permission from ref. [218] (b) In vitro cellular uptake of HA-on-ICG@MIL-100(Fe)NPs investigated using CLSM and (c) flow cytometry analysis (solutions that contained 10 $\mu\text{g}/\text{mL}$ of ICG, scale bar = 50 μm) Reprinted with permission from ref. [227] Copyright 2016 American Chemical Society.

indocyanine green (ICG) was developed for multimodal imaging-guided cancer photothermal therapy (PTT) by Liu and co-workers [227]. ICG is an FDA-approved near-infrared (NIR) organic dye for clinical application. However, its low aqueous solubility, low cancer specificity, and low sensitivity for cancer theranostics prevent

its use in practical medical applications. To overcome these limitations, ICG-infiltrated within HA-on-MIL-100(Fe) NPs were prepared by the conjugating of MIL-100(Fe) NPs with HA in aqueous solution. Following this the porous biocomposite was loaded with ICG to yield a HA-on-ICG@MIL-100(Fe) biocomposite. The ICG drug

loading reported for this system is 40 wt%. Additionally, the authors state that this system provides low cytotoxicity and photothermal stability under NIR light irradiation which is a desirable property for PTT. The cellular uptake was investigated using CLSM and flow cytometry analysis and showed the high targeting ability for CD44-positive MCF-7 cells/xenograft tumors (Fig. 17b, c). This demonstrates that ICG-infiltrated HA-on-MIL-100(Fe) NPs could be a potential theranostic platform for imaging-guided cancer treatment [227].

A dual chemo- and photodynamic therapy (PDT) system based on the PCN-224 MOF coated with HA was developed for advanced anticancer therapy by Ryu and co-workers [226]. HA-coated MOF NPs were prepared by dispersing Dox-loaded PCN-224 into an HA aqueous solution (HA-on-Dox@PCN-224) [226]. As in the case of Ghaee and co-workers [204], the interaction between HA and MOF NPs was attributed mostly to the coordination between carboxylate groups of HA and the cations of MOF surface. The formation of HA-on-PCN-224 enhances the targeting ability of the carrier towards CD44 as described previously. This feature could be used for selective drug delivery in tumor treatments. In fact, an *in vitro* experiment for the combined chemo- and PDT demonstrated Dox loaded HA-on-PCN-224 provided an enhanced cancer therapeutic effect under the chosen light irradiation conditions [226].

Another interesting example of using HA as a targeting agent in cancer therapy was reported by Yao and co-workers [228]. In this work, the authors encapsulated the antibacterial and anticancer drug Acriflavine (ACF) into MOF NPs (PCN-224) and coated them with immunologic adjuvant (CpG) and HA. This study again demonstrated a HA-mediated preferential cellular uptake behavior for targeting CD44 membrane in cancer cells [228].

For photodynamic therapy (PDT), Yu and co-workers [229] mixed Ce6 (a second-generation photosensitizer with antitumor activity) with zinc nitrate and HmIM to obtain Ce6@ZIF-8 that was subsequently exposed to HA. This configuration prevented typical agglomeration issues of Ce6. Moreover, *in vivo* experiment showed HA-on-Ce6@ZIF-8 exhibited targeting ability towards tumor bearing-mice. Furthermore, the surface modification of ZIF-8 with a hyaluronic acid coating enhanced the stability, biocirculation, and biocompatibility of Ce6@ZIF-8 NPs [229].

In another example, Zhao and co-workers [230] demonstrated that an HA conjugated MOF could improve the targeting ability of the anticancer drug doxorubicin (HA-on-Dox@ZIF-8) for chemotherapy and MR imaging [230]. The synthesis of HA-on-Dox@ZIF-8 was carried out by loading the doxorubicin into ZIF-8 followed by coating Dox@ZIF-8 with polydopamine and conjugating with hyaluronic acid via Fe^{3+} mediated coordination reaction. HA-on-Dox@ZIF-8 provided pH-responsive release of DOX in acidic environments and targeted drug delivery towards CD44-rich membranes on PC-3 cells (prostate cancer cell line). Moreover, the authors suggested that this system could be used for theranostic (cancer therapy and magnetic resonance (MR) imaging) due to Fe^{3+} coordinated to the carboxylic groups of HA coating the Dox@ZIF-8 particles [230].

4.3. The role of carbohydrates in living cell encapsulation processes to form MOF biocomposites

We and others have postulated that carbohydrates also play a significant role in the encapsulation of living cells, such as yeast cells and bacteria, within MOF composites [231,232]. The bacterial cell wall contains a variety of glycoconjugates and polysaccharides that assists structural formation and play a role in several functions of the cell [233]. For instance, in gram-negative bacteria such as *Escherichia coli* (*E. coli*), peptidoglycans can be found in the cell wall and they contribute to the mechanical strength and maintenance

of cell shape [233]. A peptidoglycan is comprised of glycan chains associated with short peptides [234]. In yeast cells, carbohydrates represent a large portion of the cell wall; indeed 85% of the yeast cell wall is made of polysaccharides [234], and in yeast and bacterial cells they contribute significantly to the overall negative surface charge [232,235,236]. For example, the yeast *Saccharomyces cerevisiae* has a negative charge due to ionized carboxylic and phosphoric acid groups on the surface [232,235]. Chen et al. studied the effect of different zinc precursors (zinc nitrate, zinc sulfate and zinc acetate) for the formation of a ZIF-8 exoskeleton on *Saccharomyces cerevisiae*. The authors elegantly explained that yeast cells are enveloped by mannoprotein which consists of 90% (w/w) carbohydrate fraction and has negative charges due to the phosphodiester bridges [232]. Given that in the biomimetic mineralization process negatively charged carbohydrates enhance MOF crystallization [206], the presence of negatively charged carbohydrates likely facilitates the MOF shell formation on living cells [232].

In the case of *Micrococcus luteus* coated with ZIF-8, we note that this bacterium also has a membrane rich in peptidoglycans [231,237], which have a negative surface charge due to the presence of teichoic acid polymers [237]. Therein, the authors postulated that peptidoglycans and glycoproteins could enhance the MOF precursor concentration, which favours the formation of a ZIF-8 exoskeleton. Later it was confirmed by experimental and computational modelling that negatively charged carbohydrates could concentrate the zinc ions in and around biomacromolecules [206]. Thus, it was postulated that peptidoglycans and glycoproteins could enhance the precursor concentration, thereby triggering the formation of a ZIF-8 exoskeleton. Another study by Chen et al. reported the formation of a ZIF-8 shell on *E. coli*. According to the authors, the surface of this type of bacteria is negatively charged because of the constituent phosphate groups in lipopolysaccharides [232,238]. Therefore, the presence of lipopolysaccharides in the outer membrane of the cell was suggested to enhance the local concentration of zinc cations, thus facilitating the nucleation and growth of ZIF-8 particles. These examples further exemplify the need to understand in detail the role of carbohydrates for biomimetic mineralization, and their affinity to MOFs, as this knowledge will progress the design new protective and perm-selective artificial coatings for living cells for applications to biomedicine.

4.4. Summary and future outlook

Progress has been made combining carbohydrates (CHs) and MOFs for biomedical applications. CH MOF biocomposites were investigated for DDS and two main configurations have been tested: CHs-on-MOFs and CHs@MOFs. The first class, which involves CH coatings on MOFs, is the most extensively studied to improve stability, targeting properties and bio-distribution of pre-formed MOF-based DDS. More recently, it was found that large clinical CH-based therapeutics can be encapsulated within MOFs using a one-pot strategy [103,206]. Because of the large number of CHs-based therapeutics in the market and in clinical trial [239], additional work is needed to develop a better understanding of the advantages and limitations of these promising systems.

5. Nucleic acids@MOF composites

Nucleic acids including oligonucleotides (ODN), ribonucleic acid (RNA) and deoxyribonucleic acid (DNA) provide promising tools for therapeutic targets [240,241]. Small interfering ribonucleic acid (siRNA) can knock down a gene in a sequence-specific manner and control a disease caused by the activity of one or several genes,

includes viral infections [242–246], dominant genetic disorders [247–249], autoimmune disease [250], and cancer [251–256]. Plasmid deoxyribonucleic acid (pDNA) encodes a wild-type gene to a “depot” organ where the subsequent secretion of the therapeutic protein from this depot has the potential to treat genetic diseases such as hemophilia [257]. The main hurdle for developing such promising therapeutics remains in overcoming the abyss of targeted delivery. To this end, both viral and non-viral vectors have been actively used to achieve this goal. Although viral gene delivery achieves high levels of gene expression, it has several disadvantages such as immunogenicity and oncogenicity that make it problematic for clinical trials [258]. Non-viral vectors have attracted much attention due to their universal application range and high safety level over viral vectors [259]. Among the different synthetic gene delivery vehicles, MOFs show great prospects due to the possibility of tuning their porosity and functionality by tailored molecular design [260]. Moreover, MOFs can overcome enzymatic and acidic digestion through endosomal escape and successfully maintain the physical and chemical integrity of the entrapped genetic materials [261]. In this section we will discuss relevant examples of the encapsulation of nucleic acids in MOF shells and the use of these biocomposites in gene expression, silencing and editing, for application in drug delivery and cell manipulation (Fig. 18).

The first examples of MOF biocomposites for the delivery of nucleic acids involved siRNA [262] and other oligonucleotides [263] bioconjugated to the MOF surface. Lin and co-workers explored multidrug resistance (MDR) gene-silencing by reporting the first example of nanoscale metal–organic frameworks (nMOFs) for the co-delivery of siRNAs and cisplatin [262]. They used Zr-based metal-organic frameworks (UiO-68), formed by heating a solution of $ZrCl_4$ and amino triphenyl dicarboxylic acid in DMF for 5 days at 80 °C, followed by loading Cisplatin prodrug via infiltration (Cis@UiO). MDR gene-silencing siRNAs were coordinated with metal ions on the UiO-68 nMOF's surface through simple mixing in water to give (siRNA-on-Cis@UiO) with 128 ± 3 nm size. siRNA-on-Cis@UiO exhibited higher siRNA uptake compared to naked siRNA by 11-fold. The release profile of siRNA in phosphate buffered saline (PBS) was higher than siRNA release in water as phosphate ions coordinate with the dissociated Zr ions after internalization leading to the destruction of the endosomal structure. Cytotoxicity studies of SKOV-3 cells treated by siRNA-on-UiO showed no toxic effects.

The concept of lysosomal escape prompted researchers to test the possibility of more advanced gene editing technology using MOFs. For example, clustered Regularly Interspaced Short Palindromic Repeats or CRISPR-associated Cas genes are essential in adaptive immunity in selected bacteria and archaea, enabling the organisms to respond to and eliminate invading genetic material [264]. Consequently, this approach can make precise, targeted changes to the genome of living cells. However, for this technique to be effective, the Cas9 protein and sgRNA need to be perfectly protected from endosomal degradation. In 2018, Khashab and co-workers reported the first example of Crispr/Cas9 delivery by one-pot co-encapsulation into nanoscale zeolitic imidazolate framework-8 (Crispr/Cas9@ZIF-8, abbreviated as CC@ZIF-8) with a size of 100 nm and excellent loading efficiency of 17% [261]. Moreover, CC@ZIFs enhanced the endosomal escape through the protonation of the imidazole moieties (Fig. 19c). The stability study of CC@ZIFs indicated that <3% of Crispr/Cas9 was released under physiological conditions (pH 7) while >60% was released at acidic conditions due to ZIF degradation at low pH (Fig. 19d). The CC@ZIFs exhibit superior efficiency for knocking down gene expression (GFP), which reached up to 37% over 4 days in Chinese hamster ovary (CHO) cells [261]. Furthermore, Khashab and co-workers improved the targetability by using a cancer cell membrane coat-

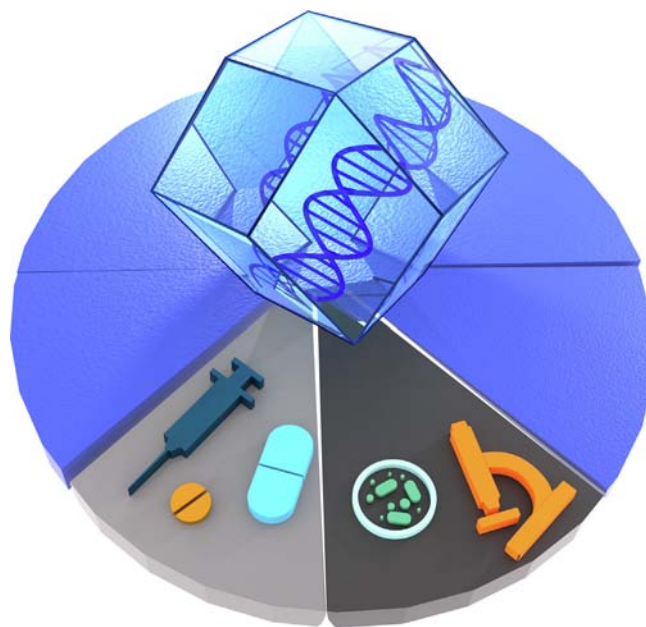


Fig. 18. Nucleic acids@MOF biocomposites and their applications in gene expression, silencing and editing, for drug delivery and cell manipulation.

ing strategy to enable cell specific delivery of Crispr/Cas9 [265]. Human breast adenocarcinoma cell membrane coated CC-ZIFs were prepared through coextrusion of CC@ZIFs and the MCF extracted membrane forming C^3 -ZIF_{MCF} with an average size of 120 nm. C^3 -ZIFs were supported by TEM and Zeta potential measurements as the charge decreased from 8.83 ± 2.96 eV to -17.3 ± 2.82 eV after coating as a result of using the negatively charged cell membrane (Fig. 19c–f). C^3 -ZIF_{MCF} efficiency for specific and targeted delivery has been demonstrated by ICP-MS, flow cytometric and CLSM where the cellular uptake of C^3 -ZIF_{MCF} was higher in MCF-7 cells compared to other cell types due to the inherent homotypic binding phenomenon. Moreover, The C^3 -ZIF_{MCF} efficiency for gene editing against EGFP expression showed a decrease of EGFP expression by 3-fold compared to MCF-7 treated by C^3 -ZIF_{HELA} only which showed a 1- fold repression in the EGFP expression. This confirms the ability to improve the targetability of MOF systems by proper functionalization [265].

In 2019, Farha and co-workers reported the successful infiltration and delivery of unmodified siRNA, utilizing a mesoporous zirconium-based MOFs (NU-1000), to the cytoplasm [23]. After activation at 100 °C for 3 days, proton NMR demonstrated that residual solvent (i.e. DMF) was successfully removed thus allowing for the subsequent loading of the NU-1000 pores with siRNA. The capability of NU-1000 to protect siRNA from enzyme degradation was demonstrated as relevant siRNA bands were observed on a polyacrylamide gel after an enzymatic attack. The location of siRNA in the MOF particles was evaluated by using fluorescence-lifetime imaging microscopy (FLIM) indicating that some siRNA was located on NU-1000 surface, while the majority of siRNA was found inside NU-1000 pores. However, in vitro studies did not show an obvious change in the mCherry expression when HEK293-mC cells were incubated with siRNA@NU-1000, at another time although the mCherry expression was similar to siRNA@lipofectamine. They hypothesized that the inconsistent change in mCherry gene knock-down is due to siRNA@NU-1000 degradation in the endosomes. The authors overcame endosomal entrapment by employing cofactors that have the ability to open endosomes such as proton-sponges (PS) and membrane opening peptides. siRNA@NU-1000 incubated with either 5.3 μg of ammonium chloride (NH₄Cl) or

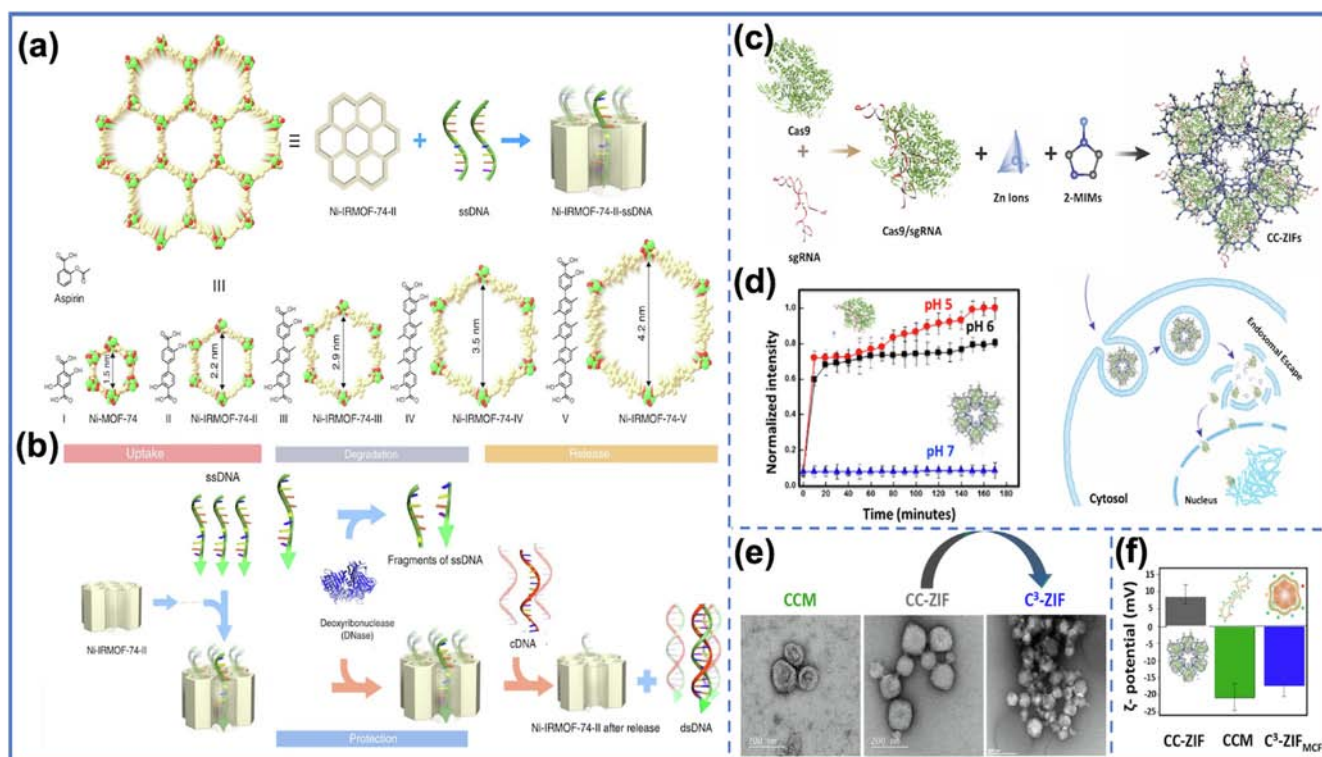


Fig. 19. (a) Illustration of ssDNA inclusion in Ni-IRMOF-74 series. Ni, C, and O atoms were labeled with green, gold, and red color, respectively. (b) Uptake, protection, and release of ssDNA using Ni-IRMOF-74-II. Adapted with permission from ref. [267]. Copyright 2018 Springer Nature. (c) Illustration of CC-ZIF synthesis and cellular uptake. (d) pH dependent release of AF-Cas9/sgRNA. Adapted with permission from ref. [261]. Copyright 2018 American Chemical Society. Characterization of C3-ZIF. (e) TEM images of cancer cell membrane (CCM), CC-ZIF, and C3-ZIF. (f) ζ -Potential of CC-ZIF, CCM, and C3-ZIF. Adapted with permission from ref. [265]. Copyright 2020 American Chemical Society.

0.04 PS resulted in decrease of mCherry expression to ca. 75% and 78% respectively compared to NU-1000 alone. Also, 0.4 μg of the amphipathic KALA cell-penetrating peptide incubated with siRNA@NU-1000 led to a decrease in mCherry signal to ca. 73% [23]. More recently, Horcajada and co-workers reported the first example of mRNA infiltration into biocompatible iron-based mesoporous MOFs [266]. In this work, iron (III) trimesate (MIL-100) and iron (III) aminoterephthalate (MIL-101-NH₂) were used as hosts for the infiltration of non-specific siRNA (as a control) and miR-145 (an onco-suppressor miRNA, for therapeutic purposes). The siRNA and miR-154 infiltration was favored by the opposite charges that the nucleic acids and the MIL particles possess in water. To investigate the localization of the loaded nucleic acids, the authors studied N₂ sorption isotherms: after the nucleic acid infiltration, the N₂ uptake, calculated surface area and pore volume were lowered, suggesting successful nucleic acids entrapment within the pores. Compared to MIL-101-NH₂, MIL-100 NPs showed better nucleic acid protection against enzymatic degradation and this behavior was associated with the smaller pore size. The authors proved also the successful delivery of RNA as RNA@bio-MOF were internalized, while the bare RNA could not penetrate the tested cells. Finally, to evaluate the RNA@bioMOF's therapeutic efficiency, SW480 cancer cells were incubated for 72 h with miR145@MIL-101-NH₂ and miR145@MIL-100 and efficient transfection activities of the delivered miR145 were demonstrated [266].

As for DNA delivery, Deng, Zhou and co-workers reported in 2018 the reversible DNA infiltration into mesoporous MOFs [267]. Different lengths of single-stranded (ssDNA) were infiltrated into a series of MOFs (Ni-IRMOF-74-II to -V) with the same hexagonal topology and different pore size (2.2 nm, 2.9 nm, 3.5 nm and 4.2 nm) (Fig. 19a). The pore environment of the Ni-IRMOF-74 series

reveal that MOF-ssDNA interaction and release are responsive to the DNA target (cDNA) existing in the cells (Fig. 19b). Furthermore, the Ni-IRMOF-74 series exhibits a better protection efficiency of ssDNA from degradation compared to UiO-66, UiO-67, and mesoporous silica, which were used as controls. Both Ni-IRMOF-74-II and Ni-IRMOF-74-III show excellent transfection efficiency in primary mouse immune cells (CD4 + T cells), 60% and 92% respectively compared to the commercial agent, Neofect (50%) [267].

Early attempts at DNA one-pot encapsulation in MOFs and delivery were initiated by Shukla and co-workers and by Tang and co-workers in 2019 [268,269]. Shukla and colleagues reported a complete gene-set (6.5 kilo base-pairs) encapsulation using zeolitic imidazolate framework-8 (ZIF-8) following the biomimetic mineralization process (Fig. 20a) [268]. They confirmed that the DNA has been completely encapsulated using the propidium iodide (PI) dye commonly used for DNA staining. Fluorescence spectroscopy detected the emission peak of PI labeled DNA at 617 nm. The absence of any emission peak when the supernatant and pEGFP@ZIF-8 were treated with PI confirms the successful encapsulation (Fig. 20b, c). Furthermore, they demonstrated that the encapsulated plasmid (pEGFP) remains functionally intact through detecting green fluorescent signals corresponding to GFP expression in human prostate cancer epithelial cells (PC-3) [268]. Tang et al. prepared pDNA (pEGFP, 4.7 kilo base-pairs) and ZIF-8 biocomposites following two encapsulation strategies: the biomimetic mineralization of pDNA@ZIF-8 and the coprecipitation of pDNA in the presence of polyethyleneimine (PEI) as a capping agent for pEGFP-C1@ZIF-8-PEI synthesis (Fig. 20d) [269]. In the presence of PEI (MW \approx 25kD), pEGFP-C1@ZIF-8-PEI nanostructures exhibit higher loading (\approx 3.4 wt%) and better stability against DNase degradation (\approx 82.3%) due to the strong electrostatic interaction between PEI and pDNA. Cellular viability study of pEGFP-

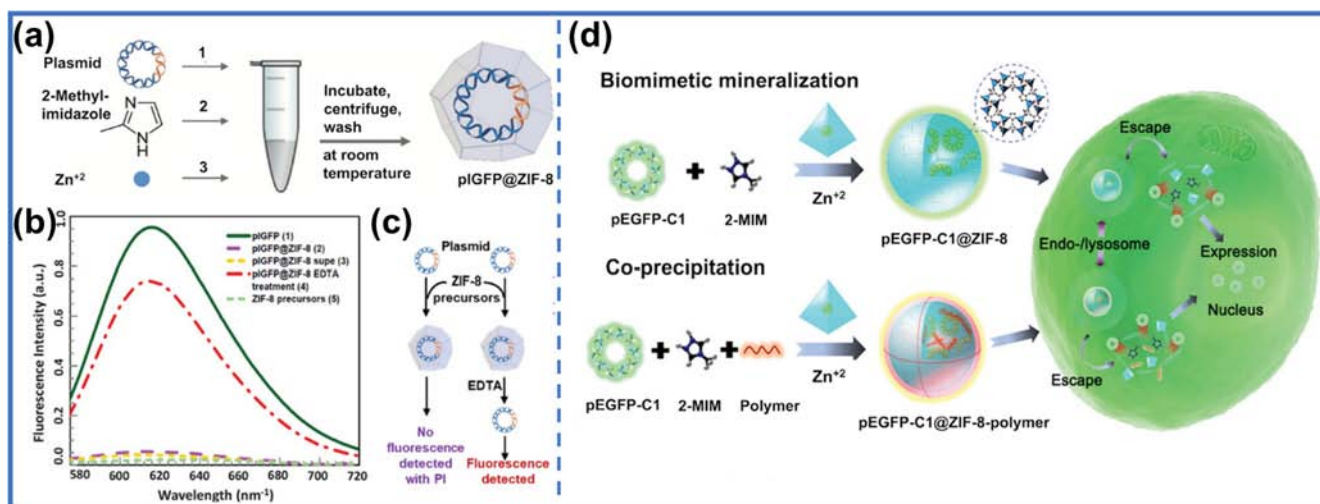


Fig. 20. (a) Schematic representation of the synthesis of pIGFP@ZIF-8. (b) Scheme of pIGFP detection using fluorescence spectroscopy. (c) Fluorescence emission spectra of pIGFP. Adapted with permission from ref. [268]. Copyright 2019 WILEY-VCH. (d) Schematic representation for synthesis of pEGFP-C1@ZIF-8 via biomimetic mineralization and pEGFP-C1@ZIF-8-polymer using coprecipitation method and their cellular delivery and expression process. Adapted with permission from ref. [269]. Copyright 2019 WILEY-VCH.

C1@ZIF-8 and pEGFP-C1@ZIF-8-PEI shows the negative impact of PEI on cytotoxicity. Moreover, pEGFP-C1@ZIF-8-PEI exhibits higher cellular uptake than pEGFP-C1@ZIF-8, probably owing to the positive charge interaction with the negatively charged cell membrane, which further facilitates the internalization of the nanostructures. ZIF-8 was also utilized for gene and photodynamic therapy as a nanocarrier for chlorin e6 (PDT agent) functionalized DNAzyme, and Zn²⁺ ions to support the biocatalytic activity of the Zn²⁺-dependent DNAzyme [270]. Western blot analysis and qRT-PCR studies indicated successful DNAzyme-mediated cleavage reaction in MCF-7 cells treated by DNAzyme@ZIF-8 [270]. The EPR effect facilitates the delivery of Ce6-DNAzyme@ZIF-8 to the cancer cells without DNAzyme degradation followed by controlled release of Ce6-DNAzyme via ZIF-8 degradation in the cytoplasm. Surprisingly, the apoptotic ratio of the photo-irradiated Ce6-DNAzyme@ZIF-8 was higher than that of the gene therapy and PDT alone, (44.9%, 19.85% and 33.6%) respectively [270].

5.1. Summary and future outlook

MOFs nanoparticles are promising vectors for genetic materials encapsulation and delivery. The main challenges in genetic material delivery are poor cellular uptake and rapid degradation. Consequently, some of the main factors that should be considered for the design of superior genetic materials delivery platforms include: 1) high protection against enzymatic degradation in the case of MOF biocomposites synthesized via one-pot encapsulation methods, or coating with cofactors such as cell membranes as nucleic acids could stay on the outer surface of MOFs due to their complex nature, charge and size; 2) enhancing the cellular uptake by controlling MOF size, coating with positively charge materials or other materials that can selectively adhere to cell membranes such as antibodies; 3) enhancing endosomal/lysosomal escape by using cofactors such as proton sponges or membrane penetrating peptides. We believe that heterogeneous coordination-based delivery systems will play a major role in the future of the design and fabrication of the next generation smart materials for automated and controlled biomedical applications.

6. Encapsulation of cells and viruses in MOFs

Among the wide variety of MOF-biocomposites, the encapsulation of cells and viruses within a MOF has been demonstrated to improve stability during manipulation, handling or storage, suggesting that encapsulation of cells and viruses in MOFs could progress cell- and virus-based therapies, diagnostics and drug screening [6,48]. However, this remains one of the most underexplored fields, mostly due to the limitations related to maintaining cell viability or preventing the virus degradation, while working with biocompatible reagents and synthetic conditions [6].

In general, the advantages that a synthetic shell could offer are numerous. For example, single-cell coatings can provide effective protection from environmental factors such as cytotoxic compounds, mechanical stress and UV radiation, which would help in enabling potential applications for cultured cells. Applications such as cell therapy and tissue engineering require *ex vivo* handling and manipulation of cells in which mechanical stress can be an important hazard [46]. For example, one of the key applications of animal cells is bioprinting and it has been reported that the shear stress suffered during the extrusion of bio-inks is a limiting factor for the development of this technique [271]. Physical forces such as shear stress in the needle during intravenous injection, shear and extensional forces during *in vitro* applications (e.g. microfluidic or bioreactor systems) and during centrifugation, damage the plasma membrane of cells, reducing cell viability due to leakage of cytosolic components [272–274]. This is particularly important for mammalian cells, since animal cells do not possess a strong cell wall or exoskeletal shell to provide structural support. The possibility of overcoming this problem by protecting the cells through micro- and nano-encapsulation has been therefore of increasing interest in the research community.

Typical strategies involve microencapsulation in hydrogel systems, nanocoatings of soft polymers and hydrogels, polyelectrolytes, mineral shells and supramolecular metal-organic complexes [275,276]. Single cell-in-shell approaches based on materials such as metal-oxides and polymers have shown good results for applications in biocatalysis (mainly photosynthesis or organic transformations), probiotics (probiotic delivery) and cell therapy (immunotherapy, blood transfusion and stem-cell ther-

apy) [276]. Various types of microbial and mammalian cells (including stem cells, red blood cells, fibroblasts, and endothelial cells) have been successfully encapsulated with these materials [277]. However, among the challenges that limit their application is the need for precise control over the perm-selective properties of the artificial exoskeletons and the necessity to recover the fully functional cells via the degradation of the synthetic shell under biocompatible conditions.

MOFs offer a number of unique features which make them applicable for live-cell encapsulation. For instance, an important aspect in the case of live-cell encapsulation is the preservation of cell's normal functions; thus the protective coating should allow for the diffusion of nutrients and stimulants, while blocking potentially cytotoxic agents. In this context, the narrow pore distribution of MOFs provides a clear advantage over other materials (i.e. silica, other metal oxides and polymers) used as coatings [6]. In addition, biological entities can trigger the self-assembly of MOFs. For example, self-standing cell walls extracted from yeast cells have been shown to be a good template for the creation of different MOF microcapsules with size-selective permeability and different compositions (ZIF-8, Cu-BTC, MIL-53) by biomimetic mineralization [278]. Additionally, the building-block approach to MOF-coatings can also afford biocomposites with abiotic properties such as magnetism, electrical conductivity, multi-wavelength fluorescence, intracellular activity sensing, selective permeability and tunable cell mechanics, which do not occur naturally on most living organisms [279].

With respect to virus encapsulation and virus-like particles (VLP), it was suggested that MOFs could provide essential protection for virus-based therapies and vaccines which typically require constant refrigeration (i.e. a cold chain) to protect the biostructures against denaturing conditions [6]. Pioneering studies in this field have been made using a common model virus (the tobacco mosaic virus or TMV), which could serve as a foundation to further develop VLP-based vaccines [47,208]. However, the exploration of different viruses, MOFs and bioconjugation strategies suggests that further research is needed to realize the full potential of MOF coatings for the protection of vaccines and viral therapeutic nanocarriers. Systematic studies on the synthesis conditions and property optimizations will be fundamental to understand the interaction between MOFs and bioentities.

To highlight the progress made so far, and to visualize more clearly the aspects where there is still opportunity for further development, we have summarized the discussed results in Table 7. From this summary, it can be seen that the synthetic strategies can be broadly divided in two: 1) biomimetic mineralization, and 2) encapsulation by depositing pre-synthesized MOF nanoparticles onto the living cell surface, with an optional additional step of cross-linking to promote NP-NP complexation. In this section we will mainly discuss MOF-encapsulated live cells and viruses with applications in biopreservation and cell and virus manipulation (Fig. 21). Although the scope of this review is focused on the applications of the bioentity@MOF composites, given the research on this topic is not widely developed we will divide the discussion into cells@MOF and virus@MOF composites, with each topic covered in subsections describing both preparation and potential applications.

6.1. Encapsulation of live cells within MOFs

In 2016, Falcaro and co-workers performed the first encapsulation of living cells in a MOF via self-assembly of zeolitic imidazolate framework-8 (ZIF-8) on the surface of *Saccharomyces cerevisiae* (baker's yeast) and *Micrococcus luteus* (a bacterium) [231] (Fig. 22a). The synthesis was performed in water and the formation of the MOF occurred spontaneously. By comparing the via-

bility of yeast cells cultured in the presence of free ZIF-8 particles with that of untreated cells (24 h incubation period), the authors found that the ZIF-8 particles did not adversely affect the viability of yeast cells. Critically, the viability before and after application of the MOF coating was also studied using two standard assays with fluorescein diacetate (FDA) and resazurin as indicators, showing no significant changes in the viability of coated yeast cells with respect to untreated cells. These results indicated that the ZIF-8 coating is non-toxic to yeast cells. The crystalline porous coating was found to form a nutrient permeable exoskeleton with perm-selective properties, which protected the yeast cells in presence of lyticase, a cytotoxic enzyme, whose size is larger than the MOF pores. The same ZIF-8 shell was also found to protect against filipin, a polyene macrolide antibiotic [280], showing that yeast cells could also be successfully shielded from large antifungal agents. Remarkably, after removing the ZIF-8 coating with EDTA, a normal reproductive rate of free yeast cells was measured (Fig. 22b). The authors postulated that the biomolecule-rich surface of living yeast cells and bacteria was the determining factor for the formation of a ZIF-8 shell [27]. In particular, negatively charged carbohydrates were found to trigger the MOF formation [103,206]; thus the glycoproteins and peptidoglycans in the cell membrane could locally increase the concentration of the MOF precursors (see Section 4.3). This hypothesis was supported by Chen et al. [232] who studied different precursors for the ZIF-8 coating (*vide infra*).

In follow-up work, Liang et al. explored the functionalization of the cellular yeast wall with β -galactosidase, and induced the formation of a ZIF-8 coating [281]. With this proof-of-concept experiment, Liang and co-workers demonstrated that the MOF coating could preserve the bioactive functionality of an enzyme immobilized on the surface of living cells (Fig. 22c) providing nutrients in an oligotrophic environment for yeast. Indeed, in a solution with lactose, β -galactosidase, which is not naturally present in yeast cells, was used to convert disaccharides into monosaccharides (a nutrient that yeast could metabolize). Experiments showed that the bioactive exoskeleton allowed the cells to survive for >7 days in a nutrient-deficient medium, where lactose was added instead of glucose. An interesting implication of this study is the demonstration that lactose, and the biocatalytically formed glucose, could diffuse through the porous coating and reach β -galactosidase and the yeast cells, respectively. The properties of this bioactive exoskeleton were further tested by exposing the coated cells to a culture medium containing lactose and cytotoxic enzymes such as lyticase or protease, to simulate a cytotoxic and nutrient-deficient environment (Fig. 22d). The MOF-coated cells were able to survive with only a minor reduction in viability (<30%) for 7 days in these extreme environments, while the naked yeast was lysed in a matter of hours. As in the previous report, the cells were confirmed to recover their full growth potential after the removal of the biocomposite shell.

A recent study by Chen et al. systematically investigated the influence of different zinc precursors on the cell viability for the biomimetic mineralization of ZIF-8 on *E. coli* and yeast cells [232]. Zinc nitrate, zinc acetate, and zinc sulfate were studied as precursors to obtain a ZIF-8 shell on both types of cells. The authors found the three zinc salts and the organic ligand (2-methylimidazole) have low toxicity to these cells; however, for concentrations above 4 mM, zinc sulfate is the precursor that impacts cell viability the most.

Other hybrid materials have been explored taking advantage of the biomimetic mineralization process on live cells for applications in biocatalysis. Qiu et al. produced a special strain of *E. coli* (BL21 (DE3)/pCDFDuet-gdh-cr) capable of asymmetrically reducing tert-butyl 6-cyano-(5R)-hydroxyl-3-oxohexanoate ((5R)-1) to (3R,5R)-2, for biocatalysis [282]. In order to protect the bacteria

Table 7
Summary of recent progress made on the encapsulation of live cells and viruses in MOF-based exoskeletons.

Type	Bioentity	MOF	Metal	Linker	Additional agents	Synthesis method	Application/effect	Refs.
Fungi	Yeast	ZIF-8	Zn ²⁺	2-mlm		Biomimetic mineralization	Protection	[231,232]
Fungi	Yeast	ZIF-8	Zn ²⁺	2-mlm	β-galactosidase	Biomimetic mineralization	Protection and lactose metabolism	[281]
Fungi	<i>Phialomyces macrosporus</i>	Ln-MOF	Tb ³⁺ , Eu ³⁺	mellitic acid		Encapsulation by pre-synthesized particles	Luminescent exoskeleton and organelles	[285]
Fungi	<i>Trichoderma sp.</i>	Ln-MOF	Tb ³⁺ , Eu ³⁺	mellitic acid		Encapsulation by pre-synthesized particles	Luminescent exoskeleton and organelles	[285]
Fungi	<i>Aspergillus niger</i>	Ln-MOF	Tb ³⁺ , Eu ³⁺	mellitic acid		Encapsulation by pre-synthesized particles	Luminescent exoskeleton and organelles	[285]
Bacteria	<i>E. coli</i>	ZIF-8	Zn ²⁺	2-mlm		Biomimetic mineralization	Protection	[231,232]
Bacteria	<i>E. coli</i> , (BL21(DE3))/pCDFDuet-gdh-cr strain	ZIF-8	Zn ²⁺	2-mlm	Activated carbon, glutaraldehyde	Biomimetic mineralization + crosslinking	Immobilization and enhanced recovery for biocatalysis	[282]
Bacteria (anaerobic)	<i>Morella thermoacetica</i>	Zr ₆ O ₄ (OH) ₄ (BTB) ₂ (OH) ₆ (H ₂ O) ₆	Zr ⁴⁺	1,3,5-benzenetribenzoate (BTB)		Encapsulation by pre-synthesized particles	Protection against ROS for artificial photosynthesis	[286]
Mammalian cell	HeLa, A549, HL-60	ZIF-8	Zn ²⁺	2-mlm	Tannic acid	Encapsulation by pre-synthesized particles + crosslinking	Protection, abiotic properties	[279]
Mammalian cell	HeLa, A549, HL-60	MIL-100 (Fe)	Fe ³⁺	trimesic acid	Tannic acid	Encapsulation by pre-synthesized particles + crosslinking	Protection, abiotic properties	[279]
Mammalian cell	Raw 264.7	UiO-66-NH ₂	Zr ⁴⁺	2-amino terephthalic acid	Tannic acid	Encapsulation by pre-synthesized particles + crosslinking	Protection, abiotic properties	[279]
Mammalian cell	HeLa	MET-3-Fe	Fe ³⁺	1H-1,2,3-triazole	Tannic acid	Encapsulation by pre-synthesized particles + crosslinking	Protection, abiotic properties	[279]
Virus	Tobacco mosaic virus (TMV)	ZIF-8	Zn ²⁺	2-mlm		Encapsulation by pre-synthesized particles + crosslinking	Protection, controlled drug delivery	[47,208,292]

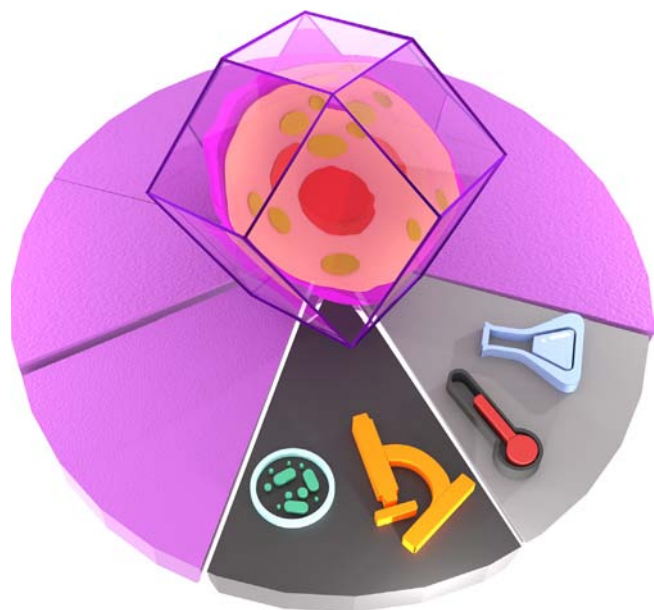


Fig. 21. Encapsulation of live cells and viruses in MOFs and their applications in biobanking and cell and virus manipulation.

and to create a recyclable robust matrix which could be used continuously, the authors combined ZIF-8 encapsulation of the bacteria, glutaraldehyde (GA) cross-linking and immobilization in

activated carbon (AC). The authors define the activity of the biocomposite in terms of one unit of activity taken as “the amount of enzyme required for 1 μmol of (3R,5R)-2 formed per minute at 30 °C, pH 7.0”. Then, the “activity recovery” was defined as the immobilized cells’ percentage of activity, compared to the original activity of the free whole-cells (taken as 100%). The authors report an activity recovery of 82.6% under the optimized conditions for the synthesized biocomposites (AC-ZIF-8@E. coli-GA), with a very high conversion yield of 99.5%. When compared with the free cells and celite-polyethyleneimine-GA immobilized E. coli (same special strain BL21(DE3)/pCDFDuet-gdh-cr), the improved stability and recyclability of AC-ZIF-8@E.coli-GA was attributed to the additional MOF exoskeleton.

Yan et al. capitalized on the combination of live-cell encapsulation with a chemical-loaded MOF for targeted cancer treatment [283]. In this work, the authors combined a specific strain of E. coli that can target tumor cells, E. coli (MG1655), with a ZIF-8 shell loaded with both an anti-cancer drug (doxorubicin, DOX), and a photosensitizer (chlorin e6, Ce6). The therapeutic-loaded ZIF-8 coating did not affect the targeting abilities, nor the viability of the bacteria. With this strategy, the authors were able to activate the therapeutic effect of the biocomposites (E. coli@ZIF-8/C&D) in mild near-infrared laser irradiation conditions. Both *in vitro* and *in vivo* tests demonstrated the efficacy of the method. Remarkably, E. coli@ZIF-8/C&D was shown to inhibit tumor growth in mice after only a one laser treatment (10 min, 660 nm, 200 mW cm^{-2}). This innovative concept combines all of the elements described in this section, as well as the drug delivery strategies discussed in Sections 2 and 3.2.

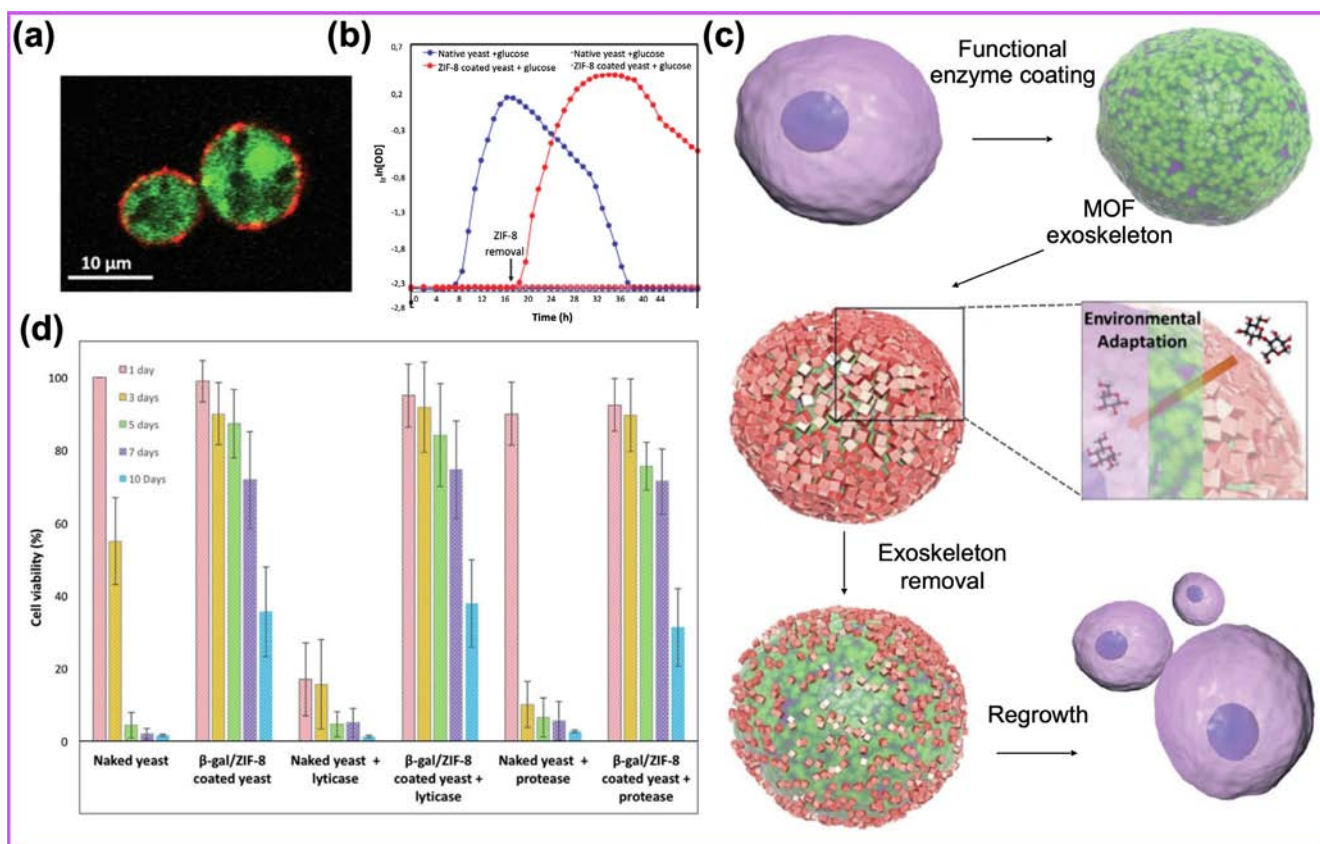


Fig. 22. (a) CLSM cross-section of the ZIF-8-coated yeast cells. Living yeast cells were labeled with FDA (green) and the ZIF-8 coatings were labeled by infiltration of Alexa Fluor 647 fluorescent dyes (red). (b) Yeast growth measurement before and after the removal of MOF coatings by EDTA for native (blue circles) and ZIF-8 coated yeast (red circles). Reprinted with permission from ref. [231]. Copyright 2016 John Wiley and Sons. Yeast @ β -gal/ZIF-8 bioactive coating: (c) Schematic of the construction of the bioactive porous shell (β -gal/ZIF-8) for adaptive cell survival. (d) Relative cell viability (%) of the biocomposites in oligotrophic and inhospitable environments (cytotoxic enzymes and lactose-rich media). Adapted with permission from ref. [281]. Copyright 2017 John Wiley and Sons.

Following the demonstration of ZIF-8 shells on live yeast and bacteria, there have been more recent developments extending this concept to different cell types and other kinds of MOFs. In 2019, Brinker and co-workers presented the concept of “SupraCells”: a versatile encapsulation approach, by which living mammalian cells were instantly encapsulated within a nanoparticle-based exoskeleton thus preventing typical endocytotic nanoparticle (NP) internalization pathways [279] (Fig. 23a). Additionally, this method preserved cell viability and functions (e.g. metabolism), since the MOF NP-based coating did not disturb the permeability of nutrients, metabolites, and signaling molecules. The authors demonstrated these properties by preparing NP-exoskeletons made of ZIF-8, MIL-100 (Fe), UiO-66-NH₂ and MET-3-Fe (see Table 7) and other inorganic coatings (mesoporous silica and iron oxide). NP-based exoskeletons were constructed via the sequential addition of a colloidal MOF solution and tannic acid to cell suspensions prepared in phosphate buffered saline (PBS) solution, in a three-step process: 1) MOF NP synthesis, 2) cell culture in colloidal NP solution and 3) incubation in tannic acid solution. By adjusting the incubation time in tannic acid between 30 s and 60 s depending on the MOF, it was possible to freeze the cellular internalization of the MOF nanobuilding blocks via tannic acid-mediated interparticle binding due to strong multivalent metal-phenolic complexation. Control experiments showed that without this crosslinking agent (tannic acid), in <5 min, the NPs were physically adsorbed onto the cellular surface and then internalized and accumulated around the nucleus. The SupraCell syn-

thesis, initially applied to HeLa cells, was successfully extended to other mammalian cell lines such as adenocarcinomic human alveolar basal epithelial cell (A549 cells), human promyelocytic leukemia cells (HL-60 cells), and Raw 264.7 cell line, all of them yielding SupraCells with continuous MOF exoskeletons. The authors demonstrated increased resistance to various stressors such as osmotic pressure, pH, reactive oxygen species (ROS), UV irradiation, and toxic NPs for the SupraCell-MIL-100(Fe) (Fig. 23d). Additionally, the authors showed that the NP functionality can be tuned to provide the cells with abiotic properties including increased mechanical stability (Fig. 23 b,c), size-selective permeability, intracellular activity sensing, magnetism and electrical conductivity. For example, the NO sensing by luminescence quenching was shown for UiO-66-NH₂ on Raw 264.7 cell line SupraCells. Electrical conductivity was also demonstrated by using metal-triazolate MOF (MET-3(Fe) NPs [284]) The authors suggested the use of this approach for cell-based sensing, regenerative medicine, immunotherapy, and tissue engineering.

A similar approach was used by Rosário et al., who synthesized a luminescent exoskeleton on live filamentous fungi using pre-synthesized lanthanide-MOF (Ln-MOF) NPs [285]. Fungal spores of *Phialomyces macrosporus*, *Trichoderma* sp. or *Aspergillus niger* were inoculated in a sterile solution containing glucose and a particulate dispersion of Ln-MOF NPs. The Ln-MOFs were prepared using Tb³⁺ and Eu³⁺ and mellitic acid (1,2,3,4,5,6-benzenehexacarboxylic acid) to give MOF particles in the 70–900 nm range. The fungi were cultured for two weeks under dark conditions, and

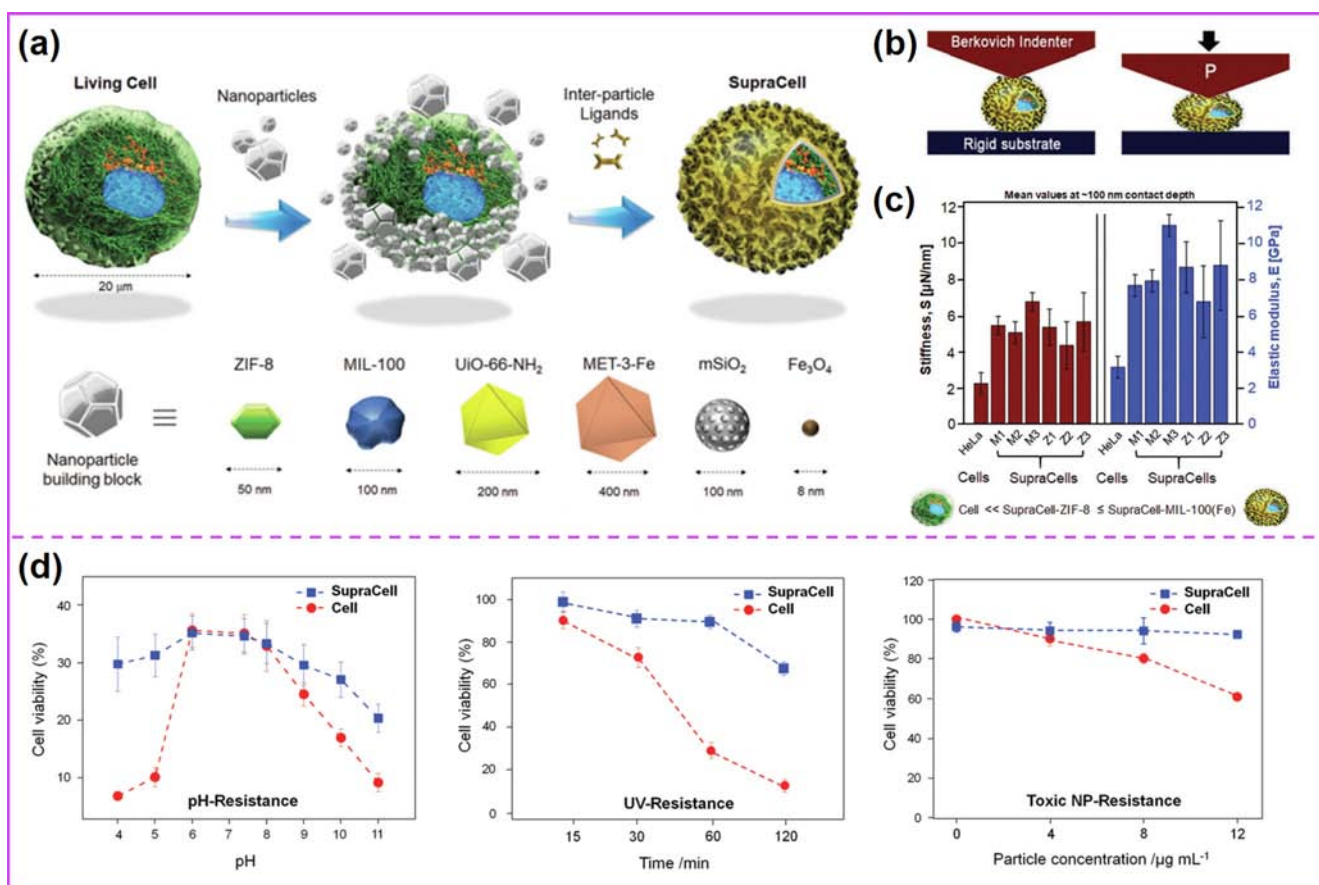


Fig. 23. (a) Schematic of SupraCell construction based on different materials (MOFs and inorganic coatings) forming artificial exoskeletons on living cells; (b) Schematic of the mechanical response test setup performed with a Berkovich Indenter imposing a P load onto cells and SupraCells using a cyclic loading–unloading function; (c) Elastic modulus and stiffness of HeLa cells and SupraCells-MIL-100(Fe) or ZIF-8 (M or Z refers to MIL-100(Fe) or ZIF-8, respectively); with different coating cycles (indicated by numbers 1–3). (d) Enhanced resistance of SupraCells against endo- and exogenous stimuli such as pH, UV irradiation and toxic NPs (blue squares SupraCells, red circles naked cells). Reprinted with permission from ref. [279]. Copyright 2018 John Wiley and Sons.

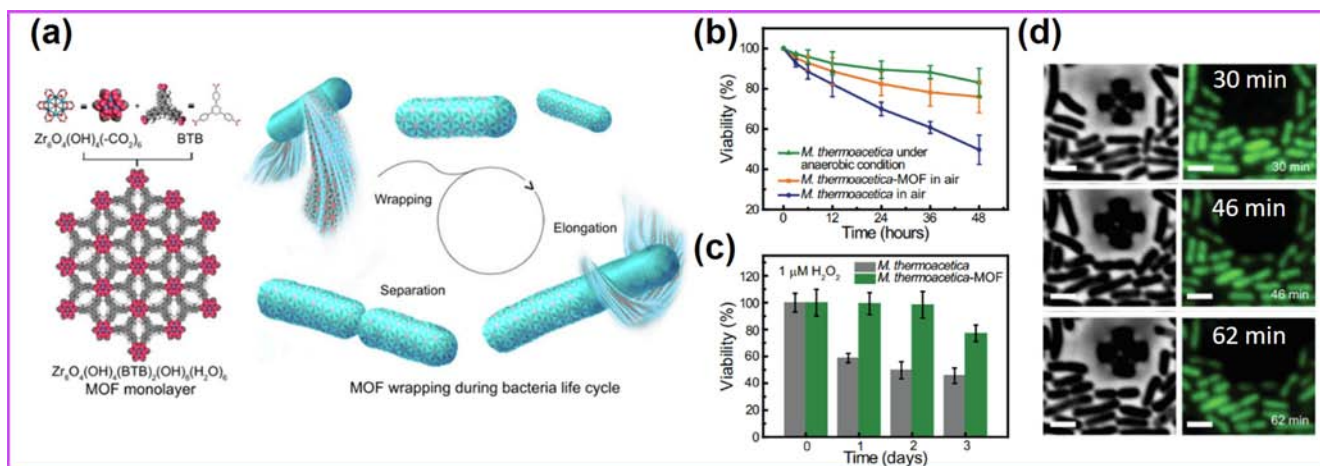


Fig. 24. (a) Design and synthesis of a MOF wrapping system on anaerobic bacteria (*M. thermoacetica*). MOF monolayers comprised of a 6-connected $Zr_6O_4(OH)_4(-CO_2)_6$ clusters and trigonal BTB linkers. (b) Cell viability studies of *M. thermoacetica* and *M. thermoacetica*-MOF in air, and bare *M. thermoacetica* under anaerobic conditions. (c) Cell viability of the anaerobic bacteria and the bacteria-MOF composites in media containing $1 \mu M H_2O_2$ solution. (d) Dark field (left) and fluorescence field (right) images of the division process of *E. coli*-MOF, taken at 30, 46 and 62 min, showing the MOF monolayer wraps around newly grown cells (Scale bars: $1 \mu m$). Adapted with permission from ref. [286].

Ln-MOF decorated mycelia were obtained and analyzed with fluorescence microscopy and further physicochemical characterizations. SEM images reveal that particulate Ln-MOFs are accumulated uniformly on tubular cells, and firmly bound in the surrounding biopolymer matrix. The results show that the controlled deposition of Ln-MOFs on filamentous fungi imparts photoluminescent properties in living entities. The authors suggested that these findings may be relevant for the development of living imaging analysis and treatment of fungal infections.

Yang, Yaghi and co-workers added pre-synthesized MOF [$Zr_6O_4(OH)_4(BTB)_2(OH)_6(H_2O)_6$; BTB = 1,3,5-benzenetribenzoate] NPs into the culture media of *Morella thermoacetica*, an anaerobic bacteria [286] (Fig. 24). The exposure of the bacteria to the MOF colloidal solution allowed for the self-assembly of a flexible NP-monolayer (1–2 nm) that could adapt to the bacteria cell wall changes, including growth and reproduction. The authors, by adding an excess of MOF to the culture media, observed the formation of a coating on newly grown cell surfaces, allowing the extension of the artificial MOF-based exoskeleton over generations of the anaerobic bacteria (Fig. 24d). We note that this type of process is not likely to be possible via biomimetic mineralization of ZIF-8 as the reproduction or growth of yeast cells is temporarily blocked until the coating is removed. The protective effect of the MOF shell on the anaerobic bacteria was investigated by assessing cell viability after exposure to O_2 and H_2O_2 for a 1–3 day period (Fig. 24b). Compared to pristine bacteria in anaerobic environments, the results showed that MOF-protected bacteria in aerobic conditions have comparable cell viability. MOF-encapsulated live anaerobic bacteria displayed “active” protection which allows an enhanced artificial photosynthesis process, reduced death of the bacteria (5 times) in presence of O_2 , and enabled continuous production of acetate from CO_2 fixation under oxidative stress. The authors attributed the protection against oxidative stress to catalytic activity (decomposition of the reactive oxygen species, ROS) by the MOF because of structural resemblance between the zirconium clusters of the MOF and active sites of zirconia. However, control experiments comparing the MOF-coated bacteria with bacteria cultured in the presence of zirconia nanoparticles, found no cytoprotective effect for the zirconia NPs. This result suggests that the proximity

of the MOF catalytic active sites to the cell, as well as their accessibility (surface active sites) are important factors.

In recent years, interesting progress has been made on coating living cells with an artificial shell comprised of a self-assembled ferric ion-tannic acid complex that spontaneously forms in presence of tannic acid (TA) and Fe^{III} . Studies performed by Caruso, Choi and co-workers, have demonstrated the feasibility and potential for protection of live yeast [287], adherent and cancerous mammalian cells, [288,289] and red blood cells (RBC) [290]. These coordination compound coatings, which lack the extended MOF periodic structure formed via coordinate bonds, showed interesting properties: 1) TA- Fe^{III} complexes formed a very thin layer and its thickness can be precisely controlled by changing the precursor concentration in the 5 to 20 nm range; 2) it is highly cyto-compatible; and, 3) it generates a protective and degradable nanoshell. In particular, experiments on red blood cells showed that the coating helped attenuate the antibody-mediated agglutination, while retaining the oxygen-carrying capability of RBCs after shell formation. The authors suggested these biocomposites could progress the development of universal blood. TA- Fe^{III} coatings were also applied to other mammalian cell lines (HeLa, NIH 3 T3, and Jurkat cells) [288]. Albeit not technically a MOF [291], we include this discussion about TA- Fe^{III} complexes in the present review as this could inspire the development of Fe-based MOF coatings for biomedicine.

6.2. Encapsulation of viruses within MOFs

The first report on virus-MOF composites was performed by Gassensmith and co-workers [292], and described the crystallization of a ZIF-8 shell on tobacco mosaic virus (TMV), a model virus (Fig. 25a). The authors achieved precise control over the thickness of the ZIF shell that could be tuned between 70 and 100 nm by changing the ligand to metal ratio (2-methylimidazole:Zn). The authors also exposed the resultant biocomposites to different environmental stressors, such as polar solvents and high temperature. The TMV@ZIF-8 composites were found to be stable in polar organic solvents (methanol and DMF) for 16 h, and for the thickest shell the biocomposites were also able to endure immersion in dichloromethane (DCM) for 16 h and boiling water for 20 min,

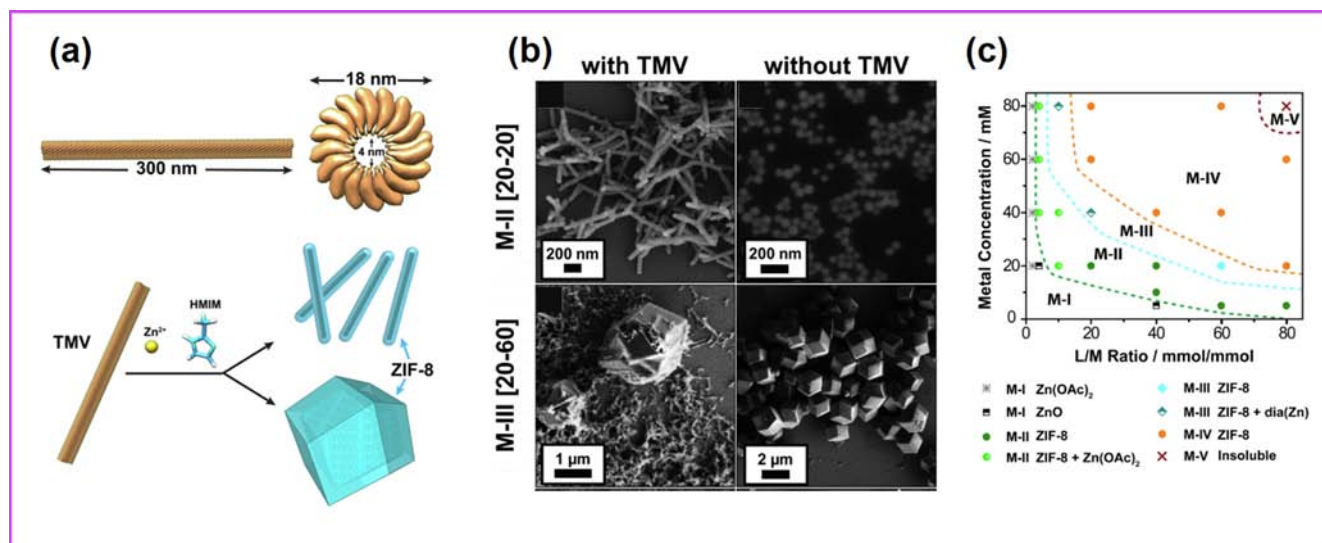


Fig. 25. (a) Top: Schematic of the tube-shaped tobacco mosaic virus (TMV) showing its dimensions (300 nm long and 18 nm diameter with a 4 nm inner channel). Bottom: Schematic illustration of TMV-templated ZIF-8 mineralization which, depending on synthetic conditions, can lead to CSBNs (top) or rhombic dodecahedral (r.d.) composites (bottom). (b) Influence of different ligand/metal ratios on the resultant morphology of the TMV@MOF particles (SEM images), at constant metal concentration (20 mM), with and without TMV. (c) Composite transformation map, correlating SEM and PXRD characterizations of the as-obtained composites to their synthetic conditions. M-I: strips of Zn(OAc)₂ (grey star) or near aggregates of ZnO (black and white box); M-II: rod-like CSBNs of either phase pure ZIF-8 (dark green circle) or a mixture of ZIF-8 and Zn(OAc)₂ (half light green circle); M-III: mixture of pure ZIF-8 phase CSBNs and r.d. crystals (light blue diamond) or a mixture of ZIF-8 and dia(Zn) of both CSBNs and r.d. crystals (half dark blue diamond); M-IV: r.d. composites with pure ZIF-8 phase (orange hexagon); M-V: solubility issues of 2mIM limiting further study (dark red ×). Reprinted with permission from ref. [208]. Copyright 2018 American Chemical Society.

without structural degradation. Furthermore, the virus itself could be reclaimed undamaged after immersion in pure methanol overnight, by using an aqueous solution of EDTA to remove the ZIF-8 coating.

A comprehensive study performed subsequently by the same group analyzed the dominating factors that influence the final morphology of TMV@ZIF-8 biocomposites [208]. The authors performed an in-depth study of the formation mechanism of the core-shell biocomposites, by exploring different ligand to metal (L/M) ratio and precursor concentrations (Fig. 25c), as well as the effect of surface charge changes induced by bioconjugation reactions on the surface of the virus. The biocomposites were divided into two sets: small core-shell bionanoparticles (CSBN), which retained the underlying morphology of the virus (~300 nm × 18 nm rods), and multiple TMV particles entrapped in micrometer-sized rhombic dodecahedral (r.d.) single crystals of ZIF-8 (Fig. 25a,b). Interestingly, the CSBN morphology was found to form most favorably in reaction conditions in which the spontaneous formation of ZIF-8 was otherwise disfavored, yielding only amorphous granules without the TMV. Using a bioconjugation strategy, the authors functionalized the TMV exterior via a Cu(I)-catalyzed azide-alkyne cycloaddition (CuAAC) reaction to attach functionalized azides that could modify the electrostatic charge of the virus capsid. The results suggest that CSBN formation proceeds in very good yields (~90%) under most circumstances, unless the surface is highly positively charged, in which case the yield is still ~70%. Time-dependent SEM characterization of the different phases revealed that the growth of ZIF-8 on the surface of the TMV proceeds at different rates from the precursor solution and is probably induced by an elevated local concentration of zinc in the microenvironment around the TMV. This is in line with studies by Doonan and co-workers on the influence of electrostatic charge of proteins in biomimetic mineralization of ZIF-8 [114].

The most recent progress on virus-based MOF biocomposites was performed by the same team, in a 2019 publication in which they apply the optimized conditions already found for the encapsulation of TMV in ZIF-8 to further study the viability of MOF-

encapsulated vaccines [47]. In this case, to evaluate the potential of ZIFs for vaccine preservation, TMV@ZIF composites were subjected to different stressors such as heat and denaturing solvents, then the ZIF-8 shell was removed and the protein was recovered and analyzed by ELISA to assess the integrity of the surface (Fig. 26a). Studies on *N. benthamiana* (tobacco) plants were performed in which the plants were inoculated and the evolution of the infection was assessed as well as a viral recovery study, measured by ELISA on harvested leaves (Fig. 26b). The study also found that the RNA of the encapsulated virus was still active, indicating that the TMV remains virulent and the RNA survives the encapsulation and release process. Finally, studies on live animal models shed light on the immune response toward these biocomposites, their biocompatibility, and the ZIF-8 shell decomposition profile and virus release *in vivo* (Fig. 26c-f). Importantly, the results of this study have shown that the crystalline porous coating grown on the viruses did not affect the structure of the proteins and their ensembles, and that it did not damage significantly the viral RNA. The results obtained from the *in vivo* studies on mice showed no alteration of tissue morphology at the injection site or distal organs (Fig. 26e). Additionally, no behavioral changes, illness or deaths were observed on the animals as a result of the TMV@ZIF administration. Based on these results, the authors propose that ZIF-8-based shells in combination with the highly tunable TMV platform could provide a safe and reliable method for the delivery of proteinaceous drugs.

6.3. Summary and future outlook

In this section we have discussed the most relevant results of live cell and virus encapsulation in MOFs. The progress made on these complex biocomposites has shown the potential of MOF-based artificial shells [6], and some systematic studies [208,279] have shed light on MOF formation mechanisms and assessed the protective properties. However, for a better understanding of these systems, further systematic studies should reveal the importance of the synthetic conditions on the protection of different cell types.

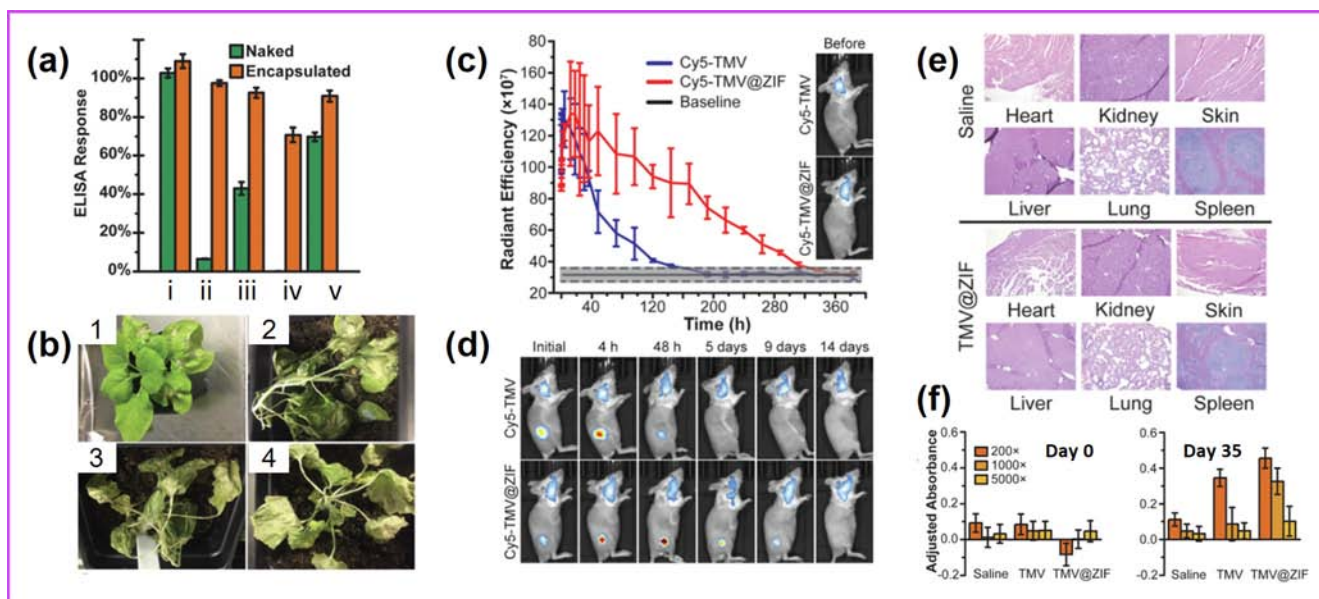


Fig. 26. (a) ELISA response of naked and encapsulated TMV subject to no stress (i), heating (ii), methanol (iii), 6 M guanidinium chloride (iv), and ethyl acetate (v). (b) Tobacco plants (*N. benthamiana*) 10 days after inoculation with (1) 0.1 M pH 7.4 potassium phosphate buffer as a negative control, (2) TMV@ZIF, (3) exfoliated TMV@ZIF, and (4) native TMV as a positive control. (c) *In vivo* experiments performed on mice after subcutaneous injection of a fluorescently-tagged ZIF-8-encapsulated TMV virus. Fluorescence intensity over time. Baseline taken by averaging the fluorescence on four mice before injection (dashed line represents error), insets show images of mice prior to injection of Cy5-TMV or Cy5-TMV@ZIF showing some initial fluorescence from the hairs on the head (mice were shaved). (d) Time point images after injection of Cy5-TMV or Cy5-TMV@ZIF. (e) Hematoxylin & eosin Y (H&E) staining of saline- and TMV@ZIF-injected mice. (f) ELISA response for day 0 and day 35 performed on blood samples from injected mice, buffer blank subtracted, serum samples were diluted 200 \times , 1000 \times , and 5000 \times . Adapted with permission from ref [47]. Copyright 2019 American Chemical Society.

In particular, an important step is the extension to different cell types and MOFs [6]. As a future perspective for this field, MOF-coatings could be used to impart control over cell aggregation and coagulation, which are critical for applications such as 3D cell printing [276] in regenerative medicine.

Another important step would be a comparison of MOF coatings with more established materials. For example, typical materials used for single-cell encapsulation are polymers deposited using a layer-by-layer approach. For these polymers, the control over shell thickness seems superior to the current control over MOF exoskeletons [277]. For example, the thicknesses of the explored coatings have ranged between 70 and 900 nm [285] to ~50–80 nm [208,279] to 1–2 nm [286], but this is strictly dependent on the MOF chosen and deposition process used. Layer-by-layer MOF growth is also possible [293,294], which suggests that adoption of polymer deposition approaches could be employed if a suitable MOF material can be identified.

It is also important to note that most of the progress for MOF coatings has been made on cells with robust cell walls (e.g. fungi, bacteria). Although the encapsulation of bacteria can be useful for applications such as whole-cell biocatalysis, for other applications such as cell therapy and tissue engineering it is fundamental to develop this field toward cytoprotective and cytocompatible coatings on mammalian cells [6,276]. The coating of mammalian cells, which are encased only in lipid bilayer membranes, remains a challenge due to their fragile nature. For this reason, they require more carefully selected precursors and processing [288] and handling conditions. Thus, coating mammalian cells with different MOFs, while preserving their viability, would significantly progress these composites toward application in regenerative medicine and cell therapy.

7. Lipids-on-MOFs: A surface functionalization approach for MOFs-based DDS

Lipids (e.g. fatty acids, sterols, glycerolipids and glycerophospholipids) play a key role in many biological processes such as cell

metabolism and signaling. In addition, lipids are fundamental structural biological components as cell membranes are mainly composed of lipids (e.g. glycerophospholipids). In the field of drug delivery, lipids are particularly attractive because of their biocompatibility and amphiphilic properties [295]. The amphiphilicity of phospholipids permits the formation of supramolecular structures in solution, such as micelles and liposomes. The vesicular structure of liposomes is used for the integration of a wide variety of active pharmaceutical ingredients (APIs) including hydrophobic drugs. This strategy is commercially viable as it enhances the drug loading and bioavailability of several clinical therapeutics via different administration routes (e.g. oral, parenteral, topical) [295].

In the field of MOF-based drug delivery systems (DDS), lipids have been employed as functional coatings on MOF-based carriers (i.e. lipid-on-MOF). The main advantages that a lipid coating can impart to MOF-based DDS are the improved colloidal stability and biocompatibility, longer circulation time and easier cellular internalization. Pioneering reports on lipid-on-MOFs were provided in 2015 by Wuttke et al. [213] and Wang et al. [296].

Wang et al. synthesized a series of hydrophilic Zr-based MOFs (UiO-66, UiO-67, and BUT-30) crystals with different particle sizes (e.g. particles in the range of 20 to 30 nm, and from 200 to 500 nm range) [296] and high affinity for polar solvents (e.g. water) (Fig. 27a). The main goal of this study was to obtain a stable colloidal suspension of the hydrophilic MOFs in low-polarity media. To obtain stable colloidal suspension of MOF NPs, the crystals were sonicated in presence of 1,2-dioleoyl-*sn*-glycero-3-phosphate (DOPA). According to $^{31}\text{P}\{^1\text{H}\}$ magic angle spinning (MAS) NMR spectroscopy results, the MOF functionalization occurred due to the phosphates of DOPA coordinating to the zirconium oxide nodes on the external surface of the MOF nanoparticle. The DOPA-functionalized MOFs retained both the crystallinity and porosity of the pristine MOF. Following this approach, the authors showed that it was possible to tailor the stability of MOF colloids in low-polarity solvents using lipids (e.g. CHCl_3).

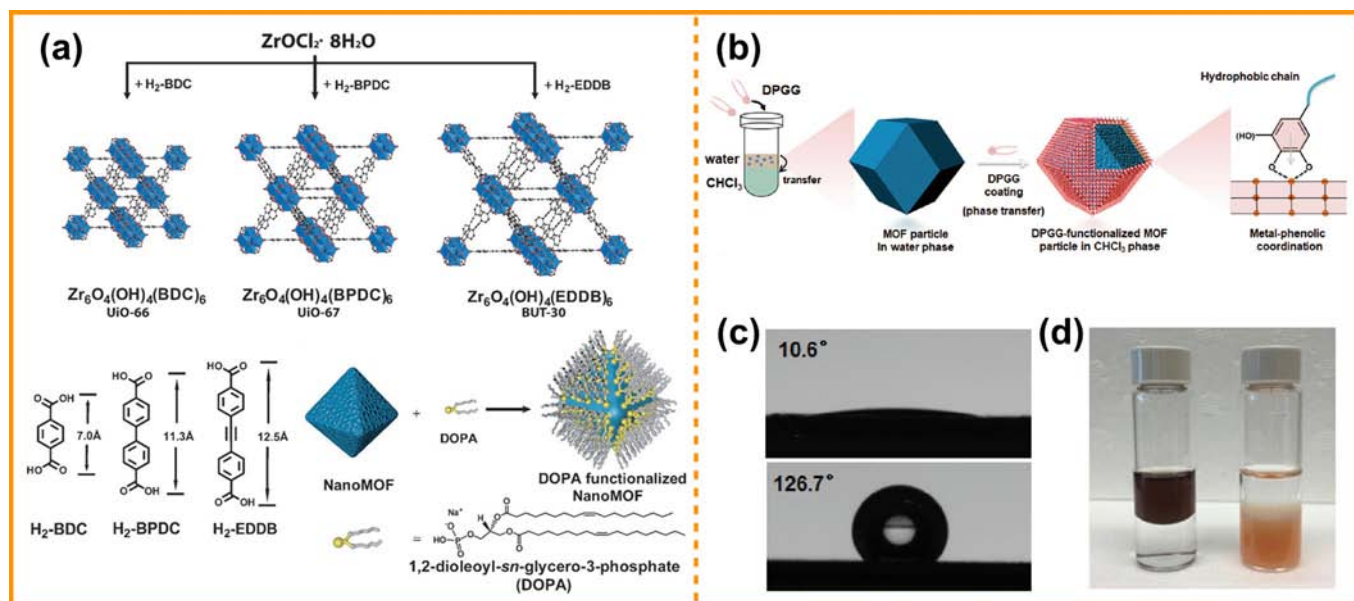


Fig. 27. (a) Functionalization of a series of Zr-based MOFs (UiO-66, UiO-67, and BUT-30) with 1,2-dioleoyl-*sn*-glycero-3-phosphate (DOPA). Reprinted with permission from ref. [296]. Copyright 2018 John Wiley and Sons. (b) Surface functionalization of MOFs with 1,2-dipalmitoyl-*sn*-glycero-3-phosphate (DPGG). (c) Contact angle images of MIL-88A before (top) and after (down) DPGA modification. (d) Pristine MOF nanoparticles suspended in aqueous phase (right), MOF nanoparticles transferred to toluene phase upon the functionalized with DPGA (left). Reprinted with permission from ref. [300]. Copyright 2018 John Wiley and Sons.

The study from Wuttke et al. on lipid-on-MOF systems demonstrated the potential use of such biocomposites in the field of drug delivery [213]. The authors prepared MIL-100(Fe) and MIL-101(Cr) nanoparticles (ca. 50 nm) and loaded a fluorescent cargo molecule (e.g. fluorescein and Atto663) in the porous framework. Then, the resultant dye@MOF particles were functionalized with a 1,2-dioleoyl-*sn*-glycero-3-phosphocholine (DOPC) bilayer via a controlled solvent-exchange deposition method: by increasing the water content in a DOPC-MOF ethanol/water dispersion, the DOPC molecules concentrated on the MOF surface leading to the formation of a lipid bilayer. The MOF structure was preserved after the coating process, and the DOPC-on-dye@MOF NPs were successfully dispersed in water showing improved colloidal stability that is a central aspect of DDS. In addition, the presence of the DOPC bilayer prevented the uncontrolled release of the cargo, an additional important property in DDS. The cellular uptake of DOPC-Atto633@MOF nanoparticles in cancer cells (T24 bladder carcinoma cells) was monitored by confocal laser scanning microscopy, and this analysis confirmed the superior uptake compared to the un-coated dye@MOF particles. As MILs could be loaded with a variety of molecules (e.g. dyes for imaging, drugs) and the lipid bilayer nature could be tailored for targeting or shielding purposes, the authors suggested that these lipids and MOF biocomposites could be suited to different applications in the biomedical field. Thus, Wuttke's group further explored different combinations of lipids and drug-loaded MOF NPs [297,298]. In 2017, they embedded MOF particles within exosome [297] shells. Exosomes are extracellular vesicles produced by eukaryotic cells with a structure that mimics the cell membrane [299]. Since these exosomes are present in body fluids and are non-immunogenic, the authors hypothesized that exosome-MOFs could circulate without being recognized by the immune system, thus providing a novel MOF-based system for drug delivery. The authors first loaded a model drug (e.g. calcein with a loading capacity of 15.8 wt%) into MIL-88A NPs (ca. 50 nm). Then the drug@MOF NPs were dispersed in water in the presence of exosomes extracted from HeLa cells, and incubated at room temperature for 2 h. The exosomes-coated particles showed a negligible premature drug release in water, as in the case

of DOPC-on-dye@MOF biocomposites, while uncoated particles leaked rapidly. The authors examined the controlled release of the cargo after cellular internalization by exposing the exosome-MOF biocomposites to an artificial lysosomal fluid (ALF), a solution that simulates the endocytosis environment inside cells. The enhanced osmotic pressure in the exosome coating caused by ALF lead to bursting of the exosome and the consequent calcein release. Finally, exosome-coated calcein@MIL-88A was incubated with HeLa cells: fluorescent microscopy studies confirmed the successful biocomposite internalization and calcein release. Motivated by these interesting results, the authors loaded an anti-cancer drug (suberohydroxamic acid, SBHA, loading = 2.3 wt%) into MIL-88A NPs and coated them with exosomes. Exosome-coated SBHA@MIL-88A were incubated with HeLa cells and the authors confirmed the apoptotic properties: after 3 days of incubation, the IC50 value (4.78 μ g/mL) was found to be 3 times higher than the IC50 of free SBHA.

After these seminal works, the coating of MOF NPs with mono- and bi-layers of lipids was expanded and applied to different MOFs and lipids [300,301]. Yang et al. synthesized nanoparticles (<200 nm) of a porphyrinic Zr-MOF (PCN-223) and coated them with a continuous monolayer of DOPC exploiting the formation of Zr-O-P bonds on the MOF surface [301]. Then, the DOPC-on-PCN-223 was further coated with DOPC and cholesterol to self-assemble into a lipid bilayer on the MOF surface. The DOPC-on-PCN-223 biocomposites showed high colloidal stability in different chemical environments (including phosphate-based media that could degrade pure PCN-223), more favorable biocompatibility and cellular uptake. Furthermore, the DOPC coating ensured the intracellular stability of the biocomposite: the authors observed that the internalized NPs maintained their rod morphology in the cytoplasmic milieu of SMMC-7721 cells after 12 h of incubation. The intracellular stability was associated with the shielding properties of DOPC that protected the MOF particles from the phosphate ions available in the intracellular environment [67]. The authors suggested the use of these coated MOFs for bioimaging and photodynamic therapies to improve the stability of MOF systems during their imaging functions. In 2018, Zhu et al. investi-

gated a versatile and reversible strategy to decorate the surface of several different MOF microparticles (e.g. MOFs based on Al, Cr, Fe, Co, Cu, Zn, Zr, In and Eu) with a phenolic-inspired lipid molecule DPGG (1,2-dipalmitoylsn-glycero-3-galloyl) via the coordination of the galloyl head groups to the metal sites on the MOF surfaces [300] (Fig. 27b). After the self-assembly of the DPGG monolayer, the DPGG-on-MOF particles showed a hydrophobic character (i.e. hydrophobic tails of the lipid were oriented opposite to the MOF surface) and colloidal stability in non-polar solvents (Fig. 27c, d). The DPGG monolayer was dis-assembled by washing in weakly acidic water, since the metal-phenol complexation is pH sensitive, and this aspect could be exploited for triggered-release applications. Then, the authors demonstrated that DPGG-on-MOF biocomposites could serve as platform for the synthesis of a variety of materials via the successive functionalization of the lipid monolayer (e.g. silica coating via silanes condensation, addition of a second lipid to form a lipid bilayer on the MOF surface) and posit that these materials can be exploited for biomedical applications (e.g. multi-compartment biocarrier, targeted delivery and photothermal therapies).

In summary, lipid-on-MOF biocomposites represent a promising platform for the development of MOF-based DDSs. The rich chemical variability of lipids can be exploited to impart additional functionality to drug-loaded or bioentity-loaded MOF particles, ranging from the improvement of MOF DDS biocompatibility, bioavailability and blood-circulation time to active targeting properties. Furthermore, the lipid functionalization strategy could be applied to different MOF systems, thus expanding their field of application from drug delivery systems to other biotechnological platforms including bioimaging and biosensing.

8. Conclusions and perspectives

In this review we have highlighted the advantages and promising applications of different bioentities@MOFs, sorted mainly into four categories based on the bioentity: proteins, carbohydrates, nucleic acids and live cells and viruses. Additionally, we have discussed the use of lipids and carbohydrates-on-MOFs as a strategy to improve targeting, blood circulation time and compatibility of the biocomposites. We have discussed different synthetic approaches for the formation of these biocomposites, experimental techniques used for their characterization and their potential application in biomedicine. We have summarized aspects that demonstrate how MOFs are an effective platform for the protection and controlled release of protein-based therapeutics, and moreover demonstrated that MOFs are emerging materials for the delivery of nucleic acids- and carbohydrate-based drugs. Azolate-based MOFs (e.g. ZIF-8, ZIF-90 and MAF-7), which feature highly in this field, afford high encapsulation efficiency and a tunable release profile, along with favorable biocompatibility, which commend them as drug delivery systems. While these MOFs have led the way, considerable scope is available to extend the encapsulation process to other MOF matrices, perhaps containing bio-derived linkers [11,302] or even to metal-free systems that are assembled from organic molecular building blocks [303].

From a preliminary assessment of the cost of the materials involved in forming ZIF-biocomposites, the MOF component is typically inexpensive with respect to the therapeutic and can range between 0.01% and 5% with respect to the total cost of the final material (MOF + encapsulated bio-therapeutic), see Table 1. Additionally, post functionalization methods could further enhance specific desired properties, including blood circulation time, cell uptake, and targeted delivery.

Where possible, we have discussed further aspects relevant to biomedicine such as particle size, encapsulation efficiency, release

properties, biocompatibility and therapeutic properties. Regarding the particle size of MOF-based biocomposites for drug delivery applications, only a few studies have investigated the effect on the biodistribution, biocompatibility and release kinetics of the cargo. However, it would be crucial to have comparative studies across different MOF carriers and several precisely controlled particle size distributions, as both the chemistry of the MOF particle and their size could influence the properties of both micro- and nano-MOF carriers. By controlling the chemistry, the particle size and the surface functionalization of MOFs, both the degradability and bioaccumulation of the carrier can be manipulated. For example, stimuli-responsive carriers have been designed where the degradation process is selectively triggered by the presence of glucose to achieve controlled insulin release.

Encapsulation of biomacromolecules within a MOF shell has been demonstrated to be an effective strategy for maintaining the bioactivity of a wide range of compounds including proteins, enzymes, antibodies and viruses, even after exposing them to denaturing conditions such as elevated temperature. Thus encapsulation has emerged as a promising technology for handling, transport, and storage of biospecimens without refrigeration, which is an attractive alternative for providing cold-chain-free transport of vaccines, and thereby reducing the shipping costs.

For other biomacromolecules such as enzymes, their embedding within a MOF shell can progress the fabrication of cost-effective biosensors for the detection of a wide variety of analytes, ranging from small molecules such as H₂O₂ and glucose, to large biomacromolecules including protein-based biomarkers and exosomes. Such platforms offer several benefits including high signal amplification, sensitivity, specificity, and reproducibility. The presented strategy is envisioned to facilitate the design of point-of-care testing devices and for real-time diagnostic analytical systems.

Finally, in this review we discussed the new trends in the encapsulation of live-cells and viruses using a MOF-based exoskeleton for the protection of bioentities. To date, most of the progress has been made on cells within robust walls (fungi, bacteria) and this could be useful for applications such as whole-cell biocatalysis. However, for applications of MOF protective coatings to cell therapy and tissue engineering, the development of protocols for the fabrication of cytoprotective and cytocompatible coatings on mammalian cells is needed. The promising results obtained for cells encapsulated in bioactive coatings suggest an opportunity to expand this research by combining the MOF shell with different biomacromolecules, which can endow the cells with new properties.

As a final remark, while the characterization of the bioentity and biomacromolecule@MOF composites has greatly improved, the use of in-situ analytical and structural characterization methods could further advance MOF biocomposites. This could shed light on critical aspects, such as the formation mechanisms of MOFs on bioentities and related MOF-to-biomacromolecule interactions. These fundamental insights will guide the use of other MOF materials as coatings for DDS, and will inform the methodologies employed to encapsulate particular classes of biomacromolecules and cells that are not robust enough for current approaches.

Declaration of Competing Interest

The authors declare that they have no known competing financial interests or personal relationships that could have appeared to influence the work reported in this paper.

Acknowledgements

The authors acknowledge support from the European Union's Horizon 2020 FETOPEN-1-2016-2017 research, LP-03, the innovation program under grant agreement 801464, and the European Research Council under the European Union's Horizon 2020 Programme (FP/2014-2020)/ERC Grant Agreement no. 771834 – POP-CRYSTAL. M.J.V.H. acknowledges The National Council of Science and Technology (CONACyT, México) for the postdoctoral scholarship (CVU 419210). E.A. acknowledges Austrian Agency for International Cooperation in Education and Research (OeAD-GmbH) for the Ph.D. scholarship. C.J.S. and C.J.D. acknowledge the Australian Research Council (DP170103531 and DP200102411).

References

- [1] K. Pal, in: *Hybrid Nanocomposites: Fundamentals, Synthesis, and Applications*, first ed., Jenny Stanford Publishing, New York, 2019, <https://doi.org/10.1201/9780429000966>.
- [2] E. Gillies, J. Frechet, Dendrimers and dendritic polymers in drug delivery, *Drug Discovery Today* 10 (1) (2005) 35–43, [https://doi.org/10.1016/S1359-6446\(04\)03276-3](https://doi.org/10.1016/S1359-6446(04)03276-3).
- [3] C.J.H. Porter, N.L. Trevaskis, W.N. Charman, Lipids and lipid-based formulations: optimizing the oral delivery of lipophilic drugs, *Nat. Rev. Drug Discovery* 6 (3) (2007) 231–248, <https://doi.org/10.1038/nrd2197>.
- [4] S. Senapati, A.K. Mahanta, S. Kumar, P. Maiti, Controlled drug delivery vehicles for cancer treatment and their performance, *Sig. Transduct. Target Ther.* 3 (2018) 1–19, <https://doi.org/10.1038/s41392-017-0004-3>.
- [5] C. Doonan, R. Riccò, K. Liang, D. Bradshaw, P. Falcaro, Metal-organic frameworks at the biointerface: synthetic strategies and applications, *Acc. Chem. Res.* 50 (6) (2017) 1423–1432, <https://doi.org/10.1021/acs.accounts.7b00090>.
- [6] R. Riccò, W. Liang, S. Li, J.J. Gassensmith, F. Caruso, C. Doonan, P. Falcaro, Metal-organic frameworks for cell and virus biology: a perspective, *ACS Nano* 12 (1) (2018) 13–23, <https://doi.org/10.1021/acsnano.7b08056>.
- [7] S. Kitagawa, R. Kitaura, S.-I. Noro, Functional porous coordination polymers, *Angew. Chem. Int. Ed.* 43 (18) (2004) 2334–2375, <https://doi.org/10.1002/anie.200300610>.
- [8] O.M. Yaghi, M. O'Keeffe, N.W. Ockwig, H.K. Chae, M. Eddaoudi, J. Kim, Reticular synthesis and the design of new materials, *Nature* 423 (6941) (2003) 705–714, <https://doi.org/10.1038/nature01650>.
- [9] H. Furukawa, K.E. Cordova, M. O'Keeffe, O.M. Yaghi, The chemistry and applications of metal-organic frameworks, *Science* 341 (6149) (2013) 1230444, <https://doi.org/10.1126/science.1230444>.
- [10] Z. Wang, S.M. Cohen, Postsynthetic modification of metal-organic frameworks, *Chem. Soc. Rev.* 38 (5) (2009) 1315, <https://doi.org/10.1039/b802258p>.
- [11] P. Horcajada, R. Gref, T. Baati, P.K. Allan, G. Maurin, P. Couvreur, G. Férey, R.E. Morris, C. Serre, Metal-organic frameworks in biomedicine, *Chem. Rev.* 112 (2) (2012) 1232–1268, <https://doi.org/10.1021/cr200256v>.
- [12] P. Horcajada, T. Chalati, C. Serre, B. Gillet, C. Sebrie, T. Baati, J.F. Eubank, D. Heurtaux, P. Clayette, C. Kreuz, J.-S. Chang, Y.K. Hwang, V. Marsaud, P.-N. Bories, L. Cynober, S. Gil, G. Férey, P. Couvreur, R. Gref, Porous metal-organic framework nanoscale carriers as a potential platform for drug delivery and imaging, *Nature Mater.* 9 (2010) 172–178, <https://doi.org/10.1038/nmat2608>.
- [13] S. Rojas, A. Arenas-Vivo, P. Horcajada, Metal-organic frameworks: a novel platform for combined advanced therapies, *Coord. Chem. Rev.* 388 (2019) 202–226, <https://doi.org/10.1016/j.ccr.2019.02.032>.
- [14] J. Huo, J. Aguilera-Sigalat, S. El-Hankari, D. Bradshaw, Magnetic MOF microreactors for recyclable size-selective biocatalysis, *Chem. Sci.* 6 (3) (2015) 1938–1943, <https://doi.org/10.1039/C4SC03367A>.
- [15] W. Cai, J. Wang, C. Chu, W. Chen, C. Wu, G. Liu, Metal-organic framework-based stimuli-responsive systems for drug delivery, *Adv. Sci.* 6 (1) (2019) 1801526, <https://doi.org/10.1002/advs.201801526>.
- [16] R.P. Welch, H. Lee, M.A. Luzuriaga, O.R. Brohlin, J.J. Gassensmith, Protein-polymer delivery: chemistry from the cold chain to the clinic, *Bioconjug. Chem.* 29 (9) (2018) 2867–2883, <https://doi.org/10.1021/acs.bioconjchem.8b00483>.
- [17] S.E. Miller, M.H. Teplensky, P.Z. Moghadam, D. Fairen-Jimenez, Metal-organic frameworks as biosensors for luminescence-based detection and imaging, *Interface Focus* 6 (4) (2016) 20160027, <https://doi.org/10.1098/rsfs.2016.0027>.
- [18] M. Bilal, M. Adeel, T. Rasheed, H.M.N. Iqbal, Multifunctional metal-organic frameworks-based biocatalytic platforms: recent developments and future prospects, *J. Mater. Res. Technol.* 8 (2) (2019) 2359–2371, <https://doi.org/10.1016/j.jmrt.2018.12.001>.
- [19] H.-S. Wang, Metal-organic frameworks for biosensing and bioimaging applications, *Coord. Chem. Rev.* 349 (2017) 139–155, <https://doi.org/10.1016/j.ccr.2017.08.015>.
- [20] S. Carrasco, Metal-organic frameworks for the development of biosensors: a current overview, *Biosensors* 8 (2018) 92, <https://doi.org/10.3390/bios8040092>.
- [21] C.-S. Liu, J. Li, H. Pang, Metal-organic framework-based materials as an emerging platform for advanced electrochemical sensing, *Coord. Chem. Rev.* 410 (2020) 213222, <https://doi.org/10.1016/j.ccr.2020.213222>.
- [22] P. Li, Q. Chen, T.C. Wang, N.A. Vermeulen, B.L. Mehdi, A. Dohnalkova, N.D. Browning, D. Shen, R. Anderson, D.A. Gómez-Gualdrón, F.M. Cetin, J. Jagiello, A.M. Asiri, J.F. Stoddart, O.K. Farha, Hierarchically engineered mesoporous metal-organic frameworks toward cell-free immobilized enzyme systems, *Chem* 4 (5) (2018) 1022–1034, <https://doi.org/10.1016/j.chempr.2018.03.001>.
- [23] M.H. Teplensky, M. Fantham, C. Poudel, C. Hockings, M. Lu, A. Guna, M. Aragones-Anglada, P.Z. Moghadam, P. Li, O.K. Farha, S. Bernaldo de Quirós Fernández, F.M. Richards, D.I. Jodrell, G. Kaminski Schierle, C.F. Kaminski, D. Fairen-Jimenez, A highly porous metal-organic framework system to deliver payloads for gene knockdown, *Chem* 5 (11) (2019) 2926–2941, <https://doi.org/10.1016/j.chempr.2019.08.015>.
- [24] Y. Chen, P. Li, J.A. Modica, R.J. Drout, O.K. Farha, Acid-resistant mesoporous metal-organic framework toward oral insulin delivery: protein encapsulation, protection, and release, *J. Am. Chem. Soc.* 140 (17) (2018) 5678–5681, <https://doi.org/10.1021/jacs.8b02089>.
- [25] W. Wang, S. Wu, J. Wang, Z. Li, H. Cui, S. Lin, J. Zhu, Q. Chen, Superoxide dismutase transcellular shuttle constructed from dendritic MOF and charge reversible protein derivatives, *Chem. Sci.* 10 (16) (2019) 4476–4485, <https://doi.org/10.1039/C8SC04160A>.
- [26] F. Lyu, Y. Zhang, R.N. Zare, J. Ge, Z. Liu, One-pot synthesis of protein-embedded metal-organic frameworks with enhanced biological activities, *Nano Lett.* 14 (10) (2014) 5761–5765, <https://doi.org/10.1021/nl5026419>.
- [27] K. Liang, R. Ricco, C.M. Doherty, M.J. Styles, S. Bell, N. Kirby, S. Mudie, D. Haylock, A.J. Hill, C.J. Doonan, P. Falcaro, Biomimetic mineralization of metal-organic frameworks as protective coatings for biomacromolecules, *Nat. Commun.* 6 (1) (2015), <https://doi.org/10.1038/ncomms8240>.
- [28] F.-K. Shieh, S.-C. Wang, C.-I. Yen, C.-C. Wu, S. Dutta, L.-Y. Chou, J.V. Morabito, P. Hu, M.-H. Hsu, K.-W. Wu, C.-K. Tsung, Imparting functionality to biocatalysts via embedding enzymes into nanoporous materials by a *de Novo* Approach: size-selective sheltering of catalase in metal-organic framework microcrystals, *J. Am. Chem. Soc.* 137 (13) (2015) 4276–4279, <https://doi.org/10.1021/ja513058h>.
- [29] H. An, M. Li, J. Gao, Z. Zhang, S. Ma, Y. Chen, Incorporation of biomolecules in Metal-Organic Frameworks for advanced applications, *Coord. Chem. Rev.* 384 (2019) 90–106, <https://doi.org/10.1016/j.ccr.2019.01.001>.
- [30] R. Ameloot, F. Vermoortele, W. Vanhove, M.B.J. Roeffaers, B.F. Sels, D.E. De Vos, Interfacial synthesis of hollow metal-organic framework capsules demonstrating selective permeability, *Nature Chem* 3 (5) (2011) 382–387, <https://doi.org/10.1038/nchem.1026>.
- [31] L. Lupica-Spannolò, D.J. Ward, J.-J. Marie, S. Lympelopoulou, D. Bradshaw, Pollen-like ZIF-8 colloidosomes via emulsion templating and etching, *Chem. Commun.* 54 (61) (2018) 8506–8509, <https://doi.org/10.1039/C8CC03511C>.
- [32] G.-Y. Jeong, R. Ricco, K. Liang, J. Ludwig, J.-O. Kim, P. Falcaro, D.-P. Kim, Bioactive MIL-88A framework hollow spheres via interfacial reaction in-droplet microfluidics for enzyme and nanoparticle encapsulation, *Chem. Mater.* 27 (23) (2015) 7903–7909, <https://doi.org/10.1021/acs.chemmater.5b02847>.
- [33] E. Yamamoto, S. Miyazaki, C. Aoyama, M. Kato, A simple and rapid measurement method of encapsulation efficiency of doxorubicin loaded liposomes by direct injection of the liposomal suspension to liquid chromatography, *Int. J. Pharm.* 536 (1) (2018) 21–28, <https://doi.org/10.1016/j.ijpharm.2017.11.035>.
- [34] T. Feczko, J. Tóth, G.y. Dósa, J. Gyenis, Optimization of protein encapsulation in PLGA nanoparticles, *Chem. Eng. Process. Process Intensif.* 50 (8) (2011) 757–765, <https://doi.org/10.1016/j.ccep.2011.06.008>.
- [35] E.P. Holowka, S.K. Bhatia (Eds.), *Drug Delivery*, Springer New York, New York, NY, 2014, <https://doi.org/10.1007/978-1-4939-1998-7>.
- [36] K. Kita, C. Dittich, Drug delivery vehicles with improved encapsulation efficiency: taking advantage of specific drug-carrier interactions, *Expert Opin. Drug Delivery* 8 (3) (2011) 329–342, <https://doi.org/10.1517/17425247.2011.553216>.
- [37] E. Piacentini, in: *Encyclopedia of Membranes*, Springer Berlin Heidelberg, Berlin, Heidelberg, 2016, pp. 706–707, https://doi.org/10.1007/978-3-662-44324-8_1945.
- [38] S.J. Wallace, J. Li, R.L. Nation, B.J. Boyd, Drug release from nanomedicines: selection of appropriate encapsulation and release methodology, *Drug Delivery Transl. Res.* 2 (4) (2012) 284–292, <https://doi.org/10.1007/s13346-012-0064-4>.
- [39] Z. Peng, S. Li, X.u. Han, A.O. Al-Youbi, A.S. Bashammakh, M.S. El-Shahawi, R.M. Leblanc, Determination of the composition, encapsulation efficiency and loading capacity in protein drug delivery systems using circular dichroism spectroscopy, *Anal. Chim. Acta* 937 (2016) 113–118, <https://doi.org/10.1016/j.jca.2016.08.014>.
- [40] K.S. Chu, A.N. Schorzman, M.C. Finnis, C.J. Bowerman, L. Peng, J.C. Luft, A.J. Madden, A.Z. Wang, W.C. Zamboni, J.M. DeSimone, Nanoparticle drug loading as a design parameter to improve docetaxel pharmacokinetics and efficacy, *Biomaterials* 34 (33) (2013) 8424–8429, <https://doi.org/10.1016/j.biomaterials.2013.07.038>.

- [41] F. Betsou, R. Barnes, T. Burke, D. Coppola, Y. DeSouza, J. Eliason, B. Glazer, D. Horsfall, C. Kleeberger, S. Lehmann, A. Prasad, A. Skubitz, S. Somiari, E. Gunter, Human biospecimen research: experimental protocol and quality control tools, *Cancer Epidemiol. Biomarkers Prevention* 18 (2009) 1017–1025, <https://doi.org/10.1158/1055-9965.EPI-08-1231>.
- [42] D. Kristensen, D. Chen, R. Cummings, Vaccine stabilization: research, commercialization, and potential impact, *Vaccine* 29 (41) (2011) 7122–7124, <https://doi.org/10.1016/j.vaccine.2011.05.070>.
- [43] D. Stigter, D.O. Alonso, K.A. Dill, Protein stability: electrostatics and compact denatured states, *Proc. Natl. Acad. Sci.* 88 (10) (1991) 4176–4180, <https://doi.org/10.1073/pnas.88.10.4176>.
- [44] C. Wang, H. Sun, J. Luan, Q. Jiang, S. Tadeipalli, J.J. Morrissey, E.D. Kharasch, S. Singamaneni, Metal-organic framework encapsulation for biospecimen preservation, *Chem. Mater.* 30 (4) (2018) 1291–1300, <https://doi.org/10.1021/acs.chemmater.7b04713>.
- [45] Y. Feng, H. Wang, S. Zhang, Y.u. Zhao, J. Gao, Y. Zheng, P. Zhao, Z. Zhang, M.J. Zaworotko, P. Cheng, S. Ma, Y. Chen, Antibodies@MOFs: an in vitro protective coating for preparation and storage of biopharmaceuticals, *Adv. Mater.* 31 (2) (2019) 1805148, <https://doi.org/10.1002/adma.201805148>.
- [46] O. Hasturk, D.L. Kaplan, Cell armor for protection against environmental stress: Advances, challenges and applications in micro- and nanoencapsulation of mammalian cells, *Acta Biomater.* 95 (2019) 3–31, <https://doi.org/10.1016/j.actbio.2018.11.040>.
- [47] M.A. Luzuriaga, R.P. Welch, M. Dharmarwardana, C.E. Benjamin, S. Li, A. Shahriarkevisshahi, S. Popal, L.H. Tuong, C.T. Creswell, J.J. Gassensmith, Enhanced stability and controlled delivery of mof-encapsulated vaccines and their immunogenic response in vivo, *ACS Appl. Mater. Interfaces* 11 (10) (2019) 9740–9746, <https://doi.org/10.1021/acsami.8b20504>.
- [48] S. Dutta, J. Kim, P.-H. Hsieh, Y.-S. Hsu, Y.V. Kaneti, F.-K. Shieh, Y. Yamauchi, K.-W. Wu, Nanoarchitectonics of biofunctionalized metal-organic frameworks with biological macromolecules and living cells, *Small Methods* 3 (11) (2019) 1900213, <https://doi.org/10.1002/smt.201900213>.
- [49] W. Liang, H. Xu, F. Carraro, N.K. Maddigan, Q. Li, S.G. Bell, D.M. Huang, A. Tarzia, M.B. Solomon, H. Amenitsch, L. Vaccari, C.J. Sumbly, P. Falcaro, C.J. Doonan, Enhanced activity of enzymes encapsulated in hydrophilic metal-organic frameworks, *J. Am. Chem. Soc.* 141 (6) (2019) 2348–2355, <https://doi.org/10.1021/jacs.8b10302>.
- [50] M. Nordberg, J. Duffus, D.M. Templeton, Glossary of terms used in toxicokinetics (IUPAC Recommendations 2003), *Pure Appl. Chem.* 76 (2004) 1033–1082, <https://doi.org/10.1351/pac200476051033>.
- [51] A.K. Singh, *Engineered Nanoparticles: Structure, Properties and Mechanisms of Toxicity*, Elsevier/AP Academic Press is an imprint of Elsevier, Amsterdam; Boston, 2016.
- [52] B. Silva Lima, M.A. Videira, Toxicology and biodistribution: the clinical value of animal biodistribution studies, *Mol. Ther. Methods Clin. Dev.* 8 (2018) 183–197, <https://doi.org/10.1016/j.omtm.2018.01.003>.
- [53] B.A. Lakshmi, S. Kim, Current and emerging applications of nanostructured metal-organic frameworks in cancer-targeted theranostics, *Mater. Sci. Eng., C* 105 (2019) 110091, <https://doi.org/10.1016/j.msec.2019.110091>.
- [54] R. Ghosh, M.A. Bhuiyan, I. Dewan, D.R. Ghosh, A. Islam, Immediate release drug delivery system (Tablets): an overview, *Int. Res. J. Pharm. Appl. Sci.* 2 (2012) 88–94.
- [55] B. Leader, Q.J. Baca, D.E. Golan, Protein therapeutics: a summary and pharmacological classification, *Nat. Rev. Drug Discovery* 7 (1) (2008) 21–39, <https://doi.org/10.1038/nrd2399>.
- [56] T. Vermonden, R. Censi, W.E. Hennink, Hydrogels for protein delivery, *Chem. Rev.* 112 (5) (2012) 2853–2888, <https://doi.org/10.1021/cr200157d>.
- [57] A. Szlachcic, M. Zakrzewska, J. Otlewski, Longer action means better drug: tuning up protein therapeutics, *Biotechnol. Adv.* 29 (4) (2011) 436–441, <https://doi.org/10.1016/j.biotechadv.2011.03.005>.
- [58] A.C. Anselmo, S. Mitragotri, An overview of clinical and commercial impact of drug delivery systems, *J. Control. Release* 190 (2014) 15–28, <https://doi.org/10.1016/j.jconrel.2014.03.053>.
- [59] Y. Pathak, D. Thassu (Eds.), *Drug Delivery Nanoparticles Formulation and Characterization*, first ed., CRC Press, Boca Raton, Florida, 2016, <https://doi.org/10.3109/9781420078053>.
- [60] R.A. Thakur, C.A. Florek, J. Kohn, B.B. Michniak, Electrospun nanofibrous polymeric scaffold with targeted drug release profiles for potential application as wound dressing, *Int. J. Pharm.* 364 (1) (2008) 87–93, <https://doi.org/10.1016/j.ijpharm.2008.07.033>.
- [61] T. Yamada, H. Onishi, Y. Machida, Sustained release ketoprofen microparticles with ethylcellulose and carboxymethylcellulose, *J. Control. Release* 75 (3) (2001) 271–282, [https://doi.org/10.1016/S0168-3659\(01\)00399-6](https://doi.org/10.1016/S0168-3659(01)00399-6).
- [62] Y. Zhou, S. Luo, B. Niu, B. Wu, J. Fu, Y. Zhao, V. Singh, C. Lu, G. Quan, X. Pan, J. Zhang, C. Wu, Ultramild one-step encapsulating method as a modular strategy for protecting humidity-susceptible metal-organic frameworks achieving tunable drug release profiles, *ACS Biomater. Sci. Eng.* 5 (10) (2019) 5180–5188, <https://doi.org/10.1021/acsbiomaterials.9b01233>.
- [63] S. Freiberg, X.X. Zhu, Polymer microspheres for controlled drug release, *Int. J. Pharm.* 282 (1–2) (2004) 1–18, <https://doi.org/10.1016/j.ijpharm.2004.04.013>.
- [64] A. Khan, K. Waqar, A. Shafique, R. Irfan, A. Gul, In vitro and in vivo animal models, in: *Omics Technologies and Bio-Engineering*, Elsevier, 2018, pp. 431–448, <https://doi.org/10.1016/B978-0-12-804659-3.00018-X>.
- [65] S. Mura, J. Nicolas, P. Couvreur, Stimuli-responsive nanocarriers for drug delivery, *Nature Mater* 12 (11) (2013) 991–1003, <https://doi.org/10.1038/nmat3776>.
- [66] J. Zhuang, C.-H. Kuo, L.-Y. Chou, D.-Y. Liu, E. Weerapana, C.-K. Tsung, Optimized metal-organic-framework nanospheres for drug delivery: evaluation of small-molecule encapsulation, *ACS Nano* 8 (3) (2014) 2812–2819, <https://doi.org/10.1021/nn406590q>.
- [67] M. de J. Velásquez-Hernández, R. Ricco, F. Carraro, F.T. Limpoco, M. Linares-Moreau, E. Leitner, H. Wiltsche, J. Rattenberger, H. Schröttner, P. Frühwirt, E. M. Stadler, G. Gescheidt, H. Amenitsch, C.J. Doonan, P. Falcaro, Degradation of ZIF-8 in phosphate buffered saline media, *CrystEngComm* 21 (31) (2019) 4538–4544, <https://doi.org/10.1039/C9CE00757A>.
- [68] J. An, S.J. Geib, N.L. Rosi, Cation-triggered drug release from a porous zinc-adeninate metal-organic framework, *J. Am. Chem. Soc.* 131 (24) (2009) 8376–8377, <https://doi.org/10.1021/ja902972w>.
- [69] Q. Hu, J. Yu, M. Liu, A. Liu, Z. Dou, Y. Yang, A low cytotoxic cationic metal-organic framework carrier for controllable drug release, *J. Med. Chem.* 57 (13) (2014) 5679–5685, <https://doi.org/10.1021/jm5004107>.
- [70] C.C. Epley, K.L. Roth, S. Lin, S.R. Ahrenholtz, T.Z. Grove, A.J. Morris, Cargo delivery on demand from photodegradable MOF nano-cages, *Dalton Trans.* 46 (15) (2017) 4917–4922, <https://doi.org/10.1039/C6DT04787D>.
- [71] Y.-D. Zhu, S.-P. Chen, H. Zhao, Y. Yang, X.-Q. Chen, J. Sun, H.-S. Fan, X.-D. Zhang, PPy@MIL-100 nanoparticles as a pH- and near-IR-irradiation-responsive drug carrier for simultaneous photothermal therapy and chemotherapy of cancer cells, *ACS Appl. Mater. Interfaces* 8 (50) (2016) 34209–34217, <https://doi.org/10.1021/acsami.6b11378>.
- [72] M. Lismont, L. Dreesen, S. Wuttke, Metal-organic framework nanoparticles in photodynamic therapy: current status and perspectives, *Adv. Funct. Mater.* 27 (14) (2017) 1606314, <https://doi.org/10.1002/adfm.201606314>.
- [73] S.L. Anderson, P.G. Boyd, A. Gładysiak, T.N. Nguyen, R.C. Palgrave, D. Kubicki, L. Emsley, D. Bradshaw, M.J. Rosseinsky, B. Smit, K.C. Stylianou, Nucleobase pairing and photodimerization in a biologically derived metal-organic framework nanoreactor, *Nat. Commun.* 10 (1) (2019), <https://doi.org/10.1038/s41467-019-09486-2>.
- [74] P. Horcajada, C. Serre, A.C. McKinlay, R.E. Morris, Biomedical applications of metal-organic frameworks, in: D. Furrusseng (Ed.), *Metal-Organic Frameworks*, Wiley-VCH Verlag GmbH & Co. KGaA, Weinheim, Germany, 2011, pp. 213–250, <https://doi.org/10.1002/9783527635856.ch10>.
- [75] T. Simon-Yarza, A. Mielcarek, P. Couvreur, C. Serre, Nanoparticles of metal-organic frameworks: on the road to in vivo efficacy in biomedicine, *Adv. Mater.* 30 (37) (2018) 1707365, <https://doi.org/10.1002/adma.201707365>.
- [76] D.S. Kohane, Microparticles and nanoparticles for drug delivery, *Biotechnol. Bioeng.* 96 (2) (2007) 203–209, <https://doi.org/10.1002/bit.21301>.
- [77] R.A. Petros, J.M. DeSimone, Strategies in the design of nanoparticles for therapeutic applications, *Nat. Rev. Drug Discovery* 9 (8) (2010) 615–627, <https://doi.org/10.1038/nrd2591>.
- [78] J. Rejman, V. Oberle, I.S. Zuhorn, D. Hoekstra, Size-dependent internalization of particles via the pathways of clathrin- and caveolae-mediated endocytosis, *Biochem. J.* 377 (1) (2004) 159–169, <https://doi.org/10.1042/bj20031253>.
- [79] H. Hillaireau, P. Couvreur, Nanocarriers' entry into the cell: relevance to drug delivery, *Cell. Mol. Life Sci.* 66 (17) (2009) 2873–2896, <https://doi.org/10.1007/s00018-009-0053-z>.
- [80] W. Yu, R. Liu, Y. Zhou, H. Gao, Size-tunable strategies for a tumor targeted drug delivery system, *ACS Cent. Sci.* 6 (2) (2020) 100–116, <https://doi.org/10.1021/acscentsci.9b01139>.
- [81] G. Kong, R.D. Braun, M.W. Dewhirst, Hyperthermia enables tumor-specific nanoparticle delivery: effect of particle size, *Cancer Res.* 60 (2000) 4440–4445.
- [82] S.A. Kulkarni, S.-S. Feng, Effects of particle size and surface modification on cellular uptake and biodistribution of polymeric nanoparticles for drug delivery, *Pharm. Res.* 30 (10) (2013) 2512–2522, <https://doi.org/10.1007/s11095-012-0958-3>.
- [83] M. Gaumet, A. Vargas, R. Gurny, F. Delie, Nanoparticles for drug delivery: the need for precision in reporting particle size parameters, *Eur. J. Pharm. Biopharm.* 69 (1) (2008) 1–9, <https://doi.org/10.1016/j.ejpb.2007.08.001>.
- [84] S. Mitragotri, J. Lahann, Physical approaches to biomaterial design, *Nature Mater.* 8 (1) (2009) 15–23, <https://doi.org/10.1038/nmat2344>.
- [85] J. Della Rocca, D. Liu, W. Lin, Nanoscale metal-organic frameworks for biomedical imaging and drug delivery, *Acc. Chem. Res.* 44 (10) (2011) 957–968, <https://doi.org/10.1021/ar200028a>.
- [86] T.W. Prow, J.E. Grice, L.L. Lin, R. Faye, M. Butler, W. Becker, E.M.T. Wurm, C. Yoong, T.A. Robertson, H.P. Soyer, M.S. Roberts, Nanoparticles and microparticles for skin drug delivery, *Adv. Drug Delivery Rev.* 63 (6) (2011) 470–491, <https://doi.org/10.1016/j.addr.2011.01.012>.
- [87] X.-X. Yang, P. Feng, J. Cao, W. Liu, Y. Tang, Composition-engineered metal-organic framework-based microneedles for glucose-mediated transdermal insulin delivery, *ACS Appl. Mater. Interfaces* 12 (12) (2020) 13613–13621, <https://doi.org/10.1021/acsami.9b20774>.
- [88] N. Mody, R. Sharma, S. Dubey, S.P. Vyas, in: *Micro and Nanotechnology in Vaccine Development*, Elsevier, 2017, pp. 259–278, <https://doi.org/10.1016/B978-0-323-39981-4.00014-2>.
- [89] F. Carraro, M. de J. Velásquez-Hernández, E. Astria, W. Liang, L. Twright, C. Parise, M. Ge, Z. Huang, R. Ricco, X. Zou, L. Villanova, C.O. Kappe, C. Doonan, P. Falcaro, Phase dependent encapsulation and release profile of ZIF-based

- biocomposites, *Chem. Sci.* 11 (13) (2020) 3397–3404, <https://doi.org/10.1039/C9SC05433B>.
- [90] X. Li, L. Lachmanski, S. Safi, S. Sene, C. Serre, J.M. Grenèche, J. Zhang, R. Gref, New insights into the degradation mechanism of metal-organic frameworks drug carriers, *Sci. Rep.* 7 (1) (2017), <https://doi.org/10.1038/s41598-017-13323-1>.
- [91] C.R. Marshall, S.A. Staudhammer, C.K. Brozek, Size control over metal-organic framework porous nanocrystals, *Chem. Sci.* 10 (41) (2019) 9396–9408, <https://doi.org/10.1039/C9SC03802G>.
- [92] M. Rubio-Martinez, C. Avci-Camur, A.W. Thornton, I. Imaz, D. Maspoch, M.R. Hill, New synthetic routes towards MOF production at scale, *Chem. Soc. Rev.* 46 (11) (2017) 3453–3480, <https://doi.org/10.1039/C7CS00109F>.
- [93] X. Feng, Y. Wang, F. Muhammad, F. Sun, Y. Tian, G. Zhu, Size, shape, and porosity control of medi-MOF-1 via growth modulation under microwave heating, *Cryst. Growth Des.* 19 (2) (2019) 889–895, <https://doi.org/10.1021/acs.cgd.8b01442>.
- [94] S. Bao, X. Cai, Y. Shi, M. Pang, Effect of modulators on size and shape-controlled growth of highly uniform In-NDC-MOF particles, *CrystEngComm* 19 (14) (2017) 1875–1878, <https://doi.org/10.1039/C7CE00308K>.
- [95] T.E. Webber, S.P. Desai, R.L. Combs, S. Bingham, C.C. Lu, R.L. Penn, Size control of the MOF NU-1000 through manipulation of the modulator/linker competition, *Cryst. Growth Des.* 20 (5) (2020) 2965–2972.
- [96] Q. Yu, Y. Tian, M. Li, Y. Jiang, H. Sun, G. Zhang, Z. Gao, W. Zhang, J. Hao, M. Hu, J. Cui, Poly(ethylene glycol)-mediated mineralization of metal-organic frameworks, *Chem. Commun.* 56 (75) (2020) 11078–11081, <https://doi.org/10.1039/D0CC03734F>.
- [97] F. Carraro, J.D. Williams, M. Linares-Moreau, C. Parise, W. Liang, W. Amenitsch, C. Doonan, C.O. Kappe, P. Falcaro, Continuous-Flow Synthesis of ZIF-8 Biocomposites with Tunable Particle Size, *Angew. Chem. Int. Ed.* 59 (21) (2020) 8123–8127, <https://doi.org/10.1002/anie.202000678>.
- [98] K.K. Jain (Ed.), *Drug Delivery Systems*, Humana, Totowa, NJ, 2008.
- [99] Z. Cheng, A. Al Zaki, J.Z. Hui, V.R. Muzykantov, A. Tsourkas, Multifunctional nanoparticles: cost versus benefit of adding targeting and imaging capabilities, *Science* 338 (6109) (2012) 903–910, <https://doi.org/10.1126/science.1226338>.
- [100] W.-H. Chen, G.-F. Luo, M. Vázquez-González, R. Cazelles, Y.S. Sohn, R. Nechushtai, Y. Mandel, I. Willner, Glucose-responsive metal-organic-framework nanoparticles act as “smart” sense-and-treat carriers, *ACS Nano* 12 (8) (2018) 7538–7545, <https://doi.org/10.1021/acsnano.8b03417>.
- [101] M. Hoop, C.F. Walde, R. Riccò, F. Mushtaq, A. Terzopoulou, X.-Z. Chen, A.J. deMello, C.J. Doonan, P. Falcaro, B.J. Nelson, J. Puigmartí-Luis, S. Pané, Biocompatibility characteristics of the metal organic framework ZIF-8 for therapeutical applications, *Appl. Mater. Today* 11 (2018) 13–21, <https://doi.org/10.1016/j.apmt.2017.12.014>.
- [102] G. Cheng, W. Li, L. Ha, X. Han, S. Hao, Y. Wan, Z. Wang, F. Dong, X. Zou, Y. Mao, S.-Y. Zheng, Self-Assembly of extracellular vesicle-like metal-organic framework nanoparticles for protection and intracellular delivery of biofunctional proteins, *J. Am. Chem. Soc.* 140 (23) (2018) 7282–7291, <https://doi.org/10.1021/jacs.8b03584>.
- [103] M. de J. Velásquez-Hernández, E. Astria, S. Winkler, W. Liang, H. Wiltzsche, A. Poddar, R. Shukla, G. Prestwich, J. Paderi, P. Salcedo-Abraira, H. Amenitsch, P. Horcajada, C.J. Doonan, P. Falcaro, Modulation of metal-azolate frameworks for the tunable release of encapsulated glycosaminoglycans, *Chem. Sci.* (2020), <https://doi.org/10.1039/D0SC01204A>.
- [104] C.-Y. Sun, C. Qin, X.-L. Wang, G.-S. Yang, K.-Z. Shao, Y.-Q. Lan, Z.-M. Su, P. Huang, C.-G. Wang, E.-B. Wang, Zeolitic imidazolate framework-8 as efficient pH-sensitive drug delivery vehicle, *Dalton Trans.* 41 (23) (2012) 6906, <https://doi.org/10.1039/c2dt30357d>.
- [105] F.-M. Zhang, H. Dong, X. Zhang, X.-J. Sun, M. Liu, D.-D. Yang, X. Liu, J.-Z. Wei, Postsynthetic modification of ZIF-90 for potential targeted codelivery of two anticancer drugs, *ACS Appl. Mater. Interfaces* 9 (32) (2017) 27332–27337, <https://doi.org/10.1021/acsmi.7b08451>.
- [106] S. Zhang, Q. Deng, Y. Li, M. Zheng, C. Wan, C. Zheng, H. Tang, F. Huang, J. Shi, Novel amphiphilic polyvinylpyrrolidone functionalized silicone particles as carrier for low-cost lipase immobilization, *R. Soc. Open Sci.* 5 (6) (2018) 172368, <https://doi.org/10.1098/rsos.172368>.
- [107] K.M. Koczkur, S. Mourdikoudis, L. Polavarapu, S.E. Skrabalak, Polyvinylpyrrolidone (PVP) in nanoparticle synthesis, *Dalton Trans.* 44 (41) (2015) 17883–17905, <https://doi.org/10.1039/C5DT02964C>.
- [108] A. Abedini, E. Saion, F. Larki, A. Zakaria, M. Noroozi, N. Soltani, Room temperature radiolytic synthesized Cu@CuAlO₂-Al₂O₃ nanoparticles, *IJMS* 13 (2012) 11941–11953, <https://doi.org/10.3390/ijms130911941>.
- [109] S. Huang, X. Kou, J. Shen, G. Chen, G. Ouyang, “Armor-Plating” enzymes with metal-organic frameworks (MOFs), *Angew. Chem. Int. Ed.* 59 (23) (2020) 8786–8798, <https://doi.org/10.1002/anie.201916474>.
- [110] Y.-R. Lee, M.-S. Jang, H.-Y. Cho, H.-J. Kwon, S. Kim, W.-S. Ahn, ZIF-8: a comparison of synthesis methods, *Chem. Eng. J.* 271 (2015) 276–280, <https://doi.org/10.1016/j.cej.2015.02.094>.
- [111] G. Lu, S. Li, Z. Guo, O.K. Farha, B.G. Hauser, X. Qi, Y. Wang, X. Wang, S. Han, X. Liu, J.S. DuChene, H. Zhang, Q. Zhang, X. Chen, J. Ma, S.C.J. Loo, W.D. Wei, Y. Yang, J.T. Hupp, F. Huo, Imparting functionality to a metal-organic framework material by controlled nanoparticle encapsulation, *Nature Chem* 4 (4) (2012) 310–316, <https://doi.org/10.1038/nchem.1272>.
- [112] F.-S. Liao, W.-S. Lo, Y.-S. Hsu, C.-C. Wu, S.-C. Wang, F.-K. Shieh, J.V. Morabito, L.-Y. Chou, K.C.-W. Wu, C.-K. Tsung, Shielding against unfolding by embedding enzymes in metal-organic frameworks via a *de Novo* approach, *J. Am. Chem. Soc.* 139 (19) (2017) 6530–6533, <https://doi.org/10.1021/jacs.7b01794>.
- [113] K. Liang, C.J. Coghill, S.G. Bell, C. Doonan, P. Falcaro, Enzyme encapsulation in zeolitic imidazolate frameworks: a comparison between controlled coprecipitation and biomimetic mineralisation, *Chem. Commun.* 52 (3) (2016) 473–476, <https://doi.org/10.1039/C5CC07577G>.
- [114] N.K. Maddigan, A. Tarzia, D.M. Huang, C.J. Sumbly, S.G. Bell, P. Falcaro, J. Christian, Doonan, Protein surface functionalisation as a general strategy for facilitating biomimetic mineralisation of ZIF-8, *Chem. Sci.* 9 (2018) 4217–4223, <https://doi.org/10.1039/C8SC00825F>.
- [115] R.D. Palmiter, The elusive function of metalloproteins, *Proc. Natl. Acad. Sci.* 95 (15) (1998) 8428–8430, <https://doi.org/10.1073/pnas.95.15.8428>.
- [116] P. Coyle, J.C. Philcox, L.C. Carey, A.M. Rofe, Metallothionein: the multipurpose protein, *Cell. Mol. Life Sci. (CMLS)* 59 (4) (2002) 627–647, <https://doi.org/10.1007/s00018-002-8454-2>.
- [117] E.A. Peroza, R. Schmucki, P. Güntert, E. Freisinger, O. Zerbe, The β E-domain of wheat Ec-1 metallothionein: a metal-binding domain with a distinctive structure, *J. Mol. Biol.* 387 (1) (2009) 207–218, <https://doi.org/10.1016/j.jmb.2009.01.035>.
- [118] G. Chen, S. Huang, X. Kou, S. Wei, S. Huang, S. Jiang, J. Shen, F. Zhu, G. Ouyang, A convenient and versatile amino-acid-boosted biomimetic strategy for the nondestructive encapsulation of biomacromolecules within metal-organic frameworks, *Angew. Chem. Int. Ed.* 58 (5) (2019) 1463–1467, <https://doi.org/10.1002/anie.201813060>.
- [119] A.F. Ogata, A.M. Rakowski, B.P. Carpenter, D.A. Fishman, J.G. Merham, P.J. Hurst, J.P. Patterson, Direct observation of amorphous precursor phases in the nucleation of protein-metal-organic frameworks, *J. Am. Chem. Soc.* 142 (3) (2020) 1433–1442, <https://doi.org/10.1021/jacs.9b11371>.
- [120] C. Hu, Y. Bai, M. Hou, Y. Wang, L. Wang, X. Cao, C.-W. Chan, H. Sun, W. Li, J. Ge, K. Ren, Defect-induced activity enhancement of enzyme-encapsulated metal-organic frameworks revealed in microfluidic gradient mixing synthesis, *Sci. Adv.* 6 (5) (2020) eaax5785, <https://doi.org/10.1126/sciadv.aax5785>.
- [121] C.-H. Ng, M.S.H. Guan, C. Koh, X. Ouyang, F. Yu, E.-K. Tan, S.P. O'Neill, X. Zhang, J. Chung, K.-L. Lim, AMP kinase activation mitigates dopaminergic dysfunction and mitochondrial abnormalities in drosophila models of Parkinson's disease, *J. Neurosci.* 32 (41) (2012) 14311–14317.
- [122] F. Du, Q. Yu, S. Yan, G. Hu, L.-F. Lue, D.G. Walker, L. Wu, S.F. Yan, K. Tieu, S.S. Yan, PINK1 signalling rescues amyloid pathology and mitochondrial dysfunction in Alzheimer's disease, *Brain* 140 (2017) 3233–3251, <https://doi.org/10.1093/brain/awx258>.
- [123] S. Mitravotri, P.A. Burke, R. Langer, Overcoming the challenges in administering biopharmaceuticals: formulation and delivery strategies, *Nat. Rev. Drug Discovery* 13 (9) (2014) 655–672, <https://doi.org/10.1038/nrd4363>.
- [124] L. Zhang, FX Gu, JM Chan, AZ Wang, RS Langer, OC Farokhzad, Nanoparticles in medicine: therapeutic applications and developments, *Clin. Pharmacol. Ther.* 83 (5) (2008) 761–769, <https://doi.org/10.1038/sj.cpt.6100400>.
- [125] X. Qin, C. Yu, J. Wei, L. Li, C. Zhang, Q. Wu, J. Liu, S.Q. Yao, W. Huang, Rational design of nanocarriers for intracellular protein delivery, *Adv. Mater.* 31 (46) (2019) 1902791, <https://doi.org/10.1002/adma.201902791>.
- [126] Y. Zhang, F. Wang, E. Ju, Z. Liu, Z. Chen, J. Ren, X. Qu, Metal-organic-framework-based vaccine platforms for enhanced systemic immune and memory response, *Adv. Funct. Mater.* 26 (35) (2016) 6454–6461, <https://doi.org/10.1002/adfm.201600650>.
- [127] T.-T. Chen, J.-T. Yi, Y.-Y. Zhao, X. Chu, Biomaterialized metal-organic framework nanoparticles enable intracellular delivery and endo-lysosomal release of native active proteins, *J. Am. Chem. Soc.* 140 (31) (2018) 9912–9920, <https://doi.org/10.1021/jacs.8b04457>.
- [128] S. Shi, X. Chen, L. Zhang, S. Ding, X. Wang, Q. Lei, W. Fang, FA-PEG decorated MOF nanoparticles as a targeted drug delivery system for controlled release of an autophagy inhibitor, *Biomater. Sci.* 6 (10) (2018) 2582–2590, <https://doi.org/10.1039/C8BM00625C>.
- [129] Z. Wang, X. Zhou, J. Li, X. Liu, Z. Chen, G. Shen, T. Guan, N. Ye, X. Wei, N. Huang, L. Yang, Y. Wei, J. Li, Suppression of hepatoma tumor growth by systemic administration of the phytotoxin gelonin driven by the survivin promoter, *Neo* 60 (2013) 469–479, https://doi.org/10.4149/neo_2013_061.
- [130] H. Cheng, J.-Y. Zhu, S.-Y. Li, J.-Y. Zeng, Q. Lei, K.-W. Chen, C. Zhang, X.-Z. Zhang, An O₂ self-sufficient biomimetic nanoplatform for highly specific and efficient photodynamic therapy, *Adv. Funct. Mater.* 26 (43) (2016) 7847–7860, <https://doi.org/10.1002/adfm.201603212>.
- [131] L. Zhang, Z. Wang, Y. Zhang, F. Cao, K. Dong, J. Ren, X. Qu, Erythrocyte membrane cloaked metal-organic framework nanoparticle as biomimetic nanoreactor for starvation-activated colon cancer therapy, *ACS Nano* 12 (10) (2018) 10201–10211, <https://doi.org/10.1021/acsnano.8b05200>.
- [132] S.B. Reddy, S.K. Williamson, Tirapazamine: a novel agent targeting hypoxic tumor cells, *Expert Opin. Invest. Drugs* 18 (1) (2009) 77–87, <https://doi.org/10.1517/13543780802567250>.
- [133] Z. Huang, M. Ge, F. Carraro, C.J. Doonan, P. Falcaro, X. Zou, Can 3D electron diffraction provide accurate atomic structures of metal-organic frameworks?, *Faraday Discuss* (2020), <https://doi.org/10.1039/D0FD00015A>.
- [134] X. Yang, Q. Tang, Y. Jiang, M. Zhang, M. Wang, L. Mao, Nanoscale ATP-responsive zeolitic imidazole framework-90 as a general platform for cytosolic protein delivery and genome editing, *J. Am. Chem. Soc.* 141 (9) (2019) 3782–3786, <https://doi.org/10.1021/jacs.8b11996>.

- [135] L. An, C. Yan, X. Mu, C. Tao, Q. Tian, J. Lin, S. Yang, Paclitaxel-induced ultrasmall gallic acid-Fe@BSA self-assembly with enhanced MRI performance and tumor accumulation for cancer theranostics, *ACS Appl. Mater. Interfaces* 10 (34) (2018) 28483–28493, <https://doi.org/10.1021/acsmi.8b10625>.
- [136] Y. Wang, J. Zhang, C. Zhang, B. Li, J. Wang, X. Zhang, D. Li, S.-K. Sun, Functional-protein-assisted fabrication of Fe-gallic acid coordination polymer nanonetworks for localized photothermal therapy, *ACS Sustainable Chem. Eng.* 7 (1) (2019) 994–1005, <https://doi.org/10.1021/acsschemeng.8b04656>.
- [137] H. Zhao, J. Xu, Y. Li, X. Guan, X. Han, Y. Xu, H. Zhou, R. Peng, J. Wang, Z. Liu, Nanoscale coordination polymer based nanovaccine for tumor immunotherapy, *ACS Nano* 13 (11) (2019) 13127–13135, <https://doi.org/10.1021/acsnano.9b05974>.
- [138] F. Duan, X. Feng, X. Yang, W. Sun, Y. Jin, H. Liu, K. Ge, Z. Li, J. Zhang, A simple and powerful co-delivery system based on pH-responsive metal-organic frameworks for enhanced cancer immunotherapy, *Biomaterials* 122 (2017) 23–33, <https://doi.org/10.1016/j.biomaterials.2017.01.017>.
- [139] Y. Miao, W. Pan, K. Chen, H. Wei, F. Mi, M. Lu, Y. Chang, H. Sung, Engineering a nanoscale Al-MOF-armed antigen carried by a “Trojan Horse”-like platform for oral vaccination to induce potent and long-lasting immunity, *Adv. Funct. Mater.* 29 (43) (2019) 1904828, <https://doi.org/10.1002/adfm.201904828>.
- [140] D.K. Wilkins, S.B. Grimshaw, V. Receveur, C.M. Dobson, J.A. Jones, L.J. Smith, Hydrodynamic Radii of native and denatured proteins measured by pulse field gradient NMR techniques [†], *Biochemistry* 38 (50) (1999) 16424–16431, <https://doi.org/Devarajan2008>.
- [141] P. Devarajan, Neutrophil gelatinase-associated lipocalin (NGAL): a new marker of kidney disease, *Scand. J. Clin. Lab. Invest.* 68 (2008) 89–94, <https://doi.org/10.1080/00365510802150158>.
- [142] N. Scholler, N. Urban, CA125 in ovarian cancer, *Biomarkers Med.* 1 (4) (2007) 513–523, <https://doi.org/10.2217/17520363.1.4.513>.
- [143] C. Wang, G. Sudlow, Z. Wang, S. Cao, Q. Jiang, A. Neiner, J.J. Morrissey, E.D. Kharasch, S. Achilefu, S. Singamaneni, Metal-organic framework encapsulation preserves the bioactivity of protein therapeutics, *Adv. Healthcare Mater.* 7 (22) (2018) 1800950, <https://doi.org/10.1002/adhm.201800950>.
- [144] S. Tadeipalli, J. Yim, S. Cao, Z. Wang, R.R. Naik, S. Singamaneni, Metal-organic framework encapsulation for the preservation and photothermal enhancement of enzyme activity, *Small* 14 (7) (2018) 1702382, <https://doi.org/10.1002/smll.201702382>.
- [145] L. Kang, S. Smith, C. Wang, Metal-organic framework preserves the biorecognition of antibodies on nanoscale surfaces validated by single-molecule force spectroscopy, *ACS Appl. Mater. Interfaces* 12 (2) (2020) 3011–3020, <https://doi.org/10.1021/acsmi.9b19551>.
- [146] D.R. Thévenot, K. Toth, R.A. Durst, G.S. Wilson, Electrochemical biosensors: recommended definitions and classification International UNION of pure and applied chemistry: physical chemistry division, commission I.7 (biophysical chemistry); analytical chemistry division, commission V.5 (electroanalytical chemistry).1, *Biosens. Bioelectron.* 16 (1–2) (2001) 121–131, [https://doi.org/10.1016/S0956-5663\(01\)00115-4](https://doi.org/10.1016/S0956-5663(01)00115-4).
- [147] M. Gutiérrez-Capitán, A. Baldi, C. Fernández-Sánchez, Electrochemical paper-based biosensor devices for rapid detection of biomarkers, *Sensors* 20 (2020) 967, <https://doi.org/10.3390/s20040967>.
- [148] R. Peltomaa, B. Glahn-Martínez, E. Benito-Peña, M. Moreno-Bondi, Optical biosensors for label-free detection of small molecules, *Sensors* 18 (2018) 4126, <https://doi.org/10.3390/s18124126>.
- [149] B. Byrne, E. Stack, N. Gilmartin, R. O’Kennedy, Antibody-Based Sensors: principles, problems and potential for detection of pathogens and associated toxins, *Sensors* 9 (2009) 4407–4445, <https://doi.org/10.3390/s90604407>.
- [150] P. Mehrotra, Biosensors and their applications – a review, *J. Oral Biol. Craniofacial Res.* 6 (2) (2016) 153–159, <https://doi.org/10.1016/j.jobcr.2015.12.00>.
- [151] A.P.F. Turner, Biosensors: sense and sensibility, *Chem. Soc. Rev.* 42 (8) (2013) 3184, <https://doi.org/10.1039/c3cs35528d>.
- [152] C.C. Winterbourn, Biological production, detection, and fate of hydrogen peroxide, *Antioxid. Redox Signal.* 29 (6) (2018) 541–551, <https://doi.org/10.1089/ars.2017.7.7425>.
- [153] D. Dębski, R. Smulik, J. Zielonka, B. Michałowski, M. Jakubowska, K. Dębowska, J. Adamus, A. Marcinek, B. Kalyanaraman, A. Sikora, Mechanism of oxidative conversion of Amplex[®] Red to resorufin: pulse radiolysis and enzymatic studies, *Free Radical Biol. Med.* 95 (2016) 323–332, <https://doi.org/10.1016/j.freeradbiomed.2016.03.027>.
- [154] Y. Yin, C. Gao, Q. Xiao, G. Lin, Z. Lin, Z. Cai, H. Yang, Protein-metal organic framework hybrid composites with intrinsic peroxidase-like activity as a colorimetric biosensing platform, *ACS Appl. Mater. Interfaces* 8 (42) (2016) 29052–29061, <https://doi.org/10.1021/acsmi.6b09893>.
- [155] D.I. Metelitzka, A.V. Litvinchuk, M.I. Savenkova, Peroxidase-catalyzed co-oxidation of halogen-substituted phenols and 4-aminoantipyrine, *J. Mol. Catal.* 67 (3) (1991) 401–411, [https://doi.org/10.1016/0304-5102\(91\)80052-5](https://doi.org/10.1016/0304-5102(91)80052-5).
- [156] C.M. Doherty, E. Knystautas, D. Buso, L. Villanova, K. Konstas, A.J. Hill, M. Takahashi, P. Falcato, Magnetic framework composites for polycyclic aromatic hydrocarbon sequestration, *J. Mater. Chem.* 22 (23) (2012) 11470, <https://doi.org/10.1039/c2jm31798b>.
- [157] Z. Fan, J. Wang, Y. Nie, L. Ren, B. Liu, G. Liu, Metal-organic frameworks/graphene oxide composite: a new enzymatic immobilization carrier for hydrogen peroxide biosensors, *J. Electrochem. Soc.* 163 (3) (2016) B32–B37, <https://doi.org/10.1149/2.0531603jes>.
- [158] J. Khawandanah, Double or hybrid diabetes: a systematic review on disease prevalence, characteristics and risk factors, *Nutr. Diabetes* 9 (1) (2019), <https://doi.org/10.1038/s41387-019-0101-1>.
- [159] X. Wu, J. Ge, C. Yang, M. Hou, Z. Liu, Facile synthesis of multiple enzyme-containing metal-organic frameworks in a biomolecule-friendly environment, *Chem. Commun.* 51 (69) (2015) 13408–13411, <https://doi.org/10.1039/C5CC05136C>.
- [160] D. Harpaz, E. Eltzov, T.S.E. Ng, R.S. Marks, A.I.Y. Tok, Enhanced colorimetric signal for accurate signal detection in paper-based biosensors, *Diagnostics* 10 (2020) 28, <https://doi.org/10.3390/diagnostics10010028>.
- [161] W. Xu, L. Jiao, H. Yan, Y. Wu, L. Chen, W. Gu, D. Du, Y. Lin, C. Zhu, Glucose oxidase-integrated metal-organic framework hybrids as biomimetic cascade nanozymes for ultrasensitive glucose biosensing, *ACS Appl. Mater. Interfaces* 11 (25) (2019) 22096–22101, <https://doi.org/10.1021/acsmi.9b03004>.
- [162] W.-H. Chen, M. Vázquez-González, A. Zoabi, R. Abu-Reziq, I. Willner, Biocatalytic cascades driven by enzymes encapsulated in metal-organic framework nanoparticles, *Nat. Catal.* 1 (9) (2018) 689–695, <https://doi.org/10.1038/s41492-018-0117-2>.
- [163] H. Liu, Y. Du, J. Gao, L. Zhou, Y. He, L. Ma, G. Liu, Z. Huang, Y. Jiang, Compartmentalization of biocatalysts by immobilizing bienzyme in hollow ZIF-8 for colorimetric detection of glucose and phenol, *Ind. Eng. Chem. Res.* 59 (1) (2020) 42–51, <https://doi.org/10.1021/acs.iecr.9b04391>.
- [164] M. Mohammad, A. Razmjou, K. Liang, M. Asadnia, V. Chen, Metal-organic-framework-based enzymatic microfluidic biosensor via surface patterning and biomineralization, *ACS Appl. Mater. Interfaces* 11 (2) (2019) 1807–1820, <https://doi.org/10.1021/acsmi.8b16837>.
- [165] X. Wu, H. Yue, Y. Zhang, X. Gao, X. Li, L. Wang, Y. Cao, M. Hou, H. An, L. Zhang, S. Li, J. Ma, H. Lin, Y. Fu, H. Gu, W. Lou, W. Wei, R.N. Zare, J. Ge, Packaging and delivering enzymes by amorphous metal-organic frameworks, *Nat. Commun.* 10 (1) (2019), <https://doi.org/10.1038/s41467-019-13153-x>.
- [166] Z. Zhao, T. Lin, W. Liu, L. Hou, F. Ye, S. Zhao, Colorimetric detection of blood glucose based on GOx@ZIF-8@Fe-polydopamine cascade reaction, *Spectrochim. Acta Part A: Mol. Biomol. Spectrosc.* 219 (2019) 240–247, <https://doi.org/10.1016/j.saa.2019.04.061>.
- [167] Z. Zhao, Y. Huang, W. Liu, F. Ye, S. Zhao, Immobilized glucose oxidase on boronic acid-functionalized hierarchically porous MOF as an integrated nanozyme for one-step glucose detection, *ACS Sustainable Chem. Eng.* 8 (11) (2020) 4481–4488, <https://doi.org/10.1021/acsschemeng.9b07631>.
- [168] J. Gao, C. Wang, H. Tan, Lanthanide/nucleotide coordination polymers: an excellent host platform for encapsulating enzymes and fluorescent nanoparticles to enhance ratiometric sensing, *J. Mater. Chem. B* 5 (37) (2017) 7692–7700, <https://doi.org/10.1039/C7TB02049J>.
- [169] W. Ma, Q. Jiang, P. Yu, L. Yang, L. Mao, Zeolitic imidazolate framework-based electrochemical biosensor for in vivo electrochemical measurements, *Anal. Chem.* 85 (15) (2013) 7550–7557, <https://doi.org/10.1021/ac401576u>.
- [170] S. Patra, T. Hidalgo Crespo, A. Permyakova, C. Sicard, C. Serre, A. Chaussé, N. Steunou, L. Legrand, Design of metal organic framework-enzyme based bioelectrodes as a novel and highly sensitive biosensing platform, *J. Mater. Chem. B* 3 (46) (2015) 8983–8992, <https://doi.org/10.1039/C5TB01412C>.
- [171] Q. Wang, X. Zhang, L. Huang, Z. Zhang, S. Dong, GOx@ZIF-8(NiPd) Nanoflower: an artificial enzyme system for tandem catalysis, *Angew. Chem.* 129 (50) (2017) 16298–16301, <https://doi.org/10.1002/ange.201710418>.
- [172] A. Jeanson, J.-M. Cloes, M. Bouchet, B. Rentier, Comparison of conjugation procedures for the preparation of monoclonal antibody-enzyme conjugates, *J. Immunol. Methods* 111 (2) (1988) 261–270, [https://doi.org/10.1016/0022-1759\(88\)90135-4](https://doi.org/10.1016/0022-1759(88)90135-4).
- [173] R. Presentini, A new covalent peroxidase conjugation method using bis (sulfosuccinimidyl) suberate as cross-linking reagent in a two-step procedure, *J. Immunoassay Immunochem.* 38 (1) (2017) 100–113, <https://doi.org/10.1080/15321819.2016.1250773>.
- [174] C. Wang, J. Gao, H. Tan, Integrated antibody with catalytic metal-organic framework for colorimetric immunoassay, *ACS Appl. Mater. Interfaces* 10 (30) (2018) 25113–25120, <https://doi.org/10.1021/acsmi.8b07225>.
- [175] L. Xue, Y. Yang, S. Wu, Y. Huang, J. Li, Y. Xiang, G. Li, In situ reduction of porous copper metal-organic frameworks for three-dimensional catalytic click immunoassay, *Anal. Chem.* 92 (4) (2020) 2972–2978, <https://doi.org/10.1021/acs.analchem.9b03677>.
- [176] Y. Wang, L. Chen, Q. Wu, Z. Wen, Y. Ren, M. Wang, An acid-responsive all-in-one signal amplification strategy for the ultrasensitive prostate-specific antigen detection, *New J. Chem.* 43 (40) (2019) 15910–15914, <https://doi.org/10.1039/C9NJ03510A>.
- [177] S. Wu, H. Tan, C. Wang, J. Wang, S. Sheng, A colorimetric immunoassay based on coordination polymer composite for the detection of carcinoembryonic antigen, *ACS Appl. Mater. Interfaces* 11 (46) (2019) 43031–43038, <https://doi.org/10.1021/acsmi.9b18472>.
- [178] R. Ren, G. Cai, Z. Yu, Y. Zeng, D. Tang, Metal-polydopamine framework: an innovative signal-generation tag for colorimetric immunoassay, *Anal. Chem.* 90 (18) (2018) 11099–11105, <https://doi.org/10.1021/acs.analchem.8b03538>.
- [179] C. Liu, J. Dong, S. Ning, J. Hou, G.L.N. Waterhouse, Z. Cheng, S. Ai, An electrochemical immunosensor based on an etched zeolitic imidazolate

- framework for detection of avian leukosis virus subgroup, *J Microchim. Acta* 185 (9) (2018), <https://doi.org/10.1007/s00604-018-2930-3>.
- [180] J. Feng, H. Wang, Z. Ma, Ultrasensitive amperometric immunosensor for the prostate specific antigen by exploiting a Fenton reaction induced by a metal-organic framework nanocomposite of type Au/Fe-MOF with peroxidase mimicking activity, *Microchim. Acta* 187 (1) (2020), <https://doi.org/10.1007/s00604-019-4075-4>.
- [181] T.-Z. Liu, R. Hu, X. Zhang, K.-L. Zhang, Y. Liu, X.-B. Zhang, R.-Y. Bai, D. Li, Y.-H. Yang, Metal-organic framework nanomaterials as novel signal probes for electron transfer mediated ultrasensitive electrochemical immunoassay, *Anal. Chem.* 88 (24) (2016) 12516–12523, <https://doi.org/10.1021/acs.analchem.6b04191>.
- [182] J.R. Edgar, Q&A: what are exosomes, exactly?, *BMC Biol.* 14 (2016) 46, <https://doi.org/10.1186/s12915-016-0268-z>.
- [183] Y. Sun, H. Jin, X. Jiang, R. Gui, Assembly of black phosphorus nanosheets and MOF to form functional hybrid thin-film for precise protein capture, dual-signal and intrinsic self-calibration sensing of specific cancer-derived exosomes, *Anal. Chem.* 92 (3) (2020) 2866–2875, <https://doi.org/10.1021/acs.analchem.9b05583>.
- [184] Y. Zhang, B. Yan, A point-of-care diagnostics logic detector based on glucose oxidase immobilized lanthanide functionalized metal-organic frameworks, *Nanoscale* 11 (47) (2019) 22946–22953, <https://doi.org/10.1039/C9NR06475C>.
- [185] E.-H. Yoo, S.-Y. Lee, Glucose biosensors: an overview of use in clinical practice, *Sensors* 10 (2010) 4558–4576, <https://doi.org/10.3390/s100504558>.
- [186] G. Freckmann, A. Baumstark, N. Jendrike, E. Zschornack, S. Kocher, J. Tshiananga, F. Heister, C. Haug, System accuracy evaluation of 27 blood glucose monitoring systems according to DIN EN ISO 15197, *Diabetes Technol. Ther.* 12 (3) (2010) 221–231, <https://doi.org/10.1089/dia.2009.0128>.
- [187] C. Wang, L. Wang, S. Tadeipalli, J.J. Morrissey, E.D. Kharasch, R.R. Naik, S. Singamaneni, Ultrarobust biochips with metal-organic framework coating for point-of-care diagnosis, *ACS Sens.* 3 (2) (2018) 342–351, <https://doi.org/10.1021/acssensors.7b00762>.
- [188] H. Yan, L. Jiao, H. Wang, W. Xu, Y. Wu, W. Gu, D. Du, Y. Lin, C. Zhu, A “sense-and-treat” ELISA using zeolitic imidazolate framework-8 as carriers for dual-modal detection of carcinoembryonic antigen, *Sens. Actuators, B* 297 (2019) 126760, <https://doi.org/10.1016/j.snb.2019.126760>.
- [189] G. Zhao, Y. Wang, X. Li, X. Dong, H. Wang, B. Du, W. Cao, Q. Wei, Quenching electrochemiluminescence immunosensor based on resonance energy transfer between ruthenium (ii) complex incorporated in the UiO-67 metal-organic framework and gold nanoparticles for insulin detection, *ACS Appl. Mater. Interfaces* 10 (27) (2018) 22932–22938, <https://doi.org/10.1021/acsaami.8b04786>.
- [190] X. Wang, X. Wang, Y. Han, H. Li, Q. Kang, P. Wang, F. Zhou, Immunoassay for cardiac troponin I with fluorescent signal amplification by hydrolyzed coumarin released from a metal-organic framework, *ACS Appl. Nano Mater.* 2 (11) (2019) 7170–7177, <https://doi.org/10.1021/acsaanm.9b01685>.
- [191] S. Mishra, K. Upadhya, K.B. Mishra, A.K. Shukla, R.P. Tripathi, V.K. Tiwari, Carbohydrate-based therapeutics, in: *Studies in Natural Products Chemistry*, Elsevier, 2016, pp. 307–361, <https://doi.org/10.1016/B978-0-444-63601-0.00010-7>.
- [192] M.I. Osborn, P.G. Evans, N. Gemmill, S.D. Osborne, Carbohydrate-based therapeutics, *J. Pharm. Pharmacol.* 56 (2004) 691–702, <https://doi.org/10.1211/0022357023619>.
- [193] S.B. Oppenheimer, M. Alvarez, J. Nnoli, Carbohydrate-based experimental therapeutics for cancer, HIV/AIDS and other diseases, *Acta Histochem.* 110 (1) (2008) 6–13, <https://doi.org/10.1016/j.acthis.2007.08.003>.
- [194] M. von Itzsteine, Novel carbohydrate-based inhibitors that target influenza a virus sialidase, in: M. Shibasaki, M. Iino, H. Osada (Eds.), *Chemiobiomolecular Science*, Springer Japan, Tokyo, 2012, pp. 261–267, https://doi.org/10.1007/978-4-431-54038-0_26.
- [195] V. Pomin, B. Mulloy, Glycosaminoglycans and proteoglycans, *Pharmaceuticals* 11 (2018) 27, <https://doi.org/10.3390/ph11010027>.
- [196] N.S. Gandhi, R.L. Mancera, The structure of glycosaminoglycans and their interactions with proteins, *Chem. Biol. Drug Des.* 72 (2008) 455–482, <https://doi.org/10.1111/j.1747-0285.2008.00741.x>.
- [197] C. Wong (Ed.), *Carbohydrate-Based Drug Discovery*, first ed., Wiley, 2003, <https://doi.org/10.1002/3527602437>.
- [198] U. Aich, M.A. Meledeo, S.-G. Sampathkumar, J. Fu, M.B. Jones, C.A. Weier, S.Y. Chung, B.C. Tang, M. Yang, J. Hanes, K.J. Yarema, Development of delivery methods for carbohydrate-based drugs: controlled release of biologically-active short chain fatty acid-hexosamine analogs, *Glycoconj. J.* 27 (4) (2010) 445–459, <https://doi.org/10.1007/s10719-010-9292-3>.
- [199] J. Hirsh, S.S. Anand, J.L. Halperin, V. Fuster, Guide to anticoagulant therapy: heparin: a statement for healthcare professionals from the american heart association, *Circulation* 103 (24) (2001) 2994–3018, <https://doi.org/10.1161/01.CIR.103.24.2994>.
- [200] H.-Y. Lee, C.-H. Hwang, H.-E. Kim, S.-H. Jeong, Enhancement of bio-stability and mechanical properties of hyaluronic acid hydrogels by tannic acid treatment, *Carbohydr. Polym.* 186 (2018) 290–298, <https://doi.org/10.1016/j.carbpol.2018.01.056>.
- [201] R. Stern, G. Kogan, M.J. Jedrzejak, L. Šoltés, The many ways to cleave hyaluronan, *Biotechnol. Adv.* 25 (6) (2007) 537–557, <https://doi.org/10.1016/j.biotechadv.2007.07.001>.
- [202] S. Jana, S. Maiti, S. Jana (Eds.), *Biopolymer-based Composites: Drug Delivery and Biomedical Applications*, Elsevier, Woodhead Publishing, Duxford Cambridge, Mass, 2017.
- [203] Y. Jiao, N. Ubrich, M. Marchand-Arvier, C. Vigneron, M. Hoffman, T. Lecompte, P. Maincent, In vitro and in vivo evaluation of oral heparin-loaded polymeric nanoparticles in rabbits, *Circulation* 105 (2) (2002) 230–235, <https://doi.org/10.1161/hc0202.101988>.
- [204] A. Abednejad, A. Ghaee, J. Nourmohammadi, A.A. Mehrizi, Hyaluronic acid/carboxylated Zeolitic Imidazolate Framework film with improved mechanical and antibacterial properties, *Carbohydr. Polym.* 222 (2019) 115033, <https://doi.org/10.1016/j.carbpol.2019.115033>.
- [205] V.V. Vinogradov, A.S. Drozdov, L.R. Mingabudinova, E.M. Shabanova, N.O. Kolchina, E.I. Anastasova, A.A. Markova, A.A. Shtil, V.A. Milichko, G.L. Starova, R.L.M. Precker, A.V. Vinogradov, E. Hey-Hawkins, E.A. Pidko, Composites based on heparin and MIL-101(Fe): the drug releasing depot for anticoagulant therapy and advanced medical nanofabrication, *J. Mater. Chem. B* 6 (16) (2018) 2450–2459, <https://doi.org/10.1039/C8TB00072G>.
- [206] E. Astria, M. Thonhofer, R. Ricco, W. Liang, A. Chemelli, A. Tarzia, K. Alt, C.E. Hagemeyer, J. Rattenberger, H. Schroettner, T. Wrodnigg, H. Amenitsch, D.M. Huang, C.J. Doonan, P. Falcaro, Carbohydrates@MOFs, *Mater. Horiz.* 6 (5) (2019) 969–977, <https://doi.org/10.1039/C8MH01611A>.
- [207] K. Liang, R. Wang, M. Bouter, C.M. Doherty, X. Mulet, J.J. Richardson, Biomimetic mineralization of metal-organic frameworks around polysaccharides, *Chem. Commun.* 53 (7) (2017) 1249–1252, <https://doi.org/10.1039/C6CC09680H>.
- [208] S. Li, M. Dharmarwardana, R.P. Welch, C.E. Benjamin, A.M. Shamir, S.O. Nielsen, J.J. Gassensmith, Investigation of controlled growth of metal-organic frameworks on anisotropic virus particles, *ACS Appl. Mater. Interfaces* 10 (21) (2018) 18161–18169, <https://doi.org/10.1021/acsaami.8b01369>.
- [209] K. Makyla-Juzak, A. Chachaj-Brekiesz, P. Dynarowicz-Latka, P. Dąbczyński, J. Zemla, The effect of dextran sulfate—as model glycosaminoglycan analogue—on membrane lipids: DPPC, cholesterol, and DPPC-cholesterol mixture. The monolayer study, *J. Membr. Biol.* 251 (5–6) (2018) 641–651, <https://doi.org/10.1007/s00232-018-0041-z>.
- [210] A. Mahmood, W. Xia, N. Mahmood, Q. Wang, R. Zou, Hierarchical heteroaggregation of binary metal-organic gels with tunable porosity and mixed valence metal sites for removal of dyes in water, *Sci. Rep.* 5 (1) (2015), <https://doi.org/10.1038/srep10556>.
- [211] B. Bueken, N. Van Velthoven, T. Willhammar, T. Stassin, I. Stassen, D.A. Keen, G.V. Baron, J.F.M. Denayer, R. Ameloot, S. Bals, D. De Vos, T.D. Bennett, Gel-based morphological design of zirconium metal-organic frameworks, *Chem. Sci.* 8 (5) (2017) 3939–3948, <https://doi.org/10.1039/C6SC05602D>.
- [212] J. Zhong, R.K. Kankala, S.-B. Wang, A.-Z. Chen, Recent advances in polymeric nanocomposites of metal-organic frameworks (MOFs), *Polymers* 11 (2019) 1627, <https://doi.org/10.3390/polym11101627>.
- [213] S. Wuttke, S. Braig, T. Preiß, A. Zimpel, J. Sicklinger, C. Bellomo, J.O. Rädler, A. M. Vollmar, T. Bein, MOF nanoparticles coated by lipid bilayers and their uptake by cancer cells, *Chem. Commun.* 51 (87) (2015) 15752–15755, <https://doi.org/10.1039/C5CC06767G>.
- [214] I. Christodoulou, C. Serre, R. Gref, Metal-organic frameworks for drug delivery: degradation mechanism and in vivo fate, in: *Metal-Organic Frameworks for Biomedical Applications*, Elsevier, 2020, pp. 467–489, <https://doi.org/10.1016/B978-0-12-816984-1.00023-8>.
- [215] D. Giliopoulos, A. Zamboulis, D. Giannakoudakis, D. Bikiaris, K. Triantafyllidis, Polymer/Metal Organic Framework (MOF) nanocomposites for biomedical applications, *Molecules* 25 (2020) 185, <https://doi.org/10.3390/molecules25010185>.
- [216] W.-L. Liu, C.-Y. Wu, C.-Y. Chen, B. Singco, C.-H. Lin, H.-Y. Huang, Fast multipoint immobilized MOF bioactor, *Chem. Eur. J.* 20 (2014) 8923–8928, <https://doi.org/10.1002/chem.201400270>.
- [217] S. Misra, V.C. Hascall, I. Atanelishvili, R. Moreno Rodriguez, R.R. Markwald, S. Ghatak, Utilization of glycosaminoglycans/proteoglycans as carriers for targeted therapy delivery, *Int. J. Cell Biol.* 2015 (2015) 1–25, <https://doi.org/10.1155/2015/537560>.
- [218] E. Bellido, T. Hidalgo, M.V. Lozano, M. Guillevic, R. Simón-Vázquez, M.J. Santander-Ortega, A. González-Fernández, C. Serre, M.J. Alonso, P. Horcajada, Heparin-engineered mesoporous iron metal-organic framework nanoparticles: toward stealth drug nanocarriers, *Adv. Healthcare Mater.* 4 (8) (2015) 1246–1257, <https://doi.org/10.1002/adhm.201400755>.
- [219] Y. Liang, K.L. Kiick, Heparin-functionalized polymeric biomaterials in tissue engineering and drug delivery applications, *Acta Biomater.* 10 (4) (2014) 1588–1600, <https://doi.org/10.1016/j.actbio.2013.07.031>.
- [220] V.R. Cherkasov, E.N. Mochalova, A.V. Babenyshev, J.M. Rozenberg, I.L. Sokolov, M.P. Nikitin, Antibody-directed metal-organic framework nanoparticles for targeted drug delivery, *Acta Biomater.* 103 (2020) 223–236, <https://doi.org/10.1016/j.actbio.2019.12.012>.
- [221] R. Ricco, L. Malfatti, M. Takahashi, A.J. Hill, P. Falcaro, Applications of magnetic metal-organic framework composites, *J. Mater. Chem. A* 1 (42) (2013) 13033, <https://doi.org/10.1039/c3ta13140h>.
- [222] P. Falcaro, F. Lapierre, B. Marmiroli, M. Styles, Y. Zhu, M. Takahashi, A.J. Hill, C. M. Doherty, Positioning an individual metal-organic framework particle using a magnetic field, *J. Mater. Chem. C* 1 (1) (2013) 42–45, <https://doi.org/10.1039/C2TC00241H>.
- [223] S. Javanbakhht, M. Pooremaeli, H. Hashemi, H. Namazi, Carboxymethylcellulose capsulated Cu-based metal-organic framework-drug nanohybrid as a pH-sensitive nanocomposite for ibuprofen oral

- delivery, *Int. J. Biol. Macromol.* 119 (2018) 588–596, <https://doi.org/10.1016/j.ijbiomac.2018.07.181>.
- [224] J.M. Wickens, H.O. Alsaab, P. Kesharwani, K. Bhise, M.C.I.M. Amin, R.K. Tekade, U. Gupta, A.K. Iyer, Recent advances in hyaluronic acid-decorated nanocarriers for targeted cancer therapy, *Drug Discovery Today* 22 (4) (2017) 665–680, <https://doi.org/10.1016/j.drudis.2016.12.009>.
- [225] C. Chen, S. Zhao, A. Karnad, J.W. Freeman, The biology and role of CD44 in cancer progression: therapeutic implications, *J. Hematol. Oncol.* 11 (1) (2018), <https://doi.org/10.1186/s13045-018-0605-5>.
- [226] K. Kim, S. Lee, E. Jin, L. Palanikumar, J.H. Lee, J.C. Kim, J.S. Nam, B. Jana, T.-H. Kwon, S.K. Kwak, W. Choe, J.-H. Ryu, MOF × biopolymer: collaborative combination of metal–organic framework and biopolymer for advanced anticancer therapy, *ACS Appl. Mater. Interfaces* 11 (31) (2019) 27512–27520, <https://doi.org/10.1021/acsami.9b05736>.
- [227] W. Cai, H. Gao, C. Chu, X. Wang, J. Wang, P. Zhang, G. Lin, W. Li, G. Liu, X. Chen, Engineering phototheranostic nanoscale metal–organic frameworks for multimodal imaging-guided cancer therapy, *ACS Appl. Mater. Interfaces* 9 (3) (2017) 2040–2051, <https://doi.org/10.1021/acsami.6b11579>.
- [228] Z. Cai, F. Xin, Z. Wei, M. Wu, X. Lin, X. Du, G. Chen, D. Zhang, Z. Zhang, X. Liu, C. Yao, Photodynamic therapy combined with antihypoxic signaling and CpG adjuvant as an *In situ* tumor vaccine based on metal–organic framework nanoparticles to boost cancer immunotherapy, *Adv. Healthcare Mater.* 9 (1) (2020) 1900996, <https://doi.org/10.1002/adhm.v9.110.1002/adhm.201900996>.
- [229] X. Fu, Z. Yang, T. Deng, J. Chen, Y. Wen, X. Fu, L. Zhou, Z. Zhu, C. Yu, A natural polysaccharide mediated MOF-based Ce6 delivery system with improved biological properties for photodynamic therapy, *J. Mater. Chem. B* 8 (7) (2020) 1481–1488, <https://doi.org/10.1039/C9TB02482D>.
- [230] F. Shu, D. Lv, X.-L. Song, B. Huang, C. Wang, Y. Yu, S.-C. Zhao, Fabrication of a hyaluronic acid conjugated metal organic framework for targeted drug delivery and magnetic resonance imaging, *RSC Adv.* 8 (12) (2018) 6581–6589, <https://doi.org/10.1039/C7RA12969F>.
- [231] K. Liang, J.J. Richardson, J. Cui, F. Caruso, C.J. Doonan, P. Falcaro, Metal-organic framework coatings as cytoprotective exoskeletons for living cells, *Adv. Mater.* 28 (36) (2016) 7910–7914, <https://doi.org/10.1002/adma.201602335>.
- [232] W. Chen, S. Kong, M. Lu, F. Chen, W. Cai, L. Du, J. Wang, C. Wu, Comparison of different zinc precursors for the construction of zeolitic imidazolate framework-8 artificial shells on living cells, *Soft Matter* 16 (1) (2020) 270–275, <https://doi.org/10.1039/C9SM01907C>.
- [233] S. Misra, V. Sharma, A.K. Srivastava, Bacterial polysaccharides: an overview, in: K.G. Ramawat, J.-M. Mérillon (Eds.), *Polysaccharides*, Springer International Publishing, Cham, 2015, pp. 81–108, https://doi.org/10.1007/978-3-319-16298-0_68.
- [234] W. Vollmer, Peptidoglycan, in: *Molecular Medical Microbiology*, Elsevier, 2015, pp. 105–124, <https://doi.org/10.1016/B978-0-12-397169-2.00006-8>.
- [235] S.M. Tazhibayeva, K.B. Musabekov, A.B. Orazymbetova, A.A. Zhubanova, Surface properties of yeast cell, *Colloid J.* 65 (2003) 122–124, <https://doi.org/10.1023/A:1022391613491>.
- [236] Z. Li, J. Ma, J. Ruan, X. Zhuang, Using positively charged magnetic nanoparticles to capture bacteria at ultralow concentration, *Nanoscale Res. Lett.* 14 (1) (2019), <https://doi.org/10.1186/s11671-019-3005-z>.
- [237] N. Malanovic, K. Lohner, Gram-positive bacterial cell envelopes: The impact on the activity of antimicrobial peptides, *Biochim. Biophys. Acta (BBA) - Biomembranes* 1858 (5) (2016) 936–946, <https://doi.org/10.1016/j.bbame.2015.11.004>.
- [238] J.K. Oh, Y. Yegin, F. Yang, M. Zhang, J. Li, S. Huang, S.V. Verkhoturov, E.A. Schweikert, K. Perez-Lewis, E.A. Scholar, T.M. Taylor, A. Castillo, L. Cisneros-Zevallos, Y. Min, M. Alkbulut, The influence of surface chemistry on the kinetics and thermodynamics of bacterial adhesion, *Sci. Rep.* 8 (1) (2018), <https://doi.org/10.1038/s41598-018-35343-1>.
- [239] J. Paderi, G.D. Prestwich, A. Panitch, T. Boone, K. Stuart, Glycan therapeutics: resurrecting an almost pharma-forgotten drug class, *Adv. Therap.* 1 (8) (2018) 1800082, <https://doi.org/10.1002/adtp.201800082>.
- [240] W. Anderson, Human gene therapy, *Science* 256 (5058) (1992) 808–813, <https://doi.org/10.1126/science.1589762>.
- [241] R. Mulligan, The basic science of gene therapy, *Science* 260 (5110) (1993) 926–932, <https://doi.org/10.1126/science.8493530>.
- [242] J. DeVincenzo, R. Lambkin-Williams, T. Wilkinson, J. Cehelsky, S. Nochur, E. Walsh, R. Meyers, J. Gollub, A. Vaishnav, A randomized, double-blind, placebo-controlled study of an RNAi-based therapy directed against respiratory syncytial virus, *Proc. Natl. Acad. Sci.* 107 (19) (2010) 8800–8805, <https://doi.org/10.1073/pnas.0912186107>.
- [243] S. Subramanya, S.-S. Kim, N. Manjunath, P. Shankar, RNA interference-based therapeutics for human immunodeficiency virus HIV-1 treatment: synthetic siRNA or vector-based shRNA?, *Expert Opin. Biol. Ther.* 10 (2) (2010) 201–213, <https://doi.org/10.1517/14712590903448158>.
- [244] Chen, G. Cheng, R.I. Mahato, RNAi for treating hepatitis B viral infection, *Pharm. Res.* 25 (1) (2008) 72–86, <https://doi.org/10.1007/s11095-007-9504-0>.
- [245] U.A. Ashfaq, M.Z. Yousaf, M. Aslam, R. Ejaz, S. Jahan, O. Ullah, siRNAs: Potential therapeutic agents against Hepatitis C Virus, *Virology* 451 (1) (2011), <https://doi.org/10.1186/1743-422X-8-276>.
- [246] D.V. Morrissey, J.A. Lockridge, L. Shaw, K. Blanchard, K. Jensen, W. Breen, K. Hartsough, L. Machemer, S. Radka, V. Jadhav, N. Vaish, S. Zinnen, C. Vargeese, K. Bowman, C.S. Shaffer, L.B. Jeffs, A. Judge, I. MacLachlan, B. Polisky, Potent and persistent *in vivo* anti-HBV activity of chemically modified siRNAs, *Nat. Biotechnol.* 23 (8) (2005) 1002–1007, <https://doi.org/10.1038/nbt1122>.
- [247] M. DiFiglia, M. Sena-Esteves, K. Chase, E. Sapp, E. Pfister, M. Sassi, J. Yoder, P. Reeves, R.K. Pandey, K.G. Rajeev, M. Manoharan, D.W.Y. Sah, P.D. Zamore, N. Aronin, Therapeutic silencing of mutant huntingtin with siRNA attenuates striatal and cortical neuropathology and behavioral deficits, *Proc. Natl. Acad. Sci.* 104 (43) (2007) 17204–17209, <https://doi.org/10.1073/pnas.0708285104>.
- [248] M.H. Farah, RNAi silencing in mouse models of neurodegenerative diseases, *Curr. Drug Deliv.* 4 (2007) 161–167, <https://doi.org/10.2174/156720107780362276>.
- [249] T. Li, S. Koshy, H.G. Folkesson, RNA interference for CFTR attenuates lung fluid absorption at birth in rats, *Respir. Res.* 9 (1) (2008), <https://doi.org/10.1186/1465-9921-9-55>.
- [250] G. Courties, J. Presumey, I. Duroux-Richard, C. Jorgensen, F. Apparailly, RNA interference-based gene therapy for successful treatment of rheumatoid arthritis, *Expert Opin. Biol. Ther.* 9 (5) (2009) 535–538, <https://doi.org/10.1517/14712590902926089>.
- [251] G. R Devi, siRNA-based approaches in cancer therapy, *Cancer Gene Ther.* 13 (9) (2006) 819–829, <https://doi.org/10.1038/sj.cgt.7700931>.
- [252] M. Abdelrahim, S. Safe, C. Baker, A. Abudayyeh, RNAi and cancer: Implications and applications, *J. RNAi Gene Silencing.* 2 (2006) 136–145.
- [253] A.L. Gartel, E.S. Kandel, RNA interference in cancer, *Biomol. Eng.* 23 (1) (2006) 17–34, <https://doi.org/10.1016/j.bioeng.2006.01.002>.
- [254] L.A. Martinez, I. Naguibneva, H. Lehrmann, A. Vervisch, T. Tchenio, G. Lozano, A. Harel-Bellan, Synthetic small inhibiting RNAs: efficient tools to inactivate oncogenic mutations and restore p53 pathways, *Proc. Natl. Acad. Sci.* 99 (23) (2002) 14849–14854, <https://doi.org/10.1073/pnas.222406899>.
- [255] S. I. Pai, Y.-Y. Lin, B. Macaes, A. Meneshian, C.-F. Hung, T.-C. Wu, Prospects of RNA interference therapy for cancer, *Gene Ther.* 13 (6) (2006) 464–477, <https://doi.org/10.1038/sj.gt.3302694>.
- [256] F. Takeshita, T. Ochiya, Therapeutic potential of RNA interference against cancer, *Cancer Sci.* 97 (8) (2006) 689–696, <https://doi.org/10.1111/j.1349-7006.2006.00234.x>.
- [257] S.S. Dhadwar, J. Kiernan, J. Wen, G. Hortelano, Repeated oral administration of chitosan/DNA nanoparticles delivers functional FVIII with the absence of antibodies in hemophilia A mice, *J. Thrombosis Haemostasis* 8 (2010) 2743–2750, <https://doi.org/10.1111/j.1538-7836.2010.04116.x>.
- [258] C.E. Thomas, A. Ehrhardt, M.A. Kay, Progress and problems with the use of viral vectors for gene therapy, *Nat. Rev. Genet.* 4 (5) (2003) 346–358, <https://doi.org/10.1038/nrg1066>.
- [259] M. Ramamoorthi, A. Narvekar, Non viral vectors in gene therapy- an overview, *J. Clin. Diagn. Res.* 9 (2015) GE01–GE06, <https://doi.org/10.7860/JCDR/2015/10443.5394>.
- [260] S. Keskin, S. Kızılel, Biomedical applications of metal organic frameworks, *Ind. Eng. Chem. Res.* 50 (4) (2011) 1799–1812, <https://doi.org/10.1021/ie101312k>.
- [261] S.K. Alsaiani, S. Patil, M. Alyami, K.O. Alamoudi, F.A. Aleisa, J.S. Merzaban, M. Li, N.M. Khashab, Endosomal escape and delivery of CRISPR/Cas9 genome editing machinery enabled by nanoscale zeolitic imidazolate framework, *J. Am. Chem. Soc.* 140 (1) (2018) 143–146, <https://doi.org/10.1021/jacs.7b11754>.
- [262] C. He, K. Lu, D. Liu, W. Lin, Nanoscale metal–organic frameworks for the co-delivery of cisplatin and pooled siRNAs to enhance therapeutic efficacy in drug-resistant ovarian cancer cells, *J. Am. Chem. Soc.* 136 (14) (2014) 5181–5184, <https://doi.org/10.1021/ja4098862>.
- [263] W. Morris, W.E. Briley, E. Auyeung, M.D. Cabezas, C.A. Mirkin, Nucleic acid-metal organic framework (MOF) nanoparticle conjugates, *J. Am. Chem. Soc.* 136 (20) (2014) 7261–7264, <https://doi.org/10.1021/ja503215w>.
- [264] L. Cong, F.A. Ran, D. Cox, S. Lin, R. Barretto, N. Habib, P.D. Hsu, X. Wu, W. Jiang, L.A. Marraffini, F. Zhang, Multiplex genome engineering using CRISPR/Cas systems, *Science* 339 (6121) (2013) 819–823, <https://doi.org/10.1126/science.1231143>.
- [265] M.Z. Alyami, S.K. Alsaiani, Y. Li, S.S. Qutub, F.A. Aleisa, R. Sougrat, J.S. Merzaban, N.M. Khashab, Cell-type-specific CRISPR/Cas9 delivery by biomimetic metal organic frameworks, *J. Am. Chem. Soc.* 142 (4) (2020) 1715–1720, <https://doi.org/10.1021/jacs.9b11638>.
- [266] T. Hidalgo, M. Alonso-Nocelo, B.L. Bouzo, S. Reimondez-Troitiño, C. Abuin-Redondo, M. de la Fuente, P. Horcajada, Biocompatible iron(III) carboxylate metal–organic frameworks as promising RNA nanocarriers, *Nanoscale* 12 (2020) 4839–4845, <https://doi.org/10.1039/C9NR08127E>.
- [267] S. Peng, B. Bie, Y. Sun, M. Liu, H. Cong, W. Zhou, Y. Xia, H. Tang, H. Deng, X. Zhou, Metal-organic frameworks for precise inclusion of single-stranded DNA and transfection in immune cells, *Nat. Commun.* 9 (1) (2018), <https://doi.org/10.1038/s41467-018-03650-w>.
- [268] A. Poddar, J.J. Conesa, K. Liang, S. Dhakal, P. Reineck, G. Bryant, E. Pereiro, R. Ricco, H. Amenitsch, C. Doonan, X. Mulet, C.M. Doherty, P. Falcaro, R. Shukla, Encapsulation, visualization and expression of genes with biomimetically mineralized zeolitic imidazolate framework-8 (ZIF-8), *Small* 15 (36) (2019) 1902268, <https://doi.org/10.1002/sml.201902268>.
- [269] Y. Li, K. Zhang, P. Liu, M. Chen, Y. Zhong, Q. Ye, M.Q. Wei, H. Zhao, Z. Tang, Encapsulation of plasmid DNA by nanoscale metal–organic frameworks for efficient gene transportation and expression, *Adv. Mater.* 31 (29) (2019) 1901570, <https://doi.org/10.1002/adma.201901570>.

- [270] H. Wang, Y. Chen, H. Wang, X. Liu, X. Zhou, F. Wang, DNAzyme-loaded metal-organic frameworks (MOFs) for self-sufficient gene therapy, *Angew. Chem. Int. Ed.* 58 (22) (2019) 7380–7384, <https://doi.org/10.1002/anie.201902714>.
- [271] A. Blaeser, D.F. Duarte Campos, U. Puster, W. Richtering, M.M. Stevens, H. Fischer, Controlling shear stress in 3D bioprinting is a key factor to balance printing resolution and stem cell integrity, *Adv. Healthcare Mater.* 5 (3) (2016) 326–333, <https://doi.org/10.1002/adhm.201500677>.
- [272] S.V. Murphy, A. Atala, 3D bioprinting of tissues and organs, *Nat. Biotechnol.* 32 (8) (2014) 773–785, <https://doi.org/10.1038/nbt.2958>.
- [273] A. Matsuzawa, M. Matsusaki, M. Akashi, Effectiveness of nanometer-sized extracellular matrix layer-by-layer assembled films for a cell membrane coating protecting cells from physical stress, *Langmuir* 29 (24) (2013) 7362–7368, <https://doi.org/10.1021/la303459v>.
- [274] M.J. Levesque, E.A. Sprague, C.J. Schwartz, R.M. Nerem, The influence of shear stress on cultured vascular endothelial cells: the stress response of an anchorage-dependent Mammalian cell, *Biotechnol. Progress* 5 (1) (1989) 1–8, <https://doi.org/10.1002/btpr.5420050105>.
- [275] J.H. Park, D. Hong, J. Lee, I.S. Choi, Cell-in-shell hybrids: chemical nanoencapsulation of individual cells, *Acc. Chem. Res.* 49 (5) (2016) 792–800, <https://doi.org/10.1021/acs.accounts.6b00087>.
- [276] B.J. Kim, H. Cho, J.H. Park, J.F. Mano, I.S. Choi, Strategic advances in formation of cell-in-shell structures: from syntheses to applications, *Adv. Mater.* 30 (14) (2018) 1706063, <https://doi.org/10.1002/adma.201706063>.
- [277] J.H. Park, S.H. Yang, J. Lee, E.H. Ko, D. Hong, I.S. Choi, Nanocoating of single cells: from maintenance of cell viability to manipulation of cellular activities, *Adv. Mater.* 26 (13) (2014) 2001–2010.
- [278] W. Li, Y. Zhang, Z. Xu, Q. Meng, Z. Fan, S. Ye, G. Zhang, Assembly of MOF microcapsules with size-selective permeability on cell walls, *Angew. Chem. Int. Ed.* 55 (3) (2016) 955–959, <https://doi.org/10.1002/anie.201508795>.
- [279] W. Zhu, J. Guo, S. Amini, Y. Ju, J.O. Agola, A. Zimpel, J. Shang, A. Noureddine, F. Caruso, S. Wuttke, J.G. Croissant, C.J. Brinker, SupraCells: living mammalian cells protected within functional modular nanoparticle-based exoskeletons, *Adv. Mater.* 31 (25) (2019) 1900545, <https://doi.org/10.1002/adma.201900545>.
- [280] J.M. Hamilton-Miller, *Chemistry and biology of the polyene macrolide antibiotics*, *Bacteriol. Rev.* 37 (1973) 166–196.
- [281] K. Liang, J.J. Richardson, C.J. Doonan, X. Mulet, Y. Ju, J. Cui, F. Caruso, P. Falcaro, An enzyme-coated metal-organic framework shell for synthetically adaptive cell survival, *Angew. Chem. Int. Ed.* 56 (29) (2017) 8510–8515, <https://doi.org/10.1002/anie.201704120>.
- [282] S. Qiu, Y.-J. Wang, H. Yu, F. Cheng, Y.-G. Zheng, t-Butyl 6-cyano-(3R,5R)-dihydroxyhexanoate synthesis via asymmetric reduction by immobilized cells of carbonyl reductase and glucose dehydrogenase co-expression *E. coli*, *Process Biochem.* 80 (2019) 43–51, <https://doi.org/10.1016/j.procbio.2019.02.019>.
- [283] S. Yan, X. Zeng, Y. Wang, B. Liu, Biomining of bacteria by a metal-organic framework for therapeutic delivery, *Adv. Healthcare Mater.* 9 (12) (2020) 2000046, <https://doi.org/10.1002/adhm.202000046>.
- [284] F. Gándara, F.J. Uribe-Romo, D.K. Britt, H. Furukawa, L. Lei, R. Cheng, X. Duan, M. O’Keeffe, O.M. Yaghi, Porous, conductive metal-triazolates and their structural elucidation by the charge-flipping method, *Chem. Eur. J.* 18 (34) (2012) 10595–10601, <https://doi.org/10.1002/chem.201103433>.
- [285] J. Rosário, L.L. da Luz, R. Geris, J.G.S. Ramalho, A.F. da Silva, S.A. Júnior, M. Malta, Photoluminescent organisms: how to make fungi glow through biointegration with lanthanide metal-organic frameworks, *Sci. Rep.* 9 (1) (2019), <https://doi.org/10.1038/s41598-019-43835-x>.
- [286] Z. Ji, H. Zhang, H. Liu, O.M. Yaghi, P. Yang, Cytoprotective metal-organic frameworks for anaerobic bacteria, *PNAS* 115 (42) (2018) 10582–10587, <https://doi.org/10.1073/pnas.1808829115>.
- [287] J.H. Park, K. Kim, J. Lee, J.Y. Choi, D. Hong, S.H. Yang, F. Caruso, Y. Lee, I.S. Choi, A cytoprotective and degradable metal-polyphenol nanoshell for single-cell encapsulation, *Angew. Chem. Int. Ed.* 126 (2014) 12628–12633, <https://doi.org/10.1002/anie.201405905>.
- [288] J. Lee, H. Cho, J. Choi, D. Kim, D. Hong, J.H. Park, S.H. Yang, I.S. Choi, Chemical sporulation and germination: cytoprotective nanocoating of individual mammalian cells with a degradable tannic acid-Fe^{III} complex, *Nanoscale* 7 (45) (2015) 18918–18922, <https://doi.org/10.1039/C5NR05573C>.
- [289] B.J. Kim, S. Han, K.-B. Lee, I.S. Choi, Biphasic supramolecular self-assembly of ferric ions and tannic acid across interfaces for nanofilm formation, *Adv. Mater.* 29 (28) (2017) 1700784, <https://doi.org/10.1002/adma.201700784>.
- [290] T. Park, J.Y. Kim, H. Cho, H.C. Moon, B.J. Kim, J.H. Park, D. Hong, J. Park, I.S. Choi, Artificial spores: immunoprotective nanocoating of red blood cells with supramolecular ferric ion-tannic acid complex, *Polymers* 9 (2017) 140, <https://doi.org/10.3390/polym9040140>.
- [291] S.R. Batten, N.R. Champness, X.-M. Chen, J. Garcia-Martinez, S. Kitagawa, L. Öhrström, M. O’Keeffe, M.P. Suh, J. Reedik, Coordination polymers, metal-organic frameworks and the need for terminology guidelines, *CrystEngComm* 14 (9) (2012) 3001, <https://doi.org/10.1039/c2ce06488j>.
- [292] S. Li, M. Dharmawardana, R.P. Welch, Y. Ren, C.M. Thompson, R.A. Smaldone, J.J. Gassensmith, Template-directed synthesis of porous and protective core-shell bionanoparticles, *Angew. Chem. Int. Ed.* 55 (36) (2016) 10691–10696, <https://doi.org/10.1002/anie.201604879>.
- [293] J.G. Hinman, J.G. Turner, D.M. Hofmann, C.J. Murphy, Layer-by-layer synthesis of conformal metal-organic framework shells on gold nanorods, *Chem. Mater.* 30 (20) (2018) 7255–7261, <https://doi.org/10.1021/acs.chemmater.8b03341>.
- [294] J.-L. Zhuang, A. Terfort, C. Wöll, Formation of oriented and patterned films of metal-organic frameworks by liquid phase epitaxy: a review, *Coord. Chem. Rev.* 307 (2016) 391–424, <https://doi.org/10.1016/j.ccr.2015.09.013>.
- [295] H. Shrestha, R. Bala, S. Arora, Lipid-based drug delivery systems, *J. Pharm.* 2014 (2014) 1–10, <https://doi.org/10.1155/2014/801820>.
- [296] S. Wang, W. Morris, Y. Liu, C.M. McGuirk, Y. Zhou, J.T. Hupp, O.K. Farha, C.A. Mirkin, Surface-specific functionalization of nanoscale metal-organic frameworks, *Angew. Chem. Int. Ed.* 54 (49) (2015) 14738–14742, <https://doi.org/10.1002/anie.201506888>.
- [297] B. Illes, P. Hirschele, S. Barnert, V. Cauda, S. Wuttke, H. Engelke, Exosome-coated metal-organic framework nanoparticles: an efficient drug delivery platform, *Chem. Mater.* 29 (19) (2017) 8042–8046, <https://doi.org/10.1021/acs.chemmater.7b02358>.
- [298] B. Illes, S. Wuttke, H. Engelke, Liposome-coated iron fumarate metal-organic framework nanoparticles for combination therapy, *Nanomaterials (Basel)* 7 (2017), <https://doi.org/10.3390/nano7110351>.
- [299] G. van Niel, G. D’Angelo, G. Raposo, Shedding light on the cell biology of extracellular vesicles, *Nat. Rev. Mol. Cell Biol.* 19 (4) (2018) 213–228, <https://doi.org/10.1038/nrm.2017.125>.
- [300] W. Zhu, G. Xiang, J. Shang, J. Guo, B. Motevalli, P. Durfee, J.O. Agola, E.N. Coker, C.J. Brinker, Versatile Surface functionalization of metal-organic frameworks through direct metal coordination with a phenolic lipid enables diverse applications, *Adv. Funct. Mater.* 28 (16) (2018) 1705274, <https://doi.org/10.1002/adfm.201705274>.
- [301] J. Yang, X. Chen, Y. Li, Q. Zhuang, P. Liu, J. Gu, Zr-based MOFs shielded with phospholipid bilayers: improved biostability and cell uptake for biological applications, *Chem. Mater.* 29 (10) (2017) 4580–4589, <https://doi.org/10.1021/acs.chemmater.7b01329>.
- [302] S.L. Anderson, K.C. Stylianou, Biologically derived metal organic frameworks, *Coord. Chem. Rev.* 349 (2017) 102–128, <https://doi.org/10.1016/j.ccr.2017.07.012>.
- [303] W. Liang, F. Carraro, M.B. Solomon, S.G. Bell, H. Amenitsch, C.J. Sumbly, N.G. White, P. Falcaro, C.J. Doonan, Enzyme encapsulation in a porous hydrogen-bonded organic framework, *J. Am. Chem. Soc.* 141 (36) (2019) 14298–14305, <https://doi.org/10.1021/jacs.9b06589>.

3. Conclusion and Outlook

This doctoral thesis presents the study of encapsulation biomacromolecules (carbohydrates and proteins) within MOFs. After screening several CHs including mono, di, and polysaccharides, it was observed that only CHs decorated with COO^- functional groups afford the encapsulation of carbohydrates within the MOF shell, whereas those functionalized with amino groups are not suitable for the CH@MOF formation. These results were supported by computational simulations, where it was found that coulombic forces between the negatively charged CHs and the zinc cations enhance the Zn^{2+} concentration around the target CHs, which allows for the formation of the MOF around the target CH. By contrast for amino-functionalized dextran depletes the concentration of zinc ions around the biomacromolecules. We demonstrated that the release of FITC-CM-dextran can be triggered by applying external stimuli such as a chelating agent (EDTA) or under acidic conditions (citrate buffer 100 mM, pH 6).

Having known that negatively-charged carbohydrates could enhance the formation of MOFs, we extended our study towards the encapsulation of the commercially important CH-based drugs. To this aim we used a selection of glycosaminoglycans (HA, HP, CS, DS, HepSYL, and GM-1111), to test their encapsulation within three different zinc-based MAFs (ZIF-8, ZIF-90, and MAF-7). The encapsulation efficiency of the resultant biocomposites ranged from 50 to 100%. By selecting the proper ZIF matrix we showed that the release kinetics can be adjusted. Finally, Heparin@ZIFs was selected to assess the biopreservation properties of the porous carriers.

During our investigation of ZIF-based biocomposites, we found that the properties of these biocomposites depend on their crystalline phases. Thus, we explored the synthesis of BSA@MOFs and In@MOFs composites within different MOF phase (MOF= $\text{Zn}(\text{mIM})_2$) by varying systematically the concentration and mass ratio of the precursors (BSA, $\text{Zn}(\text{OAc})_2$, and HmIM) as well as the post-synthetic washing treatments (washes with water or water & ethanol). Four different crystalline phases such as sodalite (*sod*), diamondoid (*dia*), ZIF-C, U13, were observed. The encapsulation efficiency of the resultant biocomposites ranged from 85 to 100% and the release kinetics were ranging from 20 to 300 min depending on the selected phase.

In summary, ZIF-8, ZIF-90, and MAF-7 have emerged as a promising platform for the encapsulation of carbohydrate-based drugs and their subsequent applications as drug delivery systems. For the latter, sustained and targeted delivery of therapeutics could be

improved by tuning the particle size, crystalline phase, and surface chemistry of biocomposites. Moreover, MOF biocomposites were demonstrated unprecedented protection properties and on-demand degradation which could be an attractive alternative strategy for biopreservation applications. Due to a large number of CH-based therapeutics in the market and clinical trial process, extended studies will be necessary for a better understanding of the advantages of these promising biocomposites which could further progress MOF systems towards applications in biotechnology and biomedicine.

4. References

- [1] O. M. Yaghi, M. O’Keeffe, N. W. Ockwig, H. K. Chae, M. Eddaoudi, J. Kim, *Nature* **2003**, *423*, 705–714.
- [2] H. Furukawa, K. E. Cordova, M. O’Keeffe, O. M. Yaghi, *Science* **2013**, *341*, 1230444.
- [3] H.-C. Zhou, J. R. Long, O. M. Yaghi, *Chem. Rev.* **2012**, *112*, 673–674.
- [4] P. Horcajada, R. Gref, T. Baati, P. K. Allan, G. Maurin, P. Couvreur, G. Férey, R. E. Morris, C. Serre, *Chem. Rev.* **2012**, *112*, 1232–1268.
- [5] R. Ricco, C. Pfeiffer, K. Sumida, C. J. Sumby, P. Falcaro, S. Furukawa, N. R. Champness, C. J. Doonan, *CrystEngComm* **2016**, *18*, 6532–6542.
- [6] S. E. Miller, M. H. Teplensky, P. Z. Moghadam, D. Fairen-Jimenez, *Interface Focus*. **2016**, *6*, 20160027.
- [7] H.-S. Wang, *Coordination Chemistry Reviews* **2017**, *349*, 139–155.
- [8] M. Bilal, M. Adeel, T. Rasheed, H. M. N. Iqbal, *Journal of Materials Research and Technology* **2019**, *8*, 2359–2371.
- [9] J. Huo, J. Aguilera-Sigalat, S. El-Hankari, D. Bradshaw, *Chem. Sci.* **2015**, *6*, 1938–1943.
- [10] K. Liang, R. Ricco, C. M. Doherty, M. J. Styles, S. Bell, N. Kirby, S. Mudie, D. Haylock, A. J. Hill, C. J. Doonan, P. Falcaro, *Nat Commun* **2015**, *6*, 7240.
- [11] C. Wang, H. Sun, J. Luan, Q. Jiang, S. Tadepalli, J. J. Morrissey, E. D. Kharasch, S. Singamaneni, *Chem. Mater.* **2018**, *30*, 1291–1300.
- [12] S. Li, M. Dharmawardana, R. P. Welch, Y. Ren, C. M. Thompson, R. A. Smaldone, J. J. Gassensmith, *Angew. Chem. Int. Ed.* **2016**, *55*, 10691–10696.
- [13] M. A. Luzuriaga, R. P. Welch, M. Dharmawardana, C. E. Benjamin, S. Li, A. Shahrivarkevishahi, S. Popal, L. H. Tuong, C. T. Creswell, J. J. Gassensmith, *ACS Appl. Mater. Interfaces* **2019**, *11*, 9740–9746.
- [14] P. Horcajada, C. Serre, M. Vallet-Regí, M. Sebban, F. Taulelle, G. Férey, *Angew. Chem. Int. Ed.* **2006**, *45*, 5974–5978.
- [15] F. Lyu, Y. Zhang, R. N. Zare, J. Ge, Z. Liu, *Nano Lett.* **2014**, *14*, 5761–5765.
- [16] F.-K. Shieh, S.-C. Wang, C.-I. Yen, C.-C. Wu, S. Dutta, L.-Y. Chou, J. V. Morabito, P. Hu, M.-H. Hsu, K. C.-W. Wu, C.-K. Tsung, *J. Am. Chem. Soc.* **2015**, *137*, 4276–4279.
- [17] S. K. Alsaiani, S. Patil, M. Alyami, K. O. Alamoudi, F. A. Aleisa, J. S. Merzaban, M. Li, N. M. Khashab, *J. Am. Chem. Soc.* **2018**, *140*, 143–146.
- [18] A. Poddar, J. J. Conesa, K. Liang, S. Dhakal, P. Reineck, G. Bryant, E. Pereiro, R. Ricco, H. Amenitsch, C. Doonan, X. Mulet, C. M. Doherty, P. Falcaro, R. Shukla, *Small* **2019**, *15*, 1902268.
- [19] S. Li, M. Dharmawardana, R. P. Welch, C. E. Benjamin, A. M. Shamir, S. O. Nielsen, J. J. Gassensmith, *ACS Appl. Mater. Interfaces* **2018**, *10*, 18161–18169.
- [20] R. Riccò, W. Liang, S. Li, J. J. Gassensmith, F. Caruso, C. Doonan, P. Falcaro, *ACS Nano* **2018**, *12*, 13–23.
- [21] S. Li, X. Zhou, Z. Chen, F. C. Herbert, R. Jayawickramage, S. D. Panangala, M. A. Luzuriaga, S. B. Alahakoon, S. D. Diwakara, X. Meng, L. Fei, J. Ferraris, R. A. Smaldone, J. J. Gassensmith, *ACS Appl. Mater. Interfaces* **2020**, *12*, 11884–11889.
- [22] K. Liang, J. J. Richardson, J. Cui, F. Caruso, C. J. Doonan, P. Falcaro, *Adv. Mater.* **2016**, *28*, 7910–7914.
- [23] C. Doonan, R. Riccò, K. Liang, D. Bradshaw, P. Falcaro, *Acc. Chem. Res.* **2017**, *50*, 1423–1432.
- [24] F. Carraro, M. de J. Velásquez-Hernández, M. Linares-Moreau, E. Astria, C. J. Sumby, C. J. Doonan, P. Falcaro, in *Metal-Organic Frameworks in Biomedical and Environmental Field*, Springer International Publishing, Switzerland, **In Press**.
- [25] M. de J. Velásquez-Hernández, M. Linares-Moreau, E. Astria, F. Carraro, M. Z. Alyami, N. M. Khashab, C. J. Sumby, C. J. Doonan, P. Falcaro, *Coordination Chemistry Reviews* **2020**, 213651.

- [26] M. de J. Velásquez-Hernández, R. Ricco, F. Carraro, F. T. Limpoco, M. Linares-Moreau, E. Leitner, H. Wiltsche, J. Rattenberger, H. Schröttner, P. Frühwirt, E. M. Stadler, G. Gescheidt, H. Amenitsch, C. J. Doonan, P. Falcaro, *CrystEngComm* **2019**, *21*, 4538–4544.
- [27] X. Yang, Q. Tang, Y. Jiang, M. Zhang, M. Wang, L. Mao, *J. Am. Chem. Soc.* **2019**, *141*, 3782–3786.
- [28] W. Cai, J. Wang, C. Chu, W. Chen, C. Wu, G. Liu, *Adv. Sci.* **2019**, *6*, 1801526.
- [29] P. Horcajada, T. Chalati, C. Serre, B. Gillet, C. Sebrie, T. Baati, J. F. Eubank, D. Heurtaux, P. Clayette, C. Kreuz, J.-S. Chang, Y. K. Hwang, V. Marsaud, P.-N. Bories, L. Cynober, S. Gil, G. Férey, P. Couvreur, R. Gref, *Nature Mater* **2010**, *9*, 172–178.
- [30] R. P. Welch, H. Lee, M. A. Luzuriaga, O. R. Brohlin, J. J. Gassensmith, *Bioconjugate Chem.* **2018**, *29*, 2867–2883.
- [31] J. Qiu, X. Li, R. Gref, A. Vargas-Berenguel, in *Metal-Organic Frameworks for Biomedical Applications*, Elsevier, **2020**, pp. 445–465.
- [32] S. Mishra, K. Upadhaya, K. B. Mishra, A. K. Shukla, R. P. Tripathi, V. K. Tiwari, in *Studies in Natural Products Chemistry*, Elsevier, **2016**, pp. 307–361.
- [33] H. M. I. Osborn, P. G. Evans, N. Gemmell, S. D. Osborne, *Journal of Pharmacy and Pharmacology* **2004**, *56*, 691–702.
- [34] S. B. Oppenheimer, M. Alvarez, J. Nnoli, *Acta Histochemica* **2008**, *110*, 6–13.
- [35] M. von Itzstein, in *Chembiomolecular Science* (Eds.: M. Shibasaki, M. Iino, H. Osada), Springer Japan, Tokyo, **2012**, pp. 261–267.
- [36] J.-P. Zhang, Y.-B. Zhang, J.-B. Lin, X.-M. Chen, *Chem. Rev.* **2012**, *112*, 1001–1033.
- [37] P.-Q. Liao, C.-T. He, D.-D. Zhou, J.-P. Zhang, X.-M. Chen, in *The Chemistry of Metal-Organic Frameworks: Synthesis, Characterization, and Applications* (Ed.: S. Kaskel), Wiley-VCH Verlag GmbH & Co. KGaA, Weinheim, Germany, **2016**, pp. 309–343.
- [38] A. Phan, C. J. Doonan, F. J. Uribe-Romo, C. B. Knobler, M. O’Keeffe, O. M. Yaghi, *Acc. Chem. Res.* **2010**, *43*, 58–67.
- [39] B. Chen, Z. Yang, Y. Zhu, Y. Xia, *J. Mater. Chem. A* **2014**, *2*, 16811–16831.
- [40] C.-Y. Sun, C. Qin, X.-L. Wang, G.-S. Yang, K.-Z. Shao, Y.-Q. Lan, Z.-M. Su, P. Huang, C.-G. Wang, E.-B. Wang, *Dalton Trans.* **2012**, *41*, 6906.
- [41] K. Kida, M. Okita, K. Fujita, S. Tanaka, Y. Miyake, *CrystEngComm* **2013**, *15*, 1794.
- [42] P. Horcajada, C. Serre, A. C. McKinlay, R. E. Morris, in *Metal-Organic Frameworks* (Ed.: D. Farrusseng), Wiley-VCH Verlag GmbH & Co. KGaA, Weinheim, Germany, **2011**, pp. 213–250.
- [43] S. Rojas, A. Arenas-Vivo, P. Horcajada, *Coordination Chemistry Reviews* **2019**, *388*, 202–226.
- [44] M. Hoop, C. F. Walde, R. Riccò, F. Mushtaq, A. Terzopoulou, X.-Z. Chen, A. J. deMello, C. J. Doonan, P. Falcaro, B. J. Nelson, J. Puigmartí-Luis, S. Pané, *Applied Materials Today* **2018**, *11*, 13–21.
- [45] K. S. Park, Z. Ni, A. P. Cote, J. Y. Choi, R. Huang, F. J. Uribe-Romo, H. K. Chae, M. O’Keeffe, O. M. Yaghi, *Proceedings of the National Academy of Sciences* **2006**, *103*, 10186–10191.
- [46] J.-P. Zhang, A.-X. Zhu, R.-B. Lin, X.-L. Qi, X.-M. Chen, *Adv. Mater.* **2011**, *23*, 1268–1271.
- [47] A. U. Ortiz, A. P. Freitas, A. Boutin, A. H. Fuchs, F.-X. Coudert, *Phys. Chem. Chem. Phys.* **2014**, *16*, 9940–9949.
- [48] H. Gao, W. Wei, L. Dong, G. Feng, X. Jiang, R. Wu, Z. Lin, W. Li, *Crystals* **2017**, *7*, 99.
- [49] S. Van Cleuvenbergen, Z. J. Smith, O. Deschaume, C. Bartic, S. Wachsmann-Hogiu, T. Verbiest, M. A. van der Veen, *Nat Commun* **2018**, *9*, 3418.
- [50] W. Morris, C. J. Doonan, H. Furukawa, R. Banerjee, O. M. Yaghi, *J. Am. Chem. Soc.* **2008**, *130*, 12626–12627.
- [51] L. Xie, M. Xu, X. Liu, M. Zhao, J. Li, *Adv. Sci.* **2020**, *7*, 1901758.
- [52] M. Rabe, D. Verdes, S. Seeger, *Advances in Colloid and Interface Science* **2011**, *162*, 87–106.
- [53] M. Hoarau, S. Badieyan, E. N. G. Marsh, *Org. Biomol. Chem.* **2017**, *15*, 9539–9551.

- [54] W. Liang, H. Xu, F. Carraro, N. K. Maddigan, Q. Li, S. G. Bell, D. M. Huang, A. Tarzia, M. B. Solomon, H. Amenitsch, L. Vaccari, C. J. Sumby, P. Falcaro, C. J. Doonan, *J. Am. Chem. Soc.* **2019**, *141*, 2348–2355.
- [55] G. T. Hermanson, in *Bioconjugate Techniques*, Elsevier, **2013**, pp. 259–273.
- [56] S. S. Wong, D. M. Jameson, *Chemistry of Protein and Nucleic Acid Cross-Linking and Conjugation*, CRC Press, **2011**.
- [57] B. Sung, M.-H. Kim, *Handbook of Intelligent Scaffolds for Tissue Engineering and Regenerative Medicine, Second Edition*, Pan Stanford, **2017**.
- [58] K. J. Stine, Ed., *Carbohydrate Nanotechnology: Stine/Carbohydrate Nanotechnology*, John Wiley & Sons, Inc, Hoboken, NJ, **2015**.
- [59] A. Abednejad, A. Ghaee, J. Nourmohammadi, A. A. Mehrizi, *Carbohydrate Polymers* **2019**, *222*, 115033.
- [60] X. Lian, Y. Fang, E. Joseph, Q. Wang, J. Li, S. Banerjee, C. Lollar, X. Wang, H.-C. Zhou, *Chem. Soc. Rev.* **2017**, *46*, 3386–3401.
- [61] N. Nakajima, Y. Ikada, *Bioconjugate Chem.* **1995**, *6*, 123–130.
- [62] P. Ling, J. Lei, L. Zhang, H. Ju, *Anal. Chem.* **2015**, *87*, 3957–3963.
- [63] Y.-H. Shih, S.-H. Lo, N.-S. Yang, B. Singco, Y.-J. Cheng, C.-Y. Wu, I.-H. Chang, H.-Y. Huang, C.-H. Lin, *ChemPlusChem* **2012**, *77*, 982–986.
- [64] C. M. Doherty, G. Greci, R. Riccò, J. I. Mardel, J. Reboul, S. Furukawa, S. Kitagawa, A. J. Hill, P. Falcaro, *Adv. Mater.* **2013**, *25*, 4701–4705.
- [65] S.-L. Cao, D.-M. Yue, X.-H. Li, T. J. Smith, N. Li, M.-H. Zong, H. Wu, Y.-Z. Ma, W.-Y. Lou, *ACS Sustainable Chem. Eng.* **2016**, *4*, 3586–3595.
- [66] Y. Sun, L. Zheng, Y. Yang, X. Qian, T. Fu, X. Li, Z. Yang, H. Yan, C. Cui, W. Tan, *Nano-Micro Lett.* **2020**, *12*, 103.
- [67] S. Wuttke, S. Braig, T. Preiß, A. Zimpel, J. Sicklinger, C. Bellomo, J. O. Rädler, A. M. Vollmar, T. Bein, *Chem. Commun.* **2015**, *51*, 15752–15755.
- [68] C. He, K. Lu, D. Liu, W. Lin, *J. Am. Chem. Soc.* **2014**, *136*, 5181–5184.
- [69] X. Qi, Z. Chang, D. Zhang, K. J. Binder, S. Shen, Y. Y. S. Huang, Y. Bai, A. E. H. Wheatley, H. Liu, *Chem. Mater.* **2017**, *29*, 8052–8056.
- [70] B. Illes, P. Hirschle, S. Barnert, V. Cauda, S. Wuttke, H. Engelke, *Chem. Mater.* **2017**, *29*, 8042–8046.
- [71] J. Navarro, N. Almora Barrios, B. Lerma Berlanga, J. J. Ruiz-Pernía, V. A. Lorenz Fonfria, I. Tuñón, C. Martí-Gastaldo, *Chem. Sci.* **2019**, *10*.1039.C9SC00082H.
- [72] W. Chen, S. Kong, M. Lu, F. Chen, W. Cai, L. Du, J. Wang, C. Wu, *Soft Matter* **2020**, *16*, 270–275.
- [73] E. Astria, M. Thonhofer, R. Ricco, W. Liang, A. Chemelli, A. Tarzia, K. Alt, C. E. Hagemeyer, J. Rattenberger, H. Schroettner, T. Wrodnigg, H. Amenitsch, D. M. Huang, C. J. Doonan, P. Falcaro, *Mater. Horiz.* **2019**, *6*, 969–977.
- [74] M. de J. Velásquez-Hernández, E. Astria, S. Winkler, W. Liang, H. Wiltsche, A. Poddar, R. Shukla, G. Prestwich, J. Paderi, P. Salcedo-Abraira, H. Amenitsch, P. Horcajada, C. J. Doonan, P. Falcaro, *Chem. Sci.* **2020**, *11*, 10835–10843.
- [75] S. Zhang, Q. Deng, Y. Li, M. Zheng, C. Wan, C. Zheng, H. Tang, F. Huang, J. Shi, *R. Soc. open sci.* **2018**, *5*, 172368.
- [76] K. M. Koczkur, S. Mourdikoudis, L. Polavarapu, S. E. Skrabalak, *Dalton Trans.* **2015**, *44*, 17883–17905.
- [77] A. Abedini, E. Saion, F. Larki, A. Zakaria, M. Noroozi, N. Soltani, *IJMS* **2012**, *13*, 11941–11953.
- [78] T.-T. Chen, J.-T. Yi, Y.-Y. Zhao, X. Chu, *J. Am. Chem. Soc.* **2018**, *140*, 9912–9920.
- [79] X. Pei, Y. Wu, J. Wang, Z. Chen, W. Liu, W. Su, F. Liu, *Nanoscale* **2020**, *12*, 967–972.
- [80] Y. Feng, H. Wang, S. Zhang, Y. Zhao, J. Gao, Y. Zheng, P. Zhao, Z. Zhang, M. J. Zaworotko, P. Cheng, S. Ma, Y. Chen, *Adv. Mater.* **2019**, *31*, 1805148.

- [81] T.-H. Wei, S.-H. Wu, Y.-D. Huang, W.-S. Lo, B. P. Williams, S.-Y. Chen, H.-C. Yang, Y.-S. Hsu, Z.-Y. Lin, X.-H. Chen, P.-E. Kuo, L.-Y. Chou, C.-K. Tsung, F.-K. Shieh, *Nat Commun* **2019**, *10*, 5002.
- [82] N. K. Maddigan, A. Tarzia, D. M. Huang, C. J. Sumbly, S. G. Bell, P. Falcaro, Christian. J. Doonan, *Chem. Sci.* **2018**, *9*, 4217–4223.
- [83] G. Chen, X. Kou, S. Huang, L. Tong, Y. Shen, W. Zhu, F. Zhu, G. Ouyang, *Angew. Chem. Int. Ed.* **2020**, *59*, 2867–2874.
- [84] H. Wang, L. Han, D. Zheng, M. Yang, Y. H. Andaloussi, P. Cheng, Z. Zhang, S. Ma, M. J. Zaworotko, Y. Feng, Y. Chen, *Angew. Chem.* **2020**, *132*, 6322–6326.
- [85] M. Sánchez-Sánchez, N. Getachew, K. Díaz, M. Díaz-García, Y. Chebude, I. Díaz, *Green Chem.* **2015**, *17*, 1500–1509.
- [86] K. Liang, C. J. Coghlan, S. G. Bell, C. Doonan, P. Falcaro, *Chem. Commun.* **2016**, *52*, 473–476.
- [87] K. Liang, J. J. Richardson, C. J. Doonan, X. Mulet, Y. Ju, J. Cui, F. Caruso, P. Falcaro, *Angew. Chem. Int. Ed.* **2017**, *56*, 8510–8515.
- [88] W. Liang, R. Ricco, N. K. Maddigan, R. P. Dickinson, H. Xu, Q. Li, C. J. Sumbly, S. G. Bell, P. Falcaro, C. J. Doonan, *Chem. Mater.* **2018**, *30*, 1069–1077.
- [89] S. Zhang, M. Du, P. Shao, L. Wang, J. Ye, J. Chen, J. Chen, *Environ. Sci. Technol.* **2018**, *52*, 12708–12716.
- [90] X. Wu, H. Yue, Y. Zhang, X. Gao, X. Li, L. Wang, Y. Cao, M. Hou, H. An, L. Zhang, S. Li, J. Ma, H. Lin, Y. Fu, H. Gu, W. Lou, W. Wei, R. N. Zare, J. Ge, *Nat Commun* **2019**, *10*, 5165.
- [91] F. Carraro, M. de J. Velásquez-Hernández, E. Astria, W. Liang, L. Twight, C. Parise, M. Ge, Z. Huang, R. Ricco, X. Zou, L. Villanova, C. O. Kappe, C. Doonan, P. Falcaro, *Chem. Sci.* **2020**, *11*, 3397–3404.
- [92] T. Simon-Yarza, A. Mielcarek, P. Couvreur, C. Serre, *Adv. Mater.* **2018**, *30*, 1707365.
- [93] R. A. Petros, J. M. DeSimone, *Nat Rev Drug Discov* **2010**, *9*, 615–627.
- [94] W. Yu, R. Liu, Y. Zhou, H. Gao, *ACS Cent. Sci.* **2020**, *6*, 100–116.
- [95] J. Rejman, V. Oberle, I. S. Zuhorn, D. Hoekstra, *Biochemical Journal* **2004**, *377*, 159–169.
- [96] H. Hillaireau, P. Couvreur, *Cell. Mol. Life Sci.* **2009**, *66*, 2873–2896.
- [97] X. Liu, Y. Chen, H. Li, N. Huang, Q. Jin, K. Ren, J. Ji, *ACS Nano* **2013**, *7*, 6244–6257.
- [98] S. D. Perrault, C. Walkey, T. Jennings, H. C. Fischer, W. C. W. Chan, *Nano Lett.* **2009**, *9*, 1909–1915.
- [99] G. Kong, R. D. Braun, M. W. Dewhirst, *Cancer Res* **2000**, *60*, 4440–4445.
- [100] S. A. Kulkarni, S.-S. Feng, *Pharm Res* **2013**, *30*, 2512–2522.
- [101] S. Mitragotri, J. Lahann, *Nature Mater* **2009**, *8*, 15–23.
- [102] M. Gaumet, A. Vargas, R. Gurny, F. Delie, *European Journal of Pharmaceutics and Biopharmaceutics* **2008**, *69*, 1–9.
- [103] J. Della Rocca, D. Liu, W. Lin, *Acc. Chem. Res.* **2011**, *44*, 957–968.
- [104] R. S. Kalash, V. K. Lakshmanan, C.-S. Cho, I.-K. Park, in *Biomaterials Nanoarchitectonics*, Elsevier, **2016**, pp. 197–215.
- [105] T. W. Prow, J. E. Grice, L. L. Lin, R. Faye, M. Butler, W. Becker, E. M. T. Wurm, C. Yoong, T. A. Robertson, H. P. Soyer, M. S. Roberts, *Advanced Drug Delivery Reviews* **2011**, *63*, 470–491.
- [106] G. Tiwari, R. Tiwari, S. Bannerjee, L. Bhati, S. Pandey, P. Pandey, B. Sriwastawa, *Int J Pharma Investig* **2012**, *2*, 2.
- [107] M. Singh, A. Chakrapani, D. O’Hagan, *Expert Review of Vaccines* **2007**, *6*, 797–808.
- [108] D. S. Kohane, *Biotechnol. Bioeng.* **2007**, *96*, 203–209.
- [109] X. Li, L. Lachmanski, S. Safi, S. Sene, C. Serre, J. M. Grenèche, J. Zhang, R. Gref, *Sci Rep* **2017**, *7*, 13142.
- [110] X. Feng, Y. Wang, F. Muhammad, F. Sun, Y. Tian, G. Zhu, *Crystal Growth & Design* **2019**, *19*, 889–895.
- [111] S. Bao, X. Cai, Y. Shi, M. Pang, *CrystEngComm* **2017**, *19*, 1875–1878.
- [112] T. E. Webber, S. P. Desai, R. L. Combs, S. Bingham, C. C. Lu, R. L. Penn, *Crystal Growth & Design* **2020**, *20*, 2965–2972.

- [113] F. Carraro, J. D. Williams, M. Linares-Moreau, C. Parise, W. Liang, H. Amenitsch, C. Doonan, C. O. Kappe, P. Falcaro, *Angew. Chem. Int. Ed.* **2020**, *59*, 8123–8127.
- [114] F. Betsou, R. Barnes, T. Burke, D. Coppola, Y. DeSouza, J. Eliason, B. Glazer, D. Horsfall, C. Kleeberger, S. Lehmann, A. Prasad, A. Skubitz, S. Somiari, E. Gunter, [International Society for Biological and Environmental Repositories (ISBER) Working Group on Biospecimen Science], *Cancer Epidemiology Biomarkers & Prevention* **2009**, *18*, 1017–1025.
- [115] D. Kristensen, D. Chen, R. Cummings, *Vaccine* **2011**, *29*, 7122–7124.
- [116] O. Hasturk, D. L. Kaplan, *Acta Biomaterialia* **2019**, *95*, 3–31.
- [117] S. Dutta, J. Kim, P. Hsieh, Y. Hsu, Y. V. Kaneti, F. Shieh, Y. Yamauchi, K. C. -W. Wu, *Small Methods* **2019**, *3*, 1900213.
- [118] M. Jarosz, J. Kapusta-Kołodziej, A. Pawlik, K. Syrek, G. D. Sulka, in *Nanostructures for Drug Delivery*, Elsevier, **2017**, pp. 299–326.
- [119] B. A. Lakshmi, S. Kim, *Materials Science and Engineering: C* **2019**, *105*, 110091.
- [120] D. Puppi, D. Dinucci, C. Bartoli, C. Mota, C. Migone, F. Dini, G. Barsotti, F. Carlucci, F. Chiellini, *Journal of Bioactive and Compatible Polymers* **2011**, *26*, 478–492.
- [121] X. Huang, C. S. Brazel, *Journal of Controlled Release* **2001**, *73*, 121–136.
- [122] B. Leader, Q. J. Baca, D. E. Golan, *Nat Rev Drug Discov* **2008**, *7*, 21–39.
- [123] T. Vermonden, R. Censi, W. E. Hennink, *Chem. Rev.* **2012**, *112*, 2853–2888.
- [124] A. Szlachcic, M. Zakrzewska, J. Otlewski, *Biotechnology Advances* **2011**, *29*, 436–441.
- [125] X.-Y. Lu, D.-C. Wu, Z.-J. Li, G.-Q. Chen, in *Progress in Molecular Biology and Translational Science*, Elsevier, **2011**, pp. 299–323.
- [126] Y. Pathak, D. Thassu, Eds. , *Drug Delivery Nanoparticles Formulation and Characterization*, CRC Press, **2016**.
- [127] S. Mura, J. Nicolas, P. Couvreur, *Nature Mater* **2013**, *12*, 991–1003.
- [128] M. A. Luzuriaga, C. E. Benjamin, M. W. Gaertner, H. Lee, F. C. Herbert, S. Mallick, J. J. Gassensmith, *Supramolecular Chemistry* **2019**, *31*, 485–490.
- [129] A. C. McKinlay, R. E. Morris, P. Horcajada, G. Férey, R. Gref, P. Couvreur, C. Serre, *Angewandte Chemie International Edition* **2010**, *49*, 6260–6266.
- [130] V. Pomin, B. Mulloy, *Pharmaceuticals* **2018**, *11*, 27.
- [131] N. S. Gandhi, R. L. Mancera, *Chemical Biology & Drug Design* **2008**, *72*, 455–482.
- [132] C. Wong, Ed. , *Carbohydrate-Based Drug Discovery*, Wiley, **2003**.
- [133] J. Paderi, G. D. Prestwich, A. Panitch, T. Boone, K. Stuart, *Adv. Therap.* **2018**, *1*, 1800082.
- [134] G. Ruiz-Gómez, S. Vogel, S. Möller, M. T. Pisabarro, U. Hempel, *Sci Rep* **2019**, *9*, 4905.
- [135] U. Aich, M. A. Meledeo, S.-G. Sampathkumar, J. Fu, M. B. Jones, C. A. Weier, S. Y. Chung, B. C. Tang, M. Yang, J. Hanes, K. J. Yarema, *Glycoconj J* **2010**, *27*, 445–459.
- [136] J. Hirsh, S. S. Anand, J. L. Halperin, V. Fuster, *Circulation* **2001**, *103*, 2994–3018.
- [137] H.-Y. Lee, C.-H. Hwang, H.-E. Kim, S.-H. Jeong, *Carbohydrate Polymers* **2018**, *186*, 290–298.
- [138] R. Stern, G. Kogan, M. J. Jedrzejewski, L. Šoltés, *Biotechnology Advances* **2007**, *25*, 537–557.
- [139] S. Jana, S. Maiti, S. Jana, Eds. , *Biopolymer-Based Composites: Drug Delivery and Biomedical Applications*, Elsevier, Woodhead Publishing, Duxford Cambridge, Mass, **2017**.
- [140] A. Abednejad, A. Ghaee, J. Nourmohammadi, A. A. Mehrizi, *Carbohydrate Polymers* **2019**, *222*, 115033.
- [141] V. V. Vinogradov, A. S. Drozdov, L. R. Mingabudinova, E. M. Shabanova, N. O. Kolchina, E. I. Anastasova, A. A. Markova, A. A. Shtil, V. A. Milichko, G. L. Starova, R. L. M. Precker, A. V. Vinogradov, E. Hey-Hawkins, E. A. Pidko, *J. Mater. Chem. B* **2018**, *6*, 2450–2459.
- [142] C.-H. Ng, M. S. H. Guan, C. Koh, X. Ouyang, F. Yu, E.-K. Tan, S. P. O’Neill, X. Zhang, J. Chung, K.-L. Lim, *Journal of Neuroscience* **2012**, *32*, 14311–14317.
- [143] F. Du, Q. Yu, S. Yan, G. Hu, L.-F. Lue, D. G. Walker, L. Wu, S. F. Yan, K. Tieu, S. S. Yan, *Brain* **2017**, *140*, 3233–3251.
- [144] S. Mitragotri, P. A. Burke, R. Langer, *Nat Rev Drug Discov* **2014**, *13*, 655–672.

- [145] L. Zhang, F. Gu, J. Chan, A. Wang, R. Langer, O. Farokhzad, *Clin Pharmacol Ther* **2008**, *83*, 761–769.
- [146] X. Qin, C. Yu, J. Wei, L. Li, C. Zhang, Q. Wu, J. Liu, S. Q. Yao, W. Huang, *Adv. Mater.* **2019**, *31*, 1902791.
- [147] Y. Zhang, F. Wang, E. Ju, Z. Liu, Z. Chen, J. Ren, X. Qu, *Adv. Funct. Mater.* **2016**, *26*, 6454–6461.
- [148] W.-H. Chen, G.-F. Luo, M. Vázquez-González, R. Cazelles, Y. S. Sohn, R. Nechushtai, Y. Mandel, I. Willner, *ACS Nano* **2018**, *12*, 7538–7545.
- [149] M. A. Mohamed, J. Jaafar, A. F. Ismail, M. H. D. Othman, M. A. Rahman, in *Membrane Characterization*, Elsevier, **2017**, pp. 3–29.
- [150] J. S. Gaffney, N. A. Marley, D. E. Jones, in *Characterization of Materials* (Ed.: E.N. Kaufmann), John Wiley & Sons, Inc., Hoboken, NJ, USA, **2012**, p. com107.pub2.
- [151] L. Hanna, J. V. Lockard, *J. Phys.: Condens. Matter* **2019**, *31*, 483001.
- [152] P. W. Atkins, *Physical Chemistry*, Oxford Univ. Press, Oxford, **2001**.
- [153] P. W. Atkins, J. De Paula, *Elements of Physical Chemistry*, Oxford University Press, Oxford, **2013**.
- [154] D. Titus, E. James Jebaseelan Samuel, S. M. Roopan, in *Green Synthesis, Characterization and Applications of Nanoparticles*, Elsevier, **2019**, pp. 303–319.
- [155] Z.-X. Low, J. Yao, Q. Liu, M. He, Z. Wang, A. K. Suresh, J. Bellare, H. Wang, *Crystal Growth & Design* **2014**, *14*, 6589–6598.
- [156] S. Bashir, J. Liu, in *Advanced Nanomaterials and Their Applications in Renewable Energy*, Elsevier, **2015**, pp. 117–180.
- [157] Y. Leng, *Materials Characterization: Introduction to Microscopic and Spectroscopic Methods*, J. Wiley, Singapore ; Hoboken, NJ, **2008**.
- [158] D. Lamba, in *Encyclopedia of Membranes* (Eds.: E. Drioli, L. Giorno), Springer Berlin Heidelberg, Berlin, Heidelberg, **2016**, pp. 2040–2042.
- [159] B. B. He, *Two-Dimensional X-Ray Diffraction*, John Wiley & Sons, Inc., Hoboken, NJ, USA, **2018**.
- [160] W. Zhou, R. Apkarian, Z. L. Wang, D. Joy, in *Scanning Microscopy for Nanotechnology* (Eds.: W. Zhou, Z.L. Wang), Springer New York, New York, NY, **2006**, pp. 1–40.
- [161] R. F. Egerton, *Physical Principles of Electron Microscopy*, Springer US, Boston, MA, **2005**.
- [162] A. R. Clarke, C. N. Eberhardt, *Microscopy Techniques for Materials Science*, CRC Press ; Woodhead Pub., Boca Raton, FL; Cambridge, England, **2002**.
- [163] L. D. S. Yadav, *Organic Spectroscopy*, Springer Netherlands, Dordrecht, **2005**.
- [164] P. J. Worsfold, in *Encyclopedia of Analytical Science*, Elsevier, **2005**, pp. 318–321.
- [165] H.-H. Perkampus, *UV-VIS Spectroscopy and Its Applications*, Springer Berlin Heidelberg, Berlin, Heidelberg, **1992**.
- [166] D. C. Harris, *Quantitative Chemical Analysis*, W.H. Freeman And Co, New York, **2010**.
- [167] M. M. Bradford, *Analytical Biochemistry* **1976**, *72*, 248–254.
- [168] S. J. Compton, C. G. Jones, *Analytical Biochemistry* **1985**, *151*, 369–374.
- [169] S. B. Frazier, K. A. Roodhouse, D. E. Hourcade, L. Zhang, *TOGLYJ* **2008**, *1*, 31–39.
- [170] T. M. C. C. Filisetti-Cozzi, N. C. Carpita, *Analytical Biochemistry* **1991**, *197*, 157–162.
- [171] Q. Bao, Y. Lou, T. Xing, J. Chen, *Inorganic Chemistry Communications* **2013**, *37*, 170–173.
- [172] O. Karagiari, M. B. Lalonde, W. Bury, A. A. Sarjeant, O. K. Farha, J. T. Hupp, *J. Am. Chem. Soc.* **2012**, *134*, 18790–18796.
- [173] M. Jian, B. Liu, R. Liu, J. Qu, H. Wang, X. Zhang, *RSC Adv.* **2015**, *5*, 48433–48441.
- [174] A. D. Katsenis, A. Puškarić, V. Štrukil, C. Mottillo, P. A. Julien, K. Užarević, M.-H. Pham, T.-O. Do, S. A. J. Kimber, P. Lazić, O. Magdysyuk, R. E. Dinnebier, I. Halasz, T. Friščić, *Nat Commun* **2015**, *6*, 6662.
- [175] M. He, J. Yao, Q. Liu, K. Wang, F. Chen, H. Wang, *Microporous and Mesoporous Materials* **2014**, *184*, 55–60.
- [176] Z. Akimbekov, A. D. Katsenis, G. P. Nagabhushana, G. Ayoub, M. Arhangel'skis, A. J. Morris, T. Friščić, A. Navrotsky, *J. Am. Chem. Soc.* **2017**, *139*, 7952–7957.

- [177] R. Chen, J. Yao, Q. Gu, S. Smeets, C. Baerlocher, H. Gu, D. Zhu, W. Morris, O. M. Yaghi, H. Wang, *Chem. Commun.* **2013**, 49, 9500.

5. Appendix

5.1 List of Scientific Publications

1. Astria, E., Thonhofer, M., Ricco, R., Liang, W., Chemelli, A., Tarzia, A., Alt, K., Hagemeyer, C.E., Rattenberger, J., Schroettner, H., Wrodnigg, T., Amenitsch, H., Huang, D.M., Doonan, C.J., Falcaro, P., 2019. Carbohydrates@MOFs. *Mater. Horiz.* 6, 969–977. <https://doi.org/10.1039/C8MH01611A>
2. Carraro, F., Velásquez-Hernández, M. de J., Astria, E., Liang, W., Twight, L., Parise, C., Ge, M., Huang, Z., Ricco, R., Zou, X., Villanova, L., Kappe, C.O., Doonan, C., Falcaro, P., 2020. Phase dependent encapsulation and release profile of ZIF-based biocomposites. *Chem. Sci.* 11, 3397–3404. <https://doi.org/10.1039/C9SC05433B>
3. Velásquez-Hernández, M. de J., Astria, E., Winkler, S., Liang, W., Wiltsche, H., Poddar, A., Shukla, R., Prestwich, G., Paderi, J., Salcedo-Abraira, P., Amenitsch, H., Horcajada, P., Doonan, C.J., Falcaro, P., 2020. Modulation of metal-azolate frameworks for the tunable release of encapsulated glycosaminoglycans. *Chem. Sci.* 11, 10835–10843. <https://doi.org/10.1039/D0SC01204A>
4. Carraro, F., Velásquez-Hernández, M. de J., Linares-Moreau, M., Astria, E., Sumby, C., Doonan, C.J., Falcaro, P., 2020. `MOFs and Biomacromolecules for Biomedical Applications´ in **Horcajada, P., Rojas Macías, S.** (eds.) Metal-Organic Frameworks in Biomedical and Environmental Field. Switzerland: **Springer International Publishing**. In press. doi.10.1007/978-3-030-63380-6
5. Velásquez-Hernández, M. de J., Linares-Moreau, M., Astria, E., Carraro, F., Alyami, M.Z., Khashab, N. M., Sumby, C. J., Doonan, C.J., Falcaro, P., 2020. Toward Applications of Bioentities@MOFs in Biomedicine. *Coordination Chemistry Review*. Accepted 9 October 2020. doi.10.1016/j.ccr.2020.213651

5.2 List of Presentations at Scientific Conferences

- 2019 Poster presentation at EuroMOF 2019, Paris
(<https://euromof2019.sciencesconf.org/resource/page/id/14>)
- 2019 Oral presentation at EuroMOF 2019 Young Investigator Symposium, Paris
(<https://euromof2019.sciencesconf.org/resource/page/id/12>)
- 2019 Poster presentation at Summer School Porous Materials@Work TU Graz
(<https://www.tugraz.at/projekte/pmw/news/>)
- 2019 Oral presentation at 1st PhD Symposium of Porous Materials@Work TU Graz
(<https://www.tugraz.at/projekte/pmw/news/>)
- 2019 Oral Presentation at Doctoral Days Chemistry NAWI Graz (2019)
(<https://www.nawigraz.at/de/neuigkeiten/detail/article/doc-days-chemie-2019/>)

5.3 Fundings and Awards

- 2020 European Research Council (ERC) grant for doctoral program funding
- 2020 CERIC access Travel and expenses reimbursement for short term
visiting research at Elettra synchrotron in Trieste, Italy
- 2019 *Internationale Kommunikation* by Österreichische
Forschungsgemeinschaft (ÖFG) for travel funding to EuroMOF
conference in Paris, France
- 2017-2020 Ernst-Mach grant Asea-Uninet by OeAD GmbH for PhD scholarship